

15th International Conference on Heavy Ion Accelerator Technology

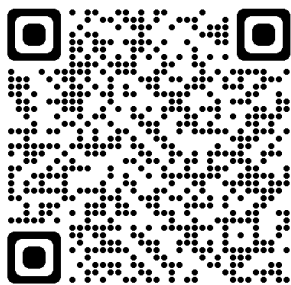
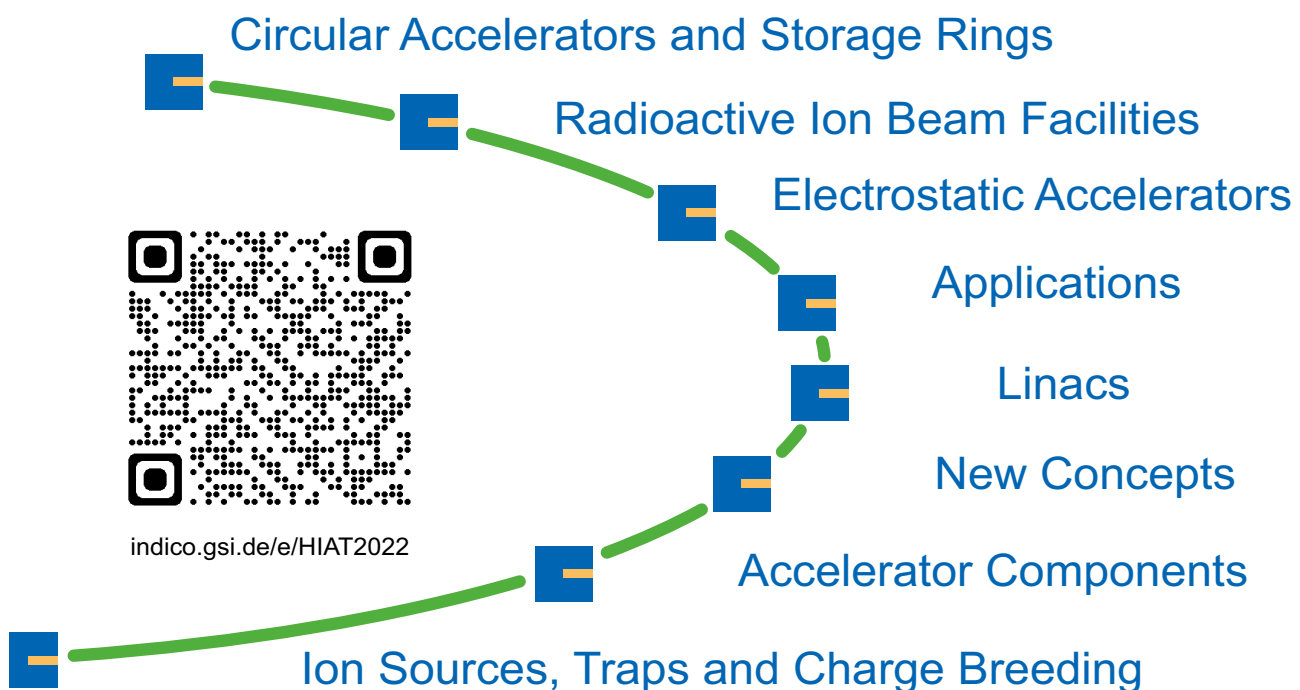
HIAT

2022 | Darmstadt

June 27 - July 1

GERMANY

Proceedings Volume



indico.gsi.de/e/HIAT2022

doi:10.18429/JACoW-HIAT2022



Dear colleague and participant of **HIAT 2022**

GSI/FAIR is honored to host the 15th International Conference on Heavy Ion Accelerator Technology in the Rhine-Main Metropolitan Region, in the City of Darmstadt, Germany. To allow for the original in person conference experience the 15th HIAT has been shifted by one year to 2022. It starts on Monday, 27 June 2022 and will last until Friday, 1 July, 2022.

HIAT 2022 is the 15th in a series of conferences, going back to 1973 in Daresbury and followed by Strasbourg (1977), Oak Ridge (1981), Buenos Aires (1985), Strasbourg-Heidelberg (1989), Legnaro (1992), Canberra (1995), Argonne (1998), Delhi (2002), Brookhaven (2005), Venice (2009), Chicago (2012), Yokohama (2015) and Lanzhou (2018).

HIAT is dedicated to the design, construction, development and operation of heavy-ion accelerators and their components. It focuses on the operational experience of existing facilities, achievements in heavy-ion accelerator physics and technology, progress on the implementation of new projects and infrastructure upgrades, and trends in the proposal, design and application of heavy ion accelerators as well as their main systems and components. Topics for the HIAT 2022 are:

- ◆ Circular Accelerators and Storage Rings
- ◆ Radioactive Ion Beam Facilities and other Facilities
- ◆ Electrostatic Accelerators
- ◆ Applications: Medical, Materials, Isotopes, Space and others
- ◆ Room Temperature and Superconducting Linacs
- ◆ Ion Source, Traps and Charge Breeding
- ◆ Accelerator Systems and Components
- ◆ New Concepts and Applications for Heavy Ion Acceleration

All sessions will be plenary and consist of invited and contributed talks. A poster session, a lab tour of the GSI/FAIR accelerator complex including the FAIR construction site, and an excursion will complete the program. Because of the still or unfortunately again difficult travel situation we also offer an option for remote participation. All together we have yy contributions, xx talks, zz posters and presently 102 participants (13 using the remote option).

A number of industrial partners kindly support this conference. You can meet them on Monday and Tuesday on the conference site and find information about them also in this book of abstracts. Their sponsorship enabled us to support 9 students and 2 post-docs to attend the conference.

On behalf of the local organizing committee I would like to welcome you to Darmstadt after a long time without proper conferences and workshops finally in person. The schedule provides ample time for the missed experience of lively discussions also on topics that only fit coffee breaks and excursions. The lab visit (a bus tour of the FAIR construction site) and excursion (a boat trip on the river rhine including the conference dinner) are combined with an open session at GSI/FAIR in the morning of the conference Wednesday.

I am looking forward to an inspiring and interesting conference HIAT2022!

Frank Herfurth
Chair HIAT2022

International Advisory Committee (IAC)

Giovanni Bisoffi	INFN-LNL, Legnaro
Luigi Celona	INFN-LNS, Catania
Yuan He	IMP-CAS, Lanzhou
Frank Herfurth	GSI/FAIR, Darmstadt
Dinakar Kanjilal	IUAC, New Delhi
Oliver Kester	TRIUMF, Vancouver
Daniela Leitner	LBNL, Berkeley
Nikolai Lobanov	ANU, Canberra
Brahim Mustapha	ANL, Argonne
Francis Osswald	IPHC, Strasbourg
Kimikazu Sasa	University of Tsukuba, Tsukuba
Jie Wei	FRIB, East Lansing

Local Organizing Committee (LOC)

Winfried Barth	GSI	
Larissa Birli	GSI	Secretarist
Wolfgang Geithner	GSI	
Frank Herfurth	GSI	LOC Chair
Ralph Hollinger	GSI	
Paola Lindenberg	GSI	Secretariat
Fabio Maimone	GSI	
Holger Podlech	IAP	
Stephan Reimann	GSI	
Udo Weinrich	GSI	

JACoW Editorial Team (JET)

Christine Petit-Jean-Genaz	CERN	
Raphael Müller	GSI	
Volker RW Schaa	GSI	Editor-in-Chief

Contents

Preface	i
Foreword	iii
Committees	iv
Contents	v
Papers	1
MO1C3 – High Voltage Upgrade of the 14UD Tandem Accelerator	1
MO2C3 – Status and Perspective of Electron Cyclotron Resonance Based Charge Breeders	6
MO3I1 – Developments towards a Compact Carbon Ion Linac for Cancer Therapy	14
MO3C2 – Establishment of the New Particle Therapy Research Center (PARTREC) at UMCG Groningen	20
MO3I3 – Heavy Ion Stripping	24
MO4I2 – Liquid Lithium Charge Stripper Commissioning with Heavy Ion Beams and Early Operations of FRIB Strippers	31
MO4C3 – Development, Fabrication and Testing of the RF-Kicker for the Acculinna-2 Fragment Separator	37
TU1C4 – A 3D Printed IH-Type Linac Structure-Proof-of-Concept for Additive Manufacturing of Linac RF Cavities	41
TU2I2 – Development and Commissioning of the K500 Superconducting Heavy Ion Cyclotron	46
TU2C4 – Beam Tuning Automation Activities at TRIUMF	52
TU3I2 – Beam Instrumentation, Challenging Tools for Demanding Projects — a Snapshot from the French Assigned Network	57
TU3C3 – Preparation of Low-Energy Heavy Ion Beams in a Compact Linear Accelerator/Decelerator	63
TUP03 – Bunch Merging and Compression: Recent Progress with RF and LLRF Systems for FAIR	67
TUP04 – New Method for Overcoming Dipole Effects of 4-Rod RFQs	72
TUP05 – Prototype Room Temperature Quadrupole Chamber with Cryogenic Installations	75
TUP06 – Cryogenic Surfaces in a Room Temperature SIS18 Ioncatcher	79
TUP07 – Efficient Heavy Ion Acceleration with High Brilliance	83
TUP08 – RF Chopper for Prebunched Radioactive Ion Beams	87
TUP09 – Tuning and RF Measurements of the LILAC RFQ	90
TUP10 – High Power Tests of a New 4-Rod RFQ with Focus on Thermal Stability	93
TUP11 – Upgrade and Operation of the ATLAS Radiation Interlock System (ARIS)	96
TUP14 – Study of Injection Line of the Cyclotrons C70XP of Arronax	100
TUP16 – Seven Decades of Science with Accelerators at IPHC	104
TUP17 – Beam Dynamics and Space Charge Studies for the InnoVaTron Cyclotron	108
TUP19 – First Tests of Model-Based Linac Phasing in ISAC-II	113
WE1I3 – FRIB Commissioning	118
WE2I1 – The New GANIL Beams: Commissioning of SPIRAL 2 Accelerator and Recent Developments	124
TH1I2 – Reinforcement Learning and Bayesian Optimization for Ion Linac Operations	130
TH1C3 – Automation of RF and Cryomodule Operation at FRIB	136
TH1C4 – Cavity Designs for the CH3 to CH11 and Bellow Tuner Investigation of the Superconducting Heavy Ion Accelerator HELIAC	140
TH2I2 – Longitudinal Beam Diagnostics R&D at GSI-UNILAC	144
TH2C4 – Signal Estimation and Analyzing of Cold Button BPMs for a Low-Beta Helium/Proton Superconducting Linac	150
TH3I1 – A Novel CW RFQ for Exotic and Stable Beams	156
TH3C2 – Alternating Phase Focusing Based IH DTL for Heavy Ion Application	162
TH3C3 – Recent UNILAC Upgrade Activities	166
TH4C3 – High Intensity Proton Beams at GSI (Heavy Ion) UNILAC	170
FR1C3 – Mode Analysis of Single Spoke Resonator Type-2 (SSR2) for RISP	174
Appendices	179
List of Authors	179
List of Institutes	183
List of Participants	188

HIGH VOLTAGE UPGRADE OF THE 14UD TANDEM ACCELERATOR

T. B. Tunningley, S. T. Battisson, A.C. Cooper, J. Heighway, H. D. Hinde, C. Kafer, T. Kitchen, N.R. Lobanov, P. Linardakis, C. Notthoff†, B. Tranter, D. Tempra, and R. Tranter
Heavy Ion Accelerator Facility, Australian National University, Canberra, ACT, Australia
R.A. Bosch, J.E. Raatz, National Electrostatics Corp. Middleton, WI, USA

Abstract

The 14UD at the Australian National University's Heavy Ion Accelerator Facility (HIAF) operated at a maximum voltage of 15.5 MV after the installation of tubes with a compressed geometry in the 1990s. In recent years, the performance of the accelerator has shown a gradual decline to a maximum operation voltage of ~14.5 MV. There are some fundamental factors that limit the high voltage performance, such as SF₆ gas pressure, field enhancement due to triple junctions and total voltage effect. In addition, there are non-fundamental factors causing high voltage degradation. These are: operation with faulty ceramic gaps; operation at inappropriate voltage and SF₆ pressure combinations; SF₆ leaks into the vacuum space; use of SF₆ and O₂ as a stripper gases; poor electron suppression in the high energy stripper and frequent use of highly reactive ions such as sulphur and fluorine. In 2019 ANU initiated a feasibility study of available options to upgrade the entire population of supporting posts, acceleration tubes and grading resistors. In this paper we will discuss the preferred technologies and strategies for successful implementation of this development. The chosen design is based on NEC tubes with magnetic electron suppression and minimized steering of ion beams.

INTRODUCTION

Accelerator users are most familiar with tubes that are the products of three commercial suppliers: NEC, HVEC and Dowlish. Each manufacturer features a particular type of electron suppression technology.

The original NEC 333 kV tubes were assembled with "dead" sections of the lowest longitudinal field containing a substantial radial component to suppress the multiplication of particles that originated on electrodes. In the later compressed geometry, "dead" sections were removed and in order to restore strong axial field modulation, the electrodes were of variable diameter and dished [1, 2]. In Munich, the 25 mm thick, 25 mm diameter heater plate was replaced by a "zero" length 25 mm diameter electrode resulting in inferior trapping efficiency for ions and electrons originating from the aperture and from ionization of residual gas. To improve the trapping, V-shaped electrodes with angles ranging from 30 up to 50 degrees were successfully introduced to replace the flat electrode.

Still, no suppression existed for gas ionizations near the axis. In the 1990s, the overall length of a single tube increased to allow for operation up to 500 kV. Each section contained 21 live gaps with V-electrodes every 10 or 11

gaps. The trapping efficiency of Vs installed in the middle of tubes was weaker. In later tube designs, the V-electrodes were removed completely and weak magnets added to provide suppression of particles that originated on apertures and in gas [3]. The transverse magnetic field rotates by 90 degrees after every ~7 gaps of the tube.

However, this scheme was not optimum. After the New Delhi machine, NEC changed the tubes to use two pieces per MV, with either 20 or 21 ceramic gaps depending on the accelerator modules. NEC has used 20 and 21 gap tubes with 50 degree cones without external magnets in at least 7 accelerators, including the 20UR at JAEA-Tokai. This solution works even though the lack of suppression may limit heavy-ion beam currents.

At the same time, NEC has used similar tubes with 22 gaps but without cones in tandems up to 6 MV, and they conditioned very well. Again, the lack of suppression may limit heavy-ion beam currents. Based on these results, NEC has made a short-term decision to add weak magnets to the 22 gap tubes for 6 MV systems. In this module, there are 4 apertures per 1 MV, without cones, with 1 aperture in the middle on each 22 gap tube, that is, 11/11. The magnetic field reaches 47 gauss on axis between apertures and falls off near each aperture because the field is rotated 90 degrees from one set of 11 gaps to the next. In the 6 MV case, the modelling shows an average electron energy of only 222 keV and, with just 6 MV of length, an easily correctable net deflection for protons. These new tubes all have one internal 1 inch aperture, so for the modules of the 14UD there would be four 10-gap intervals between apertures per MV. NEC does not use cones in any apertures. These tubes have been used in all "U-series" accelerators since New Delhi and, at least up to 6MV and 8MV, NEC finds them to be well behaved. The U-series use the ceramic posts as in the 14UD, as opposed to smaller S-series, which uses an acrylic column. Magnets are external, hidden in the spark gaps.

The focus of this study is to evaluate suppression efficiency for charged particles originating on axis and on the surfaces of Ti electrodes. Suppression devices should not compromise the transmission of the ion beam, both CW, pulsed, chopped and bounced (AMS) in the full ranges of accelerating voltages from a few MV up to 14.5 MV and mass range from M=1 (protons) up to M=244 (Pu).

The goal of this study to select an appropriate tube technology which will deliver at least the same performance of the 14UD accelerator or exceed it in terms of transmission, e-suppression and improved beam loading. This will be strongly dependent on simulations as the practical confirmation is mainly demonstrated in 6 MV machines, which are much smaller than the 14UD.

† email address: Christian.notthoff@anu.edu.au

METHODS

Experimental Evidence of Secondary Particles Generated Inside Accelerating Tubes

Experience with the 14UD tandem at ANU has shown that the interaction of the heavy ion beam with the residual gas atoms in the tube and bombardment of Ti apertures and electrodes can lead to critical limitations of the transmitted beam intensity due to beam loading and vacuum problems. Five acceleration tubes were replaced with viable used spares during a maintenance period in 2016. Three eleven-gap tubes above the high-energy stripper were removed from unit 19 and two eleven-gap tubes were removed from below the stripper in unit 20. The titanium insert electrodes within the tubes were removed and examined using an optical microscope [4].

SIMION Simulations of e-Suppression, Steering and Effect on Spread of Pulse Width

The model was constructed using a bitmap (created from an Inventor model cross section) to PA conversion in Simion SL Tools. Then it was converted to an axisymmetric array and voltages were assigned at graduations of 30kV giving a range of 0 V-990 kV across the three tubes.

To simulate the electron suppression, two groups of electrons were considered. In the first group, electrons originated on the beam side of the V electrode. The second group comprised of the electrons originated near the axis from interactions with the residual gas.

Being on or near the axis, the blue trajectories are difficult to stop and accelerate up towards the terminal.

Analytical Simulations of the Effect of Magnetic Steering Applied to the Entire LE or HE Sections of the Accelerator

Some limitations of the SIMION package would not allow a model of the full machine. However, a simple analytical model can be derived from the Lorentz equation in order to estimate beam deflection by magnets applied to the entire LE or HE sections of the 14UD. In the case of high gradient tubes with magnets, the typical tube section geometry is divided into 4 segments of length l_1 , l_2 , l_3 and l_4 in which the magnetic field is rotated by 90° from one segment to another. In segment 1, the magnetic field \mathbf{B} is applied towards the reader therefore the beam is deflected and exits this segment at angle θ_1 . In segment 2, the trajectory is nearly a straight line (in reality a parabola) as the ion is still accelerated due to \mathbf{E} but no action from \mathbf{B} in this projection. In segment 3, the ion is bent in the reverse direction as the magnetic field \mathbf{B} is the opposite polarity as compared to segment 1. In segment 4, the ion travels nearly parallel to the axis but at slightly divergent angle as the velocity is higher than in segment 1. Segments 1 to 4 describe the full pattern of motion and then repeats further down in acceleration.

The analytical solution is based on the following assumptions.

1. The magnetic field suddenly changes direction by 90 degrees between sections.
2. The velocity of the particle within the section is assumed to be constant and defined as $\beta = (\beta_{in} + \beta_{out})/2$, where β_{in} is the velocity at the entry point and β_{out} is the exit velocity.
3. The “constant velocity approximation” assumes there is no electric field in sections 1 and 3 so the particle follows a circular path.
4. We assume that the deflection in section 1 is cancelled by the opposite deflection in section 3. The trajectory in section 4 is parallel to the axis.

Because of many assumptions, the analytical model will be validated by comparing with SIMION simulations for a short section of the accelerator. The deflection of particles after passing through the consecutive sections of the tube is given by a set of equations where the index corresponds to the number of segment

$$D_1 \approx 0.16 \times Q l_1^2 B / M \beta_1 \quad (1)$$

$$D_2 \approx l_2 \times \theta_1 = 0.32 \times Q B l_1 l_2 / M \beta_2 \quad (2)$$

$$D_3 \approx 0.16 \times Q l_3^2 B / M \beta_3 \quad (3)$$

$$D_4 \approx 0, \quad (4)$$

where Q is the charge state, M is the atomic mass, $\beta = v/c$ is the particle velocity and c is the velocity of light in a vacuum. The total displacement of a particle after passing all four sections is given by the equation

$$D_{1-4} \approx D_1 + D_2 + D_3 + D_4 \quad (5)$$

Alternative Magnet Positioning and Orientation to Reduce Overall Beam Steering

Alternatively, there is an option where the positioning of magnets is optimised to cancel out any net beam steering. Just to check this concept, this study also explores a configuration “snake”.

RESULTS

Optical Investigation of Ti Electrodes

Figure 1 shows the image of the 1st (A) and 12th (B) Ti electrode removed from tube 1 in unit 19 of HE section.

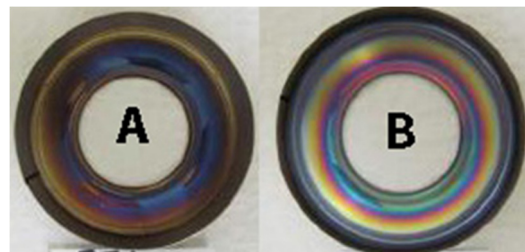


Figure 1: The image of the 1st (A) and 12th (B) Ti electrode removed from tube 1 in unit 19 after ~40 years of operation. Left image (A) is the discoloured electrode surface facing the top of accelerator and (B) is the surface of the 12th tube electrode facing the bottom of accelerator.

SIMION Calculation of Secondary e^- Trajectories

Figure 2 depicts the result of SIMION simulations of the trajectories of secondary electrons in ANU's existing tubes with V electrodes and without magnetic suppression. Blue trajectories were added to simulate electrons liberated from interactions with the residual gas.

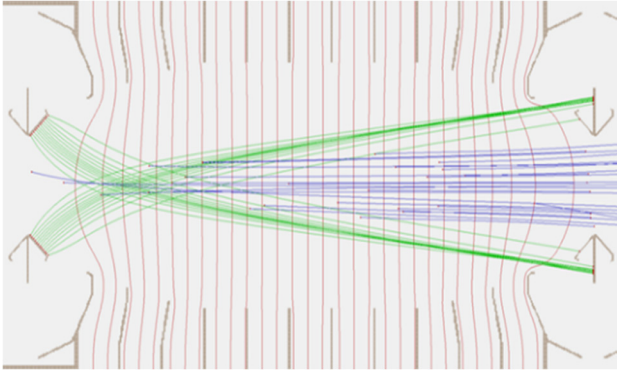


Figure 2: Electrons flying normal from Vee electrode (green) plus beam axis interactions (blue trajectories). No magnetic suppression.

Magnetic Suppression of Electrons Originating from the Aperture and from Ionization of Residual Gas

Table 1 lists the consolidated results of the simulation runs showing the percent of back-streaming electrons originating from the aperture through each section. Each section is 10 gaps defined by a 1" electrode, flat or V style. The higher the percentage, the more electrons through which is considered as negative effect. The magnets create 50 G field rotated by 90 degrees after every 7 gaps indicated as the spiral B field. The tube is the NEC 21 gap assembly.

Figure 3 shows the combined on-axis and aperture electron suppression on the 22-gap tube with both magnets and V electrodes.

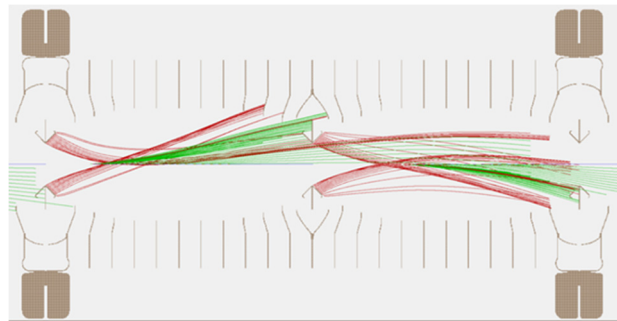


Figure 3: Electron suppression in XZ when both V electrodes and magnets are used.

The average energy at electron impact is 257 keV. For the Vee electrode generated electrons the average energy at impact is 286 keV (321 keV with no magnets).

Table 1: The percent of back-streaming electrons originating from the aperture through each section of a 21 gap high gradient tube.

Aperture	1	2	3	B-field
Flat at tube flange	100	30	0	none
Flat at tube middle	100	100	100	none
Flat with magnets				
XZ flange	0	0	0	spiral
Flat with magnets				
XZ middle	0	0	0	spiral
Flat with magnets				
YZ flange	15	0	0	spiral
Flat with magnets				
YZ middle	0	0	0	spiral
V electrode at tube flange	8	0	0	none
Flat at tube middle	100	100	100	none
V at tube flange	8	0	0	none
V at tube middle	36	9	0	none

Effect on Steering of the Ion Beam and Transmission by SIMION

In this section we will look at what effect the electron suppression magnets have on the beam steering. The tube is a 22 gap system with V electrodes and magnets rotating 90 degrees every 7 gaps. Two beams will be tested with SIMION, Proton (M=1) shown in red and Nickel (M=58) shown in green. The beams have an initial energy of 150keV and measurements are taken between magnet polarity changes. The gradient is 25kV per gap (1.97 MV/m). The overall effect is the beam steering off-axis as shown in Fig. 4.

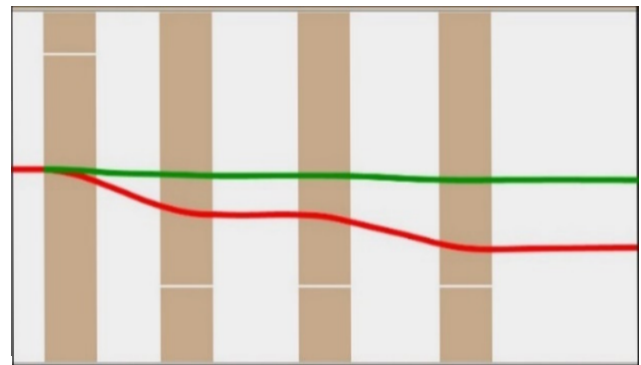


Figure 4: H^{-1} (red) and Ni^{-1} (green) beams in XZ plane stretched in the vertical axis to amplify trajectories. Each section (brown then white) indicates seven gaps and therefore the magnet orientations changing.

The beam displacement simulated with SIMION and by analytical formula is shown in Table 2.

Table 2: Beam Displacement After Passing Through Three 22 Gap Tubes with Magnets

	LE section				HE section	
	H ⁻¹ D, mm		Ni ⁻¹ D, mm		Ni ⁺¹² D, mm	
X	SIMION	(7)	SIMION	(7)	SIMION	(7)
T1 in	0	0.0	0	0.0	0	0.0
T2 in	0.9	1.0	0.11	0.1	0.3	0.3
T3 in	1.4	1.4	0.18	0.2	0.6	0.4
T3 out	1.8	1.8	0.23	0.2	0.9	0.5

The beam displacement due to the effect of magnets after travelling through the entire LE and HE sections of the 14UD accelerator calculated with the analytical formula is shown in Table 3.

Table 3: Beam displacements at the end of LE and HE sections of 14 UD calculated with the analytical formula.

	E _{inj} , MV	U _T , MV	LE section			HE section		
			M	Q	D, mm	M	Q	D, mm
H	0.1	14.5	1	1	6.0	1	1	3.2
H	0.1	3	1	1	14.0	1	1	7.0
C	0.15	14.5	12	1	2.0	12	5	3.2
C	0.15	6	12	1	2.9	12	5	5.0
Cl	0.15	14	37	1	1.1	37	7	2.3
Cl	0.15	10	37	1	1.3	37	7	2.8
Ni	0.15	14.5	60	1	0.9	60	12	2.6
Au	0.15	14	197	1	0.5	197	13	1.5

Effect on Pulsing Width

The magnetic field causes deviations in path length of particles starting at different radii. The transit time changes as $\Delta t/t = \Delta L/L$. In the case of the pelletron accelerator, the major contributor to transit time is the first section of the accelerating column, the remaining sections add only a small fraction of the transit time broadening. The SIMION simulated transit time variations are given in Table 4.

In Table 4, the Δt is the time difference in the time of flight for an on-axis particle vs particles injected at 3 mm radius.

Table 4: Variation of Transit Time Due to Path Difference in the First Three 22 Gap Sections

Ion	E _{inj} , MV	U _T , MV	no magnets Δt , ns	with magnets Δt , ns
H ⁻¹	0.07	3	0.312	0.312
Ni ⁻¹	0.15	14.4	0.120	0.124

Alternative Magnet Positioning and Orientation to Reduce Overall Beam Steering

A proton beam is injected at 150 keV in this simulation at a terminal voltage of 14.3 MV, or 25 kV/gap. The geometry of this simulation is shown in Fig. 5.

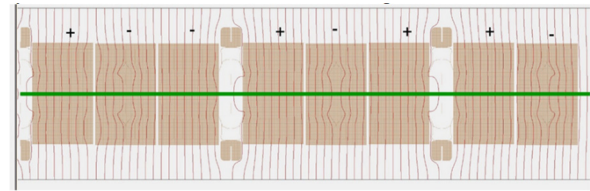


Figure 5: Single plane magnet orientation. Alternative single plane magnet orientation is shown above each plane.

A beam trajectory for single plane magnet orientation, zoomed and enlarged in radial coordinate, is shown in Fig. 6.

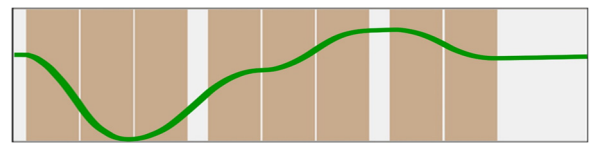


Figure 6: Single plane magnet orientation stretched in the vertical axis to amplify trajectory.

Most importantly, the magnets must still be able to suppress electrons. Here in Fig. 7 we have a distribution of electrons created in a 24 mm diameter cylinder along the length of the tubes covered by magnets. These electrons simulate those created by the beam striking residual gas particles as it travels through the 14UD.

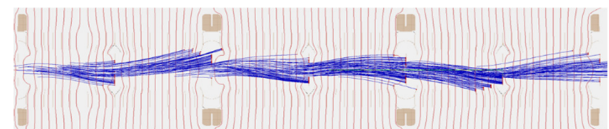


Figure 7: Electron trajectories for single plane magnet orientation.

DISCUSSION

In the LE section tube, the diameter of the ion beam injected is about 5 mm, which is much smaller than the minimum diameter of aperture of 25 mm. Therefore, charge exchange is the dominating process. The charge of the negative ion is not in equilibrium. The stripping of one or a few electrons in one collision can take place with a cross section of the order of 10^{-15} cm². In addition, the ionization of the residual gas atom can take place with considerable probability. Secondary electrons and charged particles will travel and gain some energy before they are stopped on the electrodes. They may also cause an additional ionization of residual gas and release more secondary electrons when colliding with the electrodes. In the case of the ANU suppression system based on V-electrodes, the electrons originating on axis are not stopped. One can expect a flux of high energy electrons travelling toward the terminal that are eventually intercepted by an electrode surface facing the top of accelerator as shown in Fig. 1. The discoloration

of top surface (Fig. 1, 1A) is possibly caused by bombardment of negatively charged particles travelling toward the terminal.

After passing the stripper there is a distribution of charge states but only the selected state is focused properly through the HE section. The same is valid for the HE stripper. The neighbouring charges are over-focused or underfocused with the quadrupole terminal lens. Eventually they are stopped on the electrodes or apertures in the HE tubes producing secondary electrons. One can expect electrons produced on electrodes and in residual gas to travel back to the terminal. Therefore both surfaces of the tube electrodes might be exposed to particle bombardment. The consequences are:

- (i) An additional outgassing rate produced by the bombardment of the tube electrodes
- (ii) Production of secondary particles which cause additional ionization.

The production of X-ray inside the tube, which ionizes the insulating gas leading to radial loss current between column and tank. This will result in a higher potential difference between electrodes near the terminal causing overvoltage. The feedback character of the process described determines a criticality condition for the maximum injected current.

SIMION simulations confirm that the V electrodes are an efficient suppression option for electrons originating on apertures, Fig. 2. However, this option does not eliminate e⁻ originating on the beam axis in residual gas. SIMION simulations also confirm that the magnets are a universal suppression option for electrons originating on the beam axis and on apertures as shown in Fig. 3 even without using V electrodes. Simulations addressed the suppression of electrons originating on apertures in new NEC 21 or 22 gap tubes. The following conclusions are drawn from the results shown in Table 1.

- (i) Poor suppression with flat electrodes and without magnets
- (ii) Excellent suppression with flat electrodes (or V electrodes) and B field
- (iii) Medium suppression if using V electrodes without B field
- (iv) On axis electrons generated from the beam interacting with gas are generally not able to be suppressed with V electrodes, however the magnetic field is able to steer them to terminate within a tube.

The main issue with the “spiral” magnetic field is significant steering of the beam both in LE and HE sections, Fig. 4. The analytical model was validated by comparison with SIMION simulations as per Table 2. Then it was applied to calculate beam displacement after passing through LE and HE sections of the 14UD as shown in Table 3. In the LE section the displacement was in excess of 10 mm. In the HE section the maximum displacement of the beam was about 10 mm, but this calculated value is underestimated. The displacement is higher for a beam of low M and at a lower terminal voltage. A high level of steering in both LE and HE sections makes good overall transmission through the entire accelerator impossible. This is specifically im-

portant in the case of the ANU 14UD where there is no terminal steering capability. A terminal steerer has to be implemented if “spiral” magnetic suppression is chosen. No significant effect of the magnets on pulsed beam broadening was noticed as per Table 4.

A good alternative to the “spiral” B field might be a “snake” B field configuration (Fig. 5) in which case the net offset could be negligibly small, see Fig. 6. The net offset in this case is +0.002 mm over 830 mm.

The next set of 8 magnets could be arranged in the opposite direction to try to cancel this net effect. The magnetic suppression is nevertheless not compromised, Fig. 7. The electrons seem to terminate well, mainly at the apertures with an average energy of 290 keV comparable to the 222 keV using the NEC rotated magnet arrangement.

In response to the ANU single plane proposal, NEC suggested using spiral B configuration with half gradients on entry and exit tubes in X and Y directions to compensate. In this case the field configuration would be to put ½ strength magnets on the first and last 20-gap tubes in the first 6 LE units, with, for example, the first 10 gaps in +X, the second 10 gaps in +Y, then full strength 10 gaps -X, 10 gaps -Y, 10 gaps +X, 10 gaps +Y,, down to the last tube section with half field 10 gaps -X, and finally 10 gaps -Y. The next eight units after the dead section would follow the same pattern. NEC simulations show that the net deflections in that first 6 units are very small.

CONCLUSION

The preferred technologies for successful implementation of the upgrade of the entire population of 14UD acceleration tubes is based on NEC 20 gap tubes with magnetic electron suppression and minimized steering of ion beam. The minimization of overall steering can be achieved by keeping the integral of B field distribution along beam axis to zero. This option is possible for flat B field distribution (“snake” configuration) or 2D distribution (“spiral” B configuration).

REFERENCES

- [1] D.C. Weisser and M.D. Malev, “NEC accelerator tube upgrade: 16.7 MV in a 14UD”, *Nucl. Instrum. Meth. Phys. Res., Sect A*, vol. 287, pp. 64-67, 1990.
doi: 10.1016/0168-9002(90)91767-6
- [2] C.M. Jones, K.A. Erb, D.I. Haynes, J.T. Mitchell, N.F. Ziegler, J.E. Raatz, and R.D. Rathmell, “Tests of compressed geometry acceleration tubes in the Oak Ridge 25URC tandem accelerator”, *Nucl. Instrum. Methods Phys. Res., Sect A*, vol. 268, pp. 361-367, 1988.
doi: 10.1016/0168-9002(88)90536-0
- [3] G.A. Norton, “Developments Concerning the NEC High Gradient Accelerating Tube Assemblies”, in *Symposium of North Eastern Accelerator Personnel 1987*, Tallahassee, FL, USA, World Scientific Publishing Company, pp. 235-245, 1988.
- [4] P. Linardakis, N. R. Lobanov, T. B. Tunningley, D. Tsifakis, S. T. Battison, B. Graham, J. A. Bockwinkel, and J. Heighway, “High Voltage Performance Degradation of the 14UD Tandem Accelerator”, *J. Phys.: Conf. Ser.*, vol. 1401, p. 012004, 2020.
doi: 10.1088/1742-6596/1401/1/012004

STATUS AND PERSPECTIVE OF ELECTRON CYCLOTRON RESONANCE BASED CHARGE BREEDERS

J. Angot*, T. Thuillier, M. Baylac, M. Migliore

Univ. Grenoble Alpes, CNRS, Grenoble INP, LPSC-IN2P3, Grenoble, France

O. Tarvainen

UK Research and Innovation, STFC Rutherford Appleton Laboratory,
Harwell Campus, United Kingdom

Abstract

Since their invention in the late 1990s, Electron Cyclotron Resonance (ECR) based Charge Breeders (CB) have been used in several Isotope Separation On Line (ISOL) facilities to study radioactive ions. Many developments were carried out on these devices to enhance their performances and improve the knowledge on the ECR charge breeding process in laboratories worldwide. At LPSC, recent experiments in pulse mode were carried out to estimate plasma parameters such as the ionisation, charge exchange and confinement times, providing indications on the high charge state ions confinement. A new model of the 1+ beam capture was also proposed and experimentally verified by studying the stopping of injected ions of different masses. Present ECR charge breeder optimum efficiencies vary from 10 to 20% depending on the ion species and the facilities specifications. The total efficiency ranges from 35 to 90% and the charge breeding time from 10 to 25 ms/q. Electron Beam Ion Source (EBIS) is an alternate CB technology with lower contamination yield, yet limited injection flux capability. ECR CB sustains a higher 1+ beam intensity acceptance and its prospects to improve the efficiency, charge breeding time and beam purity are identified.

INTRODUCTION

In flight and Isotope Separation On Line are complementary methods used to produce radioactive ions. For nuclear astrophysics and nucleus structure studies far from the valley of stability, the energy of the particles have to be raised in the MeV/u range. Elements are produced at rest in the ISOL case and a post accelerator is used to obtain the final energy. Several criteria must be fulfilled to allow successful investigation of these particles which are often produced at low yield or with a short half-life (<1 s) : in particular the beam purity, the possibility to tune the final energy, a low radiation background and the beam optics quality. Since the acceleration of the particles scales with the charge state, a Charge state Breeder is typically installed before the LINear ACcelerator (LINAC) or the cyclotron. Presently 8 ISOL facilities using a CB are in operation worldwide, or in final construction phase. Table 1 summarizes the characteristics of these facilities.

In these facilities, the Radioactive Ion Beam (RIB) production yield ranges between 10^2 up to 10^{10} ions/s and different

* julien.angot@lpsc.in2p3.fr

types of 1+ sources are used. The CB has to be adapted to the configuration and experiment (ion mass, 1+ beam optics, requested charge state ...) and reach optimal performances. Two different technologies are presently in use : EBIS and ECRIS (ECR Ion Source). Recently 2 facilities were converted to EBIS CB mainly to increase the purity of the re-accelerated beams. This paper presents the ECRIS CB technology and possible ways to improve its performances.

ECR CHARGE BREEDING

ECR CB Origin

Charge breeders based on the use of Electron Cyclotron Resonance ion sources emerged in the frame of the PI-AFE project [1]. Neutron rich radioactive ions with a mass ranging between 75 to 150 amu were to be produced from the bombardment of ^{235}U target by the high neutron flux (5×10^{13} n/(cm²s)) of the ILL reactor. The species were to be ionised, accelerated at 10-30 keV, mass separated and transported to LPSC (formerly named ISN) over a 400 m distance. The ion charge state had to be increased in order to allow the post acceleration of the particles with the LPSC double cyclotron system «SARA». The idea came up to use the ECR ion source plasma as a «plasma catcher» where the RIBs would be stopped before interacting with the metallic walls, thus suppressing the sticking time of the solid-state catcher which was used until then. In the same time, the ECR plasma had to increase the charge state of the incoming RIBs up to high charge states. The first charge breeding experiments with an ECR ion source were carried out in 1995 with the 10 GHz ISOL MAFIOS ion source using the «backward» injection method, i.e. through the extraction electrode. Soon the injection through the upstream side of the source was tested and adopted : comparable efficiencies were reached in a simpler way and injection in continuous mode was possible, which was of high interest for post acceleration with cyclotrons or LINACs operating in continuous mode [2]. This injection scheme is presently used by all the ECR charge breeders.

ECR CB Principle

ECR CB are based on minimum-B type ECR ion sources. Modern configurations consist of a set of 2 or 3 coils and a yoke to generate an axial magnetic field profile with a maximum B_{inj} at injection, a local maximum B_{ext} at extraction and a minimum B_{min} in between, as illustrated in Fig. 1. An

Table 1: Characteristics of the ISOL facilities equipped with a charge breeder. “LINAC”, “SC LINAC” and “RFQ” account to respectively room temperature LINAC, superconducting LINAC and Radio Frequency Quadrupole Accelerators.

Lab Facility	Prim. beam	Reaction Ionisation source	Charge Breeder I+ (pps)	Post accel. Energy
ANL CARIBU		²⁵² Cf fission fragments He gas catcher	ECRIS → EBIS	SC LINAC 10 MeV/u
CERN ISOLDE	1.4 GeV p ⁺	Spallation, fragmentation, fission Surface, laser, plasma, LIST	EBIS 10 ⁷	LINAC + SC LINAC 10.4 MeV/u at A/q=2.5
GANIL SPIRAL1	95 MeV/u C 24 MeV/u U	Fragmentation, fusion evaporation ECR, Febiad	ECRIS 10 ² to 5 × 10 ⁸	Cyclotron Up to 25 MeV/u
LNL SPES	30-70 MeV 1.5 mA H ⁺	UCx target fragmentation	ECRIS 10 ⁶	RFQ, SC LINAC Up to 10 MeV/u for A/q=7
MSU ReA	80 MeV/u	Projectile fragmentation He gas catcher	EBIT CW 10 ¹⁰	RFQ, SC LINAC 20 MeV/u light, 12 MeV/u heavy
Texas A&M	80 MeV H ⁺	(p,n) reactions He gas cell	ECRIS	Cyclotron 26-57 MeV/u
TRIUMF ISAC	500 MeV H ⁺	Spallation, fragmentation Surface, laser, plasma	ECRIS+EBIS 10 ⁵ to 10 ⁹	RFQ, LINAC, SC LINAC 0.15-9.5 MeV/u
IBS RAON	70 MeV p ⁺	UCx target fragmentation	EBIS Up to 10 ⁹	SC LINAC 20 MeV/u

hexapolar magnet is set around the plasma chamber, to produce the radial magnetic field. B_{rad} is the radial field on the poles generated by the hexapole at the wall of the plasma chamber.

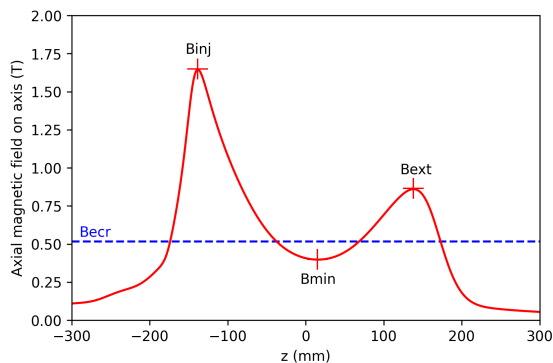


Figure 1: Typical 14 GHz ECRIS axial magnetic field profile on axis.

The combination of these components creates a magnetic trap for charged particles, where the magnetic field strength has a minimum at the center of the plasma chamber. The Electron Cyclotron Resonance allows the electron heating by the injection of microwaves into the plasma chamber. The ECR surface is defined by the iso magnetic field strength B_{ecr} value. Due to successive crossings of the ECR surface, the trapped electrons gain enough energy to ionize the atoms and ions up to a high charge state, through step by step ionisation. On the other hand, charge exchange with neutral atoms or other ions is the main phenomenon counteracting

ionisation and limiting high charge state production. Due to their lower mass, electrons are more mobile than ions in the plasma which induces an ambipolar diffusion and the build-up of an electrostatic plasma potential Φ (Fig. 2). In addition, the existence of a potential dip $\Delta\Phi$ in the center of the plasma has been proposed to explain the confinement of highly charged ions, where the dip would be due to the hot electron population strongly confined within the magnetic trap [3].

Empirical laws were formulated by Geller regarding the performances of ECRIS as a function of their configuration. One can cite, for instance, that the electron density scales with the square of the frequency [4]. Considering the magnetic trap, as experimentally demonstrated and reported in [5], the source performances can be optimized with adequate mirror ratios as a function of B_{ecr} at injection $\frac{B_{inj}}{B_{ecr}} \geq 3.5$, extraction $\frac{B_{ext}}{B_{ecr}} \geq 2$ and regarding the radial confinement $\frac{B_{rad}}{B_{ecr}} \geq 2$. In addition the balance between the ratios should respect the values $\frac{B_{min}}{B_{ecr}} \approx 0.8$ and $\frac{B_{ext}}{B_{rad}} \approx 0.9$.

In the ECR based charge breeding method, the ions are injected into the plasma, slowed down, captured, multi ionised and extracted. The capture process proposed by Geller [6] relies on the deviation of the injected ions by Coulomb collisions with the plasma ions, leading to their thermalization and trapping by the magnetic field. The energy of the injected ions is tuned by adjusting the potential difference ΔV between the 1+ source and the CB, as displayed on Fig. 2.

From this theory, the 1+ ions energy must be high enough to overcome the plasma potential and adjusted to optimize the capture, i.e. injected ions must have an average speed

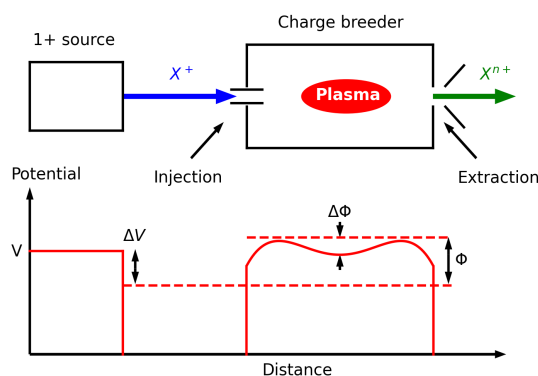


Figure 2: Electrostatic potential profile from the 1+ source to the ECR CB.

equal to the average speed of the plasma ions [6]. After their thermalization, the ions behave like the other plasma ions, they are ionised by the plasma electrons and extracted.

The ECR CB efficiency for one charge state is calculated by the formula $\eta = \frac{(I_{n+} - I_{n0+})}{(n * I_{1+})}$, where I_{1+} and I_{n+} are the electrical currents of the 1+ and n+ beams and I_{n0+} is the electrical current of the n+ beam measured when the 1+ beam is switched off. The total efficiency is calculated by summing all individual efficiencies for each charge state, for charge states ≥ 2 . It represents the proportion of 1+ ions that were effectively charge breed.

ECR CB Development

Even though the PIAFE project was not funded, the LPSC group decided to continue the R&D on ECR charge breeding for other facilities, in particular for a possible use for the SPIRAL1 project at GANIL [7]. The new 14 GHz PHOENIX type ECR CB was then conceived and commissioned in the early 2000. Two copies were manufactured, one for TRIUMF and one for ISOLDE, the last being ordered by Daresbury Laboratory. At KEK, a 12 GHz ECR ion source was turned into a CB and the obtained results were in good agreement with those achieved with the PHOENIX CB, for example regarding the CB efficiency as a function of the ion mass, charges and species [8]. A new 18 GHz ECR CB was then designed and assembled by KEK to produce ions with an A/q ratio of 7 [9]. At ANL, a 10 GHz AEER type source was severely modified and transformed into a CB for the CARIBU facility [10], whereas at Texas A&M a brand new source was designed and manufactured by Scientific Solutions (San Diego) [11]. The Daresbury CB, tested at ISOLDE as an option to the EBIS CB, was donated to GANIL in 2011 for the SPIRAL1 facility. This source was upgraded in collaboration with ANL, tested at LPSC and installed on the SPIRAL1 facility in 2016 [12]. Another PHOENIX CB was manufactured by the LPSC group for the SPES project, the source is installed on the facility and will be commissioned soon [13].

Extensive R&D work was carried out by the different groups to improve the ECR CB performances. Different

schemes to improve the efficiency of the 1+ injection were tested like the 2-stage deceleration system (TRIUMF) [14], tuning the deceleration cylindrical electrode position (ANL, GANIL) [15, 16], increasing the injection electrode diameter (LPSC) [17], or using a sextupolar ion guide injection system in the particular case of the Texas A&M CB [18]. The magnetic field at the source injection was symmetrized to prevent steering of the 1+ beam [15, 19].

The plasma conditions were also enhanced. In order to reduce charge exchange and produce higher charge states, the residual vacuum was improved. The magnetic confinement was optimized by increasing the injection axial magnetic field and changing the field gradients [20]. Regarding microwave heating, the use of two frequencies and fine frequency tuning was profitable to increase the CB efficiency and stabilize the plasma, but in some cases it was observed to affect the charge breeding time [21, 22].

The RIB purity issue in the ECR CB was early pointed out by KEK (2004) [23], LPSC (2004) [24] and TRIUMF (2006) [25]. Chemical elements, coming from the wall sputtering, the support gas or the residual vacuum are present in the ECR CB plasma. Depending on the mass of these contaminants, they can be extracted from the CB with a A/q extremely close to the RIB of interest which makes their separation difficult with the downstream spectrometer and leads to the degradation of the RIB purity. At KEK, the use of a NEG type material was tested to make a selective pumping. Pure aluminium coating on aluminium alloy plasma chamber was also used, together with a careful cleaning by sand blasting and high-pressure rinsing [9, 22]. New methods were proposed by Vondrasek [26] to reduce the contaminants in ECR CB like the CO₂ cleaning or the ultra pure aluminium coating with appropriate heating system. Atomic Layer Deposition was also introduced for in situ deposition of Al₂O₃. ECR plasma studies on the kinetic instabilities demonstrated that unstable plasma conditions enhance the level of contaminants in the extracted ion beam of the CB [27]. The contamination issue is currently addressed by a collaborative work between LNL, LPSC and GANIL [28]. Preliminary experiments were done with the LPSC CB to measure contaminant spectra that will be used as reference for comparison with future configurations. High purity liners will be inserted in the plasma chamber to minimize the number of species sputtered by the plasma as well as decontamination of the support gas and vacuum improvement.

ECR Plasma Studies

The experimental analysis of ECR plasma can hardly be done by introducing physical probes into the plasma as this would perturb the plasma equilibrium [29]. Meanwhile, some plasma properties like the electron energy distribution function, the ion temperature or the electrostatic field distribution, remain poorly known. The possibility to use the 1+ beam as a probe was early proposed by Lamy [30]. Several studies with ECR CB contributed to a better understanding of ECR plasma.

Experiments were carried out with the LPSC CB by injecting (i) Rb^+ and Cs^+ into an oxygen plasma [31] and (ii) Na^+ into a helium plasma [32]. The ion-ion collision mean free path and the lower limit of the electron density were estimated by analysing the captured portion of the 1+ beam.

The capture process was also simulated using different plasma models [33, 34] and measured ΔV curves (high charge state efficiency response as a function of ΔV) and efficiencies were used as input data to estimate the plasma potential, electron density or ion temperature. The simulated ion temperature is not in good agreement with experimental findings done by optical emission spectroscopy [35], similar to the plasma potential value from measurements done with a retarding field analyser [36].

The capture process was recently investigated with the LPSC CB injecting 1+ ions with different mass in a plasma sustained by different support gas. One conclusion of this work is that the final slowdown of the injected particles is mainly caused by the electrostatic force due to the plasma potential rather than long range Coulomb collisions, as previously postulated.

Experiments were also done by injecting short 1+ pulses [37]. The response of the n+ beam was analysed with a 0D code to estimate confinement, ionisation and charge exchange characteristic times together with other plasma parameters. These characteristic times play a key role in the charge breeding process. This short pulse method, tested by injecting K^+ with 2 different plasma conditions [38], showed that the K^{9+} efficiency increase in the new configuration was linked to a higher pile up of these ions induced by a better characteristic times configuration (minimisation of the ionisation time from lower charge state and reduction of the charge exchange time from higher charge state). This was eased in this case by the closed shell of the electronic configuration of K^{9+} . Recently, new experiments were done to improve the method accuracy [39]. The ECR plasma was probed with different isotopes and different species using a single 1+ alkali ion source pellet. The uncertainty on the fitted characteristic times was decreased by injecting different species and isotopes in the plasma, resulting in the reduction of the possible plasma parameter (electron density and average energy) matching all those configurations. The confinement times of high charge state ions were found to be in good agreement with the potential dip electrostatic trapping model which brings additional credits to this theory [40].

All these developments and studies contributed to a better understanding of the ECR CB process and to an improvement of the performances.

Discussion on the Performances of ECR CB

Table 2 summarizes the specifications of the recently developed ECR CB. These CB exhibit different performances depending on both their design and the characteristics of the accelerator facility they are installed on.

The ECR CB efficiency for a given charge state typically ranges from 5% to 20% and the total efficiency between 35% and 90%. Limited efficiencies is often due to the specifica-

tions of the facility such as high 1+ beam emittance [34] or high residual pressure. Moreover, in order to produce very high charge states, the CB may be operated with specific tuning, thus limiting the maximum value of the efficiency charge state distribution. This large variety of operation conditions makes the comparison between different charge breeders difficult.

Nevertheless, some parameters appear essential for efficient charge breeding like high magnetic mirror ratios (ANL, LPSC). This is in agreement with the ECRIS theory and it should be noticed that the mirror ratio at injection is often lower than the recommended value (≥ 3.5). The ECR CB configuration requires a port into the soft iron injection plug for the 1+ beam injection, reducing B_{inj} and so the magnetic mirror ratio. The presence of a median axial coil (case of 3 coils configuration), for the fine tuning of B_{min}/B_{ecr} , is beneficial to obtain a stable plasma with an optimum efficiency.

As illustrated by the short pulse experiments method, the plasma conditions may imply more suitable ions characteristic times and so improve the source performances. A higher microwave frequency would induce a higher electron density and reduce the ionisation times. It would improve the high charge state production together with the 1+ beam capture.

The lifetime of the high charge state ions can also be enhanced with a larger plasma chamber diameter [41] like in the case of ANL and Texas A&M. It should improve high charge state production as it increases the probability of ionisation. In addition, a lower residual vacuum, like TRIUMF, GANIL and ANL, may contribute to this goal by increasing the charge exchange times of the ions with neutral atoms. Fine frequency tuning or double frequency heating are also mandatory to enhance high charge state efficiency or optimize the efficiency on a given charge state.

Charge breeding time is measured in the range 5 to 25 ms/q which means that for high mass species, the process can take several hundreds of milliseconds. This duration can be relatively long in the case of short half-life isotopes. In some cases, a tuning providing a lower efficiency together with a shorter charge breeding time can be considered. Due to the step by step process of ionisation, shorter ionisation times obtained with a higher electron density should reduce the CB time. On the other hand, a larger plasma chamber radius would mechanically lengthen the the ion confinement time but this could be mitigated by acting on B_{ext} . In fact, reducing the axial magnetic field strength at extraction would create an electron leak on axis and, as a consequence, would reduce the ion confinement time [42].

ECR CB are robust instruments that can accept high intensity primary beam ($> 10^{13}$ ions/s) in CW or pulsed operation mode. Their performances are compared to EBIS type CB instruments, which are often operated in pulse mode for efficiency reasons, in Table3. EBIS CB require an ion cooler-buncher upstream to prepare the beam for injection. The EBIS cooler-buncher efficiency ranges between 10% and $\approx 60\%$ depending on the ion mass and the RIB flux. The total efficiency of the trap and EBIS is between 5 to 20% which is close to ECR CB performances. High charge state

Table 2: Specifications of the ECR charge breeders developed worldwide. The results are provided for stable metallic elements. SPES CB data were measured during the commissioning phase at LPSC.

Laboratory Facility	ANL CARIBU	GANIL SPIRAL1	KEK TRIAC	LNL SPES	LPSC R&D	Texas A&M	TRIUMF ISAC
Source type	AECR	PHOENIX	KEKCB	PHOENIX	PHOENIX		PHOENIX
Freq. (GHz)	10-14	14.5	18	14.5	14.5	14.5	14.5
Chamber Φ (mm)	80	72	75	72	72	90	72
Pressure (mbar)	2.5×10^{-8}	1×10^{-8}		4×10^{-7}	3×10^{-8}	1×10^{-7}	1×10^{-8}
Coils nb	2	3	3	3	3	2	3
B_{inj}/B_{ecr}	3.8	2.9	2.3	2.8	3.1	2.5	2.2
B_{rad}/B_{ecr}	2.3	1.5	1.7	1.5	1.5	2.2	1.5
ϵ_{CB} (%), A \approx 20	10.1	17.0			18.7		
ϵ_{CB} (%), A \approx 80		9.5		7.8	11.3		3.0
ϵ_{CB} (%), A \approx 130	14.1		2.4	11.7	14.1	10.0	4.0
Total eff. (%)	47 - 77	44 - 72		50-65	60 - 90		>35%
τ_{CB} (ms/q)	10 - 46	4 - 20		17-28	13 - 26		10 - 20
A/q, A \approx 20	3.3	3.3			2.9		5.5
A/q, A \approx 130	5.1	4.5	7.0	5.1	5.1	5.5	6.3
Separation $\Delta m/m$	300	10000		1000	140		250

Table 3: Order of magnitude of the performances and features of the cooler-buncher and EBIS system compared to 14 GHz ECRIS CB.

Technology	EBIS CB	ECRIS CB
Max 1^+ RIB intensity	$<10^{10}/s$	$>10^{13}/s$
CB time to n+ (ms)	15 - 200	100 - 300
Operation mode	pulsed	CW or pulsed
Robustness	medium	high
1+n+ conversion efficiency	5 - 20%	10 - 20%
RIB total contamination rate extracted	$\sim 10^5/s$	$\sim 10^9 - 10^{10}/s$
Upstream requirement	Ion cooling	None
Maximum A/q	Bare ions	3 \rightarrow A \sim 60 5-6 \rightarrow A \sim 150

ions with A/q between 2 and 7 are typically extracted from the EBIS for ISOL application [43]. The charge breeding time, taking into account both the trapping and the charge breeding steps ranges between 15 to 200 ms (for A \leq 130) which is faster than ECR CB. The maximum 1^+ beam intensity acceptance ranges between 10^8 and 10^{10} ions/s and is limited by the number of charges that can be stored in the cooler-buncher or in the electron beam of the EBIS. ECR CB can accept three orders of magnitude higher RIB flux.

For the EBIS, the n+ beam contamination mainly originates from the residual gas and the typical vacuum level to mitigate this problem is 10^{-11} mbar. In the ECRIS case, the charged particules of the plasma have more interactions with the surrounding surfaces leading to higher wall desorption and material sputtering.

Contaminants density into the ECR plasma can be reduced by increasing the plasma chamber diameter (more favorable volume over surface ratio) [41] whereas a higher plasma density, obtained with higher microwave frequency, would increase the wall sputtering and thus increase the RIB contamination.

The contamination rate can be estimated to 10^5 pps in the EBIS case and up to 10^{10} pps for the ECRIS. This is particularly problematic when a low RIB rate is produced or with low downstream separation. RIB contamination can be limited by the fine tuning of the post accelerator or the use of a stripping foil like done at TRIUMF. Nevertheless, TRIUMF decided to manufacture and install an EBIS CB as previously done at ANL. At SPIRAL1, a cyclotron is used for post acceleration allowing a high resolution mass separation ($\Delta m/m > 10000$).

ECR technology is efficient for ISOL charge breeding when the downstream separator has a high resolution. It still can be improved and it could play a key role in the frame of future facilities with high intensity RIB production.

PERSPECTIVES

Future ISOL Projects

At MSU, the FRIB project is in its final construction phase. At maximum power, the new facility will produce radioactive ions with a rate $>10^{10}$ pps. The new «HCEBIS» charge breeder was assembled to allow their post acceleration. It will operate with an electron beam current of 4 A, a density of 200 A/cm², the trapping length being ≈ 0.7 m. The expected charge capacity is 10^{11} allowing charge breeding with production rates up to 10^{10} for light ions.

In Europe, beyond the SPIRAL2 and SPES projects, the EURISOL project aims at the construction of an ISOL facility increasing the production yield by a factor of 100 or

more. It is based on a new 1 GeV proton linac with 5 MW power, 2 different types of targets and a 150 MeV LINAC. Presently, only ECR CB can accept high flux RIBs on the order of 10^{12} ions/s.

Future ECR CB Configurations

At LPSC, a development plan was set to enhance the PHOENIX type CB performances.

As a first step, the source will be implemented in the so called “5 coils configuration” (consisting in removing one axial coils among the existing 6) to ease the CB tuning and to stabilize the plasma. The yoke and coils structure will be modified to reduce the coupling between the 3 groups of solenoids generating B_{inj} , B_{min} and B_{ext} (see Fig. 1). The injection and extraction plugs will be replaced, together with the plasma chamber. The reduction of the port diameter of the injection soft iron plug will be tested to enhance the injection mirror ratio from 3.1 (see Table 2) up to 3.6, while maintaining a good 1+ beam injection. The source length will be reduced (by 80 mm) and the injection and extraction electrodes will be shortened to improve the optics. To reduce contamination, residual gas pressure will be minimized using alumina insulators with brazed metallic flanges at injection and extraction, thus limiting the number of o-rings. Contamination reduction will also be studied by introducing into the plasma chamber liners of different materials, such as Nb and Ta. All the parts have been manufactured and the assembly is planned in September 2022.

As a second step, a larger diameter plasma chamber configuration of the PHOENIX CB was designed to increase high charge state production and reduce further the contamination yield. In this design, the plasma chamber diameter is increased from 72 mm to 100 mm with a new hexapole providing a 1.1 T maximum field at the plasma chamber wall. The whole new central core parts under vacuum will be made of the same material and so, no soft iron parts will be set under vacuum in this case. Vacuum sealing will be performed exclusively with metallic gaskets. The injection coil current supply will be upgraded to reach the maximum possible current in the injection coil (1350 A) and improve the magnetic mirror ratio at injection. The magnetic configuration will allow operation up to 18 GHz (against 14 GHz today). For double frequency heating, the plasma chamber will be equipped with 2 WR62 waveguide ports and a 500 W 9-18 GHz amplifier will be purchased, also allowing fine frequency heating. Manufacturing of the parts will be completed by the end of 2022 to test this configuration in 2023.

Finally, a new concept of 18 GHz superconducting ECR CB was proposed by Thuillier [42]. The driving idea is to apply the feedback learned with ECR ion sources by the community along the past decades and apply it to define a new generation ECR CB. The design is adapted to optimize the ion capture, maximize the high charge state production and minimize the output RIB contaminants. A high tuning flexibility is obtained with a set of 8 axial coils, able to produce either short or very long ECR plasma. The radial

magnetic field is also created by a superconducting hexapole magnet tunable up to 1.4 T. The plasma chamber would have a 200 mm diameter and could be baked online up to 300°C. Ultra High Vacuum would be reached with cryogenic pumps set at each side of the source. Pure Beryllium was proposed to manufacture all parts surrounding the plasma in order to reduce the number of contaminant species produced by the plasma sputtering of the walls. This design should allow a +20% increase of the efficiency together with a -40% reduction of the charge breeding time and drastic reduction of the contaminants. Such design could be advantageously considered for next generation facilities like EURISOL where high intensity RIBs are expected.

ACKNOWLEDGMENTS

The authors are indebted to N. Bidault from CERN for the fruitful exchanges and discussions on EBIS charge breeder operation in RIB facilities.

REFERENCES

- [1] R. Geller, C. Tamburella and J.L. Belmont, “The ISOL–MAFIOS Source (invited)”, *Rev. Sci. Instrum.*, vol. 67, p. 1281, 1996. doi:10.1063/1.1146649
- [2] R. Geller, “The electron cyclotron resonance ($1+n^+$) systems and the ISOL radioactive beam facilities”, *Rev. Sci. Instrum.*, vol. 71, p. 612, 2000. doi:10.1063/1.1150342
- [3] G. Melin *et al.*, “Some particular aspects of the physics of the ECR sources for multicharged ions”, *Rev. Sci. Instrum.*, vol. 61, p. 236, 1990. doi:10.1063/1.1141305
- [4] R. Geller, *Electron Cyclotron Resonance Ion Sources and ECR Plasmas*, IOP, Bristol, UK, 1996.
- [5] D. Hitz, A. Girard, G. Melin, S. Gammio, G. Ciavola, and L. Celona, “Results and interpretation of high frequency experiments at 28 GHz in ECR ion sources”, *Rev. Sci. Instrum.*, vol. 73, p. 509, 2002. doi:10.1063/1.1429313
- [6] R. Geller, T. Lamy, and P. Sortais, “Charge breeding of isotope on-line-created radioactive ions using an electron cyclotron resonance ion trap”, *Rev. Sci. Instrum.*, vol. 77, p. 03B107, 2006. doi:10.1063/1.2151896
- [7] N. Chauvin, “La transformation d’état de charges $1^+ \rightarrow n^+$ pour l’accélération des ions radioactifs”, Ph.D. thesis, Phys. Dept., Université Joseph Fourier, Grenoble, France, 2000.
- [8] T. Lamy, R. Geller, P. Sortais, and T. Thuillier, “Status of charge breeding with electron cyclotron resonance ion sources (invited)”, *Rev. Sci. Instrum.*, vol. 77, p. 03B101, 2006. doi:10.1063/1.2149300
- [9] S.C. Jeong *et al.*, “KEKCB-18 GHz ECR charge breeder at TRIAC”, *Nucl. Instrum. Methods Phys. Res., Sect. B*, vol. 266, pp. 4411-4414, 2008. doi:10.1016/j.nimb.2008.05.072
- [10] R. Vondrasek, R. Scott, J. Carr, and R.C. Pardo, “Status of the electron cyclotron resonance charge breeder for the ^{252}Cf fission source project at ATLAS”, *Rev. Sci. Instrum.*, vol. 79, p. 02A901, 2008. doi:10.1063/1.2802580

- [11] D.P. May, G. Tabacaru, F.P. Abegglen, and W.D. Cornelius, “First operation of the charge-breeder electron-cyclotron-resonance ion source at the Texas A&M Cyclotron Institute”, *Rev. Sci. Instrum.*, vol. 81, p. 02A901, 2010. doi: 10.1063/1.3273060
- [12] L. Maunoury *et al.*, “Charge breeder for the SPIRAL1 upgrade: Preliminary results”, *Rev. Sci. Instrum.*, vol. 87, p. 02B508, 2016. doi: 10.1063/1.4935215
- [13] A. Galatà, G. Patti, C. Roncolato, J. Angot, and T. Lamy, “The new ECR charge breeder for the Selective Production of Exotic Species project at INFN—Laboratori Nazionali di Legnaro”, *Rev. Sci. Instrum.*, vol. 87, p. 02B503, 2016. doi: 10.1063/1.4933338
- [14] F. Ames, M. Marchetto, A. Mjøs, and A.C. Morton, “Charge state breeding experiences and plans at TRIUMF”, *Rev. Sci. Instrum.*, vol. 87, p. 02B501, 2016. doi: 10.1063/1.4932317
- [15] R. Vondrasek, A. Kolomiets, A. Levand, R. Pardo, G. Savard, and R. Scott, “Performance of the Argonne National Laboratory electron cyclotron resonance charge breeder”, *Rev. Sci. Instrum.*, vol. 82, p. 053301, 2011. doi: 10.1063/1.3586765
- [16] L. Maunoury *et al.*, “SPIRAL1 Charge Breeder: Performances and Status”, in *Proc. ECRIS’16*, Busan, Korea, Aug.-Sep. 2016, pp. 35–38. doi: 10.18429/JACoW-ECRIS2016-MOF001
- [17] T. Lamy, J. Angot, P. Sortais, T. Thuillier and A. Galatà, “Beam injection improvement for electron cyclotron resonance charge breeders”, *Rev. Sci. Instrum.*, vol. 83, p. 02A909, 2012. doi: 10.1063/1.3670596
- [18] D.P. May *et al.*, “Charge-breeding of radioactive ions at the Texas A&M cyclotron institute”, in *Proc. ECRIS’18*, Catania, Italy, Sep 2018, pp. 20–23. doi: 10.18429/JACoW-ECRIS2018-MOC2
- [19] T. Lamy *et al.*, “Experimental activities with the LPSC charge breeder in the European context”, in *Proc. ECRIS2014*, Nizhny Novgorod, Russia, 2014, paper WEOBMH01, pp. 120-126. <https://jacow.org/ECRIS2014/papers/weobmh01.pdf>
- [20] J. Angot *et al.*, “Recent improvements of the LPSC charge breeder”, in *AIP Conference Proceedings*, vol. 11, p. 070005, 2018. doi: 10.1063/1.5053347
- [21] R. Vondrasek, A. Levand, R. Pardo, G. Savard, and R. Scott, “Charge breeding results and future prospects with electron cyclotron resonance ion source and electron beam ion source (invited)”, *Rev. Sci. Instrum.*, vol. 83, p. 02A913, 2012. doi: 10.1063/1.3673629
- [22] R. Vondrasek *et al.*, “Operational experience with the Argonne National Laboratory Californium Rare Ion Breeder Upgrade facility and electron cyclotron resonance charge breeder”, *Rev. Sci. Instrum.*, vol. 85, p. 02B903, 2014. doi: 10.1063/1.4826329
- [23] S.C. Jeong *et al.*, “Test results of 18 GHz ECR charge breeder for KEK–JAERI RNB facility”, *Rev. Sci. Instrum.*, vol. 75, p. 1631, 2004. doi: 10.1063/1.1699453
- [24] T. Lamy *et al.*, “ECRIS charge breeding: High resolution spectra and emittance”, *Rev. Sci. Instrum.*, vol. 75, p. 1624, 2004. doi: 10.1063/1.1691472
- [25] F. Ames *et al.*, “Charge state breeding of radioactive ions with an electron cyclotron resonance ion source at TRIUMF”, *Rev. Sci. Instrum.*, vol. 77, p. 03B103, 2006. doi: 10.1063/1.2165271
- [26] R.C. Vondrasek, “Addressing contamination in ECR charge breeders”, in *Proc. ECRIS’18*, Catania, Italy, Sep 2018, pp. 90–93. doi: 10.18429/JACoW-ECRIS2018-TUP07
- [27] O. Tarvainen *et al.*, “Plasma instabilities of a charge breeder ECRIS”, in *Plasma Sources Sci. Technol.*, vol. 26, p. 105002, 2017. doi: 10.1088/1361-6595/aa8975
- [28] J. Angot, T. Thuillier, M. Baylac, M. Migliore, P. Sole, and A. Galatà, “Contaminants reduction in ECR charge breeders by LNL LPSC GANIL collaboration”, in *Proc. ECRIS2020*, East Lansing, MI, USA, Sep. 2020, to be published. doi: 10.18942/JACoW-ECRIS2020-WEZZ002
- [29] L. Maunoury *et al.*, “Charge breeders: Development of diagnostic tools to probe the underlying physics”, in *Rev. Sci. Instrum.*, vol. 93, p. 021101, 2022. doi: 10.1063/5.0076254
- [30] T. Lamy, J. Angot, M. Marie-Jeanne, J. Medard, P. Sortais, T. Thuillier, A. Galatà, H. Koivisto, and O. Tarvainen, “Fine frequency tuning of the Phoenix charge breeder used as a probe for ECRIS plasmas”, in *Proc. ECRIS2010*, Grenoble, France, paper WECOBK03, 2010. <https://jacow.org/ECRIS2010/papers/wecobk03.pdf>
- [31] O. Tarvainen *et al.*, “Injected 1+ ion beam as a diagnostics tool of charge breeder ECR ion source plasmas”, in *Plasma Sources Sci. Technol.*, vol. 24, p. 035014, 2015. doi: 10.1088/0963-0252/24/3/035014
- [32] O. Tarvainen *et al.*, “Diagnostics of a charge breeder electron cyclotron resonance ion source helium plasma with the injection of $^{23}\text{Na}^{1+}$ ions”, in *Phys. Rev. Accel. Beams*, vol. 19, p. 053402, 2016. doi: 10.1103/PhysRevAccelBeams.19.053402
- [33] A. Galatà, D. Mascali, L. Neri, and L. Celona, “A new numerical description of the interaction of an ion beam with a magnetized plasma in an ECR-based charge breeding device”, *Plasma Sources Sci. Technol.*, vol. 25, p. 045007, 2016. doi: 10.1088/0963-0252/25/4/045007
- [34] A. Annaluru, P. Delahaye, M. Dubois, and L. Maunoury, “Electron cyclotron resonance charge breeder plasma parameters from the modeling of 1+ beam stopping”, *Phys. Rev. Accel. Beams*, vol. 24, p. 073403, 2021. doi: 10.1103/PhysRevAccelBeams.24.073403
- [35] R. Kronholm *et al.*, “Spectroscopic study of ion temperature in minimum-B ECRIS plasma”, *Plasma Sources Sci. Technol.*, vol. 28, p. 075006, 2019. doi: 10.1088/1361-6595/ab27a1
- [36] O. tarvainen *et al.*, “Stopping of injected 1+ ions in charge breeder ECRIS plasma”, submitted for publication.
- [37] J. Angot, M. Luntinen, *et al.*, “Method for estimating charge breeder ECR ion source plasma parameters with short pulse 1+ injection of metal ions”, *Plasma Sources Sci. Technol.*, vol. 30, p. 035018, 2021. doi: 10.1088/1361-6595/abe611
- [38] M. Luntinen, J. Angot, O. Tarvainen, V. Toivanen, T. Thuillier, and H. Koivisto, “Measurement of ionization, charge exchange and ion confinement times in charge breeder ECR ion sources with short pulse 1+ injection of metal ions”, in *J. Phys.: Conf. Ser.*, vol. 2244, p. 012009, 2021. doi: 10.1088/1742-6596/2244/1/012009

- [39] M. Luntinen *et al.*, “Diagnostics of highly charged plasmas with multi-component 1+ ion injection”, submitted for publication.
- [40] G. Douysset, H. Khodja, A. Girard, and J.P. Briand, “Highly charged ion densities and ion confinement properties in an electron-cyclotron-resonance ion source”, in *Phys. Rev. E*, vol. 61, p. 3015, 2000. doi:10.1103/PhysRevE.61.3015
- [41] T. Thuillier *et al.*, “Effect of the plasma chamber radius on the high charge state production in an ECR ion source”, in *AIP Conf. Proc.*, vol. 2011, p. 040020, 2018. doi:10.1063/1.5053294
- [42] T. Thuillier *et al.*, “Challenges and prospects of electron cyclotron resonance charge breeders applied to radioactive ion beam facilities”, in *J. Instrum.*, vol. 14, p. P02030, 2019. doi:10.1088/1748-0221/14/02/P02030
- [43] A. Lapierre, “Electron-beam ion source/trap charge breeders at rare-isotope beam facilities”, in *Rev. Sci. Instrum.*, vol. 90, p. 103312, 2019. doi:10.1063/1.5127203

DEVELOPMENTS TOWARDS A COMPACT CARBON ION LINAC FOR CANCER THERAPY*

B. Mustapha[†], A. Nassiri, Y. Yang and D. Meyer, Argonne National Laboratory, Lemont, IL, USA
S. Kutsaev, A. Smirnov, A. Araujo and R. Agustsson
Radiabeam Technologies, Santa Monica, CA, USA

Abstract

Hadron therapy offers improved localization of the dose to the tumor and much improved sparing of healthy tissues, compared to traditional X-ray therapy. Combined proton/carbon therapy can achieve the most precise dose confinement to the tumor. Moreover, recent studies indicated that adding FLASH capability to such system may provide significant breakthrough in cancer treatment. The Advanced Compact Carbon Ion Linac (ACCIL) is a conceptual design for a compact ion linac based on high-gradient accelerating structures operating in the S-band frequency range. Thanks to this innovation, the footprint of this accelerator is only 45 m, while its capabilities are well beyond the current state of the art for hadron therapy machines and include: operation up to 1000 pulses per second, pulse to pulse energy variation to treat moving tumors in layer-by-layer regime. ACCIL is capable of accelerating all ions with mass-to-charge ratio $A/q \sim 2$ to a full energy of 450 MeV/u, and that includes protons, helium, carbon, oxygen and neon. With very short beam pulses of $\sim 1 \mu\text{s}$ and high instantaneous dose delivery, ACCIL is capable of delivering FLASH-like doses ($>100 \text{ Gy/sec}$) for most ion species. In close collaboration between Argonne and Radiabeam, we have developed different design options and prototypes of the high-gradient structures needed for ACCIL. Following an overview of the ACCIL design and its capabilities, the most recent results from the high-gradient structure R&D and future plans will be presented and discussed.

ACCELERATORS IN HADRON BEAM THERAPY – WHY NOT A LINAC?

Cyclotrons are currently dominating the field of proton therapy while synchrotrons are being used for ion beam therapy, especially carbon ions. A cyclotron is a continuous-wave (cw) fixed-energy machine; it does not offer the flexibility of adjusting the time structure or the energy of the beam by simple tuning. Energy degraders are used to adjust the beam energy, these are material blocks that also degrade the primary beam quality and generate secondary radiation requiring significant shielding.

Synchrotrons are pulsed accelerators which offer more flexibility in pulse structure and pulse-to-pulse change in energy without significant radiation or deterioration in beam quality. However, due to the multi-turn acceleration in

a synchrotron and typical beam extraction, these changes could take a few seconds.

Being a single-pass machine, a pulsed linear accelerator (linac) is in principle capable of adjusting the pulse repetition rate and the beam energy hundreds of times per second ($\sim 200 \text{ Hz}$). So, why ion linacs are not deployed in cancer therapy? Linacs have already been proposed for protons [1], but using the same technology used for high-intensity research machines [2], such a linac would be hundreds of meters long. This has limited their deployment in a hospital or university setting, and it is the main reason why synchrotrons are currently dominating the field of ion beam therapy.

However, the intensity requirements for ion beam therapy are rather modest, 10^{10} p/s for proton and 10^9 p/s for carbon, which could in principle be delivered in very short pulses ($\sim \mu\text{s}$) at a relatively low duty cycle ($\sim 10^{-4}$). Combined with the possibility of using small-aperture accelerating sections, these features enable the use of high-frequency high-voltage copper cavities. Due to the wide-spread use and commercial availability of S-band RF sources, the frequency range of $\sim 3 \text{ GHz}$ was a natural choice. And, taking advantage of high-gradient accelerating structure developments for CLIC [3], an accelerating gradient of 50 MV/m seems quite achievable in this frequency range, and was taken as a goal for current and future therapy linac proposals [4].

Finally, a fast-pulsed linac will enable the much-desired flexibility in beam tuning and the fast and efficient beam scanning to allow 3D dose painting, as well as real-time image-guided therapy and targeting of moving targets. By changing the pulse repetition rate, the beam intensity could be adjusted up to 10^9 ions per second (10^{10} for protons), typically needed for therapy. The carbon beam energy could be changed continuously up to the full energy of 430 MeV/u required to penetrate the depth of a human body, which is equivalent to a 30 cm of water. The beam delivery from a linac will be similar to synchrotron beam delivery through fixed beam lines or gantry systems. However, the beam quality of the linac could enable much smaller magnets and therefore more compact gantries.

ACCIL – THE ADVANCED COMPACT CARBON ION LINAC

The Advanced Compact Carbon Ion Linac (ACCIL) is the most compact full-energy carbon ion linac proposed for therapy [5]. In Europe, there are proposals for a combined cyclotron and linac (cyclinac) and an all-linac for carbon beams [6], in addition to the ongoing LIGHT project for a

* Work supported by the U.S. Department of Energy, Office of Science, under Contract No. DE-AC02-06CH11357

[†] brahim@anl.gov

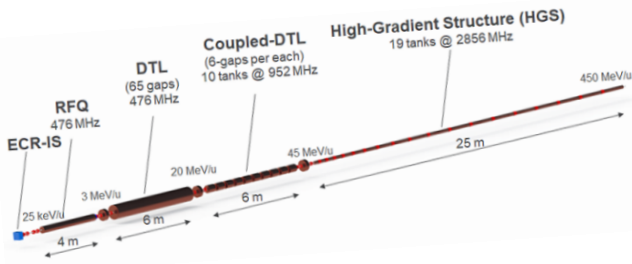


Figure 1: A schematic layout of the ACCIL linac design. A schematic layout of the ACCIL linac design.

proton therapy linac [7]. ACCIL is designed to deliver a full energy of 450 MeV/u which exceeds the energy required for carbon ion therapy. It is also capable of accelerating protons and many other ion beams to the same energy per nucleon. Figure 1 presents a schematic layout of the ACCIL design. The system is about 45 m long, but could, in principle, be folded into two 25 m long sections.

The linac is comprised of an electron cyclotron resonance ion source, followed by a radio-frequency quadrupole accelerating the carbon beam to 3 MeV/u, which is further accelerated in a drift tube linac (DTL), then in a coupled DTL linac up to 45 MeV/u. The most essential features to achieve compactness in the ACCIL design are high-gradient structures, each capable of delivering 50 MV/m, that accelerate the beam to the full energy of 450 MeV/u in ~25 m.

Main Design Features

In order to satisfy the ion beam requirements, the following design choices were made, which reflect the main design features of the ACCIL linac:

- The required carbon beam intensities can be provided by a commercial ECR ion source. A 5^+ charge state is selected for carbon ions to avoid contaminants.
- The acceleration starts with a 476 MHz RFQ designed for $^{12}\text{C}^{5+}$, followed by stripping to a 6^+ charge state.
- Further acceleration is provided by a DTL with permanent-magnet quadrupoles (PMQs) designed to focus both proton and carbon beams without tuning.
- A frequency transition to 972 MHz and further acceleration is provided by a CCDTL with compact electromagnetic quadrupoles for alternating focusing.
- The transition to an S-band frequency of 2856 MHz happens at 45 MeV/u, where a CCL using high-gradient structures is designed taking advantage of commercially available klystrons as RF sources and recent developments in high-gradient acceleration.
- High accelerating gradients up to 50 MV/m in S-band structure are possible due to very short RF pulse, less than 1 μs , and manageable voltage breakdown rates. Such short pulses are acceptable because of the low average beam current requirement.
- A relatively high repetition rate of beam pulses, ~100 Hz or higher, is required for fast tumor scanning. This is manageable by adjusting the pulse length while keeping the same overall duty cycle.

Design Parameters of the Different Linac Sections

Table 1 summarizes the most important design parameters for the different sections of the ACCIL linac:

Table 1: Main Design Parameters of ACCIL Sections

Parameter	RFQ	DTL	CCDTL	CCL
Design beam	C^{5+}	C^{6+}	C^{6+}	C^{6+}
Frequency (MHz)	476	476	972	2856
Input energy (MeV/u)	0.025	3	20	45
Output energy (MeV/u)	3	20	45	450
Section length (m)	4	6	10	25
Aperture radius (mm)	2	5	5	3
Kilpatrick factor	2.6	2	2	2.2
Accel. Gradient (MV/m)	1	3.5	12	50
Focusing lattice	–	FODO	FD	doublets
Focus. strength (T/m)	–	140	90	200
Focusing period	–	$4\beta\lambda$	$15\beta\lambda$	$8\beta\lambda$

Being a pulsed machine with a low duty cycle ($\sim 10^{-4}$), the accelerating structures could be operated at relatively high peak surface fields (Kilpatrick factor). The RFQ can be a brazed four-vane structure similar to the linac-4 RFQ operating at 352 MHz [8]. In the DTL, the focusing strength of the non-tunable PMQs is selected to satisfy the carbon beam dynamics while still providing a stable motion for the proton beam. Since the accelerating rate is the same for both beams, the transverse phase advance for protons is significantly larger, 97 deg vs. 23 deg for carbon.

Proton and Carbon Beam Dynamics Simulations

Figure 2 shows results of proton beam simulations from the ion source to the end of the linac while Fig. 3 shows the same results for carbon. The input and output beam parameters are summarized in Table 2.

Table 2: Input and Output Parameters for Proton and Carbon Beams for the ACCIL Linac

Parameter	Proton	Carbon
Input $4^* \epsilon_{t,rms,n}$ ($\pi \cdot \text{mm} \cdot \text{mr}$)	0.33	0.33
Input energy spread (%)	0.1	0.1
Output $4^* \epsilon_{t,rms,n}$ ($\pi \cdot \text{mm} \cdot \text{mr}$)	0.35	0.36
Output $4^* \epsilon_{l,rms,n}$ ($\pi \cdot \text{ns} \cdot \text{keV/u}$)	0.93	0.89
Beam transmission (%)	92	92

It is important to note that the 92% transmission corresponds to the RFQ acceleration efficiency and that no beam loss was observed through the rest of the linac. These results assume 99% stripping efficiency of C^{5+} to C^{6+} at 3 MeV/u following the RFQ.

DEVELOPMENT OF HIGH-GRADIENT STRUCTURES FOR ION BEAMS

As mentioned earlier, the essential part of the ACCIL linac are the S-band high-gradient accelerating structures

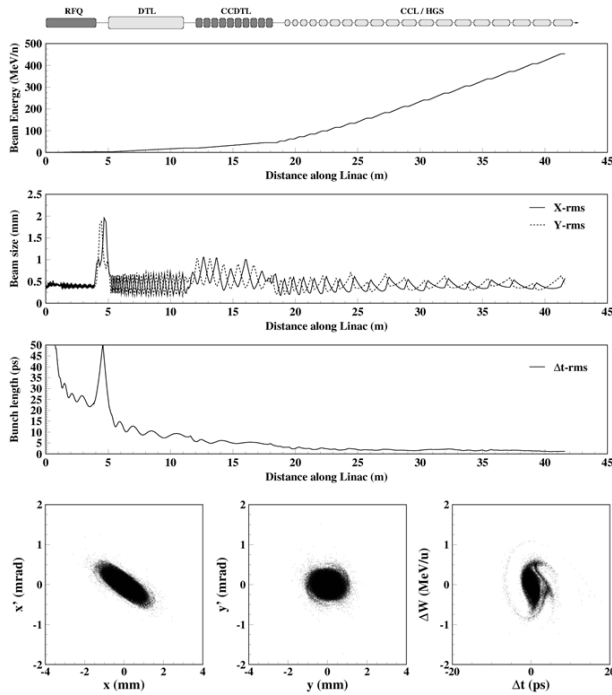


Figure 2: Simulation results for a proton beam in the ACCIL linac up to 450 MeV.

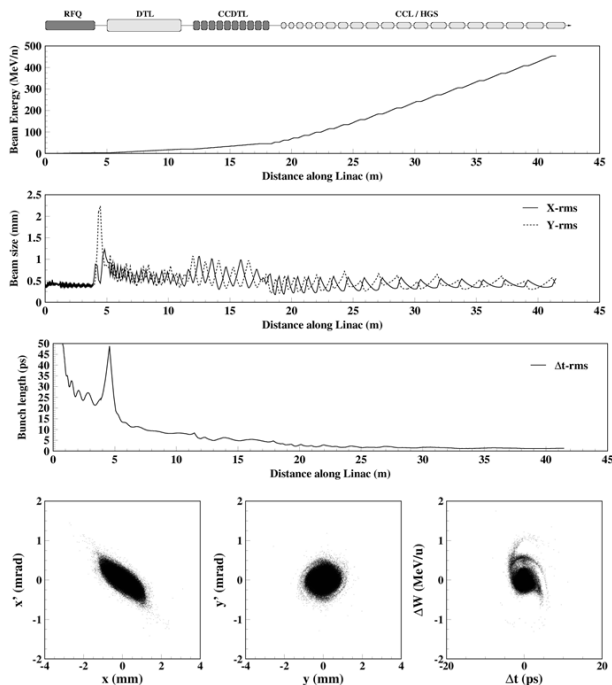


Figure 3: Simulation results for a carbon beam in the ACCIL linac up to 450 MeV/u.

used in the high-energy section of the linac and making it possible to be compact with a footprint under 50 meters.

Such a technology is well developed for electron beams, which become relativistic at an early stage of acceleration and benefit from speed of light accelerating cells, $\beta \sim 1$. In fact, a voltage gradient as high as 52 MV/m has been demon-

strated at Argonne for a five-cell electron beam structure operating at the same frequency (2856 MHz) and pulse structure required for ACCIL [5]. However, ACCIL requires these structures for ion acceleration with a relative velocity β in the 0.3–0.8 range. This makes the accelerating cells more compact compared to $\beta \sim 1$ electron cavity cells, especially at the lowest β . A shorter and more compact cell increases the rate of electric breakdowns and makes dissipating the power required for operation at such high gradients very challenging.

Research and development (R&D) in this field is being pursued at CERN [9], other European institutions and recently in the US by Radiabeam and Argonne [10]. In collaboration with Radiabeam, we have developed a novel design for a $\beta \sim 0.3$ negative harmonic traveling-wave structure capable of delivering such accelerating gradients, ~ 50 MV/m [11]. Designing the cavity to operate in the negative space harmonic leads to a longer cell where reentrant noses can be added for more efficient acceleration while easing power dissipation due to the larger cell volume. This special cavity design for the lowest velocity ions is what distinguishes ACCIL and makes it more compact than other linacs. It allows the transition to high-gradient acceleration to take place at 45 MeV/u, which is much lower than the 70 MeV/u proposed for other linacs.

Standing wave $\pi/2$ -mode options such as side-coupled (SCS) and annular-coupled structures (ACS) are promising designs capable of similar performance. These structures are made of alternating accelerating and coupling cells. The coupling is off axis on one side in the case of SCS, while it's annular surrounding the accelerating cells in the ACS design. Development and prototyping is required for low and medium velocity high-gradient structures to populate the high-energy section of the ACCIL linac.

In collaboration with Radiabeam, we have built and tested at high-power a full prototype NHS cavity for $\beta \sim 0.3$. Figure 4 shows the design, construction and test results for the NHS cavity. A power corresponding to a 50 MV/m accelerating gradient was attained, more details can be found in [12]. We have also designed and built a cold model for an ACS cavity for an ion beam velocity of $\beta \sim 0.4$ as the next accelerating cavity for ACCIL, following the NHS cavity [13]. Figure 5 shows the RF design, fabrication and testing of the cold model for the ACS cavity.

More recently, and due to the need for fast beam scanning for 3D tumor painting, an advanced model of the NHS has been designed to operate at a repetition rate as high as 1 kHz [14]. Figure 6 shows the cell geometry, rf design and engineering model of the latest NHS design. It will be built and tested in the near future.

ACCIL CAPABILITIES AND POTENTIAL APPLICATIONS

The main advantages of ACCIL are fast pulse-to-pulse beam energy change and ion beam switching capabilities. Different ion sources could be used in the front-end to allow

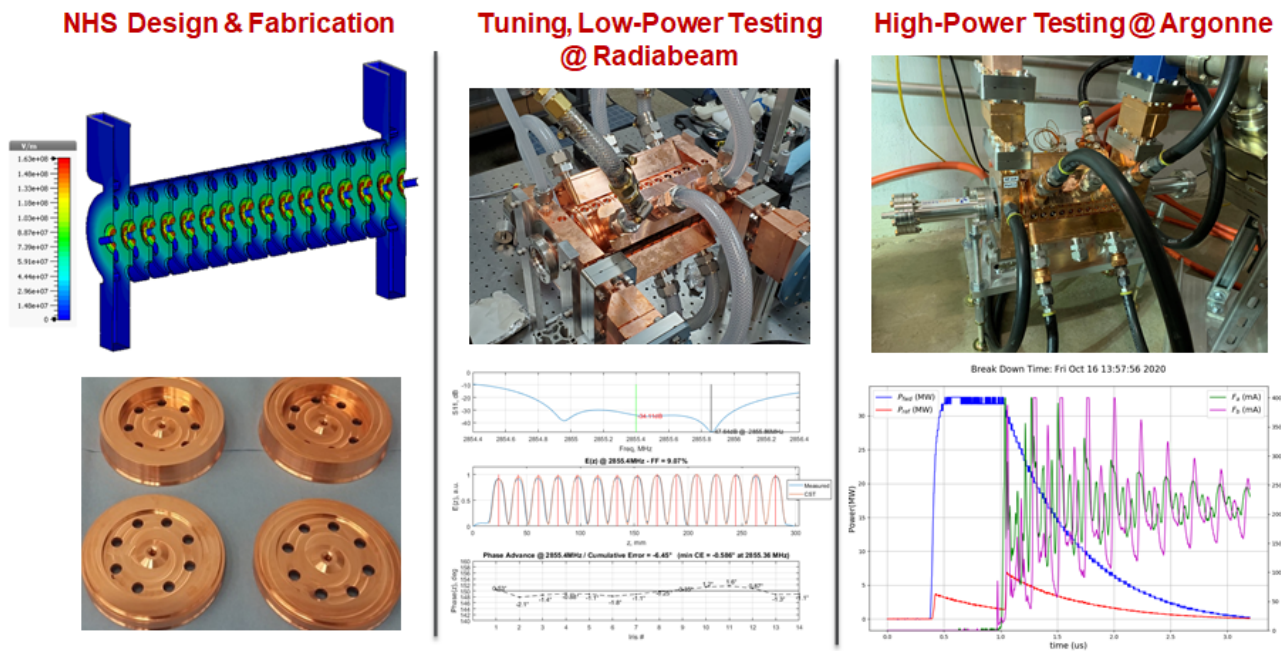


Figure 4: Design, fabrication and high-power testing of the $\beta \sim 0.3$ negative-harmonic traveling-wave structure (NHS) developed by Radiabeam in collaboration with Argonne.

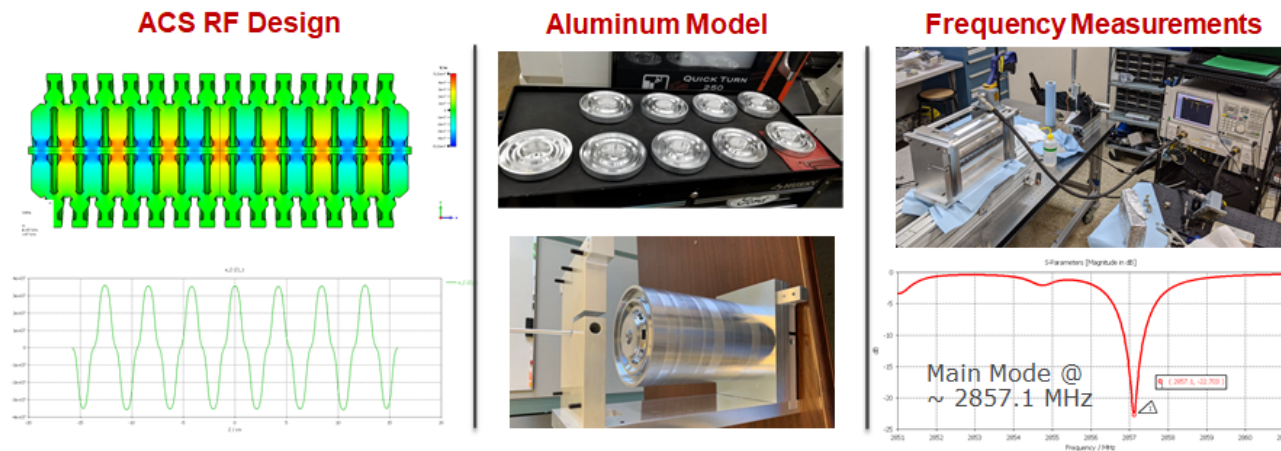


Figure 5: Design, cold model and measurements of the $\beta \sim 0.3$ annular-coupled structure (ACS) developed by Argonne in collaboration with Radiabeam.

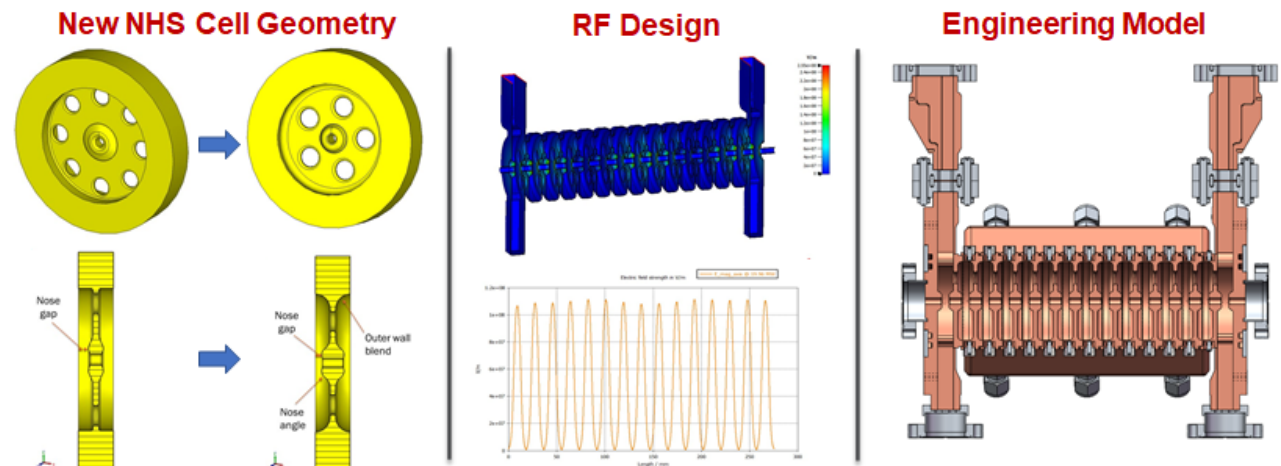


Figure 6: New cell geometry, rf design and engineering model for the latest NHS design developed by Radiabeam.

fast beam switching between different ion species. The delivered beam intensity could also be controlled by adjusting the pulse length at the source or changing the pulse repetition rate, typically from 100 to 400 pulses per second (pps) are possible, and R&D for accelerating structures capable of operating at 1000 pps is ongoing. Ultimately, the tuning flexibility of the ACCIL design will allow fast and effective variable-energy and intensity-modulated multi-ion beam therapy.

ACCIL is capable of accelerating a variety of ion beams from proton to neon, up to a maximum energy of 450 MeV/u. At this energy, ions lighter than carbon, including protons and helium ions, have ranges exceeding the depth of the human body and could therefore be used for imaging purposes, as in proton tomography. It is also possible to deliver these beams with lower energies for treatment. Despite having ranges shorter than the human body, ions heavier than carbon, like oxygen and neon, could still be used for treatment at adjustable energies up to the full linac energy.

As for FLASH therapy, ACCIL's capability is comparable to other existing proton and ion machines [15]. For example, for a proton beam of 230 MeV, losing about half of its energy in the last 10 cm, the energy deposited at 10^{10} p/s in a spot size of $\sim 5 \times 5$ mm² corresponds to a delivered dose rate of ~ 60 Gy/s, which is well within the FLASH dose requirement of 40 Gy/s to 100 Gy/s. For a carbon ion beam of 430 MeV/u, losing about half of its energy in the last 10 cm, the energy deposited at 10^9 p/s in the same stopping volume corresponds to a dose rate of ~ 150 Gy/s, which exceeds the FLASH dose requirement and calls for a larger beam spot size. However, in order to satisfy all cases, for all tumor sizes and beam energies, we would need at least 10 times more particles per second (10^{11} protons/s and 10^{10} carbon/s), which is feasible within the current ACCIL design. In addition, the higher rep. rate of ~ 1 kHz, being developed, will allow faster beam scanning and more flexibility in beam delivery.

FUTURE DEVELOPMENTS AND PLANS

In addition to the general development of high-gradient accelerator structures for low-velocity ions, we identify few areas of R&D of special importance for compact ion linacs and their applications in the medical and industrial sectors, namely:

- Investigating and pushing the beam current limit of compact ion linacs.
- Increasing the repetition rate of high-gradient structures.
- Developing RF sources capable of delivering the required high pulsed power.

In particular, to enable this technology for ion beam therapy, establishing a linac-based advanced ion therapy research center in one of the US National Labs would be a significant step forward and would allow the following applications and further developments:

- Cancer therapy and radiobiology research with all ion species up to neon.
- Imaging and Tomography with ions lighter than carbon: proton, helium, ...
- Combined real-time MRI imaging with beam delivery, significantly enhancing the outcome of ion beam therapy.
- PET imaging using positron emitters (C-11, N-13, O-15, ...) produced in the tumor for dose verification.
- FLASH ion therapy and other applications.

We mention, in particular, an ACCIL-type linac could be installed at the former IPNS site at Argonne National Lab. with the existing required infrastructure [16], which represents a significant cost saving compared to a green field installation. Following the development and commissioning phases, an initial research program including cellular radiobiology and animal therapy could be conducted prior to human therapy and clinical trials for FDA approval.

ACKNOWLEDGEMENTS

The authors would like to thank P. Ostroumov and A. Plastun of MSU/FRIB for their earlier contributions to this work. We also would like to thank J. Nolen and J. Noonan of Argonne for fruitful discussions related to future developments and directions for the proposed advanced ion therapy research center. We also would like to thank T. Smith for guidance during the high-power test of the NHS cavity at Argonne's APS.

REFERENCES

- [1] R. W. Hamm, K. R. Crandall, and J. M. Potter, "Preliminary Design of a Dedicated Proton Therapy Linac", in *Proc. PAC'91*, San Francisco, CA, USA, May 1991, pp. 2583–2586. https://jacow.org/p91/PDF/PAC1991_2583.PDF
- [2] N. Holtkamp, "Status of the SNS* Linac: An Overview", in *Proc. LINAC'04*, Lübeck, Germany, Aug. 2004, paper FR103, pp. 837-841. <https://jacow.org/104/PAPERS/FR103.PDF>
- [3] A. Grudiev *et al.*, "New local field quantity describing the high gradient limit of accelerating structures", *Phys. Rev. ST Accel. Beams*, vol. 12, p. 102001, 2009. doi:10.1103/PhysRevSTAB.12.102001
- [4] U. Amaldi *et al.*, "Proton and Carbon Linacs for Hadron Therapy", in *Proc. LINAC'14*, Geneva, Switzerland, Aug-Sep. 2014, paper THPP061, pp. 992–994. <https://jacow.org/LINAC2014/papers/THPP061.pdf>
- [5] P. Ostroumov *et al.*, "Compact Carbon Ion Linac", in *Proc. NAPAC'16*, Chicago, IL, USA, Oct. 2016, pp. 61–63. doi: 10.18429/JACoW-NAPAC2016-MOA4C004
- [6] S. Benedetti, "New Trends in Proton and Carbon Therapy Linacs", in *Proc. LINAC'18*, Beijing, China, Sep. 2018, pp. 666–671. doi: 10.18429/JACoW-LINAC2018-TH1P03
- [7] D. Ungaro, A. Degiovanni, and P. Stabile, "LIGHT: A Linear Accelerator for Proton Therapy", in *Proc. NAPAC'16*, Chicago, IL, USA, Oct. 2017, pp. 1282–1286. doi: 10.18429/JACoW-NAPAC2016-FRB1I002

- [8] S. Mathot *et al.*, “Mechanical Design, Brazing and Assembly Procedures of the Linac4 RFQ”, in *Proc. IPAC’10*, Kyoto, Japan, May 2010, pp. 807–809. <http://jacow.org/IPAC10/papers/MOPD054.pdf>
- [9] S. Benedetti *et al.*, “RF Design of a Novel S-Band Backward Travelling Wave Linac for Proton Therapy”, in *Proc. LINAC’14*, Geneva, Switzerland, Aug.-Sep. 2014, pp. 992–994. <https://jacow.org/LINAC2014/papers/THPP061.pdf>
- [10] S. Kutsaev *et al.*, “High Gradient Accelerating Structures for Carbon Therapy Linac”, in *Proc. LINAC’16*, East Lansing, MI, USA, Sep. 2016, pp. 44–47. doi:10.18429/JACoW-LINAC2016-MOOP03
- [11] S. Kutsaev *et al.*, “High-Gradient Low- β Accelerating Structure Using the first negative spatial harmonic of the fundamental mode”, *Phys. Rev. Accel. Beams*, vol. 20, p. 120401, Dec. 2017. doi:10.1103/PhysRevAccelBeams.20.120401
- [12] S. Kutsaev *et al.*, “Test Results of a High-Gradient 2.856 GHz Negative Harmonic Accelerating Waveguide”, *IEEE Microwave Wireless Compon. Lett.*, doi:10.1109/LMWC.2021.3081358
- [13] B. Mustapha *et al.*, “Design of a High-Gradient S-Band Annular Coupled Structure”, in *Proc. NAPAC’19*, Lansing, MI, USA, Sep. 2019, pp. 762–764. doi:10.18429/JACoW-NAPAC2019-WEPLM72
- [14] A. Araujo *et al.*, “Optimization of Negative-Harmonic High-Gradient Accelerating Structure for Low-Beta Ions”, presented at NAPAC’22 Conference Proceedings, Aug. 2022, Albuquerque, NM, USA, Aug. 2022, paper WEPA47, to be published.
- [15] S. Jolly *et al.*, “Technical challenges for FLASH proton therapy”, *Physica Medica*, vol. 78, pp. 71–82, Sep. 2020. doi:10.1016/j.ejmp.2020.08.005
- [16] B. Mustapha *et al.*, “Prospects for an Advanced Heavy Ion Therapy Center in the Chicago Area”, *AIP Conf. Proc.*, vol. 2160, p. 050009, 2019. doi:10.1063/1.5127701

ESTABLISHMENT OF THE NEW PARTICLE THERAPY RESEARCH CENTER (PARTREC) AT UMCG GRONINGEN

A. Gerbershagen^{*1}, L. Barazzuol^{1,2}, S. Brandenburg¹, R.P. Coppes^{1,2}, P. Dendooven¹, M.-J. van Goethem¹, E.R. van der Graaf¹, B.N. Jones^{1,2}, P. van Luijk^{1,2}, J.M. Schippers¹, S. Both¹

¹ Particle Therapy Research Center (PARTREC), Department of Radiation Oncology, University Medical Center Groningen, University of Groningen, The Netherlands

² Department of Biomedical Sciences of Cells and Systems, University Medical Center Groningen, University of Groningen, Groningen, The Netherlands.

Abstract

After 25 years of successful research in the nuclear and radiation physics domain, the KVI-CART research center in Groningen has been re-established as the PARTicle Therapy REsearch Center (PARTREC). Using the superconducting cyclotron AGOR and being embedded within the University Medical Center Groningen, it operates in close collaboration with the Groningen Proton Therapy Center.

PARTREC uniquely combines radiation physics, medical physics, biology and radiotherapy research with an R&D program to improve hadron therapy technology and advanced radiation therapy for cancer. A number of further upgrades, scheduled for completion in 2023, will establish a wide range of irradiation modalities, such as pencil beam scanning, shoot-through with high energy protons and Spread Out Bragg Peak (SOBP) for protons, helium and carbon ions. Delivery of spatial fractionation (GRID) and dose rates over 300 Gy/s (FLASH) are envisioned. In addition, PARTREC delivers a variety of ion beams and infrastructure for radiation hardness experiments conducted by scientific and commercial communities, and nuclear science research in collaboration with the Faculty of Science and Engineering of the University of Groningen.

PARTREC FACILITY

The PARTicle Therapy REsearch Center (PARTREC) is a newly established research facility at the University Medical Center Groningen (UMCG). It builds on the success of the former KVI-CART research center and utilizes the superconducting cyclotron AGOR (see Fig. 1) for experimental research, mainly in radiation physics and biology.

Built by a French-Dutch collaboration in Orsay in the period 1987 – 1994 and commissioned in Groningen in 1996, AGOR operated within the KVI-CART research center [1]. It was used for 25 years to perform research in nuclear physics and on fundamental symmetries [2] as well as for detector development, radiation hardness testing [3,4] and radiobiological experiments. Recently besides nuclear physics, radiation and accelerator physics and radiobiology, the research focus has been shifting towards medical applications and therefore the facility and its personnel was integrated into the University Medical Center Groningen (UMCG). Hence,

* a.gerbershagen@umcg.nl



Figure 1: Photograph of the AGOR accelerator.

the new structure, additional goals and the new infrastructure (described in the chapters below) have been formalized via a creation of the new research center named PARTREC (logo in Fig. 2) was created.

Working in close collaboration with the UMCG Groningen Proton Therapy Center (GPTC), PARTREC research activities encompass medical physics, radiation biology experiments, tests of different radiation therapy treatment modalities and development of detector technology. In addition, it provides opportunities for experiments in the domain of radiation hardness, for both the scientific and commercial communities, and nuclear science, in collaboration with the Faculty of Science and Engineering of the University of Groningen.

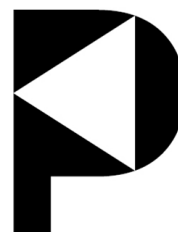


Figure 2: Logo of new PARTicle Therapy REsearch Center (PARTREC).

BEAM DELIVERY CAPABILITIES

The magnetic field of AGOR has a varying value between 1.7 to 4.1 T. It is produced by two superconducting main coils and fifteen trim coils for the precise field shaping, with three iron hill sectors for focussing and defocussing of the circulating beam (see Fig. 3).

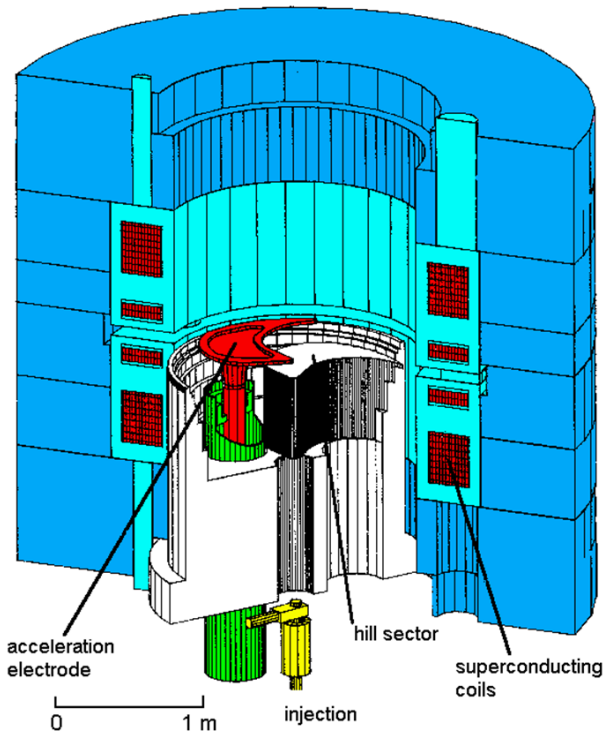


Figure 3: Schematic 3D-model of the AGOR cyclotron interior.

The acceleration is performed by three halfwave RF cavities, which can be mechanically extended or contracted to produce accelerating frequencies of 24–62 MHz with the harmonic numbers of $h = 2, 3$ or 4 . The beam is axially injected from three external ion sources, with two ECR sources for heavy ions and a multi-cusp source for light ions. The extraction happens after 300–500 turns, depending on harmonic mode. The extraction radius is about 870–890 mm (depending on E/A of the beam), with the turn separation at the extraction being in the order of 2–3 mm, which corresponds to the width of the beam.

Given the flexibility of the magnetic field, RF frequency and ion sources, AGOR routinely delivers ion beams of all stable elements up to xenon, within an energy range dependent on the charge-to-mass ratio of the ions. For radiation hardness tests, the facility provides beams of protons at different primary energies and various ions (from He to Xe) at 30 MeV/amu (see diagram in Fig. 4 and setup in Fig. 5). Experiments can be performed at 90 MeV/amu with ions up to Ne. The changeover between the different particle types at the same energy per amu takes typically less than an hour. The possibilities of extending the palette of beams towards still heavier fully stripped ions and lower energies, as suggested by Fig. 4, are under examination [5].

Proton beams with energies relevant for clinical purposes (range in water up to 230 mm) are used for preclinical radiation biology research and proton therapy related physics since twenty-five years. They can be delivered with the continuous intensity of up to 10^9 particles per second per cm^2 with the dose homogeneity level within 1% for a scanned

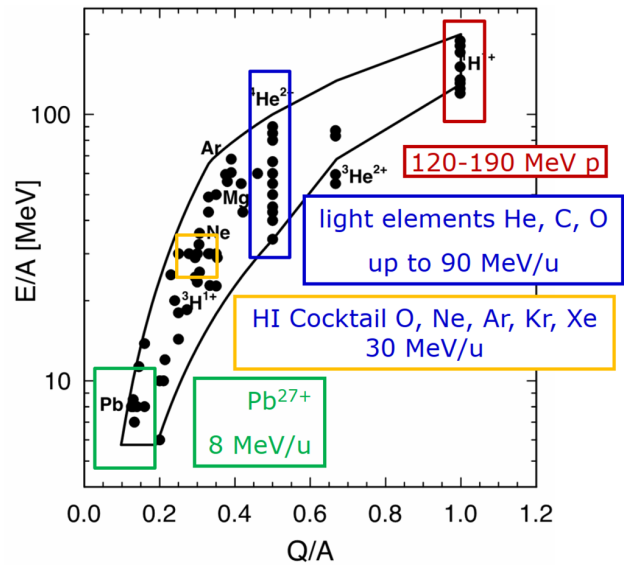


Figure 4: Ion types provided by AGOR, with their extraction energy plotted as function of their charge-over-mass-ratio.

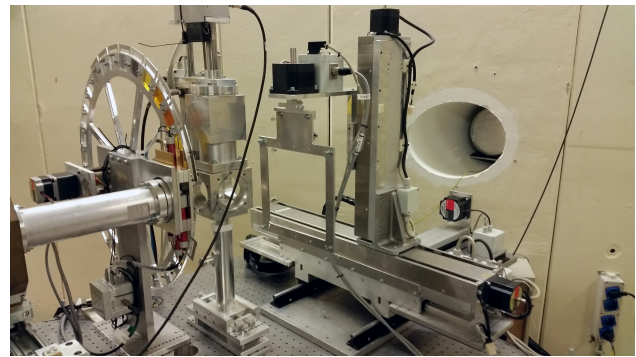


Figure 5: Photograph of the setup for heavy ion irradiations.

beam and within 2-10% for scattered beams, dependent on the irradiation field size. The intensity of the heavier ion beams depends on the ion type and can be varied in the range 10^2 - 10^5 ions / (s cm^2), with the field homogeneities comparable to the ones of proton beams. The LET can be tuned by means of a degrader system just before the sample location. The beam purity is very high (contamination below 10^{-5}) and is verified by means of a silicon detector telescope that stops the ions and provides particle identification.

RESEARCH PLANS WITH THE NEW INFRASTRUCTURE

To extend PARTREC's research capabilities, new infrastructure is currently under development and is expected to become available in 2023.

This includes design, installation and commissioning of a new beam line for the biomedical research, which will free up additional capacities at the existing beam line (see Fig. 6). The new irradiation modalities developed in the framework of this extension will also become available at the existing beam line. These include scattering and pencil



Figure 6: Photograph of the setup for radiobiological irradiations.

beam scanning, shoot-through with high energy protons as well as Spread-Out Bragg Peak for protons and helium. Additionally, the adaptation of the facility for the delivery of spatial fractionation and high dose rates in excess of 300 Gy/s (FLASH) is maturing. An active Proton Radiography program with a variety of detectors in collaboration with GPTC exists and advanced detector technologies, such as PET scanner panels around a head-shaped phantom [6, 7] for the optimization of margins for head-and-neck tumour treatment, are under development (see Fig. 7).

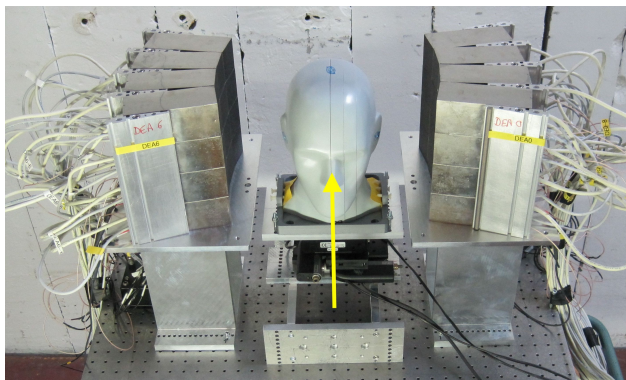


Figure 7: Experimental setup showing the head phantom in-between the 2 PET scanner panels. The head phantom sits on top of 2 orthogonal translation stages and a rotation stage. The direction of the proton beam is indicated by the arrow. The proton beam will be scanned vertically and horizontally with respect to this direction. The proton beam direction and entry point in the head phantom can be accurately controlled by combined translation and rotation of the phantom.

New experimental research [8] on the production of neutron-rich heavy nuclei using multi-nucleon transfer reactions between heavy nuclei (e.g. ^{136}Xe on ^{208}Pb) has recently been started. An upgrade to one of the electron cyclotron resonance (ECR) ion sources is under development, in addition to the work on improvement of transmission from the ion source to the cyclotron extraction. A new experimental station consisting of a 3 T superconducting solenoid frag-

ment separator and MR-ToF mass spectrometer is developed in collaboration with the University of Groningen.

The new infrastructure will allow us and our users to address various research questions such as:

- Radiation effects on electronics.
- Testing of particle detectors [9].
- Biological and physical radiation effects in space.
- Studies of radiation sensitivity variations within normal tissue and tumour.
- Mechanistic studies using various tumour and normal tissue utilizing in vitro and in vivo models to investigate interaction between radiation and systemic treatments, such as chemotherapy, immunotherapy and DNA damage response (DDR) modulators.
- LET and RBE studies for biological treatment planning.
- Advanced radiotherapy dose delivery techniques, such as GRID and FLASH.
- Therapeutic window optimization and translation to the clinic.

Medium-term, it is envisaged for PARTREC to provide users a one-stop-shop facility. This implies that PARTREC will support the users during the complete process of experiment development, the actual irradiation and its follow-up. For the animal irradiations, PARTREC will guide the users with the ethics authorisation process, animal procurement logistics, and will provide on-site animal accommodation with individually ventilated cage (IVCs) with a capacity of 200 rats and mice. For the follow-up the laboratory for animal handling prior and post irradiation could be used. The GronSAI imaging center will provide the possibilities to perform optical, structural and functional imaging of the animal models prior and post irradiation using fluorescence, bioluminescence, PET, CT, MR and multi-modality imaging systems. In addition, the local data management facilities could be used to store, process and analyze the irradiation-related data.

CONCLUSION

The new PARTREC facility will provide the physics, radiation hardness, radiation biology and medical communities with a state-of-the-art, open access research infrastructure for cell/tissue culture and small animal research. The upgrades to the infrastructure will become available from 2023.

ACKNOWLEDGEMENT

Research at PARTREC is supported by the Dutch Cancer Foundation KWF, the Dutch Organization for Scientific Research NWO, the European Union, the European Space Agency ESA, Ion Beam Applications S.A., RaySearch Laboratories, Siemens Healthineers AG, the University Medical Center Groningen and the University of Groningen.

PARTREC is a member of RADNEXT, INSPIRE, CORA-IBER, ARIEL and COST irradiation networks.

REFERENCES

- [1] S. Galès for the AGOR project group, “AGOR: A superconducting cyclotron for light and heavy ions”, in *Proc. ICCA'11*, Tokyo, Japan, Oct. 1989, paper f01, pp. 184–190.
- [2] H. W. Wilschut and K. Jungmann, “Trapped Radioactive Isotopes: micro-laboratories for fundamental Physics (TRIμP)”, *Nuclear Physics News*, vol. 17, no. 1, p. 11-15, 2007. doi:10.1080/10506890701225114
- [3] E.R. van der Graaf, R.W. Ostendorf, M.-J. van Goethem, H.H. Kiewiet, M.A. Hofstee, and S. Brandenburg, “AGOR-FIRM, The AGOR Facility for Irradiations of Materials”, in *Proc. RADECS 2009*, p. 443, 2010. doi:10.1109/RADECS.2009.5994694
- [4] F. Diblen, T. Buitenhuis, T. Solf, P. Rodrigues, E. van der Graaf, M. J. van Goethem, S. Brandenburg, and P. Dendooven, “Radiation hardness of dSiPM sensors in a proton therapy radiation environment”, *IEEE Transactions on Nuclear Science*, vol. 64, no. 7, pp. 1891–1896, 2017. doi:10.1109/TNS.2017.2705522
- [5] B.N. Jones, S.Brandenburg, and M.-J. van Goethem, “AGOR status report”, in *Proc. Cyclotrons'19*, Cape Town, South Africa, Sep. 2019, pp. 256–258. doi:10.18429/JACoW-Cyclotrons2019-TUC03
- [6] I. Ozoemelum, E.R. van der Graaf, M.-J. van Goethem, M. Kapusta, Nan Zhang, S. Brandenburg, and P. Dendooven, “Feasibility of quasi-prompt PET-based range verification in proton therapy”, *Phys. Med. Biol.*, vol. 65, no. 24, p. 245013, 2020. doi:10.1088/1361-6560/aba504
- [7] I. Ozoemelum, E.R. van der Graaf, M.-J. van Goethem, M. Kapusta, Nan Zhang, S. Brandenburg, and P. Dendooven, “Real-Time PET Imaging for Range Verification of Helium Radiotherapy”, *Front. Phys.*, vol. 8, p. 431, 2020. doi:10.3389/fphy.2020.565422
- [8] X. Chen *et al.*, “Stacked-ring ion guide for cooling and bunching rare isotopes”, *Int. J. Mass Spectrom.*, vol. 477, p. 116856, 2022. doi:10.1016/j.ijms.2022.116856
- [9] T. Teichmann, M.J.G. Torres, M.-J. van Goethem, E.R. van der Graaf, J. Henniger, A. Jahn, H.H. Kiewiet, M. Sommer, W. Ullrich, C. Weinhold, and T. Kormoll, “Dose and dose rate measurements in proton beams using the luminescence of beryllium oxide”, *J. Instrum.*, vol. 13, p. 10015, 2018. doi:10.3389/fphy.2020.565422

HEAVY ION STRIPPING

P. Gerhard*, M. Maier

GSI Helmholtzzentrum für Schwerionenforschung GmbH, Darmstadt, Germany

Abstract

Ion stripping is primarily an essential technique for heavy ion accelerators in order to reach higher beam energies within reasonable size and budget limits. Due to the stochastic nature of the stripping process, the resulting ion beam contains ions of different charge states. Therefore, high beam loss is typically associated, making the net stripping efficiency one of the decisive elements of the overall performance of an accelerator facility. Several technical implementations of strippers have been developed and are still being investigated in order to obtain optimal stripping for different ion beams by employing different kinds of stripping targets, namely gaseous, solid and more recently fluid materials. Strippers of the first two types are in operation at GSI. High beam intensities resulting in prohibitive energy deposition and target destruction are increasingly challenging. The foil stripper situated in the transfer line from the UNILAC to SIS18 employs a magnetic sweeper as a possible remedy. At the same time, it offers four stripping options to be used in parallel. Optimizing a stripper may potentially increase the overall performance by a large factor with less effort than other actions. This gave rise to the pulsed gas stripper project at the GSI UNILAC, which aims at the introduction of hydrogen as regular stripping target.

INTRODUCTION

The GSI accelerator facility consists of the UNiversal Linear ACcelerator UNILAC, the SchwerIonenSynchrotron (heavy ion synchrotron) SIS18, two storage rings (ESR and CRYRING@ESR) and the decelerator HITRAP. Several stripping devices are operated in the area of UNILAC and SIS18 in order to facilitate acceleration and deliver ions with the charge states required by the various experiments. Regarding the wide range of ion energies and beam intensities, different stripping technologies are applied. Figure 1

* p.gerhard@gsi.de

shows a schematic overview of the UNILAC and the locations of the stripping devices. Stripping at the lowest energy of 1.4 MeV/u between the high current injector and the Alvarez DTL is achieved by a gas stripper, while all subsequent strippers use foils or sheet metal. The SIS18 area and its strippers are not shown. UNILAC and SIS18 possess the unique feature to deliver individual beams made from up to three different ion species in a rapid time multiplex scheme. This has to be supported by the strippers as well.

UNILAC together with SIS18 will serve as the heavy ion injector chain for the Facility for Antiproton and Ion Research (FAIR) [1], currently under construction. The reference projectile for FAIR is the heavy ion ^{238}U . To meet the beam requirements for FAIR, upgrade programs for both accelerators have been and are being conducted to increase the delivered beam intensities especially for heavy ions. The task for the UNILAC is to deliver $\approx 3 \cdot 10^{11} \text{ U}^{28+}$ ions within 100 μs pulse length and adequate emittance at repetition rates of up to 2.7 Hz to the subsequent synchrotron. A major step in this pursuit will be the use of hydrogen in the gas stripper in addition to the traditional nitrogen operation. The hydrogen stripping target will improve the mean charge state of all stripped ions. For heavy ions, the width of the charge state distribution will be decreased, which results in an enhanced beam intensity of up to 60% [2]. This makes use of the electron capture suppression associated with low Z targets.

STRIPPING FUNDAMENTALS

A stripper consists of a gaseous or solid, infrequently liquid or plasma stripping target, which is placed in the beam line. While the ions cross it, they experience collisions with the target atoms. Many devices will therefore lead to stripping as a side effect. Stripping is the result of charge transfer processes caused by the collisions between the fast moving ions of the particle beam and the stationary target atoms.

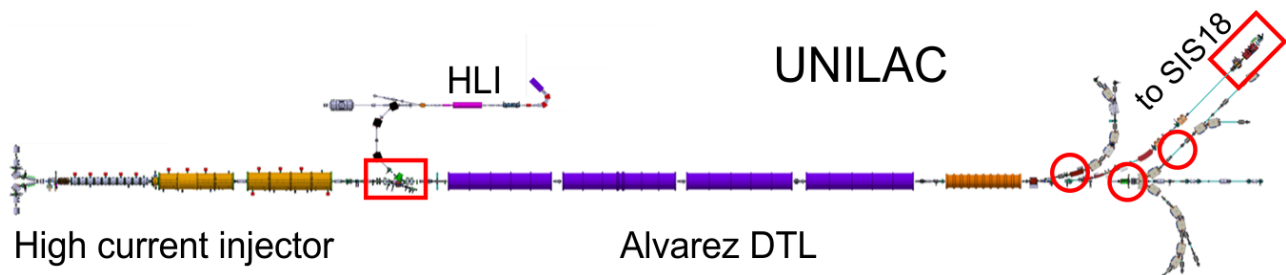


Figure 1: The UNILAC and its main constituents: The high current injector with two source terminals and an RFQ/IH-DT linac (left), the high charge state injector HLI (top centre), and the main Alvarez-DT linac (centre). To the right are several user branches and the transfer channel to the synchrotron. Stripper sections for general accelerator operation are framed with red boxes, strippers for special user requirements with red circles.

Both electron loss and capture processes happen, increasing and reducing the ion's charge state respectively. Hence, stripping is a stochastic process. The corresponding cross sections σ_L and σ_C for electron loss and capture depend on several parameters: Ion charge state q , energy E and atomic number Z , target atomic number Z_T and density ρ , and the type of transfer process, i. e. single or multiple electron.

While the ions pass through the target, their charge state (and energy) changes, which means σ_L and σ_C change. Given a target of sufficient thickness $x = x_\infty$, i. e. the number of collisions high enough, the stripping approaches an equilibrium, where $\sigma_L = \sigma_C$ ¹. Due to the statistical nature of the underlying electron loss and capture processes, the ions populate a charge state distribution. The correlation between the parameters above and the mean value \bar{q} and width d of the distribution is generally described by semi-empirical relations, especially for low energy beams.

Due to the inherent collisions with the target, the beam will experience energy loss and emittance growth by straggling, both deteriorating the beam quality. The energy deposition leads to a degradation or even destruction of the stripping target, especially with solid targets. Special effort has to be made to keep this within reasonable limits. Recently, liquid targets have been developed [3] in order to circumvent this and still profit from the density effect. As mentioned above, stripping results in a charge state spectrum. Typically, a stripper is therefore followed by a charge state separator, which selects ions of one charge state and eliminates all others². Thus, substantial loss of beam is always linked to stripping.

In most accelerator applications, one is interested in increasing the charge state in order to facilitate further acceleration of the ions. Figures of merit may be the resulting charge state and beam intensity. Optimizing the stripping may be achieved by choosing accessible target parameters accordingly. Changing the beam parameters would also do, but may rarely be possible or only at high cost. A more subtle optimization may make use of ion shell effects. The mean charge state can be increased by changes of the target density, especially for gaseous targets, or by using solid targets due to the density effect. If equilibrium is not yet reached, the target thickness may be increased, at the expense of more energy loss and emittance growth. Increasing the stripping efficiency is more challenging, because the width of the charge state distribution is generally not very sensitive to any of the parameters, including beam energy. Changing the target material can be an option: Especially low Z targets like hydrogen lead to the suppression of electron capture processes. This does not only increase the equilibrium mean charge state, but also leads to narrower distributions for heavy ions and hence to a higher fraction of ions with the charge state desired. For more basic information about stripping see for instance [4–7].

¹ Further collisions only lead to a slow change of the equilibrium due to the progressive energy loss.

² Applications using more than one charge state exist.

GAS STRIPPER

At low ion velocities, targets have to be thin but robust, since energy loss in the target is relatively high. This renders solid state targets inapplicable despite the desirable high charge states achievable. Gaseous targets are a suitable choice. The drawbacks are lower mean equilibrium charge states and the inevitable gas load in the accelerator vacuum system.

The first stripper along the UNILAC is applied to high current beams at an ion energy of 1.4 MeV/u. Figure 2 shows the corresponding stripper section schematically in its current form after the redesign, which was implemented together with the installation of the HSI in 1999 [8].

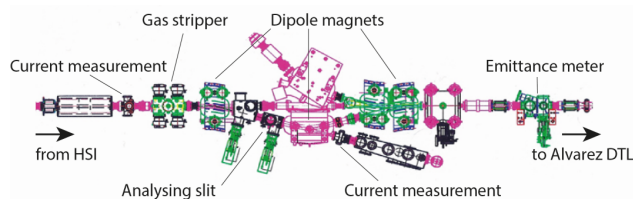


Figure 2: The UNILAC gas stripper section between the high current injector HSI and the Alvarez DTL. The central part consists of a 15°-30°-15° dogleg composed of three dipoles for charge state separation.

Heavy ions like $^{238}\text{U}^{4+}$ are provided at low charge states but with high intensity by two sources located at the high current injector (german "HochStromInjektor") HSI. This injector is designed to accelerate ions with a mass-to-charge ratio of $A/q \leq 65$ to 1.4 MeV/u. Since the following Alvarez DTL is limited to $A/q \leq 8.5$, a stripper is needed to increase A/q accordingly.

Historic Alternatives

In the early years of GSI both a foil and a gas stripper were operated between the then Wideröe type *prestripper* (today HSI) and the *poststripper* (Alvarez DTL). The foil stripper delivered higher charge states than the gas stripper (U^{41+} vs. U^{28+}) due to the density effect, which allowed for higher final energies. For particle currents above 1 μA the 40 $\mu\text{g}/\text{cm}^2$ target foils were destroyed in short time [9]. As beam intensities increased, foil operation was dropped. A comeback of foil stripping at this location was tried many years later and is described in a later section.

Current Jet Stripper

The stripping target is created by a supersonic N_2 jet generated by a Laval nozzle with a back pressure of up to 0.45 MPa, which crosses the beam line orthogonally. The main part of the gas load is pumped by a 10 000 m^3/h roots pump. Spreading of the gas along the beam line is reduced by the jet itself, which directs the gas into the pump, by two differential pumping sections next to the stripper and three aperture diaphragms reducing the conductance between them.

Content from this work may be used under the terms of the CC BY 4.0 licence (© 2022). Any distribution of this work must maintain attribution to the author(s), title of the work, publisher, and DOI

H₂ Target Development

With the current N₂ jet stripper just about 12–15% of the incoming U⁴⁺ ions are stripped into the desired charge state 28+. In order to improve the stripping efficiency for heavy ions, the width d of the charge distribution has to be reduced. In principle changing the beam energy E and the target's x_∞ , ρ , and Z_T are conceivable. Changing E is not really feasible and has no significant impact on the width, but on \bar{q} . Target thickness and density of the nitrogen jet essentially possess no potential for development, either. However, introducing a low Z gas as stripping target is known to have an effect on the width of the charge distribution for heavy ions. This is acceptable since for light ions the beam intensities achieved are already sufficient to fill the synchrotron up to the space charge limit. As a side effect, the mean equilibrium charge state for all ion species is also rising. A development was started accordingly, and about 10 years ago comparative tests using N₂, CH₄ and H₂ were carried out at the jet stripper [10]. The highest mean charge states achieved were 27+ for nitrogen and 25+ for methane, while for hydrogen no sufficient target thickness could be reached, the highest charge state observed being 21+. With methane at high pressures, the charge state separation deteriorated.

The tests revealed, that the stripper device had to be modified on order to reach sufficient target thickness for hydrogen. The pumping speed for light gases was identified as the main limiting factor. The basic idea to overcome this limitation is to exploit the low duty factor f of the ion beam. For synchrotron operation, which is the reference for FAIR, $f \ll 1\%$. The continuous operation of the jet is not required, and the gas load on the vacuum pumps can be reduced by about two orders of magnitude, if gas is injected only while a beam pulse passes the gas stripper. The pulsed gas injection was realized by applying a fast, electro-magnetically actuated gasoline valve normally used for direct fuel injection in au-

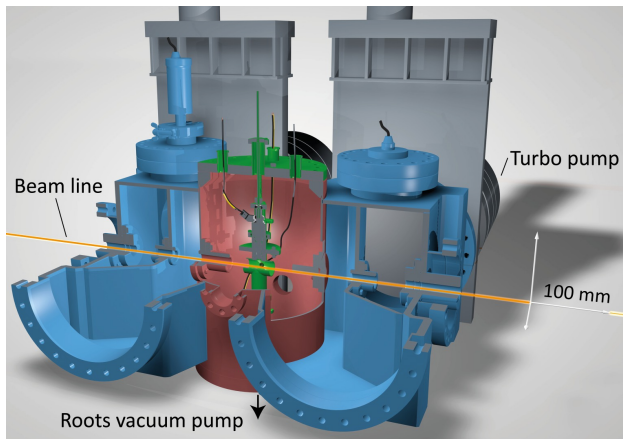


Figure 3: Schematic illustration of the pulsed gas stripper setup. The pulsed gas injection (green) is mounted on the top flange of the main chamber (red). Together with the adjacent sections (blue) this constitutes a four stage differential pumping system (from [11]).

tomotive applications. Its operation is synchronized with the accelerator timing. Shortly (≈ 0.4 ms) before the beam pulse passes the gas stripper, the valve opens to build up the gas target in the interaction zone, and closes immediately afterwards. A new setup was developed (Fig. 3), serving as a mount for the valve and replacing the Laval nozzle by a short tube enclosing the interaction zone of the stripper [11]. The gas is injected into this tube and is thereby confined, increasing the target density while at the same time reducing the gas load on the vacuum system.

Results for U ions stripped with several gases using this setup are shown in Fig. 4 [12]. For all gases except H₂, equilibrium distributions could be measured. In comparison to N₂, both He and H₂ lead to a reduced width and increased stripping efficiency of more than 20% for U²⁸⁺. Even though

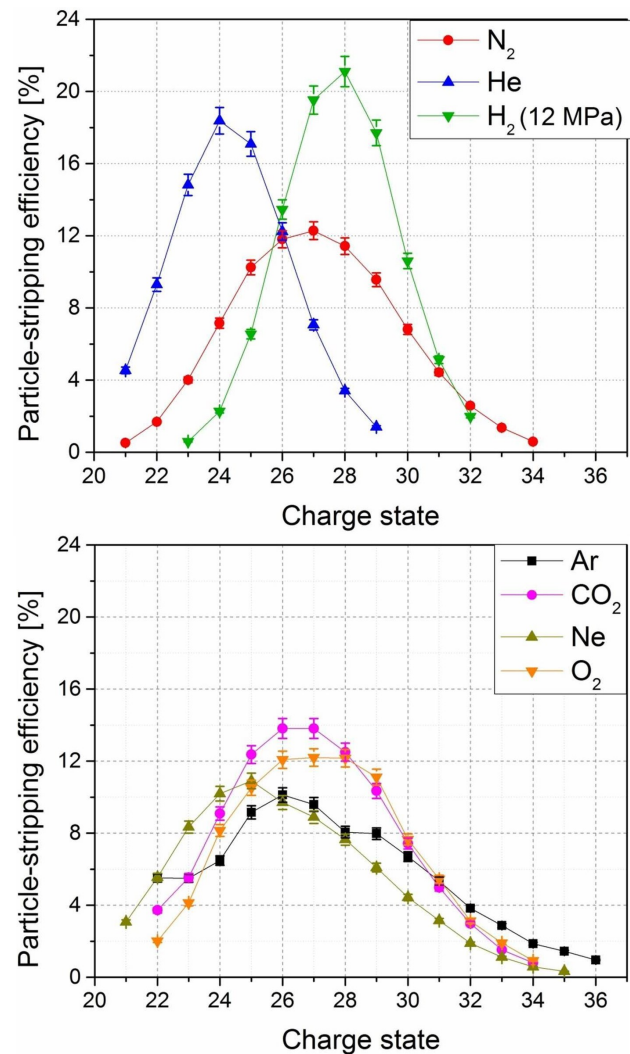


Figure 4: Charge state distributions for U stripped by N₂, He and H₂ (top), Ar, CO₂, Ne and O₂ (bottom), measured with the pulsed gas stripper at 1.4 MeV/u beam energy. The graphs show the equilibrium stripping efficiencies f_q as functions of the charge state q except for H₂, where the distribution was still not equilibrated at 12 MPa back pressure (from [12]).

equilibrium was not achieved, hydrogen also leads to a higher mean charge state of 28+, while helium shows a reduced $\bar{q} = 24$ compared to 27+ achieved with nitrogen. Ne, O₂, Ar, and CO₂ generate relatively broad charge state distributions at average charge states between 25+ and 27+. They do not provide any advantage in relation to nitrogen. With an enhanced setup, equilibrium charge state distributions could later be measured for hydrogen, too [13]. For uranium, the most populated charge state 29+ reached a fraction of 21%. For medium heavy ions like Ti or Ar, there is no significant effect on the distribution width, but the mean charge state is raised by about 3. This may enable the use of shell effects for some ion species to increase the fraction stripped into a certain charge state.

To Regular Operation with H₂

After the proof of principle was achieved, the aim is to turn the test setup into a facility suitable for regular operation. At the end of a three week test run in 2016, the fast valves showed significant leakage problems. The reason lies in the valve seating, which relies on the damping by a liquid fuel when closing. The first step on the way therefore was to find and evaluate a suitable valve. A solution was found by employing intake-manifold fuel injection valves also originating from automotive applications, but designed for gaseous fuels. The main difference is that they are operated at much lower back pressures of up to 1.2 MPa, while the direct injection valves required up to 25 MPa. The characterisation of the electrical, temporal and gas dynamical properties was carried out on a newly established test bench. It revealed, that the new valves were much slower especially when closing. In the meantime, parameters for safe and efficient operation of the valves have been established and verified with beam, and a new stripper setup was designed to accommodate two of the new valves (Fig. 5) [14].

The introduction of pulsing implicates, that temporal aspects such as build up, depletion and stability of the target are now of importance. A measurement related to this is shown in Fig. 6, where a complete target cycle (build up, flattop and depletion) is probed by a 5 ms long Ar²⁺ beam pulse. The valve is opened by applying a voltage of 90 V (yellow curve) to the valve coil about 100 μs before the beam pulse starts (red curve). This induces a steep rise of the coil current (cyan curve) despite of the coil's inductance. After 180 μs, a current of 2 A is reached and the valve opens. The subsequent build up of the stripping target can be observed by the stripped Ar¹²⁺ beam current (green curve) rising. Then the valve is kept open by a lower current and voltage for the remaining pulse duration. After 4 ms, the voltage is reversed (steep drop in yellow curve) to purge the coil current and thereby close the valve quickly. As can be seen in the green curve, it takes about 600 μs for the valve to close and the target to diminish after the current purge was initiated. During the beam pulse, the stripping efficiency stays sufficiently constant. The voltage and current profiles can be controlled by a fast, dedicated magnetic valve controller and were optimised for minimal heat load on the coil. The

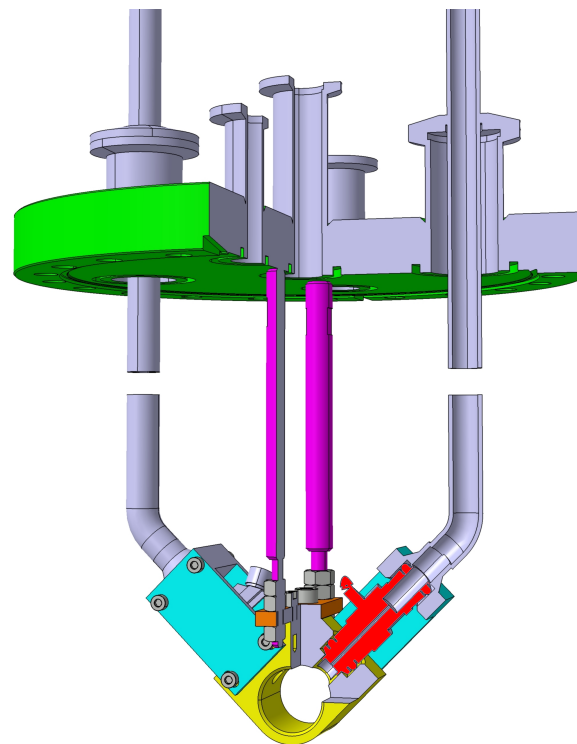


Figure 5: Sketch of the latest stripper setup accommodating two fast valves for gaseous media. One valve is indicated in red. Gas supply is from top via the tubes. The interaction zone is within the yellow tube at the bottom.

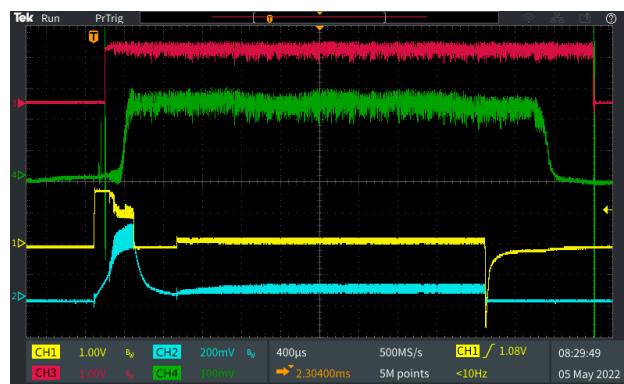


Figure 6: Stripping of Ar²⁺ ions with the pulsed gas stripper. Shown are the current of the incoming beam (red) and the stripped Ar¹²⁺ beam (green), voltage (yellow) and current (cyan) applied to the valve. Details see text.

timing for regular operation will be optimised for minimal gas load and stable target provisioning.

Several experimental beam times at the UNILAC have been successfully conducted with the new setup. No valve failures occurred. A long-time test with hydrogen operation is still pending due to the lack of an adequate safety certificate. The main challenge remains in specifying and implementing a concept for fully automated, safe operation of the whole gas stripper facility, including the provision and disposal of the hydrogen.

FOIL STRIPPER

The GSI facility was extended by the heavy ion synchrotron SIS18 and the experimental storage ring ESR at the end of the 1980s. Highly charged ions were to be provided for the synchrotron in order to reach highest beam energies for its users. Injection energy of the synchrotron was sufficiently high to allow for a foil stripper to be integrated into the beamline connecting the SIS18 to the UNILAC, the so-called transfer channel TK. For charge state separation, a dogleg inherent to the TK design consisting of two 11.25° dipoles was used. The drawback of this solution was the long distance of more than 20 m between the stripper and the charge state separation, resulting in prolonged degrading of the beam by strong space charge effects.

This foil stripper was upgraded in 1999 in the course of the HSI installation, when a fast sweeper magnet was added to distribute the energy loss over a larger foil area [15]. Another upgrade took place in 2008 with the installation of a dedicated charge state separation in the vertical plane directly behind the stripper [16]. The separator primarily consists of four 35° dipole magnets.

At the standard energy of 11.4 MeV/u, the mean charge state for uranium is 73+, exploiting the density effect of the solid target. Due to the variety of accelerated ions from Li to U and the substantial foil wear caused by the energy loss of up to 300 keV/u, the stripper is equipped with a foil carousel with 42 slots, each slot holding two foils in an aluminium frame (see Fig. 7).



Figure 7: Target frame of the transfer channel foil stripper with two foils mounted in a slot of the foil carousel. The large foil shows deformation caused by the energy deposition of the beam.

The four operating modes are illustrated in Fig. 8. Both foils can be used with low current beams in two static modes without engaging the fast sweeper. This is accomplished by deflecting the beam onto the required foil by a kicker magnet. The large foil may additionally be used in the sweeping mode for high current beams. In this mode, the beam spot is swept over the large foil within a minimal beam pulse length of 120 μs, starting at maximum deflection and ending on the regular beam axis. This is accomplished by sweeper magnets, which are precharged to maximum deflection before the beam pulse starts, and then discharged linearly within

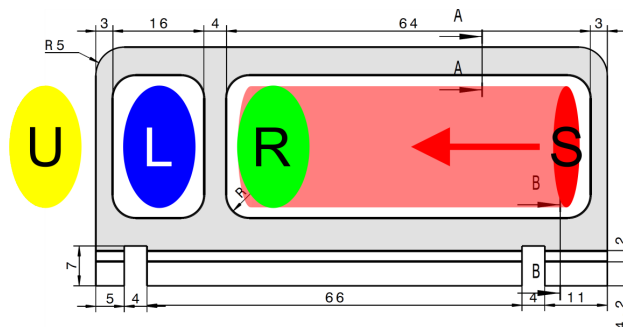


Figure 8: Illustration of the four operating modes of the transfer channel foil stripper. Coloured ellipses indicate the beam spot positions wrt the foil frame (grey) for the different operating modes. Blue spot (L) and Green spot (R): Static stripping via the left, small foil and the right, large foil, respectively. Yellow spot, U: Unstripped mode. Red spot, S: Sweeper mode, the beam spot position at the start of the beam pulse is indicated, while the light red area depicts the foil painting.

the beam pulse length. Pulses shorter than 120 μs are only painted over a part of the foil due to the limited discharge speed. The static mode can also be used to deflect the beam out of the frame and circumvent the stripper. This enables the delivery of the same ion in a high and low charge state simultaneously and represents the fourth, unstripped mode of operation.

Both modes use different beam dynamics. For the static mode, the beam spot on the foil is maximised in order to spread the energy loss over the foil. In the sweeper mode, the beam is focused in the horizontal plane, which is used for sweeping and also for filling the phase space of the synchrotron during injection. Thereby, the emittance growth in that plane is minimised, which matches the reduced acceptance of the synchrotron in that plane. In the vertical plane, the beam spot is matched to the foil size again to spread the heat.

For regular operation, carbon foils made by the GSI target laboratory with thicknesses of approximately 200, 400 and 600 μg/cm² are used. For special purposes, foils between 50 and 1000 μg/cm² have been applied. Each slot is equipped with foils of different thicknesses and all combinations of the standard types are loaded into the carousel. This enables the optimal stripping of different light and heavy ions at the same time in terms of energy loss, foil degradation, emittance growth and charge state. The number of slots usually holds enough spare foil combinations to last for a whole beam time.

Other Foil Strippers At GSI

In the experimental hall of the UNILAC, three more foil strippers are operated for the low energy beam branches. According to the needs of the different users, each of these strippers contains a simple target ladder mounted on a linear drive actuated either by a stepper motor or pneumatically, depending on the number of target positions. The ladders

are equipped with carbon foils with thicknesses typically in the range of 50–150 $\mu\text{g}/\text{cm}^2$. A similar ladder is shown in Fig. 9.

High Energy Stripper Another stripper is located in the High Energy Beam Line HEBT following the SIS18. It offers nine target positions arranged in a 3-by-3 matrix, containing thin sheet metal targets made from copper, tantalum, and beryllium as well as carbon targets. Corresponding to the much higher energies of the ions accelerated in the synchrotron, target thicknesses range from 5 to 100 mg/cm^2 . The mean charge state for uranium at 300 MeV/u stripped through a 40 mg/cm^2 Cu target equals 91+, i. e. hydrogen like uranium. Fully stripped heavy ions can be produced with high efficiencies given high enough ion velocity, as the mean equilibrium charge state can be pushed above the atomic number, eliminating the width of the charge distribution. Another consequence of the high ion velocities is the negligible energy deposition, which means that the targets show no deterioration. This stripper can therefore be operated for long times with high intensity beams without the need for a target service.

Low Energy Foil Stripping In 2010 an attempt was made again to use carbon foils instead of the gaseous N_2 target at the location of the gas stripper. Stripping efficiencies around 20% for U^{39+} and U^{40+} were achieved, depending on the foil thickness of 20–50 $\mu\text{g}/\text{cm}^2$ [17]. However, the lifetime of the foils was generally limited to a few hours due to thermal stress and irradiation effects. Some foils survived only a few beam pulses. Figure 9 shows one of the foil target holders used during these tests before and after the foils were irradiated with a high current beam. Considerable effort was put into investigations on the strongly differing lifetimes of individual foils, and to develop a procedure how to enhance the durability. The initiative was not successful, and foil stripping was not adopted for regular operation at this location.

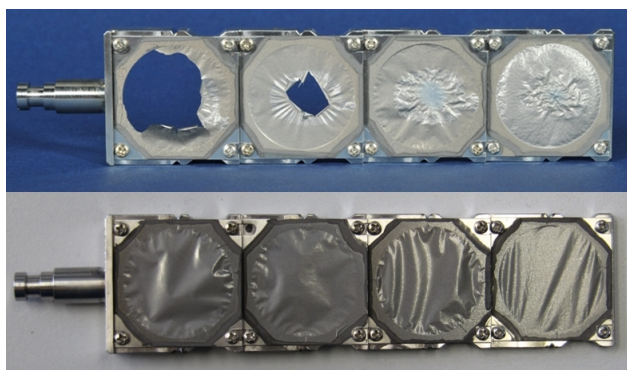


Figure 9: Foil ladders used during the 2010 low energy foil stripper tests. The same foil stripper before (bottom) and after (top) high current operation. 11 kJ were deposited in the third foil from left without any observed influence on the beam parameters [17].

LIQUID STRIPPER

Over the past years, a stripper based on a liquid lithium target has been developed and recently commissioned at FRIB [3, 18] for high current, medium energy heavy ion beams. This approach tries to combine the advantages of a quickly renewing target like a gas stripper with the beneficial stripping properties of a solid state stripper. The obvious challenge is handling of the liquid and therefore hot and highly reactive lithium. Special development and effort also had to be put into generating a sufficiently large, thin and homogeneous target without any backing in the interaction zone.

PLASMA STRIPPER

End of the 1980s, an experiment about energy loss of heavy ions in a plasma target was conducted by Hoffmann *et al.* at the location of the UNILAC gas stripper [19]. While the main topic was energy loss, this work also deals with the stripping of heavy ions in a plasma target. The results show that at 1.4 MeV/u, far higher charge states can be achieved by stripping in a hydrogen plasma in comparison to a conventional cold gas target. The drawback, of course, is the increased energy loss.

CONCLUSION

The operation of the GSI heavy ion accelerator facility would not be feasible without the repeated application of stripping devices along the beam line in order to increase the charge state. The physics of stripping requires different technological solutions and links significant beam loss inseparably to it. At low energies, target destruction by high current beams make gaseous targets the best choice, limiting the charge states reachable. Improvements can be achieved by introducing low Z targets. This is pursued at GSI by replacing the standard nitrogen with hydrogen. The main goal is to increase the stripping efficiency for heavy ions. A corresponding development is in progress, but safety requirements are especially challenging in the environment of a nearly 50 year old accelerator facility. Commissioning of the regular hydrogen stripping is anticipated for 2025. At medium energies, foil stripping can already be applied operationally, permitting access to higher charge states by the density effect. Additional effort is necessary to spread the energy loss over extended foil areas. At GSI, this is achieved by a magnetic sweeper. Stripping at high energies after the synchrotron is more relaxed since it involves no energy deposition in the target. The targets need to be thicker and are mechanically more robust.

REFERENCES

- [1] FAIR Baseline Technical Report, vol. 2, GSI Darmstadt, pp. 335ff, 2006.
- [2] W. Barth *et al.*, “ U^{28+} -intensity record applying a H_2 -gas stripper cell”, *Phys. Rev. ST Accel. Beams*, vol. 18, p. 040101, 2015. doi: 10.1103/PhysRevSTAB.18.040101

- [3] F. Marti, P. Guetschow, J.A. Nolen, Y. Momozaki, and C.B. Reed, “Development of a Liquid Lithium Charge Stripper for FRIB”, in *Proc. HIAT’15*, Yokohama, Japan, Sep. 2015, paper TUA1I01, pp. 134–138.
- [4] H.-D. Betz, “Charge states and charge-changing cross sections of fast heavy ions penetrating through gaseous and solid media”, *Rev. Mod. Phys.* vol. 44, no. 3, p. 465, 1972.
- [5] H. Okuno *et al.*, “Low-Z gas stripper as an alternative to carbon foils for the acceleration of high-power uranium beams”, *Phys. Rev. ST Accel. Beams*, vol. 14, p. 033503, 2011. doi: 10.1103/PhysRevSTAB.14.033503
- [6] H. Kuboki *et al.*, “Charge state distribution of ^{86}Kr in hydrogen and helium gas charge strippers at 2.7 MeV/nucleon”, *Phys. Rev. ST Accel. Beams*, vol. 17, p. 123501, 2014. doi: 10.1103/PhysRevSTAB.17.123501
- [7] I. Yu. Tolstikhina and V. P. Shevelko, “Influence of atomic processes on charge states and fractions of fast heavy ions passing through gaseous, solid, and plasma targets”, *Phys.-Usp.*, vol. 61, no. 3, p. 247, 2018.
- [8] W. Barth and P. Forck, “The new gas stripper and charge state separator of the GSI high current injector”, in *Proc. LINAC’00*, Monterey, USA, Aug. 2000, paper MOD13, pp. 235-237.
- [9] N. Angert, K. Blasche, B. Franczak, B. Franzke, and B. Langenbeck, “The Stripper-Section of the Unilac”, in *Proc. LINAC’76*, Chalk River, Canada, Sep. 1976, paper E08, pp. 286–290.
- [10] B. Schlitt *et al.*, “Charge Stripping Tests of High Current Uranium Ion Beams with Methane and Hydrogen Gas Strippers and Carbon Foils at the GSI UNILAC”, in *Proc. IPAC’13*, Shanghai, China, May 2013, paper THPWO010, pp. 3779–3781.
- [11] P. Scharrer *et al.*, “Stripping of High Intensity Heavy-Ion Beams in a Pulsed Gas Stripper Device at 1.4 MeV/u”, in *Proc. IPAC’15*, Richmond, VA, USA, May 2015, pp. 3773–3775. doi: 10.18429/JACoW-IPAC2015-THPF035
- [12] P. Scharrer *et al.*, “A Pulsed Gas Stripper for Stripping of High-Intensity, Heavy-Ion Beams at 1.4 MeV/u at the GSI UNILAC”, in *Proc. HIAT’15*, Yokohama, Japan, Sep. 2015, paper TUA1C01, pp. 144–147.
- [13] P. Scharrer *et al.*, “Developments on the 1.4 MeV/u Pulsed Gas Stripper Cell”, in *Proc. LINAC’16*, East Lansing, MI, USA, Sep. 2016, pp. 387–389. doi: 10.18429/JACoW-LINAC2016-TUOP03
- [14] P. Gerhard *et al.*, “Development of Pulsed Gas Strippers for Intense Beams of Heavy and Intermediate Mass Ions”, in *Proc. LINAC’18*, Beijing, China, Sep. 2018, pp. 982–987. doi: 10.18429/JACoW-LINAC2018-FR1A05
- [15] J. Glatz, J. Klabunde, U. Scheeler, and D. Wilms, “Operational Aspects of the High Current Upgrade at the UNILAC”, in *Proc. LINAC’00*, Monterey, CA, USA, Aug. 2000, paper MOD12, pp. 232–234.
- [16] W. Barth, L. A. Dahl, P. Gerhard, L. Groening, M. Kaiser, and S. Mickat, “Commissioning of the New GSI-Charge State Separator System for High Current Heavy Ion Beams”, in *Proc. LINAC’08*, Victoria, Canada, Sep.-Oct. 2008, paper MOP046, pp. 175–177.
- [17] W. A. Barth *et al.*, “High Current U40+-operation in the GSI-UNILAC”, in *Proc. LINAC’10*, Tsukuba, Japan, Sep. 2010, paper MOP044, pp. 154–156.
- [18] T. Kanemura, “Liquid lithium charge stripping commissioning with heavy ion beams”, presented at HIAT’22, Darmstadt, Germany, June 2022, paper MO4I2, this conference.
- [19] D. H. H. Hoffmann *et al.*, “Energy loss of heavy ions in a plasma target”, *Phys. Rev. A* vol. 42, p. 2313, 1990. doi: 10.1103/PhysRevA.42.2313

LIQUID LITHIUM CHARGE STRIPPER COMMISSIONING WITH HEAVY ION BEAMS AND EARLY OPERATIONS OF FRIB STRIPPERS*

T. Kanemura[†], N. Bultman, M. LaVere, R. Madendorp, F. Marti, T. Maruta, Y. Momozaki¹, J. A. Nolen¹, P. N. Ostroumov, A.S. Plastun, H. Ren, A. Taylor, J. Wei, and Q. Zhao, FRIB, Michigan State University, East Lansing, MI, USA
¹also at Argonne National Laboratory, Lemont, IL, USA

Abstract

The Facility for Rare Isotope Beams (FRIB) at Michigan State University is a 400 kW heavy ion linear accelerator. Heavy ion accelerators normally include a charge stripper to remove electrons from the beams to increase the charge state of the beams thus to increase the energy gain. Thin carbon foils have been the traditional charge stripper but are limited in power density by the damage they suffer (sublimation and radiation damage) and consequently short lifetimes. Because of the high beam power, FRIB had decided to use a liquid lithium charge stripper (LLCS), a self-replenishing medium that is free from radiation damage. FRIB recently commissioned a LLCS with heavy ion beams (³⁶Ar, ⁴⁸Ca, ¹²⁴Xe and ²³⁸U beams at energies of 17-20 MeV/u). Since there had been no experimental data available of charge stripping characteristics of liquid lithium, this was the first demonstration of charge stripping by a LLCS. The beams were successfully stripped by the LLCS with slightly lower charge states than the carbon foils of the same mass thickness. The LLCS started serving the charge stripper for FRIB user operations with a backup rotating carbon foil charge stripper. FRIB has become the world's first accelerator that utilizes a LLCS.

INTRODUCTION

The Facility for Rare Isotope Beams (FRIB) at Michigan State University produces rare isotopes through nuclear reactions between a production target and heavy ions that are accelerated to energies above 200 MeV/u by a driver linac [1]. Figure 1 shows the configuration of the FRIB driver linac, which consists of three linac segments and two folding segments. At FRIB, the charge stripping occurs in the 1st folding segment (FS1), where beams are accelerated to 17-20 MeV/u after the 1st linac segment (LS1). When the facility is operated at the full power, the beam power at the stripper would reach 40 kW.

It is known that heavier ion beams deposit higher energy in matters as the beams traverse them [2]. Full power uranium beams at FRIB would deposit a thermal power of 1600 W within a 1.5 mg/cm² thick carbon foil, or a thermal density of about 70 MW/cm³ assuming the beam diameter is 2 mm. This ultra-high thermal load would cause serious damages to the carbon foil. The solid carbon foil would also suffer radiation damages. Even the best performance

carbon foil that has been successfully used in RIKEN's Radioactive Isotope Beam Factory (RIBF) [3] would not allow continuous full power operations at FRIB.

To overcome this, a self-replenishing medium was sought because it is free from radiation damage and could be a good heat remover. A helium gas stripper has been successfully operated at RIKEN's RIBF [4], and a new charge stripping device based on the helium gas stripper (charge stripper ring, CSR) has been proposed [5]. A drawback of using a gas as the stripping medium is that the equilibrium charge state is significantly lower than solids or liquids. Therefore FRIB has decided to use liquid lithium as the stripper medium as proposed by Nolen [6]. FRIB also considered the helium gas stripper as a backup option of the liquid lithium charge stripper. The key technology to develop was an efficient isolation between the high-pressure helium cell and the ultra-high-vacuum beamline. Because of the limited space available in the driver linac, FRIB cannot use a differential pumping system like the one used in RIKEN, thus sought to develop a "plasma window" [7]. The recent results are published elsewhere [8].

Recently FRIB commissioned a liquid lithium charge stripper (LLCS) with heavy ion beams [9], which was the world's first demonstration of a LLCS. FRIB has also started user operations after the successful completion of its construction. The LLCS as well as a rotating carbon foil charge stripper were used in user operations. This paper describes the results obtained in those tests and operations.

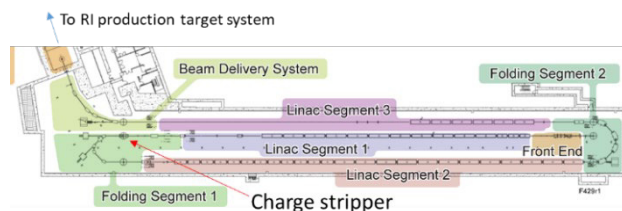


Figure 1: FRIB driver linac configuration. There are three linac segments (LS1, LS2 and LS3) and two folding segments (FS1 and FS2). The charge stripper is located at FS1 before the beam makes a 180 degree turn where the desired charge state(s) is selected for the acceleration at LS2 and LS3.

LIQUID LITHIUM CHARGE STRIPPER SYSTEM AT FRIB

Figure 2 shows a sketch of the FRIB LLCS system. Since liquid lithium is reactive with air, water, and many other materials, safety in use of liquid lithium is the key to

* Work supported by the U.S. Department of Energy Office of Science under Cooperative Agreement DE-SC0000661

[†] kanemura@frib.msu.edu

Content from this work may be used under the terms of the CC BY 4.0 licence (© 2022). Any distribution of this work must maintain attribution to the author(s), title of the work, publisher, and DOI

successful operations. The system has several safety controls to prevent / mitigate lithium-related hazards. The most notable is the secondary containment vessel that completely encloses the lithium loop and is always filled with argon during operations. Thus, even if a liquid lithium leak develops, it will not lead to fire and the system will be kept safe.

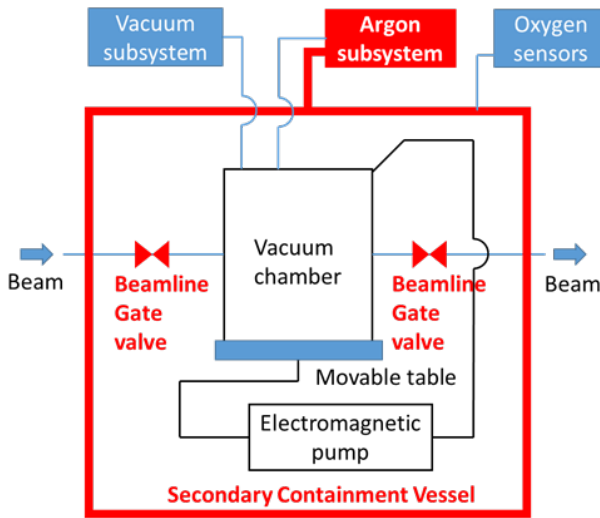


Figure 2: FRIB liquid lithium charge stripper system. The liquid lithium loop is completely enclosed by a secondary containment vessel as a safety control. Noted by red are safety controls.

The LLCS system consists mainly of an argon subsystem, a vacuum subsystem, and a lithium subsystem. The vacuum subsystem is connected to the vacuum chamber, which is part of the lithium loop, where a lithium stripper

film is formed. The vacuum chamber is placed on a table that can be moved with stepper motors. This enables scanning of the film while the beam stays in its beam axis.

Figure 3 shows a photograph of the LLCS film formed in the FRIB linac, and a sketch for what is seen in the photograph. The lithium film is made by a round jet issuing from a 0.5 mm orifice impinging on a flat surface with a sharp edge, so-called deflector.

The flow speed was >50 m/s, which is required to not only produce a stable film but also to remove a heat deposited from high power beams. Under a collaboration with Argonne National Laboratory (ANL), the superior heat removal performance of a liquid lithium film flowing at >50 m/s was demonstrated with a proton beam [10]. The volumetric power deposition during this demonstration was higher than the one foreseen during full power uranium beam operations.

To generate a high-speed jet, a custom made direct current (DC) electromagnetic pump was fabricated [11], which can pump liquid lithium at pressures of higher than 1 MPa. The liquid lithium loop is operated at 220°C with electrical heaters to keep lithium melted (the melting point of lithium is 181°C). The vacuum pressure in the vacuum chamber is typically around 1e-8 Torr. As a main vacuum pump, a cryopump was selected. Among advantages of using cryopumps in a liquid lithium system, most notable is that they can operate in a closed environment unlike turbo molecular pumps, which always need an auxiliary backing pump, and cannot create a physical boundary between atmosphere and the lithium environment. Use of a turbo pump in a liquid lithium system would require a reliable gate valve that isolate the lithium environment from atmosphere in case of pump failures.

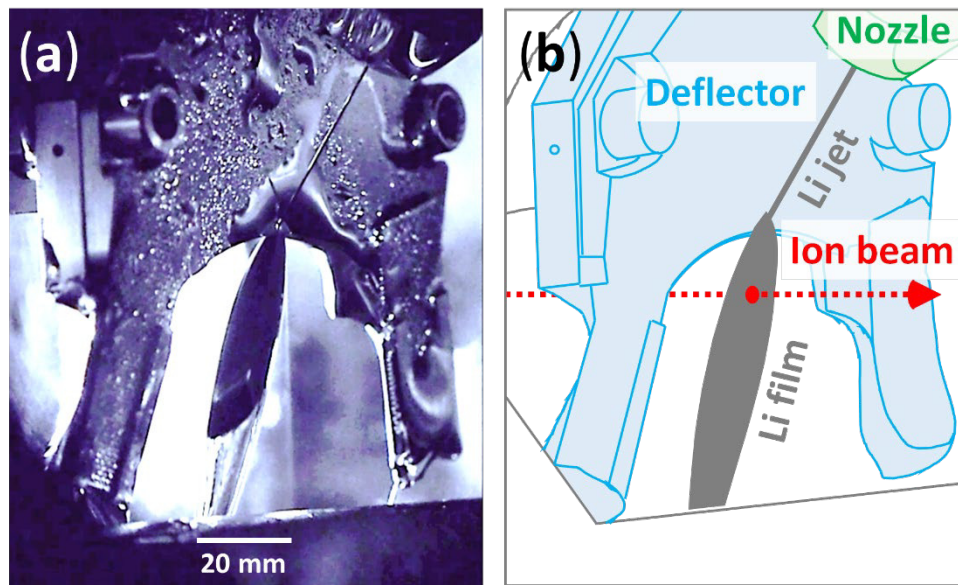


Figure 3: Liquid lithium charge stripper formed in a vacuum chamber which is part of the FRIB linac beamline. (a) Photograph of the lithium film and (b) sketch of what's seen in the photograph. A round jet of liquid lithium being issued from a nozzle impinges on a flat surface ("deflector"). The jet is then deflected forming a stable film that intercepts beams. The film is stable enough to have a mirror surface that reflects the surrounding components in the vacuum chamber or its inner wall.

COMMISSIONING WITH HEAVY ION BEAMS

After a series of offline commissioning tests without beams was completed, the LLCS system was transported to the linac tunnel, mated to the linac beamline, and commissioned with heavy ion beams. Three heavy ions ($^{36}\text{Ar}^{10+}$, $^{124}\text{Xe}^{26+}$, $^{238}\text{U}^{36+}$) were used for the commissioning. Table 1 summarizes the beam conditions. The commissioning tests included measurement of LLCS film thickness, measurement of charge states after the LLCS, and high power beam test. The root-mean-square (rms) beam radius was estimated to be 0.5 mm at the stripper.

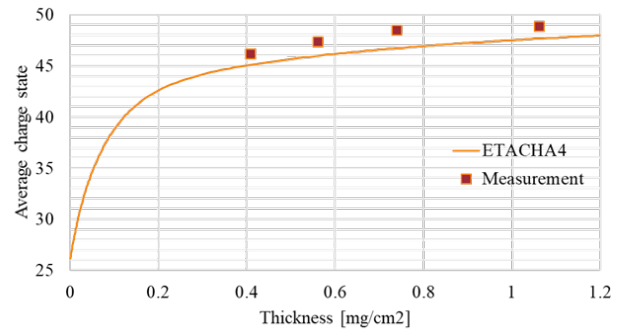
Table 1: Heavy Ions Used During LLCS Commissioning With Heavy Ion Beams

Ions	Energy
$^{36}\text{Ar}^{10+}$	17 MeV/u & 20 MeV/u
$^{124}\text{Xe}^{26+}$	17 MeV/u
$^{238}\text{U}^{36+}$	17 & 20 MeV/u

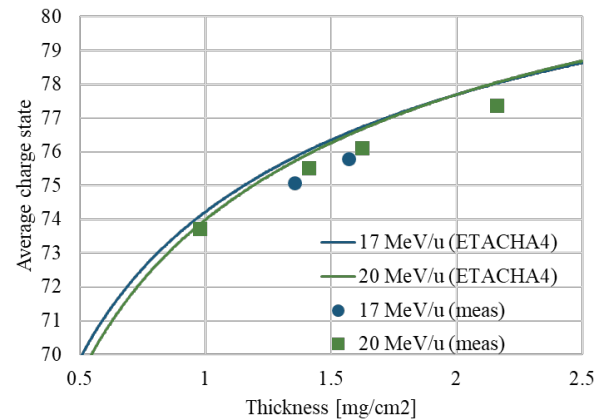
Measurement of the film thickness was conducted with combination of experiment and calculation. A 20 MeV/u $^{36}\text{Ar}^{10+}$ beam was used for the experiment. In the experiment, the beam energy loss at the stripper was measured, and then using the energy loss per unit length obtained from the SRIM code [12], the thickness was estimated. The energy loss was measured over the entire film by moving the table where the vacuum chamber is placed. The measured film was thicker, and its gradient was steeper at locations closer to the impinging point [9]. In other words, at some distance away from the impinging point, the film was uniform enough for the 0.5-mm-radius beam. The measured mass thickness ranged from 0.5 to 1.5 mg/cm², which corresponds to physical thickness of approximately 10 to 30 μm . This result was consistent with past measurements using low energy electron beams [13]. The fluctuations of the beam energy after the stripper was less than 0.1% of the incoming beam energy over a period of 2.5 hours, which is acceptable in the further acceleration in the linac. These energy fluctuations were found to be correlated with the temperature fluctuations of the vacuum chamber. By improving the temperature control scheme, this energy fluctuations could be eliminated. Those observations indicated that the film was stable and spatially stationary.

Measurement of charge states was conducted by scanning the current of the first dipole magnet after the stripper and analysing the intensity of beams that pass through a slit after the dipole magnet. The measured charge states were compared with simulation results obtained with the ETACHA code [14,15]. Results showed that the average charge states obtained with the Ar and Xe beams were higher than the calculated values. On the other hand, the average charge states obtained with the U beams were lower than the calculated values, as shown in Figure 4. Figure 5 shows charge state distributions of the xenon (red) and uranium (blue) beams after the LLCS. The beam energy was 17

MeV/u for both beams. The film thickness was 1.05 and 1.40 mg/cm² for the xenon and uranium beams, respectively. Figure 6 shows charge state distributions of the 20 MeV/u argon beam after the LLCS and a carbon foil stripper. Thickness was 1.6 mg/cm² and 1.2 mg/cm² for the lithium and the carbon, respectively. Even though the lithium film was thicker than the carbon foil, the lithium film produced a lower fraction of the fully stripped $^{36}\text{Ar}^{18+}$. The charge state distributions of the 20 MeV/u uranium beam were also measured in the liquid lithium and a carbon foil at 1 mg/cm² thickness. It was found that the average charge states are 73.7 and 76.9 for the liquid lithium and carbon, respectively.



(a) Average charge states of xenon beam stripped by lithium.



(b) Average charge states of uranium beam stripped by lithium

Figure 4: Average charge states of heavy ion beams stripped by lithium as a function of lithium thickness. The lines show the simulation results with ETACHA4, and symbols show the measured values.

Content from this work may be used under the terms of the CC BY 4.0 licence (© 2022). Any distribution of this work must maintain attribution to the author(s), title of the work, publisher, and DOI

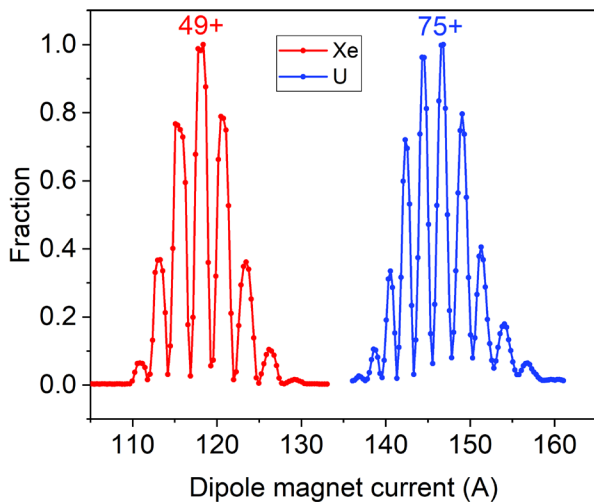


Figure 5: Xenon (red) and uranium (blue) charge state distributions after the liquid lithium stripper. The thickness is 1.05 mg/cm² for the xenon beam and 1.40 mg/cm² for the uranium beam.

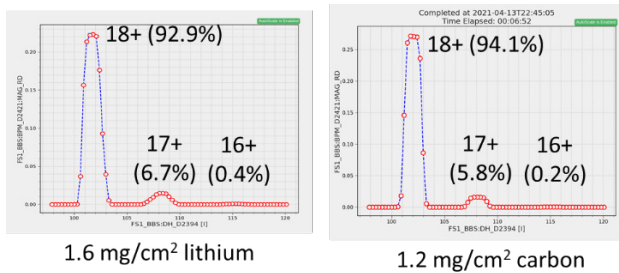


Figure 6: Charge state distributions of 20 MeV/u argon beam after the LLCS and carbon foil stripper. Thickness was 1.6 mg/cm² and 1.2 mg/cm² for the lithium and the carbon, respectively.

To test thermal responses of the LLCS to a high power heavy ion beam, the LLCS was irradiated by a high-intensity 17 MeV/u ³⁶Ar¹⁰⁺ beam. The beam power that can be transported to a beam dump in FS1 is limited to 500 W. Therefore, to conform to this limitation but utilize the maximum peak power available, the beam intensity was kept to the maximum value of 12 particle μA that the ion source was able to produce while the beam duty cycle was limited to 5.4% with the repetition rate of 10 Hz. With these parameters, the average beam power was 400 W while the peak power was 7400 W at the stripper during each 5.4 ms period. Since it took approximately 20 μs for the flowing lithium at 50 m/s to completely cross the beam spot of 1 mm, it was considered that the longest time constant of any thermal and fluid dynamic responses of the lithium flow was 20 μs. Thus the 5.4 ms long beam, which was 270 times longer than the longest time constant, may be considered well representing a continuous beam. If this beam had been transported to the production target in the CW mode, the final power at the target would have been more than 74 kW. The peak volumetric power deposition into the lithium was estimated to be 6 MW/cm³ (peak power loss

50 W) during the test, which is about 10% of the FRIB full power uranium beam operation value. As expected from the past thermal performance test at a higher volumetric power deposition [10], the beam parameters and LLCS system operating parameters were stable during the test without an issue. Figure 7 shows the beam energy after the LLCS during the test. Figure 8 shows a photo of beam spot on the film during the test.

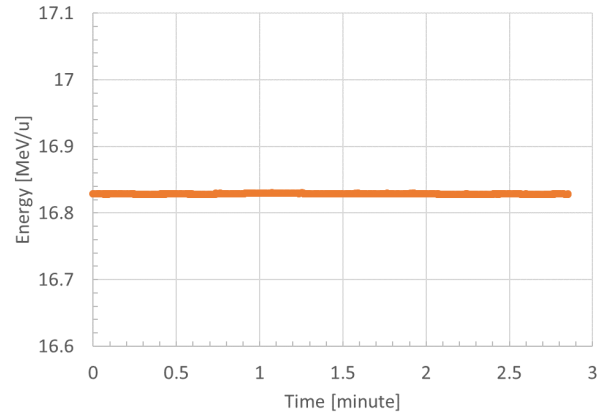


Figure 7: ³⁶Ar beam energy after the lithium stripper during the high-intensity irradiation test (peak intensity 12 particle μA, peak beam power 7400 W (average 400 W, duty cycle 5.4%), peak power loss 50 W (volumetric power deposition 6 MW/cm³).

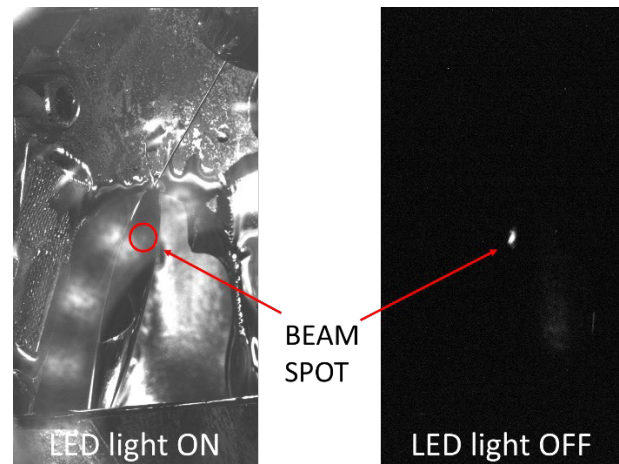


Figure 8: Beam spot on the LLCS during the high-intensity irradiation test. The LED light was turned off on the right photo to take a clear beam spot.

EARLY OPERATION EXPERIENCES

FRIB officially started the user program in May 2022 [16,17]. The LLCS was used during the first user operation conducted in May 2022. The primary beam was ⁴⁸Ca and beam power was up to 1 kW at the production target (about 100 W at the stripper). Rare isotopes were successfully delivered to the user station. The long-term operation with the

primary ^{48}Ca beam was validated. Figure 9 shows an example of the beam energy after the LLCS during the operation.

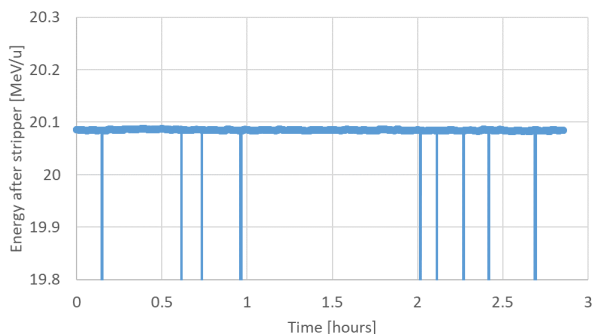


Figure 9: ^{48}Ca beam energy after the lithium stripper. At downward spikes the beam was tripped.

A rotating carbon foil charge stripper was also used for user operations. The carbon stripper is located in FS1, adjacent to the LLCS, as shown in Figure 10. These strippers are lined up tandemly in the beamline. This configuration was adopted to use the carbon stripper as a backup stripper. The carbon stripper cannot be used for high power heavy ion beams, but this flexibility gives an option of switching one stripper to another. When the facility operates at a high power (>10 kW), we use the LLCS. But in case it fails, our plan is to switch to the carbon stripper with a reduced beam power to continue delivering beams to users.

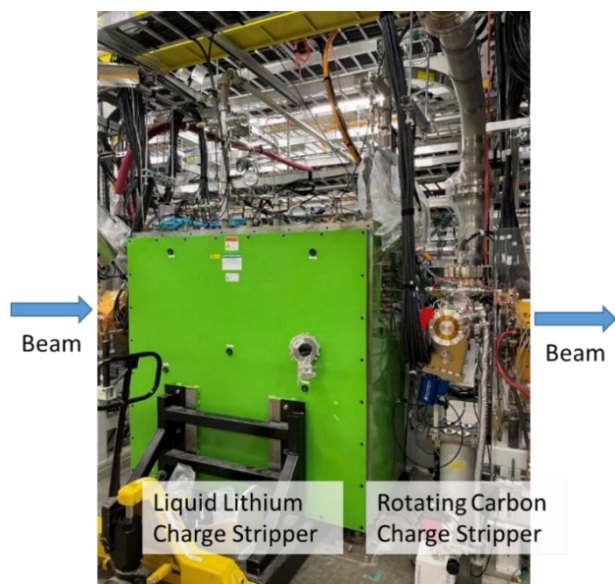


Figure 10: Photograph showing the LLCS and the carbon charge stripper connected in series in FS1 of the FRIB linac. The LLCS is located upstream of the carbon stripper.

The carbon stripper system is equipped with two independent motors that can rotate and move vertically a 100-mm-radius carbon foil. This mechanism increases the available area of the foil for irradiation, and thus reduces

the local fluence of ions passing through the foil, which can longer the foil lifetime. The rotational motion is intended to reduce the maximum temperature of the foil. Thus the combination of both motions reduces thermal and radiation damages to the foil, prolonging its lifetime.

During the second user operation in June 2022, a 1.5 mg/cm^2 graphene foil purchased from Applied Nanotech Inc served as the stripper for this operation. The primary beam was ^{82}Se . The beam energy and power at the stripper were 20.3 MeV/u and 270 W, respectively. Among 270 W, about 5 W was estimated to be deposited to the carbon foil (about $50 \text{ kW}/\text{cm}^3$ volumetric heat deposition). Except for the initial thickness reduction (about 3%) during the conditioning, the foil didn't show a significant thickness reduction over a week. It contributed to the successful user operation.

SUMMARY

The Facility for Rare Isotope Beams (FRIB) at Michigan State University has become the world's first accelerator in which a liquid lithium charge stripper (LLCS) is used [9]. The LLCS was successfully commissioned with heavy ion beams: $^{36}\text{Ar}^{10+}$, $^{48}\text{Ca}^{10+}$, $^{124}\text{Xe}^{26+}$, and $^{238}\text{U}^{36+}$. For the first time, the charge stripping efficiency of a lithium film was measured and compared with simulation results. Charge state evolutions tend to agree with simulations, but the average charge states didn't show a good agreement with simulations. The beam energy loss measurement showed that the lithium film was stable enough for the beam to be accelerated in the subsequent stages of the linac. Measured charge states after the lithium stripper were lower than those after the carbon stripper of the same thickness. The peak heat deposition of $6 \text{ MW}/\text{cm}^3$ from ^{36}Ar beam, which is equivalent to a condition of >74 kW beam at the target, didn't cause any issue in the lithium stripper. After the successful commissioning, the LLCS started serving as a charge stripper for FRIB user operations with a backup rotating carbon foil charge stripper.

ACKNOWLEDGEMENTS

The authors would like to thank all the FRIB staff members for their contributions to the successful commissioning of the liquid lithium charge stripper with heavy ion beams. This work is supported by the U.S. Department of Energy Office of Science under Cooperative Agreement No. DE-SC0000661, the State of Michigan, and Michigan State University.

REFERENCES

- [1] J. Wei *et al.*, "Accelerator commissioning and rare isotope identification at the Facility for Rare Isotope Beams," *Mod. Phys. Lett. A*, vol. 37, no. 9, p. 2230006, 2022. doi:10.1142/S0217732322300063
- [2] J. A. Nolen and F. Marti, "Charge Strippers of Heavy Ions for High Intensity Accelerators," *Rev. Accel. Sci. Technol.*, vol. 06, pp. 221-236, 2013. doi:10.1142/S1793626813300107

- [3] H. Hasebe *et al.*, “Development of a rotating graphite carbon disk stripper,” *Proc. AIP Conf.*, vol. 1962, no. 1, p. 030004, 2018. doi:10.1063/1.5035521
- [4] H. Imao *et al.*, “Charge stripping of ^{238}U ion beam by helium gas stripper,” *Phys. Rev. ST Accel. Beams* vol. 15, no. 12, p. 123501, 2012. doi:10.1103/PhysRevSTAB.15.123501
- [5] H. Imao, “Charge Stripper Ring for RIKEN RI Beam Factory,” *J. Inst.*, vol. 15, p. P12036, 2020. doi:10.1088/1748-0221/15/12/P12036
- [6] J. A. Nolen *et al.*, “Argonne Physics Division 2000 Annual Report,” Argonne National Laboratory, Lemont, USA, Rep. ANL-01/19, 2001.
- [7] W. Gerber *et al.*, “The Plasma Porthole: a Windowless Vacuum-Pressure Interface With Various Accelerator Applications,” *Proc. AIP Conf.*, vol. 475, pp. 932-935, 1999. doi:10.1063/1.59299
- [8] A. LaJoie, J. Gao, and F. Marti, “Study of High-Flow Argon Through Cascaded Arc for Use as a Gas Target Isolator,” *IEEE Trans. Plasma Sci.*, vol. 47, no. 5, pp. 2752-2758, May 2019. doi:10.1109/TPS.2019.2907767
- [9] T. Kanemura *et al.*, “Experimental Demonstration of the Thin-Film Liquid-Metal Jet as a Charge Stripper,” *Phy. Rev. Lett.*, vol. 128, no. 21, p. 212301, May. 2022. doi:10.1103/PhysRevLett.128.212301
- [10] Y. Momozaki *et al.*, “Proton beam-on-liquid lithium stripper film experiment,” *J. Radioanal. Nucl. Chem.*, vol. 305, pp. 843-849, 2015. doi:10.1007/s10967-015-4074-9
- [11] F. Marti, P. Guetschow, Y. Momozaki, J.A. Nolen, and C.B. Reed, “Development of a Liquid Lithium Charge Stripper for FRIB,” in *Proc. 13th International Conference on Heavy Ion Accelerator Technology (HIAT’15)*, Yokohama, Japan, Sep. 2015, pp. 134-138.
- [12] J. F. Ziegler, M. D. Ziegler, and J. P. Biersack, “SRIM – The stopping and range of ions in matter (2010),” *Nucl. Instrum. Methods Phys. Res., Sect. B*, vol. 268, no. 11-12, pp. 1818-1823, 2010. doi:10.1016/j.nimb.2010.02.091
- [13] C. B. Reed, J. Nolen, Y. Momozaki, J. Specht, D. Chojnowski, and R. Lanham, “FRIB lithium stripper thickness and stability measurements,” Argonne National Laboratory, Lemont, USA, Rep. ANL/NE-11/01, 2011.
- [14] E. Lamour *et al.*, “Extension of charge-state-distribution calculations for ion-solid collisions towards low velocities and many-electron ions,” *Phys. Rev. A*, vol. 92, p. 042703, 2015. doi:10.1103/PhysRevA.92.042703
- [15] LISE++, <http://lise.nslc.msu.edu/etacha.html>
- [16] J. Wei *et al.*, “FRIB Commissioning and Early Operations,” presented at the 13th Int. Particle Accelerator Conf. (IPAC’22), Bangkok, Thailand, June 2022, paper TUI-YGD3, submitted for publication.
- [17] P. N. Ostroumov *et al.*, “FRIB at MSU: Status and Opportunities/Commissioning Experience at FRIB,” presented at the 15th Int. Conf. Heavy Ion Accelerator Technology (HIAT’22), Darmstadt, Germany, June 2022, paper WE113, this conference.

DEVELOPMENT, FABRICATION AND TESTING OF THE RF-KICKER FOR THE ACCULINNA-2 FRAGMENT SEPARATOR

W. Beeckman*, F. Forest, O. Tasset, E. Voisin, SIGMAPHI, Vannes, France
A. Bechtold, NTG Neue Technologien GmbH & Co KG, Gelnhausen, Germany
A. Fomichev, A. Gorshkov, S. Krupko, G. Ter-Akopian
Flerov Laboratory of Nuclear Reactions, JINR, ubna, Russia

Abstract

The Acculina-2 radioactive beam separator was designed and built between 2012 and 2014, installed and tested by Sigmaphi in 2015 and in full operation since 2016 at the Flerov laboratory of JINR in Dubna. In order to achieve efficient separation of neutron-deficient species, an RF kicker was foreseen since the beginning of the project but was put on hold for many years.

In 2016 Sigmaphi got a contract to study, build, install and test an RF kicker with a variable frequency ranging between 15 and 21 MHz and producing 15kV/cm transverse electric fields in a 10 cm gap over a 1m distance.

The paper briefly recalls the rationale of an RF-kicker to separate neutron-deficient species. It then goes through the different steps of the study, initial choice of the cavity structure, first dimensioning from analytical formulas, finite elements computations and tuning methods envisioned, down to a final preliminary design.

The fabrication and tests of a 1/10 mock-up and final study, design, construction and factory testing of the real cavity are presented but, because of U400M cyclotron closure, no beam tests have been performed so far.

INTRODUCTION

A detailed description of the Acculina-2 RI beam separator and a comparison with other separators can be found in [1–3] and references therein. The purpose of the RF kicker in the Acculina-2 separator is outlined in [2] and with more details in [3], which, as a review paper, provides a very complete panorama of intended experiments with Acculina-2.

In the present paper, we describe the design, fabrication, installation and testing of the RF kicker. The choice of Sigmaphi by JINR is the continuation of the long-time collaboration during which Sigmaphi studied, built, installed and helped starting a large part of the Acculina-2 facility.

The reader will find information on the rationale for RF kickers for RIB beamlines in references [4–6] and we only briefly summarize them here for consistency. Proton-rich (aka neutron-deficient) isotopes, are difficult to separate because

- being close to the dripline, they are usually produced with very low yields.
- their magnetic rigidity $B\Delta$ is similar to the rigidity of the low energy tail of species close to the stability zone, which are produced in much larger quantities. Hence, they are shadowed by a more intense background and magnetic separation is inefficient.

However, these “magnetically entangled” species differ in their velocities v , hence in the time TOF it takes for them to travel the distance D between their point of production and a further away location in the beamline.

$$B\rho = \left(\frac{p}{Qq}\right) = \left(\frac{mv}{q}\right) \left(\frac{A}{Q}\right) = \frac{1}{TOF} \left(\frac{Dm}{q}\right) \left(\frac{A}{Q}\right),$$

$$TOF = \left(\frac{Dm}{B\rho q}\right) \left(\frac{A}{Q}\right) = C^{ste} \left(\frac{A}{Q}\right).$$

In the case of fully stripped ions, we have

$$TOF = C^{ste} \left(\frac{Z+N}{Z}\right) = a + \frac{b}{Z},$$

a and b being 2 constants, which we can summarize as: For the same number of neutrons and identical rigidities, the time-of-flight increases as atomic number decrease.

Every such “TOF-different” component of the beam enters the kicker at a different time and experiences inside it a different vertical electric field, kicking some components up, some down -and any in-between- according to the time structure of the beam and that of the electric field. After some drifting distance, the vertical kick is transformed into a vertical distance to the optical axis and a suitable set of slits and vertical steering magnets allow selecting the part of the beam one is interested in. An RF-kicker/deflector/sweeper is a TOF to vertical deflection transformer.

SCOPE OF WORK

- Cavity design: variable frequency and high mechanical and thermal stability, cooling, vacuum pumps and gauges.
- Motorized coupling, tuning and fine-tuning loops, measuring pick-up loops
- Cavity fabrication and factory tests
- RF generator and amplifier
- Command and control system
- On-site start-up and tests

CAVITY DESIGN

Most requirements are given in Table 1 (identical required and achieved values), to which we must add maximum height of 2300 mm and weight of 3000 kg. See also graphical summary of these parameters in Fig. 1.

The dimensional constraints advocate for a quarter-wave coaxial resonator, a cavity of a similar type as the one built for RIBF [7]. Analytical formulas for such a simple geometry e.g. [8] permit fast preliminary estimates.

In order to address the frequency change in the rather large requested range, modifying the inductance, the capacitance or a mix of both were envisioned.

Changing the inductance requires a sliding short-circuited plate around the central pillar that reduces the cavity length

* wbeeckman@sigmaphi.fr

Content from this work may be used under the terms of the CC BY 4.0 licence (© 2022). Any distribution of this work must maintain attribution to the author(s), title of the work, publisher, and DOI

Table 1: Comparison of Kicker Parameters in the RIBF [7], Acculinna-2 and NSCL [9] Facilities

Parameter	RIBF	Acc-2	NSCL
Type	$\lambda/4$	$\lambda/4$	$\lambda/2$
Length [mm]	1600	1650	1500
R_{cavity} [mm]	800	1400	
$L_{electrode}$ [mm]	700	700	1500
$w_{electrode}$ [mm]	120	120	
gap [mm]	40	70	50
V [kV]	100	120	100
f_{low} [MHz]	11	14.8	19
f_{high} [MHz]	19	22.7	27
Q_{low}	13000	13200	7500*
Q_{high}	18000	16600	10000*

* Most pessimistic - different papers present different values

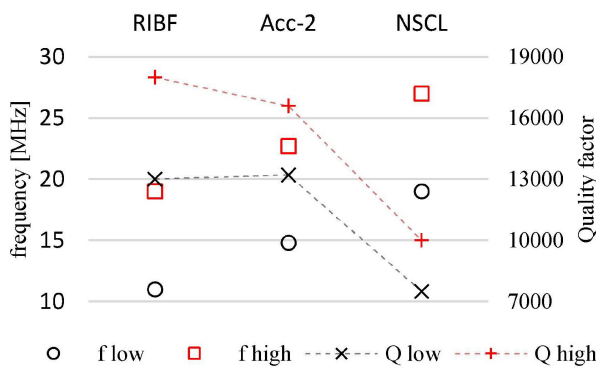


Figure 1: Comparison of frequency ranges and quality factors for 3 RF-kickers with comparable goals, showing a nice match to the trend of the Acculinna-2 kicker.

but the frequency range involved requires a 600 mm stroke which makes it mechanically complex and, moreover, it influences other functions as the possibility to insert the coupling loop, pick-ups and pumping from the top.

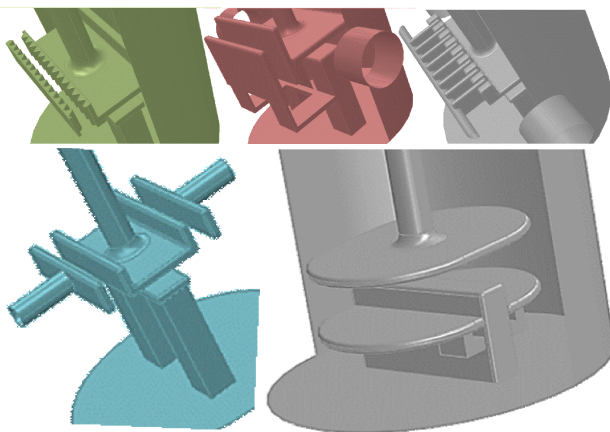


Figure 2: Many different geometries for capacitive change were tried, among which a few examples are shown (top row and bottom left). The chosen solution is displayed in the bottom right-hand part of the picture.

A capacitive method looks easier, being located in the vicinity of the electrodes and therefore having little influence on other functions but care must be taken to preserve a good field pattern in the gap. A rather large space is needed to cover the whole range.

The capacitive solution is also the one chosen for other existing kickers [5, 7, 9]. Figure 2 shows a series of Soprano (Opera3d RF module) models with different solutions for the capacitance modification. The chosen solution is also displayed. Although the RIBF cavity [7] has a geometry close to ours, we preferred keeping a fully cylindrical geometry instead of a mixed cylinder/rectangle to avoid close unwanted modes and make construction easier.

A design featuring an inductively modified frequency through magnetically saturable ferrite rings in an external magnetic field was also envisioned but, despite a very attractive reduced size (Fig. 3), it was judged too radical.

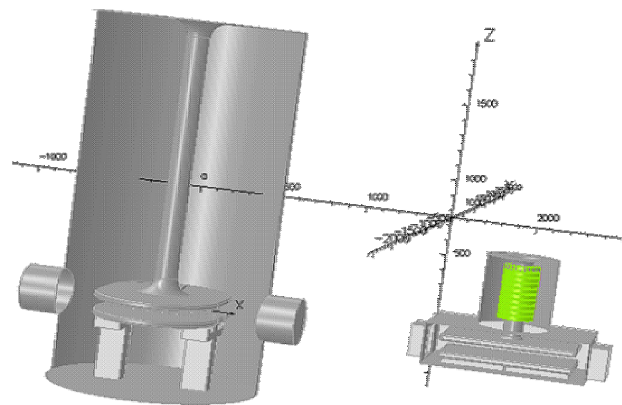


Figure 3: Soprano models of the conventional version using capacitive tuning (15-22 MHz) and of the version with saturable ferrite inductive tuning (15-45 MHz) are displayed on the same scale.

MOCK-UP TESTS

We built a 1/10 scale model of the cavity with which we could check calculation results as shown in Fig. 4.

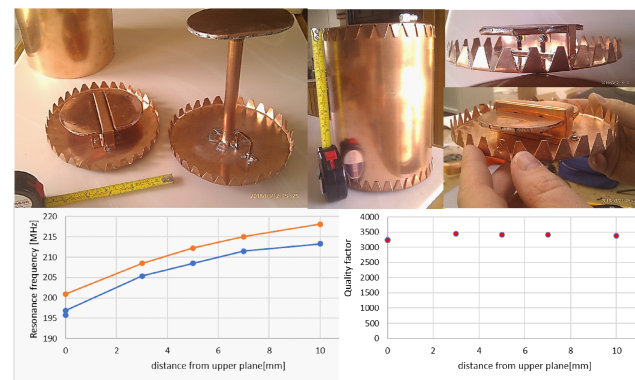


Figure 4: A 1/10 scale mock-up (top) was used to check Soprano predictions as frequency variation vs distance of the tuning plates (bottom left) and a low sensitivity of the coupling to this distance (bottom right).

The discrepancies between calculations and mock-up come from slightly different geometries from the use of commercially available copper parts, inaccuracies in the measurement of the gap (0.5 mm is enough), openings not taken into account, etc. Other important lessons were learned, among others on coupling.

CAVITY FABRICATION

The NTG company was contracted to build the cavity according to the preliminary design provided by Sigmaphi. A full cross-check using another code (CST Microwave Studio) was performed, as well as a detailed study of all sub-components like sliding contacts, coarse and fine tuners, pick-up probes, etc. (see Fig. 5). Mechanical stability, deformations, thermal and cooling issues were also addressed.



Figure 5: Cavity parts during fabrication. Central pillar and top electrode (left), moving bottom electrodes disassembled (mid top) and assembled with the central electrode on the bottom main flange (mid bottom), with outside drum at the rear of the picture. The right-hand picture shows the complete cavity under vacuum tests.

An examples of factory tests results is show in Fig. 6.

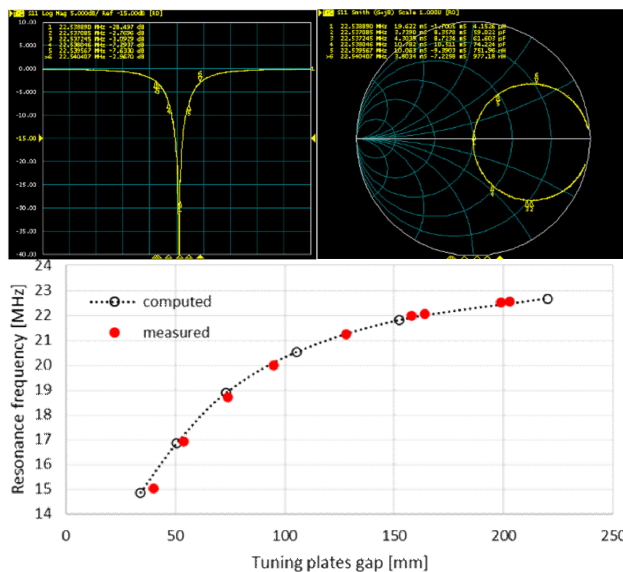


Figure 6: Factory tests results. Top pictures show the resonance peak (left) and Smith chart (right) at 22.539 MHz. At bottom measured and calculated values of the resonance frequency as a function of the distance between the bottom moving electrodes and their top counterpart.

The transmission peak measured at 22.539 MHz delivers a quality factor $Q_{\text{meas}} = 14818$ in almost perfect agreement (<4%) with the calculated value $Q_{\text{calc}} = 14256$ while the Smith chart shows an almost ideal coupling. We also see that measurements and model predictions agree very well on the frequency change generated by moving electrodes throughout the whole tuning range.

POWER AND CONTROL

The kicker is driven by a solid-state HFA-15 RF amplifier from QEI (installed and put in operation by AR France) in CW mode and delivering up to 15 kW in a 14–22 MHz frequency range with a full power bandwidth >200 kHz.

The control system is designed, built and put into operation by Cosylab. It takes care of the full operation of the kicker, from the synchronization with the UM400 cyclotron signal, amplifier set up and power input, coarse and fine frequency tuning, pick-up readings, interlocks, etc.

ON-SITE INSTALLATION AND TESTING

The kicker was rigged in the Acculinna-2 beamline during the 2nd week of June 2019 and full assembly and first test were performed during the last week of July 2019.

A 2 years refurbishment shutdown of the U400M cyclotron which delivers beams to the Acculinna-2 experimental facility was planned by June 2020. Hence, most available beamtime after July 2019 was used by the Acculinna-2 team to collect data to be processed during this 2 years closure period. No further operation was performed on the kicker until a one-week slot was made available in mid-February 2020.

The 2 main goals during this week were to:

- achieve proper coupling in 15-19 MHz range (Figs. 7, 8 and 9).
- overcome multipactoring in the vicinity of 18.0 MHz for first experiments with ^{20}Ne beams.

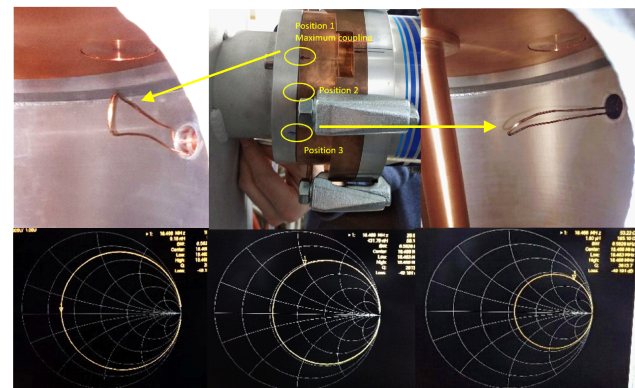


Figure 7: The coupler is rotated in 3 positions defined by the flange. Position 1 (left) gives a strong over-coupling, position 2 (mid) is still over-coupled and position 3 (right) is a bit under-coupled. The loop, in position 3, is then slightly deformed to increase its active surface and reach ideal coupling.

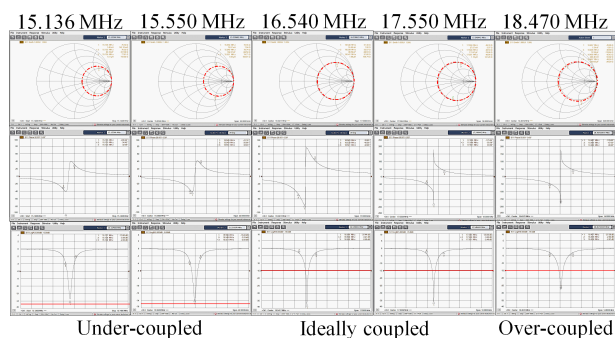


Figure 8: Smith chart (top), phase (mid) and transmission (bottom) for a series of frequencies up to 18.5 MHz. The red line in the bottom part shows the -15 dB value.

Figure 9 compares calculated and measured transmission showing that a better-than-expected transmission is achieved. The coupling must probably be retuned for the high frequency range but the present setting matches at best the cyclotron capabilities.

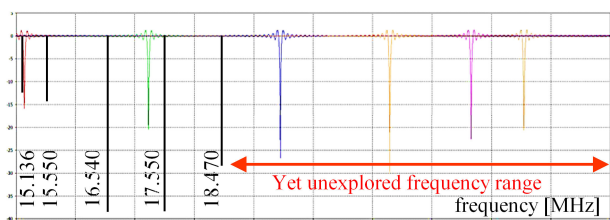


Figure 9: Comparison of calculated (coloured peaks) and measured (black lines and values) transmission ($+5$ to -40 dB) at a series of frequencies.

To overcome multipactoring, the cavity is conditioned by short sequences of pulses separated by long «blanks». The number of pulses in the sequence is then increased as power is accepted until a continuous signal can be input.

Figure 10 are oscilloscope displays of a 2 ms 900 W impulse (top) and continuous (bottom) signals at 18.4 MHz. The time evolution (left to right) shows a progressive increase of the transmitted (green) and pick-up (pink) signals and a concomitant disappearance of the reflected (blue). Yellow on top is the driving from frequency generator.

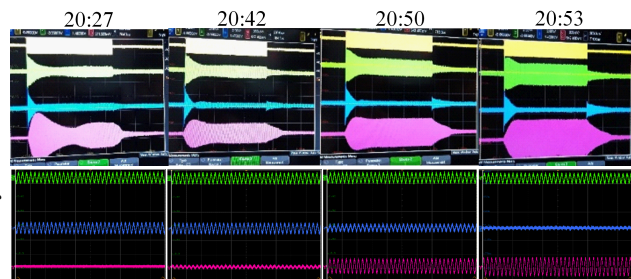


Figure 10: 2 ms 900 W impulse (top) and continuous (bottom) signals at 18.4 MHz. Time of the photo for the impulse signal (top of the picture) shows that conditioning takes place in less than 30 minutes.

Because of the limited time slot, experiments were conducted on a limited frequency range and no test with beam was done yet. U400M operation should resume in the end 2022 and RF-kicker operation will have a high priority in day-one experiments.

CONCLUSION

The Acculinna-2 RF-kicker was successfully designed, built and tested. It is a collaborative achievement.

On-site tests showed equal-to or better-than expected results which we hope to be confirmed in the future operation with beam.

ACKNOWLEDGEMENTS

We want to thank Claude Bieth who unfortunately left us in 2020 for his important advices from the very start of the project. We also thank Bernard Bessot of AR France for his help on power amplifier, Jernej Podlipnik of Cosylab on the control system, Anna Orlova of Sigmaphi Electronics for on-site debugging, Antonio Palmieri of INFN Legnaro for his advices on start-up and multipactoring and Antonio Caruso of INFN Catania for his advices on protection.

REFERENCES

- [1] W. Beeckman *et al.*, “Status of the Acculinna-2 RIB fragment separator”, in *Proc. HIAT 2015*, Yokohama, Japan, 2015, pp. 33-35. doi: 10.18429/JACoW-HIAT2015-M0A2C03
- [2] A. Gorshkov *et al.*, “Current status of the new fragment separator ACCULINNA-2 and the first-day experiments”, *Eurasian J. Phys. Funct. Mater.*, vol. 3, p. 46-52, 2019. doi: 10.29317/ejpfm.2019030106
- [3] A.S. Fomichev, L.V. Grigorenko, S.A. Krupko, S.V. Stepantsov, and G.M. Ter-Akopian, “The ACCULINNA-2 project: The physics case and technical challenges”, *Eur. Phys. J. A*, vol. 54, p. 97-119, 2018. doi: 10.1140/epja/i2018-12528-0
- [4] T. Baumann *et al.*, “The Radio Frequency Fragment Separator: A Time-of-Flight Filter for Fast Fragmentation Beams”, in *Proc. Cyclotrons’13*, Vancouver, BC, Canada, 2013, pp. 467-469. <https://jacow.org/cyclotrons2013/papers/fr1pb03.pdf>
- [5] R.C. Pardo, J. Bogaty, S. Sharamentov, and K.E. Rehm, “An RF beam sweeper for purifying in-flight produced secondary ion beams at ATLAS”, *Nucl. Instr. Methods Phys. Res., Sect. A*, vol. 790, p. 1-5, 2015. doi: 10.1016/j.nima.2015.03.046
- [6] K. Yamada, T. Motobayashi, and I. Tanihata, “RF deflector system for proton-rich RI beams in RIKEN”, *Nucl. Phys. A*, vol. 746, p. 156c-160c, 2004. doi: 10.1016/j.nuclphysa.2004.09.064
- [7] H. Miyazaki, Y. Kumata, and K. Hoshika, “Development of RF deflector”, *Sumitomo Heavy Industries Technical Review*, vol. 153, p. 57-60, Dec. 2003.
- [8] P. Vizmuller, “Resonators – Coaxial resonators”, in *RF Design Guide – Systems, Circuits, and Equations*, Artech House, Norwood, MA, USA: Wiley, 1995, pp. 237-239.
- [9] D. Bazin *et al.*, “Radio Frequency Fragment Separator at NSCL”, *Nucl. Instr. Methods Phys. Res., Sect. A*, vol. 606, p. 314-319, 2009. doi: 10.1016/j.nima.2009.05.100

A 3D PRINTED IH-TYPE LINAC STRUCTURE – PROOF-OF-CONCEPT FOR ADDITIVE MANUFACTURING OF LINAC RF CAVITIES*

H. Hähnel[†], A. Ateş, U. Ratzinger

Institute of Applied Physics, Goethe University, Frankfurt a. M., Germany

Abstract

Additive manufacturing (AM or "3D printing") has become a powerful tool for rapid prototyping and manufacturing of complex geometries. A 433 MHz IH-DTL cavity has been constructed to act as a proof of concept for additive manufacturing of linac components. In this case, the internal drift tube structure has been produced from 1.4404 stainless steel using 3D printing. We present the concept of the cavity as well as first results of vacuum testing and materials testing. Vacuum levels sufficient for linac operation have recently been reached with the AM linac structure.

INTRODUCTION

Additive manufacturing (AM) of metal parts may provide an interesting new way to manufacture accelerator components. As technology is evolving, the quality and accuracy of parts manufactured this way is improving. Recently, a number of studies on the topic of AM for linear accelerator components have been published [1–5]. Based on these promising results, we aim to evaluate the suitability of AM parts for direct manufacturing of normal conducting linac structures. To that end, a reproduction of the beam pipe vacuum tests in [2, 3] was performed and upon success, a prototype cavity with a fully printed drift tube structure was constructed. The cavity is designed to be UHV capable and includes cooling channels reaching into the stems of the drift tube structure for power testing with a pulsed 30 kW rf amplifier.

Prototype Design and Concept

The prototype cavity was designed for a resonance frequency of 433.632 MHz, which is a harmonic of the GSI UNILAC operation frequency [6]. In combination with a targeted proton beam energy of 1.4 MeV this scenario allows for a compact accelerator at the limits of feasibility and is therefore a good benchmark for the new approach. The internal drift tube structure is fully 3D printed from stainless steel (1.4404), see Fig. 1a. Due to the lower complexity of the cavity frame and lids, they are manufactured by CNC milling of bulk stainless steel. Printing those parts would not be cost efficient.

The cavity is just 22 cm wide and 26 cm high (outer walls), with a length of 20 cm on the beamline (flange to flange). A center frame acts as the foundation for the cavity. This 7 cm high center frame provides the precision mount points for the girder-drift tube structures and end-drift tubes. While the end-drift tubes are mounted in vacuum, the girders have a vacuum sealing surface at the bottom. Two half shells are

mounted on the top and bottom of the center frame. The cavity is equipped with four CF40-Flanges for vacuum, rf-coupler and tuner, as well as metal sealed KF40 flanges for the beamline and smaller ports for diagnostics. Rf simulations show that the bulk of the rf losses during the operation of this cavity is concentrated on the drift tube structure and the cavity frame. Therefore, water channels are included in the girders up to the drift tubes and also in the center frame. A 3D CAD view of the full construction is shown in Fig. 1b.

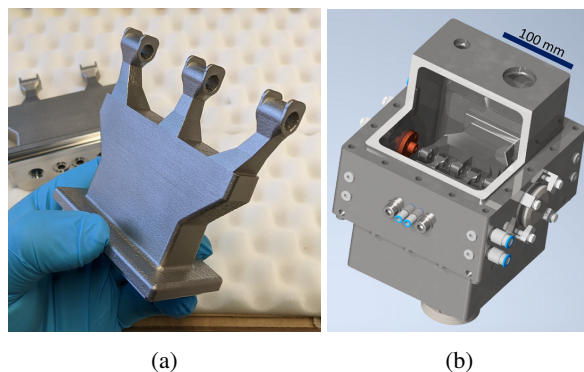


Figure 1: Overview of the cavity geometry and printed parts. (a) 3D printed girder drift tube structure. (b) Cross section of the assembled cavity model.

RF Simulations

The cavity design was optimized for a frequency of 433.632 MHz. To minimize the need for support structures during the manufacturing process, the shape of the girder-drift tube structure was optimized to reduce overhang. Simulations of electromagnetic fields in the cavity were performed with the CST Microwave Studio eigenmode solver. Figure 2 shows the resulting electric field distribution in the cavity, with the typical characteristics of a $\beta\lambda/2$ IH-type structure. From the idealized design model, the simulated dissipated power for the effective acceleration voltage of $U_{eff} = 1$ MV is $P_{loss} = 24.82$ kW. With an inner wall length of 146 mm, this corresponds to an effective shunt impedance of $Z_{eff} = 287.13$ Ω/m^1 , showing the high efficiency of such an IH-type structure.

EXPERIMENTS

Since the first construction of the cavity in late 2020/early 2021, several experiments have been conducted to evaluate certain aspects of the cavity suitability for linac operation. The following sections will explore the different experiments.

¹ The stated value in [7] was much too low, due to a typo.

* Work supported by BMBF 05P21RFRB2

[†] haehnel@iap.uni-frankfurt.de

Content from this work may be used under the terms of the CC BY 4.0 licence (© 2022). Any distribution of this work must maintain attribution to the author(s), title of the work, publisher, and DOI

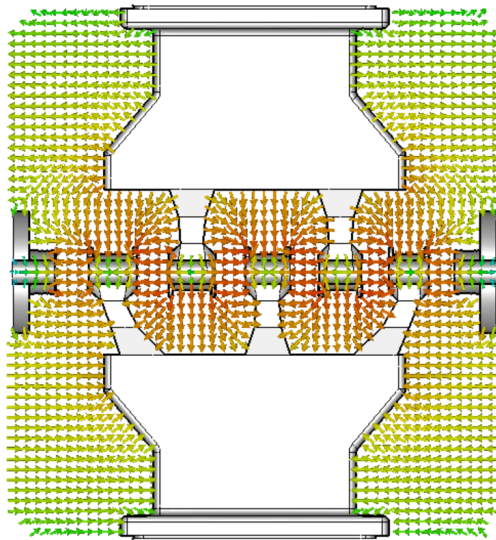


Figure 2: Electric field distribution in the prototype cavity.

Water Flow Measurements

Both girder-drift tube structures, as well as the center frame of the cavity are water cooled. While the water cooling in the center frame is quite conventional and realized with deep-hole drilled channels, the water cooling in the girders is more complex. To ensure, that the water channels in the girders are working as intended and not blocked by, for example, residual metal powder, some flow measurements were performed. The setup is provided with a water pressure of 8 bar. The tubing used is Festo tubing with an outer diameter of 6 mm. Measurements were performed with a Kobold digital inductive flow meter. Measurement results are summarized in Table 1.

Table 1: Waterflow Measurement

Scenario	Water Flow
Source	10.8 L/min
6 mm tubing	7.2 L/min
Girder 1	4.8 L/min
Girder 2	5 L/min
Girder 1&2 parallel	7.6 L/min

As expected, the complex inner structure of the cooling channels leads to a reduction in flow. However, the measurements show that significant cooling can be expected for these structures.

Preliminary Vacuum Tests

To evaluate the performance of 3D printed components in a UHV environment, preliminary tests were performed with 3D printed beam pipes with KF40 flanges (see Fig. 3). These pipes were printed in 1.4404 stainless steel and the sealing surfaces on both ends were turned down on a lathe at the IAP workshop to provide a good vacuum seal. The inside and outside surfaces of the pipes were left as manufactured. A commercially available conventionally manufactured beam pipe of identical dimensions was acquired from Pfeiffer Vac-

uum for comparison. Both the printed and the conventional pipes were then connected to a small 18 L/s turbomolecular pump and repeatedly evacuated and flushed with nitrogen gas.

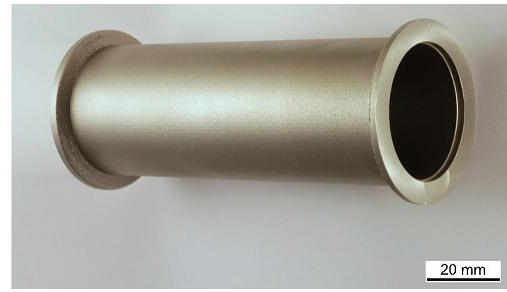


Figure 3: KF 40 pipe printed from stainless steel.

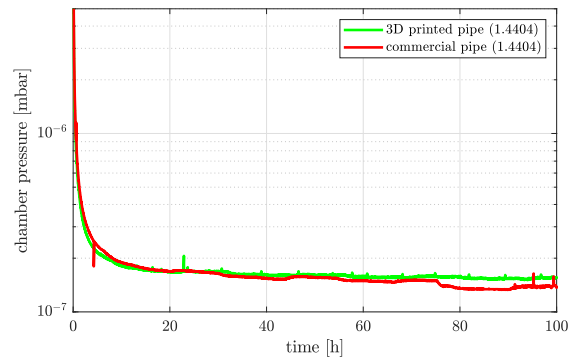


Figure 4: Pumpdown curve of the fourth vacuum cycle of the KF40 test pipes.

Since these pipes were not cleaned and were used as manufactured, some initial outgassing was expected. The experiment showed some interesting results. For one, as expected with each pumping and flushing cycle, the pump down time to a certain pressure point was taking less time with each iteration. Also, it seems, that the rough surface on the inner wall of the printed pipe does not pose a big problem. In the end, both pipes performed very similar and the pumping curve as well as the achieved final pressure were indistinguishable within the accuracy limitations of the experiment. Pressure data of the fourth pumping cycle are shown in Fig. 4.

The final pressure achieved was about 2×10^{-7} mbar for both the conventional and the printed pipe. Similarly promising results were reported in, for example, [3,4]. These results certainly show promise for the UHV capability of printed parts.

Printed Material Properties

To assess the material properties, one of the printed stainless steel pipes was sent to a materials testing lab. Surface roughness was found to be in the order of $R_z = 16.05\text{--}37.52 \mu\text{m}$ dependent on location and orientation of the measurement. Material porosity was determined to be 0.04 % by optical analysis of material cross-sections (see e.g., Fig. 5a,c). Larger cavities in the material were found on the outside of the flange, especially in the areas, where the flange extends outward from the pipe. The pipe was printed standing

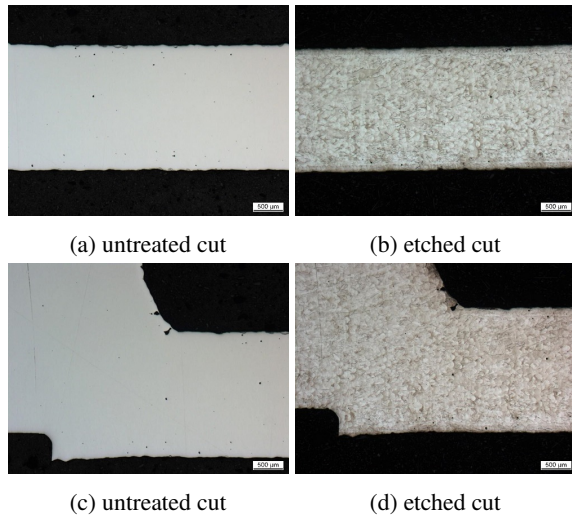


Figure 5: Prepared cross sections of printed KF40 pipe wall material (bright areas = steel). The top images show a cross-section of the pipe wall, the bottom images show the region around the KF 40 flange. Courtesy of GSI Darmstadt, pLinac project.

upright and therefore this area was not supported by bulk material during the printing process. Within the bulk material of the pipe, no large cavities were found. The melt-pool structure of the bulk material, which is caused by the manufacturing process, can be seen in the etched cross-sections in Fig. 5b,d. Overall, the material seems well suited for vacuum applications as the degree of the porosity is not concerning. Depending on the application, further surface treatment will be necessary to reduce surface roughness.

Polishing and Copper Plating

The initial batch of AM IH-structures has been polished in a slide grinding machine. The results are promising, however for the current geometry there are some areas that cannot be reached by the granule particles as well as the flat sides. Consequently, a new geometry is currently being designed to mitigate these issues. Following the surface polishing, the structures have been copper plated with an approximate layer thickness of 50 μm . Optical inspection shows a very clean result of the copper plating (see Fig. 6). Vacuum and rf tests with the copper plated components are planned to assess the quality of the copper layer.

FULL CAVITY VACUUM TESTS

The cavity was fully assembled in early May 2021 (see Fig. 7). For first vacuum tests, the cavity was attached to a turbo-molecular pump (Pfeiffer HiPace80) via one of the top CF40 flanges. A vacuum gauge (Pfeiffer PKR261) was used to measure and log the cavity vacuum. The cavity lids, as well as the girder drift tube structures were sealed using 1.5 mm aluminum wire. Following the publication of [7], where a chamber pressure of 1.19×10^{-6} mbar was reached, the cavity was disassembled and some revisions to sealing

surfaces, as well as additional provisions for a dedicated pre-vacuum system were made.

New Vacuum measurements were performed in early 2022 and a pressure of 1.4×10^{-7} mbar was reached. This demonstrates, that even direct vacuum sealing surfaces can be manufactured with 3D printing. Of course, the surface has to be milled flat after printing, as the surface roughness of a raw printed part would not suffice. At this vacuum level, high power rf experiments are possible. Further improvements of the vacuum are expected from heat treatment to speed up outgassing. This pump-down curve from the latest measurement is shown in Fig. 8.

LOW-LEVEL RF TESTS

Low-level rf measurements were performed with a network analyzer to confirm the frequency and Q-factor of the cavity without any copper plating. For comparison, CST simulations were performed with the final design CAD geometry of the components, to get as close to the manufactured cavity as possible. Simulations were performed with an electrical conductivity of $\sigma_{Cu} = 5.8 \times 10^7$ S/m and $\sigma_{1.4404} = 1.3 \times 10^6$ S/m for copper and stainless steel respectively. Table 2 compares the simulation results with the performed measurements. At critical coupling, the measured resonance frequency is only 79 kHz higher than simulated. The measured unloaded quality factor of the cavity $Q_0 = 1132$ is also reasonably close to the simulated value of $Q_0 = 1321$ for stainless steel. Calculating the quality factor for stainless steel relies on the actual conductivity value of the steel used during manufacturing an can therefore only be approximated based on spec-sheets.

Table 2: Comparison of rf simulation and measurement

Parameter	Simulation	Measurement
f_{res}	433.445 MHz	433.524 MHz
Q_0 (steel)	1321	1132
Q_0 (copper)	8715	-
Z_{eff} (copper)	241.2 M Ω /m	-

CONCLUSION

Most recent vacuum tests showed, that a cavity pressure of 1.4×10^{-7} mbar could be reached without issue. First low-level rf measurements confirmed the operating frequency and also showed good agreement for the stainless-steel Q-factor of the cavity. Overall, the current results show promise for the reality of 3D printed linacs in the near future. The project aims to further investigate the pros and cons of this technology.

NEXT STEPS

Next up are low-level rf measurements with the printed copper plated IH-structures. After these measurements, the cavity lids and center frames will also be copper plated soon. Finally, the structure will be tested at full power with a 30 kW pulsed rf amplifier.

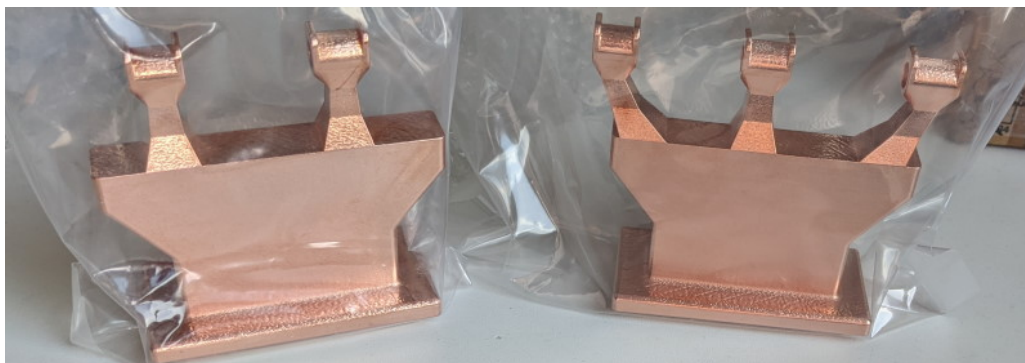


Figure 6: First iteration of AM stainless-steel IH-structures after polishing and galvanic copper-plating.

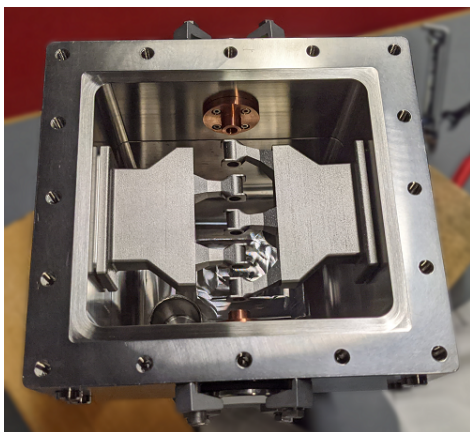


Figure 7: Top view of the cavity during first assembly with installed drift tube structure.

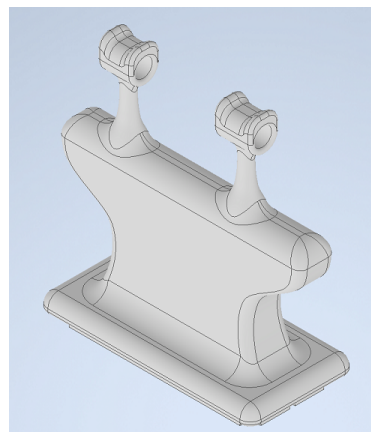


Figure 9: Improved geometry for the AM IH-structure.

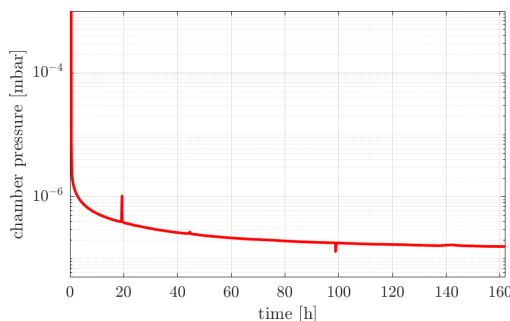


Figure 8: Pumpdown curve of the fully assembled cavity after revision and reassembly in 2022. Peak at 20 h corresponds to opening of the dedicated pre-vacuum valve.

Girder Design Improvements

A first design improvement was done in late 2021 by the inclusion of a dedicated pre-vacuum system. Currently, the overall shape of the girder-drift tube structures is being improved to achieve several goals:

- improved printing performance,
- improved polishing results,
- rf performance improvements.

A first draft of this improved geometry is shown in Fig. 9. The smooth transitions improve the polishing performance, as well as reduce peak fields during copper plating and operation. A set of the improved structures will be printed soon.

ACKNOWLEDGEMENTS

The authors would like to acknowledge the contribution of material analysis of printed parts, which was organized and funded by the GSI Darmstadt proton linac project team.

REFERENCES

- [1] P. Frigola *et al.*, “Advance Additive Manufacturing Method for SRF Cavities of Various Geometries”, in *Proc. SRF’15*, Whistler, Canada, Sep. 2015, pp. 1181–1184. doi:10.18429/JACoW-SRF2015-THPB042
- [2] S. Jenzer *et al.*, “Study of the Suitability of 3D Printing for Ultra-High Vacuum Applications”, in *Proc. IPAC’17*, Copenhagen, Denmark, May 2017, pp. 3356–3358. doi:10.18429/JACoW-IPAC2017-WEPVA043
- [3] G. Sattonnay *et al.*, “Is it Possible to Use Additive Manufacturing for Accelerator UHV Beam Pipes?”, in *Proc. IPAC’19*, Melbourne, Australia, May 2019, pp. 2240–2243. doi:10.18429/JACoW-IPAC2019-WEXXPLS3
- [4] C. R. Wolf, F. B. Beck, L. Franz, and V. M. Neumaier, “3D Printing for High Vacuum Applications”, in *Proc. Cyclotrons’19*, Cape Town, South Africa, Sep. 2019, pp. 317–320. doi:10.18429/JACoW-CYCLOTRONS2019-THC04
- [5] N. Delerue *et al.*, “Prospects of Additive Manufacturing for Accelerators”, in *Proc. IPAC’19*, Melbourne, Australia, May 2019, pp. 4118–4120. doi:10.18429/JACoW-IPAC2019-THPTS008

- [6] U. Ratzinger, “The New High Current Ion Accelerator at GSI and Perspectives for Linac Design Based on H-Mode Cavities”, in *Proc. EPAC’00*, Vienna, Austria, Jun. 2000, paper TUZF204, pp. 98-102.
- [7] H. Hähnel, U. Ratzinger, “First 3D Printed IH-Type Linac Structure – Proof-of-Concept for Additive Manufacturing of Linac RF Cavities”, in *Instruments*, vol. 6, no. 1, p. 9, 2022. doi:10.3390/instruments6010009

DEVELOPMENT AND COMMISSIONING OF THE K500 SUPERCONDUCTING HEAVY ION CYCLOTRON*

Sumit Som[†], Arup Bandyopadhyay, Samit Bandyopadhyay, Sumantra Bhattacharya, Pranab Bhattacharyya, Tamal Kumar Bhattacharyya, Uttam Bhunia, Niraj Chaddha, Jayanta Debnath, Malay Kanti Dey, Anjan Dutta Gupta, Surajit Ghosh, Aditya Mandal, Paris Yalagoud Nabhiraj, Chinmay Nandi, Md. Zamal Abdul Naser, Sandip Pal, Sarbajit Pal, Umashankar Panda, Jedidiah Pradhan, Anindya Roy, Subrata Saha, Sudeshna Seth, Sajjan Kumar Thakur
VECC, Variable Energy Cyclotron Centre, Kolkata, India

Abstract

The K500 Superconducting Cyclotron (SCC) has been developed indigenously and commissioned at VECC. The three-phase Radio-Frequency (RF) system of SCC, consists of three half-wave cavities placed vertically 120 deg. apart. Each half-wave cavity has two quarter-wave cylindrical cavities tied together at the centre and symmetrically placed about median plane of the cyclotron. Each quarter-wave cavity is made up of a short circuited non-uniform coaxial transmission line (called "dee-stem") terminated by accelerating electrode (called "Dee"). The SCC, operating in the range 9 to 27 MHz, has amplitude and phase stability within 100 ppm and 0.1 deg. respectively. The overview of all the subsystems of the cyclotron along with low-level RF (LLRF), high and low power RF amplifiers, cavity analysis, absolute Dee voltage measurement using X-ray method, amplitude and phase control loops will be presented in the talk. The commissioning of the cyclotron with first harmonic Nitrogen⁴⁺ beam extracted at 252 MeV, while operating at 14 MHz RF frequency, along with the correction of first harmonic magnetic field error by repositioning the cryostat within 120 micron accuracy, will be discussed briefly.

INTRODUCTION

The Variable Energy Cyclotron Centre (VECC) at Kolkata, India, has been focused on building cyclotrons as a tool for nuclear physics experiments and medical applications. The center has developed a K130 cyclotron with normal conducting coils and a K500 cyclotron with superconducting coils. Also, VECC has been operating IBA-make 30MeV Medical Cyclotron from production of radioisotopes.

Recently, the first harmonic Nitrogen⁴⁺ beam of 18 MeV/A was extracted from the K500 SCC (as shown in Fig. 1). A 14 GHz Electron Cyclotron Resonance (ECR) ion source (Fig. 2) is integrated with the cyclotron using 28 meters long low energy beam transport line. Initially, the internal beam could be accelerated up to the extraction radius, but could not be extracted due to imperfection of ~ 50 Gauss of 1st harmonic magnetic field (B_1) at the extraction region prohibiting the beam's extraction. The root cause of the imperfection was a damaged dowel resulting in erroneous position of the coil and cryostat. The

machine was dismantled and corrected. Subsequently, the coil and cryostat were repositioned with an accuracy within 120 μm , by devising a new positioning mechanism for precise radial movement of the cryostat. Three radial screws were used to move the 12 Tonnes cryostat. Dial gauges at the outer radius of the cryostat were used to estimate the movement of the cryostat. The final measurement of the cryostat position was taken with a portable CMM machine. Extensive mapping of magnetic field at different excitations of primary coils was carried out. The gross reduction of the imperfection of B_1 achieved to ~7 Gauss at extraction radius resulted in successful extraction of the beam.



Figure 1: The K500 superconducting cyclotron at VECC.



Figure 2: 14GHz ECR ion source and injection beam line.

* Work supported by the DAE, Government of India.

[†] email: ssom@vecc.gov.in

The superconducting cyclotron consists of several challenging technologies that took a considerable time to prepare for the operation, e.g., the NbTi (niobium-titanium) wired magnet, the cryogenic system, the cryo-panel-cooled vacuum system, independently driven three-dee radio-frequency acceleration system, compact magnetic field mapping system, compact electrostatic deflectors, etc.

SUPERCONDUCTING MAGNET

The main component of the K500 superconducting cyclotron is a pill-box type dipole magnet, with a cylindrical iron structure energized by NbTi coil, operating at liquid 4.2K. It produces high magnetic field (up to 5 Tesla) to bend the charge particle beams in a near-circular orbit, which spirals out as energy of the beam increases. The superconducting cyclotron has $K_{\text{bend}}=520$ and $K_{\text{foc}}=160$. The basic design of the machine is based on the superconducting cyclotrons built at Michigan State University and Texas A&M University in USA [1, 2, 3].

Iron Frame

The magnet frame is a cylindrical pill-box structure made of about 80 Tonnes of low carbon magnetic steel (AISI 1020), as shown in Fig. 3. The magnet poles are attached to the circular end-plates at the top and bottom. The outer ring (yoke) supports the end plates and serves as the magnetic flux return path. The coil sits in the annular space between the return path and the poles. The poles are of 0.654 meter radius. Both the poles have three spiral hills, each covering an angle of 46° at the outer radii. The average spiral constant is $(1/33.02)$ rad/cm. The gap

between the upper and lower hills is 64 mm. The valley regions between the adjacent hills have much more significant gaps, varying radially in three steps. These hill-valley structures create the necessary azimuthal variation of the magnetic field. The whole structure has median-plane reflection symmetry. The magnet iron frame is 3.048 meters in diameter and 2.2 meters in height. It is installed on three piers levelled within an accuracy of $800 \mu\text{m}$. The lower and the upper half of the magnet iron pole are shown in Fig. 3.

Superconducting Coil and Cryostat

The cryostat sits in the annular space between the pole and the return yoke (from 0.654 meter to 1.066 meter radius). It houses the two pairs of independently powered superconducting coils, usually called the α coil and the β coil. The coils are made of NbTi multifilament composite superconducting cable (with critical current 1030 A at 5.5 Tesla and 4.2 K), consisting of 500 filaments of 40 micron diameter embedded in the copper matrix (in 1:20 ratio). The superconducting coils are wound on a bobbin made from stainless steel (SS316L). Annular Stainless Steel (SS) sheets are welded to the top and bottom edges of the bobbin all along the periphery to form the liquid-helium chamber containing the coils to cool them down at 4.2 K for cryogenic stability. It is then wrapped with several multi-layer insulation (MLI) sheets. A liquid-nitrogen (LN) cooled thermal shield made of copper sheets encloses the liquid-helium chamber. Several layers of MLI wrappings are provided outside the LN-shield also. The entire coil assembly is then inserted into an annular magnetic steel chamber called coil-tank, as shown in the Fig. 4.



Figure 3: Different parts of iron frame of the magnet: lower half of the magnet (at top-left), three spiral hills (at top-right), return yoke ring (at bottom-left), upper half of the magnet (at bottom-right).

Content from this work may be used under the terms of the CC BY 4.0 licence (© 2022). Any distribution of this work must maintain attribution to the author(s), title of the work, publisher, and DOI



Figure 4: Different parts of cryostat and coil assembly: bobbin made of Stainless Steel (at top-left), Coil-winding machine (at top-middle), superconducting primary coils (at top-right), Copper made liquid nitrogen cooled radiation shield (at bottom-left), MLI wrapped coil plus shield being inserted into the cryostat vacuum chamber made of magnetic steel (at bottom middle), Coil tank with its radial inserts being installed on magnet (at bottom-right).

Nine glass-epoxy support links keep the coil suspended inside the coil tank, three from the top, three from the bottom and three in radial directions. By adjusting the tension in these supports, the coil position is changed. Twenty radial penetrations are welded on the outer surface of the coil tank at the median plane to insert the drives for electrostatic deflectors and magnetic channels, beam diagnostic elements, etc. Cryogenic lines and the power feed-throughs are connected from the top. The cryostat is installed on the lower part of the magnet structure and the upper half of the magnet is lowered down on it using a motorized system to complete the installation. One needs to raise the upper half to access the cyclotron beam chamber.

Trim Coils

Thirteen numbers of field trimming copper coils are wound around each of the six spiral pole-tips (as shown in Fig. 5). All these 78 numbers of trim coils are made of water-cooled copper conductor. The leads of these coils penetrate through the circular holes in the magnet end-plates. All the six trim coils at a particular radius – the upper and lower pairs in all three sectors – are connected in series, except the innermost and outermost trim coils. In case of these two, coils of individual sectors are powered independently, so that they can be used to produce harmonic fields other than 3N harmonics (N=3) and average field contribution. There is a circular trim coil mounted on the central-plug.



Figure 5: The trim coils are mounted on the pole tip and then vacuum impregnated with epoxy resin.

RF Acceleration System

The RF cavity (as shown in Fig. 6) of K500 superconducting cyclotron (SCC) at VECC consists of three half-wave ($\lambda/2$) cavities placed vertically 120 degree apart. Each half-wave cavity [4] has two quarter-wave ($\lambda/4$) cylindrical cavities tied together at the centre and symmetrically placed about median plane of the cyclotron. Each quarter-wave cavity is made up of a short circuited non-uniform coaxial transmission line (called "dee-stem") terminated by accelerating electrode (called "Dee"). The RF cavity is analysed using 3D CST Microwave Studio code and RF parameters like Shunt impedance, Quality factor and cavity size etc. have been calculated in the operating frequency range of 9–27 MHz. During the

commissioning of RF system, absolute Dee voltage calibration has been done by using AMPTEK make CdTe (Cadmium Telluride) X-ray detector and the calculated RF parameters have been validated by the measured absolute Dee voltage [5], RF power and quality factor of the cavity.

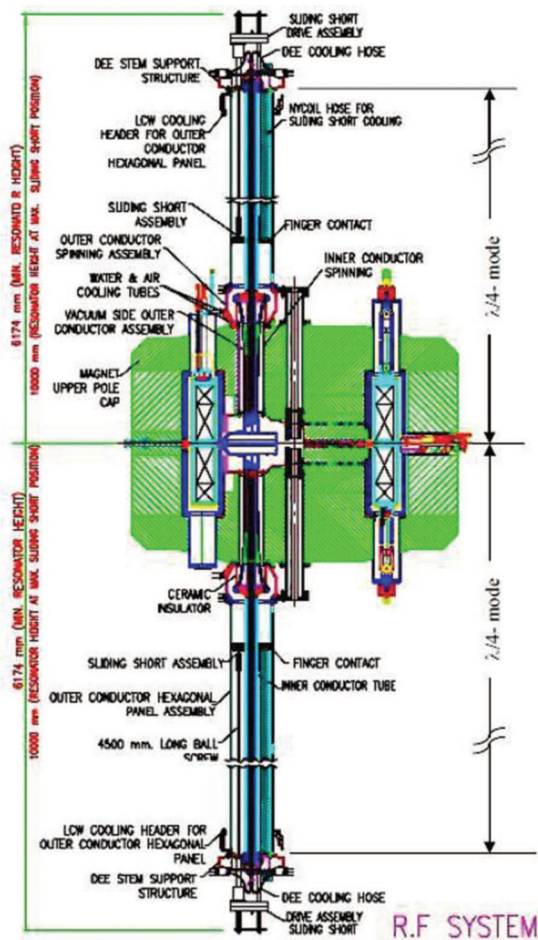


Figure 6: Half-wave coaxial RF cavity of SCC.

The phase control system has the option to change the relative phase difference between any two RF cavities and maintain the phase stability [6] within $\pm 0.1^\circ$ during round-the-clock cyclotron operation. The said precision phase loop consists of both analog In-phase/Quadrature (I/Q) modulator to achieve faster response and also Direct Digital Synthesis (DDS) based phase shifter to achieve wide dynamic range as well. Three spiral Dees are situated in the three spiral valley regions (as shown in Fig. 7). Dee-stem consists of uniform coaxial line (in air) and also tapered line (in vacuum). The sliding short plate is electrically connected to the outer and inner conductors of coaxial line by Be-Cu contact finger with silver-graphite (99% silver +1% graphite) contact balls at the tip.

Each of the three half-wave cavity is fed with rf power (80 kW max.) from each of the three high power tetrode based final RF amplifiers (as shown in Fig. 8), developed in-house. RF system of SCC has been operated at 14 MHz with dee voltage in the range of 45 - 50 kV, to extract the first harmonic 252 MeV Nitrogen⁴⁺ and 360 MeV Neon⁶⁺ beam.



Figure 7: Lower dees and Liner.

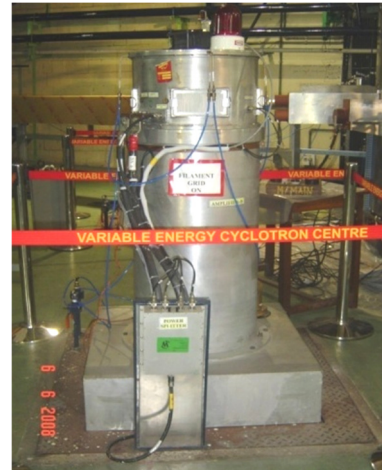


Figure 8: Tetrode based final RF Amplifier.

Magnetic Field Mapper

The magnetic field was mapped with a search coil and NMR set up on a polar (r, θ) grid at the median plane of cyclotron with 0.1-inch radial step and 1° azimuthal step. The mechanical system comprises of a cantilever arm assembly, the radial drive assembly, angular drive and transducer assembly. The arm assembly consists of a straight track, a support bar, a cart carrying the search coil and a linear encoder. All materials of the arm assembly, placed inside the cyclotron, are non-metallic and non-magnetic to avoid distortion because of the high magnetic field and eddy current forces on them. A linear encoder made of a photo sensor assembly head that moves on a linear optical strip with 360 lines/inch was used to measure the radial position of the search coil during mapping. A drive mechanism consisting of a DC brush-less servo motor, spur-gear set and a pulley-drum was used to move the search coil radially at a uniform velocity of about 40 cm/sec. A Kevlar string wound on the pulley-drum was connected to the search coil through the hollow angular drive shaft. The search coil moved from -50 mm to 685 mm on the base track along the radial direction of the cyclotron. The zero (0 mm) in this scale represents the mapping centre. One out of every thirty-six pulses from the encoder was used to trigger the digital integrator unit to read and integrate the search coil output between two successive triggers. After completing each radial scan for a particular angular position, the arm assembly was rotated

Content from this work may be used under the terms of the CC BY 4.0 licence (© 2022). Any distribution of this work must maintain attribution to the author(s), title of the work, publisher, and DOI

in 1° or 0.5° angular steps using an angular drive mechanism. The angular position of the search coil carrying arm is determined by an absolute rotary Inductosyn encoder with an accuracy of 1.7 arc-sec, which was obtained using two dual channel preamplifier and AWICS converter board. A micro-controller based interface module was used to read the angular position online.

COMMISSIONING

Magnetic Field Correction

The mapping system consists of a search coil that moves on a radial track with an optical sensor mounted on the coil cart. The counts in the digital integrator were calibrated using two absolute field values by a Nuclear Magnetic Resonance (NMR) probe placed at the center of the machine and in specific hill and valley locations, where the field uniformity meets the requirement of NMR locking. The 360° polar map covers a radius of 668 mm with a radial and azimuthal step size of 2.54 mm and 1° , respectively. The linear encoder that provides the position of the search coil has an accuracy of 10 μm . The measurement accuracy of the angular encoder is 1.7 arc sec.

Positioning the coil-tank and coils coaxially with the iron mass is a significant concern in K500 superconducting cyclotron since it introduces 1st harmonic field imperfection in the extraction region cyclotron [7, 8]. It is undesirable because the equilibrium orbit (EO) is off-centered due to 1st harmonic field imperfections as the beam passes through $\nu_r = 1$ resonance. In K500 SCC, the beam passes through $\nu_r = 1$ resonance near the machine's center and again near the extraction zone. The stable regions of phase space also shrink to zero at these resonance zones. In addition, the off-centering of the orbit may excite the critical Walkinshaw resonance ($\nu_r = 2\nu_z$) resulting vertical blow-up of the beam.

About 28 Gauss 1st harmonic field in the central region and 50 Gauss in the extraction region were observed (Fig. 9). The first harmonic peaks show an iron-produced component nearly independent of coil excitations. The 1st harmonic field introduced due to misalignment of the superconducting coils was current dependent, as in the radial range from 400 mm to 600 mm. The peak near 650 mm radius was due to positioning error of the coil-tank.

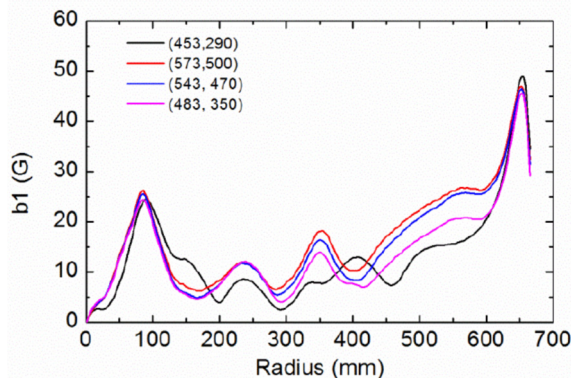


Figure 9: The 1st harmonic field amplitude vs. radius.

The 1st harmonic field near centre was reduced below 10 Gauss by a suitable trimming of iron in large-hill-addition, as shown in Fig. 10.

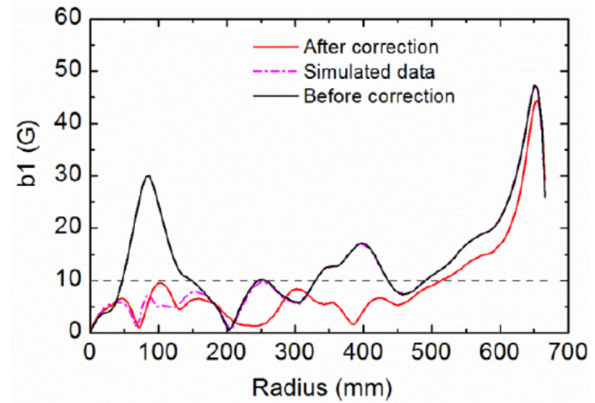


Figure 10: 1st harmonic amplitude ($I_\alpha = 453\text{A}$, $I_\beta = 290\text{A}$) before and after correction of large-hill-addition.

It was noted that the optimum coil position to minimize 1st harmonic component might increase the radial force on the support links. Therefore, keeping the coil in a compromised place was necessary. Following the careful repositioning of the coil and the coil tank with an accuracy of $\pm 100.0\ \mu\text{m}$, the measured 1st harmonic field amplitude reduced below 10 Gauss, as shown in Figs. 11 and 12.

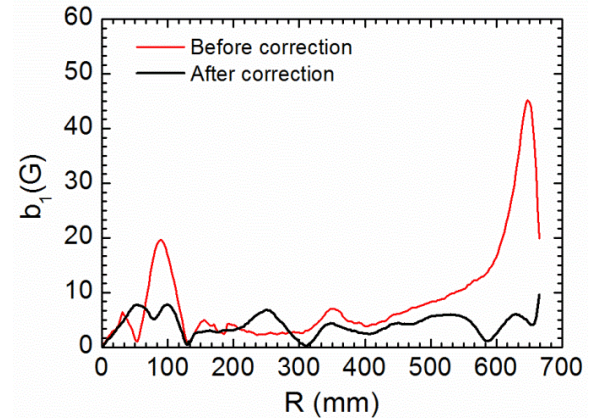


Figure 11: 1st harmonic field before and after correction of cryostat position.

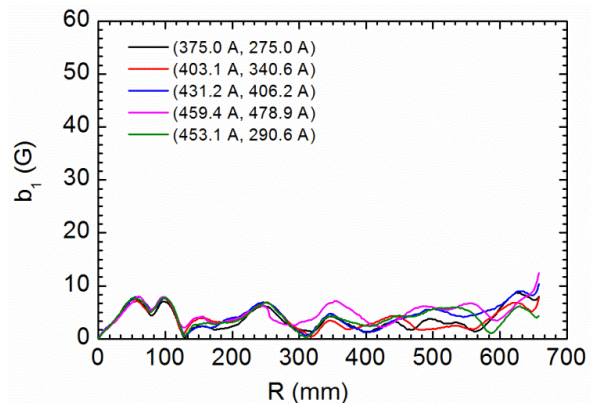


Figure 12: 1st harmonic amplitude at different excitations of main coils.

BEAM EXTRACTION

The magnetic field correction led to successful extraction of the beam from K500 SCC at VECC [9–12]. Isochronous field fitting code TCFIT was used to calculate the current settings of 2 main coils and 14 trim coils using the measured magnetic field data. Nitrogen²⁺ beam at 4.5 MeV/u in 2nd harmonic mode of operation and Nitrogen⁴⁺ beam at 18 MeV/u in 1st harmonic mode of operation are extracted from the cyclotron and transported to the experimental cave. The profile of accelerated and extracted beam current is shown in Fig. 13.

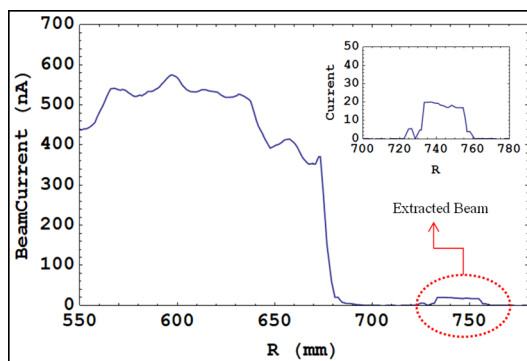


Figure 13: Beam current vs. radius for N²⁺, 4.5 MeV/u beam ($f_{rf} = 14$ MHz, in 2nd harmonic mode of operation); First deflector entry was at 668.0 mm.

ACKNOWLEDGEMENTS

I am thankful to VECC scientists, engineers and technical staff who have put their relentless effort in successfully extracting the second and first harmonic beam from K500 superconducting cyclotron.

REFERENCES

- [1] H. G. Blosser, “The Michigan State University superconducting cyclotron program”, *IEEE Trans. on Nucl. Sci.*, vol. 26, no. 2, p. 2024, Apr. 1979.
doi:10.1109/TNS.1979.4329804
- [2] D. P. May *et al.*, “Status of the Texas A&M K500 Superconducting Cyclotron”, in *Proc. 10th Int. Cyclotron Conf. and Their Applications (Cyclotrons'84)*, East Lansing, MI, USA, Apr.-May 1984, paper F05, pp. 267-270.
- [3] R. K. Bhandari, “Status of the Calcutta K500 Superconduction Cyclotron Project”, in *Proc. 16th Int. Conf. on Cyclotrons and Their Applications (Cyclotrons'01)*, East Lansing, MI, USA, May 2001, paper C-4.

- [4] S. Som *et al.*, “Development Of Rf System For K500 Superconducting Cyclotron at VECC Kolkata”, in *Proc. 18th Int. Conf. on Cyclotrons and Their Applications (Cyclotrons'07)*, Giardini-Naxos, Italy, Oct. 2007, pp. 473-475.
- [5] Sumit Som, Sudeshna Seth, Aditya Mandal, Saikat Paul, Anjan Duttagupta, “Radio frequency cavity analysis, measurement and calibration of absolute Dee voltage for K500 superconducting cyclotron at VECC, Kolkata”, *Rev. Sci. Instrum.*, vol. 84, p. 023303, 2013.
doi:10.1063/1.4789784
- [6] Sumit Som, Surajit Ghosh, Sudeshna Seth, Aditya Mandal, Saikat Paul, Suprakash Roy, “Precision phase control for the radio frequency system K500 superconducting cyclotron at Variable energy Cyclotron Centre, Kolkata”, *Rev. Sci. Instrum.*, vol. 84, p. 113303, 2013.
doi:10.1063/1.4828670
- [7] M. K. Dey *et al.*, “Coil Centering Of The Kolkata Superconducting Cyclotron Magnet”, in *Proc. 18th Int. Conf. on Cyclotrons and Their Applications (Cyclotrons'07)*, Giardini-Naxos, Italy, Oct. 2007, pp. 438-440.
- [8] F. Marti and P. S. Miller, “Magnetic Field Imperfections in the K500 Superconducting Cyclotron”, in *Proc. 10th Int. Cyclotron Conf. and Their Applications (Cyclotrons'84)*, East Lansing, MI, USA, Apr.-May 1984, paper B25, pp. 107-110.
- [9] J. Debnath, U. Bhunia, M. K. Dey, J. Pradhan, A. Dutta, S. Paula, A. Dutta Gupta, A. Bandyopadhyay and S. Som, “Optimization of compensation of magnetic field imperfection in K500 superconducting cyclotron”, *J. Instrum.*, vol. 15, no. 9, Sep. 2020.
doi:10.1088/1748-0221/15/09/t09004
- [10] J. Pradhan, J. Debnath, M. K. Dey *et al.*, “Median plane and Beam Diagnosis in the Central region for Compact Superconducting Cyclotron”, *Nucl. Instrum. Methods Phys. Res., Sect. A*, vol. 993, p. 165084, Mar. 2021.
doi:10.1016/j.nima.2021.165084
- [11] J. Pradhan, J. Debnath, M. K. Dey, *et al.*, “Characteristics of beam loss in compact superconducting cyclotron”, *J. Instrum.*, vol. 15, Aug. 2020.
doi:10.1088/1748-0221/15/08/T08006
- [12] S. Paul, U. Bhunia, J. Debnath, M. K. Dey *et al.*, “A beam dynamics study for efficient extraction from the VECC K500 superconducting cyclotron”, accepted in *J. Instrum.*, Mar. 2022.
doi:10.1088/1748-0221/17/03/P03029

BEAM TUNING AUTOMATION ACTIVITIES AT TRIUMF*

S. Kiy, J. Adegun, F. Ames, A. Andres, R. Baartman, H. Bagri, K. Ezawa,
W. Fedorko, P. Jung, O. Kester, K. Lucow, J. Nasser, T. Planche, S.D. Rädcl,
B. Schultz, O. Shelbaya, B. Stringer, D. Thomson, D. Wang, K. Wu
TRIUMF, Vancouver, BC, Canada

Abstract

The particle accelerator complex at TRIUMF provides beams for secondary particle production including rare isotopes. The post acceleration of rare isotope ions demands frequent changes of beam properties like energy and changes of the ion species in terms of isotope and charge state. To facilitate these changes to beam properties and species, a High Level Applications (HLA) framework has been developed that provides the essential elements necessary for app development: access to sophisticated envelope simulations and any necessary beamline data, integration with the control system, version control, deployment and issue tracking, and training materials. With this framework, one can automate collection of beam data and subsequently pull that data into a model which then outputs the necessary adjustments to beam optics. Tuning based on this method is model coupled accelerator tuning (MCAT) and includes pursuits like the training of machine learning (ML) agents to optimize corrections benders. A summary of the framework will be provided followed by a description of the different applications of the MCAT method — both those currently being pursued, and those envisioned for the future.

MOTIVATION

Programs that aid accelerator operation are often developed in an ad-hoc manner by physicists — *particularly for themselves as end-users* — as the facility expands.

In the case of TRIUMF, a lab more than 50 years old, there are various tools and programs that have been developed by experts for different operating systems using different programming languages for a variety of different accelerators across the campus. However, this approach does not scale well as the size and complexity of the lab increase — too many tools can end up being duplicated and not all are well maintained.

The newly installed e-linac and upcoming new proton beamline from the main cyclotron will drive rare isotope beam (RIB) production via new target stations and associated beamlines in ARIEL. This is expected to triple the number of deliverable RIB hours to experiments.

To allow for reliable operation in this new era, a High Level Applications (HLA) task force was established at TRIUMF in 2017 [1] with the mission to reduce facility overhead and improve beam reliability [2]. To accomplish this, the taskforce was to create a standard software framework for

creating applications that can be easily used at any of our many accelerator facilities, as depicted below in Fig. 1.

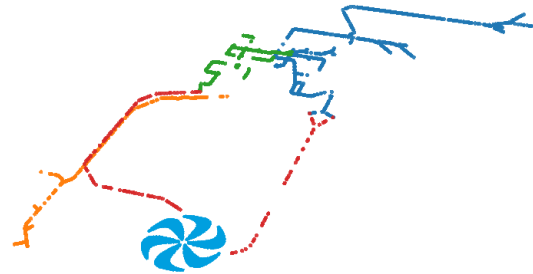


Figure 1: Layout of TRIUMF beamlines based on data from acc xml files. E-linac devices are shown in orange, primary proton beamlines in red, the new ARIEL RIB transport beamlines in green, and ISAC RIB transport beamlines in blue.

HLA FRAMEWORK

The software development framework itself is critical to the development of robust apps as well as enticing staff members to contribute to existing code repositories rather than working alone.

Jaya – Integration with the Control System

Jaya is a web application acting as the middle layer that allows communication with the underlying low-level control system. It currently maintains channel access (CA) monitors on over 5000 process variables (PVs) distributed over five independent EPICS subnets at TRIUMF.

PV values are stored in an in-memory database (Redis). This way, any HLAs that request to read PV values only poll the HLA server database and don't produce any additional load on the EPICS networks.

A second noteworthy component of jaya is the additional backend processes that allow for long running measurements. Jaya uses a Python task queue package called Celery, which allows passing of jobs between the jaya web application and the Celery backend process via Redis. Using this tool, jaya allows users to create custom scans or measurements that allow for setting, waiting, and saving of data as required by the users. An example of this functionality is shown in Fig. 2. In the measurement shown [3], the current of a magnetic quadrupole was changed in various step sizes and directions, while saving magnetic field data to an HLA database used for storing beam measurements (beamDB).

* Funded under a contribution agreement with NRC (National Research Council Canada).

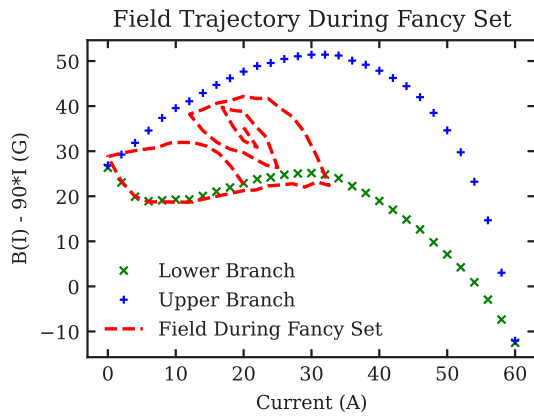


Figure 2: Field during algorithm for setting of magnetic quadrupoles.

Acc – xml Description of Beamline Information

Acc is a collection of xml files describing TRIUMF’s beamlines that are intended to contain all necessary information needed to locate devices, generate envelope simulations, load and scale optics settings, and more. It contains the necessary references to all relevant design drawings from which beamline positions were attained.

The acc files are stored in a version controlled (git) repository and available via the DevOps platform Gitlab. Over 20 staff members have contributed to over 1000 commits in this repository, demonstrating the interest and utility in an easily accessible open-source tool such as this.

beamDB – Database of Beam Measurements

Coordination and consistency in saving and accessing beam related measurements can be difficult. Historically users have saved data from diagnostics to a shared file server on a case by case basis. Filenames are chosen by users, other relevant data is difficult to link, and the end result is a large flat directory of data which can be hard to navigate. This could pose a significant issue as we look forward to applications of machine learning on the operation of beamlines and accelerators.

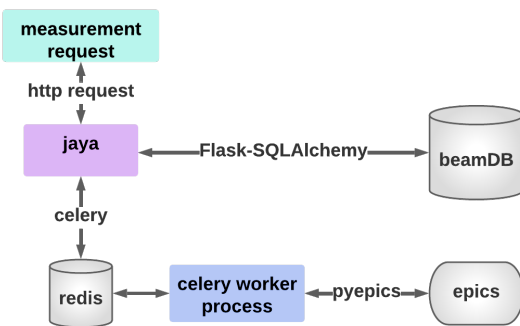


Figure 3: Schematic of the fundamental elements for automation - jaya, the beamDB, backend processes, and connection to EPICS.

To improve the way in which beamline/tuning related data is saved and later searched/utilized, we have implemented a database solely to store measurements of various particle beams [4]. We are using a PostgreSQL database accessed via jaya using Flask-SQLAlchemy, as shown in Fig. 3.

For the RIB facilities of TRIUMF, the beamDB stores beam properties, optics settings, and a user-defined collection of diagnostics measurements all linked together in various tables. Paired with the automation capabilities in the backend of jaya, this has enabled us to begin building a large training dataset that can in the future used to training various ML agents.

Profiles – Package for Processing Data

Measuring the profiles of various particle beams is an essential part of understanding both the machine and beam properties. One of the most common instruments for measuring beam profiles at TRIUMF is a wire scanner type device, called a rotary profile monitor (RPM). The raw data output from an RPM is two arrays: one a voltage (representing position) and the other a current.

These devices (and others) have various different features that can complicate processing of the profile data. This can include electrical noise, mechanical issues, potentiometer issues, and more. To provide a consistent approach that all HLA users and apps can utilize, a co-op project was completed [5] which developed a Python package to process profile data. This package utilizes a random forest classifier (RFC) system to select the most appropriate of four deterministic algorithms for processing the data. The RFC was trained by having staff members with experience of the various wire scanned failure modes classify a large set of RPM data into a number of different categories. Quality data processing of a beam profile (Fig. 4) accepts all data points that are really representative of the underlying beam distribution, while rejecting other data. Poor profile processing often incorrectly includes noise or background in the calculation of the beam size (Fig. 5).

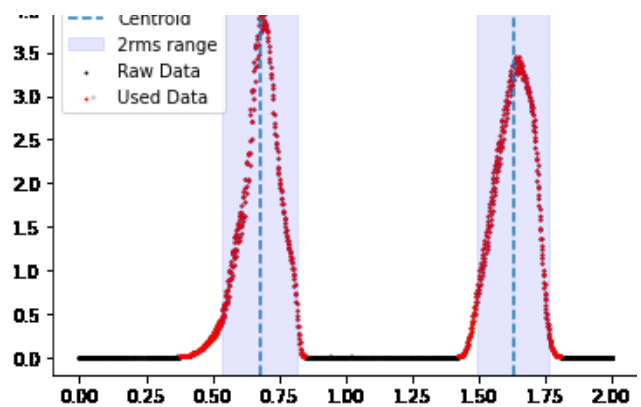


Figure 4: Example of good data processing of an RPM scan.

Content from this work may be used under the terms of the CC BY 4.0 licence (© 2022). Any distribution of this work must maintain attribution to the author(s), title of the work, publisher, and DOI

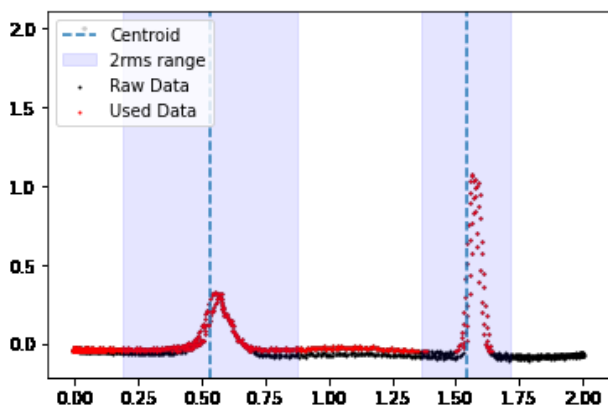


Figure 5: Example of poor data processing of an RPM scan.

accpy and fancy_set – Interfacing with acc and jaya

accpy is a Python package built with a number of different modules. One module provides a collection of functions to connect to the jaya backend running on the server to get and set data to the control system. A second module allows users to easily query and pull beamline information from the acc xml file structure.

A recent addition to accpy was from a co-op project [3]. This project added an algorithm to improve the way in which magnetic optics are set such that effects of hysteresis are minimized. This new ramping technique, fancy_set, is particularly of use for quadrupoles with unipolar power supplies. The routine cycles the quadrupole setpoint around the desired final current at successively smaller amplitudes as shown in Fig. 6 and the resulting path the magnetic field takes is shown earlier in Fig. 2.

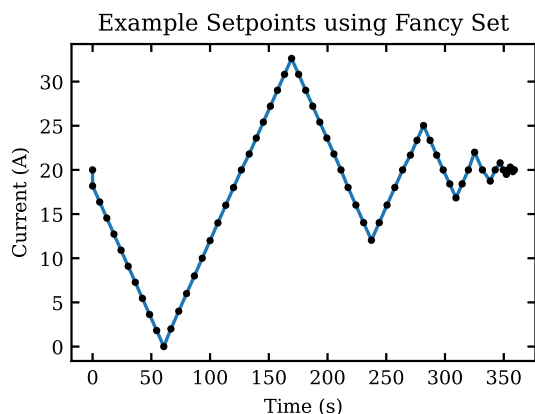


Figure 6: Quadrupole current vs time using the fancy_set routine.

This new routine is expected to help establish more accurate and stable tunes, thus reducing tuning time for operators overall. Initial tests have also been carried out to use this routine for ramping of the main cyclotron magnet.

Gitlab – DevOps Platform

To enable the development of HLAs at TRIUMF, a Gitlab server was established. Gitlab is a DevOps¹ platform that has many benefits. This include the Continuous Integration/Continuous Deployment (CI/CD) feature, which allows custom pipelines of jobs to be executed when new versions of code are committed. With this, we are able to have applications automatically redeploy when new code is committed to gitlab, which can be to either a development or production machine. Gitlab also allows us to serve up repositories of packaged Python code which can easily be installed by users or applications. Last, Gitlab includes an issue tracking feature through which requests, bugs, and improvements are tracked, allowing for easy collaboration.

Docker and Kubernetes

Applications developed are now being built and deployed primarily as Docker images within a Kubernetes cluster. This has a number of significant benefits including: basically fully eliminating dependency issues both when developing and deploying; improving scalability - Kubernetes can start extra processes of an app when demand is high; further simplifying and expediting the deployment process.

APPLICATIONS

Automation

The long-running backend measurements enabled by jaya give students and physicists the ability to code custom measurements. This can be done both on a local Python script which posts the measurement request to be approved by a control room console, or within apps themselves. One recent example of this was to enable multi-parameter scans of a FEBIAD (Forced Electron Beam Induced Arc Discharge) ion source, shown in Fig. 7. This ability assists both with the analysis of FEBIAD models and the identification of optimal operating settings.

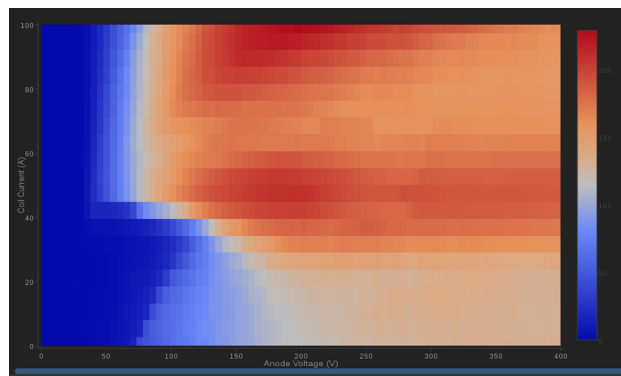


Figure 7: Heatmap showing ion beam intensity for varying FEBIAD source settings (Coil current and Anode voltage).

¹ Software development and IT operations. DevOps is an approach toward expediting the cycle between developing and deploying new code.

Snapshot – Data Collection

In order to populate the beamDB quickly with well categorized information, there was a need to improve the way in which beam current, profiles, and optics settings were collected. Historically data had been collected via buttons on EPICS Extensible Display Manager (EDM) screens and a Perl/TK tool. Information was then stored as html tables and screenshots in an electronic logbook.

A project led by an operator leveraged the existing HLA framework to create a web application that automates these processes and stores the data into the beamDB. In its first year of use this app has already noticeably reduced the work load on operators and has contributed to the over 1000 data sets saved to the beamDB. Figure 8 shows the UI view of two beam profiles saved with snapshot.

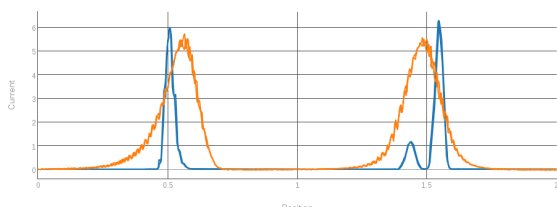


Figure 8: Webpage UI showing profiles stored in the beamDB that were automatically collected using the snapshot app.

Model Based Phasing of ISAC-II Linac

The ISAC-II superconducting heavy ion linac at TRIUMF accelerates both stable and radioactive ions up to as high as 16.5 MeV/u through 40 quarter wave resonators distributed over eight cryomodules. The cavities are individually controlled and their configuration regularly changes depending on cavity performance and requested beam properties from the experiments it serves.

Also utilizing the HLA framework, a project for modelling and automating the phasing of the cavities is nearing completion. The phase offsets and amplitudes of the cavities have been investigated and calibrated allowing for initial tests of an automated phasing routine [6] which has been demonstrated to reduce overhead in switching linac configuration from over eight hours to less than one.

Model-Coupled Accelerator Tuning (MCAT)

The envelope code TRANSOPTR [7], in use at TRIUMF since 1984 [8], has recently been expanded to include RFQs [9] and KONUS DTLs [10]. Its native FORTRAN is capable of executing start to end accelerator simulations in under one second, suitable for real-time use. Using the code's internal optimizers (simulated annealing or downhill simplex), it is possible to rapidly re-compute entire machine tunes, using on-line beam diagnostic data as inputs [11]. This technique of model coupled accelerator tuning (MCAT) is being developed at the ISAC-I linac, aiming to produce a closed loop, diagnostic driven feedback control system for the accelerator.

Machine Learning Based Beam Steering

Tuning the steerers of a particle accelerator is a complex process, often with a high dimensional parameter space and limited observables. These characteristics make it potentially suited for reinforcement algorithms. The ultimate goal is to reduce the tuning time for such facilities. The training process is an iterative process in steps in which the agent takes the state s_t of a beam line as an input and predicts an action a_t sampled from a policy $\pi(a_t|s_t)$. The policy is updated using Recurrent Deterministic Policy Gradient (RDPG) algorithms based on the so-called reward (calculated from beam transmission) [12, 13]. The optimization process for different steps on a simulated beam line using TRANSOPTR is shown in Fig. 9. Initial investigations and tests of this approach [14] have been carried out over the past year using the offline ion source (OLIS) at TRIUMF.

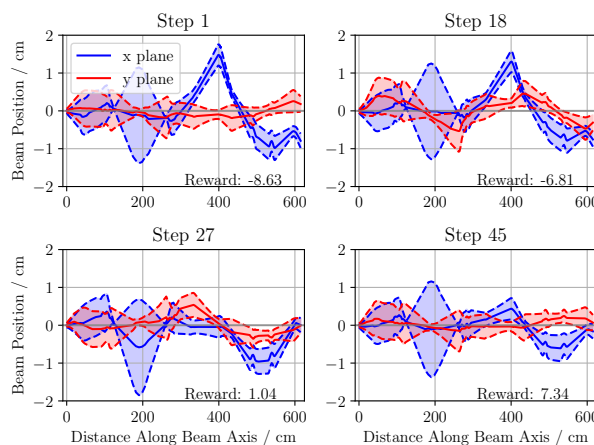


Figure 9: A validation of a trained agent on the simulated OLIS beam line. The panels show the evolution of the steerer predictions of a trained agent for different steps. The reward (calculated from the beam transmission) is increasing during the optimization process.

CONCLUSION

Automation of beam tuning activities is a major area of interest in labs around the world. TRIUMF has now implemented a robust framework using modern tools that has allowed development of apps for automation, high-level physics modelling and feedback, and user-defined measurements that can be saved to a properly indexed database. All software is available openly within the TRIUMF network for other staff members to utilize and contribute to. Further automation is expected in the near future as we strive to accumulate large data sets for future applications of machine learning.

REFERENCES

- [1] C.B. Barquest *et al.*, “Web-Based Control Room Applications at TRIUMF”, in *Proc. IPAC'18*, Vancouver, Canada, Apr.-May 2018, pp. 4832–4835. doi: 10.18429/JACoW-IPAC2018-THPML078

- [2] C. Barquest, “A brief history of high level applications at TRIUMF,” TRIUMF, Tech. Rep. TRI-BN-19-01, 2019.
- [3] J. Nasser, R. Baartman, O. Kester, S. Kiy, T. Planche, S. Räd-
 el, and O. Shelbaya, “Algorithm to mitigate hysteresis in
 magnets with unipolar power supplies,” in *Proc. IPAC’22*,
 Bangkok, Thailand, Jun. 2022, to be published. doi:10.
 18429/JACoW-IPAC2022-MOPOST039
- [4] O. Shelbaya, “HLA-beamData: An Elementwise Database
 for Passive Beam Data Accumulation,” TRIUMF, Tech. Rep.
 TRI-BN-19-16, 2019.
- [5] K. Wu, “Profile Monitor Classification using Random Forest
 Classifier,” TRIUMF, Tech. Rep. TRI-BN-21-11, 2021.
- [6] S. Kiy, R. Baartman, O. Kester, and O. Shelbaya, “First Tests
 of Model-Based Linac Phasing in ISAC-II,” presented at the
 15th Heavy Ion Accelerator Technology Conf. (HIAT’22),
 Darmstadt, Germany, June 2022, paper TUP19, this confer-
 ence.
- [7] R. Baartman, “TRANSOPTR Reference Manual,” TRIUMF,
 Tech. Rep. TRI-BN-22-08, 2022.
- [8] R. Baartman, “TRANSOPTR: Changes since 1984,” TRIUMF,
 Tech. Rep. TRI-BN-16-06, 2016.
- [9] O. Shelbaya, R. Baartman, and O. Kester, “Fast radio fre-
 quency quadrupole envelope computation for model based
 beam tuning,” *Phys. Rev. Accel. Beams*, vol. 22, no. 11,
 p. 114602, 2019. doi:10.1103/PhysRevAccelBeams.22.
 114602
- [10] O. Shelbaya, T. Angus, R. Baartman, P.M. Jung, O. Kester,
 S. Kiy, T. Planche, and S. D. Räd-
 el, “Autofocusing drift tube
 linac envelopes,” *Phys. Rev. Accel. Beams*, vol. 24, no. 12,
 p. 124602, 2021. doi:10.1103/PhysRevAccelBeams.24.
 124602
- [11] O. Shelbaya, R. Baartman, P. Jung, O. Kester, S. Kiy,
 T. Planche, Y.-N. Rao, and S. Räd-
 el, “On-Line Retuning
 of ISAC Linac Beam with Quadrupole Scan Tomography,” in
Proc. IPAC’21, Campinas, SP, Brazil, May 2021, pp. 4187–
 4189. doi:10.18429/JACoW-IPAC2021-THPAB205
- [12] T.P. Lillicrap, J.J. Hunt, A. Pritzel, N. Heess, T. Erez, Y. Tassa,
 D. Silver, and D. Wierstra, “Continuous control with deep re-
 inforcement learning,” 2019. doi:10.48550/arXiv.1509.
 02971
- [13] N. Heess, J.J. Hunt, T.P. Lillicrap, and D. Silver, “Memory-
 based control with recurrent neural networks,” 2015. doi:
 10.48550/arXiv.1512.04455
- [14] D. Wang, R. Baartman, H. Bagri, W. Fedorko, P. Jung,
 O. Kester, S. Kiy, C. Macdonald, T. Planche, and O. Shelbaya,
 “Accelerator tuning with deep reinforcement learning,” in
*Proceedings of the Fourth Workshop on Machine Learning
 and the Physical Sciences (NeurIPS)*, 2021.
[https://ml4physicalsciences.github.io/2021/
 files/NeurIPS_ML4PS_2021_125.pdf](https://ml4physicalsciences.github.io/2021/files/NeurIPS_ML4PS_2021_125.pdf)

BEAM INSTRUMENTATION, CHALLENGING TOOLS FOR DEMANDING PROJECTS – A SNAPSHOT FROM THE FRENCH ASSIGNED NETWORK

F. Poirier¹, T. Durand¹, C. Koumeir¹, C. Jamet², S.M. Ben Abdillah³, N. Delerue³, H. Guler³, T. Adam⁴, E. Bouquerel⁴, C. Maazouzi⁴, F. R. Osswald⁴, C. Thiebaut⁵, M. Verderi⁵, L. Daudin⁶, A. Husson⁶, B. Lachacinski⁶, J. Michaud⁶, B. Cheymol⁷, D. Dauvergne⁷, M.-L. Gallin-Martel⁷, R.Molle⁷, C. Peaucelle⁷

¹ARRONAX, Saint-Herblain, ²GANIL, Caen, ³IJCLAB, Orsay, ⁴IPHC, Strasbourg, ⁵LLR, Palaiseau, ⁶LP2I, Gradignan, ⁷LPSC, Grenoble

France

Abstract

Particle accelerators are thrusting the exploration of beam production towards several demanding territories that is beam high intensity, high energy, short time and geometry precision or small size. Accelerators have thus more and more stringent characteristics that need to be measured. Beam diagnostics accompany these trends with a diversity of capacities and technologies that can encompass compactness, radiation hardness, low beam perturbation, or fast response and have a crucial role in the validation of the various operation phases. Their developments also call for specialized knowledge, expertise and technical resources. A snapshot from the French CNRS/IN2P3 beam instrumentation network is proposed. It aims to promote exchanges between the experts and facilitate the realization of project within the field. The network and several beam diagnostic technologies will be exposed. It includes developments of system with low beam interaction characteristics such as PEPITES, fast response detector such as the diamond-based by DIAMMONI, highly dedicated BPM for GANIL-SPIRAL2, emittance-meters that deals with high intensity beams and development for MYRRHA, SPIRAL2-DESIR and NEWGAIN.

NETWORKS AT THE IN2P3

The scientific programs carried out at the French National Institute of Nuclear and Particle Physics (IN2P3) require specific instruments that can only be developed within the laboratories themselves. Indeed, the expected performance of the instruments are more and more constrained in terms of granularity, sensitivity, dynamics, resolution, speed, tolerance to radiations, integration and transparency.

Instrumentation therefore mobilises a large number of professions and skills and becomes, in itself, a strategic axis of Research & Technology (R&T). The hyper-specialisation of professions and the current context of resources have led to rationalising this R&T upstream, by promoting the emergence of networks of experts across laboratories around the main families of detectors and associated transverse techniques for examples mechanics, gas detectors, cryotechnics, semi-conductors, photo-detection, beam instrumentation.

These networks are intended to be privileged exchange tools allowing experts to best share the know-how acquired

between projects and between laboratories. They are an important factor of cohesion and efficiency, just as they generate specific training.

This network organisation makes it possible to identify emerging technologies, local skills, and to support them. Exchanges between experts promote the sharing of best practices, the identification and management of common engineering tools, and the rationalisation of resources.

THE BEAM INSTRUMENTATION NETWORK (RIF)

The Beam Instrumentation Network (in French, RIF i.e. Réseau Instrumentation Faisceau) is one of the identified transverse structures in the IN2P3. The RIF was born at the end of 2018 with the aim of bringing together experts in the field of diagnostics and associated instrumentation for particle beams in accelerators.

Missions

The Network animates, coordinates, encourages, and promotes interdisciplinary initiatives carried out in the various fields of beam instrumentation. As part of these missions, the network undertakes structuring actions that aim to:

- Take an active part in scientific and technological monitoring and, in particular, on the subject of the evolution of research support.
- Identify and promote the skills and expertise of the Network by updating pools of experts, and by ensuring a prospective analysis of skills in conjunction with the IN2P3.
- Ease communication and skills and/or information exchange between its members (sharing of good business practices, know-how) in the form of seminars or feedback.
- Pool experiences, with a view to solve particular technical problems, and capitalise to eventually make available, and manage a set of common tools, operating methods or best practices.
- Develop proposals relating to its missions for CNRS bodies, institutes and, more broadly, higher education and research bodies.
- Identify and help promote one or more research themes relating to technological locks in the field in order to boost R&D.

- Identify R&T projects in addition to IN2P3 Masters Projects to overcome certain technological obstacles in the field.
- Develop, if necessary, specific training offers relating to beam instrumentation in conjunction with the IN2P3 training Mission Manager. Promote learning and internships in the field of instrumentation within IN2P3 units.

In order to support its mission, the network is gathering almost 40 active members disseminated throughout several laboratories in France. It has led more than 22 meetings since its creation. The subjects of the presentations have been on a wide spectrum of diagnostics ranging from beam position monitor and emittance-meters to diagnostics tools for complete beamlines in leptons and ions machines and has produced a report for the IN2P3 2020-30 prospects[1].

Within its years of existence, several Working Groups (WG) have been created: one WG had the task to perform a survey of the domain and the experts in the field. It showed the large range of specialty and tools necessary for the experts to perform their work, i.e. from physics and electric modelling tools, to mechanics and computing. The survey also pointed out the training, the need for exchanges, and some specifics as, for example, the implication of the experts in the development phases of the diagnostics (see diagnostics section). A second WG focused on establishing an overview on emittance-meter as discussed later on.

IONS ACCELERATORS WITHIN THE RIF

The accelerators presented in the next section pertain to machines in operation, through machines in commissioning and towards projects.

The ARRONAX Cyclotron

ARRONAX uses a 4-sectors isochronous cyclotron 70XP that produces protons from 34 MeV up to 70 MeV, deuterons from 15 MeV up to 35 MeV, and alpha particles at a fixed extracted energy of around 67.4 MeV [2]. Its operational average intensity usage ranges from a few pA to 350 μ A with bunches separated by 32.84 ns (Freq=30.45MHz) with a continuous beam. As the machine can use several beamlines at the same time it can operate up to 52 kW beams. In 2021 the RF equivalent running time was 4700h. In the last few years, the injection has been adapted to perform trains of bunches with a chopper system. The trains of bunches can thus be shortened to a few μ s (with non-dominating transit time, otherwise it is a few 100s of ns) with a repetition up to ~50KHz. The application of the beams is from short time ultra-high dose rates for flash-like experiments, and, long period of irradiations for radio-isotope production, to very low intensity irradiation for physics and detector studies. For the machine, beam instrumentation has been developed as a first purpose for machine protection i.e. with external beam loss monitor and intensity monitors [3]. Low intensity diagnostics are also being extensively investigated as detailed below and with this respect, the ARRONAX cyclotron pro-

vides a test-beam for future medical and application instrumentation. The compact injection (~5 m long line) has also seen as well dedicated studies with, for example, the use of a newly built emittance-meter (see later), and is at the present time the focus of a study for a compact instrumented multi-layer collimators system.

The SPIRAL2 Linac

The SPIRAL2 accelerator is a facility characterised by a wide range of operations, both for the different types of accelerated ions, for the energy and intensity ranges, and a wide duty cycle range. The accelerator consists of a 5 mA p-d ion source, a 1 mA heavy ions source ($A/Q \leq 3$), a CW RFQ and a superconducting linac. The linac is composed of 26 cavities divided into two sections: a first low energy section ($\beta=0.07$) with 12 cryomodules, each containing one cavity, and a second high energy section ($\beta=0.12$) with seven cryomodules, each containing two cavities. This high power CW superconducting linac accelerates beams up to 200 kW (D+) and produces beams with a wide range of intensity (from few 10 μ A to 5 mA), as well as energies from 0.75 MeV/u to 33 MeV/u. The duty cycle range applied on the chopper is included between 100 μ s per second to a continuous wave mode [4].

Beam diagnostic monitors were designed to best meet these requirements and those of the machine protection system. Protections to control the operation field, the limitation of equipment activation, the beam power and losses have also been considered. To obtain the commissioning authorisation of the French Safety Authority, AC and DC current transformers (intensity and transmission control), Time of Flight (ToF) and beam loss monitors (energy control) were built to the standards of quality assurance rules, including Failure Modes and Effect Analysis (FMEA).

Modifications of measurement systems are still in progress to improve their sensitivity and increase their measurement range at low intensities.

The DESIR Facility at SPIRAL2

The DESIR facility [5, 6] will be, in a few years, the SPIRAL2 experimental hall at GANIL dedicated to the study of nuclear structure, astrophysics, and weak interaction at low energy. New 10–60 keV exotic ion beams from (i) the upgraded SPIRAL1 facility [7] and (ii) the super separator spectrometer S3 [8] under commissioning will be transferred to high precision experiments in the DESIR building. SPIRAL1 will continuously produce ions at a maximum rate of about 10^8 ions/s, meaning a 20 pA CW single charged ion beam to be transferred to the DESIR Hall. The beams from S3 will be similar, except the time structure (Bunched beams). To guarantee high purity beams to perform high precision measurements on specific nuclei, three main devices are currently being developed at LP2i Bordeaux: a High Resolution Separator (HRS) [9], a General Purpose Ion Buncher (GPIB), and a double Penning Trap named “PIPERADE” [10]. On one hand, the final resolution of the HRS will mainly depend on the correction of optical aberrations. These aberrations can be studied

through the beam emittance figure. The use of a commercial pepperpot-type emittance-meter to correct the HRS aberrations is described in [9]. On the other hand, specific instrumentation developments described in [11] have been developed and are still being improved to characterise the low energy (3 keV) bunches produced by the GPIB. This RFQ-Cooler-Buncher is designed to handle large samples (10^6 ions in a $1\mu\text{s}$ bunch) with the best transverse and longitudinal emittances [12].

The NEWGAIN Project

The NEWGAIN project (NEW GAnil INjector) aims to construct a second injector $A/q=7$ [13], so as to produce very intense Super Heavy Elements, well beyond the performance of the existing injector. With the addition of this new injector, the SPIRAL2 LINAC will deliver, within its energy interval of operation, the most intense beams in the world over a large variety of ions (up to uranium). This second injector will be designed to be fully compatible with the existing facility; it will be composed of a high-performance superconducting ion source, a first low energy beam transport line connecting the superconducting ion source to the RFQ, a second LEBT connecting the existing ion source PHOENIX V3 ($A/q=3$) to the RFQ, an RFQ that will accelerate heavy ions up to the injection energy for the superconducting LINAC, and a medium energy beam line connecting the RFQ to the LINAC.

The MYRRHA Project

The MYRRHA (Multi-purpose hYbrid Research Reactor for High-tech Applications) project [14] requires a proton beam of 4mA at 600 MeV operated in continuous mode. It aims at demonstrating the feasibility and operability of an efficient transmutation of nuclear waste products. MYRRHA will use external neutron produced by protons coming from Accelerator Driven Systems (ADS). The beam will be delivered to the reactor vertically from above through an achromatic beam line and window. Currently under design, MYRRHA is foreseen to release first beams at 100 MeV in few years now.

DIAGNOSTICS IN THE RIF

The design of beam diagnostic monitors involves the consideration of many parameters and requirements (i.e. mechanics, vacuum, beam parameters, safety and human-machine interfaces). These domains are important and continue iteratively throughout the design phase of the diagnostics and accelerator advancements.

As illustrated in Fig. 1, the development of diagnostics can go through several phases, here, separated as a pre-project, a prototype, and an operation phase. The pre-project phase starts up with the definition of the physics phenomena to be measured and might include pre-testing on a beam test. A prototype phase, for a specific accelerator, is usually necessary, except in the case where existing measurement systems can make it possible to carry out laboratory validation tests. Prototyping makes it possible to vali-

date technical solutions that meet measurement and operating requirements. This can also involve the design and use of a laboratory measurement bench. In the case of safety requirements, it is necessary to quantify the measurement uncertainties by listing all the influencing parameters and evaluating their effect on the measurements. The reception tests of the final equipment, coming from the suppliers, are carried out first in the laboratory and then on the accelerator before the beam commissioning.

Interfaces with the command-control are essential but not so easy to specify. Definitions of the exchange data include both the various commands for setting the measurements, the measured data, and the operating and default status, for experts and for operation.

The last steps concern the beam commissioning, operation verifications of the beam diagnostic monitors, the measured values between diagnostics, and the level of disturbances in the electromagnetic environment. Modifications, optimisations, and evolutions are often necessary.

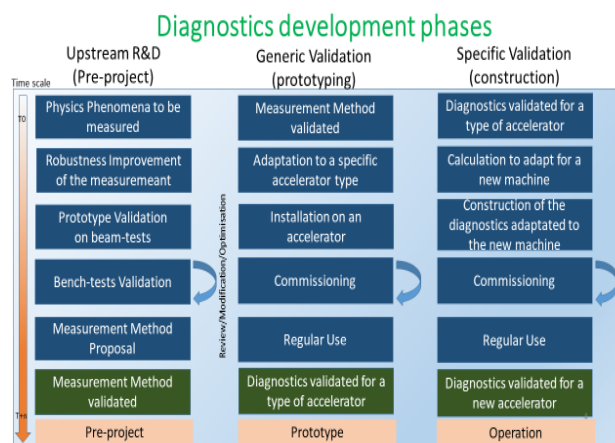


Figure 1: Diagnostics development phases: the pre-project, generic validation, and specific validation.

In the case of SPIRAL 2 injector commissioning, a test bench (Diagnostic plate) with all diagnostic monitors was installed at the exit of the RFQ [15,16]. This test bench had two main objectives: qualify the beam at the RFQ exit and qualify and validate the diagnostic monitors of SPIRAL2. The D-plate allowed to measure:

- Intensities with Faraday cups, ACCT, and DCCT,
- Transverse profiles with classical multi-wire profilers and ionisation gas monitor (MIGR),
- H and V transverse emittances with Allison type scanners,
- Energies with a Time of Flight (TOF) monitor,
- Phases with the TOF and 2 BPMs,
- Longitudinal profiles with a Fast Faraday Cup (FFC), and a Beam Extension Monitor (BEM),
- Beam position and ellipticity ($\sigma_x^2-\sigma_y^2$) with the BPMs.

The test bench allowed optimising and developing diagnostics, such as ToF energy measurements and the fast Faraday cup. Difficulties arose with the BPM qualification tests due to the lack of beam profilers installed in the test bed. A detailed analysis of the measurement needs must be carried out before the design of the test bench.

A New Emittance-meter for the Community

A new emittance-meter has been constructed and commissioned at IPHC in 2020 [17]. This device is based on the Allison principle and follows other similar achievements done in the framework of SPIRAL2 and MYRRHA projects and soon NEWGAIN [18]. The newly developed instrument was installed in the injection channel of the ARRONAX cyclotron in Nantes at the beginning of 2021. The aim of the experiment was to investigate beam properties and improve current intensity [19].

Since then, the device has been used to characterise beams at the exit of DESIR/SPIRAL 2 High Resolution Spectrometer at LP2I Bordeaux, and on the ARIBE beam line of the CIMAP/GANIL facility in Caen. The system is now fully operational and is shared by the community at IN2P3, the beam instrumentation network. It is currently installed on a secondary beam line of the ALTO facility at IJCLab, Orsay, in order to characterise beams of new ion sources before the summer 2022.

The goal of the collaborative work is not only to share equipment, but also to discuss, analyse measurements, and improve collective knowledge of emittance-meter, ion-beam behaviour and data analysis.

Perspective of Ion Beam Emittance Measurements

Performance limitations of Allison-based systems are well known and IPHC's system ones have been investigated in order to propose improved phase-space distribution measurements, see summary in Table 1.

Table 1: IPHC's Emittance-meter Performance Limits

Front-end electronics	1 nA total beam, EMI issues (as shielding)
Data acquisition	BW limitation at ~10 MHz, limited dynamic capabilities
Power dissipation	300 W (5 mA at 60 keV)
Resolution	0.1 mm, 1 mrad, not sufficient for small beams and halo definition
Accuracy	10-20%, integration of different subsystems errors and internal beam-optics defects
Packaging	Weight and dimensions are penalising

Apart from the technical limitations, there are several issues raised by the shared use of the instrument: its versatility in respect to the different applications at IN2P3 (with time and resources required for adaptation), its availability over the year (an experiment takes several months), and radioprotection and transport between laboratories (preliminary dose and radiation exposure evaluation, activation inventory, decay time estimation, safety procedures, and regulations are mandatory) [20]. A commercial solution is expensive and shows little flexibility. IPHC, as, a unique ex-

ternal lab involved in installation, commissioning, support and feedback on the different facilities, does not have sufficient resources for long-term sustainability. The future will favour open source solutions with sharing of drawings, knowledge and community experiences, which are not only unique to this instrument.

DIAMMONI Monitor

Compared to other semiconductors, diamond exhibits a high resistivity ($>10^{13} \Omega \cdot \text{m}$) associated to a large electronic gap (5.48 eV) that results in an almost negligible leakage current, and thus a low noise level. The high charge carrier mobility leads to a very fast response allowing tens of picoseconds time resolution and high count-rate capabilities [21]. Diamond detectors are also highly resistant to radiation [22]. For beam monitoring purposes, CVD-diamonds (Chemical Vapor Deposition) are used as solid-state ionisation chambers. Diamonds are metallised (~100 nm Al layer) to permit charge collection. In addition, the very original lift-off process allows a large number of user-defined electrode designs to satisfy beam profile requirements.

The DIAMMONI pulsed proton beam tagging monitor is foreseen to be equipped with the largest possible sensors ($> 1 \text{ cm}^2$, CVD single crystals or polycrystals). In order to ensure short charge carrier drift time and limit the detector current (compulsory for very intense beam pulses), their thickness needs to be optimised. Furthermore, to provide spatial resolution and low detector capacitance values, the diamond detectors are to be segmented with double-sided metallic strip readouts (X and Y directions). Indeed, DIAMMONI objectives are a spatial resolution of the order of a millimetre linked to the transverse dimension of the diamond strip metallisation. Finally, a high dynamic range for particle counting can be reached: from a single particle up to bunches of thousands of protons (or He ions) while beam intensity is monitored with a current integration mode that relies on a QDC design. As a result, a first prototype of DIAMMONI, made of a 150 μm thick CVD single crystal read-out by a QDC developed at LPSC, demonstrated, in May 2022 at ARRONAX, its capability to perform particle counting in 100 μs trains of nano-pulses. The beam intensity was raised up to 5 μA (measured on the diamond surface), which corresponds to an average of 10^6 protons per nano-pulse every 30 ns, with an energy deposit of 500 GeV/bunch over a 7 mm^2 detector area.

PEPITES Profiler

PEPITES [23] is a brand new operational prototype of an ultra-thin ($<10 \mu\text{m}$ water-equivalent thickness), radiation-resistant, SEE-based beam profiler capable of continuous operation on mid-energy (O(100 MeV)) charged particle accelerators. Characterised at ARRONAX with 68 MeV proton beams and at medical energies at CPO-Orsay, the system has been exposed to doses of up to 10^9 Gy without showing significant degradation. A demonstrator with a new ASIC 32-channel electronics is installed at ARRONAX in a dedicated chamber.

SPIRAL2 Beam Position Monitor

SPIRAL2 BPM [24] instrumentations are used to measure positions and phases of ion beams, and also transverse shapes, called ellipticity, as well as beam energy. Specifications involve knowing and calculating the sensitivities in position and in ellipticity as a function of the beam velocities. The β values in the linac are from 0.04 up to 0.26 for the 33 MeV proton beam.

The BPM specifications to tune the SC linac cavities are given in (Table 2).

Table 2: BPM Specifications

Parameter	Resolution	Range
Position	+/- 150 μm	+/-20 mm
Phase	+/-0.5 deg.	+/-180 deg.
Ellipticity	+/-20 % or +/- 1.2 mm ²	

These also impose small amplitude differences between channels, which require precise calibration of electronics. At low velocities, sensitivities in position and ellipticity are a function of the beam beta and the frequency harmonic. One of the objectives was to find a formula to calculate the ellipticity sensitivity correction.

BPM systems process signals either at the 88.0525 MHz fundamental frequency or at the second harmonic for both amplitude and phase measurements. Horizontal and vertical positions, ellipticity, amplitude and phase of the vector-sum are calculated from both h1 and h2 measurements. The design of the BPM system is based on the scheme of auto-gain equalisation using offset tone. In this scheme, the gain of the different channels is equalised with respect to the injected offset tone.

In order to obtain the required resolutions, two solutions were implemented in the electronic process: a very precise calibration, and stabilisation of the four gains and phases.

After numerous modifications and optimisations, position and ellipticity values calculated from the level measurements at harmonic 1 (88 MHz) and at harmonic 2 (176 MHz) are very close, and confirm the correctness of the formulas of the sensitivity coefficients.

In early 2021, an improved cavity tuning procedure using beam energy measurements from the BPMs was tested. A new calibration procedure, taking into account the phase drift from BPM outputs, was applied to correct these phase shifts and to have the same phase reference for the 20 BPM monitors.

In July 2021, with a helium beam at 40 MeV, beam energies were measured using the Time of Flight monitor (ToF) located at the linac exit to check the BPM measurements. The energy differences were relatively small and validated the BPM phase accuracies and the phase accuracy from BPMs.

The current actions concern an automation of the calibrations and an increase of the sensitivity towards the very low levels.

DESIR Diagnostics

The DESIR transfer beamline will use Faraday Cups (FC) coupled with a low-bandwidth transimpedance linear

amplifier called PicoLIN [24] to cover a very wide range of CW beam intensity measurements, from 50 fA to 100 μA . These diagnostics, developed at GANIL, are crucial to optimise the beam transport efficiency. The other main diagnostics used are Beam Profile Monitors (BPM) based on secondary electron emission of 47 tungsten wire harps (0.5 mm step) for both horizontal and vertical planes [25]. Equipped with high-sensitivity charge preamplifiers, these semi-interceptive BPM, also developed at GANIL, are used to monitor down to a few tens of pA ion beams with a transparency higher than 90% to obtain the beam position, size, and shape on focal plane of each optical section.

Ion bunches generated by the GPIB can be detected by the FC, coupled to a fast commercial I/V converter (FEMTO DHPA-100). This detection system can be used only for high-intensity bunches ($>10^4$ particles in a 1 μs bunch), the lower ion number limit strongly depending on the time distribution of the bunch. A commercial RedPitaya board is used to readout the bunch intensity signal close to the diagnostics and serve it as an EPICS [26] Process variable on the Ethernet network. Micro-Channel-Plates (MCP) are also used to measure low-intensity beams in counting mode and to perform Time-Of-Flight (TOF) measurements, using a LP2i-Bordeaux FPGA development called "RedPiTOF" [11] implemented into a dedicated Red Pitaya board. The TOF spectra has been constructed in the RedPiTOF and is used daily to commission the GPIB RFQ-Cooler-Buncher but also to test and perform in-trap techniques in a similar manner as with the PIPERADE Penning traps at Bordeaux.

Additive Manufacturing

Studies are also ongoing in France to see how additive manufacturing can benefit to accelerators. As an example, a beam position monitor was developed and thanks to additive manufacturing, a thin electrodes were built and tailored to be closer to the optimal impedance [27].

CONCLUSION

The present network keeps working efficiently on its activities, organises meetings and technical exchange, to align its work-in-progress with the demands of the experts in the field. This means also taking into account the past two years' events, experienced by the world from a health and military point of view, that have affected projects and collaborations. Though, the development of the network is consistent with the recommendations on the IN2P3 2020-30 prospects that occurred in 2021, as its report outlined "prime importance to guarantee a suited scientific and technical support for accelerators development" and "to strengthen the connection between accelerators and detectors community" "particularly R&D activities on beam instrumentation". A potential future would be the integration of the network within a larger structure that would allow sharing information within fields that are not usually nor specifically close to beam instrumentation.

ACKNOWLEDGEMENTS

The authors would like to thank the IN2P3 management team for initiating and financing this network. The authors

also thank all the actors of this network (mainly from CNRS and CEA) who feed the exchanges and contribute greatly to its life and its improvement.

REFERENCES

- [1] J.L. Biarrotte, R. Clédassou, *et al.*, Report of the GT07 working group: Particle Accelerators & associated instrumentation, CNRS/IN2P3
<https://box.in2p3.fr/index.php/s/ZgCZtszNAf2zkmx>
- [2] F. Poirier *et al.*, “Studies and Upgrades on the C70 Cyclotron Arronax”, in *Proc. CYCLOTRONS'16*, Zurich, Switzerland, Sep. 2016, pp. 235-237.
doi:10.18429/JACoW-Cyclotrons2016-TUD02
- [3] F. Poirier *et al.*, “The Pulsing Chopper based System of the Arronax C70XP Cyclotron”, in *Proc. IPAC'19*, Melbourne, Australia, May 2019, pp. 1948-1950.
doi:10.18429/JACoW-IPAC2019-TUPTS008
- [4] A. K. Orduz *et al.*, “Beam commissioning of SPIRAL2 in *Proc. IPAC'21*, Campinas, SP, Brazil, May 2021.
doi:10.18429/JACoW-IPAC2021-WEXB05
- [5] B. Blank *et al.*, “Perspectives for mass spectrometry at the DESIR facility of SPIRAL2,” *Int. J. Mass Spectrom.*, vol. 349, pp. 264-269, Sep. 2013.
doi:10.1016/j.ijms.2013.03.006
- [6] DESIR presentation website, <https://www.ganil-spiral2.eu/scientists/ganil-spiral-2-facilities/experimental-areas/desir/>, accessed 20th June 2022.
- [7] P. Delahaye *et al.* “New exotic beams from the spiral 1 upgrade”, *Nucl. Instrum. Methods. Phys. Res., Sect. B* vol. 463, pp. 339 – 344, 2020.
doi:10.1016/j.nimb.2019.04.063
- [8] F. Déchery *et al.*, “The super separator spectrometer s3 and the associated detection systems: Sirius and leb-reglis3”, *Nucl. Instrum. Methods. Phys. Res., Sect. B*, vol. 376, pp. 125 – 130, 2016.
doi:10.1016/j.nimb.2016.02.036
- [9] J. Michaud *et al.*, “Status on the DESIR High Resolution Separator Commissioning”, Mar. 2022.
doi:10.48550/arXiv.2203.11214
- [10] P. Ascher *et al.*, “PIPERADE: A double Penning trap for mass separation and mass spectrometry at DESIR/SPIRAL2”, *Nucl. Instrum. Methods. Phys. Res., Sect. A*, vol. 1019, p. 165857, 2021.
doi:10.1016/j.nima.2021.165857
- [11] L. Daudin *et al.*, “CENBG Control System and Specific Instrumentation developments for Spiral2-DESIR setups”, in *Proc. ICALEPCS'21*, Shanghai, China, Oct. 2021, pp. 98–103.
doi:10.18429/JACoW-ICALEPCS2021-M0PV002
- [12] M. Gerbaux *et al.*, “The General Purpose Ion Buncher : a radiofrequency quadrupole cooler-buncher for DESIR at SPIRAL2”, to be published.
- [13] D. Ackermann, B. Blank, L. Caceres, M. Caamaño, G. de France, *et al.* “NEWGAIN White Book - Science Requirements - Work Package Physics”, Technical Report, GANIL – document, 2021. <https://www.ganil-spiral2.eu/scientists/ganil-spiral-2-facilities/accelerators/newgain/>
- [14] D. Vandeplassche, J.L. Biarrotte, *et al.*, “The MYRRHA Linear Accelerator”, in *Proc. IPAC'11*, San Sebastian, Spain, May 2011, WEPS090, pp. 2718-2720.
- [15] R. Ferdinand *et al.*, “Final Results of the SPIRAL2 Injector Commissioning”, in *Proc. IPAC'19*, Melbourne, Australia, May 2019, pp. 848-851. doi:10.18429/JACoW-IPAC2019-MOPTS006
- [16] P. Ausset *et al.*, “SPIRAL2 Injector Diagnostics”, in *Proc. DIPAC'09*, 25-27 May 2009, Basel, Switzerland, pp. 110-112.
- [17] F. Osswald *et al.*, “Transverse phase space scanner developments at IPHC”, in *Proc. IBIC'19*, Malmö, Sweden, Sep. 2019, pp. 293-296. doi:10.18429/JACoW-IBIC2019-TUPP007
- [18] E. Bouquerel and C. Maazouzi, “IPHC emittance-meters: design and development”, *Journal of Instrumentation*, vol. 16, no. 6, p. T06009, Jun. 2021. doi:10.1088/1748-0221/16/06/t06009
- [19] F. Poirier *et al.*, “Investigation on the injection of the Arronax Cyclotron 70XP”, in *Proc. IPAC'21*, Campinas, SP, Brazil, May 2021, pp. 873-876.
doi:10.18429/JACoW-IPAC2021-MOPAB276
- [20] F. Poirier *et al.*, “Installation, Use and Follow-Up of an Emittance-Meter at the Arronax Cyclotron 70XP”, in *Proc. IPAC'21*, Campinas, SP, Brazil, May 2021, pp. 877-880. doi:10.18429/JACoW-IPAC2021-MOPAB277
- [21] S. Curtoni *et al.*, “Performance of CVD diamond detectors for single ion beam-tagging applications in hadrontherapy monitoring”, *Nucl. Instrum. Methods. Phys. Res., Sect. A*, vol. 1015, p. 165757, 2021.
doi:10.1016/j.nima.2021.165757
- [22] L. Bäni *et al.*, “A study of the radiation tolerance of polycrystalline and single-crystalline CVD diamond to 800 MeV and 24 GeV protons”, *J. Phys. D : Appl. Phys.*, vol. 52, p. 465103, 2019. doi:10.1088/1361-6463/ab37c6
- [23] C. Thiebaut *et al.*, “Development of a transparent profiler based on secondary electrons emission for charged particle beams”, in *Proc. CYCLOTRONS'19*, Cape Town, South Africa, Sep. 2019. doi:10.18429/JACoW-Cyclotrons2019-THB04
- [24] C. Jamet *et al.*, “Beam Diagnostic Overview of the SPIRAL2 RNB Section”, in *Proc. DIPAC'11*, Hamburg, Germany, May 2011, paper TUPD06, pp. 314-316.
- [25] J. L. Vignet *et al.*, “The Beam Profile Monitor for SPIRAL2”, in *Proc. DIPAC'09*, Basel, Switzerland, May 2009, paper TUPB07, pp. 176-178.
- [26] L. Dalesio *et al.*, “The experimental physics and industrial control system architecture: past, present and future”, *Nucl. Instr. And Meth. In Phys. Res. Sect. A*, vol. 352, p. 179, 1994. doi:10.1016/0168-9002(94)91493-1
- [27] S. Jenzer *et al.*, “Study of the performances of a 3D printed BPM”, *Journal of Physics: Conference Series*, vol. 1067, no. 8, p. 082026, 2018. doi:10.1088/1742-6596/1067/8/082026

PREPARATION OF LOW-ENERGY HEAVY ION BEAMS IN A COMPACT LINEAR ACCELERATOR/DECELERATOR

Z. Andelkovic, S. Fedotova, W. Geithner, P. Gerhard,
F. Herfurth, I. Kraus, M. Maier, A. Reiter, G. Vorobyev
GSI Helmholtzzentrum für Schwerionenforschung, Darmstadt, Germany
N. Stallkamp

Goethe Universität Frankfurt, (IKF) Institut für Kernphysik, Frankfurt, Germany

Abstract

High precision tests of fundamental theories can often unfold their full potential only by using highly charged ions (HCI) at very low energies. Although in light of the envisaged energies at FAIR, experiments in the keV to MeV range may sound like backpedaling, these two techniques are in fact complementary, since the production of heavy HCI is virtually impossible without prior acceleration and electron stripping. However, subsequent preparation, transport, storage and detection of low-energy HCI bring new, surprising sets of problems and limitations. Here we will give an overview of the CRYRING@ESR local injector [1] and the HITRAP linear decelerator [2]. These two facilities consist out of one or two accelerator or decelerator stages, with a total length of around 10 meters, making them “compact” in comparison to other GSI accelerators. The following sections describe their main design parameters, the achieved ion numbers, challenges of beam detection, as well as some special features such as multi-turn injection and single-shot energy analyzers. The conclusion will present the current status and will also give an outlook of the planned applications of low-energy ions at the FAIR facility.

WHAT ARE LOW ENERGIES?

Although the term “low-energy” is often used with ease to describe stored ion beams, there is no strict definition of the term and the actual energy can range over several orders of magnitude. In a storage ring, beams of highly charged ions are labeled as slow already below 10 MeV/u, although their velocity still amounts to about 10% the speed of light c . A small-scale linear accelerator brings charged particles to a few hundred keV/u, while in a linear decelerator and a subsequent ion trap, ions can be slowed down almost to rest, pulling the energy over eight orders of magnitude to the sub-eV range. Therefore a more practical description of “low energies” would relate to a diffuse lower limit of a system, behind which a different way of handling ions is necessary, if compared to a “high energy” range of the same system, e.g. an accelerator. It should be noted that the reason for this discrepancy can be both physical, such as scaling of cross sections [3] or beam emittance, and technical, such as device stability or detector noise.

For precision experiments, low energy storage rings like CRYRING@ESR, or Penning traps like HITRAP are the devices of choice. They can provide excellent experimental conditions since effects like Doppler corrections and cor-

responding uncertainties at low energies are either smaller and/or they can be controlled with higher accuracy, while providing high luminosity or density at the same time. At CRYRING@ESR, electron cooling at comparably low beam energies is enhanced by transversal expansion of the electron beam upon leaving the high magnetic field produced by a superconducting magnet [4]. This process effectively reduces the temperature of the electron beam and consequently of the ion beam, enabling unprecedented experimental accuracy.

Even lower energies can be reached by extracting the ion beam from a storage ring and then employing a linear decelerator, such as HITRAP. Given the energy after multi-stage deceleration is sufficiently low for electrostatic manipulation, ions can be injected into a Penning trap [5], such as the cooling trap of HITRAP, giving the possibility to store ions basically at rest. Trapped ions are then either readily available for experiments, or they can be prepared according to the needs of an experiment and extracted at a desired energy. At this point, for convenience, the energy unit of eV/mass unit (u) commonly used for magnetic beam steering is replaced by eV/charge (q) which is more suitable for electrostatic, low-energy beam manipulation. The HITRAP transport beamline [6] typically operates at 4 keV/q, which requires a separation of doublets around a meter over the full transport length, with diagnostic elements after each pair, before the beam either hits a target or is retrapped by an experiment.

CRYRING@ESR LINEAR ACCELERATOR

The magnetic rigidity ranging from 1.4 Tm down to 0.08 Tm offers the CRYRING@ESR storage ring the possibility to work with very low ion energies. Next to heavy, highly charged ion beams from the GSI accelerator, CRYRING@ESR can also store lighter ions from a local compact injector without the use of the full accelerator chain. The properties of this compact ion source and linear accelerator are given in Table 1.

Typically, a compact electron-cyclotron resonance ion source (ECRIS) is used to deliver up to 50 μ A of mass-separated D^+ ions in chopped ion bunches 7–50 μ s in length. Also multiple charge states like Ne^{3+} are possible, though with considerably lower intensity. A Nielson type ion source (MINIS) is used as a backup, delivering slightly lower ion currents. Both ion sources are constructed in a high voltage cage, allowing extraction energies of up to 40 kV/q.

Table 1: Parameters of the CRYRING@ESR Local Injector

Parameter	min.	typ.	max.
MINIS [μA]	0.2	5	10
ECRIS [μA]	0.2	10	50
ion pulse [μs]	1	50	500
RFQ in [keV/u]	0.8	10	10
RFQ out [keV/u]	0.8	292	305
dp/p [%]	0.5	1	1

The radio-frequency quadrupole (RFQ) accelerates ions with mass-to-charge (m/q) ratio of up to 3 to the designed value of 300 keV/u. Depending on the applied RF power, the final energy and the dispersion will vary in a range 292 – 305 keV/u and 0.5 – 1% respectively. Ions with $m/q > 3$ can be only transported through the RFQ towards the ring with the energy of the ion source. Interestingly, this presents another limit for injection into CRYRING@ESR, since ions with $m/q < 7$ at ion source potential are too slow (i.e. the beam is “too soft”) for the lowest possible storage ring rigidity of 0.08 Tm. In summary, the CRYRING@ESR local injector uses two modes of operation:

1. **Acceleration** for ions $m/q < 3$ with $E = 292$ keV/u at injection
2. **Transport** for ions $m/q > 7$ with $E = 40$ keV/q (corresponds to 1 – 6 keV/u) at injection

Ion beam detectors along the injector comprise a combination of a YAG scintillation screen and a Faraday cup driven on the same axis in and out of the ion beam path. The use of micro channel plate detectors, Chromox or Phosphorus fluorescent screens proved to be either too sensitive for the energy range, or not sufficiently sensitive. The destructive detectors are supplemented with an AC and a DC current transformer to monitor the ion source output before and after mass separation by a dipole magnet.

The injection is done with an electrostatic and a magnetic septum as well as an electrostatic bumper to break the closed orbit of the ring. The bumper power supply is a home-made device, constructed with solid-state 15 kV fast switching units, followed by a series of resistors arranged in a switching matrix with high voltage relays. Together with the natural capacity of the electrodes, the resistors slow down the otherwise too fast exponential slope of the rising/falling edge of the bumper voltage, while the switching matrix enables the operator to choose the appropriate slope for a given ion species and energy. Typical fall times (90% to 10%) range between 5 and 10 times the ion revolution time in the ring. Figure 1 shows stored beam intensity as an ion pulse equal to the ring revolution time is stepwise delayed across the falling voltage of the bumper and injected. It shows that by using this multi-turn arrangement around 4 turns (i.e. ion revolution times) can be injected from the local injector with reasonable stored beam intensity, until the bumper voltage becomes either too large or too low for proper injection, or ultimately, until the phase space is completely filled. Efforts are ongoing to improve on this result.

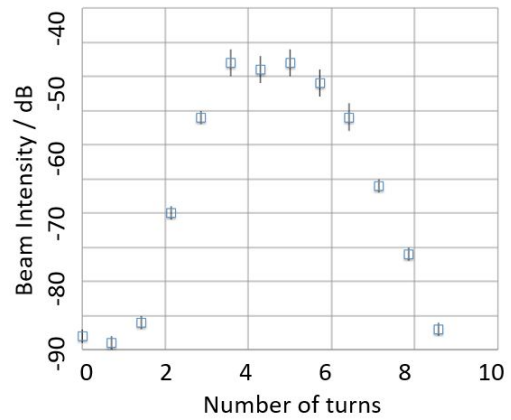


Figure 1: Stored beam intensity as a function of injection time with respect to the bumper trigger. One injection corresponds to one revolution time in the ring (one “turn”). The peak corresponds to ions which were efficiently injected, with the bumper voltage either too low or too high for proper injection outside of this region.

The low energy of the particles injected from the local injector imposes certain restrictions on the diagnostic elements of the storage ring. After the first round is established by using destructive detectors, multi-turn beam storage is typically optimized by observing the beam position monitors (BPM). These are constructed as capacitive pick-up electrodes shaped as diagonally cut hollow cylinders. The noise level of the BPM amplifiers competes with the signal from the stored ion beam and sets the lower intensity limit to about $5 \cdot 10^5$ charges, while reliable measurements significantly above the background noise level require $> 4 \cdot 10^6$. Other non-destructive detectors of coasting beams, such as Schottky noise or DC current transformer offer even lower sensitivity at the given energies. Consequently, the lowest intensity an ion source for the CRYRING@ESR local injector has to deliver amounts to about $3 \cdot 10^7$ charges, in order to reach the minimal storage ring intensity after mass separation and the usual transport losses.

The ion position monitor (IPM) images the beam profile by guiding the residual gas particles, ionized by the circulating beam, towards an MCP with a resistive anode. The field cage of the IPM operates at voltages around 5 kV, which is seen by the incoming particles as a fixed-field electrostatic steerer. If the acceleration mode of the injector’s RFQ is used, the kick amounts to 1 mrad and does not significantly influence the stored beam. At higher energies, e.g. after acceleration or with beam injected from the GSI accelerator, this angle is even smaller. However, if the transport mode of the RFQ is used, the IPM kick amounts to 143 mrad, which destroys the beam in a single turn. Thus, even though beam profiling would be possible after acceleration, the IPM is effectively not available for low-energy particles which are lost upon injection. Efforts are ongoing to construct a new version of the IPM which will make injection possible by either voltage switching or active compensation.

HITRAP LINEAR DECELERATOR

The GSI accelerator facility can deliver a large scope of elements at almost any charge state and prepare them for experiments. This process typically involves several acceleration and electron stripping stages, resulting in up to 10^8 highly charged ions stored at the Experimental Storage Ring (ESR). Starting from the initial energy of 30–400 MeV/u, the ions are decelerated to 4 MeV/u, electron cooled and extracted in 1 μ s bunches (roughly 1 m long). The full process of preparing the beam takes 30–60 seconds, defining the delivery rate for further deceleration. The extracted ion bunch, comprising typically $10^6 - 10^7$ ions, is guided through several meters of a transport beamline before entering the HITRAP cave. There, the bunch is first reshaped into micro-bunches by two double-drift-bunchers operating at 108 MHz and 216 MHz. Two phase probes monitor the beam energy by measuring the phase advance between individual micro-bunches and overlaying the data for multiple periods. The energy of 4.02(1) MeV/u necessary for injection into the first deceleration stage can then be fine-tuned by adjusting the electron cooler voltage of the ESR.

The interdigital H-structure (IH) is designed to decelerate ions from 4.02 to 0.495 MeV/u with an efficiency of up to 60%. Unlike particle acceleration where the beam successively enters regions with higher magnetic rigidity, in the case of deceleration the subsequent beam steering elements are designed for lower energies while the non-decelerated fraction of the main beam remains unaffected. Therefore a dedicated single-shot energy analyzer was developed in order to set-up deceleration and monitor the efficiency. It consists of a 0.5 T permanent magnet followed by a micro-channel plate (MCP) detector. A narrow slit in front of the energy analyzer increases the accuracy and decreases the non-decelerated beam intensity on the MCP at the same time. With this setup it was possible to separate individual energy components with a resolution of around 0.01 MeV/u. Figure 2 shows the design of the energy analyzer and the energy spectrum directly behind the IH decelerator. The image reveals the non-decelerated beam on the top together with several mid-energy stages, followed by full deceleration to 0.5 MeV/u in the lower part.

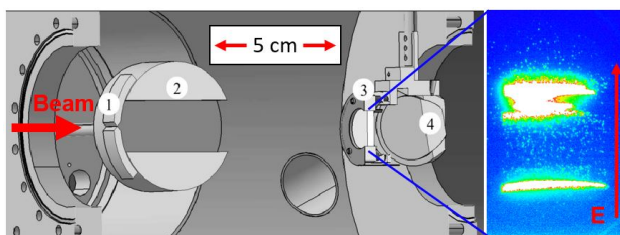


Figure 2: The HITRAP single-shot energy analyzer, comprising a slit (1), a permanent 0.5 T magnet (2), an MCP with a phosphorus screen (3) and a mirror (4) for reflecting the image towards an externally mounted CCD camera (not shown). The image on the right hand side shows the energy spectrum.

After the IH decelerator the particles are rebunched by another beam buncher in order to match the requirements for efficient injection of the decelerated beam into the second deceleration stage - a radio-frequency quadrupole (RFQ). The acceptance in terms of phase and energy are $\pm 3^\circ$ and 495 ± 5 keV/u respectively, requiring precise tuning of both beam direction and the IH structure. Without prior experience, if the full phase and amplitude ranges are taken into account, this can be a very tedious task with a beam repetition rate of 30-60 seconds. If the correct parameters are set, the ions leave the RFQ with about 6 keV/u. As in the case of IH, the decelerated beam is accompanied by the non-decelerated components at 4 and 0.5 MeV/u. This energy spectrum is analyzed in the same fashion as shown on Fig. 2. The resulting distribution can be seen on Fig. 3.

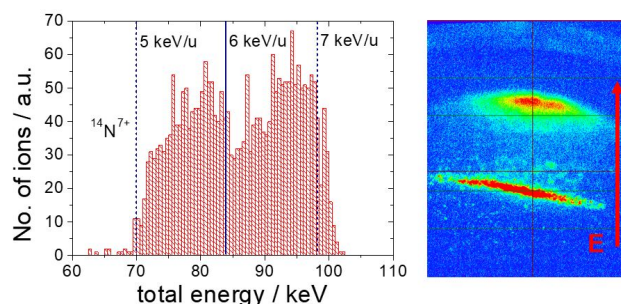


Figure 3: Left: energy distribution of decelerated ions behind the RFQ (simulation). The image on the right-hand side shows the energy spectrum recorded on the RFQ single-shot energy analyzer.

Transport between the RFQ and the ion trap is realized with six einzel lenses operating at voltages up to -40 kV, guiding the beam through two pumping barriers and some 2.5 m of beamline. Figure 4 shows the simulations of such an ion beam with an energy distribution of 18 ± 2 keV/q and an emittance of 200π mm mrad.

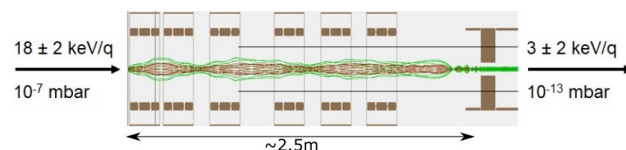


Figure 4: Simulation of the transport beamline between RFQ and entrance of the trap. Beam trajectories in different colors represent different energies.

However, with the dispersion of 30% and a very large emittance, the decelerated beam leaving the RFQ is very challenging for further transport and requires cooling. This is realized by the so-called HITRAP cooling trap, a seven-electrode, nested Penning trap, designed to capture and cool the decelerated HCI by mixing them with externally produced, pre-cooled electrons [7]. Energy is transferred via Coulomb-interaction from HCI to the electrons, which are being constantly cooled by emitting synchrotron radiation in the strong 4 T magnetic field of the Penning trap. Finally,

the cooled ions are extracted and can be transported via a low-energy beamline [6] towards various experiments.

Besides the heavy HCI provided by the GSI accelerator infrastructure, a small dedicated electron beam ion trap (EBIT) [8] attached to the low-energy beamline is used as an offline ion source, in a similar fashion as the local injector described in the previous section provides ions for CRYRING@ESR. The EBIT has a typical output of about 10^6 charges, usually bringing up to 10^5 mass separated, medium-heavy highly charged ions, available for cooling trap commissioning or experiments.

CURRENT STATUS AND PLANS

Since its commissioning in 2016 the local accelerator has produced and injected into CRYRING@ESR the following ion species: H_2^+ , D^+ , ${}^7Li^+$, ${}^{12}C^+$, ${}^{16}O^{2...6+}$, ${}^{20}Ne^{2...3+}$, ${}^{24}Mg^+$, ${}^{25}Mg^+$, ${}^{40}Ar^+$, with D^+ being by far the simplest and most used ion, mostly for commissioning and machine experiment purposes. Typical intensities at injection range between $10\ \mu A$ for singly charged, gaseous elements like D^+ , over $1\ \mu A$ for higher charge states like ${}^{20}Ne^{3+}$, to a few $100\ nA$ for ${}^{25}Mg^+$, as a less abundant natural isotope from an ion source oven. Translated into number of particles, this corresponds to $10^8 - 10^9$ stored D^+ to $10^6 - 10^7$ stored Mg^+ , both coming close to the space-charge limit of the storage ring due to the incoherent tune shifts. The injector has thus proven to be a versatile tool for operation of CRYRING@ESR without the use of the GSI accelerator chain, both for commissioning and for experiments with low-energy ion beams.

The last time ions were injected into HITRAP was 2014, before the FAIR shutdown and upgrade period of the GSI accelerator. The linear decelerator has remained in standby for several years, with only the low-energy beamline and the ion trap seeing some operation with ions produced by the local EBIT. The ion trap has also been modified to accommodate higher stability and easier operation [7]. Recommissioning in 2022 brought both deceleration stages back into operation and ions at 6 keV/u were reestablished, while the low-energy beam transport and ion trapping still remain as open tasks for the online beam. Nevertheless, efforts are ongoing to establish ion cooling offline by experimenting with ions from the EBIT. At the same time the FAIR control system is being expanded to include the full HITRAP facility, ensuring continuity and making further commissioning more effective.

As a part of FAIR, a new low-energy facility is planned within the framework of NUSTAR collaboration. The MATS-LaSpec facility [9] will be located at the very end

of the superconducting fragment separator (SFRS), taking decelerated rare isotopes produced online by nuclear reactions. These short-lived isotopes will be directed at 5 keV/q through several meters of beamline, a cooler and buncher RFQ, to reach experimental setups for in-trap mass measurements (MATS) or in-flight laser spectroscopy (LaSpec). As commonly the case with low-energy experiments, new challenges of ion handling are mostly compensated by the prospect of both high precision measurements of shortest-lived isotopes and decay studies, as well as high sensitivity and accuracy for the study of very exotic nuclides that will be possible only at the FAIR facility.

REFERENCES

- [1] W. Geithner *et al.*, “Status and outlook of the CRYRING@ESR project”, *Hyperfine Interact.*, vol. 238, p. 13, 2017. doi:10.1007/s10751-016-1383-5
- [2] F. Herfurth *et al.*, “The HITRAP facility for slow highly charged ions”, *Phys. Scr.*, vol. T166, p. 014065, 2015. doi:10.1088/0031-8949/2015/T166/014065
- [3] A. Müller and E. Salzborn, “Scaling of cross sections for multiple electron transfer to highly charged ions colliding with atoms and molecules”, *Phys. Lett.*, vol. 62A, p. 391, 1977. doi:10.1016/0375-9601(77)90672-7
- [4] C. Krantz *et al.*, “Recommissioning of the CRYRING@ESR Electron Cooler”, in *Proc. IPAC’21*, Campinas, SP, Brazil, May 2021, pp. 1816–1818. doi:10.18429/JACoW-IPAC2021-TUPAB178
- [5] G. Gabrielse, L. Haarsma, and S.L. Rolston, “Open-endcap Penning Traps for high precision experiments”, *Int. J. Mass Spectrom. Ion Processes*, vol. 88, p. 319, 1989. doi:10.1016/0168-1176(89)85027-X
- [6] Z. Andelkovic *et al.*, “Beamline for low-energy transport of highly charged ions at HITRAP”, *Nucl. Instr. Meth. Phys. Res. A*, vol. 795, p. 109, 2015. doi:10.1016/j.nima.2015.05.055
- [7] Z. Andelkovic *et al.*, “Development of the HITRAP cooling trap and the EBIT offline ion source”, *Hyperfine Interact.*, vol. 240, p. 69, 2019. doi:10.1007/s10751-019-1605-8
- [8] G. Vorobjev, A. Sokolov, A. Thorn, F. Herfurth, O. Kester, W. Quint, T. Stöhlker, and G. Zschornack, “Demonstration of charge breeding in a compact room temperature electron beam ion trap”, *Rev. Sci. Instrum.*, vol. 83, p. 053302, 2012. doi:10.1063/1.4719668
- [9] D. Rodríguez *et al.*, “MATS and LaSpec: High-precision experiments using ion traps and lasers at FAIR”, *Eur. Phys. J. Spec. Top.*, vol. 183, pp. 1–123, 2010. doi:10.1140/epjst/e2010-01231-2

BUNCH MERGING AND COMPRESSION: RECENT PROGRESS WITH RF AND LLRF SYSTEMS FOR FAIR

D. E. M. Lens*, R. Balß, H. Klingbeil¹, U. Laier, J. S. Schmidt, K. G. Thomin,
 T. Winnefeld, B. Zipfel, GSI, Darmstadt, Germany
¹also at Technische Universität Darmstadt, Darmstadt, Germany

Abstract

Besides the realization of several new RF systems for the new heavy-ion synchrotron SIS100 and the storage rings CR and HESR, the FAIR project also includes an upgrade of the RF systems of the existing accelerator rings such as SIS18. The SIS18 RF systems currently comprise two ferrite cavities, three broadband magnetic-alloy cavities and one bunch-compressor cavity. In addition, the low-level radio frequency (LLRF) system has been continuously upgraded over the past years towards the planned topology that will be implemented for all FAIR ring accelerators. One of the challenges for the SIS18 RF systems is the large RF frequency span between 400 kHz and 5.4 MHz. Although the SIS18 upgrade is still under progress, a major part of the functionality has already been successfully tested with beam in machine development experiments (MDE). This includes multi-harmonic operation such as dual-harmonic acceleration and further beam gymnastics manipulations such as bunch merging and bunch compression. Many of these features are already used in standard operation. In this contribution, the current status is illustrated and recent MDE results are presented that demonstrate the capabilities of the RF systems for FAIR.

INTRODUCTION

During the past years, the low-level radio frequency (LLRF) system at the heavy-ion synchrotron (Schwer-Ionen Synchrotron) SIS18 has been gradually upgraded towards the planned LLRF topology [1] for the Facility for Antiproton and Ion Research (FAIR).

The currently available radio frequency (RF) cavity systems with selected technical parameters that are currently used during standard machine operation are summarized in Table 1, where N denotes the number of cavities of the given type in the ring. Besides cavities loaded with ferrite ring cores, magnetic alloy (MA) cavities have been installed that enable, among other scenarios, a dual-harmonic acceleration. In addition, a bunch compressor cavity (BC) has been commissioned for a fast bunch rotation in longitudinal phase space before extraction [2].

The revolution frequency in SIS18 varies between 215 kHz and 1.36 MHz and typical harmonic numbers are $h = 2$ for the MA cavities and $h = 4$ for the ferrite cavities. Nevertheless, a variety of other harmonic numbers (e. g. $h = 1, \dots, 8$) has been used for different scenarios and beam manipulations. The LLRF system has been designed to cope

with this flexibility, including changes of harmonic numbers at dedicated White Rabbit (WR) timing events. Particular challenges are the large frequency span, fast ramping rates of the RF frequency of at least 10 MHz/s, and a required phase and amplitude accuracy under dynamic conditions of $\pm 3^\circ$ and $\pm 6\%$, respectively.

Table 1: SIS18 RF Cavity Systems

Type	N	RF frequency	Typical voltage per cavity
Ferrite	2	800 kHz - 5.4 MHz	up to 14 kV _p
MA	3	400 kHz - 2.7 MHz	up to 13 kV _p
BC	1	800 kHz - 1.2 MHz	30 kV _p

At SIS18, the cavity systems produce single-harmonic RF voltages and multi-harmonic operation is realized by operating different systems at different harmonic numbers. In contrast to multi-harmonic cavity systems (e. g. [3]), the local signal generation for one cavity is therefore simpler, but the complexity of the higher-level LLRF is higher. In the following, we demonstrate the status and performance of the SIS18 LLRF systems.

SIS18 LLRF TOPOLOGY

A simplified diagram of the LLRF topology of SIS18 is shown in Fig. 1 with an emphasis on the cavity synchronization that ensures a synchronization of the gap voltages of all involved RF cavity systems (which may be configured to different harmonic numbers) in frequency and phase. The main signal sequence is as follows: The measured gap voltages are transmitted from the accelerator tunnel to the RF supply area.¹ In the supply area, the gap signals are distributed to a Switch Matrix. This matrix also receives reference signals from Group DDS (direct digital synthesis) modules that are based on clock signals of the bunch phase timing system (BuTiS, cf. [4]). At SIS18, four such modules exist ($i \in \{A, B, C, D\}$) that are configured independently with a harmonic number h_i , such that each module generates a reference signal with frequency $f_{RF,i} = h_i \cdot f_R$ as a multiple of the revolution frequency f_R . A phase calibration eliminates remaining phase errors between the analog output signals of the Group DDS [5].

Via equally structured signal paths using lines of the same type that have been assembled to a specified electrical delay, it is ensured that all input signals of the Switch Matrix have

¹ For FAIR, a signal transmission via optical and via coaxial lines is planned. At SIS18, the coaxial lines are currently the main transmission path.

* d.e.m.lens@gsi.de

Content from this work may be used under the terms of the CC BY 4.0 licence (© 2022). Any distribution of this work must maintain attribution to the author(s), title of the work, publisher, and DOI

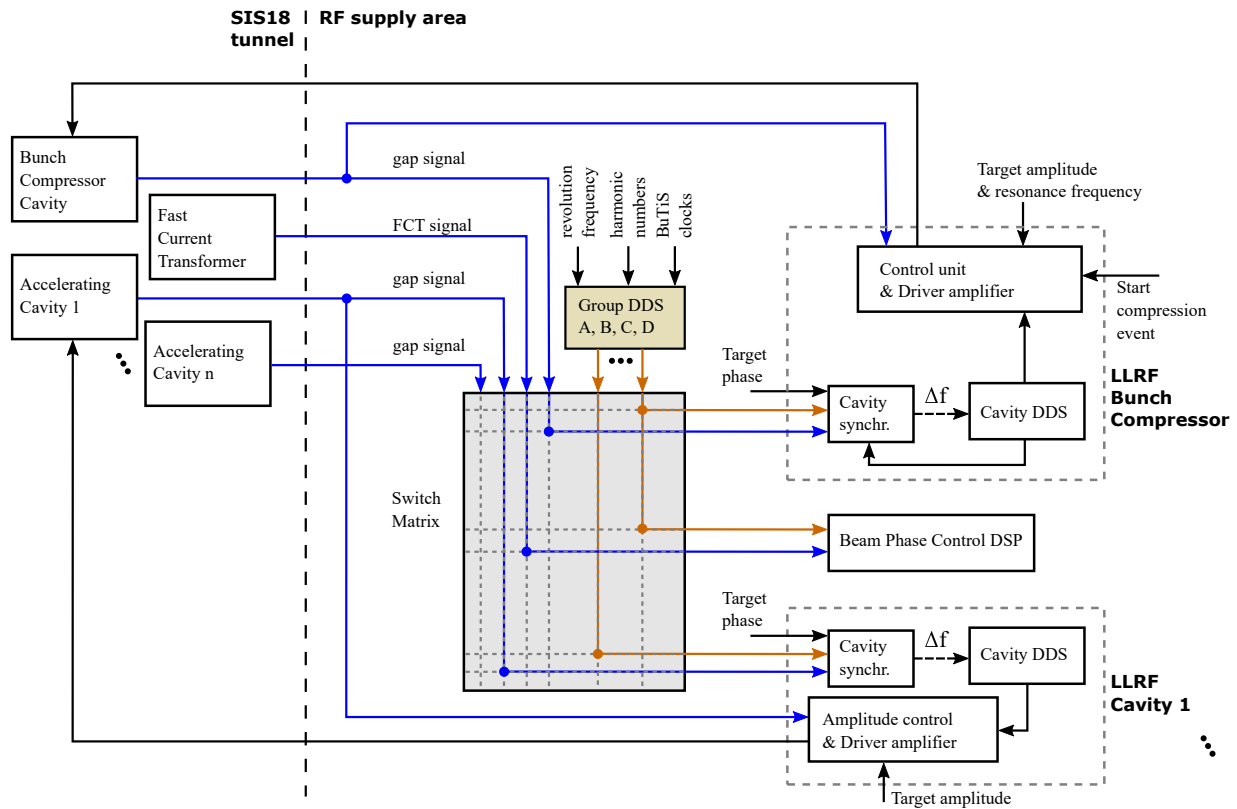


Figure 1: SIS18 LLRF topology with the cavity synchronization for the bunch compressor and one accelerating cavity (ferrite or MA). Some LLRF subsystems are omitted, e. g. the resonance frequency tuning loop for the ferrite cavities and calibration subsystems.

the same delay and can thus be compared with respect to the phase. This has been implemented for most lines of the SIS18 LLRF. However, some lines (such as the Group DDS delay lines) still have to be harmonized, because they are not yet of the correct type.

The Switch Matrix is configured such that a gap and a Group DDS reference signal with the same RF frequency $f_{RF,i}$ are selected and transmitted to the local LLRF subsystem of the respective cavity system. Depending on the phase difference of both signals, the cavity synchronization system corrects the local Cavity DDS with a frequency offset Δf . This eventually leads to a phase shift of the driver amplifier output signal (and thus the gap signal) until the phase between the gap and reference signal equals the target phase. The cavity synchronization also includes a (cavity) calibration to eliminate remaining, inevitable frequency-dependent amplitude and phase errors [6].

For the BC system, the synchronization topology is slightly different, as shown in Fig. 1. Since it is a pulsed system that has to deliver the RF peak voltage within a few tens of microseconds, its cavity synchronization system uses the Cavity DDS signal instead of the gap voltage. This has the advantage that the synchronization loop can already lock on the corresponding Group DDS signal before the start of the compressor pulse. Of course, the drawback of this procedure is that the subsequent subsystems (control unit, driver

amplifier and cavity including power amplifier) are operated in a feedforward manner, which makes a calibration curve for the target phase mandatory.

BUNCH MERGING

Bunch merging experiments have turned out to be a suitable benchmark scenario to test the overall phase accuracy of the SIS18 RF systems. On December 19th, 2019, a 8:4:2 merging was performed at SIS18 with about 1 mA of $^{40}\text{Ar}^{18+}$ ions on flattop at 130 MeV/u ($f_R = 663$ kHz) with one ferrite cavity at $h = 8$ and two MA cavities at $h = 4$ and $h = 2$, respectively.

The merging scenario was fully controlled by the Central Control System (CCS), only the phase ramps were trimmed manually to optimize the two merging processes (8:4 and 4:2). First of all, the first merging was optimized by trimming the target phase of the cavity with $h = 8$. Afterwards, the target phase of the cavity with $h = 2$ was trimmed to achieve an optimized second merging. The resulting waterfall plot is shown in Fig. 2.

Figure 3 shows the optimization of the second merging 4:2 between the two MA cavities, where the target phase of the cavity with $h = 2$ was varied. A phase offset of a few degrees influenced the symmetry of the merging process noticeably. The best result was obtained for a phase offset of -3° with respect to the default CCS settings. Since this

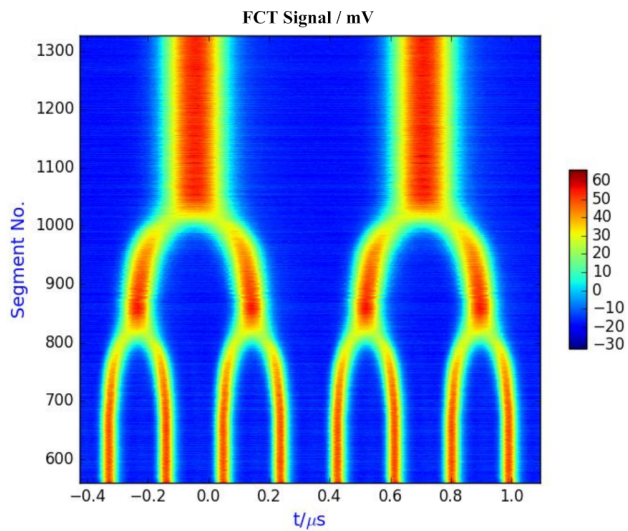


Figure 2: Waterfall plot of FCT signal after optimization of the two bunch merging sequences.

was close to the CCS default value, this is an indication that the cavities that were involved in this merging process had achieved the required phase accuracy of $\pm 3^\circ$.

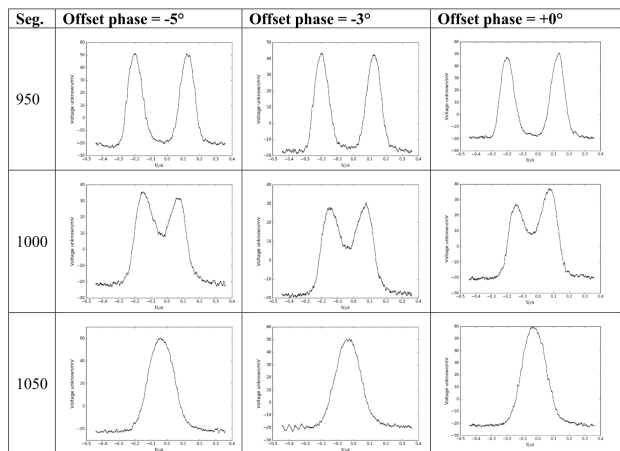


Figure 3: Optimization of 4:2 merging: FCT signal of two bunches merging into one (from top to bottom row) depending on the offset phase of the cavity with $h = 2$ (right column: default CCS settings with 0° offset).

The optimized first merging is shown in Fig. 4 as mountain range plot. It needed a much larger phase offset of 25° for the target phase of the ferrite cavity at $h = 8$. Although it can be expected in general that some systematic errors such as signal delay differences will be multiplied by the harmonic number at which the cavity system is operated, and therefore higher phase offsets may occur at higher harmonic numbers, this clearly is beyond the required accuracy. The precise error source is still under investigation, but since the LLRF upgrade at SIS18 has not yet been fully implemented, it is expected that the remaining phase errors can be decreased further. In particular, there are still some remaining unequal-

ities in the signal distribution lines between the ferrite and MA cavity systems that have to be harmonized.

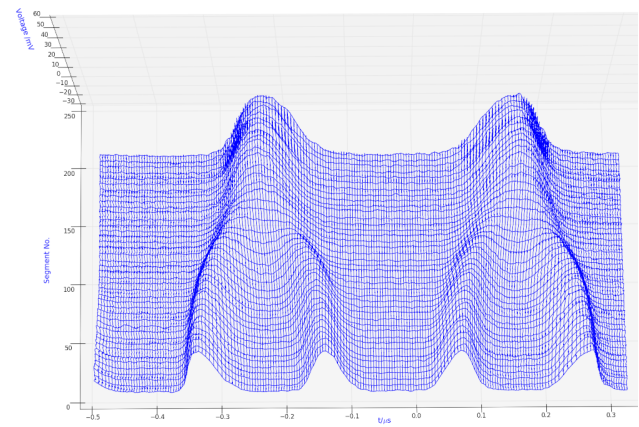


Figure 4: Mountain range plot of the FCT signal for the optimized 8:4 merging (segments 700 to 900) with phase offset $+25^\circ$ for the ferrite cavity with $h = 8$.

BUNCH COMPRESSION

The SIS18 bunch compressor was re-commissioned with beam in 2021 with the new FAIR control system based on LSA and FESA [7, 8]. In the MDE that took place on June 13th, 2021, a single bunch was compressed on flattop before fast extraction. The main parameters of the experiment are summarized in Table 2.

Table 2: MDE Bunch Compression Parameters (Flattop)

Parameter	Value
Ion species	40Ar^{18+}
Cavities used	2 (1 MA and 1 BC)
Energy	300 MeV/u
Rev. frequency	904.9 kHz
Harmonic number	$h = 1$
Beam current (typ.)	2.75 mA
RF voltage	760 V_p (MA), 30 kV_p (BC)

A beam phase control (BPC) system as shown in Fig. 1 was used to tune the target phase for the bunch compressor system during commissioning with beam. The BPC was operated in open loop² and allowed the measurement of the beam phase with respect to the Group DDS signal at $h = 1$ during the bunch compression. By minimizing the beam phase variation during compression, the target phase could be calibrated efficiently. The resulting waterfall plot of the FCT beam signal is shown in Fig. 5. The measurement was triggered by a dedicated WR timing event, which also triggered the start of the bunch compressor voltage pulse with a (configurable) delay of $240\ \mu\text{s}$. Note that in this experiment, the beam extraction was intentionally set to an instant of time after the point of maximum compression to

² The feedback for damping coherent bunch oscillations was switched off.

Content from this work may be used under the terms of the CC BY 4.0 licence (© 2022). Any distribution of this work must maintain attribution to the author(s), title of the work, publisher, and DOI

study the compression in detail. Of course, during standard operation, the extraction would have to take place earlier.

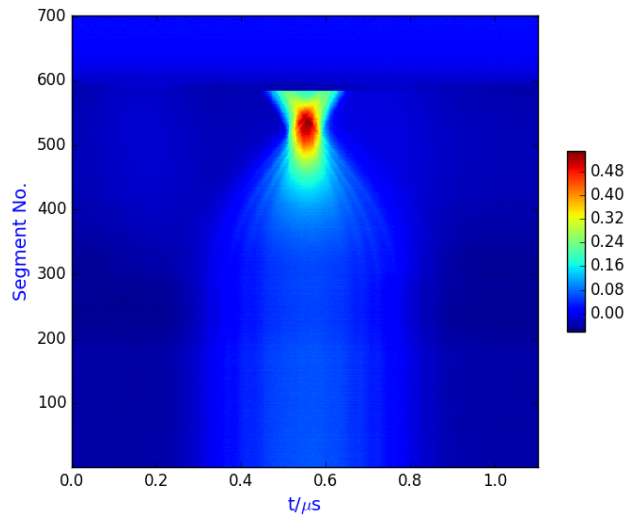


Figure 5: Waterfall plot of FCT signal for the bunch compression with extraction near segment 600. Each segment corresponds to one revolution period ($T_R = 1.1 \mu s$).

Figure 6 shows the obtained bunch profiles before and at maximum compression. From these profiles, a full width at half maximum (FWHM) value of 410 ns before compression and of 67 ns at highest compression is obtained. This leads to a compression factor of

$$K_{CF,achieved} = \frac{410 \text{ ns}}{67 \text{ ns}} \approx 6.1,$$

which is close to the theoretical value of

$$K_{CF,theory} = \sqrt{\frac{\hat{V}_{BC+MA}}{\hat{V}_{MA}}} = \sqrt{\frac{30 \text{ kV}_p + 760 \text{ V}_p}{760 \text{ V}_p}} \approx 6.4.$$

Thus, the compression efficiency was almost ideal during the experiment.

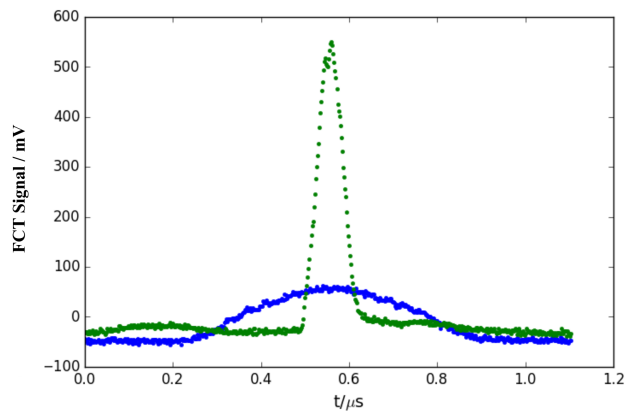


Figure 6: Comparison of bunch profiles before (blue) and at maximum compression (green).

The amplitude of the bunch compressor voltage is shown in Fig. 7. The voltage starts rising shortly after the set delay of 240 μs and reaches the maximum value after 40 μs .

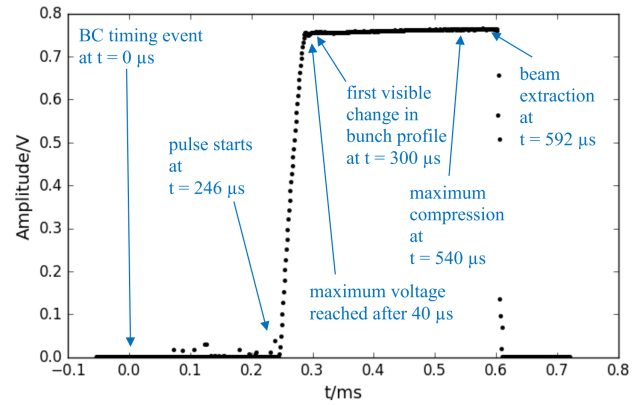


Figure 7: Bunch compressor voltage amplitude, scale 1:40,000 (obtained by a sine fit algorithm on the measured gap voltage signal; the smaller outliers before the pulse are numerical artefacts of the sine fit).

CONCLUSION AND OUTLOOK

Although many important aspects of the FAIR LLRF topology have been installed at SIS18, still a lot of effort has to be invested during the following years to reach the full functionality for the users. This includes the full control system integration of the bunch compressor cavity, the Switch Matrix, and the beam phase control loop. In addition, some subsystems and signal distribution channels of the older ferrite cavity systems have to be harmonized with the newer systems to reach the required phase accuracy for all SIS18 RF systems. Also, a driver amplifier upgrade of the MA systems is planned to decrease the energy consumption. Finally, an LLRF system that distributes optical phase and frequency corrections to the Group DDS modules is needed in order to enable manipulations of higher-level systems such as beam phase control, RF knock-out extraction, and full features of the new bunch-to-bucket transfer system in standard operation.

ACKNOWLEDGEMENTS

The authors would like to thank A. Andreev, P. Hülsmann, A. Klaus, H. G. König, K.-P. Ningel, D. Penza, A. Stuhl, C. Thielmann, and S. Schäfer for many technical contributions to the RF and LLRF systems. For the organization and approval of beam time, we would like to thank in particular P. Spiller, J. Stadlmann, and S. Reimann. We are also grateful for the help of several individuals from different GSI departments (e. g. ACO, SYS, BEA, OPE). This includes (but is not limited to) R. Bär, D. Beck, P. Kainberger, H. Liebermann, D. Ondreka, and H.J. Reeg.

REFERENCES

- [1] H. Klingbeil *et al.*, “New digital low-level rf system for heavy-ion synchrotrons”, *Phys. Rev. ST Accel. Beams*, vol. 14, no. 5, p. 102802, 06.10.2011.
 doi : 10.1103/PhysRevSTAB.14.102802

- [2] P. Hülsmann, R. Balß, H. Klingbeil, and U. Laier, “Bunch Compression for FAIR”, in *Proc. 23rd Particle Accelerator Conf. (PAC’09)*, Vancouver, Canada, May 2009, paper TU5PFP023, pp. 864–866.
- [3] P. Ausset *et al.*, “A High-Power Multiple-Harmonic Acceleration System for Proton- and Heavy-Ion Synchrotrons”, in *Proc. 16th Particle Accelerator Conf. (PAC’95)*, Dallas, TX, USA, May 1995, paper WPQ26, pp. 1781-1784.
- [4] B. Zipfel and P. Moritz, “Recent Progress on the Technical Realization of the Bunch Phase Timing System BuTiS”, in *Proc. 2nd Int. Particle Accelerator Conf. (IPAC’11)*, San Sebastian, Spain, Sep. 2011, paper MOPC145, pp. 418–420.
- [5] A. Andreev, H. Klingbeil, and D.E.M. Lens, “Phase Calibration of Synchrotron RF Signals”, in *Proc. 8th Int. Particle Accelerator Conf. (IPAC’17)*, Copenhagen, Denmark, May 2017, pp. 3945–3947.
doi:10.18429/JACoW-IPAC2017-THPAB097
- [6] U. Hartel *et al.*, “Precise Verification of Phase and Amplitude Calibration by means of a Debunching Experiment in SIS18”, in *Proc. 4th Int. Particle Accelerator Conf. (IPAC’13)*, Shanghai, China, May 2013, paper THPEA004, pp. 3155–3157.
- [7] R. Mueller *et al.*, “Supporting Flexible Runtime Control and Storage Ring Operation with the FAIR Settings Management System”, in *Proc. ICALEPCS’21*, Shanghai, China, Oct. 2021, pp. 768–773.
doi:10.18429/JACoW-ICALEPCS2021-WEPV047
- [8] R. Huhmann *et al.*, “The FAIR Control System - System Architecture and First Implementations”, in *Proc. 14th Int. Conf. on Accelerator and Large Experimental Physics Control Systems (ICALEPCS’13)*, San Francisco, CA, USA, Oct. 2013, paper MOPPC097, pp. 328–331.

SIMULATION

Analysis

In the ideal case, the voltage between the upper electrode pair V_u and the lower electrode pair V_l is the same, but with inverted polarity (see Fig. 4). The dipole mode perturbs this equality, increasing one of the voltages and decreasing the other by means of superposition. The strength of this perturbation effect can be expressed by the dipole factor DF with the following definition:

$$DF = 1 + \frac{V_u - V_l}{V_l}, \quad (1)$$

where V_u and V_l are the absolute values of the voltages between the upper and lower electrode pairs, respectively. Depending on which of the voltages is greater, DF will be greater, equal or less than 1. A value greater than one ($DF > 1$) means that the current path of the short stem is shorter than the current path of the long stem—the system is undercompensated. Accordingly, a value less than one ($DF < 1$) means that the short stem current path is too long—the system is overcompensated.

The dipole factor is an important parameter for RFQ designs, but it is not the only figure of merit. The specific shunt impedance R_p , the resonant frequency f_0 (fundamental eigenmode) and the Q-factor have been also checked.

The specific shunt impedance R_p describes the RF power losses of the resonator structure and is defined as follow:

$$R_p = \frac{V^2}{P/l}, \quad (2)$$

where V is the effective inter-rod voltage averaged over the resonator chamber length l and P is the power loss within the resonator chamber.

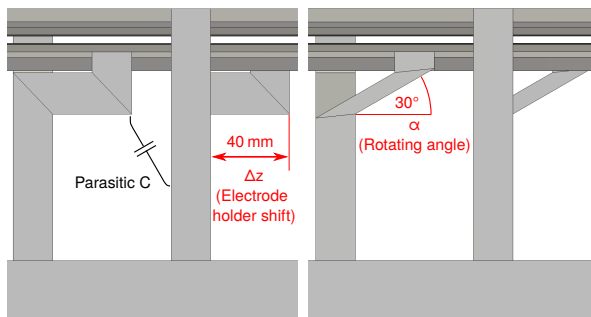


Figure 3: Side view of two variants of the model. Both variants use $\Delta z = 40$ mm with $\alpha = 0^\circ$ and 30° . Additionally depicted is the parasitic capacitance between one stem and the following stem.

Results

Simulation results show a decreasing dipole factor with an increasing Δz (see Fig. 5). Depending on α the dipole factor decreases with different gradients. Simulations were performed with hexahedral and tetrahedral meshes, both

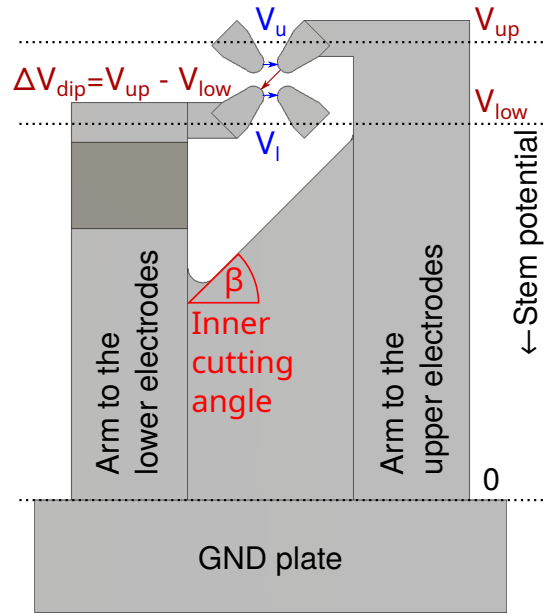


Figure 4: Front view of the model, showing the stem for one cell. V_{up} and V_{low} showing the potentials of the long and short arm in reference to the ground plate, ΔV_{dip} is the resulting dipole voltage. V_u and V_l are the calculated voltages used for the dipole factor calculation.

mesh types show good agreement. For tetrahedral meshes the current path balance point was found around $\Delta z = 29$ mm for $\alpha = 0^\circ$ and $\Delta z = 35$ mm for $\alpha = 15^\circ$. The model with $\alpha = 30^\circ$ did not reach $DF = 1$ even at the maximum $\Delta z = 40$ mm—it stays undercompensated. Noticeable is the slight increase of the dipole factor at 10 mm.

We see a decrease in shunt impedance for increasing Δz (see Fig. 6). There are only slight differences of the shunt impedance depending on α . Interestingly hexahedral and tetrahedral meshes show quite different values of 100 kΩ m and 70 kΩ m, respectively, at $\Delta z = 0$ mm. The same phenomenon holds true for the Q-factor values (see Fig. 8).

Like expected, the resonant frequency f_0 decreases with greater Δz values. The effect is stronger for lower α (see Fig. 7).

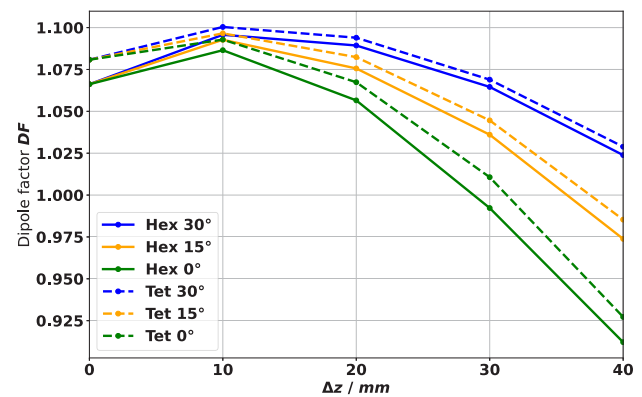


Figure 5: Dipole factor DF vs. Δz for tetrahedral and hexahedral meshes at different α .

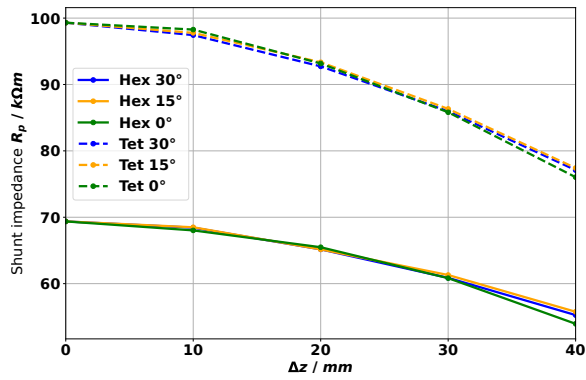


Figure 6: Shunt impedance vs. Δz for tetrahedral and hexahedral meshes at different α .

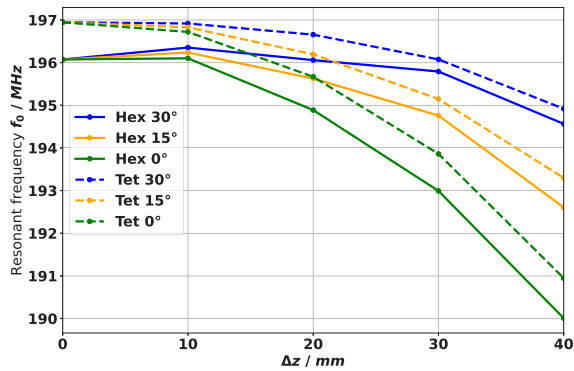


Figure 7: Resonant frequency f_0 vs. Δz for tetrahedral and hexahedral meshes at different α .

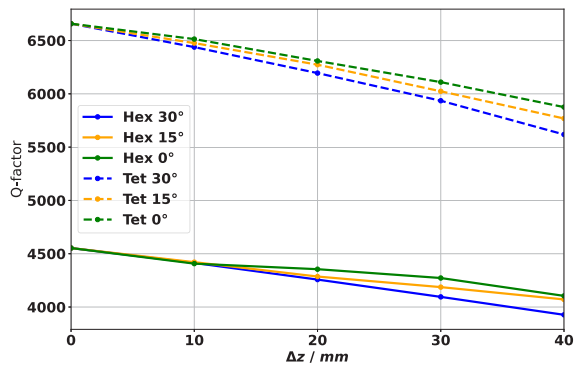


Figure 8: Q-factor vs. Δz for tetrahedral and hexahedral meshes at different α .

Discussion

We see a strong dependence of the dipole factor from α . This can be explained by the current path length. A smaller α means longer current paths and therefore compensates the dipole factor with smaller Δz values. The slight increase of the dipole factor at 10 mm can be explained by having a look at the stem thickness of 20 mm. If the stem thickness is greater than Δz , then there is no real increase of the effective

current path length. So, a mitigation of dipole effect cannot be expected.

Resonant frequency changes in dependence of α can be explained by the parasitic capacitance between one stem and the next (see Fig. 3). Resonant frequency of a 4-rod RFQ can be modeled as coupled LC circuits, that means that increasing the capacitance—i.e. by increasing the parasitic capacitance—should lead to a reduction of the resonant frequency [5]. In theory a larger α should mitigate this effect, since the effective capacitive coupling area between one stem and its neighbor is reduced (see Fig. 3). The parasitic capacitance also decreases shunt impedances and Q-factors with greater Δz values. Another possible explanation is, that parts of the stem structure run in parallel with the electrodes, therefore induced currents produce more power dissipation within the structure, also dependent on Δz .

Differences in hexahedral and tetrahedral meshes are quite strong for shunt impedance and Q-factor calculations. In tendency, tetrahedral meshes produce higher accuracy results with less cells. Exact reasons for the deviation have to be reviewed.

CONCLUSION

A new type of 4-rod RFQ stem design was developed and simulated. The simulation results show that the new method can compensate the dipole field components successfully.

This is a preliminary study to prove the principle of the method. More detailed studies will be performed in the future, especially focusing on the open questions:

- To improve shunt impedances and Q-factors, which suffered from the new style dipole compensation.
- To understand the difference of the simulation results using hexahedral and tetrahedral meshes.

REFERENCES

- [1] B. Hofmann, “Untersuchungen an einem RFQ-Beschleuniger für hohe Betriebsfrequenzen,” Diplomarbeit, Goethe University Frankfurt, 2004.
- [2] B. Koubek, H. Podlech, and A. Schempp, “Design of the 325 MHz 4-Rod RFQ for the FAIR Proton Linac,” in *Proc. IPAC’15*, Richmond, VA, USA, May 2015, pp. 3733–3735. doi: 10.18429/JACoW-IPAC2015-THPF022
- [3] K. Kümpel, A. Bechtold, H. Lenz, N. Petry, H. Podlech, and C. Zhang, “Dipole Compensation of the 176 MHz MYRRHA RFQ,” in *Proc. IPAC’17*, Copenhagen, Denmark, May 2017, pp. 2240–2242. doi: 10.18429/JACoW-IPAC2017-TUPVA070
- [4] *CST Studio Suite*. www.cst.com
- [5] C. Tan, J. Schmidt, and A. Schempp, “Simple lumped circuit model applied to field flatness tuning of four-rod radio frequency quadrupoles,” *Physical Review Special Topics - Accelerators and Beams*, vol. 17, no. 1, p. 012002, 2014. doi: 10.1103/physrevstab.17.012002

PROTOTYPE ROOM TEMPERATURE QUADRUPOLE CHAMBER WITH CRYOGENIC INSTALLATIONS

S. Aumüller*, L. Bozyk, P. Spiller

GSI Helmholtzzentrum für Schwerionenforschung, Darmstadt, Germany

K. Blaum, Max-Planck-Institut für Kernphysik, Heidelberg, Germany

Abstract

The synchrotron SIS100 at FAIR accelerator complex at the GSI Helmholtzzentrum will generate heavy ion beams of ultimate intensities. As medium charge states have to be used, the probability for charge exchange in collisions with residual gas particles of such ions is much larger than for higher charge states.

In the last years, several measures have lowered the residual gas density to extreme high vacuum conditions. For example 55% of the circumference of SIS18 have already been coated with NEG, which provides high and distributed pumping speed. Nevertheless, this coating does not pump noble and noble-like components, which have very high ionization cross sections. A cryogenic environment at e.g. 50-80 K provides a high pumping speed for all heavy residual gas particles. The only typical residual gas particle that cannot be pumped at this temperature is hydrogen. With the pumping speed of an additional NEG coating in these areas, the pumping will be optimized for all residual gas particles.

The installation of cryogenic installations in the existing room temperature synchrotron SIS18 at GSI has been investigated. Measurements on a prototype chamber and simulations of SIS18 with cryogenic installations based on these measurements are presented.

INTRODUCTION AND MOTIVATION

The SIS100 synchrotron at the FAIR accelerator complex will provide high intensity heavy ion beams, with a goal of $5 \cdot 10^{11}$ [1] particles per pulse. To achieve this goal, medium charge states have to be used as this will shift the space charge to higher numbers of particles and avoids stripping losses. However the probability for charge exchanges of medium charge ions with the residual gas particles is much higher than for higher charge states. Ions with a different charge state than the reference ion will be deflected differently and hit the vacuum chamber wall at some point, see Fig. 1. At the impact location they will release gas particles into the vacuum chamber via ion impact induced desorption processes. This leads to a localized higher density of residual gas particles, resulting increase in charge exchanges in this area. As a result even more ions hit the vacuum chamber walls downstream. This self-amplification process is called dynamic vacuum and can evolve up to complete beam loss [2].

To avoid this process, several upgrade measures have been realized in the existing heavy ion synchrotron SIS18, at

* s.aumueller@gsi.de

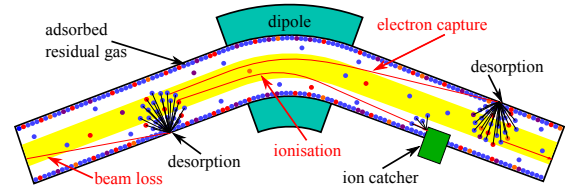


Figure 1: Principle of ionization loss and dynamic vacuum [2].

GSI [3]. Ion-catchers with low desorption surfaces have been installed to reduce the gas production by ionization beam losses. Furthermore to lower the residual gas density 65% of SIS18 vacuum chamber walls have been coated with NEG. This provides a high pumping speed for light residual gas particles like hydrogen. With these upgrades an improvement of the beam intensity was achieved [4]. However this current setup cannot reach the intensity goal for FAIR, as shown by different simulations of SIS18 [2]. Since the NEG coating only provides a high pumping speed for light particles and not for noble and noble-like gases, like argon and methane [5], which unfortunately have a high cross section for charge exchanges with U^{28+} [6], see Fig. 2, these particles have to be pumped differently to reduce the density of this residual gas particle species even further. However these can be pumped by cryogenic installations around 77 K. These pumps in combination with the already existing NEG coating can pump every residual gas component in SIS18 efficiently.

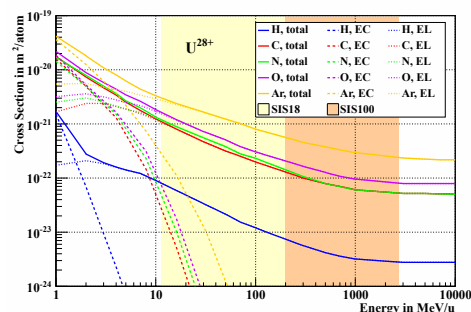


Figure 2: Cross sections for charge exchange of U^{28+} for different targets, distinguished for electron capture (EC), electron loss (EL) and total cross section. The energy regimes of SIS18 and SIS100 are marked [7].

PROTOTYPE TEST SETUP

To test the performance of cryogenic installations in a room temperature environment, a prototype quadrupole

Content from this work may be used under the terms of the CC BY 4.0 licence (© 2022). Any distribution of this work must maintain attribution to the author(s), title of the work, publisher, and DOI

chamber is used. This prototype structure is similar to the set up of SIS18's quadrupole chambers.

Like the quadrupole chamber now installed in SIS18, this prototype is a thin-walled chamber with one turbo molecular pump (TM) on one side and an ion getter (IG) pump on the other side, Fig. 3. Lengthwise, there's a difference to the existing quadrupole chambers of SIS18 with the prototype's length being 3 m while the existing chambers covering more than 4 m. The thin-walled part is divided by thicker parts to install measurement gauges (measuring chambers). Four of them are installed along the prototype, to measure a pressure profile. In addition one residual gas analyzer (RGA) is mounted, to identify the residual gas species.

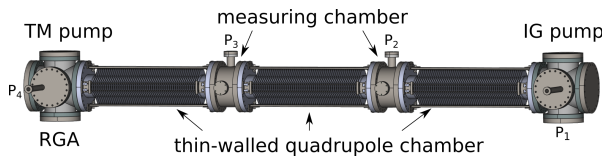


Figure 3: Sketch of the prototype quadrupole chamber with the positions of the pressure sensors p_i .

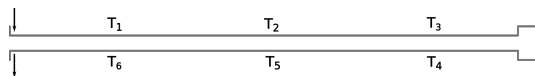


Figure 4: Sketch of the installed pipes with the positions of the temperature sensors T_i . The direction of the flow is marked.

Two pipes with a diameter of 8 mm are integrated into the chamber which can be cooled with liquid nitrogen or helium and can be used either in series as shown in Fig. 4 or independently of each other. Three sensors on each pipe measure the temperature, Fig. 4 shows their location.

In Fig. 5 measurements of the residual gas analyzer of the prototype chamber are presented. Both pipes were cooled

with liquid nitrogen to about 80 K. The major masses of all common residual gas particles of SIS18 are plotted without the measurement of argon and molecular oxygen, which are present in SIS18 but were only detectable in insufficient amounts in the prototype. Some of the residual gas particles could only be presented together due to their major masses being indistinguishable. Furthermore to show the temperature of the pipes two sensors are included. These are the ones which will be cooled first (bright violet) and last (dark violet), respectively.

The results show that pumping of different residual gas particles with pipes at 80 K is not very effective. Furthermore only hydrogen (turquoise) did not get pumped, it seems that its amount rised during the measurement. In contrast water (bright blue) pumped most efficiently, as it was expected. Every other measurable common residue like nitrogen/carbon monoxide (red), methane/oxygen (blue) and carbon dioxide (green) are already pumped by the pipes at moderate temperatures. However this pumping is not effective enough to lower the residual gas density to extreme high vacuum conditions. As the pumping speed of cryogenic pipes scales with the temperature, one way to achieve this would be to cool pipes to even lower temperatures using for example liquid helium. Other measures would be to increase the surface of the pipes or to use a different coating.

In the near future the residual gas situation in SIS18 will be simulated by a gas inlet system with a dosing valve and additional argon. With this measure the cryogenic installation can be tested on all common residual gas particles. To maximize the pumping speed the system will be tested at lower temperatures with pipes cooled by liquid helium. In addition, saturation effects and capacity of the cryogenic installations are tested in order to evaluate the pumping performance of the prototype in the long term.

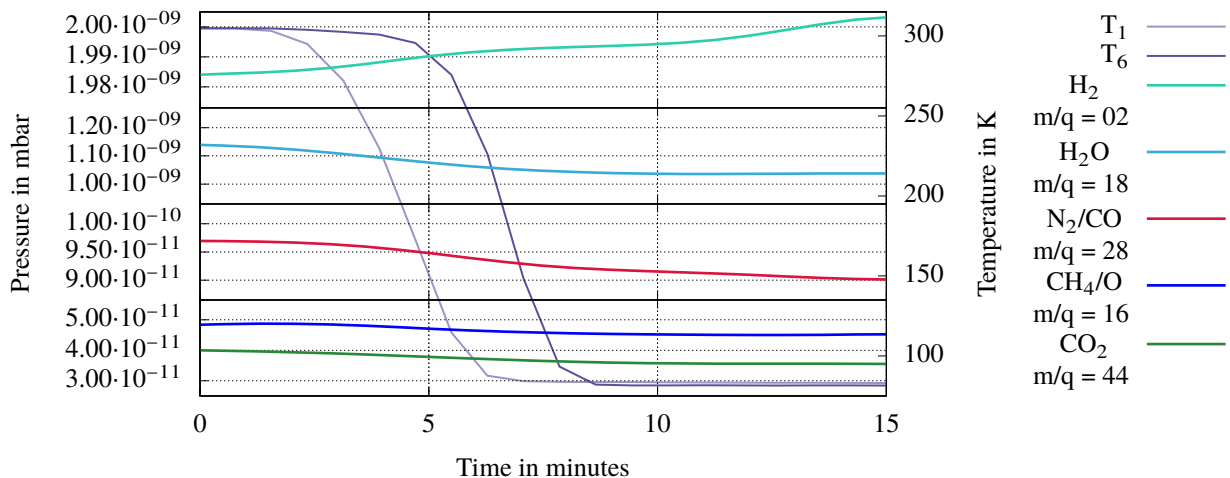


Figure 5: Residual gas analyzer measurement with both pipes cooled to ≈ 80 K. Presented are the main masses of the most common residual gas particle of SIS18 except argon and molecular oxygen. The position of the sensors can be seen in Fig. 3 and 4. All Curves have been smoothed.

SIMULATION OF U^{28+} IN SIS18 WITH CRYOGENIC INSTALLATIONS

To simulate the effect of cryogenic installations in SIS18 the software StrahlSim is used. This program is developed at GSI and is a unique code to simulate dynamic vacuum effects in circular accelerators.

The simulations presented here concentrate on two different types of cryogenic installations. The first one consists of two pipes like in the prototype quadrupole chamber. The second one features cryogenic surfaces close to the outer walls of the entire chamber. For a prototype chamber with such an installation see [8] of this conference. SIS18 is simulated with both of these installations in quadrupole and ion catcher chambers.

The SIS18 is simulated in the so called booster mode. This is the mode for injection of particle beams into the SIS100 at FAIR. Its consist of four individual cycles, a so called super cycle, following by a short break.

Presented are the number of extracted particles of U^{28+} per pulse as a function of the number of injected intensities and cycle frequencies for different scenarios. The simulation parameters can be found in Table 1. The following figures compare the operating SIS18 as it is now, blue line, with different options of cryogenic installations. The first option are pipes in the quadrupole, red line, and ion-catchers chambers, dark green. The second one are surfaces in the ion-catchers chambers, bright green. Thirdly a combined option with pipes in the quadrupole and surfaces in the ion-catcher chambers are simulated, purple line.

Table 1: Simulation Parameters for the Shown Simulations in Fig. 6 and 7.

Number of injected particles	3 to $20 \cdot 10^{10}$ U^{28+}
Ramp rate	10 T/s
Cycle frequency	1 to 2.7 Hz
Temperature of installations	15 K
Injection losses	5%

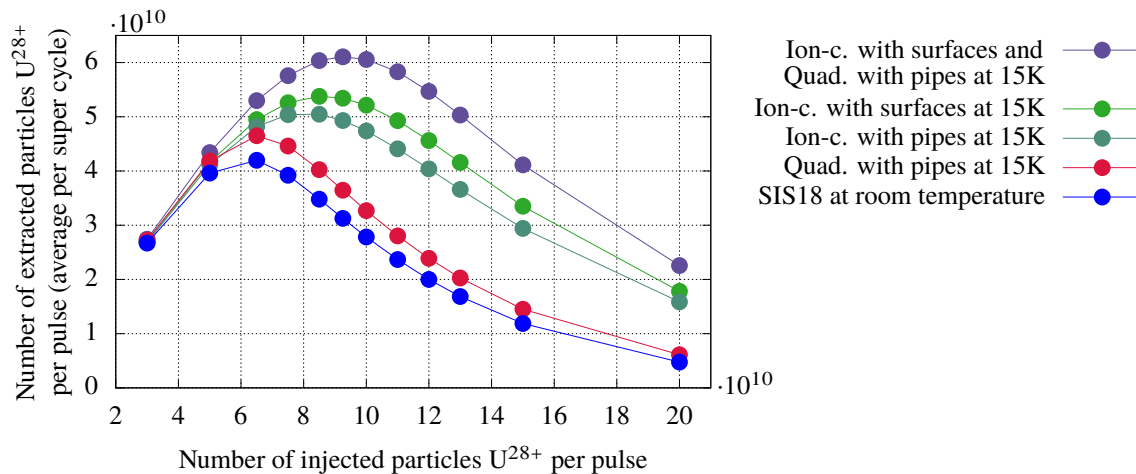


Figure 6: Results from simulations with cryogenic installations in the quadrupole and ion-catcher chambers at 15K with a cycle frequency of 2.7 Hz. More parameters are shown in Table 1.

Figure 6 shows the simulation results with the highest cycle frequency of SIS18 at 2.7 Hz, although simulations with lower frequencies have been done. At first the number of extracted particles rises with increasing number of injected particles, however after reaching a maximum, the correlation inverts. This effect is a result of the dynamic vacuum. The results in Fig. 6 show that cryogenic installations will not only lead to higher number of extracted particles, but also shift the limit for a positive correlation between number of injected and extracted particles to higher numbers. The limit of this positive correlation could be shifted from $6.5 \cdot 10^{10}$ at room temperature to 10^{11} particles of U^{28+} with the combined cryogenic options. The results show that cryogenic installations in the ion-catcher chambers could shift the number to higher number of injected particles while cryogenic installations in the quadrupole chambers only resulted in higher numbers of extracted particles.

In Fig. 7, the maximum number of extracted particles per cycle frequency are presented. This figure shows that cryogenic installations rise the number of extracted particles for every cycle frequency, but also that the ion loss is getting bigger with rising cycle frequency. However, by calculating the average intensity of extracted particles per second from the results shown in Fig. 7, one can see that the resulting particle numbers increases with higher frequencies.

The simulation results predict that the peak intensity in SIS100 could be created from a super cycle of pulses from SIS18 using cryogenic pipes and surfaces in the quadrupole chambers and ion-catcher chambers respectively employing a cycle frequency of 1 Hz. The number of injected U^{28+} particles from SIS18 in SIS100 per pulse could be increased with cryogenic installations from 2.71 to $3.27 \cdot 10^{11}$. By using the same cooling scheme at a cycle frequency of 2.7 Hz the average intensity per second of extracted U^{28+} particles would increase from 1.13 to $1.65 \cdot 10^{11}$. Although the FAIR intensity of $5 \cdot 10^{11}$ U^{28+} per pulse could not be reached, cryogenic installations are a basis for further optimization.

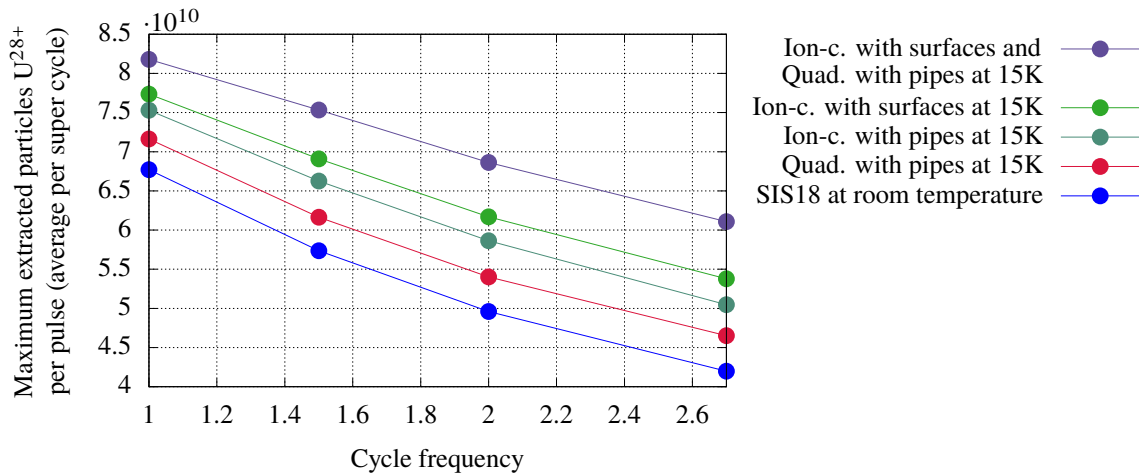


Figure 7: Maximum number of extracted particles U^{28+} from simulations with cryogenic installations in the quadrupole and ion-catcher chambers at 15 K. More parameters are shown in Table 1.

SUMMARY AND OUTLOOK

The quadrupole prototype chamber could be used successfully to show that every measurable common residual gas particle in SIS18 except for hydrogen can be pumped with cryogenic installations at 80 K. However, the measurements also showed that the achievable pumping speed is not very effective. To lower the residual gas density to extreme high vacuum conditions, for example lower temperatures have to be used. This will be tested in near future along with other measurements such as saturation effects.

Simulations of SIS18 with cryogenic installations at lower temperature have been done. They have shown the cryogenic installations could effectively lead to higher number of extracted particles and also shift the limit for a positive correlation between the number of injected and extracted particles to higher numbers of injected particles.

REFERENCES

- [1] “FAIR Technical Design Report SIS100”, December 2008
- [2] L. H. J. Bozyk and P. J. Spiller, “Ionization Loss and Dynamic Vacuum in Heavy Ion Synchrotrons”, in *Proc. 8th Int. Particle Accelerator Conf. (IPAC'17)*, Copenhagen, Denmark, May 2017, pp. 2201–2204. doi:10.18429/JACoW-IPAC2017-TUPVA056
- [3] P. J. Spiller, L. H. J. Bozyk, and P. Puppel, “SIS18 – Intensity Record with Intermediate Charge State Heavy Ions”, in *Proc. 2nd Int. Particle Accelerator Conf. (IPAC'11)*, San Sebastian, Spain, Sep. 2011, paper WEPS003, pp. 2484–2486.
- [4] P. J. Spiller *et al.*, “Status of the FAIR Synchrotron Projects SIS18 Upgrade and SIS100”, in *Proc. 5th Int. Particle Accelerator Conf. (IPAC'14)*, Dresden, Germany, Jun. 2014, pp. 1857–1860. doi:10.18429/JACoW-IPAC2014-WE0BA01
- [5] C. Benvenuti, “Extreme High Vacuum Technology for Particle Accelerators (Invited)”, in *Proc. 19th Particle Accelerator Conf. (PAC'01)*, Chicago, IL, USA, Jun. 2001, paper ROPB002, pp. 602–606.
- [6] L. Bozyk, F. Chill, M.S. Litsarev, I.Yu. Tolstikhina and V.P. Shevelko, “Multiple-electron losses in uranium ion beams in heavy ion synchrotrons”, *NIM-B*, vol. 372, pp. 102–108, 2016. doi:10.1016/j.nimb.2016.01.047
- [7] P. J. Spiller, L. H. J. Bozyk, C. Omet, I. Pongrac, and St. Wilfert, “Technologies for Stabilizing the Dynamic Vacuum and Charge Related Beam Loss in Heavy Ion Synchrotrons”, in *Proc. 7th Int. Particle Accelerator Conf. (IPAC'16)*, Busan, Korea, May 2016, pp. 977–980. doi:10.18429/JACoW-IPAC2016-MOPOY055
- [8] L.H.J. Bozyk, S. Aumüller and P.J. Spiller “Cryogenic Surfaces in a Room Temperature SIS18 Ion Catcher”, presented at HIAT'22, Darmstadt, Germany, May 2022, paper TUP06, this conference.

CRYOGENIC SURFACES IN A ROOM TEMPERATURE SIS18 IONCATCHER

L.H.J. Bozyk*, S. Aumüller, P.J. Spiller

GSI Helmholtzzentrum für Schwerionenforschung, Darmstadt, Germany

Abstract

For FAIR operation, the existing heavy ion synchrotron SIS18 at GSI will be used as booster for the future SIS100. In order to reach the intensity goals, medium charge state heavy ions will be used. Unfortunately, such ions have very high ionization cross sections in collisions with residual gas particles, yielding in beam loss and a subsequent pressure rise via ion impact stimulated gas desorption. To reduce the desorption yield, room temperature ioncatcher have been installed, which provide low desorption surfaces. Simulations including cryogenic surfaces show, that their high sticking probability prevents the vacuum system from pressure built-ups during operation. Such, the operation with heavy ion beams can be stabilized at higher heavy ion intensities, than solely with room temperature surfaces. A prototype ioncatcher containing cryogenic surfaces has been developed and built. The surfaces are cooled by a commercial coldhead, which easily allows this system being integrated into the room temperature synchrotron. The development and first laboratory tests including fast pressure measurements of this system will be presented.

MOTIVATION

The FAIR accelerator complex will provide heavy ion beams of highest intensities. The goal is to reach $5 \cdot 10^{11}$ particles per pulse [1]. In order to reach this intensity goal, medium charge state heavy ions have to be used to avoid stripping losses and to shift the space charge limit to higher number of particles. Unfortunately the probability for further charge exchange of medium charge state heavy ions in collisions with residual gas particles is much higher than for higher charge states. Ions which underwent a charge exchange process will be separated from the circulating beam in ion optical elements, as their magnetic rigidity differs from the reference ion. These ions will get lost at the vacuum chamber wall and release a huge amount of gas via ion impact induced gas desorption. This increases the rest gas density locally, which in turn increases the probability for further charge exchange. Such, a self-amplification up to complete beam loss can evolve. The rest gas density is no more constant during operation, wherefore this process is also called "dynamic vacuum". It limits the maximum achievable heavy ion beam intensity. The process is also illustrated in Fig. 1.

To shift this limit to higher intensities, several measures are possible. One is to reduce the residual gas density, another is the installation of low desorbing surfaces, which are called "ioncatcher". Both measures, besides others, have

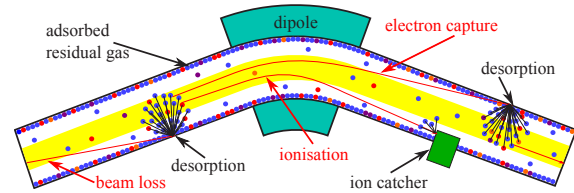


Figure 1: The principle of ionization loss and dynamic vacuum.

been carried out in SIS18. 65% of its vacuum chamber wall, including the ioncatcher chamber are coated with Non-Evaporable-Getter (NEG) [2]. This did lead to an increase of the maximum achievable intensity [2]. But the intensity goal could still not yet be reached. Even prediction from simulations do not reach the goal [3]. The same sort of simulation however hints, that the installation of cryogenic surfaces would increase the maximum intensity, as the sticking probability of such surfaces is much higher than on NEG surfaces.

In [3] cryogenic magnet chamber were assumed. Different approaches are currently investigated. One approach is the installation of cryogenic pipes cooled by liquids inside the quadrupole magnet chambers [4]. Another approach, which is subject of this proceeding, is the installation of coldhead cooled surfaces around the ioncatcher. This is the location, where most of the gas gets produced during operation by ion impact stimulated desorption and an increased sticking probability shows maximum effect.

MECHANICAL DESIGN

In cryogenic systems, temperatures well below 18 K are desirable. Even Hydrogen, the main part of the desorption gases, will get pumped by such temperatures. Commercially available coldheads can reach 4.2 K while still providing a reasonable cooling power of 1.0 W^1 . The biggest issue of coldheads in combination with UHV-system is, that coldheads can not be baked out because of their delicate mechanics. Even if one removes the sensitive parts, which is already outside of the usual application, only temperatures up to $60^\circ\text{C} - 100^\circ\text{C}$ can be used without the risk of damage at the coldhead housing. This is far below the activation temperature of the NEG coatings of $250^\circ\text{C} - 300^\circ\text{C}$, rendering coldheads useless for a baked room temperature vacuum system. On the other hand, a coldhead is more simple in application, than cooling with cryogenic liquids.

A way had to be found for being able to remove a coldhead from the system without breaking the vacuum. To find

* L.Bozyk@gsi.de

¹ Coldhead RDK-408D2 with compressor F50 by Sumitomo

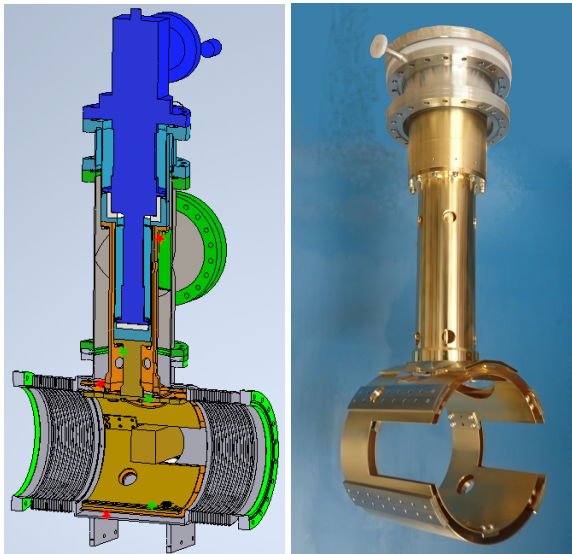


Figure 2: Left: Sectional view of the SIS18 ioncatcher 3D-model with cryogenic surfaces. Details: see text. Right: Photography of the surfaces mounted to the UHV-onset with cryogenic surfaces. (G.Schroeder, ILK)

a solution for this issue and get a prototype, an order consisting of development, construction and manufacturing has been placed to ILK, Dresden. A device which connects the removable coldhead to the UHV-system with including cryogenic surfaces, was the outcome. Figure 2 shows details. On the left, a sectional view illustrating the principle is shown. The coldhead (blue) is housed by the so-called “UHV-onset”, which is shown in turquoise. On the top, both are bolted together. Inside, the first and second stage of the coldhead are contacted by flexible heat transfer parts (white) to the UHV-onset. These parts do not only provide the thermal contact, but also have to cope with the thermal contraction during cooldown. As the coldhead shrinks first, the contact has to be maintained over 1.2 mm varying distance. During bakeout, the coldhead is replaced by a blind flange, without venting the UHV-system. The volume inside the UHV-onset can be evacuated by the small pipe, visible on the top flange in photography on the right of Fig. 2.

The UHV-onset “transfers” the two stages of the coldhead into the UHV-system. A thermal shield (orange) connected to the first stage surrounds the actual cryogenic surfaces (gold) which is connected to the second stage. Everything is mounted inside the existing ioncatcher vacuum chamber (gray with green flanges). The thermal shield could not be designed opaque from room temperature. On the one side, it would have increased the complexity for manufacturing and mounting, on the other side an opening for the circulating is required. Charge exchanged ions shall hit the ioncatcher and sufficient vacuum conductance to the cold surfaces is necessary, too. To reduce the radiation heat transfer despite the non-opaque thermal shield, all surfaces have been coated with a reflecting gold surface. The design of the cold surfaces



Figure 3: Photography inside the ioncatcher chamber with mounted cryogenic surfaces. The view is against beam direction. The flange at the backside houses vacuum diagnostics and feedthroughs.

cooperates for a good vacuum conductance on the one hand, and as much heat transfer via bulky material on the other hand.

Figure 3 shows a photography inside the vacuum chamber, contrary to beam direction. The gold-coated room temperature ion-catcher blocks stick from left and right into the cryogenic surfaces. The backside is covered by cluster-flange housing several diagnostics devices. The flange where the picture was taken is closed by a pump.

TEST SETUP

The ioncatcher-chamber with cryogenic surfaces is part of a test stand. Several properties will be measured, to learn about the performance of the cryogenic surfaces. The test setup is equipped with the following items:

- A turbomolecular-pump, which can be sealed-off by an all-metal gate valve. This allows outgassing-measurements.
- An extractor gauge and a widerange vacuum gauge to measure the total vacuum pressure.
- A residual gas analyzer for partial pressure measurements.
- A dosing valve for controlled gas inlet, used for saturation measurements.
- A piezo dosing valve for short gas inlets, used for dynamic vacuum measurements.
- Six temperature sensors inside the vacuum system on the cold surfaces, three on each stage.
- Eight temperature sensors on the atmospheric surfaces, used for monitoring during bakeout but also during cooldown.

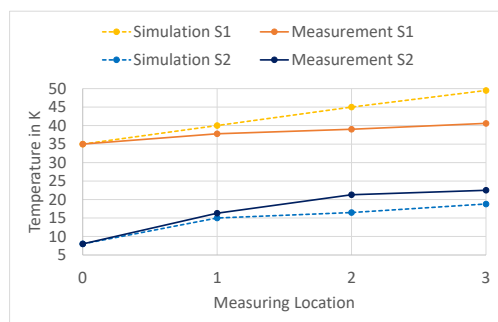


Figure 4: Measured and simulated temperatures at the respective measuring locations. The numbers increase with distance to the coldhead.

The inner temperature sensors have been placed at the following positions, for both stages respectively:

1. As close as possible to the UHV-onset, to measure the heat transfer from coldhead through the UHV-onset.
2. On the upper side of the cryogenic surface, but as close as possible to the thermal connection: These points measure the heat transfer through the support structures.
3. On the lower side of the cryogenic surface, as far away as possible from the UHV-onset, here one gets a feeling about the surface's thermal homogeneity.

In Fig. 2 (left) the locations are marked by red stars for stage 1 and green stars for stage 2.

All measurement devices are connected to a readout software. This software also allows turning on and off the coldhead compressor, to control the dosing valve by a stepping motor, and to control the piezo-dosing valve. Moreover, sequences can be programmed, which allow for semi-automatic measurement sequences without human interference. The sequences can only be operated by given time intervals, but also by e.g. falling below certain temperatures or pressures. Such, time-consuming measurement series become automated and reproducible.

MEASUREMENTS AND RESULTS

Temperature Measurements

As a thermal connection between UHV-onset and coldhead, an aluminum fleece has been pressed into form and been used for the first measurements. As the cooling was not sufficient to reach hydrogen pumping, the UHV-onset was filled with gaseous helium instead of vacuum, to increase the thermal contact. By monitoring the decreasing pressure inside the UHV-onset it could be verified, that the coldhead reaches temperatures to liquefy helium. The simulated (simulation by ILK using Ansys) and measured temperatures are shown in Fig. 4. The expected temperatures of the two

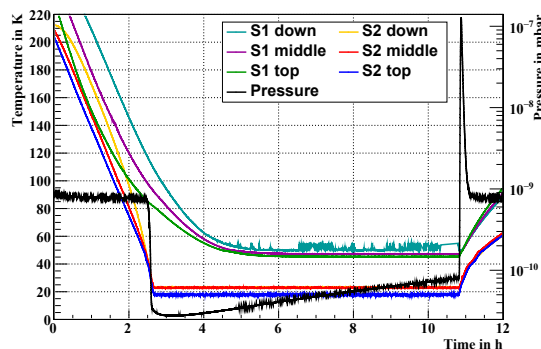


Figure 5: Temperature and pressure evolution during cooldown (0 h - 2.5 h), saturation measurement with hydrogen via dosing valve (2.5 h - 11 h), and the beginning of warmup (later than 11 h) with the fast pressure increase by the release of all adsorbed hydrogen. During saturation measurements, the lowest temperature sensor at stage one "S1 down" was subjected to distortions.

coldhead stages are shown for reference. On the first stage, the simulation was too pessimistic. The measured temperatures and their differences are lower than expected. On the second stage, in contrast, the thermal contacts have been overestimated in the simulations.

The temperatures of the atmospheric surfaces remain unchanged during cooldown. This hints to a very low emission coefficient of the gold plated cryosurfaces, as it was desired. Only the temperature at the uppermost flange of the UHV-onset drops by up to 9 °C during cooldown. This is due to thermal conductance between the coldhead's first stage and this flange. During warmup, the temperature drops by further 4 °C, before it starts to rise. The interpretation is, that the liquefied helium inside the UHV-onset evaporates and increases the thermal exchange between room temperature and cold surfaces.

By repeated partial warming to temperatures around 60 K at the second stage and subsequent cooling, the minimum temperature could be decreased slightly by 750 mK to even 1.25 K. The effect is not fully understood. A possible explanation is some rearrangement of helium inside the thermal connection between the second stage and the UHV-onset. A new version of the thermal connection is under development. A higher mass density shall increase the thermal conductivity.

A complete cooldown takes roughly 4.5 hours. Warming up requires 25 hours.

Pressure Measurements

Preceding to pressure measurements, the UHV-system has been baked to temperatures of 150 °C for about 50 hours. At room temperature, pressures in the range of $2 \cdot 10^{-10}$ mbar are reached. Via pressure rise measurements an outgassing rate of $8.2 \cdot 10^{-9}$ mbar l/s or $4 \cdot 10^{-13}$ mbar l/(s cm²) were determined.

SUMMARY AND OUTLOOK

A prototype test setup with cryogenic surfaces inside a SIS18 ioncatcher chamber has been developed and built. The cold surfaces are cooled by a coldhead, which can be removed without venting the UHV-system. Such, the system can be baked out and NEG-surfaces can be activated. The inner surfaces reach temperatures sufficiently low to pump hydrogen via cryosorption. Nevertheless, the capacity for hydrogen pumping could be higher. Therefore improved thermal connections are under development to reach lower temperatures and increase the hydrogen capacity.

The dynamic vacuum properties of the cryogenic surfaces will be analyzed. A fast pressure measurement will allow to analyze the the response to a short pressure pulse coming from a piezo dosing valve. The pressure decay time and such the sticking probability will be examined as an input for dynamic vacuum simulations.

In a later step, the vacuum chamber with its cryogenic surfaces will be installed into SIS18. Effects onto the operation with medium charge state heavy ions will be investigated.

REFERENCES

- [1] "FAIR Baseline Technical Report", December 2008
- [2] P.J. Spiller, L.H.J. Bozyk, and P. Puppel, "SIS18 – Intensity Record with Intermediate Charge State Heavy Ions", in *Proc. 2nd Int. Particle Accelerator Conf. (IPAC'11)*, San Sebastian, Spain, Sep. 2011, paper WEPS003, pp. 2484–2486.
- [3] L.H.J. Bozyk and P.J. Spiller, "Ionization Loss and Dynamic Vacuum in Heavy Ion Synchrotrons", in *Proc. 8th Int. Particle Accelerator Conf. (IPAC'17)*, Copenhagen, Denmark, May 2017, pp. 2201–2204. doi:10.18429/JACoW-IPAC2017-TUPVA056
- [4] S. Aumüller, L.H.J. Bozyk, P. Spiller, and K. Blaum, "Prototype Room Temperature Quadrupole Chamber with Cryogenic Installations", presented at HIAT 2022, Darmstadt, Germany, 2022, paper TUP05, this conference.

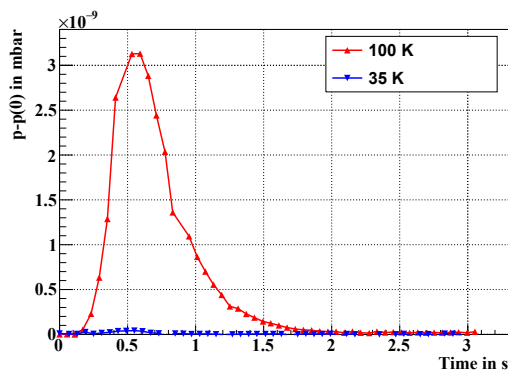


Figure 6: First fast pressure measurements using a piezo dosing valve and ambient air. The pressure difference with respect to the first value is shown.

At the end of cooldowns, a sudden pressure drop down to $2 \cdot 10^{-11}$ mbar can be observed, see Fig. 5. Here, the dosing valve was open during the whole measurement time, yielding in a higher pressure at the start and the end of the measurements than $2 \cdot 10^{-10}$ mbar. The sudden pressure drop is the start of hydrogen adsorption which means, at least parts of the cold surfaces have temperatures sufficiently low for hydrogen pumping. A capacity of $2 \cdot 10^{-3}$ mbar l for hydrogen at minimum temperatures was determined by the help of the dosing valve. The inner surface's NEG coating was not activated at this time.

In order to measure the dynamic vacuum behavior, a piezo dosing valve and a fast pressure measurement have been set up. The piezo dosing valve allows for short and repeatable gas inlet pulses. To establish a fast pressure measurement, the ion current of the extractor gauge is read out by a triggerable current measurement device². Such, a reproducible gas pulse will be analyzed in terms of peak height and decay time for different temperatures and surface saturations. Figure 6 shows first measurements with ambient air for two different temperatures.

² 65 ms interval length have been reached so far

EFFICIENT HEAVY ION ACCELERATION WITH HIGH BRILLIANCE

Chuan Zhang[#], GSI Helmholtz Centre for Heavy Ion Research, Darmstadt, Germany
 Holger Podlech, Institute for Applied Physics, Goethe-University, Frankfurt a.M., Germany

Abstract

It is challenging to realize an efficient and brilliant RFQ for accelerating high current heavy ion beams, as space charge effects are most pronounced at the low energy end. Here “efficient” means an as short as possible accelerating structure with minimum RF power consumption, while “brilliant” means high beam transmission and low emittance growth. Using the > 9 m long HSI RFQ accelerator, one of the longest RFQs in the world, as an example, a promising solution has been presented.

INTRODUCTION

As the starting accelerating structure of the UNILAC that is the main injector to the GSI accelerator complex, the 36.136 MHz HSI RFQ can accelerate a wide variety of particle species from protons to uranium ions in the energy range of 2.2 keV/u – 120 keV/u. Some major milestones in the development of the HSI RFQ are as follows:

- In 1996: the design of the first HSI RFQ (design ion: U^{4+} , design beam current I_{in} : 16.5 emA) was started [1].
- In 1998: the first HSI RFQ (hereafter referred to as Version-1998) was constructed [2].
- In 1999: the Version-1998 RFQ was put into operation.
- In 2004: the electrodes were renewed with an improved radial matching section for a larger acceptance.
- In 2008: the second HSI RFQ (hereafter referred to as Version-2008) was designed (still for U^{4+} but I_{in} was increased to 20 emA) and produced [3]. For this upgrade, the inter-vane voltage U was increased from 125 kV to 155 kV.
- In 2009: the Version-2008 RFQ was put into operation.
- From 2009 until now: the Version-2008 RFQ is in routine operation (in 2019, the electrodes were renewed but still based on the same design).
- Since 2015: in order to meet the beam intensity requirement for FAIR, the R&D for a third version of the HSI RFQ has been started.

The main design parameters of the two constructed HSI RFQs can be found in Table 1. The design goals for the new version are as follows:

- $I_{in} = 20$ emA with $T \geq 90\%$ (for real operation, 18 emA and 16.2 emA will be expected at the entrance and the exit of the RFQ, respectively).
- The maximum surface electric field $E_{s, max}$ should be lower than that of the Version-2008 RFQ.
- L should be kept same so that the same tank can be used.

[#] email address: c.zhang@gsi.de

Table 1: Design Parameters of the Constructed HSI RFQs

Parameters	Version-1998	Version-2008
W [keV/u]	2.2 – 120	2.2 – 120
U [kV]	125	155
I_{in} [emA]	16.5	20
$\epsilon_{t, in, un, total}$ [π mm-mrad]	138	210
$\epsilon_{t, in, n, rms}$ [π mm-mrad]	0.050	0.076
$\alpha_{Twiss, t, in}$	0.43	0.6
$\beta_{Twiss, t, in}$ [cm/rad]	4.6	13.6
$E_{s, max}$ [MV/m]	31.8	31.2
L [cm]	921.749	921.7
T [%]	89.5	88.5

DESIGN STRATEGY

For the third HSI RFQ, several solutions have been already proposed:

- In 2016: using one single cavity with $U = 125$ kV [4] and $E_{s, max} = 30.2$ MV/m.
- In 2020: using multiple short and independent cavities with $E_{s, max} = 30.9$ MV/m (U varies from 120 kV to 147 kV, but it is constant in each cavity) [5].

All these solutions have not only lowered maximum surface electric field of the electrodes but also improved beam performance.

The motivation for this new study is to develop another single-cavity design at $U = 120$ kV to further lower $E_{s, max}$, save more RF power, and improve beam quality.

The brilliance is an important index to measure the beam quality. There are different definitions for the brilliance B and the one used by this study is given as follows:

$$B \equiv \frac{I}{\epsilon_x \epsilon_y} \quad (1)$$

where I is the beam current in mA and ϵ_x and ϵ_y are the transverse emittances in π mm mrad (for B , the factor $1/\pi^2$ can be left out). No matter which definition is used, for a given input beam, a design with a high B means high beam transmission and low emittance growth.

For the new HSI RFQ design with $U = 120$ kV (hereafter referred to as Design-2022), the high efficiency has been achieved by using the New Four Section Procedure that

supports to realize a fast main bunching with a relatively low U under balanced transverse and longitudinal forces [6], and the high brilliance has been achieved by using the recently developed MEGLET (Minimizing Emittance Growth via Low Emittance Transfer) method [7]. Different from previously proposed methods, which always try to avoid emittance transfer, the MEGLET method minimizes emittance growth by:

- Allowing low emittance transfer when the ratio of transverse emittance to longitudinal emittance can be held in the range of $0.9 \leq \frac{\varepsilon_t}{\varepsilon_l} \leq 1.4$ (see Fig. 1).
- Using two emittance-transfer periods (in which the emittance transfer is in opposite directions) to minimize the net emittance growth.

To obtain a high B for the new HSI RFQ, the emittance transfer in the 2nd period has been designed to be stronger than that in the 1st period so that one can get smaller transverse output emittances.

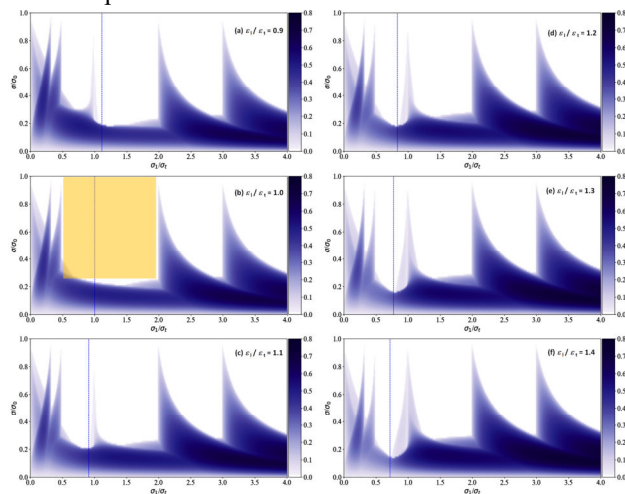


Figure 1: Hofmann charts (generated using TraceWin [8]) for the emittance ratios $\frac{\varepsilon_t}{\varepsilon_l} = 0.9 - 1.4$ [7]. The rectangle marked in orange covers the safe area for tune footprints.

DESIGN-2022 HSI RFQ

Figure 2 shows the evolution of the main parameters along the Design-2022 HSI RFQ.

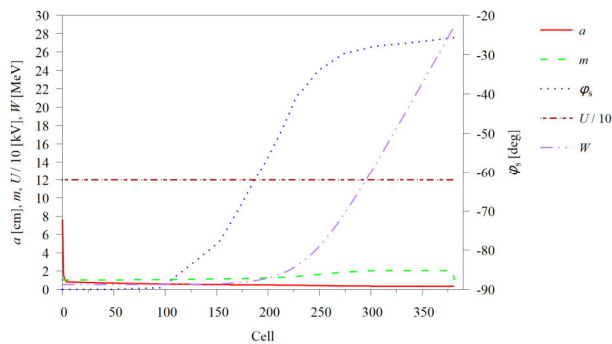


Figure 2: Main design parameters of the Design-2022 HSI RFQ, where a is the minimum electrode aperture, m is the electrode modulation, φ_s is the synchronous phase, U is the inter-vane voltage, and W is the beam energy.

In Table 2, one can see that:

- U is $\sim 25\%$ lower in the new design, which will considerably save the RF power (the power is proportional to U^2).
- $E_{s, \max}$ becomes < 30 MV/m.
- The average mid-cell aperture of the electrodes $r_{0, \text{avg}}$ is now only 0.02 cm smaller so that the current rings for carrying electrodes should be still applicable.
- The new RFQ is slightly shorter, which leaves a little room for the fine tuning of the design.

Table 2: Comparison between the Version-2008 and Design-2022 HSI RFQs

Parameters	Version-2008	Design-2022
U [kV]	155	120
$r_{0, \text{avg}}$ [cm]	0.60	0.58
$E_{s, \max}$ [MV/m]	31.2	29.9
Total number of cells	409	381
L [cm]	921.7	920.1

The beam dynamics simulation of the Design-2022 HSI RFQ was performed using the PARMTEQM (PAR) code [9] with a 4D Waterbag (particles are generated randomly in a 4D transverse hyperspace with a uniform phase spread and no energy spread) input distribution. The same input emittances ($\varepsilon_{t, \text{in, un, total}} = 210 \pi$ mm mrad or $\varepsilon_{t, \text{in, n, rms}} = 0.076 \pi$ mm mrad) and Twiss parameters (see Table 1) as the Version-2008 were adopted. The Design-2022 is also checked with an input distribution generated by the DYNAC (DYN) code [10] with $\varepsilon_{t, \text{in, n, rms}} = 0.076 \pi$ mm mrad and the same Twiss parameters (but in the transverse directions, the distributions are Gaussian). The transverse phase spaces of the two used input distributions are shown in Fig. 3, which shows that the beam size and the maximum divergence angle are much larger in the Gaussian case.

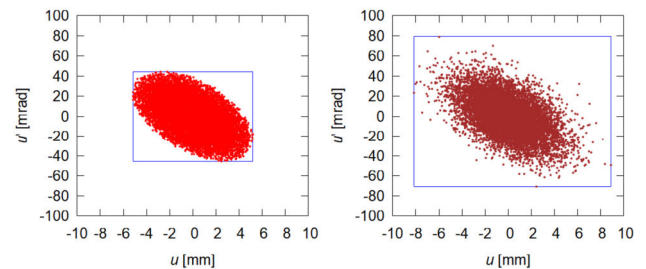


Figure 3: 4D Waterbag (left) and Gaussian (right) transverse input distributions (u represents the x or y direction).

In Fig. 4 and Fig. 5, the longitudinal and transverse emittances are plotted as functions of cell number for the Waterbag and Gaussian cases, respectively, where the emittance curves for 99% of particles are used to show the performance of the main beam by excluding 1% outmost particles. In the part marked in orange, the tune footprints of the beam are inside the so-called “safe rectangle” with $0.5 \leq \frac{\sigma_l}{\sigma_t} \leq 2.0$ and $0.25 \leq \frac{\sigma}{\sigma_0} \leq 1.0$ (corresponding to the area marked in orange in Fig. 1). Generally speaking, the two

figures are similar. For the Waterbag case, the emittance ratio of the main beam is well held in the range of $0.9 \leq \frac{\varepsilon_{\perp}}{\varepsilon_{\parallel}} \leq 1.4$ along the main part of the RFQ, as required by the MEGLET method. For the Gaussian case, the emittance transfer is stronger, but the maximum emittance ratio of the main beam is 1.7, still not far away from the optimum range.

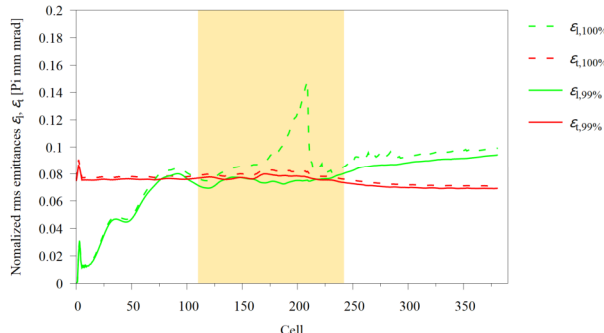


Figure 4: Evolution of emittances for 100% and 99% of particles along the Design-2022 HSI RFQ (Waterbag case).

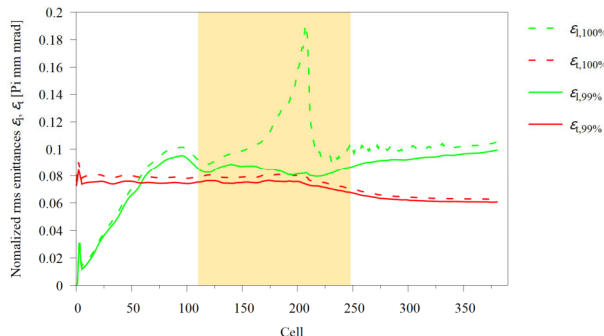


Figure 5: Evolution of emittances for 100% and 99% of particles along the Design-2022 HSI RFQ (Gaussian case).

BENCHMARK

For a benchmark, the DYNAC code [10] has been taken. A comparison of the main simulation results given by the two codes is made in Table 3, which shows that no matter beam transmission or output emittances are comparable.

Table 3: Simulated beam transmission and normalized rms output emittances (π mm mrad)

	PAR Waterbag	PAR Gaussian	DYN Waterbag	DYN Gaussian
T [%]	96.2	90.3	96.1	90.9
$\varepsilon_{x, out}$	0.070	0.063	0.079	0.068
$\varepsilon_{y, out}$	0.072	0.063	0.077	0.068
$\varepsilon_{z, out}$	0.099	0.105	0.088	0.097

With the Gaussian input beam, more losses happened due to the larger total emittance (see Fig. 3). But for all cases, the beam transmission is still $> 90\%$. Except the transverse emittances of the DYNAC simulation in the Waterbag case are slightly $> \varepsilon_{t, in, n, rms}$, all other transverse emittance values are much smaller than $\varepsilon_{t, in, n, rms}$. This indicates a high brilliance of the Design-2022 HSI RFQ. As 120 kV is much lower than 155 kV used by the current HSI

RFQ, the efficiency of the Design-2022 HSI RFQ can be clearly seen.

Figure 6 shows that the output particle distributions simulated by DYNAC are similar to those given by PARMTEQM for both the Waterbag case and the Gaussian case, especially in the transverse planes.

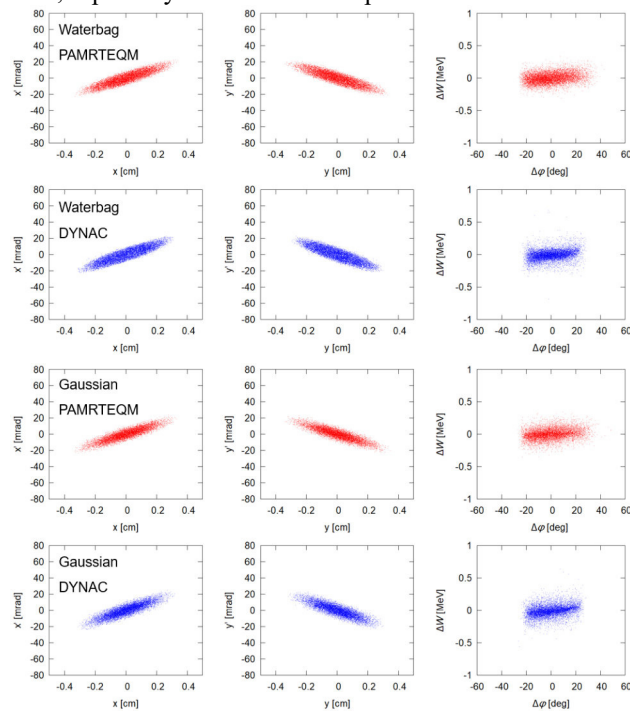


Figure 6: Output particle distributions.

ACKNOWLEDGEMENTS

Special thanks go to Hartmut Vormann for providing the information about the two constructed HSI RFQs and Eugene Tanke for the discussions on the DYNAC simulation.

REFERENCES

- [1] A. Schempp, “Design of Compact RFQ’s”, in *Proc. 1996 Linear Accelerator Conf. (LINAC’96)*, Geneva, Switzerland, 26-30 August 1996, pp. 53-55, paper MOP03.
- [2] U. Ratzinger, K. Kaspar, E. Malwitz, S. Minaev, and R. Tiede, “The GSI 36 MHz High-Current IH-Type RFQ and HIIF-Relevant Extensions”, *Nuclear Instruments and Methods in Physics Research Section A: Accelerators, Spectrometers, Detectors and Associated Equipment*, vol. 415, issues 1–2, pp. 281-286, 21 September 1998, doi: 10.1016/S0168-9002(98)00395-7
- [3] A. Kolomiets, S. Minaev, W. Barth, L. Dahl, H. Vormann, and S. Yaramyshev, “Upgrade of the Unilac High Current Injector RFQ”, in *Proc. 2008 Linear Accelerator Conf. (LINAC’08)*, Victoria, BC, Canada, 29 September – 3 October 2008, pp. 136-138.
- [4] C. Zhang, L. Groening, O. Kester, S. Mickat, H. Vormann, M. Baschke, H. Podlech, U. Ratzinger, and R. Tiede, “HSI RFQ Upgrade for the UNILAC Injection to FAIR”, in *Proc. 2016 IPAC’16*, Busan, Korea, May 8-13, 2016, pp. 877-879. doi: 10.18429/JACoW-IPAC2016-MOPOY016
- [5] C. Zhang, H. Podlech, and E. Tanke, “Realizing Long Radio-Frequency Quadrupole Accelerators with Multiple Shorter

- [5] C. Zhang, H. Podlech, and E. Tanke, "Realizing Long Radio-Frequency Quadrupole Accelerators with Multiple Shorter and Independent Cavities", *Physical Review Accelerators and Beams*, vol. 23, no. 042003, April 2020, doi:10.1103/PhysRevAccelBeams.23.042003
- [6] C. Zhang and A. Schempp, "Beam dynamics studies on a 200mA proton radio frequency quadrupole accelerator," *Nuclear Instruments and Methods in Physics Research Section A: Accelerators, Spectrometers, Detectors and Associated Equipment*, vol. 586, no. 2, pp. 153–159, Feb. 2008. doi:10.1016/j.nima.2007.12.001
- [7] C. Zhang, "Minimizing Emittance Growth via Low Emittance Transfer", *Physical Review Accelerators and Beams*, vol. 25, no. 034201, March 2022, doi:10.1103/PhysRevAccelBeams.25.034201
- [8] TraceWin code, <http://irfu.cea.fr/dacm/logiciels/>
- [9] *Manual of the LANL RFQ Design Codes*, LANL Report No. LA-UR-96-1836, Jun. 2005.
- [10] DYNAC, <https://github.com/dynac-source/dynac-source>

RF CHOPPER FOR PREBUNCHED RADIOACTIVE ION BEAMS

Alec Gonzalez, Alexander Plastun

Facility for Rare Isotope Beams, Michigan State University, East Lansing, MI, United States

Abstract

An RF chopper system is being designed for the Re-Accelerator (ReA) linac at the Facility for Rare Isotope Beams (FRIB) at Michigan State University (MSU). The chopper system is designed to clean out satellite bunches and produce a 16.1 MHz bunch structure, which allows for time-of-flight separation of the isotopes. The chopper system's location in the beamline is between the ReA3 and ReA6 cryomodules. In ReA, the beam can be prebunched at the frequency of 16.1 MHz and accelerated in a 80.5 MHz RFQ, producing four satellite bunches for every one high-intensity bunch. The chopper system includes an RF deflector operating at 64.4 MHz, which is the beat frequency of 80.5 MHz and 16.1 MHz. The deflector deflects every bunch to spatially separate high-intensity and satellite bunches. The beam trajectory is biased by a constant magnetic field to ensure the high-intensity bunches do not experience any total deflection. The kicked bunches are low in intensity and will be sent to a beam dump, resulting in a clean 16.1 MHz beam structure injected into the ReA6 cryomodule.

INTRODUCTION

The Re-Accelerator [1] is a superconducting linear accelerator that "re-accelerates" rare isotopes produced in experiments done with the FRIB linear accelerator. ReA was commissioned in 2015 and includes three general purpose beamlines and a beamline dedicated to astrophysics experiments. The ReA6 cryomodule was added in 2021 to provide higher beam energies. ReA can accelerate ions with an A/Q ratio between 2 and 5. The chopper system will produce a beam with a clean 16.1 MHz bunch structure, which will allow ReA users to perform time-of-flight measurements. The ReA beamline includes a radio-frequency quadrupole

electric field with a frequency of 64.4 MHz and a static magnetic field to deflect the satellite bunches while keeping the main bunches on axis. Two potential locations were considered for the chopper system. The first location, between the RFQ and the first ReA3 cryomodule, has a lower beam energy (0.5 MeV/u), but was not chosen because there is limited space (only about 70 cm) for the chopper system. The second location, shown in Fig. 1, is between the ReA3 cryomodules and the ReA6 cryomodule. The beam energy at this location is around 3 MeV/u. This location was chosen because there is plenty of space for both the chopper and a beam dump for the deflected satellite bunches. The beam dump will be located about 1.4 meters downstream of the chopper.

DESIGN

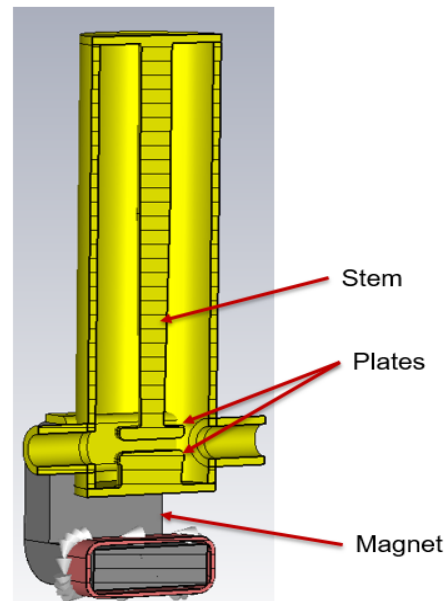


Figure 2: Cross-section view of the final RF chopper cavity model designed in CST Studio (dimensions shown in Table 1).

RF Deflection

The RF chopper design is based on a quarter-wave resonant cavity (QWR) with deflecting plates that kick the beam bunches in a vertical direction. The cavity cross-section is shown in Fig. 2. The resonant frequency of the cavity is 64.4 MHz, which in combination with the bunch frequency of 80.5 MHz (driven by the RFQ frequency) produces a 16.1 MHz deflection waveform. Indeed, the cavity resonates at the beat frequency of the actual bunch frequency and the desired 16.1 MHz bunch repetition rate. At this frequency, the QWR is a 1.1 meter-high cavity, whereas the 16.1 MHz

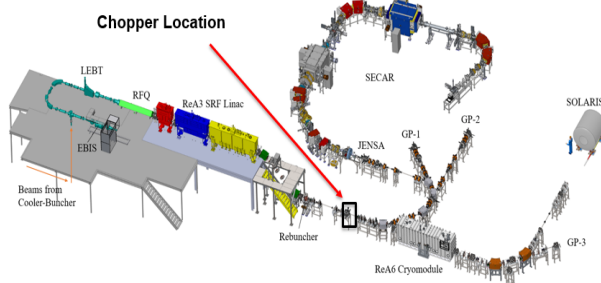


Figure 1: ReA layout.

(RFQ), which generates an 80.5 MHz bunch repetition rate. Upstream from the RFQ is a multi-harmonic buncher (MHB) which produces high-intensity bunches at a frequency of 16.1 MHz. This means that, after the RFQ, there are four low-intensity ("satellite") bunches for every one intense ("main") bunch. This chopper system uses a combination of an RF

Content from this work may be used under the terms of the CC BY 4.0 licence (© 2022). Any distribution of this work must maintain attribution to the author(s), title of the work, publisher, and DOI

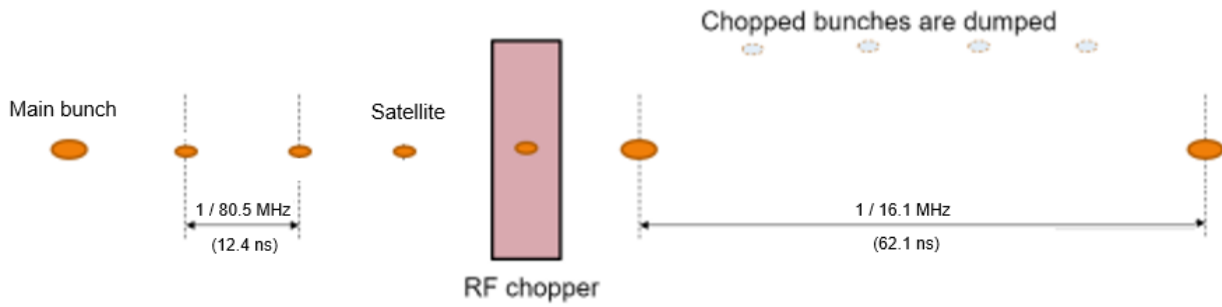


Figure 3: Bunch structure before and after the RF chopper system.

Table 1: Important Design Parameters of the RF Chopper System

Parameter	Value
Cavity Height	1130 mm
Cavity Diameter	340 mm
Plate Length	168 mm
Gap Between Plates	30 mm
Power	10 kW
Electric Field in Gap	4.6 MV/m
Voltage in Gap	137 kV
Peak Electric Field	7.9 MV/m
Magnetic Field in Gap	68 mT

resonator would require a coil inductor [2]. The peak electric field inside the cavity is limited by electric breakdown. The peak electric field in the chopper system is 7.9 MV/m, which is 80% of the Kilpatrick limit [3] at 64.4 MHz (9.7 MV/m). The length of the plates was set to 168 mm, which corresponds to $0.9 * \beta\lambda / 2$. This length is a trade-off between the deflection strength and the gap capacitance and was chosen to optimize RF power consumption by the cavity. After multiple simulations, we determined that the minimum required kick angle of about 18 mrad can be achieved at 10 kW of power to the cavity. The bunch structure of the beam can be seen in Fig.3, while Fig. 4 shows the kick waveform at 10 kW.

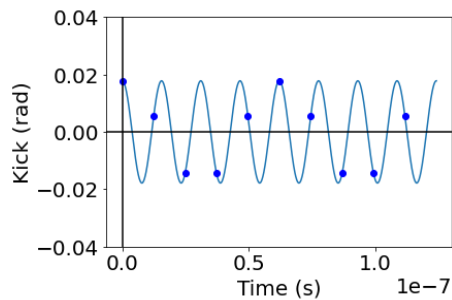


Figure 4: Average bunch deflection in the chopper due to the RF electric field overlaid onto a 64.4 MHz waveform.

Magnetic Bias

In order to keep the main bunches on axis, a static magnetic bias is needed to cancel out the deflection the main bunches feel from the RF electric field inside the cavity. The magnetic bias comes from an iron-dominated, C-shaped

dipole, which is designed to produce a magnetic field of 68 mT inside the cavity. The magnet is located on the cavity so the bunches can experience both the electric and magnetic deflections in the same space. If we used one magnet upstream and one magnet downstream of the cavity then the bunches would enter the cavity already deflected off the beam axis, which requires a larger gap and higher voltage. One magnet after the cavity would not work either because it cannot cancel out both offset and angle of the beam trajectory. The dipole requires about 1 kW of power and it uses water-cooled hollow copper conductors for the coil. Figure 5 shows the effect of the magnetic field on the deflection of the bunches. The intense bunches are on the peak of the waveform and biased to zero kick in Fig. 5, compared to the pure RF deflection case where they experience a deflection of around 18 mrad.

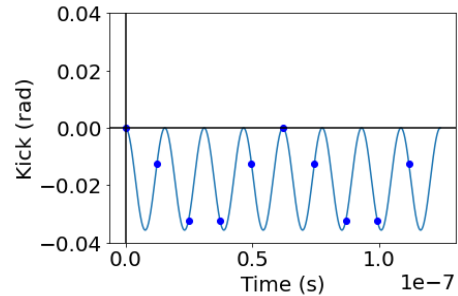


Figure 5: Average bunch deflection in the chopper due to the RF electric field combined with the static magnetic field provided by the chopper dipole overlaid onto a 64.4 MHz waveform.

Beam Dumping

The satellite bunches are dumped on the beampipe and on a circular aperture 1.4 meters downstream from the chopper. The aperture has a diameter of 1.0 cm, which allows all the particles in the main bunches to pass through and intercept the satellites before they reach the ReA6 cryomodule as shown in Fig. 6.

BEAM DYNAMICS

CST Studio

The 3D model of the chopper was constructed in CST [4]. The initial particle distribution was exported from the

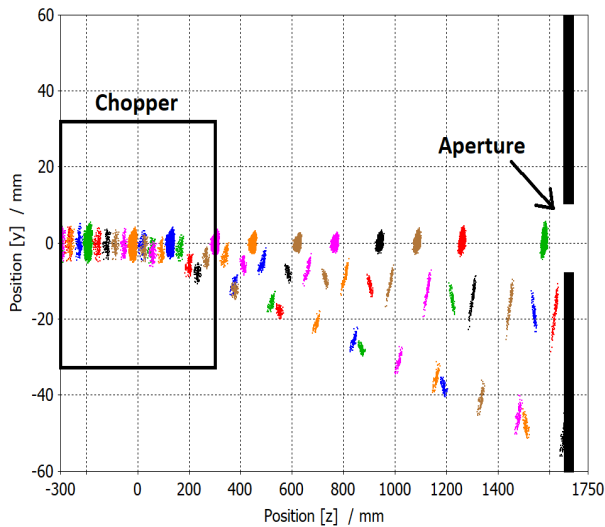


Figure 6: CST Studio simulation of the trajectory of bunches through the chopper, drift space, and the aperture.

TRACK model of the ReA beamline and imported into the CST PIC solver. The electric field inside the cavity was scaled to a level corresponding to 10 kW of input RF power and the magnetic field was adjusted to provide zero deflection for the main bunches. A snapshot of the bunches produced in CST can be seen in Fig. 6.

TRACK

In addition to our CST simulations, we also used TRACK [5] to simulate the motion of the beam. However, TRACK cannot simulate an RF electric field and a static magnetic field in the same element. To simulate the chopper system, we imported the 3D RF electric field map of the chopper from CST and then used two zero-length dipole corrector elements on each side of the cavity to simulate the magnetic bias produced in the chopper. The results from these simulations are shown in Fig. 7. It can be seen in the y - y' plot after the chopper in Fig. 7 that the average kick of each bunch is the same as in the design waveform in Fig. 5. Thanks to great time resolution of the bunches, the purity of the main bunches is 100%.

CONCLUSION

The ReA chopper system was designed in CST studio and the design was validated by simulations in both TRACK and CST Studio. The chopper uses a combination of an RF electric field and a static magnetic field to deflect low-intensity bunches in the negative y direction, while keeping the intense 16.1 MHz bunches on the beam axis. The electric field requires a moderate RF power of 10 kW and the dipole magnet requires around 1 kW of power. The chopper will provide deflections of 15 mrad and 35 mrad to the satellite bunches ensuring 100% purity of the main intense bunches. These deflected bunches will be cleaned out by a circular

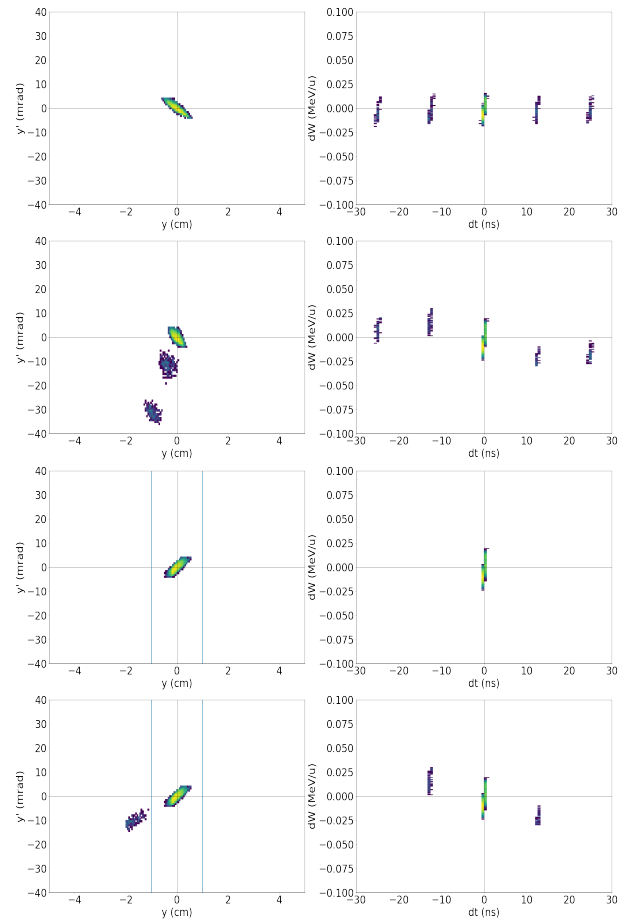


Figure 7: Y - Y' (left) and longitudinal (right) beam snapshots simulated by TRACK: before the chopper, after the chopper, before the beam dump, and after the beam dump (vertical lines represent aperture size).

aperture with an opening radius of 1 cm placed 1.4 meters downstream of the chopper system.

REFERENCES

- [1] A.C.C. Villari *et al.*, “ReAccelerator Upgrade, Commissioning and First Experiments at the National Superconducting Cyclotron Laboratory (NSCL) / Facility for Rare Isotope Beams (FRIB)”, in *Proc. IPAC'22*, Bangkok, Thailand, Jun. 2022, pp. 101–103. doi: 10.18429/JACoW-IPAC2022-MOPOST021
- [2] E.W. Blackmore *et al.*, “An RF separator for cloud muons at TRIUMF”, *Nucl. Instrum. Methods Phys. Res., Sect. A* 234.2 (1985), pp. 235–243. doi: 10.1016/0168-9002(85)90911-8
- [3] T. P. Wangler, *RF Linear accelerators*. Hoboken, NJ, USA: John Wiley & Sons, 2008.
- [4] *CST Studio Suite*, <https://www.3ds.com/products-services/simulia/products/cst-studio-suite/>.
- [5] P.N. Ostroumov, V. Aseev, and B. Mustapha, “TRACK—a code for beam dynamics simulation in accelerators and transport lines with 3D electric and magnetic fields”, 2006. <http://www.phy.anl.gov/atlas/TRACK>

TUNING AND RF MEASUREMENTS OF THE LILAC RFQ*

H. Höltermann[†], H. Hähnel, B. Koubek, H. Podlech, U. Ratzinger
 BEVATECH GmbH, Frankfurt, Germany

Abstract

A new linac for the NICA ion collider is under construction for JINR at BEVATECH GmbH. As first cavity the 2.5 m long RFQ was manufactured. Within this length it accelerates particles with a mass to charge ratio up to three to an energy of 600 keV/u. The operation frequency is 162.5 MHz and the 4-Rod structure consists of 23 RF cells that need to be adjusted using tuning blocks in order to provide the required field distribution along the electrodes. The status of the manufacturing and the upcoming tuning process including the overall RF setup of the RFQ are summarized in this paper.

INTRODUCTION

The NICA collider will be fed with various ion beams accelerated in the Nuclotron [1]. Heavy particles with $A/Q=6.25$ will use the HILAC (Heavy Ion Linac) [2] as injector and will be injected into the booster synchrotron before they will be finally accelerated by Nuclotron. Light ions with $A/Q=3$ will use the Light Ion Linac (LILAC) [3] and directly injected into the Nuclotron. LILAC will be fed with ions from two different ion sources, the SPI (Special Polarized Ion Source) for protons and deuterons, and LIS – a Laser Ion Source for ions such as C^{3+} for example [1]. Between the ion sources and the LILAC RFQ a LEBT will transport and focus proton beams with 50 keV from the ion source. In addition deuterons with only 25 keV/u beam energy from the ion source will be post-accelerated and matched to the RFQ acceptance. A solution to match the carbon beams is under investigation.

The emittance of the beam from the ion source is limited to 0.3 mm mrad which was measured as worst case for the SPI. Larger emittances can be transported by the LEBT, but will not be accepted by the RFQ.

RFQ DESIGN

Based on the measured output from the SPI and LIS, the LEBT beam dynamics design and the required matching to the following IH Drift Tube Linac, the LILAC RFQ beam dynamics design parameters are listed in Table 1. The design plots in Figure 1 show a stable output emittance against changes of the input emittance for an injected C^{3+} beam with maximum 15mA of beam current. For the worst case input emittance of 0.3 mm mrad (rms), the LILAC RFQ design provide transmissions of around 89%. The LILAC RFQ is chosen to be of the 4-Rod type RFQs.

The RF design parameters of the RFQ resonant structure have been simulated in CST. The RF design was performed taking the longitudinal end fields [4] as well as dipole correction [5] into consideration. The RF design parameters are listed in Table 2.

Table 1: LILAC RFQ Beam Dynamics Design Parameters

Parameter	Value	Unit
Input energy	25	keV/u.
Output energy	600	keV/u.
Input emittance	0.3	mm
$\epsilon_{n,rms,xy}$		mrad
Output emittance	0.31	mm
$\epsilon_{n,rms,xy}$		mrad
Energy spread (@15 mA, A/Q=3)	1.8	%
Transmission ¹	89	%

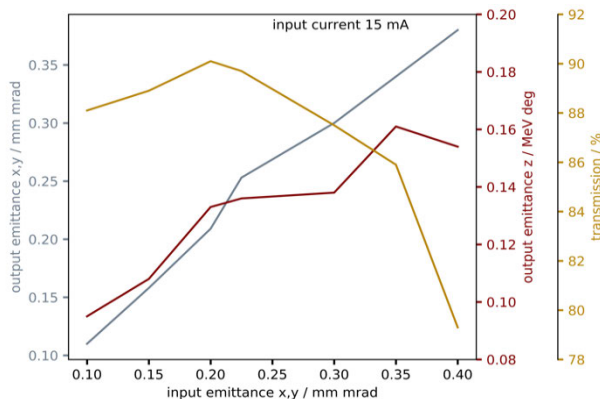


Figure 1: Output emittance and transmission as a function of the input emittance for a beam current of 15mA.

Table 2: LILAC RFQ Design Parameters

Parameter	Value	Unit
Operating frequency	162.5	MHz
Shunt impedance Z_{eff} (CST)	116	k_{Ω}^*m
Recommended RF power (Amplifier)	300	kW
Quality factor (CST)	5800	
Flatness	± 3.5	%
Kilpatrick	1.60	

TECHNICAL DESIGN

The base of the technical design of this RFQ is derived from a well established and successful design of rectangular RFQ tanks [6,7] which have water cooling feedthroughs realised in the ground plate. In the case of the LILAC RFQ only the stems will be cooled. In addition, the rectangular tank has a cover plate allowing for easy access to the 4-rod structure and tuning plates. The tuning plates are mounted

¹ For input emittances 0.3 mm mrad

with screws to the stems and offer advanced electrical and thermal conductivity, see Figure 2.

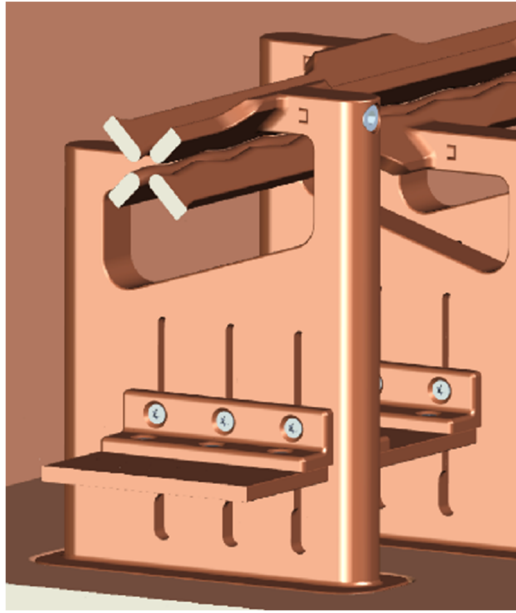


Figure 2: Mounting of tuning plates via screws.

Find below in Table 3 the technical design parameters of the 4-Rod structure and the tank dimensions.

Table 3: RFQ Technical Design Parameters

Parameter	Value	Unit
Electrode length	2422	mm
Tank inner length	2440	mm
Tank outer length	2540	mm
Tank height	400	mm
Tank width	400	mm

The RFQ vacuum will be generated using a combination of an ion-getter pump together with a turbo molecular pump sitting each on DN 160 CF flanges located on both ends of the RFQ tank. The beam entrance and exit flanges realised as DN 200 CF are shaped as lids housing each an ACCT for current transmission measurements during operation.

The power coupler for the RFQ consists of a hollow, optionally water-cooled, loop yoke made of copper and a 6 1/8" (EIA) transmission line connector for the connection to the rigid line. Detection of the transmitted signal in the cavity will be done with one of three available pick-up antennas oriented along the side of the tank. Power coupler and antennas have rotatable flanges for optimisation of the loop positions. During operation the RF tuning of the LILAC RFQ will be performed by a MTCA based LLRF control system [8] which is developed in co-operation with DESY's Tech Lab. The tuner algorithm implemented in this MTCA control system stabilises small amplitude and phase deviations. Frequency stabilisation is realised through a dynamic piston tuner with perturbation body which is coupled to the MTCA system over ModBus. The tuner can be optionally water cooled.

MANUFACTURING

During manufacturing the tank was welded from stainless steel parts, machined and polished before sent to copperplating. In Figure 3 one can see the LILAC RFQ tank and the cut-outs for the stems in the ground plate. One can easily see the alternating displacement of the stems which is simulated and used to counteract dipole components on-axis.



Figure 3: RFQ stainless steel tank with cut outs for the stems.

The tank was copperplated in Q4 2021 while the machining of the electrodes and stems had to be partially postponed into Q1 of 2022 due to difficulties in supply of raw materials. After a test mounting of the 4-rod structure followed by precision measurements the procedure of precision milling of the stems to allow precise alignment of the rods was performed in May 2022, see Figure 4.

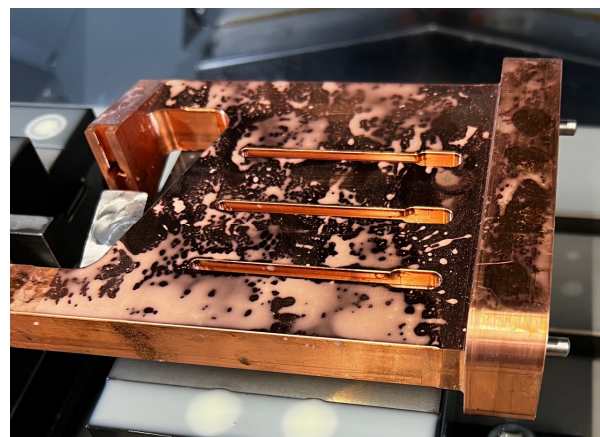


Figure 4: RFQ Stem during precision milling.

First vacuum tests with power coupler and pickup loops showed a leak in the delivered power coupler which is currently under repair. It is expected to be fixed by beginning of July which will then be followed by the tuning and RF measurements of the LILAC RFQ.

TUNING AND RF MEASUREMENTS

After successful FAT and basic tests such as vacuum and cooling water tests, the RFQ will be investigated and set up in regard to low level RF. All measurements will be performed using appropriate equipment (mostly using a vector network analyzer and corresponding cables). The LLRF setup comprises mainly the following steps.

- Measurement of the resonant frequency and the mode spectra of the RFQ
- Adjustment of the field flatness with the tuning plates
- Setup of the power coupler in terms of coupling beta and its corresponding angular position
- Determination of quality factors (Q_0 , Q_L , Q_{ext})
- Setup and adjustment of pickup antennas
- Measuring and optimisation of the tuning range of dynamic tuner

In a first step, it must be guaranteed that the nominal frequency of the RFQ is matched. At 162.5 MHz only a medium sensitivity of the RFQ on manufacturing inaccuracies, with no significant offset of the nominal frequency is expected. Nevertheless, a backup plan is foreseen to be able to adjust the frequency in a worst-case scenario.

A mode spectra and mode identification by comparing with higher order modes (HOMs) found in simulations assures a proper operation of the cavity. Also, possible other modes introduced by the piston tuner can be investigated and suppressed during the RF setup.

The voltage distribution of the RFQ will be measured using the perturbation capacitor technique.

The objective of the power coupler setup is a proper matching of the coupling loop, a determination of the coupling β and the different quality factors. This enables an efficient power transfer towards the cavity and compensates the additional losses caused by beam loading.

The pickup antennas provide the feedback signals for the LLRF system. The desired attenuation can be adjusted by the loop size and angle of the pickup antenna during the RF setup.

The tuning and RF measurement processes will be followed by a low power conditioning of up to 100 W cw to eliminate the most critical multipacting barriers.

CONCLUSION

The production of the LILAC RFQ is completed. A leak in the power coupler led to a delay in the tuning and RF measurements which were planned for end of May/beginning of June 2022. These measurements will now be performed in July and August in 2022.

The experience with the technical layout of this 4-rod RFQ design inside the square shaped stainless steel tank which is galvanically copper plated is well known and well proven and we do not expect major surprises in the final measurements.

With the introduction of concepts such as the inclusion of longitudinal end fields and dipole correction, which led to significant improvements of the role of 4-rod RFQs in the linear accelerator community, we expect a very well performing RFQ.

REFERENCES

- [1] A. Martynov *et al.*, "Injection Complex Development for the NICA Project", in *Proc. LINAC'18*, Beijing, China. doi:10.18429/JACoW-LINAC2018-TH1P02
- [2] A. V. Butenko *et al.*, "Commissioning of the New Heavy Ion Linac at the NICA Project", in *Proc. RuPAC'16*, Saint Petersburg, Russia, Nov. 2016, pp. 157-160. doi:10.18429/JACoW-RUPAC2016-FRCAMH03
- [3] A. Martynov *et al.*, "Light Ion Accelerator up to 7 AMeV for NICA", in *Proc. RuPAC'18*, Protvino, Russia, doi:10.18429/JACoW-LINAC2018-WECAMH02
- [4] M. Schuett, M. Syha, and U. Ratzinger, "Compensation of longitudinal entrance and exit gap field effects in RFQ's of the 4-Rod type", *Nucl. Instrum. Methods Phys. Res., Sect. A*, vol. 928, pp. 58-64, 2019. doi:10.1016/j.nima.2019.02.071
- [5] K. Kümpel, H. C. Lenz, N. F. Petry, H. Podlech, A. Bechtold, and C. Zhang, "Dipole Compensation of the 176 MHz MYRRHA RFQ", in *Proc. IPAC'17*, Copenhagen, Denmark, May 2017, pp. 2240-2242. doi:10.18429/JACoW-IPAC2017-TUPVA070
- [6] R. W. Garnett *et al.*, "LANSCE H+ RFQ Status", in *Proc. IPAC'15*, Richmond, VA, USA, May 2015, pp. 4073-4075. doi:10.18429/JACoW-IPAC2015-THPF148
- [7] B. Koubek, A. Schempp, J. S. Schmidt, and J. Haeuser, "RF Setup of the MedAustron RFQ", in *Proc. LINAC'12*, Tel Aviv, Israel, Sep. 2012, paper SUPB014, pp. 35-37.
- [8] B. Koubek *et al.*, "LILac Energy Upgrade to 13 MeV", in *Proc. IPAC'21*, Campinas, Brazil, May 2021, pp. 651-653. doi:10.18429/JACoW-IPAC2021-MOPAB192

HIGH POWER TESTS OF A NEW 4-ROD RFQ WITH FOCUS ON THERMAL STABILITY

S. Wagner*, D. Koser, H. Podlech¹

Institut für angewandte Physik (IAP) at Goethe-University, Frankfurt am Main, Germany

M. Basten², GSI, Darmstadt, Germany

¹also at Helmholtz Research Academy for FAIR (HFHF), Frankfurt, Germany

² also at Helmholtz-Institut Mainz (HIM), Mainz, Germany

Abstract

Due to strong limitations regarding operational stability of the existing HLI-RFQ a new design and prototype were commissioned. Three main problems were observed at the existing RFQ: A strong thermal sensitivity, modulated reflected power, and insufficient stability of the contact springs connecting the stems with the tuning plates. Although the last problem was easily solved, the first two remained and greatly hindered operations. To resolve this issue and ensure stable injection into the HLI, a new RFQ-prototype, optimized in terms of vibration suppression and cooling efficiency, was designed at the Institute of Applied Physics (IAP) of Goethe University Frankfurt. To test the performance of this prototype, high power tests with more than 25 kW/m were performed at GSI. During those, it was possible to demonstrate operational stability in terms of thermal load and mechanical vibrations, calculating the thermal detuning, and proof the reliability of the proposed design.

INTRODUCTION

In 2010, a new 4-rod RFQ had been commissioned and integrated into the existing High Charge State Injector (HLI) at GSI [1].

Shortly after the implementation, several problems occurred. Those included the contact springs between the tuning plates and stems, periodically reflected power due to mechanical oscillations of the electrodes, and a high thermal sensitivity. Even though the first one could be resolved rather quickly, the mechanical oscillations and thermal sensitivity posed big challenges for the operator, since only several pulse lengths were accepted by the RFQ, and thermal detuning limited the possible power increase. [3]

To overcome those problems and ensure stable operation conditions, the development of a new RFQ was commissioned. This RFQ was optimized in terms of mechanical vibration suppression as well as efficient cooling while still reaching the set goals for power efficient acceleration. [2, 4]

To test the success of the proposed design, a prototype had been constructed. This shorter RFQ with an electrode length of roughly one fourth of the final design had been conditioned up to high power levels. During this process, mechanical observations had been performed as described in [5], to verify the success in terms of reduced mechanical vibrations. Additionally, the heating had been carefully observed as well as compared to simulations.

*s.wagner@iap.uni-frankfurt.de

EXPERIMENTAL SETUP

A schematic depiction of the experimental setup is shown in Figure 1. Overall, the setup was divided into two parts: The bunker with the RFQ, tuner, and sensors; and the RF-gallery with the RF-sender (see Figure 2), power meter, and observation station. Especially to mention is the fact that the tuner was manually controlled through a voltage source.

Even though the RFQ was designed for CW-capable usage, due to restrictions by the sender the maximum pulse length was 6.5 ms in a 20 ms interval.

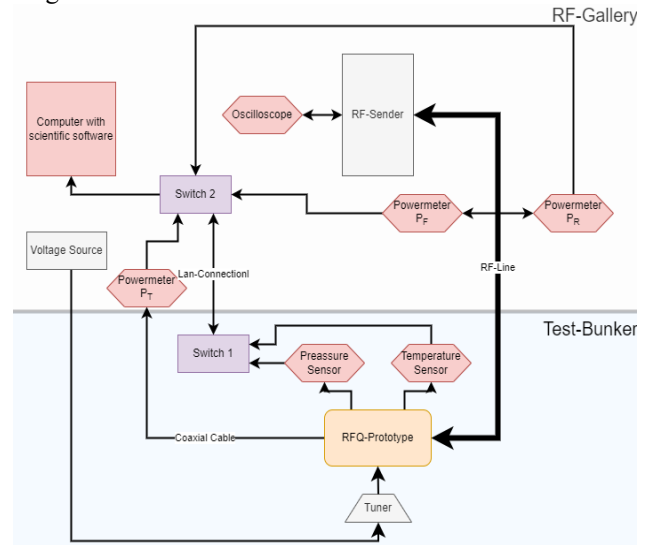


Figure 1: Schematic depiction of the experimental setup at GSI Darmstadt.

CONDITIONING PROCESS

Usually during RF conditioning, the power inside the cavity is slowly increased. Several conditioning effects, as multipathing, degassing, and flashovers, pose great threats to the conditioned cavity as well as the used equipment. This makes conditioning in most cases a time intensive and complicated endeavor.



Figure 2: RF-Sender used.

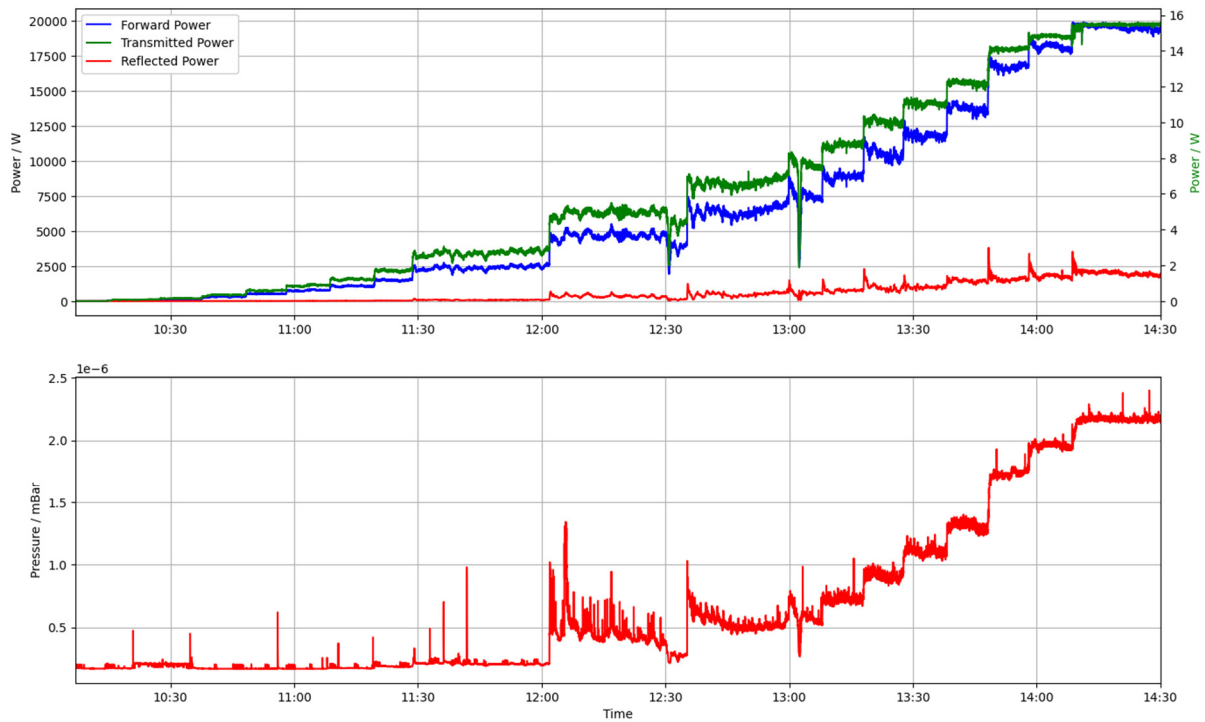


Figure 3: Conditioning process from 0 W up to 20 kW median forward power.

RF Conditioning

The RFQ was preconditioned at the IAP in Frankfurt [4], so that many problems, typically encountered in the low energy area, were quickly resolved. To achieve maximum median powers, most of the conditioning was performed using the maximum available pulse length. Additionally, to test the maximum inter-vane voltage possible, a pulse length as short as of 2 ms had been used. Using this setup, peak powers of 86.8 kW were reached, corresponding to an inter-vane voltage of 116.8 kV.

The maximum achieved values for a pulse length of 6.5 ms are presented in Table 1. There, the results are also compared to the target values which had been calculated by scaling the final design values to the length of the prototype.

To verify the capability of the prototype to accept all power levels, a final conditioning process from 0 W to roughly 20 kW forward power had been performed (see Figure 3). For this procedure, the power had been increased in steps as small as possible, and every power level has been held for several minutes to make sure the cavity reaches thermal equilibrium and no anormal effects take place. This was achieved without major issues, as can be seen in the depicted graph. The two visible power drops at around 12:30 and 13:00 were caused by either a too slow or wrong driving of the tuner, and thus were caused by the experimenter themself. In both cases the former power level was restored quickly and without any issues.

Thermal Analysis

A large problem regarding the old HLI RFQ was its sensitivity to thermal detuning [3]. To overcome this problem,

huge effort was made to ensure an efficient cooling within the new design.

Table 1: Targeted values, derived from the final design, compared to values achieved during conditioning of the prototype. Depicted values were measured for the maximum pulse length of 6.5 ms.

	Final Design	Prototype
Dissipated Power [kW]	10.3	17.8
Dissipated Power per length [kW/m]	14.7	25.4
Inter-vane Voltage [kV]	40	92.7

The heating of several components of the RFQ during a conditioning process from 0 to 25.4 kW median dissipated power is shown in Figure 4. Regarding all components, the electrodes and stems heated the most. The unevenly heating of the different components have two reasons: First, the dissipated power is not the same for every component. For the stems this largely depends on their position inside the RFQ. The farther the stem is from the center of the RFQ, the less power is dissipated. For the electrodes, more power is dissipated on the lower ones. Combining this with the measured water flow through the cooling channels and estimating the transferred heat to adjacent components, the difference between the estimated and measured heating is inside the expected error range.

To measure the thermal detuning, the usual procedure is to compensate the detuning with the tuner and then examine the tuner detuning for the corresponding position. Here, due to the manual control of the tuner, the exact position was unknown. To resolve this problem, the tuner had been

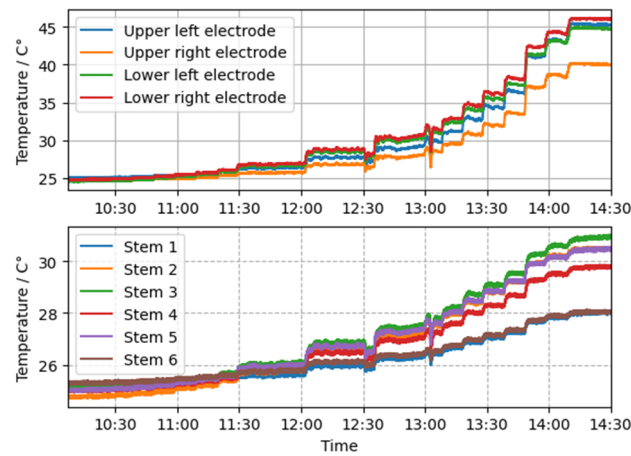


Figure 4: Measured cooling water temperatures for selected points, corresponding to the RF conditioning depicted in Figure 3.

held static while the power was stepwise increased. A controlled detuning was the result. Using the coefficient between reflected and forward power,

$$\Gamma(\omega) = \frac{\beta - 1 - i\beta Q_0 \delta}{\beta + 1 + i\beta Q_0 \delta}, \quad (1)$$

where β is the coupling factor, Q_0 the quality factor and

$$\delta = \frac{\omega}{\omega_0} - \frac{\omega_0}{\omega}, \quad (2)$$

with the frequency ω and resonance frequency ω_0 , the detuning can be calculated. Since the power had been increased in eleven steps, eleven clusters of measuring points are the result as shown in Figure 5. Those clusters can be fitted, with the slope as thermal detuning per power.

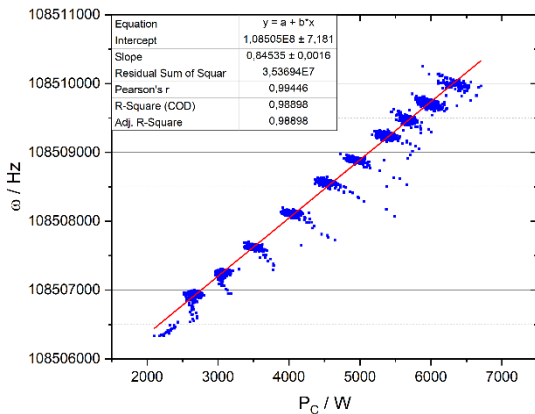


Figure 5: Calculated thermal detuning of the RFQ prototype.

CONCLUSION AND OUTLOOK

The acceptance of a multiple of the desired power per length as well as inter-electrode voltage was demonstrated. Additionally, it was possible to calculate the thermal detuning of the RFQ prototype, even though the exact position of the tuner was unknown. In combination with the increased mechanical stability, which is discussed in [5], it is possible to say that the new design overcomes all issues the old HLI RFQ encountered.

Overall, the process worked, after some initial problems with the setup, very smooth, and no major problems were encountered.

ACKNOWLEDGEMENTS

The authors thank the Helmholtz Research Academy Hesse for FAIR (HFHF) and the GSI Helmholtz Centre for Heavy Ion Research for their financial support. We received further financial support from the BMBF under contract number 05P18RFRB1, for which we are very grateful. Finally, we thank Jörg Mohr, who operated the RF transmitter at GSI, and helped us perform the presented research.

REFERENCES

- [1] L. Dahl, W. Barth, P. Gerhard, S. Mickat, W. Vinzenz, and H. Vormann, "UNILAC upgrades for coulomb barrier energy experiments", in *Proc. LINAC'10*, Tsukuba, Japan, pp. 148-150.
- [2] D. Koser, P. Gerhard, and H. Podlech, "Mechanical vibration analysis of the 4-rod RFQ at the high charge state injector at GSI", *Nucl. Instrum. Methods Phys. Res., Sect. A*, vol. 917, pp. 47-55, Feb. 2019.
doi:10.1016/j.nima.2018.10.162
- [3] P. Gerhard *et al.*, "Experience with a 4-ROD radio frequency quadrupole", in *Proc. LINAC'12*, Tel-Aviv, Israel, pp. 825-827.
- [4] D. Koser, "Development of a 108MHz 4-Rod CW RFQ-Design for High Duty Cycle Acceleration of Heavy Ion Beams at the GSI-HLI", Ph.D, Institut für angewandte Physik (IAP), Goethe Universität Frankfurt am Main, Frankfurt, Germany, 2020.
- [5] S. Wagner, D. Koser, K. Bahrke-Rhein, M. Basten, H. Podlech, and K. Kümpel, "High power tests of a new 4-Rod RFQ with focus on mechanical vibrations", in *Proc. IPAC'22*, Bangkok, Thailand, Jun. 2022, pp. 1523-1525.
doi:10.18429/JACoW-IPAC2022-TUP0MS043

UPGRADE AND OPERATION OF THE ATLAS RADIATION INTERLOCK SYSTEM (ARIS)*

B. R. Blomberg, B. B. Back, K. J. Bunnell, J. A. Clark, M. R. Hendricks, C.E. Peters,
J. Reyna, G. Savard, D. Stanton, L. Weber, Argonne, IL, USA

Abstract

ATLAS (the Argonne Tandem Linac Accelerator System) is a superconducting heavy ion accelerator which can accelerate nearly all stable, and some unstable, isotopes between hydrogen and uranium. Prompt radiation fields from gamma and or neutron are typically below 1 rem/hr at 30 cm, but are permitted up to 300 rem/hr at 30 cm. The original ATLAS Radiation Interlock System (ARIS), hereafter referred to as ARIS 1.0, was installed 30 years ago. While it has been a functional critical safety system, its age has exposed the facility to high risk of temporary shutdown due to failure of obsolete components. Topics discussed will be architecture, hardware improvements, functional improvements, and operation permitting personnel access to areas with low levels of radiation.

THE ATLAS FACILITY AND ARIS

ATLAS

ATLAS is a DOE user facility [1] located at Argonne National Laboratory outside Chicago, Illinois in the United States. ATLAS has three ion sources: two ECR sources, and an EBIS source used as a charge breeder coupled to the CARIBU radioactive ion source [2]. ATLAS can deliver beams consisting of stable and unstable isotopes from protons through uranium. Superconducting Radio Frequency (RF) cavities accelerate ions from 10 to 20 MeV/A for light mass ions. During a typical year, ATLAS hosts several hundred users from as many as a dozen countries. Experiments at ATLAS range from 2 days to a month, with the average length being a week. At the end of which the ATLAS operations staff will reconfigure the facility and tune a new beam of differing mass, energy, and current, all in under 24 hours. Despite the constant reconfiguring for new experiments and regular maintenance, ATLAS delivers ~6000 operational hours per year.

The ATLAS operations group and Argonne Physics Division Radiation Safety Committee have developed controls to allow users and staff access to accelerator and experimental areas with low-level radiation (< 5mrem/hr @ 1m from source), including areas which may have beam present. Given the wide range of ion species, energies, and various experimental end stations, this level of facility access is vital for setup and debugging new experiments in 24 hours or less.

The main safeguard against unnecessary radiation exposure includes a combination of training, administrative controls, and shielding. ARIS is an engineered control (safety system), designed to protect personnel from radi-

ation exposure should the other safeguards fail. ARIS serves as active monitoring of radiation in 16 experimental and accelerator areas as well as adjacent areas, these areas are referred to as ARIS-controlled areas. ARIS-controlled areas are equipped with radiation monitors, interlocked gates, and area status displays that are connected to ARIS. Access to these areas is allowed, provided certain conditions are satisfied and the area is in the correct access state (access states will be discussed in greater detail later).

ARIS 2.0

ARIS 1.0 has been in operation since August 1st, 1992 [3], during which time there has been no accidental personnel radiation exposure. However, the system's age has presented various limitations concerning system improvements and expansion. Additionally, an upgrade was needed to avoid accelerator operation interruptions caused by possible malfunctions of outdated components of the ARIS 1.0 system and to add functionality to the system that augments administrative controls with engineered controls. ARIS 2.0 was developed as an extension and upgrade of ARIS 1.0 system and began service on June 22nd, 2021. Below is an overview of ARIS 2.0 architecture, operating principles, and improvements over ARIS 1.0.

Architecture

The ARIS system uses a computer-PLC network composed of the following nodes (Fig. 1) [4]:

- A Programmable Logic Control computer system, the ARIS PLC, which has sensing, control, and some informational functions.
- A Linux-based PC, the ARIS Linux PC, which performs only sensing, informational, and logging/recording functions.
- Ancillary Linux PC, which performs informational and logging/recording functions.

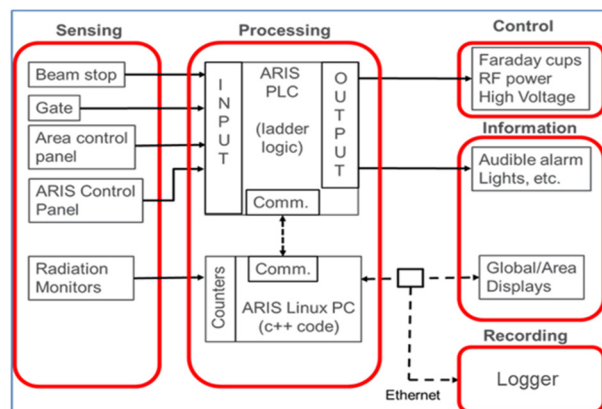


Figure 1: Schematic overview of the ARIS computer-PLC network.

* This material is based upon work supported by the U.S. Department of Energy, Office of Science, Office of Nuclear Physics, under contract number DE-AC02-06CH11357

Content from this work may be used under the terms of the CC BY 4.0 licence (© 2022). Any distribution of this work must maintain attribution to the author(s), title of the work, publisher, and DOI

Hardware Improvements

ARIS 2.0 includes several hardware improvements over its predecessor, the two most notable of which are an improvement in the hardware used for the processing side of the system architecture. The ARIS 1.0 PLC system was a SY/MAX manufactured by squared. This was replaced with an M580 safety PLC by Schneider. The new PLC has a Safety Integrity Level (SIL) of 3 while ARIS 1.0 was manufactured before SIL ratings were in use. Sensing of the radiation monitors, data logging, and information for area and global displays was initially performed via an IBUS computer with counting cards. The IBUS computer was replaced with a Linux PC and new counting cards to measure counts (pulsed outputs) from radiation monitors. Additionally, the ARIS 1.0 IBUS computer used serial communication to send information to the data logger and displays. The new Linux PC hosts servers with the displays and logger acting as clients which receive data and information via ethernet communication. This system provides a significant boost in speed to the system.

Area displays and global displays were replaced with new displays which use Raspberry Pi's, which serve as a client to the ARIS Linux PC.

ARIS 1.0 used a dot matrix printer to print off information regarding radiation monitor counts, changes to access states and changes to beam paths. This was replaced with a Raspberry Pi which tracks far more information and graphically displays it in the ATLAS control room on a Grafana dashboard.

Functional Improvements

ARIS 2.0 includes several functional improvements over ARIS 1.0. It is more user-friendly, reduces downtime, and improves the facility's overall safety.

ARIS 1.0 monitored 13 areas within the ATLAS facility and was only capable of monitoring areas on the beam path; adjacent areas were not monitored and thusly were required by administrative controls to be locked until a health physics technician could perform a survey of the area to assess radiation levels. ARIS 2.0 expanded the number of monitored areas to 16. Additionally, all areas are simultaneously monitored, removing the frequent need for surveys from health physics technicians.

Each ARIS monitored area previously had an area display at the main entrance to that area; with ARIS 2.0, we added area displays to every entrance from within the building (not from outside) and significantly increased the information displayed. This increased information helps operators more quickly diagnose problems and gives ATLAS staff a better idea of the potential radiation hazards in that area and the effect of opening a gate will have on the access state.

Previously, ARIS had one global display, which was located in the ATLAS control room. Two other global displays were added to high-traffic areas throughout the facility; this provides information on the accessibility of ARIS-controlled areas without the need to contact the control room.

ARIS 2.0 has a consistent set of logic to change each area from one access state to another, whereas previously ARIS-controlled areas had their own unique logic. This consistent set of rules across all areas reduces training time for operators, makes diagnosing problems more straightforward, and sets a standard - should ARIS ever be expanded to include additional ARIS-controlled areas.

As mentioned above, the new ARIS logger tracks a wealth of information not previously tracked, and this information is stored on a computer, whereas it was originally printed out. This change makes it far easier to look at current and historical data.

Access to ARIS-Controlled Areas

An advantage of the ATLAS facility is access to one of 18 areas (Fig. 2) [4] with the possibility for low levels of radiation. Each area is equipped with interlocked gates or access gates at each entrance. These gates have redundant sense switches that allow ARIS to detect if the gate is open or closed. ARIS-controlled areas fall into two categories: radiation generating, and adjacent areas.

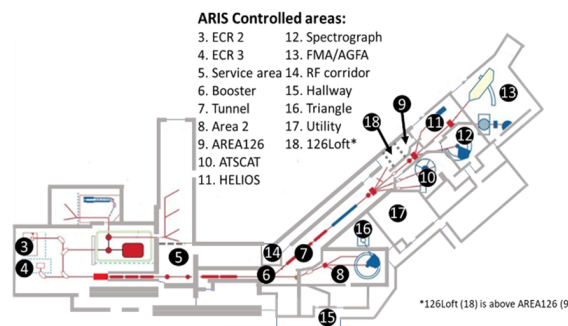


Figure 2: ATLAS floor plan indicating ARIS-controlled areas. 16 areas are shown but counting starts at 3 as we plan to add 2 additional areas.

Radiation generating areas are divided into two sub-categories, beam areas, and RF areas. An RF area is any area with accelerating structures that may have RF power applied to them. Beam areas are anywhere in which beam may potentially be delivered into the area. The ATLAS facility has several forks in the beamline, which lead to different target areas. The beam can only be delivered down one path to one target area at a time. Each fork in the beam path is defined by a single open beam stop at the exit of the fork. An adjacent area can be changed to a radiation generating area by either putting the area on the beam path through the opening of an ARIS beam stop or requesting RF power be applied to the accelerating structures.

Adjacent areas are any areas adjacent to a radiation generating area. These areas are not on the beam path and do not have any RF cavities on that could potentially produce radiation. Radiation detected by monitors is scaled to account for monitor efficiency and distance from source. Radiation monitors in adjacent areas are scaled differently from monitors in radiation generating areas. For example, they are scaled to assume the highest point of radiation is from the shared wall between that area and an adjacent radiation-generating area.

ARIS-controlled areas can be in one of seven different access states. The access state of an ARIS-controlled area depends on the current radiation level and past radiation history in the area. The ARIS PLC system assigns the actual ‘access state’ for an ‘ARIS-controlled area’ based on its various sensors, including radiation level information transmitted by the ARIS Linux PC. The seven areas and their associated maximum allowed radiation at 1 m distance from the source of radiation can be seen in Table 1.

Table 1: Possible Access States for ARIS Controlled Areas and their Associated Max Radiation

Access State	Max allowed radiation
Open	2 mrem/hr
Restricted Access Occupied	5 mrem/hr
Restricted Access Not Occupied	5 mrem/hr
No Access	100 mrem/hr
Locked	20 rem/hr
Inhibit	2 mrem/hr
Tripped	2 mrem/hr

Personnel are only permitted in ARIS-controlled areas in the Open, Restricted Access Occupied, Inhibit, and Tripped States. ATLAS operators can change the access state of an ARIS-controlled area from an Open or Restricted Access Occupied state to a Restricted Access Not Occupied or Locked state via a sweep (search and secure) procedure. This same procedure can be used to change from a Tripped or Inhibit state to a Locked or Restricted Access Not Occupied state. This procedure is executed by pressing an interior reset button, walking a specific path through the area, closing the access gate, and pressing an exterior reset button.

In the Inhibit state, ARIS inhibits all radiation sources in the area from beam by inserting an ARIS-controlled Faraday cup (Fig. 3) [4] and RF-generated sources by deactivating relays to the power supplies. Inhibit states are the result of the regular operation of the interlock system. In the Tripped state, ARIS uses the same means to stop all radiation sources in the area, both beam-generated and RF-generated, in response to an unwarranted occurrence. The Tripped state also inhibits beam upstream via the F1 cup (Fig. 3). An occurrence of a Tripped state must be investigated and reported by the ATLAS operators.

An ARIS-controlled area can only be set to Open if the following criteria are met: the area is an adjacent area, radiation in the area is below 2 mrem/hr and has been below 2 mrem/hr for the last 30 minutes. In this state, ARIS permits free access. If the radiation goes above the maximum allowable (2 mrem/hr), ARIS will set the area to the Inhibit state.

In the Restricted Access Not Occupied state, low-level radiation may be present in the area, but the system has verified that the area is absent of personnel via a valid sweep procedure. The area will remain in this state so long as no access gates are opened, and the radiation remains below the max allowed listed in Table 1.

ARIS Controlled Faraday Cups

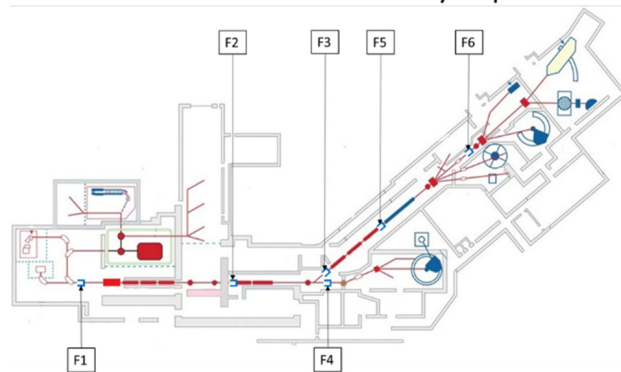


Figure 3: Location of ARIS-controlled Faraday cups.

If an access gate is opened after the area has been swept into a Restricted Access Not Occupied, the area will switch to Restricted Access Occupied. In this access state, ARIS assumes personnel is present in the area. Low-level radiation may be present, but ARIS permits access without inhibiting RF or beam so long as the radiation is below the max listed in Table 1 for this state. Should the radiation exceed the max allowable while in this state, the area will switch to the Inhibit state.

If an ARIS-controlled area is in the Restricted Access Not Occupied state and the radiation exceeds the max allowed for this state, the area will automatically enter the No Access state. The system has verified that the area is absent of personnel since a sweep procedure was required to enter the Restricted Access Not Occupied state, and no access gates have been opened. If the max allowable radiation is exceeded, the area will be placed into the Tripped state.

ARIS-controlled areas can be set to the Locked state after a sweep procedure, and additionally, locking the covers on the access gate handles so they cannot be opened from the outside. The area will be placed in the Tripped state if the radiation exceeds the max allowable or if an access gate senses it has been opened.

Additionally, for the Open and Restricted Access Occupied states, ARIS only allows an accumulated dose, from the previous 8-hour period, of 20 mrem. Anything above this and ARIS will set the area to the Tripped state.

SUMMARY

Access to radiation-producing areas is not allowed at most accelerator facilities. Since the conception of the original ARIS, the ATLAS operations group has leveraged this safety system to increase access throughout the facility and productivity. ARIS 1.0 proved successful in keeping the physics division staff’s total measurable dose below the physics division ALARA goals, and in its first year of operation (Fig. 4), starting in 2021, ARIS 2.0 has continued this trend in radiation safety all while improving operational efficiency.

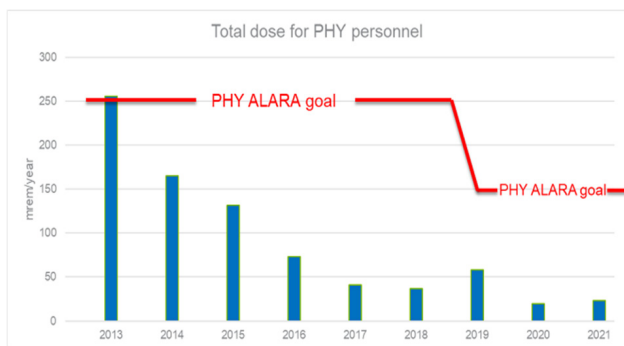


Figure 4: Dosimetry for all Argonne physics division staff.

REFERENCES

- [1] L.M. Bollinger *et al.*, "ATLAS: A Proposal for a Precision Heavy Ion Accelerator at Argonne National Laboratory", Argonne National Laboratory, 1978, ANL-78-XX-68. <https://digital.library.unt.edu/ark:/67531/metadc303815/>
- [2] R. C. Pardo *et al.*, "Neutron-Rich Beams from 252Cf Fission at ATLAS - The CARIBU Project", in *Proc. PAC'09*, Vancouver, Canada, May 2009, paper MO3GRI02, pp. 65-69. <https://jacow.org/PAC2009/papers/mo3gri02.pdf>
- [3] B. B. Back *et al.*, "ATLAS Report RA-3, ATLAS Radiation Interlock System (ARIS)", Version 2.0, Argonne National Laboratory, Internal document.
- [4] B.B. Back *et al.*, "Specification for the ATLAS Radiation Interlock System Upgrade", Argonne National Laboratory, Internal document.

STUDY OF INJECTION LINE OF THE CYCLOTRON C70XP OF ARRONAX

Teddy Durand¹⁻², Ferid Haddad¹⁻², Freddy Poirier¹⁻⁴, Robin Bellamy¹, Chris Castel¹,
Charbel Koumeir¹, Herve Trichet¹, Francis René Osswald³, Thomas Adam³, Philippe Graehling³,
Marcel Heine³, Chaker Maazouzi³

¹ARRONAX, Saint-Herblain, France, ²SUBATECH, Nantes, France, ³Université de Strasbourg,
CNRS, IPHC UMR 7178, Strasbourg, France, ⁴CNRS – DR17, Rennes, France

Abstract

The cyclotron C70XP is an accelerator built for the production of non-conventional radionuclides for nuclear medicine, research in physics, radio-chemistry and biology. Its injection section has been designed for 4 types of ions (HH+, D-, He2+ & H-), 3 types of ions reach the end of the beamline (H+, He2+ & D+) at the maximum energy of 70 MeV (H- & He2+). It is important that regular and standard runs provide similar beam features with a good emittance quality. An investigation, focused on the beam in the injection, cover beam measurements and potential beam geometry constraints. The beam transverse characteristics in the injection line has been studied with an Allison-type emittance meter and a simple instrumented collimator installed inside the injection line. With these 2 devices, it is scrutinized how the beam emittance evolves as a function of settings of the injection magnets and the source parameters. Dependencies found between the emittance, beam hotspots and tunings are discussed, as well as the protection performed by the collimator. Future of this work with a potential collimator design is introduced.

INTRODUCTION

The Arronax Public Interest Group (GIP Arronax) aims at providing well-defined transverse ion-beam dimensions. This, to secure reliable production of radio-isotopes at high intensity and deliver an adequate beam as-homogeneous-as-possible at low intensity for research and detector studies. A study program of the beam in the various sections of the accelerator, mainly transport beamlines and injection section, has been put in place. The study includes first emittance measurements performed in the injection section [1]. The installation of the emittance-meter and the outcomes of the measurements are described in the paper, including the code devised to analyze the data. The observations have pointed out that several high-density spots could be obtained, depending on the machine parameter settings. To check the rejection capacity of these spots, a slit was mounted in the injection section. Measurements of the beam dimensions at the end of two beamlines were performed. The results trigger the need to explore the design of a new collimator system adapted to low energy and high intensity beams.

MEASUREMENTS WITH THE EMITTANCE-METER

Installation

A 2D (x,x') Alison type emittance meter built in the frame of the EmitM collaboration [2] was installed in the injection line of the C70XP for a measurement campaign [3].

The injection line is composed of two ion-sources (a multicusp for H-/D- ions and an ECR for He2+ ions), a first solenoid, a first steerer, a 90° selection dipole, a quadrupoles triplet, a second steerer, a second solenoid, and a buncher.

A flange on the injection line was modified to allow the insertion device, i.e. a lengthened dedicated flange was built, the penning IKR050 gauge was deported as well as the PV AL25PK pipeline vacuum valve, and the Faraday-cup of the injection line was removed.

Due to the limited space available for the installation 30 cm downstream the buncher, the emittance-meter was positioned in a single plane measurement mode only.

The emittance-meter was aligned by a vertical laser at the geometrical center of the line to define the reference point of the displacements of the head of the emittance-meter.

Experimental Preparation

To ensure the comparability of the measurements, each morning at the start of the day, series of measurements are carried out with the low energy beam (~40keV). For this, systematic emittance measurements are achieved while increasing the arc current of the multicusp source.

Also every morning, the source and magnetic elements were set for low and high beam intensity, and emittance measurements were performed for later comparison.

For the measurement, we start with the optimization for high beam current, each parameter of the injection line was studied systematically and in defined step before returning to the starting value.

During the whole manipulation, no parameter that could affect the acquisition of the signal was changed. All these precautions have been taken in order to make the measurements as comparable as possible.

Prior to the emittance measurements, the reference beam intensity is measured on a radial probe inside the cyclotron at 150 mm of the center of the cyclotron, downstream the spiral inflector.

EMITTANCE MEASUREMENTS RESULTS

Emittance measurements have shown three major features. First, emittance measurements, combined with the intensity measurements, show a higher transmission rate with an off-axis beam.

Second, beam hotspots, performed with the H- beam, are present within the majority of-the measurements (Fig. 1). The beam hotspots are high density regions of current measurements on the emittance plots.

Third, a 4mm slit, helps to mitigate the number of hotspots. The slit is installed upstream the emittance-meter, on the top of the buncher, and positioned 90° compared to the slits of the emittance-meter.

Analysis Code

For the analysis of the results, a C++ code using the open-source data analysis ROOT framework [4] was developed. This code is based on a matrix for signal background separation and data fitting by a 2D Gaussian as described below.

The matrix cleaning routine is based on two experimental observations, at first a constant mean of back ground noise (BGN) during all experimentation following a Gaussian distribution, at second the signal is positive and reunite in spot inside the emittance measurement.

To separate the signal from the noise, a part of the emittance measurement data is extracted in the form of a matrix (order: $N * M$) around a point of study. The order need to be chosen carefully, the higher is the order of the matrix, the more side effects will appear, and at lower order of the matrix falser positive data will appear.

The number of points above the average BGN is counted inside the extract matrix. If the number of points counted outrun the number N_c [Eq. (1)], the study point inside the matrix are considered like a part of the signal and be kept, see Fig. 1

The number N_c is 50% of the number of entries of matrix extracted data multiplied by the factor of convergence of the random normal law function.

$$N_c = 0.5 * N * M * \left(1 + \frac{1}{\sqrt{N * M}}\right) \quad (1)$$

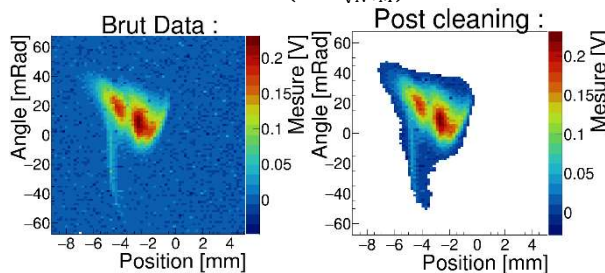


Figure 1: Before and after the matrix cleaning, with beam hotspots and tail, the extraction order is 9*9 in this case.

The matrix cleaning, in the present case, is more effective than the simple 2D Gaussian fitting. We estimated the emittance (not normalized value) for a high beam current optimized with the filament of the source at 4 A. The radial probe measurement indicating the total beam current inside

the cyclotron is 283 μA and the emittance is 20.3 mm.mrad. With a particular optimization of the source, the radial probe measurement becomes 361 μA and the emittance 7.6 mm.mrad. This optimization concerns the puller, the electron suppressor and the high tension of the ion-source.

IMPACT OF THE SLIT

Experiments were performed to determine the impact of the same 4 mm slit located in the injection section on the transverse geometry of the beam of a beamline after the cyclotron compatible with high intensity runs (i.e. $>10 \mu A$) and another beamline which accommodates an exit window. This latter is particularly adapted to host dedicated in-air beam diagnostics for low intensity beams such as industrial radiographic films. We noticed that, the beam dimensions and the operation methodology is dependent on the type of beamline in use. At the low current beamline, a shape of the beam with beam hotspots is investigated, and on the high current line, the emittance is studied with a scan of the last quadrupole of the beamline.

High Intensity Beamline Experiment

On the high current beamline, the beam was optimized to maximize the intensity on the target. To perform a scan of the transverse dimensions of the beam, the current of the quadrupole upstream a four-finger collimator was swept from 40A down to -20A. The intensity deposition on the collimator's isolated left and right fingers were added up and normalized by the total intensity, measured on the collimator and target. A parabola-like curve was obtained, with a beam waist inversely proportional to the emittance i.e. a lower emittance corresponds to a larger width [5]. With the slit in operation a reduction of the emittance was visible, which is as shown in Fig. 2.

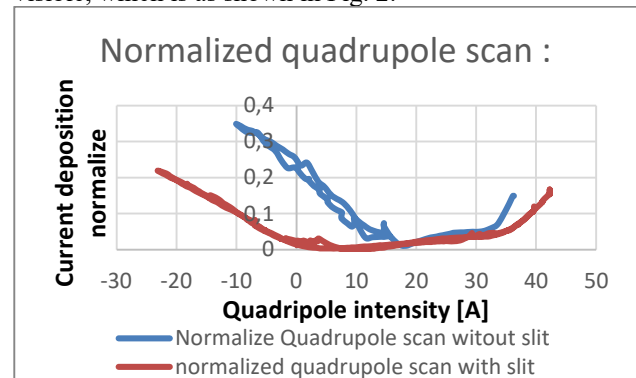


Figure 2: Quadrupole scan on the high intensity beamline with and without the injection slit.

Low Intensity Beamline

On the low current line, the measurements were made on two consecutive Gafchromic™ HD-V2 films, respectively located 130 mm and 630 mm downstream of the exit of the beamline.

The first film was installed to study the beam geometry and the second film to check the alignment of the beam. The beam was stopped inside an aluminum block located 2 m away.

Content from this work may be used under the terms of the CC BY 4.0 licence (© 2022). Any distribution of this work must maintain attribution to the author(s), title of the work, publisher, and DOI

The total beam current at the exit of the line was measured with a photomultiplier (PM), measuring the ionization of nitrogen in the air. The PM was calibrated at the start of the experiment [6]. The dose of the film was calculated according to the total beam current measured on the PM, and thus by the measurement of the density of gray deposit inside the film.

On the image below (Fig. 3) the density distribution (spot) of the beam, on the y -vertical and x -horizontal plane of the first film, is visible in term of dose deposition.

The coordinates of the beam are between 2 and 10 mm on the x -horizontal plane and -5 and 7 mm one the y -vertical plane.

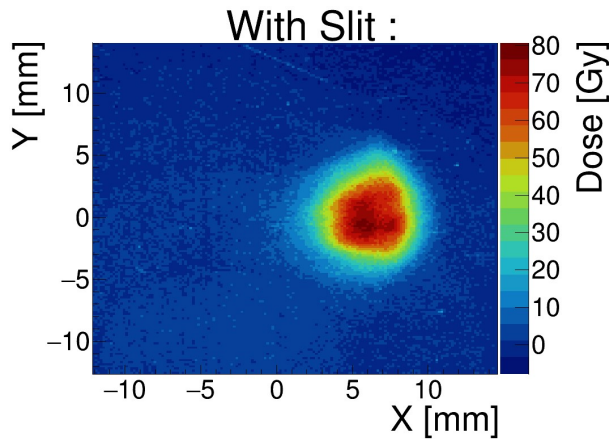


Figure 3: Beam shape on the Gafchromic™ HD-V2 film, 130 mm downstream the exit of the beamline, case with the slit.

Without the slit and with the same optimization it is possible to find other beam hotspots and the beam current increases by 20 – 25 %, see Fig. 4.

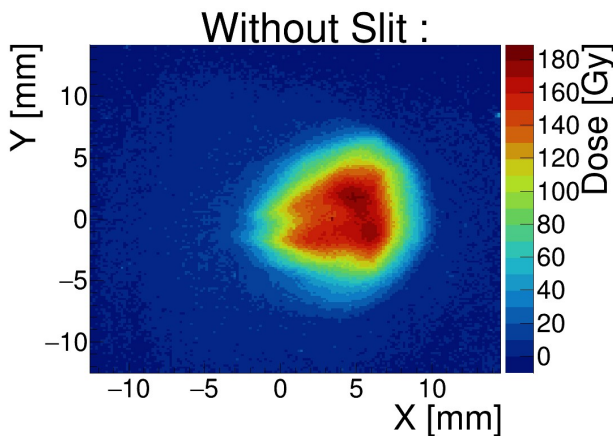


Figure 4: Beam shape on Gafchromic™ HD-V2 130 mm downstream of the exit of the beamline, case without the slit.

When is compare the two images (Fig. 3, Fig. 4), an increase of the transverse dimensions is visible without the slit

Two experimental outcomes were observed: the slit reduce the beam size and the emittance is reduced at the end of the beamline.

FUTURE COLLIMATOR

It is necessary to determine the maximum aperture of the collimator with the least possible impact on the beam. A circular collimator of 42 mm aperture diameter has been installed on the top of the buncher to validate the design. Initial measurements with the collimator indicated a beam current collection of a few nA.

Following previous emittance measurements, specifications for the future collimator were partly determined: the collimator aperture has to be offset by a few mm. In order to allow positioning indication, the collimator requires at least 4 individual instrumented markers (so called fingers). Each finger should ideally be able to move freely for the adjustment of the aperture. The specifications of the collimator should include the reduction of the emittance i.e. they should define the longitudinal extension. They should also define the safety role for the sensitive elements in the accelerator e.g. the spiral inflector.

The variable aperture of the collimator is mandatory because it is important for the operations to be able to adjust the beam cross-section, especially in the Y -vertical plane.

The future design is foreseen to be modelled with a G4beamline [7] simulation to investigate the potential geometry of the collimator.

CONCLUSION

Emittance measurements have been performed in the injection section of the C70XP cyclotron and highlight several hotspots in the beam. With the adequate tuning of the source parameters, these hotspots have been mitigated and allows now high transmission in the injection section. To deepen the exploration, a slit has been installed in the injection section. in order to modulate the transverse beam dimensions downstream the cyclotron in two different beam lines. Although the hotspots have not totally disappeared, the measurements indicate an increase of the transmission. It can be noticed that with the use of a slit, the operation tunings converge faster and the beam shows a more homogenous density. This advocates the ongoing studies for a future adjustable collimator in the injection section.

ACKNOWLEDGEMENTS

Work supported by grants from the French National Agency for Research, Arronax-Plus n°ANR-11-EQPX-0004, IRON n°ANR-11-LABX-18-01 and Next n°ANR-16-IDE-0007 and PhD scholarship from the IN2P3/CNRS.

REFERENCES

- [1] F. Poirier *et al.*, “The Injection and Chopper-Based System at Arronax C70XP Cyclotron”, in *Proc. Cyclotrons'19*, Cape Town, South Africa, Sep. 2019, pp. 159-161.
 doi: 10.18429/JACoW-Cyclotrons2019-TUP006

- [2] F. R. Osswald, T. Adam, P. G. Graehling, M. Heine, C. Maazouzi, and E. K. Traykov, "Transverse Phase Space Scanner Developments at IPHC", in *Proc. IBIC'19*, Malmö, Sweden, Sep. 2019, pp. 293-296.
doi:10.18429/JACoW-IBIC2019-TUPP007
- [3] F. Poirier et al., 'Installation, Use and Follow-Up of an Emittance-Meter at the Arronax Cyclotron 70XP', in *Proc IPAC'21*, Campinas, Sao Paolo, Brazil.
doi:10.18429/JACoW-IPAC2021-MOPAB277
- [4] Root, <https://root.cern>
- [5] F. Poirier *et al.*, "Studies and Upgrades on the C70 Cyclotron Arronax", in *Proc. Cyclotrons'16*, Zurich, Switzerland, Sep. 2016, pp. 235-237.
doi:10.18429/JACoW-Cyclotrons2016-TUD02
- [6] V. Villoing et al., "Proton beam dosimetry at ultra-high dose rates (FLASH): Evaluation of GAFchromic™ (EBT3, EBT-XD) and OrthoChromic (OC-1) film performances", *Medical Physics*, vol. 49, no. 4, pp. 2732-2745, 2022.
doi: 10.1002/mp.15526
- [7] G4beamline, <http://g4beamline.muonsinc.com>

SEVEN DECADES OF SCIENCE WITH ACCELERATORS AT IPHC

F. Osswald[†], Université de Strasbourg, CNRS, IPHC UMR 7178, Strasbourg, France

Abstract

The Institut Pluridisciplinaire Hubert Curien (IPHC) is a laboratory with solid foundations and perspectives to overcome future challenges. It is a component of the Centre National de Recherche Scientifique (CNRS) and the University of Strasbourg. It has been founded in 2006 after fusion of three local laboratories leading research in the field of analytical chemistry, ecology/environment and subatomic physics. The activities related with subatomic physics present a rich history which goes back to the 40's and is now evolving towards new challenges at the frontier of the knowledge with the contribution of other sciences as biology, chemistry, medicine and radiobiology. The paper will cover a number of past and current activities with emphasis on the link between research and technology.

INTRODUCTION

Before being a well-established laboratory in the French and European landscape IPHC went through several periods marked by continuous evolution, contrasting activities and remarkable results. Among the various fields of research explored today such as chemistry, ecology, ethology, physiology, radiobiology and subatomic physics, this article focuses on the activities developed with accelerators. The history of the Institute will be covered through six periods: origin, growth, confirmation, maturation, change in trend and metamorphosis.

THE ORIGIN

Activities related with nuclear physics applied to medicine have started in 1941 during second war, German occupation and evacuation of Strasbourg's university in Clermont-Ferrand and Dordogne. The "Medizinisches Forschungs Institut" is built inside the hospital and near the faculty of medicine with four departments in biology, chemistry, medicine and physics, see Fig. 1.



Figure 1: First accelerator building with Cockcroft Walton neutron generator at the civil hospices in Strasbourg DC, 1944.

[†] francis.osswald@iphc.cnrs.fr

First beam was produced after the liberation of the city in 1944 and the ensuing turbulences in 1948 with a neutron generator based on a 1.5 MV Cockcroft Walton accelerator, see Fig. 2. The goal was to produce isotopes for radiotracers (³²P) with ²H beam induced neutrons on Be target and to perform radiobiology on cells, one of the first facility in Europe at the time. Research is driven by recent discoveries: neutron as a new particle, induced radioactivity, fission, etc. Activities are stimulated by competition with Heidelberg and two French laboratories, that of F. Joliot located in Ivry and the Collège de France.



Figure 2: Cockcroft Walton 1.5 MV electrostatic accelerator stands on the putting green nowadays of IPHC on the Strasbourg campus.

These investments were supplemented by a new X-rays generator, an electron microscope and a cyclotron purchased in 1942. It should be noted that the first lecture in the field of nuclear physics was given in 1947 by Pr S. Gorodetsky, a friend of F. Joliot-Curie. From the beginning, the research has been characterized by the support of leading scientists, a strong interaction between theory and experiment, and the sustainability of the program in the field of nuclear physics (structure of the nucleus, spectroscopy, EM transition, interactions and life time measurements), and nuclear chemistry (chemical effects of nuclear reactions and ionizing radiations). These developments appear after the first works started in the 1930s on X-rays at 100 keV, the sources of natural radioactivity (gamma at 2 MeV with ²²⁶Ra source) and the need to study deeper effects with more energetic light ions [1-6].



Figure 3: New nuclear physics research center built in the western part of Strasbourg in 1959.

THE GROWTH

The Institute experienced a period of significant growth between 1950 and 1970. The “Institut de Recherches Nucléaires” was created in 1951, transformed into a “Centre de Recherches Nucléaires” in 1955 and finally moved to a spacious and dedicated place in the West part of the city in 1958, see Fig. 3. The first $^4\text{He}^{2+}$ beam was produced at 5.5 MeV in 1959 with a brand new Van de Graaff accelerator installed in a new building, see Fig. 4 (the 6th CN in the world). The research is dedicated to the spin study of excited states of the light nucleus, to the measurement of the cross-section of nuclear reactions (with ^1H - ^4He ions), to the angular distribution of the γ emission and to the measurement of β decay measurement (with time scale of 10^{-10} s). Other VDG accelerators were commissioned between 1960 and 1965: a 2 MV (HVEC), 2 units at 3 MV (HVEC), and a 4 MV (HVEC). Considerable progress is being made in the field of technology: new beam lines, γ spectroscopy, spectrometers, electronics and semiconductor detectors. During the 1960s, new contributions from local groups to high-energy experiments at CERN (ISOLDE) and Saclay (properties of the antiproton, positron and muon), and international collaborations with Heidelberg, Krakow, Yale, Stanford, BNL and other labs are launched. Diversification is on the way. To mention, a local study of a new linear proton accelerator in 1968 and the dawn of heavy ions physics with larger accelerators e.g. the creation of GANIL in Caen and the project to install a new electrostatic tandem accelerator in Strasbourg in order to cross the Coulomb barrier for heavier nucleus (MP10).

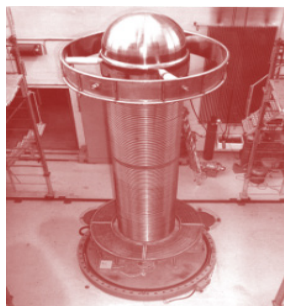


Figure 4: CN Van de Graaff accelerator operated at 5.5 MeV at IRN in 1959. Coaxial ring electrodes installed along acceleration column with terminal at the top.

THE CONFIRMATION

The 1970s were marked by the commissioning of a HEVC Tandem referenced MP10 (1972), started at 9 MV and upgraded to 18 MV, see Fig. 5. The acceleration of new ions over a wide mass range is now possible: ^1H – ^{197}Au [7]. Specific research is carried out in the field of nuclear γ spectroscopy, high-spin nuclear shape (a field of excellence ever since), neutron capture and measurement of fusion cross-section (e.g. $^{40}\text{Ca}/^{16}\text{O}$), interaction of heavy ions (e.g. $^{12}\text{C}/^{32}\text{S}$), γ and particle emission for different nuclear reactions. On the other hand, new fields of research are confirmed with the expansion of high-

energy physics activities, the contribution to CERN/SPS experiments, the search for weak interactions (measurement of the mass of particles, questioning of the SM), and collaboration on detectors for LEP. More complex reactions are carried out in the form of linked and cascade reactions of fusion-fission, fusion-evaporation, inelastic collision, interaction between heavy-ions, etc. At that time, a nuclear reactor was in operation on campus, producing targets and sources of ^{241}Am , ^{210}Po , ^{56}Co , neutron activation and performing 1400 irradiations per year. The reactor was stopped in 1997. High-energy and neutrino physics are progressing with participation in the DELPHI, ISR and NA36 experiments at CERN. Post-acceleration with a K500-60 MeV/A cyclotron was planned in 1978.



Figure 5: The new MP VDG tandem accelerator commissioned at 9 MV in 1972 and upgraded at 18 MV.

THE MATURATION

During the 1980-1990 decade, most research programs in physics were intensified due to favorable economic conditions. Nuclear physics detectors achieve unparalleled performance (see the “Château de cristal”). The number of experiments at CERN increased and numerous collaborations were established during this period: with G. Charpak, GANIL, GSI, LBNL, BNL, RIKEN, etc. The nuclear chemistry department is also developing in many fields with expertise in beam-matter interaction (ions, neutrons, γ), ion implantation at high current (at 4 MV), modification of surface properties, thin film deposition, surface analysis (Si, GaAs, PIXE), nuclear waste management, radiotracers production (with accelerators), research on CMOS circuits, solar cells, liquid crystals, positron annihilation (B-field influence), and dating of samples. It should be noted that the interest in fundamental research, multi-disciplinary activities, and education through science already grew in 1981. Industrial applications were developed such as high performance laser and pico-second camera, and spin-off companies were founded in 1984 (VIVIRAD) and in 1985 (AERIAL).

Each coin has two sides. Mega-science projects appear with increased size, duration, manpower and energy consumption (LHC R&D is launched), fixed-target experiments decrease at CERN and interest in applications to society becomes a must. For example, research on boron-neutron therapy (BNT) was launched with ^{10}B fixed in the tumour, activated by neutrons and production of alpha particles at 2.8 MeV with ^7Li in 1990.

CHANGE IN TREND

The years 1990 to 2005 were a boiling time in the research center with much energy expended to build, commission and operate a new large electrostatic accelerator, see Fig. 6. The first beam was produced in 1994 but the installation was dismantled ten years later. In the meantime many low-energy nuclear physics experiments have been carried out, for example with a $^{28}\text{Si}^{8+}$ beam of 250 nAe at 145 MeV [8, 9]. These experiments allowed research on exotic nuclear structures and the observation of extremely deformed high-spin nuclei (e.g. hyper-deformation observed in 1996 with 10^{20} rotation/s), unstable nuclei (on the time scale 10^{-12} - 10^{-15} s), SHE synthesis (A 252, N much larger than Z), and symmetry breaking (e.g. pear shape with aspect ratio 3:1). Significant progress is being made in the field of nuclear spectrometry, reaction mechanisms and the study of fragments (fusion-fission, elastic scattering, evaporation). To cite only the field of excellence developed at the time at CRN: germanium multi-detectors called Eurogam and Euroball (nucleus excitation and de-excitation) with a precision unequalled in the world.

The direction of the CRN was changed in 1996 and the laboratory became the “Institut de Recherches Subatomiques” in 1997 (IReS). As if to announce the next period of upheaval, major developments are looming on the horizon. Recruitment is decreasing at IReS as well as the number of disciplines, publications and groups, but a greater specialization of the activities can be noticed. The LHC R&D program is expended to CMS, ALICE and Atlas detectors. European programs are becoming more and more attractive, physics research shows an aggregation of ever larger accelerators in Europe like CERN, GSI, GANIL, due to the worldwide trend towards higher energies, international collaborations (Japan, USA, JINR, INFN, etc.) and industrial applications leaving less space for more modest installations.

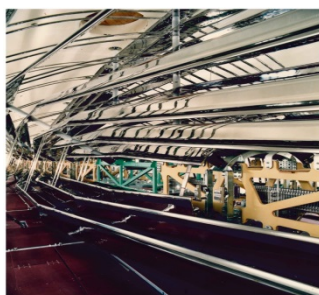


Figure 6: The Vivitron, a 20 MV large tandem. View on the terminal, longitudinal structure and intermediate polarized porticos distributed radially.

THE METAMORPHOSIS

The evolution of nuclear physics, the applications, the need to consider interactions between different disciplines to produce cutting-edge research, and the availability of new instruments at a reasonable price have contributed to the metamorphosis of the Institute and led to the creation

of the “Institut Pluridisciplinaire Hubert Curien” (IPHC) in 2006. A new 24 MeV cyclotron is purchased, see Figs. 7-8, and activities start in 2012 with the production of radionuclides applied to medical imaging.



Figure 7: TR24 cyclotron with open structure. Coils, magnet and vacuum chamber are removed.



Figure 8 Global view with yoke of magnet and beam line inside cave in controlled area.

The so called CYRCé facility is a hub for conducting research and experimentation in three main areas. The first concerns imaging and diagnostic techniques as PET, SPECT, the evolution of in-vivo tumours and the development of new detectors (time of flight, multimode, etc.), see Fig. 9. The second field is hadron therapy such as tomography with protons, cross-section measurement, in-vivo and in-vitro radiobiology, the interaction between the proton and the cell (radiochemistry) and the development of simulation code (G4-DNA). The last area is dosimetry with neutron, X-rays and proton detection techniques, and radiation dose control. ^{18}F and ^{64}Cu are the main radionuclides produced by accelerated protons and the external target (mainly ^{18}O in the electroplated substrate). The first is used as a radiotracer to study hypoxia and cell death in oncology. It should be noticed that this latest development involves the participation of several laboratory teams and therefore requires the collaboration of different experts in different fields: nuclear physicists, physiologists, analytical chemists, molecular engineering, electronics, mechanics and accelerator physicists.



Figure 9: Hot cell of CYRCé facility used for radiobiology, hadron therapy and medical imaging research at IPHC. Equipment is adapted to the manipulation of cells, samples, hot targets, radionuclides and other components.

Alongside these activities, other significant research programs are carried out by several IPHC teams through collaborations with CERN, in particular high-energy physics at the LHC with the rewarding discovery of the Higgs boson in 2012 and more discoveries to come [10]. Some scientific drivers are the search for exotic nuclei and rare isotopes, nuclear synthesis, nuclear astrophysics, the origin of elements and star formation, the search for the maximum number of nucleons (with the heaviest nucleus and proton/neutron distribution), identification of hidden mass and new interactions (dark matter, dark energy). The IPHC is now firmly anchored in the national landscape, see Fig. 10, and on the world map, see Fig. 11.



Figure 10: National landscape of CNRS/IN2P3 laboratories, and IPHC located on the East part.



Figure 11: Map of the international collaborations with IPHC.

ACKNOWLEDGEMENTS

The author would like to salute the invaluable inspiration brought by G. Frick during the first years of his career.

REFERENCES

- [1] Laboratory status reports, 1960-1996.
- [2] B. Ring, “Etude historique du CRN”, 1991-1992 (unpublished).
- [3] R. Casel, “Rapport Recherche nucléaire 1941-1951”, 1992.
- [4] G. Frick, Internal reports, 1983, 1994, 1997 (unpublished).
- [5] Laboratory internal letters, 2002-2004.
- [6] F. Olivier-Utard, “Les conventions entre le CNRS et l’université de Strasbourg : une expérience pionnière”, La revue pour l’histoire du CNRS [En ligne], 11 | 2004, mis en ligne le 04 septembre 2007, consulté le 27 juin 2022. <http://journals.openedition.org/histoire-cnrs/691>
doi:10.4000/histoire-cnrs.691
- [7] R. Hellborg, “Electrostatic accelerators”, Springer 2005. doi:10.1007/b138596
- [8] Private communication, F. Haas, 2016.
- [9] F.A. Beck, “A historical overview of nuclear structure studies in Strasbourg Laboratories: instrumentation, measurements and theory modelling hand-in-hand”, Phys. Scr., vol. 93, no. 5, p. 053002, 2018. doi:10.1088/1402-4896/aab757
- [10] IN2P3, 50 ans de physique des deux infinis, <https://50ans.in2p3.fr/timeline-iphc/>

BEAM DYNAMICS AND SPACE CHARGE STUDIES FOR THE INNOVATRON CYCLOTRON*

G. D'Agostino[†], W. Kleeven

Ion Beam Applications (IBA), Louvain-La-Neuve, Belgium

Abstract

At IBA a high-intensity compact self-extracting cyclotron is being studied. There is no dedicated extraction device but instead, a special shaping of the magnetic iron and the use of harmonic coils to create large turn-separation. Proton currents up to 5 mA are aimed for. This would open new ways for large-scale production of medical radioisotopes. The main features of the cyclotron are presented. A major variable of the beam simulations is the space charge effect in the cyclotron centre. Using the SCALA-solver of Opera3D, we attempt to find the ion source plasma meniscus and the beam phase space and current extracted from it. With these properties known, we study the bunch formation and acceleration under high space charge condition with our in-house tracking code AOC. We also discuss a new tool that automates optimization of cyclotron settings for maximizing beam properties such as extraction efficiency.

INTRODUCTION

Radioisotopes for nuclear medicine can be produced either by reactors or accelerators. Commercial cyclotrons ($E = 15\text{--}70$ MeV) achieve currents up to or just above 1 mA. Large-scale production of radioisotopes needs a high-intensity cyclotron technology. The self-extracting cyclotron is a promising tool for producing high quantities of SPECT radioisotopes such as Tc-99m or new emerging PET radioisotopes [1]. The InnovaTron 14 MeV H^+ machine features a magnetic field with a very steep fall-off near the outer pole radius, allowing the beam to extract spontaneously. First harmonic coils increase the turn-separation at the entrance of the extraction path. The prototype, installed in Fleurus (Belgium) in 2000, achieved a current close to 2 mA [2]. More details on the concept can be found in [3]. Main goals set for the project are: i) improvement and optimization of the magnet, extraction elements and central region, ii) space charge simulations, iii) improvement of turn-separation at extraction. We discuss results obtained for i) and ii).

MAGNET OPTIMIZATION

The following improvements have been implemented as compared to the prototype: i) the magnet (and also the accelerating structure) has perfect 2-fold symmetry. This allows irradiation of two targets stations at opposite exit ports and to place two internal ion sources. The latter will increase cyclotron reliability and uptime, ii) the groove in the extraction

path used in the prototype (Fig. 1a) is replaced by a “plateau” (Fig. 1b). This reduces the strong sextupole component in the extraction path and improves the extracted beam quality, iii) the pole gaps still have a quasi-elliptical shape, decreasing towards larger radii, but the iso-gap contours follow equilibrium orbits. This enables a steeper transition from the internal stable orbit towards the non-stable extracted orbit.

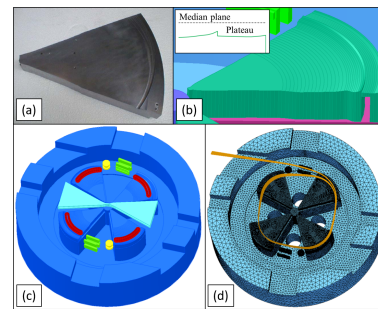


Figure 1: InnovaTron improved magnet design.

Figure 1c shows a view on the lower half of the magnet developed in Opera3D. The harmonic coils (in red) and the dees (in light blue) are also shown. The gradient correctors (in green) provide radial focusing to the extracted beam. The beam separators (in yellow) are used to intercept parts of the beam that are not properly extracted. A beam simulation of the last 5 turns superimposed on the FEM model is shown in Fig. 1d. Automatic and parametrized FEM models have been developed, for the magnet but also for the central region and dees. More details are given in [4].

CENTRAL REGION STUDIES

We do an effort for a self-consistent simulation of the space charge dominated beam in the central region. This method consists of three steps. In the first step the SCALA space charge solver of Opera3D [5] is used to find the plasma meniscus of the ion source. In the second step the same central region model is solved again, but now with the TOSCA electrostatic solver of Opera3D. Here the meniscus surface is put at ground potential. This provides the 3D electric field map everywhere in the central region, including the source-puller gap. In a third step the beam extracted from the meniscus is simulated in the 3D field map using the self-consistent in-house space-charge code AOC [6]. This code has been extended to also simulate the bunch formation process in the first gap.

SCALA Simulations

The plasma-free boundary module of SCALA calculates the plasma meniscus and the extracted beam phase space and current density on the meniscus, in a DC electric field.

* Work supported by the European Union's Horizon 2020 research and innovation programme under the Marie Skłodowska-Curie grant agreement No 886190.

[†] grazia.dagostino@iba-group.com

SCALA does not solve the plasma itself: the meniscus surface is determined by the Child-Langmuir condition where the external electric field on the surface is cancelled by the space charge electric field. The surface is found in an iterative process. The electric field in a cyclotron central region is not DC but RF. The RF frequency however, is so high that it will be impossible for the plasma meniscus to follow it, in its motion. The maximum velocity of a material wave is roughly equal to the speed of sound in the material which, for a plasma, will be close to the Bohm-velocity $v_B = \sqrt{kT_e/m_p}$, where T_e is the plasma electron temperature and m_p is the proton mass. Assuming $kT_e \approx 10$ eV we find that the meniscus could move only about 0.1 mm in a quarter of the wave period at 70 MHz. So it seems that the meniscus will move only weakly in the RF electric field; we therefore make the assumption that the meniscus shape and position can be found by solving the problem for the rms-value of the gap-voltage. It is clear that this is a strong assumption and an important simplification which we can, at this point not further validate.

For the solution of the SCALA problem we only need to model the local geometry of the source-puller gap. Our example is shown in Fig. 2. In this geometry the puller (C) and the dee (E) are placed at high (negative) potential and the chimney (A) and the dummy-dee (D) are at ground potential. The ion source full slit aperture in our example is

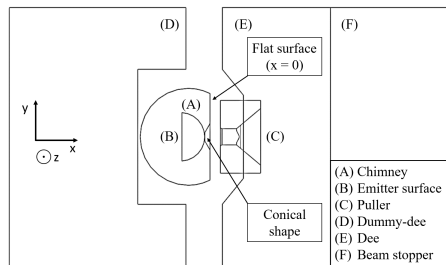


Figure 2: Top view of the SCALA source-puller model.

$\Delta y \times \Delta z = 1 \times 8 \text{ mm}^2$. SCALA launches beamlets from the (flat) emitter surface (B), which move to the right towards the ion source slit. At this position, space charge builds up which limits the flow of extracted particles. Besides the geometry, the two important parameters in the simulation are i) the dee-voltage V_{dee} and ii) the emitter current density J_{emit} . Two additional but less critical parameters are iii) the electron temperature T_e and iv) the meniscus voltage V_m .

Figure 3 shows examples of four different cases: a) ($V_{dee}=42.1 \text{ kV}$, $J_{emit}=0.4 \text{ A/cm}^2$), b) $V_{dee}=9.5 \text{ kV}$, $J_{emit}=0.4 \text{ A/cm}^2$, c) ($V_{dee}=38.9 \text{ kV}$, $J_{emit}=0.2 \text{ A/cm}^2$) and d) ($V_{dee}=38.9 \text{ kV}$, $J_{emit}=2 \text{ A/cm}^2$). The first column in the figure is a vertical section through the chimney and shows the position and shape of the meniscus (only the upper half is shown). The middle column shows the vertical beam profile (seen from the $-y$ direction) and the right column shows the horizontal beam profile (seen from the $+z$ direction). The extracted DC currents for the four cases are 100 mA (a), 36.7 mA (b), 67.4 mA (c) and 222 mA (d).

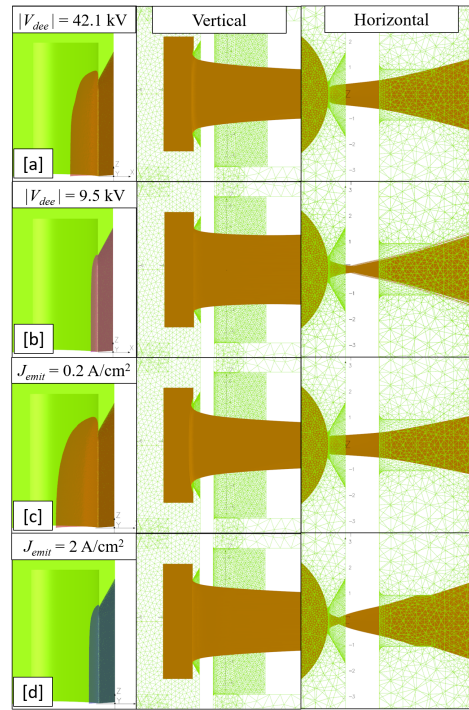


Figure 3: Examples of meniscus shape and beam projections.

A close inspection shows that the extracted current is (almost perfectly) proportional to the surface of the meniscus times the emitter current density. The beamlets cross the meniscus (almost perfectly) perpendicularly and the flow is (almost perfectly) laminar. It is seen that higher V_{dee} pushes the meniscus to the left and higher J_{emit} pushes the meniscus to the right. Horizontally the beam is strongly converging, with an (over-) focus close to the slit and vertically the beam is weakly converging. This relates directly to the slit dimensions which make that the meniscus is strongly curved in the xy -plane and much more flat in the xz -plane.

Figure 4 shows the extracted current and meniscus position as function of the four parameters V_{dee} , J_{emit} , T_e and V_m . The position is the distance between the extreme meniscus x -coordinate and the intersect between x -axis and plasma chamber cylinder.

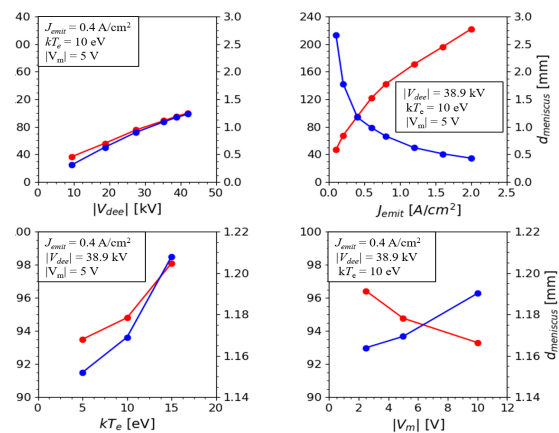


Figure 4: DC extracted current (red) and meniscus position (blue) as function of the four main parameters.

TOSCA Simulations

We extract from the beamlets calculated by SCALA (those who are extracted from the ion source), the particle position coordinates, the velocity components and the beamlet current at the meniscus intersect. These data are used to fit the meniscus x -coordinate, the transverse divergencies (y' , z') and the beamlet currents as a function of y and z . The latter two are considered as independent variables. We use a double polynomial fit up to order 7 (the sum of the y and z exponents) and take into account the symmetry: x is even in y and z ; y' is odd in y and even in z ; z' is even in y and odd z . This allows to represent the surface of the meniscus as a wire-edge structure with a triangular mesh. This surface is included in the TOSCA model of the central region, where it is put at ground potential (see Fig. 5). With this, one can simulate precisely the value and shape of the 3D electric field in the source puller gap. The representation also allows to create a file with particle starting conditions for tracking, when y and z are generated randomly and the other variables (x, y', z') are calculated from the fits. Figure 6 shows projections of the fitted phase space on the planes xy, xz, yy' and zz' . There are three cases shown: $V_{dee} = 38.9$ kV, $J_{emit} = 0.4$ A/cm² (green), $V_{dee} = 18.8$ kV, $J_{emit} = 0.4$ A/cm² (blue), $V_{dee} = 38.9$ kV, $J_{emit} = 2$ A/cm² (red).

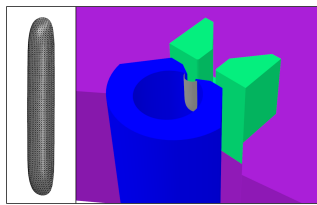


Figure 5: Modeling of the plasma meniscus in TOSCA.

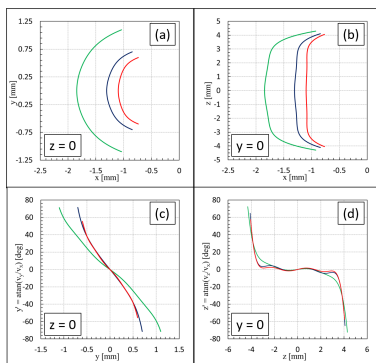


Figure 6: Fitted phase space projections.

Figure 7 shows in (a) the TOSCA electric field in the source-puller gap for three different cases. One case is for the chimney with the conical shape as shown in Fig. 2; for the other two cases this cone is not present. The meniscus was calculated at $V_{dee} = 35.3$ kV for the first case (green curve) and 18.8 kV for the other two cases. For all three cases, the electric field drops quickly in the space in between the meniscus and the chimney slit ($x < x_{slit}$). As a consequence, the particles must leave early from the meniscus surface in order to be able to cross the gap. This is illustrated in

Figs. 7(b-d). They show the particle energy gain as a function of time for different starting RF phases ranging from -180° (the moment of zero dee-voltage) up to -130° in steps of 5° (with $V_{dee} = 55$ kV). Later starting phases are not properly accelerated by the central region. The worst case is (b) where the energy gain is the lowest and the energy spread is the largest. For this case, the electric field near the meniscus is the lowest and the particles are lost after a few turns in the central region. For cases (c) and (d) the electric field near the meniscus is higher and a phase range of about 40° can be accepted and accelerated. Case c is the best as it has good energy gain and the smallest energy spread.

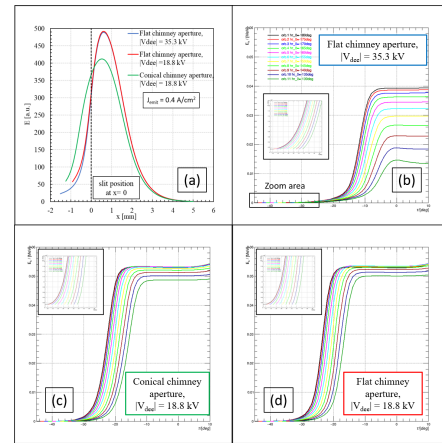


Figure 7: Electric field and energy gain in the first gap.

Space Charge in AOC

In the default use of AOC, the full 6D phase space of the initial particles in the bunch must be specified. Recently a new option has been added for simulating the formation of the bunch extracted from the ion source meniscus. In this case, the particle properties on the meniscus must be defined and also the number of time-steps that are needed to complete the bunch formation. The bunch will be sliced according to the number of time-steps. For each new step, the bunch is re-defined by adding the additional slice and then advanced using the iterative process. After completing the formation of the bunch, it is continued in the usual way.

FULL BEAM TRACKING

We track a full beam through the central region shown in Fig. 8. The position and orientation of the ion source and the first few accelerating gaps in this CR are optimized in order to obtain good beam centering and good vertical electric focusing. Some additional tools have been made in AOC that allow to slightly rotate/translate the central region geometry without the need to each time solve its 3D FEM model.

The collimators (shown in blue) are optimized to limit the accelerated RF phase range to about 40° and by so to remove particles that would otherwise be lost at higher energies. Note that the beam shown in Fig. 8 only includes the “successful” particles. The starting beam, obtained from a

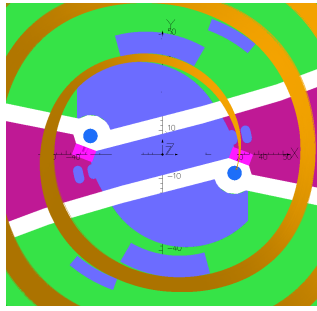


Figure 8: The 2-fold rotational symmetric central region.

SCALA simulation ($J_{emit} = 0.4 \text{ A/cm}^2$ and $V_{dee} = 18.8 \text{ kV}$) and representing a starting average current of 100 mA on the meniscus, is sampled with 100000 particles in a RF phase range between -180° and 0° . Figure 9 shows transmission (a), centering (b), vertical beam-size (c) and vertical emittance (d) of the accelerated beam during the first 25 turns. In the representation shown, the particles are binned according to their RF-starting phase on the meniscus in four groups of each 10° wide. Only particles in the phase range between -180° and -140° are accepted. The particles must leave early from the meniscus as explained before. Figure 9 (a) shows that there are high losses in the first 2 turns. This is not only due to the unfavorable transit time but also to the strong over-focusing action in the horizontal plane at the ion source exit (see Fig. 3). Only about 1.7% of the particles is accepted, corresponding to an average beam current of 1.7 mA.

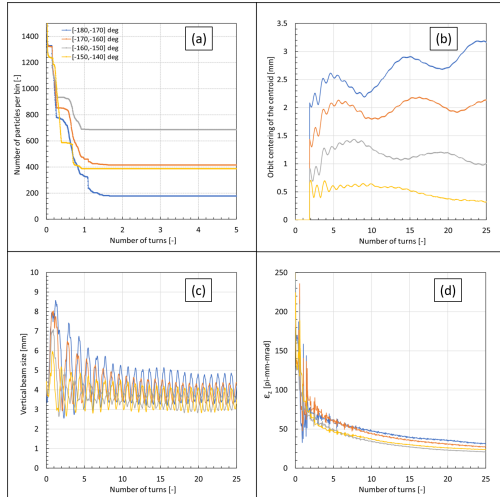


Figure 9: Beam rms properties, binned according to RF starting phase: (a) transmission, (b) beam centroid off-centering, (c) vertical beam size (2σ value), (d) normalized vertical emittance (2σ value).

The losses are distributed as follows: about 88.7% on the chimney+puller+puller collimators, about 5.8% in the phase selecting collimators and about 3.9% vertically on the dees and dummy dees. Beyond the 2nd turn all beam properties stabilize. Figure 10 (a) shows the shape of the accelerated bunches by their projection on the xy-plane, followed during 25 turns at moments when the RF phase equals zero. In

another (earlier) simulation we started a bunch just beyond the source-puller gap with an average beam current of 5 mA, horizontal and vertical emittances of about $20 \pi \cdot \text{mm} \cdot \text{mrad}$ (1σ) and a total bunch length of about 3 mm (corresponding to 30° RF width). The shape of the bunches for this case is shown (for the first 20 turns) in Figure 10 (b). Here we observe the appearance of circular bunches (with a tail however) which probably is due to the well-known vortex motion [7], turned on by high space charge forces.

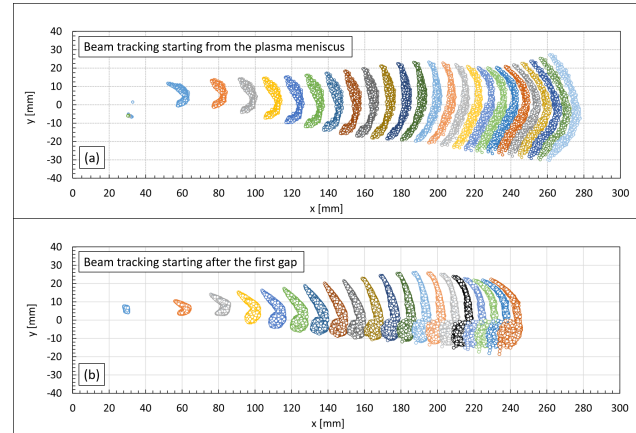


Figure 10: XY projection of accelerated bunches started (a) on the ion source meniscus and (b) after the first gap.

Optimization of Cyclotron Settings

Extracted beam optimization is a difficult and tedious process as it depends on multiple parameters (for example harmonic coil settings, dee-voltage, collimator geometry etc.) and requires full beam tracking (if possible with space charge) from the ion source up to the cyclotron exit. In order to facilitate this process an optimization program (project_optimizer) was written. This program uses standard optimization routines to optimize a task (project). The task is defined by a user-defined script which is executed by the program in an iterative process. It reads new values of independent variables as suggested by the program, executes the task and writes its results (new values of the objectives) to a file. The program then resumes and compares the results of the script with the (user defined) objectives in order to calculate the fitting error and suggest new values for the variables. This process is repeated until the fitting error is smaller than a given tolerance. In the present study, the script reads all AOC input data and adjust input field maps as needed. Then it runs AOC and post-process its results in order to extract the objective values. Three standard multiple dimension optimization routines have been implemented (Downhill Simplex Method, Direction SET Powell Method and Simulated Annealing Method) [8]).

The process has been tested (without space charge) for a beam of 2000 particles, tracked from the ion source position up to extraction. The starting conditions at the ion source were taken as: $E = 100 \text{ eV}$, $\epsilon_x = 125 \pi \cdot \text{mm} \cdot \text{mrad}$, $\epsilon_z = 500 \pi \cdot \text{mm} \cdot \text{mrad}$, slit aperture $w \times h = 1 \times 4 \text{ mm}^2$ and starting RF phases $-145^\circ < \Phi < -115^\circ$. The settings

of the two pairs of harmonic coils were optimized by project_optimizer to obtain maximum extraction efficiency on the first exit port. We found an extraction efficiency of 91% with 7.7% losses on the first beam separator and 1.3% extracted towards the 2nd exit port. Figure 11 illustrates the process of optimization of extraction efficiency as function of harmonic coil settings. Note that this case was still done “by hand”.

Extraction efficiency [%] 1 st exit port	Dee voltage 55.17 KV	Harmonic coils currents on the long poles					
		-0.35	-0.3	-0.25	-0.2	-0.15	-0.1
	Harmonic coils current on the short poles	-0.35	59.2	63.1	68.5	76.0	78.7
-0.3	59.8	67.0	78.4	82.1	82.2	81.1	
-0.25	60.9	77.2	87.7	87.9	84.9	84.3	
-0.2	81.8	89.6	89.4	89.2	83.7	69.0	
-0.15	91.3	87.3	82.2	68.5	52.3	45.7	
-0.1	76.9	66.3	65.0	72.5	67.6	12.6	

Figure 11: Optimization of extraction efficiency.

Figure 12 (a,b) shows the extracted phase space just beyond the beam separator. At this point we find (1σ) emittances and energy spread of: $\epsilon_x = 104 \pi\text{-mm-mrad}$, $\epsilon_z = 1.25 \pi\text{-mm-mrad}$, $\Delta E/E = 0.44\%$. As can be seen, there is a large X vs Z asymmetry; the vertical emittance is nicely linear.

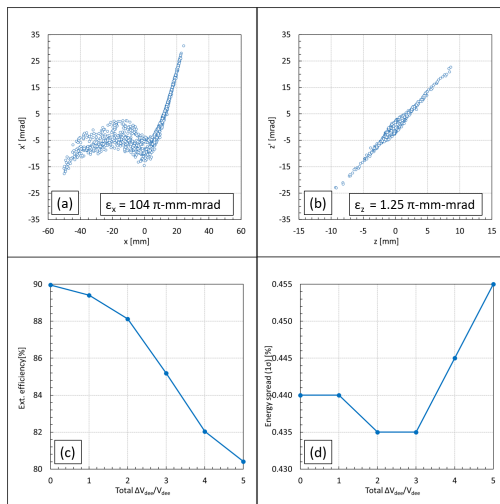


Figure 12: Extracted emittances and dependence of extraction efficiency and energy spread on dee-voltage ripple.

For the self-extracting cyclotron, good turn separation helps to obtain high extraction efficiency. Turn-separation

may be reduced or lost if the RF dee-voltage is rippled. At high beam intensities this may happen due to beam loading of the RF cavity, if the injected beam intensity is noisy. Internal ion sources indeed are rather noisy. Figure 12 (c,d) shows the decrease of extraction efficiency and the beam energy spread as function of a simulated dee-voltage ripple. It is seen that the RF control system should keep this ripple as low as possible.

CONCLUSION

We developed new tools i) for the study of space charge beams extracted from the plasma meniscus and bunch formation in the source-puller gap and ii) for automated optimization of cyclotron settings aiming at highest extraction efficiency. Further studies are planned, to see if the turn-separation at extraction can be improved.

REFERENCES

- [1] R. Alberto and H. Braband, “SPECT/PET Imaging with Technetium, Gallium, Copper, and Other Metallic Radionuclides”, in *Comprehensive inorganic chemistry II: From elements to applications*, Amsterdam: Elsevier, pp. 785-817, 2013. doi:10.1016/B978-0-08-097774-4.00331-4
- [2] W. Kleeven *et al.*, “The IBA self-extracting cyclotron project”, in *Proc. Nukleonika*, vol. 48, pp. S59-S67, 2003.
- [3] W. Kleeven, “Isochronous cyclotron and method of extraction of charged particles from such cyclotron”, Patent No.: US 6,683,426 B1, Date: 27 January 2004
- [4] G. D’Agostino *et al.*, “InnovaTron: An Innovative High-Intensity Industrial Cyclotron for Production of Tc-99m and Other Frontier Medical Radioisotopes”, in *Proc. IPAC’21*, Campinas, Brazil, May 2021, pp. 1841–1844. doi:10.18429/JACoW-IPAC2021-TUPAB188
- [5] OPERA, <https://www.3ds.com/>
- [6] J. G. M. Kleeven *et al.*, “AOC, A Beam Dynamics Design Code for Medical and Industrial Accelerators at IBA”, in *Proc. IPAC’16*, Busan, Korea, May 2016, pp. 1902–1904. doi:10.18429/JACoW-IPAC2016-TUPOY002
- [7] J. G. M. Kleeven, “Some Examples of Recent Progress of Beam-Dynamics Studies for Cyclotrons”, in *Proc. Cyclotrons’16*, Zürich, Switzerland, Sep. 2016, pp. 244–250. doi:10.18429/JACoW-Cyclotrons2016-WEA01
- [8] William H. Press, Saul A. Teukolsky, William T. Vetterling, and Brian P. Flannery. “Numerical Recipes in C, The Art of Scientific Computing, Second Edition”, Cambridge University Press, 1992. ISBN 0-521-43108-5.

FIRST TESTS OF MODEL-BASED LINAC PHASING IN ISAC-II

S. Kiy*, R. Baartman, O. Kester, O. Shelbaya
TRIUMF, Vancouver, BC, Canada

Abstract

As the e-linac and ARIEL facilities at TRIUMF progress, the impending complexity of operating three simultaneous rare ion beams (RIBs) approaches. To help prepare for this, a framework for the development of High Level Applications has been constructed, upon which multiple avenues for improvement towards model-based and automated tuning are being pursued. Along one of these avenues, the 40-cavity superconducting ISAC-II heavy ion linac has been studied and modelled in the envelope code transoptr. This has allowed for real-time integration through the on-axis fields, fitting focal strengths of solenoids to achieve desired beam waists, and calculation of necessary cavity phases to achieve a desired output energy for given input beam parameters. Initial tests have been completed, successfully phasing up to 37 cavities using the transoptr model and achieving a final output energy within 1% of the expected while maintaining nominal (>90%) transmission. A summary of the calibration of the model to the machine is given, followed by results of the phasing tests and an outlook towards future improvements.

INTRODUCTION

The Isotope Separator and ACcelerator (ISAC) facility at TRIUMF serves a wide assortment of experiments that study nuclear structure, materials science, nuclear astrophysical reaction rates, and more. Stable beams from the Off-line Ion Source (OLIS) or radioactive ion beams from the target stations can be delivered to low, medium, or high energy sections depending on the amount of post-acceleration required. The ISAC-I medium energy section, completed in 2001 [1], provides ion beams from 0.15 to 1.8 MeV/u while the ISAC-II high energy section, completed in two phases in 2006 and 2010 [2], can deliver beams from 1.5 up to as high as 16.5 MeV/u.¹

Acceleration in the ISAC-II linac is provided by forty superconducting two-gap quarter wave niobium cavities, operating at 4.2 K. Cavities are distributed over eight cryomodules, each containing one superconducting solenoid.

MOTIVATION

Typical experiments served by the ISAC-II linac run for approximately 7 days. Overhead for these experiments to adjust the accelerators for new beam properties is typically scheduled for 24 hours. The portion of this overhead required for the optimization of the ISAC-II linac is regularly over 8 hours and requires expert assistance or senior operators.

The optimization itself is a complex process, as it involves the user turning on one cavity at a time and scanning the phase to identify the desired setpoint. This is further complicated by the large energy gain relative to the incoming energy for the first few cryomodules, which impacts the transverse tune and requires re-optimization of solenoids and quadrupoles.

Basically, it is a problem of a large configuration space with interdependent tuning parameters:

- 40 cavities x 2 adjustable parameters (phase, amplitude)
- 8 solenoids x 1 adjustable parameter (current)
- 8 cryomodules x 2 adjustable parameters (x, y steerers)

This has motivated a more model-based approach to the operation of the ISAC-II superconducting linac.

HIGH LEVEL APPLICATIONS AT TRIUMF

The high-level applications (HLA) taskforce [3, 4] is tasked with using model-based tuning integrated with the control system to improve beam quality and reduce tuning overhead. This project is one of multiple such areas of study at TRIUMF and utilizes various components of the HLA framework, including python to EPICS communication, xml beamline information, and TRANSOPTR for beam envelope simulations.

MODEL CALIBRATION

Diagnostics

The time structure of the beam at three locations of known distance along the beamline are measured using flight time monitors (FTMs). Shown below in Fig.1, FTMs are an assembly consisting of a 50 μ m diameter biased tungsten wire that intersects the beam and emits secondary electrons.

These electrons are detected by a micro-channel plate (MCP) detector with a time resolution of < 100 ps, giving a resulting energy/nucleon resolution of under 0.1% [5]. The velocity of the ion beam is calculated as a weighted average using the arrival time at each of the possible 3 pairs of monitors [6].

With no time diagnostics within the linac itself, these three monitors located approximately 3, 5, and 14 metres downstream of the last accelerating cavity are the primary diagnostics used for both measuring the beam velocity and calibrating cavity phases in the model.

Phase Shifters

The forty cavities in the ISAC-II linac are each driven independently, so each cavity has its own designated phase

* spencerkiy@triumf.ca

¹ 16.5 MeV/u is achievable here for A/q of 2.

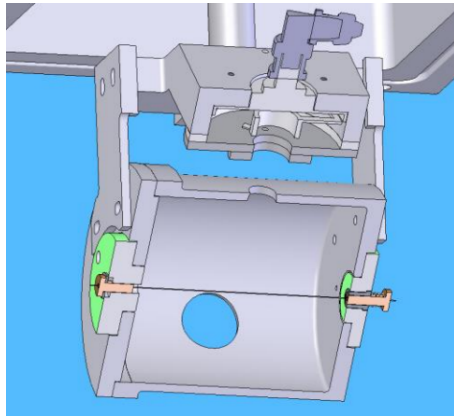


Figure 1: A model cutaway of one of the FTMs, showing the Tungsten wire as well as the beam port (bottom, centre of the picture) and the port for the MCP.

shifter to allow the user to adjust the cavity timing to the arrival of the beam. To allow for automated phasing, the exact behaviour of the phase shifter circuits was investigated. A vector voltmeter was used to measure the phase difference between the RF reference signal arriving at the phase shifter circuit to the output. This difference was recorded for varying setpoints of the phase shifter in the control system to measure the real phase change vs control system.

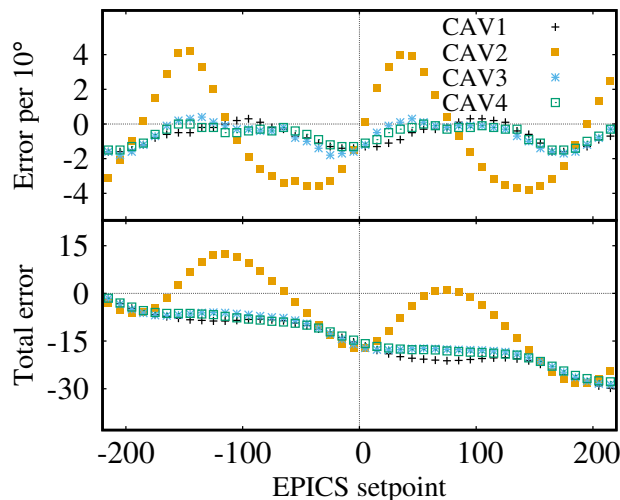


Figure 2: Measured error in phase per 10 degree step (above) and cumulative error from starting point of -220 degrees (below) vs setpoint in the control system.

As shown in Fig. 2, the relationship is non-linear and varies from one cavity to the next. To handle this, the phase behaviour was measured for all fourty cavities as well as three available global phase shifters, and input into a python package which converts between the control system setpoint and a phase in degrees prior to modelling.

The ISAC-II Linac Model in TRANSOPTR

TRANSOPTR is a first-order beam envelope code written in FORTRAN and developed at TRIUMF [7]. It calculates

the beam's sigma matrix, representing the beam envelope in 6-dimensional phase space (x, P_x, y, P_y, z, P_z) . Notable benefits include the available expertise at TRIUMF, fast execution times (on the order of 1 second), and the ability to integrate through an-axis field maps of accelerating cavities [8].

While model-based calculations of the necessary cavity phase could also use a drift-kick model and the transit-time factor approach - use of an envelope code like TRANSOPTR is advantageous as it also allows the desired optimization of transverse focusing elements.

For a given configuration of the linac, the cavity amplitudes from the control system are fed into the model, which can then model RF defocusing effects and run optimizations of solenoid strengths to achieve the desired beam waist at the desired location between each cryomodule.

TRANSOPTR takes as inputs the on-axis magnetic field (B_z) for the solenoids and the on-axis electric field (\mathcal{E}_z) for the superconducting RF cavities. The B_z field maps were measured by the vendor, Accel, in Germany for the superconducting solenoids while the \mathcal{E}_z field maps, shown in Fig. 3 were simulated in CST microwave studios (V. Zvyagintsev, personal communication, November 11, 2021).

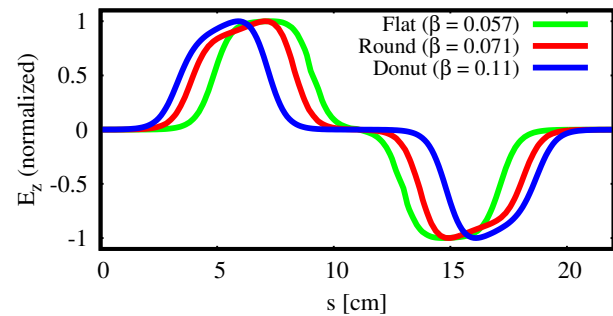


Figure 3: Normalized \mathcal{E}_z field maps of the three cavity types found in the ISAC-II linac.

The evolution of the sigma matrix is governed by the envelope equation [8]

$$\sigma' = F \cdot \sigma + \sigma \cdot F^T \quad (1)$$

Where σ is the sigma (or covariance) matrix representing the beam in 6-dimensional phase space. The prime denotes a derivative with respect to s , the distance along design orbit. F is the infinitesimal transfer matrix, defined by:

$$X' = FX \quad (2)$$

Where X is the vector (x, P_x, y, P_y, z, P_z) . The infinitesimal transfer matrix for an axially symmetric RF field [8] depends only on the longitudinal component of the on-axis electric field,

$$\mathcal{E}_z(s, t) = \mathcal{E}_z(s) \cdot \cos(\omega t + \phi_i - \theta) \quad (3)$$

Where \mathcal{E}_z is the longitudinal electric field map, ω is the RF angular frequency, ϕ is the control system phase, and θ is the cavity phase offset.

TRANSOPTR solves Eq. 1 by carrying out Runge-Kutte integration with an adaptive step size. The code also solves for the equations governing the total energy and time of flight.

BEAM-BASED CALIBRATION

Cavity Calibrations

The length of the RF lines for the fourty cavities differ, both from the master oscillator to the LLRF boards and amplifiers as well as from the amplifiers along the RF transmission lines to the cavities. To properly align the model with the machine, the phase offset of cavities, θ , must be established. The scaling between the control system amplitude and the peak electric field in the accelerating gaps must also be known.

To accomplish this, a calibration tune was established using a manual phasing method. Cavities are turned on one at a time and the control system phase is varied to a minimum of 5 different values, while using the FTM system to calculate the energy per nucleon at each of the phases. An optimization routine is then run to find the parameters θ and C that minimize the sum of the squared residuals as shown below in Eq. 4

$$S = \sum_{i=1}^m (E_i - f(\phi_i, C, \theta))^2 \quad (4)$$

Where

$$f(\phi_i, C, \theta) = W_{in} + \Delta E \quad (5)$$

Where W_{in} is the incoming energy of the beam. From Eq. 3, we have

$$\Delta E = q \int A \cdot C \cdot \mathcal{E}_{norm}(s) \cdot \cos(\omega t + \phi_i - \theta) ds \quad (6)$$

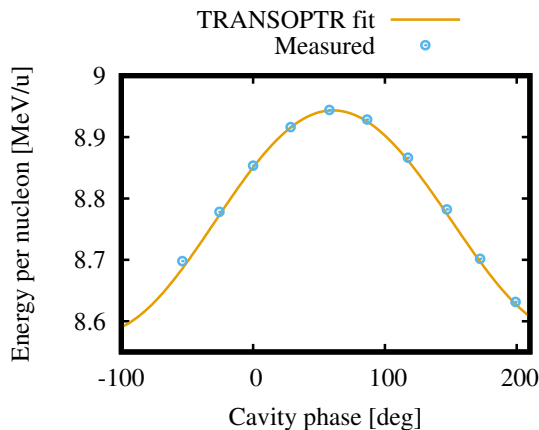


Figure 4: Energy vs cavity phase plot for one cavity, showing resulting fit between measured behaviour and the model.

Where q is the charge state of the beam, and the \mathcal{E}_z field map has been broken down into the normalized field map shown in Fig. 3, the control system amplitude A , and the scaling parameter C . An example of a typical fit to the collected data is shown above in Fig. 4.

IMPLEMENTATION AND UI

Initial tests were carried out running the model from a terminal. Of course, a more robust and user-friendly interface will be required to transfer this automated phasing tool to operations.

To this end, a web-interface is being established using the HLA framework to provide operators with a UI. This phasing tool is being built in to an existing app which is a python process running within a Docker container. The app sends the long running optimization request to a backend process via celery, which the client's machine then polls periodically until the process is complete. An overview of the current operator interface is shown in Figures 5 and 6.

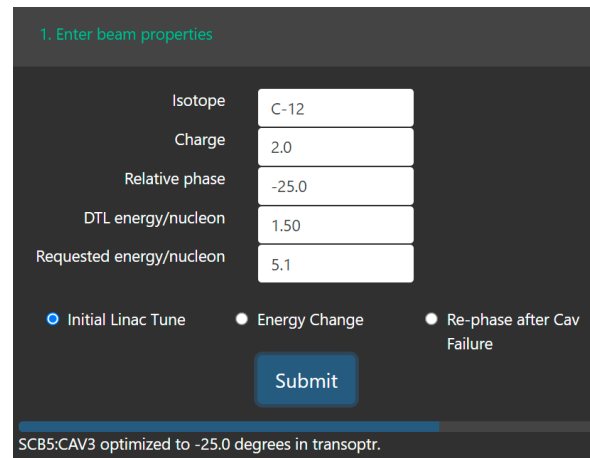


Figure 5: Web interface for operations to run the ISAC-II model for automatic calculation of cavity phases and solenoid strengths.

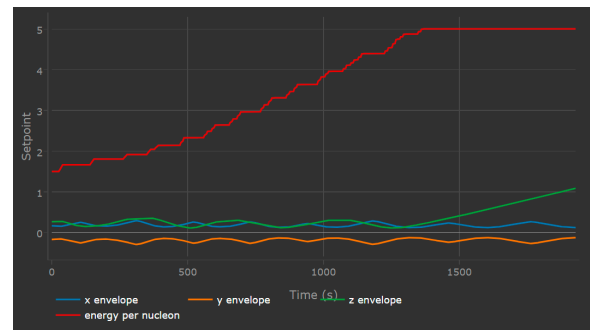


Figure 6: Envelope displayed on UI after model optimization.

ONLINE TESTS

A test was completed with 35 operational cavities, based on a single calibration tune at A/Q 4.5 from May of 2021.

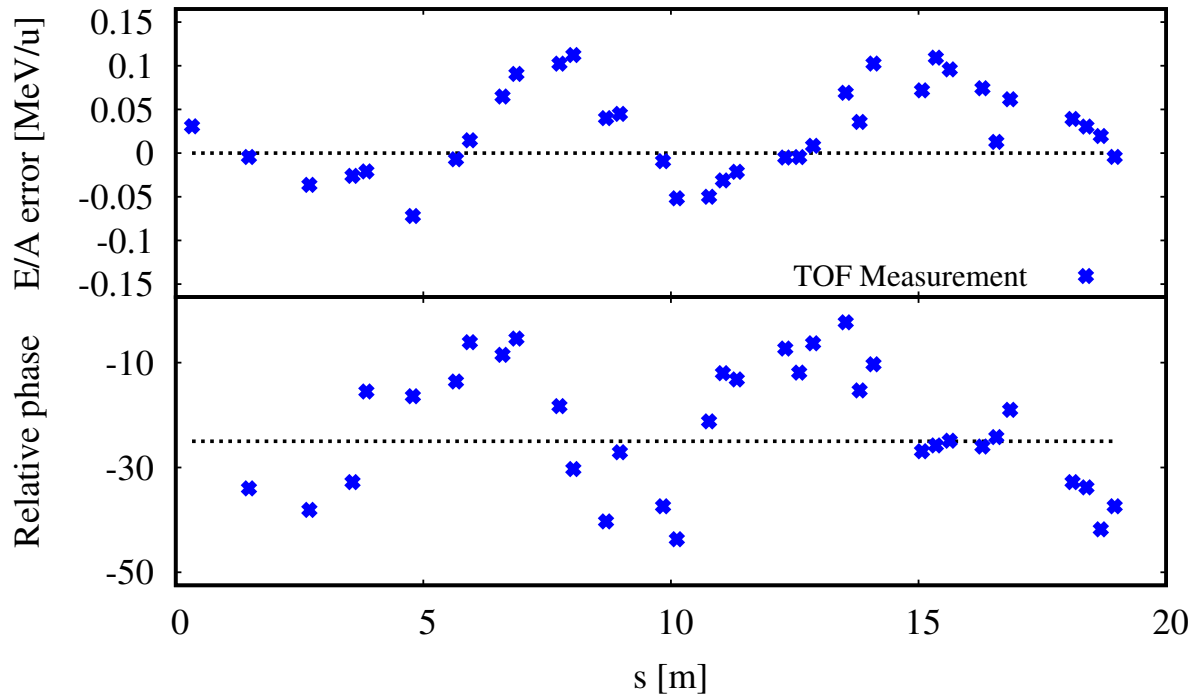


Figure 7: Measured energy and phase after each cavity of the test (blue) compared to expectations from the model (dashed line). X-axis is distance along the beamline.

The calibrated model was used to calculate the desired control system phase that gave a -25 degree relative phase and the expected energy output of each cavity.

To assess the accuracy of the model calculations, cavities were then turned on one at a time. Each cavity had its phase vs output energy behaviour measured (as done in calibration, shown in Fig. 4) and fit to quantify how far off the model was from the desired -25 degree relative phase. Finally, the cavity was set to the phase calculated by the model and transmission and energy were measured for further comparison to the model.

DISCUSSION

Shown above in Fig. 7, the energy per nucleon error in this test was less than 0.15 MeV/u while the cavity phase error was less than 20 degrees for all available cavities. Linac transmission averaged over 90% and the established tune was successfully used for delivery to an experiment.

The initial few cryomodules are suspected to be primary cause of error observed in Fig. 7. As demonstrated by the very first data point from the left on the top plot in Fig. 7, the energy error after the very first cavity is 0.03 MeV/u, which corresponds to an error of $\sim 10\%$ in the energy gained from this cavity. This could come solely from an error in the fit amplitude parameter C , from a phase error in the first cavity of ~ 4 degrees, or a combination of the two.

Due to the relatively low velocity through the first few cryomodules, this size of an energy error can produce a significant phase error at the next cavity - in this test the next operational cavity was 1.15 metres downstream, meaning the

0.03 MeV/u introduces a 20 degree phase error at the next cavity. Even if the rest of the cavities are set precisely correct, the mean energy and phase of the beam will now oscillate around the synchronous particle, similar to the behaviour seen in Fig. 7. For contrast, a 0.03 MeV/u energy error at 8.0 MeV/u over 1.15 m would only cause an error of 2 degrees at the next cavity.

Further work is planned to more carefully calibrate the early cavities in the linac, including a full 360 degree scan of the energy-phase output of the cavities at smaller step sizes. This can be difficult, as the relatively large energy gains of the first linac cavities have a significant impact on the transverse optics which require re-optimization to transport beam the $\sim 32m$ downstream to reach all three FTMs. However, this initial model-based phasing approach will now expedite this process, enabling continuous improvement of the model and linac operation.

CONCLUSION

The ISAC-II linac has been modelled in TRANSOPTR and various calibration necessary for the model have been investigated. Tests of automated phasing have been carried out and have demonstrated the capability to now setup the linac for a new experiment in under an hour where it historically has required over 1 shift (8 hours).

REFERENCES

- [1] R. E. Laxdal *et al.*, "Beam Commissioning and First Operation of the ISAC DTL at TRIUMF", in *Proc. 19th Particle Accel-*

- erator Conf. (PAC'01), Chicago, IL, USA, Jun. 2001, paper FPAH112, pp. 3942–3944.
- [2] M. Marchetto *et al.*, “The ISAC-II Linac Performance”, in *Proc. 13th Int. Conf. on Heavy Ion Accelerator Technology (HIAT'15)*, Yokohama, Japan, Sep. 2015, paper WEM2101, pp. 175–179.
- [3] C. B. Barquest *et al.*, “Web-Based Control Room Applications at TRIUMF”, in *Proc. 9th Int. Particle Accelerator Conf. (IPAC'18)*, Vancouver, Canada, Apr.-May 2018, pp. 4832–4835. doi: 10.18429/JACoW-IPAC2018-THPML078
- [4] S. Kiy *et al.*, “Beam Tuning Automation Activities at TRIUMF,” presented at the 15th Heavy Ion Accelerator Technology Conf. (HIAT'22), Darmstadt, Germany, June 2022, paper TU2C4, this conference.
- [5] V.A. Verzilov, R.E. Laxdal, M. Marchetto, and W.R. Rawnsley, “Time Domain Diagnostics for the ISAC-II Superconducting Heavy Ion Linac”, in *Proc. 8th European Workshop on Beam Diagnostics and Instrumentation for Particle Accelerators (DIPAC'07)*, Venice, Italy, May 2007, paper WEPB07, pp. 247–249.
- [6] D. Lanaia and M. Marchetto, “ISAC-II Phasing High Level Application in MATLAB”, TRIUMF, Tech. Rep. TRI-DN-13-18, 2014.
- [7] R. Baartman, “TRANSOPTR: Changes since 1984”, TRIUMF, Tech. Rep. TRI-BN-16-06, 2016.
- [8] R. A. Baartman, “Fast Envelope Tracking for Space Charge Dominated Injectors”, in *Proc. 28th Linear Accelerator Conf. (LINAC'16)*, East Lansing, MI, USA, Sep. 2016, pp. 1017–1021. doi: 10.18429/JACoW-LINAC2016-FR1A01

FRIB COMMISSIONING*

P.N. Ostroumov[†], F. Casagrande, K. Fukushima, K. Hwang, M. Ikegami, T. Kanemura, S.-H. Kim, S. Lidia, G. Machicoane, T. Maruta, D. Morris, A.S. Plastun, H. Ren, J. Wei, T. Xu, T. Zhang, Q. Zhao, S. Zhao
Facility for Rare Isotopes Beams, Michigan State University, East Lansing, MI, USA

Abstract

The Facility for Rare Isotope Beams (FRIB), a major nuclear physics facility for research with fast, stopped and reaccelerated rare isotope beams, was successfully commissioned and is in operation. The acceleration of Xe, Kr, and Ar ion beams above 210 MeV/u using all 46 cryomodules with 324 superconducting cavities was demonstrated. Several key technologies were successfully developed and implemented for the world's highest energy continuous wave heavy ion beams, such as full-scale cryogenics and superconducting radiofrequency resonator system, stripping of heavy ions with a thin liquid lithium film, and simultaneous acceleration of multiple-charge-state heavy ion beams. In December 2021, we demonstrated the production and identification of ⁸⁴Se isotopes and, in January 2022, commissioned the FRIB fragment separator by delivering a 210 MeV/u argon beam to the separator's focal plane. The first two user experiments with primary ⁴⁸Ca and ⁸²Se beams have been successfully conducted in May-June 2022.

INTRODUCTION

The FRIB includes a high-power superconducting driver accelerator, an isotope production target, and a fragment separator. The layout of the FRIB superconducting driver linac is shown in Fig. 1. The linac will provide stable nuclei accelerated to 200 MeV/u for the heaviest uranium ions and higher energies for lighter ions with 400 kW power on the target [1]. The progress with the FRIB linac construction, development, and testing was reported in multiple publications; see, for example, [2–4]. The 400 kW ion beams will be delivered to a thin fragmentation target which is followed by a large-acceptance high-resolution fragment separator (FS). The FRIB rare isotope FS has an angular acceptance of ± 40 mrad in both transverse directions, and momentum acceptance of $\pm 5\%$. The maximum magnetic rigidity of the FS can reach 8 T·m. While many isotopes will be studied in the in-flight experiments, some isotopes will be stopped and re-accelerated up to 12 MeV/u.

In a continuous wave (CW) superconducting (SC) linac, the beam power of 400 kW can be achieved with a low beam current, below 1 emA. Therefore, the space charge effects are mostly negligible in the linac except for the ion source and the Low Energy Beam Transport (LEBT). Although the performance of Electron Cyclotron Resonance Ion Sources

(ECRIS) has significantly improved in the past decades, they still cannot produce sufficient intensities of the heaviest ions to reach 400 kW on target in a single charge state. To achieve 400 kW power on the target for the heaviest ion beams, multiple charge states of the same ion species are accelerated simultaneously. Particularly, in the case of uranium, two charge states (U^{33+} and U^{34+}) will be accelerated before the stripping and five charge states after the stripping at 17 MeV/u. Additionally, multiple-charge-state acceleration after the stripper dramatically reduces the power of unwanted charge states dumped in a charge selector in the first folding segment. The multiple-charge-state acceleration will be used for all ion species with mass numbers above ~ 60 .

LINAC COMMISSIONING

The staged beam commissioning was adopted for the FRIB and started in 2017 and continued until January 2022. The current view of the linac tunnel is shown in Fig. 2. Each of the seven beam commissioning stages took less than two weeks. The results of each stage were reported in multiple journal publications and summarized in the HB'21 paper [5]. In the current paper, we report the completion of the beam commissioning at FRIB and initial experience working with 1 kW ion beams for the first two nuclear physics user experiments.

On April 25, 2021, the FRIB accelerator became the highest energy continuous wave linear accelerator in the world after acceleration of ⁸⁶Kr ion beam to 212 MeV per nucleon (MeV/u), achieving 100-percent beam transmission. Later, ¹²⁴Xe ion beam was accelerated to the same energy of 212 MeV/u. All 46 cryomodules with a total of 324 superconducting cavities were powered for the acceleration of ion beams. Successful beam commissioning of the FRIB linac validates the operation of all accelerator systems per design specifications.

Later, in December 2021, we demonstrated the production of ⁸⁴Se isotopes from ⁸⁶Kr ions of the primary beam. The FRIB project was completed in January 2022, and the preparation for user experiments has started [6].

Front End (FE)

Since the early commissioning stages in 2017, significant experience has been gained in operation and tuning of the FE for various ion beam species. The tuning procedure of the FE for any ion beam species from scratch has been developed. Currently, there is a library of settings for about ten different ion beam species.

* Work supported by the U.S. Department of Energy Office of Science under Cooperative Agreement DE-SC0000661, the State of Michigan and Michigan State University.

[†] ostroumov@frib.msu.edu

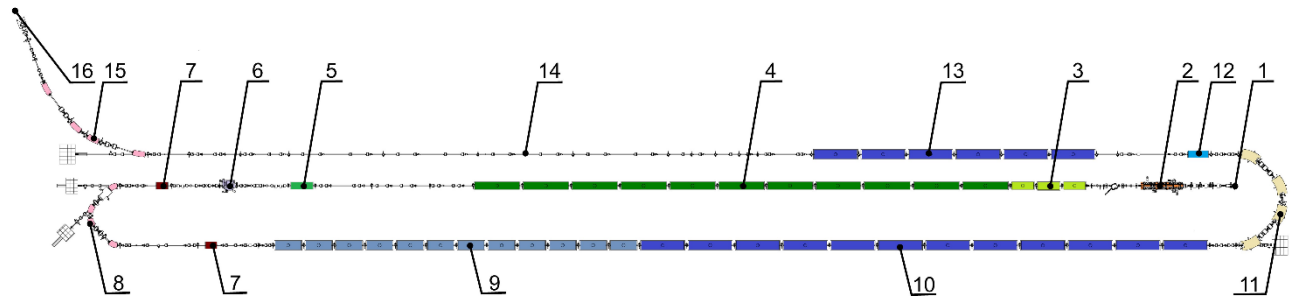


Figure 1: Layout of the FRIB accelerator in the tunnel (the above-grade portion of the Front End is not shown). 1 – ten-meter vertical drop from ion sources (above ground); 2 – 0.5 MeV/u RFQ; 3 – three $\beta=0.041$ QWR cryomodules; 4 – eleven $\beta=0.085$ QWR cryomodules; 5 – $\beta=0.085$ bunching cryomodule; 6 – Lithium and carbon stripper modules; 7 – multi-gap buncher; 8 – room temperature folding segment; 9 – twelve $\beta=0.29$ HWR cryomodules; 10 – twelve $\beta=0.54$ HWR cryomodules; 11 – superconducting folding segment; 12 – $\beta=0.53$ bunching cryomodule; 13 – six $\beta=0.54$ HWR cryomodules; 14 – beam transport to the target; 15 – beam delivery system; 16 – fragmentation target.



Figure 2: FRIB tunnel after the completion of installation.

The FRIB LEBT, unlike many other LEBTs elsewhere, has been designed and built to extract and accelerate all ion beam components produced in the ECRIS. The energy of the ions of interest is 12 keV/u. The accelerated beam components are separated and selected after the first 90° bending magnet. The charge selection segment and the whole FRIB LEBT can provide the no-loss achromatic transport of dual-charge-state heavy ion beams.

ECR ion sources have many parameters that cannot be measured directly, are cross-coupled, and fluctuate during the ion source operation. Therefore, the parameters of multi-component ion beams extracted from the ECRIS are also changing. We found the 6D vector of the beam position in the phase space downstream of the RFQ is one of the most sensitive beam properties. We also noticed that if the ECRIS is cold started to produce the same ion species that were used previously, there is a slight deviation of the beam phase space parameters after the charge state selection.

If the transport system is slightly misaligned, the 4D beam position of the ions of interest in the multi-component ion beam depends on the space-charge forces. It results in a change of the 6D beam position vector downstream of the RFQ. The beam energy and phase after the RFQ are sensitive to the beam transverse misalignment in the multi-harmonic buncher and the first accelerating cells of the RFQ. There is a correlation of the 6D beam vector downstream of the RFQ with the total ECRIS platform drain current even if the current of the ion of interest remains unchanged. We

have developed a beam dynamics model to adjust the parameters of the LEBT and re-tune the beam 6D vector in the MEBT to the reference value if the beam extracted from the ECR behaves differently. This model will be improved by using machine learning shortly.

Auto-start of Resonators

FRIB consists of 324 SC [8] and 8 Room Temperature (RT) resonators operating at five different frequencies. The stable operation of resonators is provided by the FRIB-developed digital Low-Level RF (LLRF) control system [9]. The operational experience shows that the peak-to-peak errors of the amplitudes and phases of RF fields are mostly within $\pm 0.2\%$ and $\pm 0.1^\circ$, which are an order of magnitude less than the original specification. Since the early stage of RF conditioning of resonators, an automated turn-on procedure has been developed. The auto-start code implemented at the Input-Output Control (IOC) level reduces the resonator turn-on time to about 40 seconds and excludes possible human operator errors. Most HWRs experience multipacting after a warm-up event and, therefore, require reconditioning. Now, this procedure is also automated.

The auto-start and fast-recovery capabilities are especially beneficial to meet the high availability requirement of the RFQ operating in CW mode. The cold start of the RFQ requires up to 45 minutes to the highest power level due to using of the cooling water flow for the frequency tuning. Whereas the fast-recovery in a warm state takes no more than 30 seconds.

Model-Based Beam Steering Correction

There are 144 Beam Position and Phase Monitors (BPM) and 127 correctors distributed along the linac. The orbit response matrix (ORM) method was applied previously for the beam steering correction in the first segment of the linac [10]. This method was based on the measured response matrix elements. This method works well but takes too much time for the measurements. Therefore, we have decided to use a response matrix calculated with the computer model of the linac. This approach also works well, and it is

much faster. The model-based ORM method works best if it is applied to short sections of the linac containing 10 correctors and a slightly larger number of BPMs. In most cases, the one iteration is sufficient for the beam trajectory alignment within ± 0.5 mm. The second iteration sometimes is necessary for longer linac sections due to misalignment of the beam optics devices and minor hysteresis in the superconducting (SC) dipole coils.

Phase Scan Procedures

The phase scan procedure was applied to set the synchronous phases for SC resonators and bunchers. This procedure constitutes the measurement of the beam-induced signal in downstream BPMs as a function of the resonator RF field phase, as described in [11]. Since the auto-start of resonators has become available, the phase scan procedure is also automated and can be applied to many cavities without human intervention. The phasing of short sections of the linac (6–8 cavities) is usually alternated with the model-based beam steering correction to align the beam with the accelerator axis.

The experiments with rare isotope beams last just about a week or less. For different experiments the FRIB linac should provide various primary beams at different energies, and shortening the accelerator setup time is, therefore, critical to meet the requirements of the FRIB Users community. An automated phase scan procedure reduces the tuning time, but setting up a new velocity profile in the entire linac requires at least 15 hours.

Recently we developed and tested a model-based instant phase setting in the linac segments 1, 2, and 3. The coordinates of the resonators along the linac are well known from the alignment survey, and RF field distributions are available from simulation models. The accelerator model can calculate the phase settings of all resonators for the required energy of the given ion species if the cavity calibration data is provided. The field levels in resonators are calibrated with the beam time-of-flight measurements. The phase calibration of each resonator and BPM is generated using the standard phase scan procedure with the beam of known energy. As a result of such calibration, a static phase shift in each RF line and BPM cable can be determined with respect to the RF reference clock. The model-based Instant Phase Setting (IPS) was verified with standard phase scan procedure in all linac segments. Currently, we use IPS routinely for the machine setting to run 1 kW beams and quickly recover from fault-cavity cases. The IPS dramatically reduced the machine setting time. In April 2022, the beam tune from the ion source to the target was established in just 6 hours. With minor adjustments near the charge stripper this tune was used during the first FRIB user experiment.

Liquid Lithium Stripper Testing

To achieve the design heavy ion beam energies above 200 MeV/u and beam power up to 400 kW, the FRIB linac requires a stripper at an intermediate energy of 17–20 MeV/u. The solid foils used previously for stripping heavy ions

are easily damaged at the beam intensities required for the FRIB primary beams on the fragmentation target. To overcome the existing technical limitations associated with the stripping of high intensity heavy ion beams, FRIB developed and commissioned a liquid lithium stripper [12]. The charge stripper is based on a molten liquid lithium film with thickness of ~ 10 – 20 μm , flowing at ~ 60 m/s in the ultra-high vacuum environment. We experimentally confirmed that the windowless liquid lithium thin film could be used as a charge stripper by successfully running ^{124}Xe , ^{36}Ar , and ^{238}U beams through the charge stripper. Figure 3 shows the charge state distributions of xenon and uranium beams after the liquid lithium stripper. The long-term operation with the liquid lithium stripper was tested during the user experiment with the primary ^{48}Ca beam.

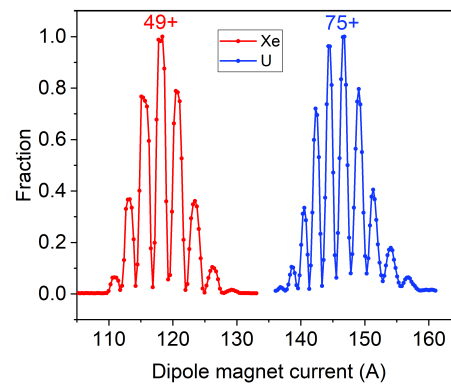


Figure 3: Xenon (red) and uranium (blue) charge state distributions after the liquid lithium stripper. The thickness is 1.05 mg/cm² for the xenon and 1.40 mg/cm² for uranium beams.

EARLY OPERATION

The Linac has been tuned for the ^{48}Ca primary beam in April 2022 to enable the first FRIB experiment for the production of rare isotopes. In June, we ran ^{82}Se for the second FRIB experiment. Currently, 1 kW beam power on the target is limited by the operational safety envelope. In October, the linac will provide up to 3 kW beam power on the target with the following increase to 10 kW in a year.

Carbon Stripper

While the liquid lithium stripper was used for extended operation during the first experiment, we have decided to use a rotating carbon stripper for the beam power on a target below 10 kW. The carbon stripper is attractive due to the simplicity of operation. The carbon foils with a diameter of 100 mm and thickness of 1.0 mg/cm² and 1.5 mg/cm² are being used for stripping FRIB ion beams. The foil's rotation speed can be as high as 150 rpm. Also, the foil is moved vertically to cover the entire area. The calculations show that for the heaviest ions at 10 kW on the target, the stripper lifetime is limited by radiation damage and equals

to about a week. The damaged stripper foil can be replaced in several hours. Figure 4 shows the viewer image of the stripper foil, rotating at 101 rpm with a 440 W, 20 MeV/u krypton beam on it. In this particular case, the temperature of the interaction spot can reach $\sim 600^\circ\text{C}$, and a long tail of the heated area is seen in the image.

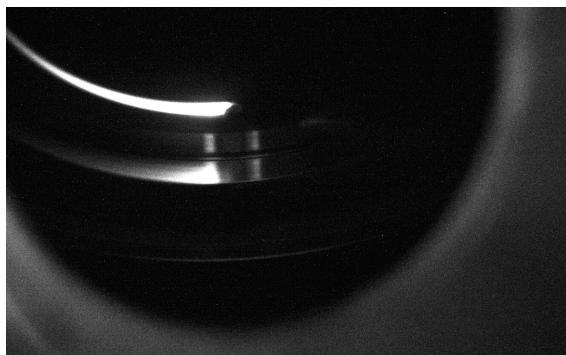


Figure 4: Krypton beam on the rotating carbon stripper.

Beam energy after the stripper fluctuates due to the slight difference in the foil thickness at different radii, as shown in Fig. 5.

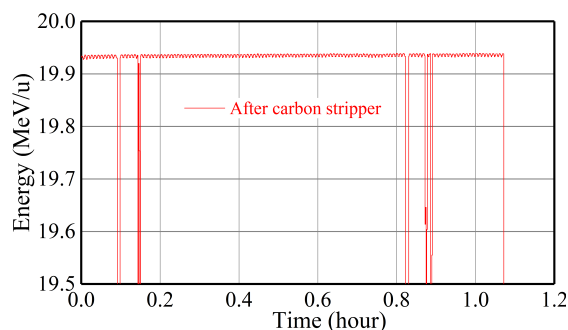


Figure 5: ^{82}Se beam energy after the stripper.

Linac Operation

Since the preparation for the first experiment, the linac started to operate around the clock, and the training of operators to support the machine operation was a high priority for the accelerator physicists. The linac "reference tune" is developed and set up for the operation by accelerator physicists. Several user-friendly high-level applications have been developed and handed over to operators to verify the beam quality and restore the reference tune. The "Settings Manager" application has been developed to manage the accelerator physics settings, which features convenient device settings loading and saving and value scaling to work with various ion species. The "Settings Manager" was recently upgraded to save beam signals from non-interceptive diagnostics devices.

During the linac operation for the rare isotope production, the operators watch the beam parameters from 144 BPMs. Typical BPM readings plotted as differences between live and reference linac signals are shown in Fig. 6. The gradual increase of the phase difference in ~ 100 m drift space

after the LS3 corresponds to a slight change of the beam energy by ~ 20 keV/u with respect to the reference energy of 165 MeV/u. The higher magnitude of the BPM live read-out corresponds to a slightly higher beam current and power than for the reference tune. The operators can identify possible issues with the accelerator subsystems by watching the live differential data from the BPMs.

Run permit and machine protection systems (MPS) are fully functional at the FRIB facility. The MPS system watches the status of nearly all devices, namely the RF resonators, bending magnets, charge stripper rotation, vacuum levels, target state, etc.. For the operation with 1 kW beam power, the Beam Loss Monitors (BLM) were incorporated into the MPS system.

Beam Power

The FRIB was designed and built to deliver a 400 kW beam to the target and produce rare isotopes for science. We have developed a plan to increase the beam power on the target within six years. There are two main reasons for such an approach:

- many experiments do not require high power and it is reasonable to conduct these experiments in early stages of the FRIB operation;
- we need to gain experience with maintaining the linac with low uncontrolled beam losses and handling high power beams in the target hall.

The machine setting is developed using a low average power pulsed beam. The power ramp-up of the CW beam is performed using attenuators and slits in the LEPT. While working with a 1-kW beam, we do not see notable uncontrolled beam losses. Figure 7 shows the ^{82}Se beam current along the linac. The beam current increases after the stripping (D2353) and drops after selecting the charge state 33^+ . The signals from the Halo Monitor Rings (HMR), Neutron Detectors (ND), and Ionization Chambers (IC) [13] in the post-stripper linac are plotted in Fig. 8. We see elevated neutron flux coming from the stripper and target. The beam losses were not observed on the HMRS installed between the cryomodules.

The primary beam has been tuned to the target with the 0.3 mm-rms radius. The 1 kW beam image on the beryllium target is shown in Fig. 9. A four-segment collimator with temperature sensors upstream of the target helps to control the beam position.

CONCLUSION

The FRIB linac beam commissioning is complete, and various primary beams are available for rare isotope production for user experiments. Two nuclear physics experiments have been conducted with 1 kW primary beams.

ACKNOWLEDGEMENTS

The authors are grateful to the entire FRIB team for supporting the beam commissioning and achieving the project goals.

Content from this work may be used under the terms of the CC BY 4.0 licence (© 2022). Any distribution of this work must maintain attribution to the author(s), title of the work, publisher, and DOI

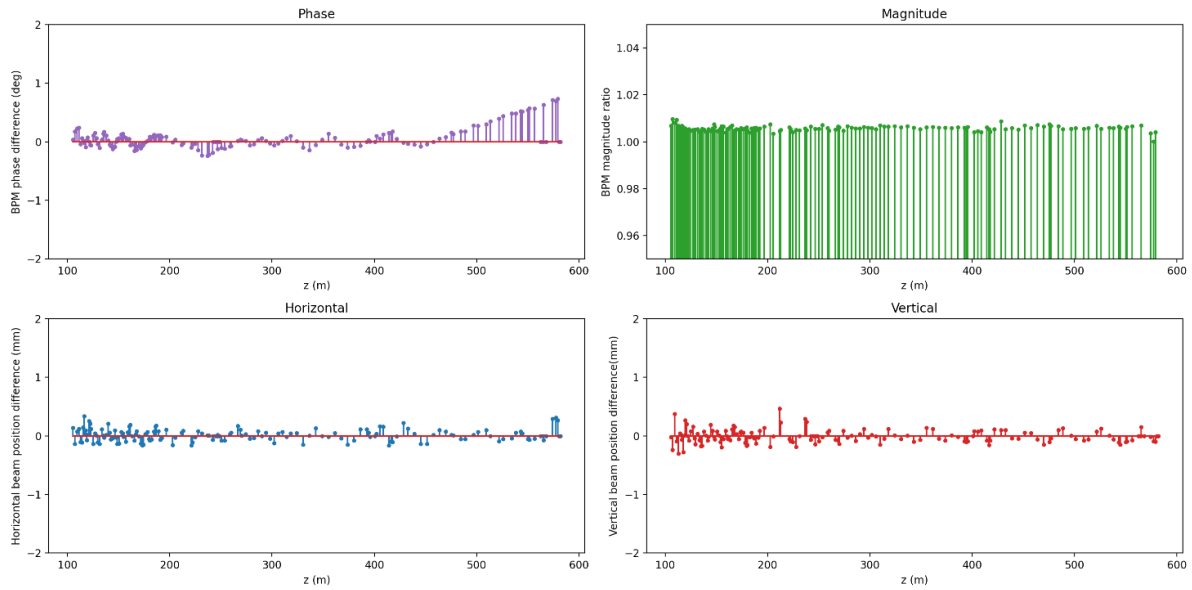


Figure 6: BPM readings during the operation. Plots show the difference between the readout and reference setting of the linac for the bunch phase (top-left), horizontal and vertical (bottom) beam positions. Plot (top-right) shows the BPM signal magnitude normalized to the reference signal strengths.

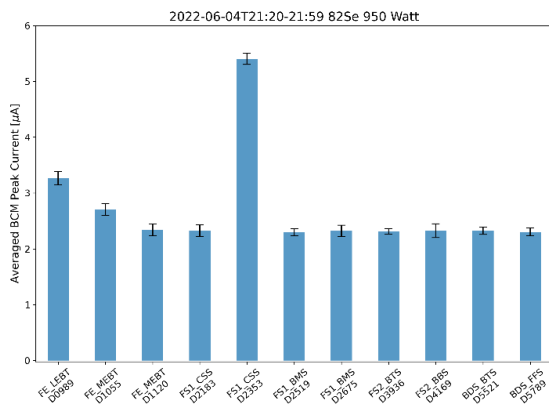


Figure 7: The ^{82}Se beam current averaged over the 60 sec along the linac. The error bar shows the standard deviation due to the noise in the signal. The D-numbers near the horizontal axis show the location of the BCMs along the linac in decimeters. The first BCM is located upstream of the RFQ. The last BCM is located upstream of the target.

REFERENCES

- [1] J. Wei *et al.*, “Advances of the FRIB project”, *Int. J. Mod. Phys. E*, vol. 28, no. 3, p. 1930003, 2019. doi: 10.1142/S0218301319300030
- [2] Q. Zhao *et al.*, “FRIB Accelerator Beam Dynamics design and Challenges”, in *Proc. HB’12* Beijing, China, Sep. 2012, paper WEO3B01, pp. 404-408.
- [3] J. Wei *et al.*, “Accelerator Challenges of Hadron Linacs and the Facility for Rare Isotope Beams – Extending High Beam Power for Protons to Heavy Ions”, in *Proc. HB’14*, East Lansing, MI, USA, paper MOZLR07, pp. 12-17.
- [4] J. Wei *et al.*, “FRIB Commissioning and Early Operation”, in *Proc. IPAC’22*, Bangkok, Thailand, Jun. 2022, pp. 802–807. doi: 10.18429/JACoW-IPAC2022-TUIYGD3

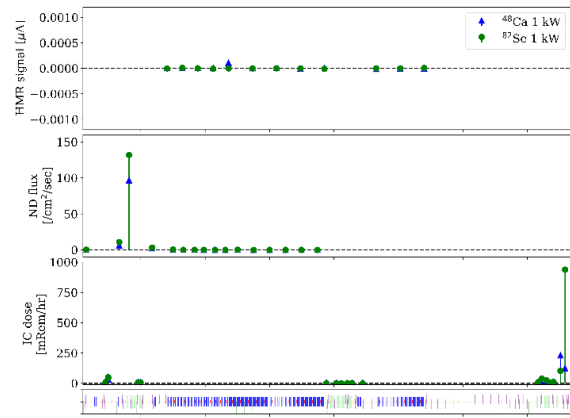


Figure 8: The signals from the beam loss monitors in the post-stripper section of the linac.

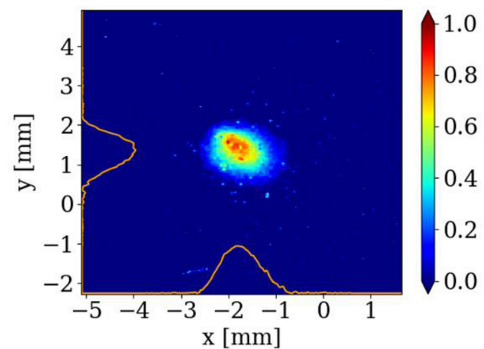


Figure 9: The 1 kW ^{82}Se beam image on the beryllium target.

- [5] P.N. Ostroumov *et al.*, “Status of FRIB Commissioning”, in *Proc. HB’21*, Fermilab, Batavia, Illinois, October 2021, pp. 205-207. doi: 10.18429/JACoW-HB2021-WEDC3

- [6] J. Wei *et al.*, “Accelerator commissioning and rare isotope identification at the Facility for Rare Isotope Beams”, *Mod. Phys. Lett. A*, vol. 37, p. 2230006, 2022.
doi:10.1142/S0217732322300063
- [7] E. Pozdeyev *et al.*, “FRIB Front End Construction and Commissioning”, in *Proc. IPAC’18*, Vancouver, BC, Canada, April 2018, pp. 58–62.
doi:10.18429/JACoW-IPAC2018-M0ZGBF1
- [8] T. Xu *et al.*, “Completion of FRIB Superconducting Linac and Phased Beam Commissioning”, in *Proc. SRF’21*, East Lansing, MI, USA, Jun.-Jul. 2021, pp. 197–202.
doi:10.18429/JACoW-SRF2021-M00FAV10
- [9] S. Zhao *et al.*, “The LLRF Control Design and Validation at FRIB”, in *Proc. NAPAC’19*, Lansing, MI, USA, Sep. 2019, pp. 667-669.
doi:10.18429/JACoW-NAPAC2019-WEPLM03
- [10] P.N. Ostroumov *et al.*, “Beam commissioning in the first superconducting segment of the Facility for Rare Isotope Beams”, *Phys. Rev. Accel. Beams*, vol. 22, p. 080101, Aug. 2019. doi:10.1103/PhysRevAccelBeams.22.080101
- [11] P.N. Ostroumov, M. Hausmann, K. Fukushima, T. Maruta, A.S. Plastun, M. Portillo, J. Wei, T. Zhang, and Q. Zhao, “Heavy ion beam physics at Facility for Rare Isotope Beams”, *J. Instrum.*, vol. 15, p. P12034, 2020.
doi:10.1088/1748-0221/15/12/p12034
- [12] T. Kanemura *et al.*, “Experimental Demonstration of the Thin-Film Liquid-Metal Jet as a Charge Stripper”, *Phys. Rev. Lett.* vol. 128, p. 212301, May 2022.
doi:10.1103/PhysRevLett.128.212301
- [13] S. Lidia *et al.*, “Overview of Beam Diagnostic Systems for FRIB”, in *Proc. IBIC’15*, Melbourne, Australia, 2015, p. 221-225. doi:10.18429/JACoW-IBIC2015-MOPB071

THE NEW GANIL BEAMS: COMMISSIONING OF SPIRAL 2 ACCELERATOR AND RESENT DEVELOPMENTS

H. Frånberg-Delahaye*, GANIL, Caen, France

Abstract

The GANIL installation at Caen in France has been operating with warm temperatures cyclotrons for heavy ion beam physics since 1983. The accelerated stable beams widely ranges from Carbon to Uranium beams. Low energy and post accelerated radioactive ion beams are also being provided.

The GANIL laboratory has newly increased their different ion beams and energies available with the installation and commissioning of a superconducting linear accelerator – SPIRAL2 and its experimental areas. The construction of SPIRAL2 started in 2011, the first beam was extracted at low energy in late 2014 with pre-acceleration in 2017 and since 2021 the new installation delivers beam for nuclear physics experiments.

This paper will cover the commissioning and power ramp up of the SPIRAL2 installation at GANIL with its superconducting LINAC – but also the latest development of stable and radioactive ion beams at the cyclotron facility of GANIL.

GANIL COMPLEX

GANIL will in November 2022 celebrate the 40 years from the first extracted beam from the two separated sector cyclotrons (SSC). The first accelerated and extracted beam was a $^{40}\text{Ar}^{16+}$ beam, accelerated to 44 MeV/A. The same beam was used for an experiment 2 months later in January 1983.



Figure 1: The Running GANIL facilities in 2022. On the right is the cyclotron facility and on the left is the SC-LINAC facility.

In the 2015 version of HIAT conference O. Kamalou presented an article of the GANIL Operation Status and New Range of Post-Accelerated Exotic Beams [1]. In the same conference J. M. Lagniel presented the Advances of the SPIRAL2 PROJECT [2] which had just commissioned the ion sources and the low energy beam transfer lines (LEBT), the SC-LINAC was still under installation.

* hanna.franberg@ganil.fr

Today GANIL is running two separated facilities, not yet connected as can be seen in Fig. 1. On the right hand side of the Fig. 1 is the cyclotron complex. The ion beams are produced on the far right hand side before accelerated in one or two steps in the two SS cyclotrons up to 95 MeV/A. On the left in the cyclotron buildings are the RIB factory SPIRAL1. The experimental halls, where the users from different fields explore the stable and radioactive beams, are on the upper part of the figure. On the left hand side in Fig. 1 is the SPIRAL2 installation with a more detailed description in Fig. 2. The four injectors used at GANIL are opposite to

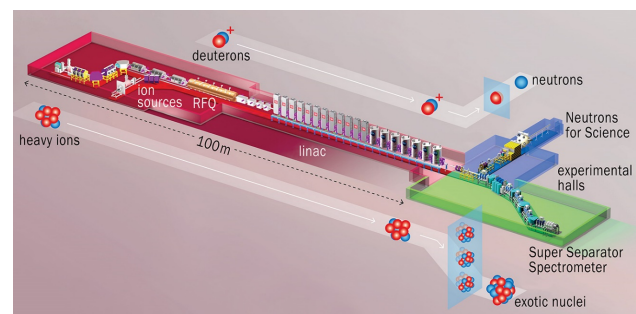


Figure 2: A schematic view over the SPIRAL2 installation, the two injectors on the right hand side.

each other in the two facilities. In the near future the two facilities will be connected and beam from either of the two facilities will be used in a new experimental area as seen in the section “Next steps for GANIL”.

From here we will refer to the cyclotron facility and the SC-LINAC facility (Fig. 3). In total GANIL is running seven ECR ion sources, one FEBIAD ion source, one ECR charge breeder, four injectors, five cyclotrons, one RFQ and one superconducting LINAC, delivering stable ion beams (SIB) and radioactive Ion beams (RIB) to nine experimental areas. The facility is operated 24h 7 days a week for 8 to 9 months per year. Since 2019 the cyclotrons and the SC-LINAC facilities are sharing the operation time, meaning that at GANIL there is a cyclotron season and a super conducting LINAC season. This arrangement divide individually the two facilities into separate 4-6 months uptime periods with 6-8 months maintenance and upgrading periods each year. This gives an opportunity to work on upgrades and regular improvements of ion beam transport and new beams while providing beams 8-9 months a year.

While the Cyclotron facility celebrate 40 years of operation the SC-LINAC is still in the first years of regular operation. In here we will present the resent upgrades at the cyclotron facility presented in details in several articles [3] and a short resume of the SC-LINAC commissioning as requested [4].

Content from this work may be used under the terms of the CC BY 4.0 licence (© 2022). Any distribution of this work must maintain attribution to the author(s), title of the work, publisher, and DOI

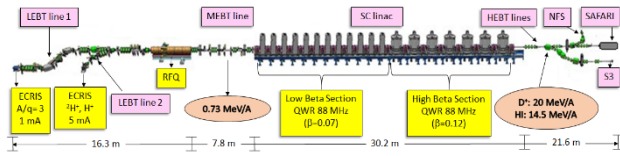


Figure 3: SC LINAC layout. At the left hand side the two injectors coming together in the LEFT beam line. The RFQ and the MEFT beam line and then the 26 accelerating cavities and their cryo-modules, each one separated by a warm quadrupole section and a beam diagnostic.

SC-LINAC – SPIRAL2 PROJECT

The SPIRAL2 project, launched in 2005 was designed to produce high-power proton, deuteron and heavy-ion beams to be accelerated in a superconducting linear accelerator. The beams were to be delivered in three different experimental areas for nuclear physics research. Two of the experimental areas are constructed and the third one was put on hold in 2013 [5]. The experimental areas and the production of RIBs were a part of the initial project. The idea was to produce RIB in one InFlight (S3) and one ISOL facility (Phase 2) to complement the neutron rich side of the table of isotopes and the production of super heavy ion for fundamental applications.

The construction was limited to the injectors and the high-power superconducting LINAC with two experimental areas called “Neutrons for Science” (NFS) [6] and “Super Separator Spectrometer” (S3) [7] (see Fig. 3).

The new facility was constructed with two injectors, the proton/deuteron source is a 2.45 GHz ECR source (SILHI like [8] it is designed to produce 5 mA proton and deuteron beams in CW or pulsed modes or pulsed modes.

The heavy-ion source was initially an 18 GHz ECR source PHOENIX V2 using three normal conducting coils and a large permanent magnet. It was designed to produce heavy ions with $A/q \leq 3$ with a total extracted beam current up to 15 mA CW at 60 kV. The design allows the installation of a dedicated oven reaching 1600 °C for the production of metallic ion beams [9]. It was later on upgraded to a Phoenix V3 [10] also operating at 18 GHz. This modification was performed to be able to provide the intensities of the beams needed for the S3 experiments.

The installation and the commissioning of the accelerator complex was programmed in phases taking into account the availability of the personnel while continuing the operation of the cyclotron facility. The start-up and tests of all equipment have been performed with staff from GANIL and the external collaborating facilities for SPIRAL2. The ion sources and their low energy beam transport (LEBT) lines was commissioned while parts of the SC LINAC was still under installation.

The design goals of the installation are to be seen in Table 1.

The first SPIRAL2 beam at GANIL (protons) was produced by the proton/deuteron source on December 19, 2014. Later on, in January 2020, the first beam of $^{40}\text{Ar}^{14+}$ was

Table 1: The Technical Design Goals of the SPIRAL2 Installation

Particle	H ⁺	D ⁺	Ions	Future
A/q	1	2	3	7
Max I (mA)	5	5	1	1
Max energy (MeV/A)	33	20	14	8.5
Max beam power (kW)	165	200	44	51

produced, with an intensity of 100 μAe , and since then ^{58}Ni at 40 kV and 40 μA have been produced, as requested by the S3 experimental facility. A strong and intense development program is ongoing for the injector, the focus of the next beams to be produced; extracted and accelerated are ^{48}Ni , $^{48,50}\text{Ti}$, $^{50,54}\text{Cr}$ for the S3 experiments, with intensities up to 2 μA for A/Q around 3 [3].

The building of SPIRAL2, is actually constructed by free standing blocks due to seismic reasons. The ion sources and LEBT are in one block and the RFQ, Medium energy beam transport line (MEBT), SC LINAC and high energy beam transport section (HEBT) in a second block and the two experimental halls in a third and fourth block. This was taken advantages of during the installation and commissioning of the equipment in the separated blocks. The RFQ and the MEBT was done in parallel of the commissioning of the ion sources from 2014. The low level RF tuning operations of the RFQ, including the voltage law bead-pull measurements and the 40 plunger adjustments ended in March 2015. From these primary tests the TOUTATIS simulations indicated that the theoretical transmission of beam should be 99.7%. The resonance frequency of the RFQ is 88.0159 MHz, and the beam is accelerate up to 0.75 MeV/A. The RFQ and the MEBT was commissioned using a specific diagnostic box before the SC LINAC, physically separating it from the LINAC but allowing to calibrate the beam and adjust the RFQ operation completely before the commissioning of the LINAC. The RFQ was commissioned at 114 kV with a pulsed 4.8 mA proton beam with 100% transmission in end of 2015 [11].

In the years of 2015–2018 the commissioning the RFQ and the MEBT was performed with beams of H⁺, $^4\text{He}^{2+}$, $^{18}\text{O}^{6+}$ and $^{40}\text{Ca}^{14+}$. The diagnostic box installed [12] before the SC-LINAC confirmed 100% transmission [13] showing no beam losses during this first accelerator stage of the installation (Fig. 4).

The diagnostic plate included temporary diagnostic tools for commissioning of the RFQ. The diagnostics used were ACCT and DCCT [14] for intensity monitoring, wire profilers for the beam size and position, Alison type scanners for emittance measurements in H and V direction, TOF (Time of Flight) monitor for energy measurements and phase coupled with two BPMs [15] (Beam profile monitor), a BEM (Beam extension monitors) [16] for the longitudinal emittance measurements [17] and FFC (fast faraday cups).

The validation of the RFQ line was done in November 2018 and the D-plate was removed, the full MEBT was

Content from this work may be used under the terms of the CC BY 4.0 licence (© 2022). Any distribution of this work must maintain attribution to the author(s), title of the work, publisher, and DOI

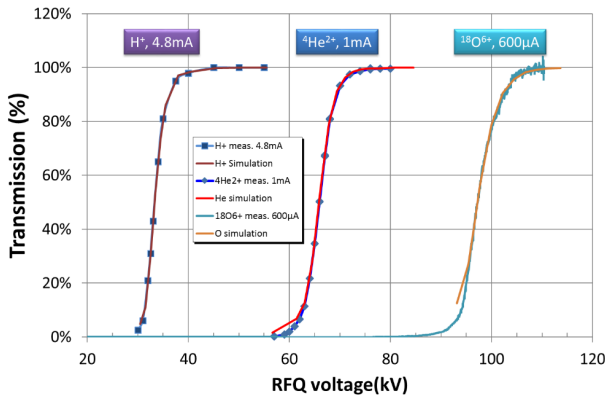


Figure 4: Transmission in the RFQ of the three reference Q/A.

installed and the line was physically connected to the LINAC. In the full MEBT line the three re-bunchers and a beam bunch selector (SBS) [18] was installed. The SBS allows an operation of 1 bunch over 100 up to 1/10000, needed primarily for experiments requiring a precise timing between the bunches to insure that there is no overlap of the bunches for precise energy measurements.

In the meantime the SC-LINAC installation was ongoing and in 2017 the cryogenic system for the cryo-modules were commissioned with a first complete cool down in November 2017 [19]. The RF tests in the LINAC were performed in parallel to the operation of the cyclotrons during the first semester in 2019.

The GANIL cyclotron and SPIRAL2 installations are constructed and operated under French nuclear authority regulations. Before the authorisation of construction a file explaining the full operation and safety measurements were sent in. The different systems for the safety controls were then constructed and tested. The final authorisation to start the facility with acceleration of the beams in the LINAC was followed four months later after having complete testing and documentation of the different safety systems. Only after this the full authorisation was given and the beam could finally be sent to the LINAC.

The SC LINAC is designed with 26 cavities, 12 A-type cryo-modules each comprising one low- β cavity and 7 B-type cryo-modules with two high- β cavities [20, 21].

The Power Up of the Beams

In an early stage of the project the strategy for the beam commissioning of the LINAC was to go in four phases as shown in Fig. 5. The proton beam, were to be sent to the SAFARI beam dump during this commissioning.

1. Beam transmission at low energy as given by the RFQ.
2. Increase of the Beam energy through the LINAC
3. Increase of the Beam intensity while opening the slits cutting the beam in the LEBT.
4. Increase of the duty cycle.

During the phases 3 and 4 the beam losses were controlled in all the LINAC by the beam loss monitors (BLM) installed

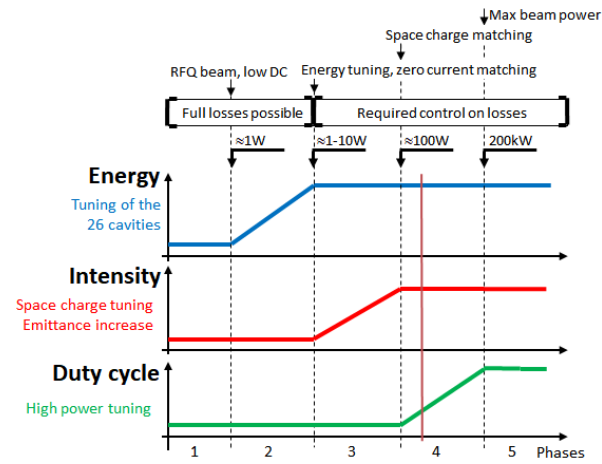


Figure 5: Transmission in the RFQ of the three reference Q/A.

around the LINAC, the intensity (ACCTs) and the pressure variations all along the LINAC.

The first beam, a 1 W proton beam, without energy increase and at low intensity was transported through the SC-LINAC tuned in a rebuncher mode in the middle of November 2019. During the following two weeks a beam energy increase up to 33 MeV with a pencil beam of 200 μ A and a full 6.4 W beam was sent to the SAFARI beam dump. Before the winter shut down in December, this beam was sent to the NFS experimental area for full identification of the energy and composition of the beam.

From here on, the LINAC operation is performed with the GANIL teams, also working on the operation of the Cyclotrons. The beam commissioning of the LINAC are therefore limited to 4–5 months every year at the moment.

The phase three continued in the second semester of 2020, after the cyclotron run programmed for the first semester of 2020. After restarting the full complex, retuning the beam and do all the initial tests as in the end of 2019, the proton beam intensity was increased to 4.8 mA and the in the following week, the beam power were then increased to 16 kW (Fig. 6) using a 10% duty cycle, with a beam transmission near of 100% into the LINAC and high energy lines.

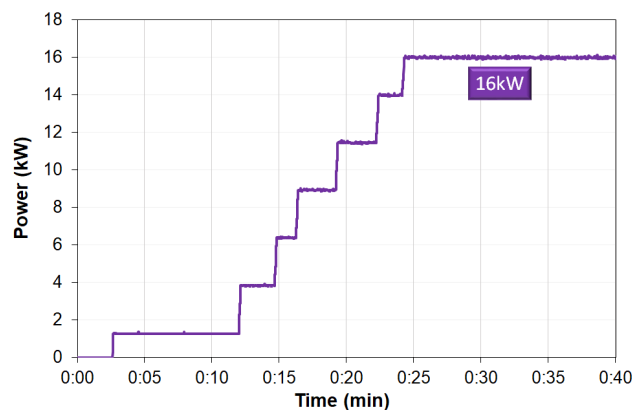


Figure 6: The beam power up to 16 kW proton beam.

For each step of the power up the beam the transmission was monitored throughout the installation from the MEBT section, all through the LINAC and in the HEBT section [4]. The results was compared to theoretical TRACEWIN calculations for confirmation.

The next step in the commissioning were to proof the capacity of accelerating heavier ions, starting with deuterons. Although, accelerating the deuterons, an eventual problem of activation should be minimized. So, in the last weeks of operation in 2020 a 4He beam were accelerated to simulate the deuteron beam transport.

After the run in 2019 and 2020, 2021 was the start of the physics experiments and real challenges of the accelerator. The different systems (security, RF, LLRF, diagnostics) was pushed to their limits to validate the operation. While in 2020 the technical and scientific goals were to proof the operability and the capacity of the different systems of the installation, showing the capabilities of controlling and maintaining an accelerated beam of high intensity. The 2021 program was to proof different beams for physics could be produced, accelerated and delivered for physics. The commissioning is no longer driven by pushing the limits of the installation as designed but is in concurrence with the need for physics. It should be remembered that the SC LINAC installation was designed for a 200 kW deuteron beam (40 MeV / 5 mA) in continuous mode and the NFS experiments are requesting proton and deuteron beams of very low repetition rate. The constructed S3 experimental area is to be commissioned with beam within two years. Their needs are heavy ion beams from the $A/q \leq 3$ ion source in a first time.

The first beam of 2021 was a deuteron beam of 20 MeV/A. Starting with the same procedure as in Fig. 5, the duty cycle went from 1 to 100 Hz using the SBS. A first experiment of 11 MeV/A deuteron beam on a Be and Li converter was performed in the middle of September in NFS followed by a 20 MeV/A beam on the rotational converter for the neutron beam production at NFS. Beam intensities of 47 μ A was used during these tests.

During the shutdown periods, technical modifications have been performed and corrections identified during the run have been made. During the 2021 run one of the cavities went out of operation, to continue the program foreseen, the accelerator was tuned without this cavity. The tuning was performed and this mode validated before the correction of the breakdown during the winter break.

Experimental Areas for LINAC

The S3 installation will be ready for stable beams as of end of 2023. During the second semesters of 2022 and 2023 the facility shall proof the possibility to accelerate the ion beams of 48Ni, 48,50Ti, 50,54Cr with intensities up to 2 μ A for A/Q around 3. A new injector increasing the capacities for heavy ion production with a goal of $A/q \leq 7$ are under study for GANIL. A superconducting ion source, a second RFQ for pre-acceleration and bunching should be installed. This project is under development, fully founded and should be installed and commissioned in 2026 as of the plans today.

CYCLOTRONS

The Cyclotron facility combined with the SPIRAL1 facility provides Stable Ion Beams (SIB) since 1983 and Radioactive Ion Beams (RIB) since 2001 for Physics experiments.

Two ECR4 ion sources, commissioned in 1992, are coupled to two cyclotrons (C01) and two separated section cyclotrons (SSC) where the beams can be successfully accelerated after stripping and bunching in between.

At the cyclotron facility the SIB can be produced at three positions, any of the two injectors consisting of ECR4 (14.5 GHz) ion sources, or by the ECR booster directly.

The beam can therefore be delivered to five experiments in parallel if requested from three points in the production of the SIB. A low energy experimental area directly after the injectors (0.3 to 1 MeV/A), a medium energy experimental area (3.7–13.7 MeV/A) take the beams after the first SSC and finally after the full acceleration (24–95 MeV/A). The beam can then be shared by two experimental areas at the same time. In parallel, a SIB can be produced directly at the SPIRAL 1 installation, either from the ECR1+ ion source or the ECR booster, and sent to a dedicated experimental room.

If RIBs are requested, it can be delivered either as 1^+ low energy or as post-accelerated beams from SPIRAL1, with the ISOL method. In one of the experimental areas there is the possibility to use a rotating or fixed target for beams up to 2 kW for fragmentation reactions with Inflight method to be used directly or on a secondary target.

The eight experimental areas at the cyclotron facility as seen on the right hand of the cyclotrons in Fig. 1 can take any of the SIB for experiments of fundamental nuclear physics, applied physics, industrial applications or any application needed SIB.

There are continuously ongoing upgrades and developments for the stable beams at the cyclotrons, driven by request from the physics.

The most recent developments are presented in [3] as the Tellurium beams and a $^{232}\text{Th}^{30+}$ beam have been produced (results should be published in a short time), using LCO heating [22]. Developments on adapting the MIVOC technique to the ECR4 sources are still ongoing to enlarge isotopes available to produce beams. It is the same group that work on the operation and development of the 4 injectors, p/d source, Phoenix V3 and ECR4 ion sources. The development of new beams and more stable operation are therefore mutualised.

Since the 2015 paper [1] an upgrade has been made of the SPIRAL1 facility shown in Fig. 7. This upgrade was motivated by the capacity to produce a larger span of radioactive ion beams at GANIL [23].

At the cyclotron facility there are two possibilities for production of RIBs, either through Fragmentation at the inflight facility LISE or by the ISOL method at the SPIRAL1 facility. The RIBs produced today [24] at the SPIRAL1 facility are seen in Fig. 8, this list is being updated regularly due to the ongoing developments.

Content from this work may be used under the terms of the CC BY 4.0 licence (© 2022). Any distribution of this work must maintain attribution to the author(s), title of the work, publisher, and DOI

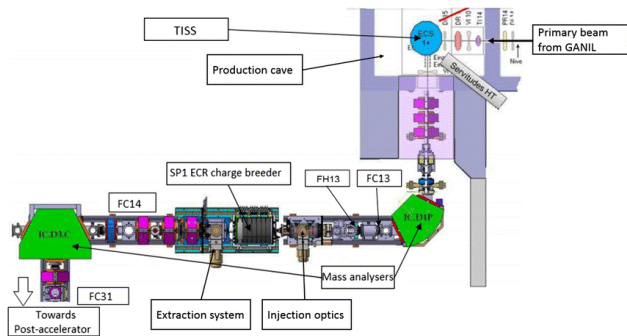


Figure 7: The SPIRAL1 for production of 1^+ radioactive ion beams with the possibility of charge breeding in the ECR booster before post acceleration in the CIME cyclotron.

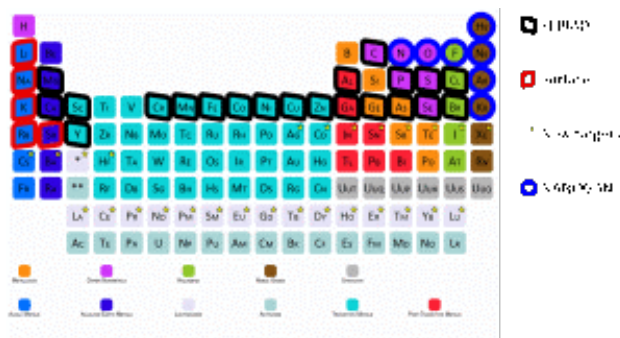


Figure 8: List of beams from the SPIRAL1 facility.

The SPIRAL1 Installation

The SPIRAL1 installation, running in 2001–2014, underwent an upgrade to increase the capacity to deliver RIBs for the physics. This upgrade led to changing totally the design of the target, ion source and the complete beam lines and install a Charge breeder to continue to permit the post accelerated beams for physics. At the SPIRAL1 installation the target is an ISOL target where the stable beams of ^{12}C at 95 MeV/A up to ^{238}U at 8 MeV/A from the SSC are stopped in a thick target (targets of $Z < 41$) or thin targets (no Z restriction). The elements are ionised either by an ECR or FEBIAD ion source. A charge breeder [25] allows to send all the RIBs to a post-accelerator CIME cyclotrons and use this beam for any of the eight experimental areas.

Since the upgrade a dense program for production of new elements is prepared every year and a new exciting exploration of these beams for physics are in the starting block opening up new scientific possibilities for the users of GANIL. Since 2019 the beams are produced with intensities of 106 pps. A $^{47}\text{K}^{10+}$ @7 MeV/A beam was used for physics in 2021. In complementary to the noble gases already produced earlier at GANIL beams of Na, Al, Mg, Cl, K, Rb have successfully been produced, the production of Br was recently produced but still under analysis while writing this article and are ready for further explorations for the needs for physics. The use of molecular beams, broken up in the charge breeder are under investigation and opens up further possibilities of RIBs for the users [26]. The charge breeder

have been upgraded with variable 8–18 GHz RF injection at a power of 200 W. This allows to optimise further the charge state efficiencies and then the RIBs to be post-accelerated with CIME.

NEXT STEPS FOR GANIL

The installation of the S3 installation is ongoing and the installation should be ready for the first beams in end of 2023. The installation will in the first years use the beams from the $A/q \leq 3$ ion source before going to the beams from the $A/q \leq 7$ ion source (2026–2027).

In the end of the S3 installation is a low energy branch [27] consisting of a gas cell setup. This part of S3 installation will be installed before the commissioning of the S3.

As seen in Fig. 9 the DESIR facility is to be installed between the current cyclotron and SC Linac facilities. The construction is foreseen to start in 2023, this installation consist of 150 m of transport beam lines from the SPIRAL1 and the S3-LEB installation towards the low energy experimental hall of DESIR. Exploration of the radioactive ion beams from either of the facilities will therefore be possible in this new experimental complexes as from 2026 after the full installation.

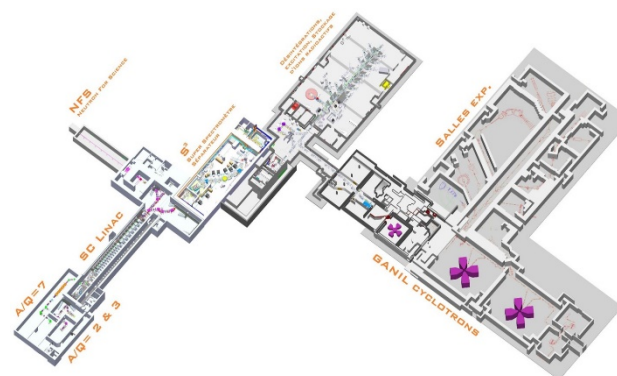


Figure 9: The full GANIL facility as from 2026.

CONCLUSIONS

The last 5 years have been exciting for GANIL, upgrades of the current 40 year old cyclotron facility and the new installation of SPIRAL2 have largely increased the capacity of beams and the capacity of interesting physics to be performed at the installation. The next 5 years will follow by further installations and further commissioning of the installations already in place. As in the span of 5–10 years even more beams, stable and radioactive will come available for the users. For what is the program from 10–30 years from now, new plans are already discussed.

ACKNOWLEDGEMENTS

I like to thank A.K. Orduz, G. Normand and M. Dubois for the help in writing this article.

REFERENCES

- [1] O. Kamalou *et al.*, “GANIL Operation Status and New Range of Post-Accelerated Exotic Beams”, in *Proc. HIAT'15*, Yokohama, Japan, Sep. 2015, paper MOA1C02, pp. 20–22. doi: 10.18429/JACoW-HIAT2015-MOA1C02
- [2] J.-M. Lagniel *et al.*, “Advances of the Spiral 2 Project”, in *Proc. HIAT2015*, Yokohama, Japan, September 2015, paper TUA2I01, pp. 148–152. doi: 10.18429/JACoW-HIAT2015-TUA2I01
- [3] M. Dubois *et al.*, “Radioactive and Stable Ion Beam production at GANIL”, *J. Phys.: Conf. Ser.*, vol. 2244, p. 1012070, 2022. doi: 10.1088/1742-6596/2244/1/012070
- [4] A. K. Orduz *et al.*, “Commissioning of a high power linac at GANIL: Beam power ramp-up”, *Phys. Rev. Accel. Beams*, vol. 25, p.1060101, 2022. doi: 10.1103/PhysRevAccelBeams.25.060101
- [5] P. Dolegieviev, R. Ferdinand, X. Ledoux, H. Savajols, and F. Varenne, “Status of the SPIRAL2 project”, in *Proc. IPAC'19*, Melbourne, Australia, 2019, pp. 844–847. doi: 10.18429/JACoW-IPAC2019-MOPTS005
- [6] X. Ledoux *et al.*, “The neutrons for science facility at SPIRAL 2”, *EPJ Web Conf*, vol. 146, p. 03003, 2017. doi: 10.1051/epjconf/201714603003
- [7] S3 collaboration, “Toward the drip lines and the superheavy island of stability with the Super Separator Spectrometer S³”, *Eur. Phys. J. A.*, vol. 51, p. 66, 2015. doi: 10.1140/epja/i2015-15066-3
- [8] O. Tuske *et al.*, “Light ion source for proton/deuteron production at CEA Saclay for the Spiral2 project”, *Rev. Sci. Instrum.*, vol. 83, p. 102A316, 2012. doi: 10.1063/1.3665963
- [9] C. Barue *et al.*, “Metallic beam developments for the SPIRAL 2 project”, *Rev. Sci. Instrum.*, vol. 85, p. 102A946, 2014. doi: 10.1063/1.4847236
- [10] T. Thuillier *et al.*, “First Plasma of the PHOENIX V3 ECR Ion Source”, in *Proc. ECRIS2016*, Busan, Korea, Aug.-Sep. 2016, paper TUAO05, pp. 48–49. doi: 10.18429/JACoW-ECRIS2016-TUAO05
- [11] M. Di Giacomo *et al.*, “RF Commissioning of the SPIRAL2 RFQ in CW Mode and Beyond Nominal Field”, in *Proc. IPAC'19*, Melbourne, Australia, May 2019, pp. 2804–2806. doi: 10.18429/JACoW-IPAC2019-WEPRB007
- [12] C. Jamet *et al.*, “SPIRAL2 Diagnostic Qualifications with RFQ beams”, in *Proc. IBIC'19*, Malmö, Sweden, Sep. 2019, pp. 188–192. doi: 10.18429/JACoW-IBIC2019-MOPP036
- [13] R. Ferdinand, M. Di Giacomo, H. Franberg, J.-M. Magniel, G. Normand, and A. Savalle, “Final Results of the SPIRAL2 Injector Commissioning”, in *Proc. IPAC'19*, Melbourne, Australia, May 2019, pp. 848–851. doi: 10.18429/JACoW-IPAC2019-MOPTS006
- [14] S. Leloir *et al.*, “Measurement Uncertainty Assessments of the Spiral2 ACCT/DCCT”, in *Proc. IBIC2016*, Barcelona, Spain, Sep. 2016, pp. 713–715. doi: 10.18429/JACoW-IBIC2016-WEPG39
- [15] J. L. Vignet *et al.*, “The Beam Profile Monitor for Spiral2”, in *Proc. DIPAC'09*, Basel, Switzerland, May 2009, paper TUPB07, pp.176-178.
- [16] R. V. Revenko and J. L. Vignet, “Bunch Extension Monitor for LINAC of SPIRAL2 Project”, in *Proc. IBIC'16*, Barcelona, Spain, Sep. 2016, pp. 486-490. doi: 10.18429/JACoW-IBIC2016-TUPG59
- [17] G. Normand *et al.*, “SPIRAL2 RFQ bunch lengths and longitudinal emittance measurements”, *J. Phys.: Conf. Ser.*, vol. 1350, p. 1012098, 2019. doi: 10.1088/1742-6596/1350/1/012098
- [18] M. Di Giacomo *et al.*, “Proton beam commissioning of the SPIRAL2 Single Bunch Selector”, *J. Instrum.*, vol. 15, p. T12011, Dec. 2020. doi: 10.1088/1748-0221/15/12/T12011
- [19] A. Ghribi, P.-E. Bernaudin, R. Ferdinand, and A. Vassal, “Cryogenic Tests of the SPIRAL2 LINAC Systems”, in *Proc. IPAC'19*, Melbourne, Australia, May 2019, pp. 1240–1243. doi: 10.18429/JACoW-IPAC2019-TUPMP006
- [20] G. Olry *et al.*, “Spiral2 Cryomodules B Tests Results”, in *SRF'13*, Paris, France, 2013, pp. MOP010, pp. 95-99. <https://jacow.org/srf2013/papers/mop010.pdf>
- [21] C. Marchand *et al.*, “Performances of SPIRAL 2 Low and High Beta Cryomodules”, in *Proc. SRF2015*, Whistler, BC, Canada, 2015, paper WEBA04, pp. 967–972. doi: 10.18429/JACoW-SRF2015-WEBA04
- [22] F. Lemagnen *et al.*, “New metallic stable beams for GANIL”, in *Proc. ECRIS'20*, East Lansing, MI, USA, Sep. 2020, pp. 54–56. doi: 10.18429/JACoW-ECRIS2020-MOZZO04
- [23] P. Dolegieviev *et al.*, “New exotic beams from the SPIRAL 1 upgrade”, *Nucl. Instrum. Methods Phys. Res., Sect. B.*, vol. 463, pp. 339-344, 2020. doi: 10.1016/j.nimb.2019.04.063
- [24] *Chart of beams at GANIL, stable and radioactive*, <https://u.ganilspiral2.eu/chartbeams/>
- [25] P. Delahaye, L. Maunoury, and R. Vondrasek, “Charge breeding of light metallic ions: Prospects for SPIRAL”, *Nucl. Instrum. Methods Res., Sect. A.*, vol. 693, pp. 104-108, 2012. doi: 10.1016/j.nima.2012.07.016
- [26] L. Maunoury *et al.*, “Charge Breeder at GANIL: metal charge-bred elements”, *J. Phys.: Conf. Ser.*, vol. 2244, p. 1012066, 2021. doi: 10.1088/1742-6596/2244/1/012066
- [27] R. Ferrer *et al.*, “In gas laser ionization and spectroscopy experiments at the Superconducting Separator Spectrometer (S³): Conceptual studies and preliminary design”, *Nucl. Instrum. Methods Phys. Res., Sect. B.*, vol. 317, pp. 570-581, 2013. doi: 10.1016/j.nimb.2013.07.028

REINFORCEMENT LEARNING AND BAYESIAN OPTIMIZATION FOR ION LINAC OPERATIONS*

J. Martinez-Marin, B. Mustapha, B. Blomberg, E. Letcher, G. Dunn, D. Stanton, and K. Bunnell
Physics Division Argonne National Laboratory, ANL, Lemont, IL, USA

Abstract

The use of artificial intelligence can significantly reduce the time needed to tune an accelerator system such as the Argonne Tandem Linear Accelerator System (ATLAS) where a new beam is tuned once or twice a week. After establishing automatic data collection procedures and having analysed the data, machine learning models were developed and tested to tune subsections of the linac. Models based on Reinforcement Learning (RL) and Bayesian Optimization (BO) were developed, their respective results are discussed and compared. RL and BO are well known AI techniques, often used for control systems. The results were obtained for a subsection of ATLAS that contains complex elements such as the radio-frequency quadrupole (RFQ). The models will be later generalized to the whole ATLAS linac, and similar models can be developed for any accelerator with a modern control system.

INTRODUCTION

The Argonne Tandem Linear Accelerator System (ATLAS) [1] is a DOE/NP User Facility for studying low-energy nuclear physics with heavy ions. It operates ~6000 h per year. The facility (see Fig. 1), uses three ion sources and services six target areas at energies from ~1–15 MeV/u. To accommodate the total number of approved experiments and their wide range of beam-related requirements, ATLAS reconfigures once or twice per week over 40 weeks of operation per year. The start-up time varies from ~12 to 48 hours depending on the complexity of the tuning, which will increase with the upcoming Multi-User Upgrade designed to deliver beams to two experimental stations simultaneously [2].

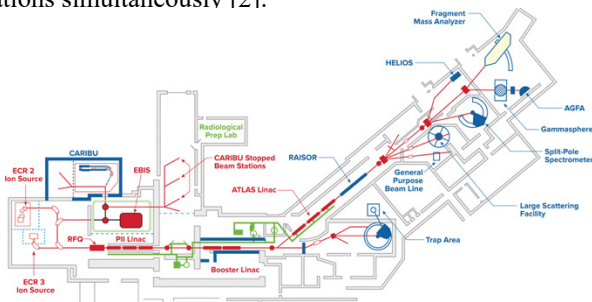


Figure 1: ATLAS Layout.

The procedure of tuning such an accelerator system is time-consuming and relies heavily on the intuition and experience of the operators. The uncertainties involved in tuning are in part due to unknown misalignments of the beamline components and the limited number of diagnostic devices to properly characterize the beam. The use of machine learning (ML) and artificial intelligence (AI) has the potential of filling the information gap and significantly reduce the time needed to tune the accelerator.

By reducing the time for beam tuning, more beam time will be available to help relieve the over-booked experimental nuclear physics program at ATLAS. In addition to beam tuning, AI/ML models can be used to improve beam quality with the installation of new diagnostics and real-time data acquisition. These improvements will increase the facility's scientific throughput and the quality of the data collected.

To support these developments, DOE/NP has approved a project to use AI/ML to support ATLAS operations. Following a description of the project objectives and future plans, the results from the most recent developments will be presented and discussed.

PROJECT OBJECTIVES & PLANS

The main project goal is to use AI/ML techniques to streamline beam tuning and help improve machine performance. The idea is to leverage artificial intelligence for linac operations, as shown in Fig. 2., with the ultimate goal of developing an AI model to tune the machine while also acquiring all kind of information from the AI model that could help improve operations.

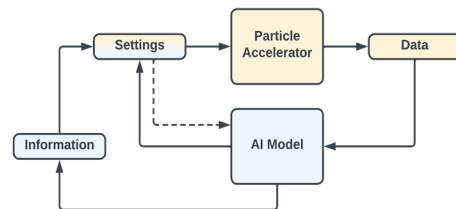


Figure 2: Basic representation of how an AI model could help particle accelerator operations.

The project objectives are threefold:

- Establish data collection, organization, and classification, towards a fully automatic and electronic data collection for both machine and beam data.
- Develop an online tuning model to optimize operations, shorten beam tuning time and make more beam time available for the experimental program.
- Develop a virtual machine model to enhance our understanding of the machine behavior, improve machine performance, optimize particular aspects and help develop new operating modes.

DATA COLLECTION

In any AI project, data collection is the first and most important step. Along with the data collection, cleaning and organizing the data are also the most time-consuming tasks. Therefore, the primary focus at the beginning of this project was on collecting the data on the state of the machine and the beam to be used for AI/ML modeling to support beam tuning and daily machine operations. Due to the

Content from this work may be used under the terms of the CC BY 4.0 licence (© 2022). Any distribution of this work must maintain attribution to the author(s), title of the work, publisher, and DOI

challenges that come with training with a real machine and the lack of ATLAS availability, the first steps in designing and training a model should use data from beam physics simulations codes.

Before moving to the developments on the data collection, it is important to know which diagnostic devices are typically available at ATLAS and what kind of data can be obtained from them. Figure 3 shows a typical beamline at ATLAS. The elements that can be found throughout ATLAS beamline are beam profile monitors, electrostatic and electromagnetic quadrupoles that form doublets and triplets, steering magnets, dipoles, faraday cups, accelerator sections, valves, etc.

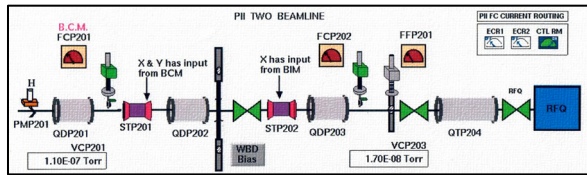


Figure 3: Beamline of a sub-section of ATLAS located between the multi-harmonic buncher and the RFQ.

Therefore, the information that can be obtained from the accelerator comes from faraday cup current readings, beam profiles and voltage and current settings of beamline elements. Currently, efforts are being made to have a functional pepper-pot device that will provide more information through beam imaging.

Prior to this project, the settings (concerning the data collection) could be saved automatically using the Control System, which uses *Vsystem* [3]. However, data from the faraday cups and beam profile monitors could not be saved and access to the devices was not automated. For example, to get a beam profile, several buttons had to be manually pressed on the control system screen. The system was capable of saving setting configurations in a data base to load old beam tunes into the accelerator but was not prepared for any kind of AI work integration.

After understanding how the Control System works, a python package was developed to communicate with it from a server that has direct access to the control system database, see Fig. 4 for a scheme of this communication between systems. The python interface was developed in a way so as to make it useful for any AI related work, thus allowing it to automatically collect and save beam profiles, faraday cup readings and beamline element settings as well as changing the settings of the accelerator.



Figure 4: Scheme representing the communication with the Control System from an existing server through the new python package.

Because the idea is to train and deploy AI models with the accelerator, an API was developed that enables communication from any computer with the server, and thus the Control System, exposing only the required functionalities

needed when training or deploying a model (see Fig. 5 for a representation of this new communication line). This was necessary because of the old servers that are still in place and are the only ones with direct access to the Control System. This added API layer allows the use of more powerful computers and provides the freedom needed for AI in setting up the software environment.

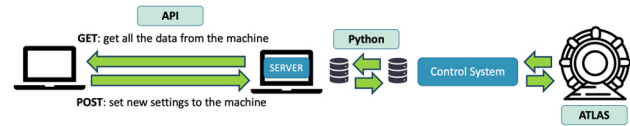


Figure 5: Scheme that represents the communication of a computer with the server and Control System through an API.

Apart from the work done on the data collection with the actual machine, a python wrapper was developed around a particle accelerator simulation code, TRACK, to allow the simulation of the actual machine, thereby generating a lot of data with different conditions and inputs and its integration with AI modelling. The AI training offline using a simulation code is key when much time is required for training because of the challenges that come with training directly on the actual machine and the lack of machine availability.

TUNING MODEL

For beam tuning and machine control, the most frequently used AI techniques are reinforcement learning with neural networks [4] and Bayesian optimization using Gaussian processes [5]. Many of these tools and platforms already exist and are available to implement ML models.

The ultimate goal for the tuning model is to optimize operations and shorten beam tuning time, and in order to achieve this the following steps were proposed:

- Develop a baseline model to tune/control a small section of ATLAS Linac using Simulation Data (see Fig. 6).

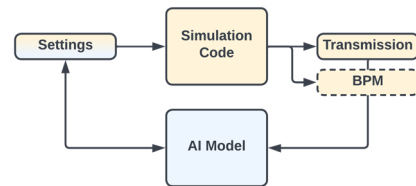


Figure 6: Scheme for model training using simulation code.

- Use alternatives approaches such as Bayesian Optimization with Gaussian Processes and Deep Reinforcement Learning.
- Test the baseline models on the real machine (see Fig. 7). Currently, the project is in this phase.

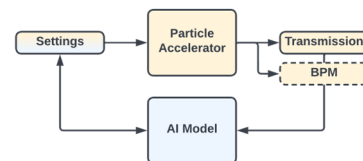


Figure 7: Scheme for model training using the accelerator.

- Improve models to enhance performance and reduce tuning time.
- Expand the model to other parts of the Linac to finally design a tuning model for the whole Linac.

Bayesian Optimization with Gaussian Processes

Bayesian optimization was chosen because of its wide use and because it combines the complementary strengths of human and numerical optimization: life-long learning, learning by experience, juggling many things at once, quick decisions, estimating its own uncertainty, reaching global optimum in a minimum number of steps, etc. This method starts with a prior belief regarding the objective function and then updates it based on samples drawn from the system in order to better approximate the objective function. It uses a probabilistic surrogate model for approximating the objective function and acquisition function that instructs where to query the system next for a more likely improvement

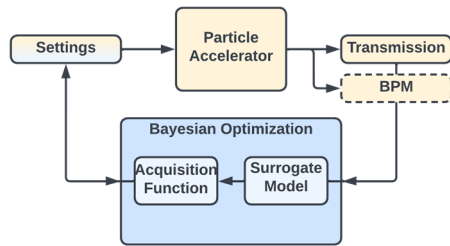


Figure 8: Scheme of how Bayesian Optimization works.

For the baseline model, Gaussian Process with a Matérn kernel, Gaussian likelihood and expected improvement as the acquisition function were used. In addition, the tools employed for BO with GP were GPyTorch and BoTorch libraries.

Simulation Data Using the beamline shown in Fig. 2 and TRACK as the simulation code, different scenarios were optimized by BO with GP. The objective is to maximize the transmission varying the settings.

1. Case for 9 quadrupoles (3 doublets and 1 triplet) and initial set of configurations randomly selected. The model was able to optimize the transmission in around 30 iterations. The initial set, although randomly generated, has a couple of configurations with around 80% transmission, see Fig. 9.
2. Case for 9 quadrupoles, RFQ and initial set of configurations randomly selected. Because the RFQ was added, the beam must match the acceptance of the RFQ; therefore, the randomly selected configurations have very low transmission through the beamline, and the model will need much more time to learn how to adjust the configuration to match the RFQ acceptance. In the following figure less than 30% transmission is achieved after more than 200 iterations, see Fig. 10.
3. Case for 9 quadrupoles, RFQ and initial set of configurations based on historical beam tunes. The initial set of configurations was scaled from old beam tunes from a historical data base. This provided reasonable transmissions for the model to learn from, which

translated into achieving the maximum transmission through the RFQ, around 80% in around 30 iterations, see Fig. 11.

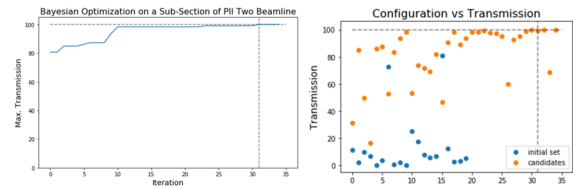


Figure 9: Results obtained for case 1. (Left) Maximum transmission achieved after a number of iterations. (Right) Transmission achieved with different configurations, in blue the initial set of points and in orange the proposed candidates by the model.

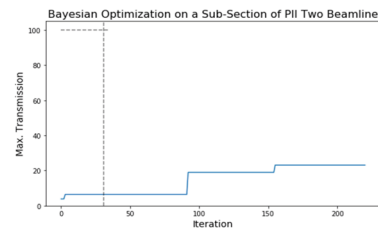


Figure 10: Results obtained for case 2. Maximum transmission achieved after a number of iterations.

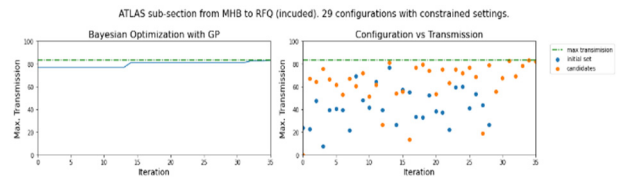


Figure 11: Results obtained for case 3. (Left) Maximum transmission achieved after a # of iterations. (Right) Transmission achieved with different configurations, in blue the initial set of points and in orange the proposed candidates by the model.

This experiment with simulation data confirms two things: first, that it is possible to optimize a beamline in a reasonable amount of time using a basic BO model, and second, the importance of good initial data in the training process when comparing case 2 against case 3.

Real Data The next step was to test the model with the real accelerator. For this experiment, 3 quadrupoles and 2 steering magnets were used (the first ones in Fig. 2). Therefore, there are 7 input parameters, since the 2 steerers have both horizontal and vertical component, and the objective remains to optimize the transmission after the RFQ.

1. Case of $^{14}\text{N}^{3+}$: the initial set was composed of 29 historical tunes plus 33 random configurations. The results are shown in Fig. 12. The model was able to converge in a few iterations (~6), although the maximum transmission was achieved around 40 iterations which was higher than the one achieved that day by the operators represented by the green dashed line in Fig. 12 left plot. The final optimum configuration was close but different from the one obtained by the operators, see Fig. 12 right plot.

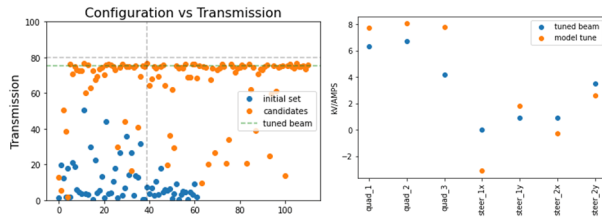


Figure 12: Results obtained for the case of $^{14}\text{N}^{3+}$. (Left) Transmission achieved with different configurations, in blue the initial set of points and in orange the candidates proposed by the model. (Right) In blue the element settings from the tuned beam by the operators and in orange the optimum settings proposed by the model.

2. Case $^{40}\text{Ar}^{9+}$: the initial set was composed of 29 historical tunes, the randomly selected configurations were not included because they did not provide an additional value owing to their very low transmissions. Similar performance is achieved in this case as in the previous one. Still showed slight improvement in transmission compared to operator configuration, see Fig. 13.

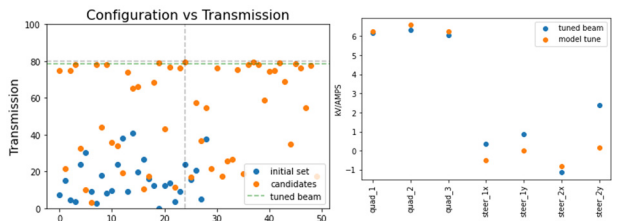


Figure 13: Results obtained for the case of $^{40}\text{Ar}^{9+}$. (Left) Transmission achieved with different configurations, in blue the initial set of points and in orange the proposed candidates by the model. (Right) In blue the settings from the tuned beam by the operators and in orange the optimum settings proposed by the model.

Reinforcement Learning

Reinforcement Learning was the other approach chosen for this study. Reinforcement learning is one of the three basic machine learning paradigms, alongside supervised learning and unsupervised learning. RL does not require labeled data because it learns from interactions between an AI agent and its environment. The idea behind using RL to tune/control a particle accelerator arises due to the complexity of a particle accelerator. Taking a look at the classic control problem (Fig. 14), it might seem like creating a single large function would be more difficult than building a control system with piecewise subcomponents; however, this is where reinforcement learning can help.

In essence, RL tries to map situations to actions in order to maximize a numerical reward. Figure 15 shows the different elements of an RL problem.

There are different kinds of algorithm that can be applied, and the one selected as a baseline model was the Deep Deterministic Policy Gradient (DDPG) [6], which is an actor-critic approach that mixes policy optimization and Q-learning method (Fig. 16). Policy optimization methods

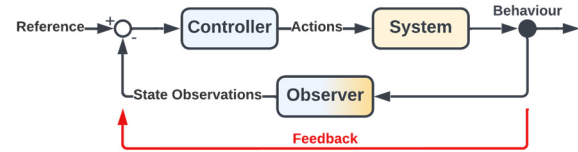


Figure 14: Classic control schema.

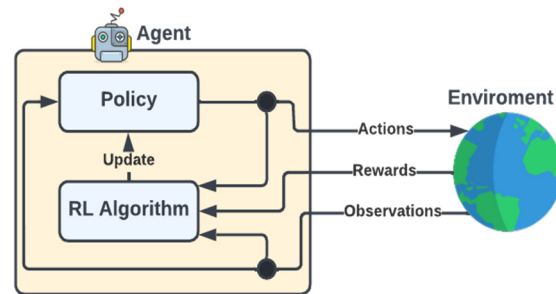


Figure 15: Scheme of how reinforcement learning works and the different elements involved.

tend to be more stable and reliable, and Q-learning methods are substantially more sample efficient, although the latter cannot work with continuous action space, which is the case for accelerators. DDPG works for continuous action spaces because the critic only needs to look at the single action that the actor took and does not need to try to find the best action by evaluating all of them.

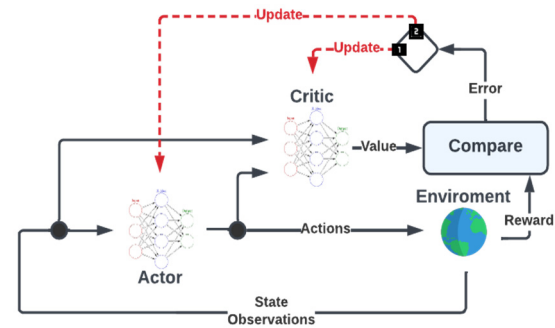


Figure 16: Scheme of how the actor-critic approach works and the different elements involved.

The *actor* is a neural network that tries to take what it thinks is the best action given the current state, as seen within the policy function method. The *critic* is a second neural network that tries to estimate the value of the state and the action that the actor took, as seen within the value function method.

Simulation Data The first scenario to test the performance of a DDPG baseline model was to train a model that minimizes the beam size by varying 3 electrostatic quadrupoles based on simulation data using the TRACK code. The rewards were defined as a logarithmic function of the beam size. Several penalties were added when the settings deviated from the given limits. The limits for the quadrupoles are from 2 kV to 10 kV and the maximum possible action is ± 0.25 kV. See Fig. 17 for the training (top) and prediction (bottom) results.

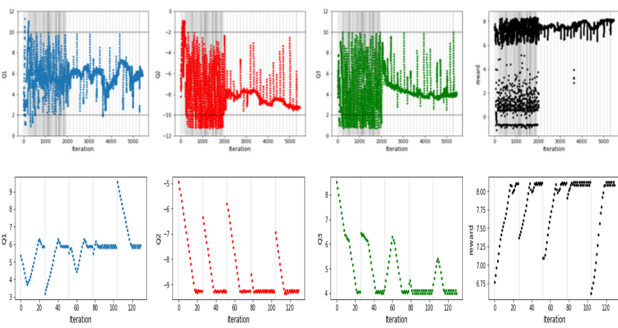


Figure 17: Results obtained for a baseline RL model using DDPG and the TRACK Code. The model optimized the beam size by varying 3 electrostatic quadrupoles. (Top) The results of the training. (Bottom) The results for 5 different predictions starting from 5 different random configurations.

Based on the training results, Fig. 17 top, the model learned first the limits of each quadrupole (up to iteration #2000), and after that, it learned how to optimize the beam size. Regarding the prediction, Fig. 17 bottom, it can be seen how the reward converges in each different scenario to a value corresponding to a minimum beam size.

Real Data After developing the simulation RL model, the next step was to test the baseline model in the real machine. In this case, the objective was to maximize the transmission, which was the reward function, through the selected beamline, see Fig. 2 for more detail. The selected beamline was composed of 4 electrostatic quadrupoles and 2 steering magnets. This gives 8 input parameters in total. The electrostatic quadrupoles were limited from 3 kV to 10 kV with a maximum action of ± 0.25 kV and the steering magnets from -1 A to 1 A and a maximum action of ± 0.25 A. Although the training was never completed because of limited experiment time with the real machine, some interesting conclusions were drawn. See Fig. 18 for the training results, in the figure it can be seen that the model was able to learn and identify the limits for almost every element of the selected beamline; it needed more time to finish learning all the elements' limits and optimize the transmission.

Moreover, this experiment confirmed the need to train the RL model offline using simulation code such as TRACK in order to perform only a fine-tune online with the machine. However, there are elements, such as the RFQ, whose simulations are considerably time consuming because of multiple accelerating cells using 3D fields calculations.

Surrogate Model

Following the need of an offline training for some approaches like RL, alongside with the time-consuming simulation of some elements like the RFQ, the idea of developing surrogate models to speed up the simulations was raised. In recent years it has successfully been shown how surrogate models can help in speeding up particle accelerator optimization [7, 8].

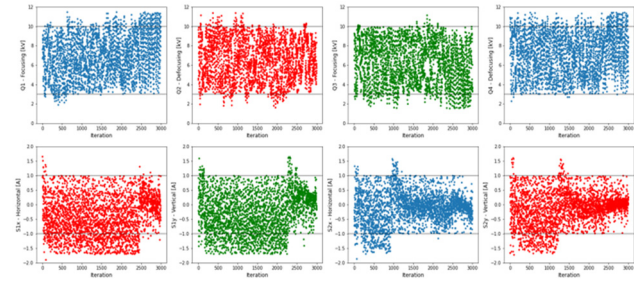


Figure 18: Results obtained for the training of a baseline RL model using DDPG in a subsection of ATLAS. This subsection was composed of 4 electrostatic quadrupoles (top) and 2 steering magnets with both vertical and horizontal components (bottom).

A surrogate model can be trained on beam simulation data to reliably reproduce the physics results in very short time; then it could be enhanced with experimental data. ML Surrogate Model can be used for virtual diagnostics, offline experiment planning, design of new setups, control and tuning.

In order to speed up the RL offline training through the RFQ, a surrogate model for the ATLAS RFQ can be used. A surrogate model was developed previously using the TRACK code [9] and could be used for RL offline training. The model was based on neural network architecture. – specifically, it was composed of two hidden layers and two residual blocks. The main objective was to predict beam transmission and output beam Twiss parameters as functions of input beam parameters which include the beam emittances and input Twiss parameters. The agreement between the simulation code and the surrogate model was excellent and is consistent with the comparison of two beam dynamics codes. Therefore, the surrogate model can be considered reliable and capable of reproducing the physical results, with the big advantage of being $\sim 30,000$ faster than the 3D model in this case. This is exactly what is needed for speeding up simulations.

CONCLUSIONS AND NEXT STEPS

Bayesian Optimization and Reinforcement Learning can be considered as analogous concepts with different terminology and often different settings. BO and RL both are useful for high-level tuning and control but excel in different regimes. BO seems to be more exploratory – ideal for optimizing new settings and situations in the limited data regime or slow measurements, while RL needs significantly more data to be trained and focusing more on continuous control.

From these preliminary results it seems that BO would be more suitable for new tuning configurations and RL for continuous control after being pre-trained offline.

The project has reached several milestones such as automated data collection, integration of new devices as the pepper-pot, integration of AI modelling with the accelerator and the successful training and deployment of a BO with GP on a subsection of ATLAS. In addition, the first step for a successful RL model has been made in demonstrating the model's learning the limits of the elements.

However, there is still a lot to do, and the next steps will be focused on testing the pepper-pot integration with the control system and the modelling, getting more useful data from the machine, fine tuning the RL with the machine after training offline, and improving existing models. To do so, other architectures, new type of data such as beam profiles and pepper-pot images, the use of surrogate models and the incorporation of more Physics information into the systems will be considered and included. And last, but not least, one of the current challenges encountered during the experiments was the possible damage to some devices when the beam is lost during model training. A solution is being investigating.

REFERENCES

- [1] P. N. Ostroumov *et al.*, “Completion of Efficiency and Intensity Upgrade of the ATLAS Facility”, in *Proc. LINAC'14*, Geneva, Switzerland, Aug-Sep. 2014, paper TUPP005, pp. 449-451.
- [2] B. Mustapha *et al.*, “The ATLAS multi-user upgrade and potential applications”, *J. Instrum.*, vol. 12, p. T12002, Dec. 2017. doi:10.1088/1748-0221/12/12/t12002
- [3] P. Clout, “The status of Vsystem”, *Nucl. Instrum. Methods Phys. Res., Sect. A*, vol. 352, pp. 442-446, 1994. doi:10.1016/0168-9002(94)91565-2
- [4] V. Kain, S. Hirlander, B. Goddard, F. M. Velotti, G. Z. Della Porta, N. Bruchon, and G. Valentino, “Sample- efficient reinforcement learning for CERN accelerator control,” *Phys. Rev. Accel. Beams*, vol. 23, p. 124801, Dec 2020. doi:10.1103/PhysRevAccelBeams.23.124801
- [5] M. W. McIntire, T. M. Cope, S. Ermon, and D. F. Ratner, “Bayesian Optimization of FEL Performance at LCLS”, in *Proc. IPAC'16*, Busan, Korea, May 2016, pp. 2972-2975. doi:10.18429/JACoW-IPAC2016-WEP0W055
- [6] T.P. Lillicrap, J.J. Hunt, A. Pritzel, N. Heess, T. Erez, Y. Tassa, D. Silver, and D. Wierstra, “Continuous control with deep reinforcement learning”, 2016. doi:10.48550/arXiv.1509.02971
- [7] M. Kranjčević, B. Riemann, A. Adelman, and A. Streun, “Multiobjective Optimization of the Dynamic Aperture Using Surrogate Models Based on Artificial Neural Networks”, *Phys. Rev. Accel. Beams*, vol. 24, p. 014601, 2021. doi:10.1103/PhysRevAccelBeams.24.014601
- [8] L. Gupta, A. Edelen, N. Neveu, A. Mishra, C. Mayes, and Y.-K. Kim, “Improving surrogate model accuracy for the LCLS-II injector frontend using convolutional neural networks and transfer learning”, *Mach. Learn.: Sci. Technol.* vol. 2, p. 045025, 2021. doi:10.1088/2632-2153/ac27ff
- [9] B. Mustapha, B. Blomberg, C. Dickerson, J. M. Marin, and C. Peters. “AI-ML Developments for the ATLAS Ion Linac Facility”, in *Proc. IPAC'21*, Campinas, SP, Brazil, May 2021, pp. 4122-4125. doi:10.18429/JACoW-IPAC2021-THPAB181

AUTOMATION OF RF AND CRYOMODULE OPERATION AT FRIB*

S. Zhao†, E. Bernal-Ruiz, W. Chang, E. Daykin, E. Gutierrez, W. Hartung,
S. Kim, S. Kunjir, T. Larter, D. Morris, J. Popielarski, H. Ren, T. Xu
Facility for Rare Isotope Beams, Michigan State University, East Lansing, MI, USA

Abstract

The Facility for Rare Isotope Beams (FRIB) has been commissioned, with rare isotopes first produced in December 2021 and the first user experiment conducted in May 2022. The FRIB driver linear accelerator (linac) uses 6 room temperature cavities, 324 superconducting cavities, and 69 superconducting solenoids to accelerate ions to more than 200 MeV/nucleon. Because of the large scale, automation is essential for reliable linac operation with high availability. Automation measures implemented during linac commissioning include turn-on of the cavities and solenoids, turn-on and fast recovery for room temperature devices, and emergency shut down of linac devices. Additional automated tasks include conditioning of multipacting barriers in the cavities and calibration of the control valves for the pneumatic tuners. To ensure a smooth transition to operations, we are currently working on real-time health monitoring of the linac cryo-modules, including critical signals such as X-ray levels, RF coupler temperatures, and cryogenic parameters. In this paper, we will describe our automation procedures, the implementation details, and the experience we gained.

INTRODUCTION

Facility for Rare Isotope Beams (FRIB) is a new heavy ion linear accelerator (linac) facility just came online recently, following the completion of technical construction in January 2022 [1]. The ribbon cutting event on May 2, 2022 marks the commencement of the FRIB user program and the first scientific user experiment was conducted in the weeks that followed in May 2022.

The FRIB driver linac includes 6 room temperature cavities and 324 superconducting (SC) cavities along with 69 SC solenoids housed in 46 cryomodules [2]. It is capable of accelerating heavy ions (up to uranium) to an energy of more than 200 MeV/nucleon. There are also 19 SC magnets spread in the folding segment 2 (FS2), target hall, vertical pre-separator and fragment separator areas (see Fig. 1).

FRIB single event effects (FSEE) facility is a purpose-built beamline at the end of the linac segment 1 (LS1), with experimental station, and user control room with complete diagnostic equipment and controls. The dedicated FSEE experimental area allows users to test the effects of radiation on their devices to make sure they are safe for commercial and scientific use. FSEE facility uses its linear particle accelerator to accelerate ions to the proper specifications that can best match space radiation conditions.

* Work supported by the U.S. Department of Energy Office of Science under Cooperative Agreement DE-SC0000661.

† zhaos@frib.msu.edu

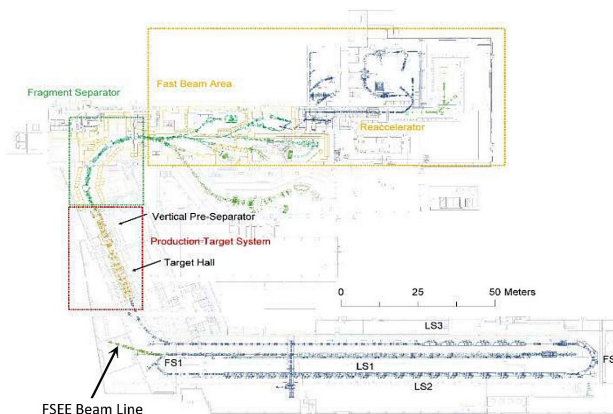


Figure 1: FRIB driver linac layout.

THE IMPORTANCE OF AUTOMATION

For a facility with hundreds of devices like FRIB, operation with high availability can only be achieved by automation.

First, automation reduces time for turning on/off devices, therefore increases time available for scientific experiments.

Automation not only improves efficiency and productivity, it also provides consistency to task execution and eliminates potential human errors. Also for certain tasks that require immediate response, for example fast recovery for room temperature cavities from a trip, automation is the only choice.

The essence of automation is to formalize the operation experience of system experts into routines, and perfect them through iterations. Eventually the devices become “smart” and require minimal human intervention. This allows operators to run complex devices without expert-level training for each type of device.

As a result, the system experts are freed from routine work and can devote more time for creative work. This also reduces the level of training required for operators.

DEVICE LEVEL AUTOMATION

During the construction phase of the FRIB project, the re-accelerator (ReA) program [3] at the National Superconducting Cyclotron Laboratory (NSCL) was already in operation. From the ReA operation experience we learned that it is important to have the auto turn on feature. We started with the quarter wave resonators (QWRs) and then expanded it to the room temperature (RT) cavities. Lastly we applied it to the half wave resonators (HWRs). During the FRIB front end (FE) commissioning, due to the long turn on time (30 to 40 minutes) of the radio frequency quadrupole (RFQ) we realized fast recovery is also very important for RT cavities. Later we applied the similar idea

to the magnet turn on process. Below are the details about each case.

Cavity Auto Turn On

To efficiently and reliably operate a large scale facility with over 300 cavities of various types could be very challenging. Automatic turn on procedures have been developed and implemented on the input/output controller (IOC) level for all FRIB cavity types to address this challenge. After resolving the difficulty in pneumatic tuner control, the auto on feature was implemented and tested for the HWRs [4].

Figure 2 shows a typical HWR auto turn on process. After the auto start command is issued by the operator, the high voltage for the bias tee is turned on and the tuner valves are enabled. The RF drive is enabled at the initial level (1.5 MV/m) afterward, followed by enabling the tuner control. Once the cavity is on resonance, the amplitude control switches to closed-loop and starts ramping to the final amplitude set-point. The phase control will switch to closed-loop once the final amplitude set-point is reached and the automatic turn on process completes. The whole process takes about 35 seconds. During the first beam run of the 4th accelerator readiness review (ARR4) in March 2020, without the auto turn on, each HWR was turned on manually and took about 2 minutes for each cavity.

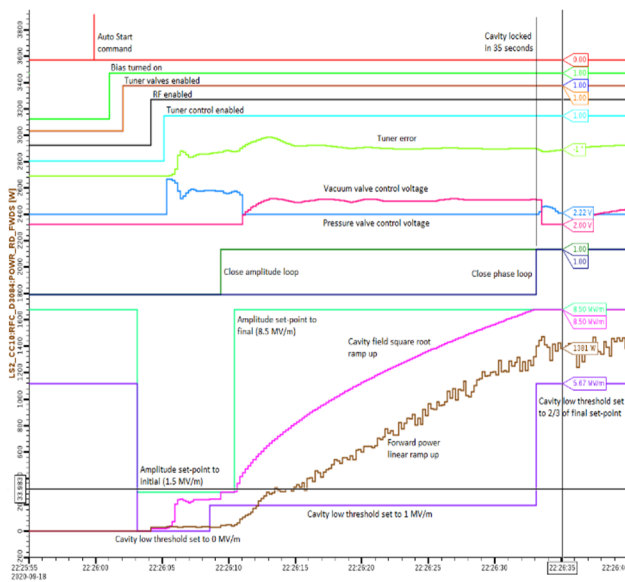


Figure 2: HWR auto turn on process.

Room Temperature Cavity Fast Recovery

For room temperature cavities, in certain cases (typically reflected power high or s11 high events due to sparking), it's important to recover the power of the device in a few seconds to keep the temperature of the cavity which is essentially the tuning of the cavity. So that the cavity can be resumed for beam operation with minimal delay. It was demonstrated that the RFQ operating at 100 kW continuous wave (CW) can resume beam operation in less than 20 seconds [5] (Figure 3).

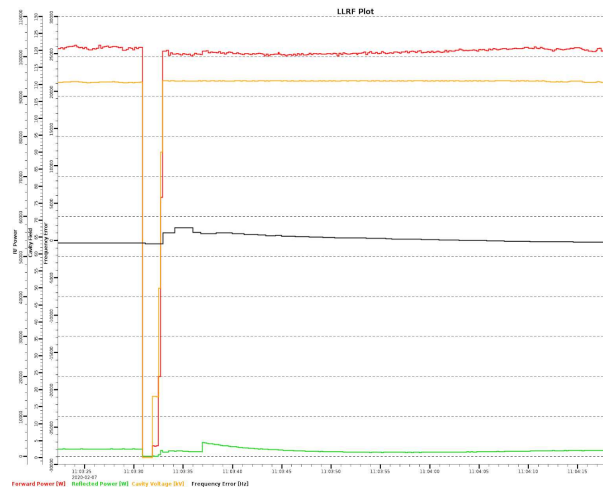


Figure 3: RFQ fast recovery after an s11 trip.

Solenoid Auto Turn On

Solenoid auto turn on is relatively simple. It is a two step ramp up process. At each step the stability of the power supply current is checked (see Figure 4).

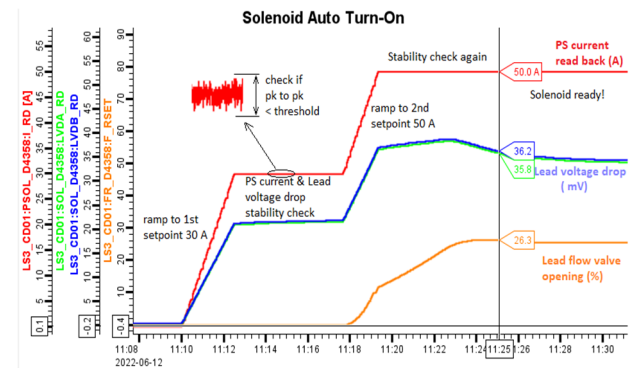


Figure 4: Solenoid auto turn on sequence.

FSEE OPERATION

Unlike typical scientific experiments, for which the beam is sent to the experimental area on the ground level, the FSEE experiments happen in the tunnel. The users usually need to frequently access the experimental area and each time tunnel access is requested, all superconducting radio frequency (SRF) cavities need to be turned off. This can happen 4 to 5 times a day.

This presents a challenge to the accelerator operation. First turning on and off the SRF cavities frequently perturbs the cryogenic system. Second, even with automatic turn on implemented, turning on cavities one at a time (104 SRF cavities are used for FSEE operation) still takes a lot of time.

To address the challenges mentioned above, heater compensation is first applied to stabilize the cryogenic operation. The accelerator physicist group provides cavity amplitude set-points for the experiment; SRF group calculates expected heat load for each cavity; cryo control group sets the heater compensation values based on the calculation. A hard-wired signal is sent from the low level radio fre-

Content from this work may be used under the terms of the CC BY 4.0 licence (© 2022). Any distribution of this work must maintain attribution to the author(s), title of the work, publisher, and DOI

quency (LLRF) controller to the programmable logic controller (PLC) to indicate the RF on/off status, which triggers the heater. Figure 5 shows the heater being turned off and on as the SRF cavities are being turned on and off.

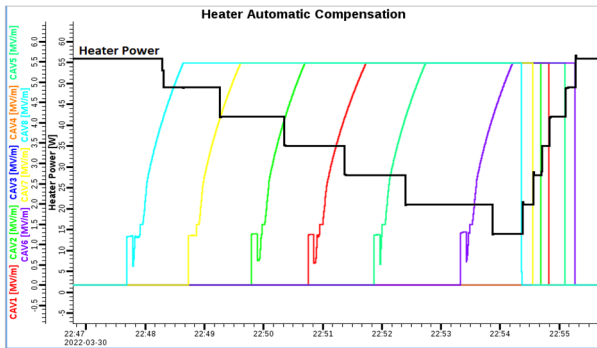


Figure 5: Cryo heater compensation based on cavity status.

Secondly, a much more simplified operator interface (OPI) is also developed with only six buttons (Figure 6) to operate all of the QWRs.



Figure 6: OPI for turning on/off LS1 SRF cavities.

With the proper heater compensation for stable cryo system operation and the simplified OPI, the LS1 SRF cavities can be turned on in 2 minutes and turned off in 2 seconds as shown in Fig. 7.

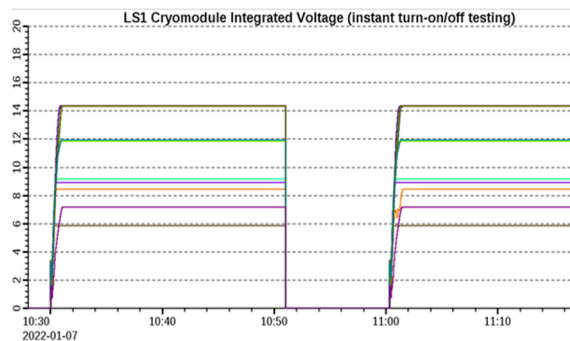


Figure 7: Efficient turning on and off of LS1 SRF cavities.

IMPLEMENTATION CONSIDERATION

There are different ways to implement the automation tasks. Below we will discuss several options being used at FRIB and their use cases.

Python script is a very powerful tool with versatile libraries and provides maximum flexibility. Since no compilation is needed, the development can be iterated very quickly. It has been used to prototype the auto turn on and

fast recovery of the cavities. For the same reason, it's also prone to mistakes. That is why FRIB has a script use policy that prohibits the use of scripts for safety features and when beam power is greater than 2 W. However Python scripts can be safely used to handle read only tasks, e.g. parameter checking, health monitoring, etc.

The sequencer module in the IOC can be utilized to automate tasks as well. The development follows a more rigorous process. The source code is version controlled and peer reviewed. Testing of IOC scripts requires a work control plan and deployment of IOC scripts requires a configuration change request. After prototyping, the auto turn on and fast recovery Python scripts for cavities are all converted to IOC scripts to enforce formality. The emergency shutdown for the cavities and solenoids is also implemented in the IOC scripts.

Lastly, some tasks can be automated at the device level, provided the device has its own processor to run software routines. The power ramp up of RT cavities is done in the self-excited loop mode. During the process the feed-forward phase setting needs to be adjusted. Previously this was done in the IOC scripts. Later we migrated the implementation to the LLRF controller software to remove the complexity of dealing with network delay. This results in a significant code size reduction from 60 lines in IOC to 30 lines in LLRF controller. Meanwhile the code runs at a much faster rate of 20 Hz in LLRF instead of 0.5 Hz in IOC.

ONGOING TASKS

Now as FRIB transits from construction and commission to operations, efficient automation tools for performance tracking and real-time health monitoring will be needed.

Currently we are working on automatic health monitoring for critical signals of the cavities and cryomodules, such as He level, X-ray levels, coupler temperatures, etc. which were monitored by experts previously. Abnormal patterns will be identified and warnings or alarms will be set depending on the severity of the situation.

Another important task is cavity trip troubleshooting and action recommendation. For some trips it is easy to identify the cause, but for others it may be time consuming. We envision a single button solution. When a cavity trip event happens, the operators only need to click the button and the script will generate a trip report and provide recommendations of actions, such as reset and restart, or contact system experts in case of potential hardware failures.

Other maintenance tasks such as pre-run check and LLRF controller firmware/software update can also benefit from automation.

SUMMARY

In this paper, we shared our experience of automating the RF and cryomodule operation at FRIB. The motivation is naturally strong for large scale facilities. We gave examples of the automated tasks at the device level as well as the facility level. The pros and cons of the different implementation approaches were compared. We hope this provides some useful information for future accelerator projects.

REFERENCES

- [1] P. Ostroumov *et al.*, “FRIB Commissioning,” presented at HIAT’22, Darmstadt, Germany, Jun.-Jul. 2022, paper WE113, this conference.
- [2] T. Xu *et al.*, “Completion of FRIB Superconducting Linac and Phased Beam Commissioning”, in *Proc. SRF’21*, East Lansing, MI, USA, Jun.-Jul. 2021, pp. 197-202. doi:10.18429/JACoW-SRF2021-M00FAV10
- [3] O. K. Kester *et al.*, “The MSU/NSCL Re-Accelerator ReA3”, in *Proc. SRF’09*, Berlin, Germany, Sep. 2009, paper MOOCAU05, pp. 57-61.
- [4] S. Zhao *et al.*, “RF System Experience for FRIB Half Wave Resonators,” in *Proc. SRF’21*, East Lansing, MI, USA, Jun.-Jul. 2021, pp. 226-229. doi:10.18429/JACoW-SRF2021-M0PTEV010
- [5] E. Pozdeyev *et al.*, “FRIB Front End Construction and Commissioning”, in *Proc. IPAC’18*, Vancouver, Canada, Apr.-May 2018, pp. 58-62. doi:10.18429/JACoW-IPAC2018-M0ZGBF1

CAVITY DESIGNS FOR THE CH3 TO CH11 AND BELLOW TUNER INVESTIGATION OF THE SUPERCONDUCTING HEAVY ION ACCELERATOR HELIAC*

T. Conrad[†], M. Busch, H. Podlech¹, M. Schwarz, IAP, Frankfurt am Main, Germany
K. Aulenbacher^{2, 3}, W. Barth³, M. Basten², F. Dziuba³, V. Gettmann², M. Heilmann,
T. Kuerzeder², S. Lauber², J. List³, M. Miski-Oglu², A. Rubin, A. Schnase, S. Yaramyshev²
GSI, Darmstadt, Germany
¹also at HFHF, Frankfurt am Main, Germany
²also at HIM, Mainz, Germany
³also at IKP, Mainz, Germany

Abstract

New CH-DTL cavities designs of the planned Helmholtz Linear Accelerator (HELIAC) are developed in collaboration of HIM, GSI and IAP Frankfurt. The in cw-mode operating linac with a final energy of 7.3 MeV/u, is intended for various experiments, in particular with heavy ions at energies close to the Coulomb barrier for research on SHE. Twelve sc CH cavities are foreseen, divided into four different cryostat each equipped with two dynamic bellow tuner. After successful beam tests with CH0, CH3 to CH11 were designed. Based on the experience gained so far, optimizations were made, which will lead to both an increase in performance in terms of reducing the peak fields limiting superconductivity and a reduction in manufacturing costs and time. In order to optimize manufacturing, attention was paid to design many parts of the cavity, such as lids, spokes, tuner and helium shell, with the same geometrical dimensions. In addition, a tuner test rig was developed, which will be used to investigate the mechanical properties of the bellow tuner. For this purpose, different simulations were made in order to realize conditions as close as possible to reality in the test rig.

INTRODUCTION

The HELIAC at GSI in collaboration between IAP, HIM and GSI is a superconducting Linac operating in cw to be built. Since UNILAC, which is currently as part of the FAIR project being upgraded, will no longer be suitable for superheavy element (SHE) synthesis experiments, HELIAC will replace it for these kind of experiments [1]. For this purpose, a demonstrator cavity CH0 was already designed, built and successfully tested [2]. After this the two identical cavities CH1 and CH2 were designed, built and also successfully characterized in cold state [3]. Through various experiments at GSI, HIM [2, 4–7] and IAP [8–17] as well as different adaptations and investigations of the CH cavity design, different experiences could be gained. The HELIAC will consist of four cryomodules, each containing three superconducting CH cavities, two superconducting bunchers

and one solenoid. In summer 2018 the design of the remaining nine 216.816 MHz sc CH-cavities (CH3 to CH11) for the HELIAC has started [18]. The design of these cavities is based on the design of the CH1 and CH2 cavities [3]. During this design process, various adjustments were made to the design. A modular cavity design for superconducting CH cavities was developed at IAP, which simplifies manufacturing and thus reduces both production time and costs. In addition to the design cavities, a bellow tuner test bench was designed, which is planned to be used to test the mechanical properties of the bellow tuners made of pure niobium.

CAVITY DESIGN

The basic design of the 216.816 MHz sc CH cavities is the same for all cavities (see Fig. 1). They differ only in some parameters like the number of gaps, the gap lengths, the radius and the total length. All cavities are designed to incorporate two static tuners for frequency adjustment during manufacture and two dynamic bellow tuners for frequency adjustment during operation.

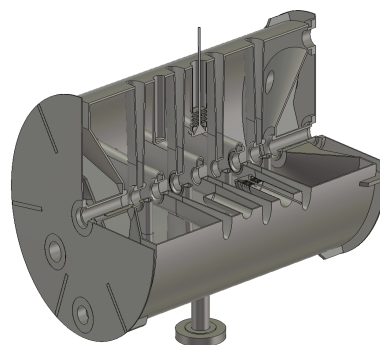


Figure 1: Layout of CH-cavity CH4 without helium vessel. The basic design of all cavities is the same except for the number of gaps, the gap lengths, the radius and the length.

The radius of the individual cavities increases steadily from CH3 to CH11, since the increasing beta causes the gap mean distances to increase from cavity to cavity and thus the capacity on the beam axis decreases. The total length of the cavities, on the other hand, varies strongly, since the gap

* Work supported by the Federal Ministry of Education and Research (BMBF, contract no. 05P21RFRB2)

[†] conrad@iap.uni-frankfurt.de

mean distances are larger, but the number of gaps decreases (see Fig. 2).

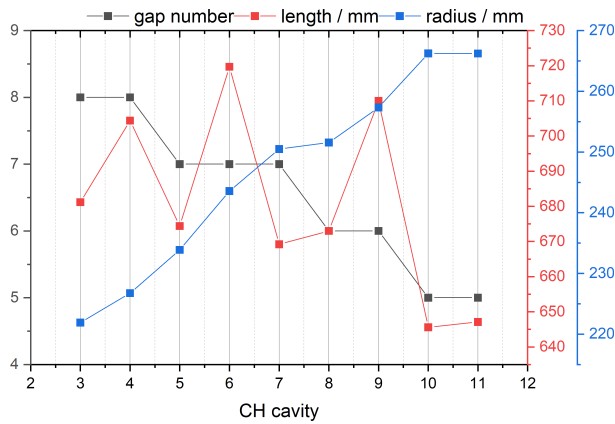


Figure 2: Graphic representations of the geometric differences of the cavities CH3 to CH11

Special attention was paid to optimizing the design of the new cavities in terms of performance. For this purpose, particular attention was paid to reducing the peak fields. Compared to the two predecessor cavities CH1 and CH2, the peak fields were significantly reduced in almost all cavities. Thus, CH1 and CH2 showed an $B_{\text{peak}}/E_a = 8.5$ and an $E_{\text{peak}}/E_a = 6.5$ [3]. The values for the nine cavities CH3 to CH11 are shown in Fig. 3.

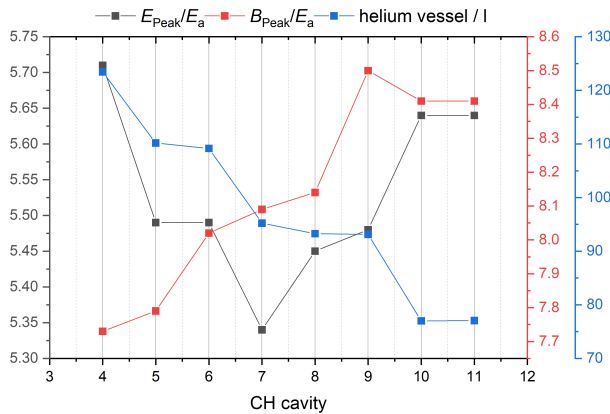


Figure 3: Plot of the values for E_{peak}/E_a and B_{peak}/E_a of the cavities CH3 to CH11 as well as the total volume of the helium reservoir in liter.

Modulare Cavity Design

In addition to optimization in terms of performance, great attention was paid to simplifying the manufacturing. After discussions with some manufacturers, a modular cavity design was developed based on their experience and knowledge. The spokes, the flanges, the tuners, the lids, and the helium tank are all manufactured with the same geometry and then adapted to the respective sizes of the cavities. This modular system allows to use the supports and tools needed for the production for each cavity, so that no additional costs

or time are needed for the production of these. Figure 4 shows the geometry of the identical spokes and lids for all cavities. The excess material can then be adapted to the geometric requirements of the cavity.

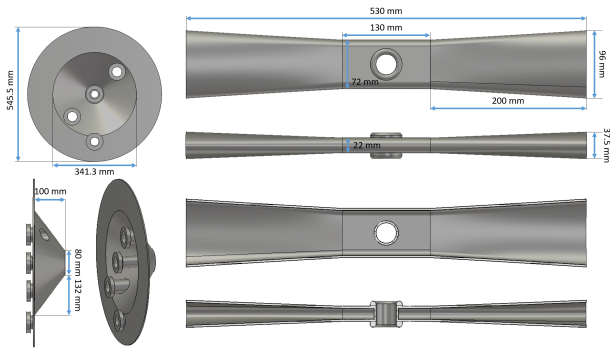


Figure 4: Representation of the spokes (right) and lids (left) of all nine cavities.

The helium shells of all cavities will also have identical radii. They are designed to have the maximum possible diameter. The four cryomodules are designed for cavities with a total radius of 325 mm. So the radius of the helium shell is 320 mm, so that there is still sufficient space for working during assembly in the cryomodules. Since the cavities radii increase within the tanks, the amount of liquid helium decreases from CH3 to CH11 (see Fig. 3), however, the amount of liquid helium is sufficient for cooling to ≈ 4 K.

TUNER TEST BENCH

When the dynamic bellow tuner of cavity CH1 were measured for the first time, it was noticed that hysteresis effects already occur even with a slight overload of the bellow tuner. For this reason, it was decided to set up a bellow tuner test bench to investigate hysteresis effects due to material fatigue as well as the maximum load capacity of the material before fracture occurs. Since the dynamic bellow tuner of superconducting CH cavities are firmly welded to the cavity, damage to the bellow tuner means damage to the whole cavity, which would lead to a time- and cost-intensive repair and downtime. To set up the test bench, a pillbox cavity will be modified so that the tuner can be cooled with liquid nitrogen and the resonant frequency can be measured to determine the possible deformation. The greatest difficulty of the modification is the required cooling. Since niobium becomes more flexible at low temperatures, it is necessary to operate the test bench at low temperatures in order to be able to make a realistic prediction for the later operation. It was decided to first operate the test bench with liquid nitrogen, since cooling with liquid helium represents an enormous financial and safety effort. In order to be able to operate the test bench safely with liquid nitrogen, a filling system was developed with which the tuner can be filled with liquid nitrogen (see Fig. 5). This includes a filling lance, so that the tuner can be filled from below, and a nitrogen cup, which prevents uncontrolled spattering during filling.

Content from this work may be used under the terms of the CC BY 4.0 licence (© 2022). Any distribution of this work must maintain attribution to the author(s), title of the work, publisher, and DOI

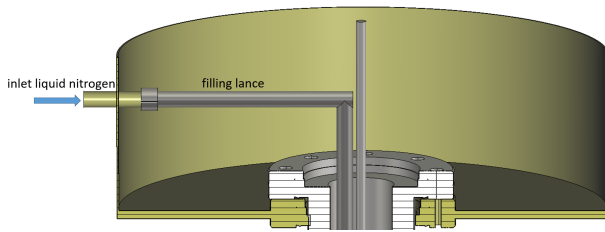


Figure 5: Planned filling system of the tuner test bench.

Since the intended pillbox cavity has a much larger radius than the later CH cavities, the bellow tuner to be examined must be adapted. Since the wall thickness of the tuner is only 1 mm, a thicker tube is used for the extension of the tuner than for the later tuners in order to exclude possible additional degrees of freedom (see Fig. 6).

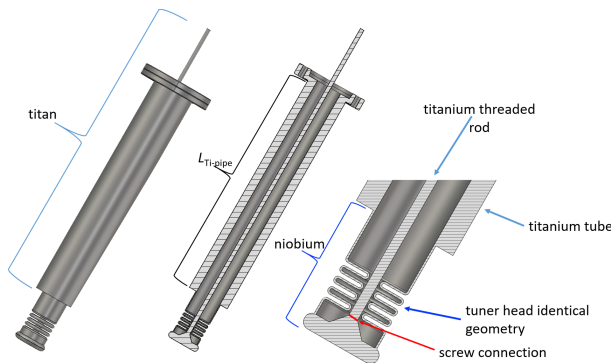


Figure 6: Bellow tuner adapted for tuner test bench.

In order to keep the manufacturing costs for the adapted tuner as low as possible, all parts that are not of interest for the actual investigation will be made of titanium, since titanium has a similar thermal expansion coefficient as niobium and is also less expensive. Thus, in the end, only the head and the bellows of the tuner will be made of niobium. Additional simulations were made to check whether the thickness of the titanium tube or the length of the niobium tube between the niobium head and the titanium tube has an effect on the validity of the test bench (see Fig. 7).

It could be shown that only the bellow is decisive for the displacement and the mechanical load of the tuner (see Fig. 8).

CONCLUSION

Based on the design of the CH1 and CH2 cavities, a total of nine new superconducting CH cavities were developed for the HELIAC at GSI in Darmstadt. A modular cavity design could be developed, which allows to reduce the production costs as well as the production time of these nine cavities. In addition to this simplification of production, it was also possible to significantly increase the performance of the cavities. Also a bellow tuner test bench was developed based on an existing pillbox cavity. A cooling concept for liquid nitrogen was developed, which allows a safe and efficient operation of the test bench. The tuner to be tested was

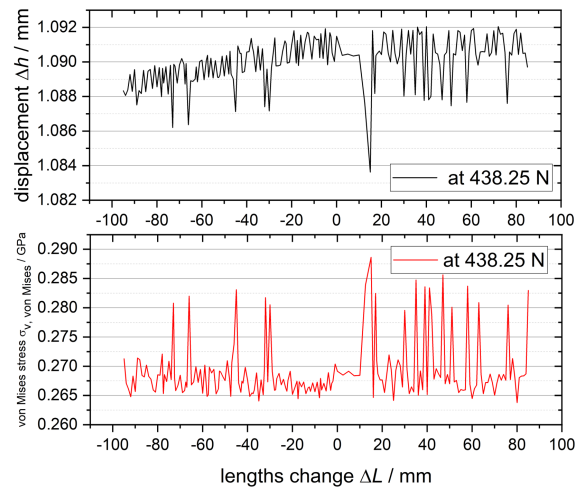


Figure 7: Simulation results done with CST Studio Suite [19] regarding the displacement and internal stress with respect to the length of the niobium tube between the niobium head and the titanium tube. The force of 438.25 N was thereby iteratively determined in simulations as the force required to displace the tuner ≈ 1 mm.

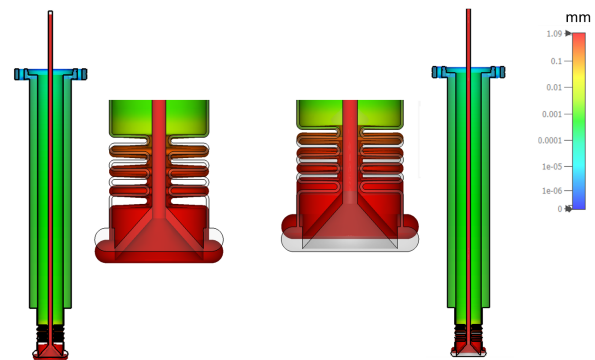


Figure 8: Simulation done with CST Studio Suite [19] of the displacement of the tuner in tension and compression. It can be seen that only the bellow contracts or expands under both forces.

successfully adapted to the requirements of the test bench without compromising the validity of the test bench, which was confirmed in additional simulations.

ACKNOWLEDGEMENTS

This work is supported by BMBF, HGS-HiRe, HFHF and Stiftung Giersch.

REFERENCES

- [1] S. Mickat *et al.*, "Superconducting, energy variable heavy ion linac with constant beta, multicell cavities of CH-type", *Phys. Rev. ST Accel. Beams*, vol. 12, p. 120101, 2009. doi: 10.1103/PhysRevSTAB.12.120101
- [2] W. Barth *et al.*, "First heavy ion beam tests with a superconducting multigap CH cavity", *Phys. Rev. Accel. Beams*, vol. 21, p. 020102, 2018. doi: 10.1103/PhysRevAccelBeams.21.020102

- [3] M. Basten, “Entwicklung und Inbetriebnahme zweier supraleitenden 217 MHz CH-Kavitat fur das HELIAC-Projekt”, in *PhD Thesis, Goethe Universitat Frankfurt am Main*, Frankfurt am Main, Germany, 2019.
- [4] W. Barth *et al.*, “Superconducting CH-Cavity Heavy Ion Beam Testing at GSI”, *J. Phys.: Conf. Ser.*, vol. 1067, p. 052007, 2018. doi:10.1088/1742-6596/1067/5/052007
- [5] F. D. Dziuba *et al.*, “Performance Tests of the Superconducting 217 MHz CH Cavity for the CW Demonstrator”, in *Proc. SRF’17*, Lanzhou, China, Jul. 2017, pp. 440–443, doi:10.18429/JACoW-SRF2017-TUPB024
- [6] F. D. Dziuba *et al.*, “First Cold Tests of the Superconducting cw Demonstrator at GSI”, in *Proc. RuPAC’16*, Saint Petersburg, Russia, Nov. 2016, pp. 84–86. doi:10.18429/JACoW-RUPAC2016-WECBMH01
- [7] S. Lauber *et al.*, “A dynamic collimation and alignment system for the Helmholtz linear accelerator”, *Rev. Sci. Instrum.*, vol. 92, p. 113306, 2021. doi:10.1063/5.0069824
- [8] M. Miski-Oglu *et al.*, “Progress in SRF CH-Cavities for the HELIAC CW Linac at GSI”, in *Proc. SRF’19*, Dresden, Germany, Jun.-Jul. 2019, pp. 1206–1212, doi:10.18429/JACoW-SRF2019-FRCAA4
- [9] T. Conrad *et al.*, “Cavity Designs for the CH3 to CH11 of the Superconducting Heavy Ion Accelerator HELIAC”, in *Proc. SRF’19*, Dresden, Germany, Jun.-Jul. 2019, pp. 396–398. doi:10.18429/JACoW-SRF2019-TUP005
- [10] M. Basten *et al.*, “Latest Cryogenic Test Results of the Superconducting $\beta = 0.069$ CH-cavities for the HELIAC-project”, in *Proc. SRF’19*, Dresden, Germany, Jun.-Jul. 2019, pp. 392–395. doi:10.18429/JACoW-SRF2019-TUP004
- [11] M. Schwarz *et al.*, “Advanced Beam Dynamics Design for the Superconducting Heavy Ion Accelerator HELIAC”, in *Proc. IPAC’19*, Melbourne, Australia, May 2019, pp. 928–931. doi:10.18429/JACoW-IPAC2019-MOPTS034
- [12] H. Podlech *et al.*, “Superconducting CH structure”, *Phys. Rev. ST Accel. Beams*, vol. 10, p. 080101, 2007. doi:10.1103/PhysRevSTAB.10.080101
- [13] M. Schwarz *et al.*, “Beam Dynamics Simulations for the Superconducting HELIAC CW Linac at GSI”, in *Proc. IPAC’22*, Bangkok, Thailand, Jun. 2022, pp. 86–89. doi:10.18429/JACoW-IPAC2022-MOPOST015
- [14] M. Schwarz *et al.*, “Beam Dynamics Simulations for the New Superconducting CW Heavy Ion LINAC at GSI”, *J. Phys.: Conf. Ser.*, vol. 1067, p. 052006, 2018. doi:10.1088/1742-6596/1067/5/052006
- [15] M. Basten *et al.*, “First Measurements of the Next SC CH-cavities for the New Superconducting CW Heavy Ion Linac at GSI”, in *Proc. SRF’17*, Lanzhou, China, Jul. 2017, pp.433–436. doi:10.18429/JACoW-SRF2017-TUPB022
- [16] M. Busch *et al.*, “Further Tests on the SC 325 MHz CH-cavity and Power Coupler Test Setup”, in *Proc. SRF’17*, Lanzhou, China, Jul. 2017, pp.437–439. doi:10.18429/JACoW-SRF2017-TUPB023.
- [17] F. D. Dziuba *et al.*, “Superconducting CH Cavities for Heavy Ion Acceleration”, in *Proc. IPAC’13*, Shanghai, China, May2013, paper THPWO016, pp. 3794–3796. doi:10.18429/JACoW-SRF2017-TUPB023
- [18] W. Barth *et al.*, “High brilliance uranium beams for the GSI FAIR”, *Phys. Rev ST Accel. Beams*, vol. 20, p. 050101, 2017. doi:10.1103/PhysRevAccelBeams.20.050101
- [19] CST Microwave Studio (2014 - 2021), Computer Simulation Technology GmbH; CST Studio Suite; CST Microwave Studio, www.cst.com

LONGITUDINAL BEAM DIAGNOSTICS R&D AT GSI-UNILAC

R. Singh*

GSI Helmholtzzentrum für Schwerionenforschung, Darmstadt, Germany

Abstract

GSI UNILAC provides a wide variety of ion types from energies ranging from 1.4 MeV/u to 11.5 MeV/u with a large dynamic range in the beam intensities to the experimental users or to the downstream accelerators. This flexibility in beam parameters requires a frequent tuning of the machine parameters for optimal operation of the UNILAC. Therefore, there has been a constant and pressing need for operationally convenient, accurate, fast and potentially non-destructive beam diagnostics for longitudinal charge profile and energy distribution. This contribution discusses the recent progress on longitudinal charge profile distribution measurements at GSI UNILAC. The outcome of recent devices like Fast Faraday cups (FFCs), transition radiation in GHz regime (GTR) is shown in comparison with phase probes or pick-ups. Other past developments aimed at longitudinal diagnostics at UNILAC like single particle detectors and RF deflector type methods are also briefly discussed.

INTRODUCTION

GSI Universal linear accelerator (UNILAC) is a complex set of resonators where detailed knowledge of longitudinal phase space is desired for optimizing the beam brilliance under flexible beam settings [1]. Past experiences suggest that the crucial locations for longitudinal phase determination is at the exit of High current injector (HSI), charge stripper sections and transfer channel to SIS-18. Figure 1 shows a schematic of the UNILAC where the various components of the UNILAC are shown along with the longitudinal diagnostics installations. Also marked is the measurement station X2 where most of the measurements discussed in this contribution were performed.

* r.singh@gsi.de

Longitudinal diagnostics are primarily concerned with the measurement of beam kinetic energy W_k , energy spread ($\delta = \Delta W_k/W_k$) and particle time/phase ($\Delta t/\Delta\phi$) of arrival spread with respect to the RF. Kinetic energy measurements are performed with Time of Flight (ToF) measurement between two or more phase probes (also referred as pick-ups/BPMs) and is routinely done at several locations along the UNILAC. The correlated distributions of beam energy spread and phase spread with respect to synchronous particle form an ellipse in longitudinal phase space. The area of the phase space ellipse is referred to as longitudinal emittance. The orientation of the ellipse at various accelerator locations can be controlled via bunchers and drifts. Typical strategy of determining full longitudinal phase space ellipse is by measuring one of the projection of longitudinal phase space) under various buncher settings and then performing tomographical reconstruction [2]. The measurement of phase/time of arrival spread also referred to as "longitudinal charge distribution" or loosely just "bunch length or bunch shape" is considered more accessible. The problem of longitudinal emittance determination is thus reduced to accurate measurement the longitudinal charge distribution. The devices used for longitudinal charge distribution is the main topic of this paper.

Longitudinal charge distribution measurements for relativistic charges ($\beta \approx 1$) or "long" charge distributions ($\Delta t \gg 1$ ns) is satisfactorily and non destructively performed using phase probes or wall current monitors until the electromagnetic design limitations. However, for UNILAC energies, i.e. $\beta < 0.15$ and the particle arrival time spread of about 0.4–2 ns (σ of a Gaussian distribution), the beam transverse field distribution is elongated significantly in comparison to charge distribution. This effect is here onward referred to as "field dilution". Equation 1 shows the expression of the transverse field of a moving charge q with

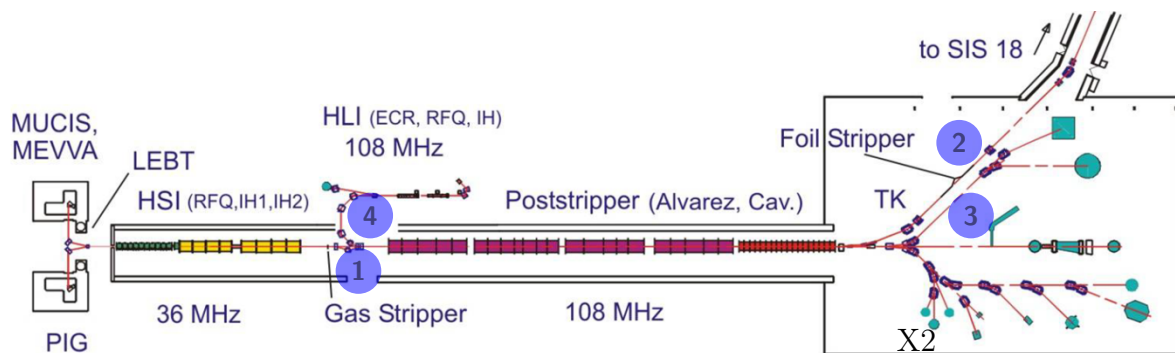


Figure 1: Schematic showing the UNILAC facility marking the location of various diagnostics. 1) Particle detectors 2) Dispersive section with RF deflector and screens 3) Gas Ionization BSM and 4) Feschenko BSM. R&D on FFC and GTR is ongoing in the area marked as "X2".

Content from this work may be used under the terms of the CC BY 4.0 licence (© 2022). Any distribution of this work must maintain attribution to the author(s), title of the work, publisher, and DOI

velocity βc at a distance R , which is the shortest perpendicular distance between charge propagation axis and phase probe.

$$E_T(R, \beta, t) = \frac{q}{4\pi\epsilon_0} \cdot \frac{\gamma R}{[R^2 + (\gamma\beta ct)^2]^{3/2}} \quad (1)$$

Figure 2 shows an example charge distribution and the corresponding transverse field at $R = 30$ mm for different charge velocities in accordance to Eq. (1). The dashed lines indicate the signal induced on the phase probe. The signal induction is based on the assumption that the contribution of phase probe to ground capacitance to the transfer impedance is negligible in the frequency range of interest.

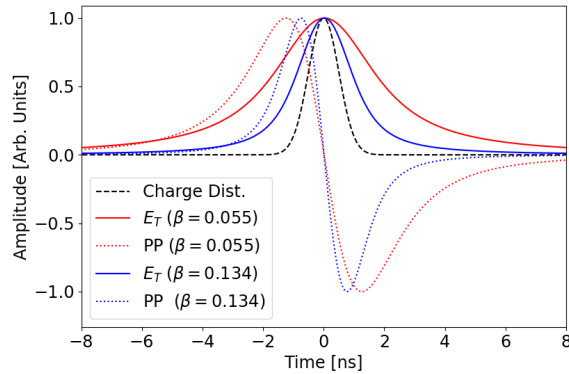


Figure 2: For the charge distribution ($\sigma_t = 0.5$ ns) showed by dashed lines, solid curves indicate the transverse field elongation for non-relativistic beam while dotted lines show the corresponding phase probe signal.

Figure 3 (top) shows 3 RF periods in a macropulse where charge distribution measured by a fast Faraday cup in comparison to the field distribution measured by a phase probe for $100 \mu\text{A}$ He^{1+} beam for the kinetic energy of 1.4 MeV/u ($\beta = 0.055$). The dotted lines mark the 108 MHz RF. The phase probe (PP) was located about ≈ 1 m upstream of the Faraday cup. Figure 3 (bottom) shows the averaged measurements over the full macropulse [3]. Also shown is the convolution of the FFC measurement with the analytical phase probe impulse response (Eq. (1)) which should ideally coincide with the phase probe measurement. The edges of the convolved signal are affected by the noise and it appears that the measured longitudinal charge distribution at FFC is smaller than the PP.

In the next section, alternate methods for longitudinal phase space determination historically used at UNILAC are discussed. Following that, recent R&D efforts on Fast Faraday cup measurements are discussed. Finally, a novel method for bunch length monitoring based on GHz transition radiation (GTR) is presented. The accuracy of FFC and GTR measurements are validated using simultaneous phase probe measurements.

BUNCH SHAPE MONITORS

Before the advent of fast oscilloscopes, two common approaches existed for charge distribution measurements for

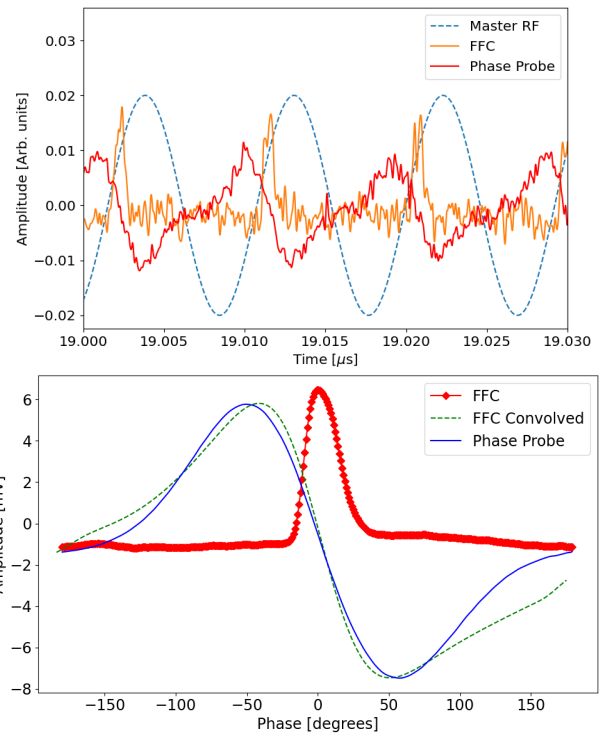


Figure 3: (Top) Snapshot of charge and field distribution measurements with FFC and PP within the macropulse. (Bottom) Averaged FFC and PP measurements along with convolution of FFC signal with impulse phase probe response.

non relativistic beams. The first one relies on scattering of the primary beam using a heavy metal foil (Tantalum, Gold etc.). The scattered beam is detected using charged particle detectors and time to digital converters (TDC) to measure particle time of arrival with respect to RF. At GSI, this principle is extended such that the scattered beam is detected twice, first via secondary electrons emitted from interaction with a thin aluminium foil followed by deposition in a diamond detector. This, in principle allowed for a simultaneous energy and phase spread measurements. The phase spread measurements were reliable while energy spread measurements were shown to be defective due to scattering foil non-uniformities. More details can be found here [4, 5] and references therein. Other facilities have used surface barrier detectors as charged particle detector with an otherwise similar principle [6].

Another commonly used method for bunch shape measurement is via generation of secondary electrons by irradiating a target material using primary beam. The low energy secondary electrons thus generated are carefully transported to a electron multiplier and a time to space conversion is performed in correlation with the master RF. The time-to-space conversion is performed via RF phase scan and slits or via the streak camera principle. Two devices, Feschenko BSM and Gas ionization based BSM which follow essentially the same principle described above, yet quite different realizations have been used at GSI. More details on these devices can be found here [5, 7] and references therein.

FAST FARADAY CUPS

Fast Faraday cups are variants of the regular Faraday cups optimized for measuring fast time structures and not the beam current. The major challenges for accurate time structure of the beam using a Fast Faraday cup are

1. The FFC structure should be optimized for deposition of the charged particles and passing the induced signal until high frequencies. This includes matching to 50 Ω co-axial cables for signal transfer. The bandwidth of the system should be at least five times the signal 3 dB cut-off in frequency domain i.e. $BW > \frac{5}{2\pi\Delta t}$
2. It should avoid the field dilution effects, i.e. measuring the preceding field of non-relativistic charges or it will encounter similar issues as with phase probes.
3. Suppress the distortion of induced signal due to secondary electron emission from the FFC collector. This is especially relevant for charged ion beams, since the number of secondary electrons scale with the charge state due to electronic stopping being the dominant mechanism.
4. Material damage to the FFC due to heating or melting of the cup under high intensity ion beams.

The problems listed above are known since the first Faraday cups were designed [8]. Earliest known design is an open ended tapered axially coupled co-axial structure [9, 10]. Currently, there is a repertoire of FFC designs based on modified co-axial cables and striplines. A front coupled stripline was used at SNS and Elettra [11] while a side coupled stripline was designed at BARC [12]. In this contribution, we will present the results of a radially coupled co-axial FFC obtained on loan from Fermilab.

The basic idea of this design is providing a blind hole from the side of a co-axial through the dielectric medium into the central conductor. The choice of hole width (1 mm) and depth (2 mm) is to minimize the escape of emitted secondary electrons. The blind hole in the central conductor of the co-axial is covered with a Titanium Zirconium Molybdenum Alloy (TZM) disk with a small 0.8 mm hole. The distance between TZM disk and the central conductor is optimized to reduce the field dilution effects. Detailed design is shown in Fig. 2 of this reference [13] along with further details. This device was successfully tested with low energy and low charge state beam and compared with a Feschenko monitor earlier [3]. In this contribution, beam with higher UNILAC energy and charge states was used for further validation measurements.

A 50 μs long Ar¹⁰⁺ beam macropulse with a kinetic energy of 8.6 MeV/u and 0.6 mA pulse current was measured at the FFC using 20 dB amplifier and 4 GHz, 40 GSA/s oscilloscope. Signal from a phase probe installed roughly 30 cm upstream was also simultaneously recorded using a comparable signal chain and acquisition electronics. The phase of one of the single gap resonators in the end section of UNILAC was utilized to vary the bunch shapes. Figure 4 shows the average bunch shape along with the phase probe signals for three buncher phase settings. A change in bunch shape

is visible and interpreted as the defocusing of the beam at increased buncher phase settings. The detailed bunch shape evolution is shown in Fig. 5. From the bunch shape evolution, it appears that energy spread is not uniform and evolves along the macropulse.

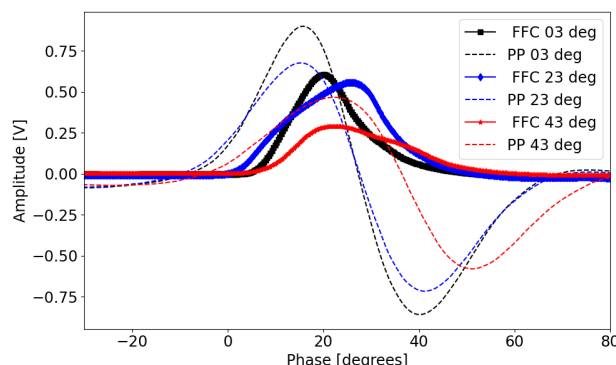


Figure 4: FFC bunch shape measurements with change in single gap resonator phase marked in the plot.

This bunch shape change along the macropulse is a general observation under various machine settings for moderate to high intensity beams in UNILAC and calls for “fast” measurements instead of “slow” averaged measurements.

Second validation measurement was performed by DC biasing of the FFC central conductor. This was performed to see the effect of secondary electrons emitted on the beam irradiation. This measurement was performed with 8.6 MeV/u 0.4 mA O⁶⁺ beam. Figure 6 shows a significant bunch “tail” of around 3ns is observed in the measured profile. The tail was suppressed on application of +ve bias and increased on application of -ve bias. Empirical estimates of secondary electron energy spectra suggest [14] that more than 90% electrons have energies below 30 eV and 30–50 V DC bias should be sufficient to suppress the signal distortion due to secondary emission. This measurement highlights the need of always positively biasing the central conductor when used with ion beams especially with higher charge states.

Another validation of the charge profile measured by FFC was performed by comparing it with the phase probe signal. Figure 7 shows the waterfall plot of the +25 V biased FFC and PP signal for the same macropulse.

While the FFC shows a phase/energy modulation along the macropulse, similar movement is not obvious in the PP signal. Figure 8 shows the comparison of the FFC signal convolved with PP impulse response and it appears that the FFC measured a reduced longitudinal charge profile in comparison to the PP. The potential reason is that, since the FFC is located in a dispersive section, it performs an energy selection of the beam through its 0.8 mm hole as depicted in Fig. 9.

This also makes it more sensitive to energy changes along the macropulse in comparison to the Phase probe. In nutshell, it should be emphasized that FFC should be placed in non-dispersive regions for trivial interpretation of its output. The signal obtained from FFCs placed in dispersive sections

require a careful analysis and might even be useful scanning the phase space with FFC movement in the dispersive plane.

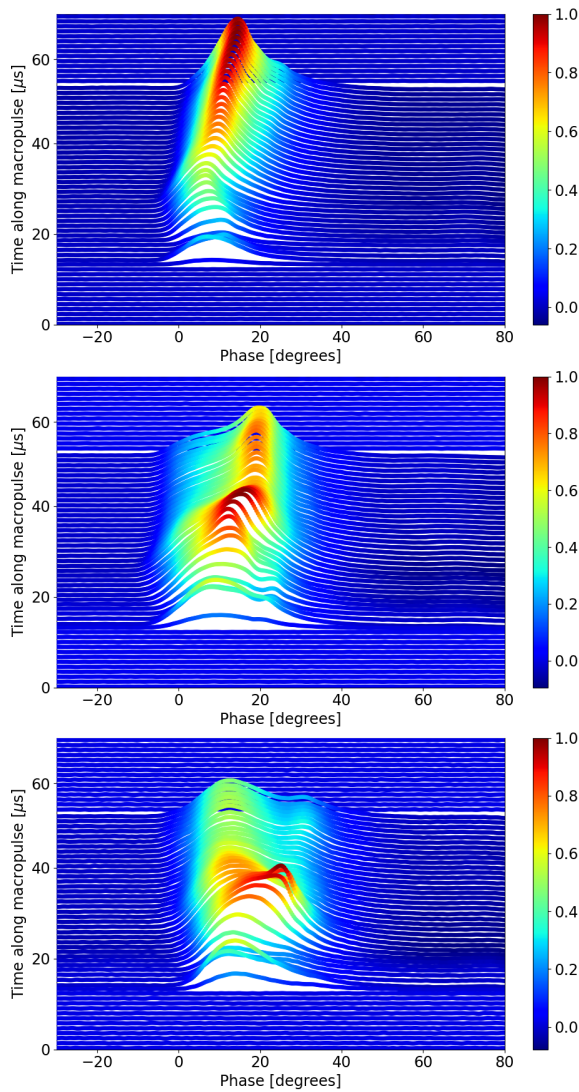


Figure 5: FFC bunch shape evolution for various single gap resonator phase (Top) 3 degrees, (Middle) 23 degrees and (Bottom) 43 degrees.

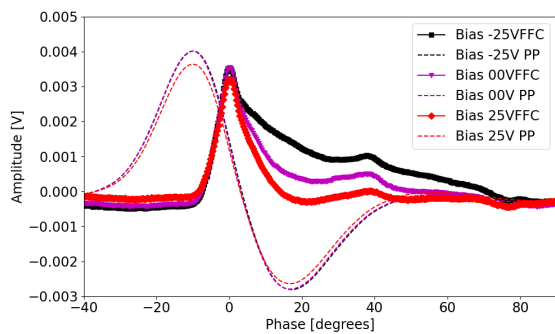


Figure 6: The longitudinal charge profile measurement averaged for a macropulse with application of various DC bias voltages on the FFC central conductor.

GHZ TRANSITION RADIATION MONITOR

Transition radiation in GHz regime is coherent for sub-n bunches. This frequency regime was utilized for bunch length measurements for the first time as reported earlier [15]. The E-Field of the coherent transition radiation for charge normally incident on a target in the far-field region is given as,

$$\vec{E}(t) = \frac{q\beta}{2\pi\epsilon_0 c R} \frac{\sin\theta \cdot \delta(R/c - t)}{1 - \beta^2 \cos^2\theta} \cdot (\hat{e}_x \cos\theta + \hat{e}_z \sin\theta) \quad (2)$$

R is the distance from the target center to the measurement location while θ is the angle between the target normal and measurement location in the plane of observation (refer Fig. 1 in [15]).

Detailed discussion on E-field analytical expressions in near field and corresponding CST simulations can be found

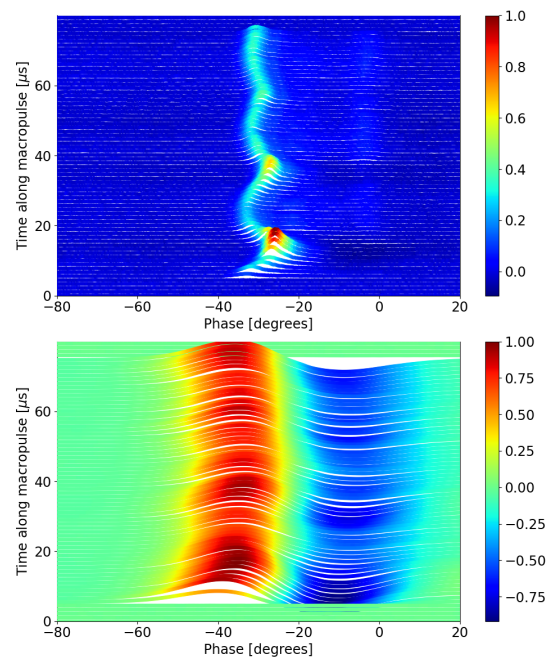


Figure 7: The waterfall plot showing the simultaneously recorded FFC and PP signal evolution along the macropulse. A phase modulation along the macropulse is visible.

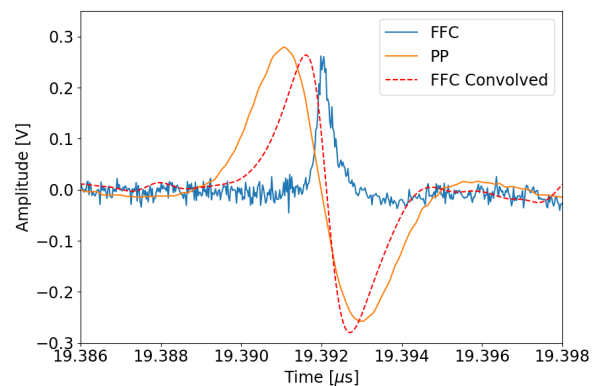


Figure 8: The FFC response convolved with the PP impulse response is much narrow in comparison to the PP signal.

Content from this work may be used under the terms of the CC BY 4.0 licence (© 2022). Any distribution of this work must maintain attribution to the author(s), title of the work, publisher, and DOI

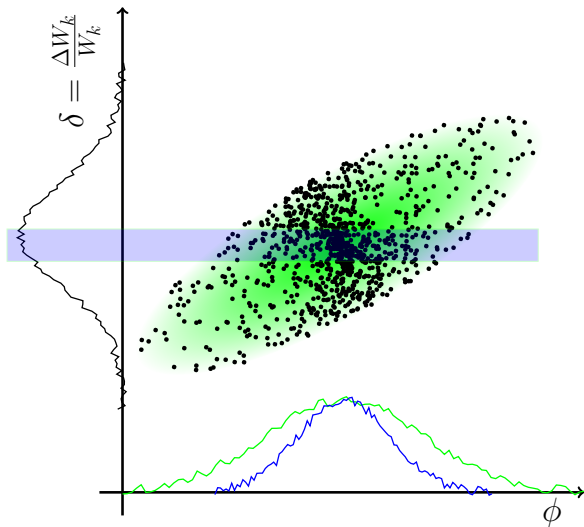


Figure 9: A schematic showing the effect of energy selection with dispersion on the measured bunch shape measured by the FFC.

here [15]. The radiation is polarized, broadband and proportional to the beam current. For 10 pC charge constrained in a 100 ps bunch, the peak measurable signal on a commercial biconical antenna is expected to be 10 mV. Other important concepts for transition radiation based measurements are the *effective source size* and radiation *formation zone*. *Effective source size* is the field elongation of the largest wavelength λ of interest and is given as, $\beta\gamma\lambda/2\pi$. The GTR target should at least be of this size in order not to cut-off useful lower frequencies required to reconstruct the bunch length via the radiated fields. Typically a small hole (10% of the effective source size) can be accommodated in the target for beam to go through without significantly affecting the induced radiation field. The *formation zone* is the area around the target where the radiation field is still transient. The radiation zone is generally dependent on the angle of radiation θ , however a simple yet conservative formula for the distance from target R which can be considered outside formation zone is given as $R = \gamma^2\lambda$. The measurement apparatus should be kept in the far field outside of the formation zone. The detailed consideration of all these concepts is discussed in [15].

The GTR measurement set-up is shown in Fig. 10. Prominent components include EM vacuum window made out of Quartz glass for the electromagnetic radiation to couple out of the vacuum and a Tantalum target with 3mm hole. There is a narrow tapered section to reject waveguide modes from leaving the beam pipe and interfere with the measurement device. A wideband biconical antenna (not shown) with a bandwidth of 4.5 GHz is placed at a distance of 1.0 m and 40 degrees with respect to beam axis from the target.

Figure 11 shows the bunch evolution in the macropulse measured by GTR and PP for 11.4 MeV/u Bi²⁶⁺ with 0.4 mA average macropulse current. The trend in absolute signal strength and bunch shape is almost identical. The time of flight between PP and GTR monitor was also measured and matched to the expected beam velocity.

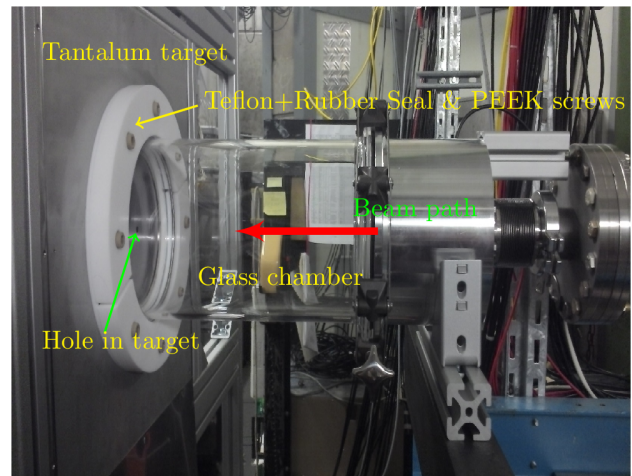


Figure 10: GTR measurements set-up

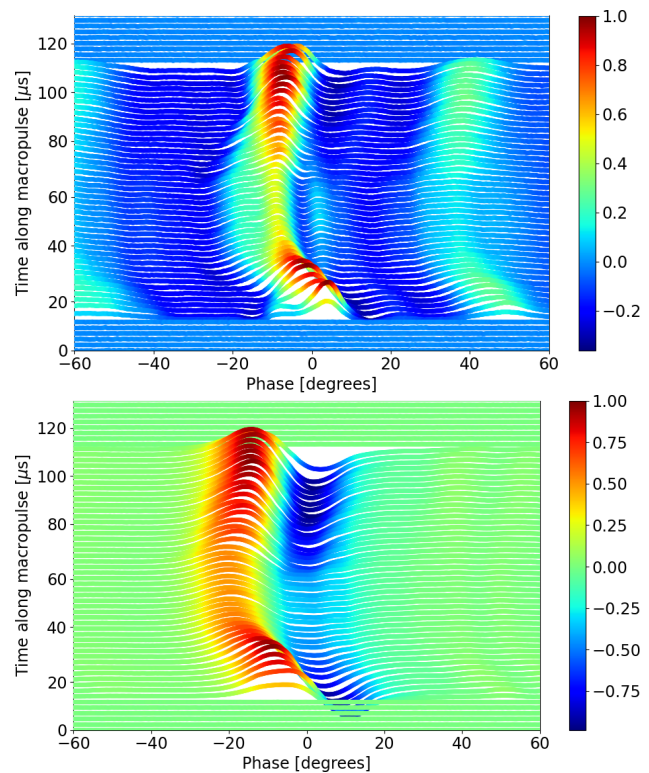


Figure 11: GTR and PP waterfall plot showing the bunch shape evolution along the macropulse.

In order to validate the accuracy of measured bunch shape by the GTR, the measured GTR signal was convolved with the analytical phase probe impulse response corresponding to $\beta = 0.154$ and compared with the phase probe signal. The outcome is shown in Fig. 12 and there is a good agreement between sampled phase space among the two devices. The wiggling behavior in the calculated convolution outside the bunch is due to enhancement of interferences by the convolution procedure. The various reflections from the glass window and metal parts in the measurement location are also visible and still pose a challenge for the GTR measurement.

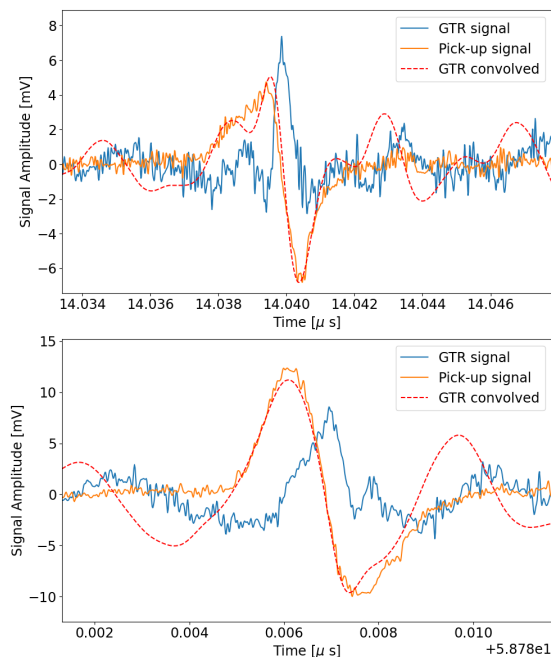


Figure 12: GTR signal along with its convolution through the PP response in comparison with the phase probe signal. A precise agreement between GTR and PP signal is seen.

CONCLUSION

The longitudinal charge distribution at UNILAC is seen to evolve within the macropulse in addition to pulse to pulse variation under moderate beam currents. These fast variations make the slower and established measurement options based on long averaging insufficient. Fast devices are therefore being sought and tested to obtain the longitudinal phase space and thus optimize the UNILAC. Based on the recent measurements, it was established that FFC is a compact and promising option and the central conductor should be biased with 30-50V. Further the FFC should be placed in a non-dispersive section to sample the complete phase space simultaneously and results should be validated against the phase probe signal. GTR monitor is a novel development and first results show precise agreement with the phase probe signal. It also allows non-invasive measurements of charge distribution which might be crucial for very high beam currents at high duty cycles.

ACKNOWLEDGEMENTS

The author would like to especially thank P. Forck and T. Reichert for many useful discussions and for providing DC biasing measurement data of the FFC. Colleagues from beam instrumentation, LINAC department and the machine operating team are gratefully acknowledged for the large support during this work on various aspects of installation and measurements. V. Scarpine, D. Sun and A. Shemyakin from FNAL for providing the FFC on loan as well as K. Mal and G. Rodrigues from IUAC for the simulation support of the FFC.

REFERENCES

- [1] W. Barth *et al.*, “High brilliance beam investigations at universal linear accelerator”, *Phys. Rev. Accel. Beams*, vol. 25, p. 040101, 2022. doi: 10.1103/PhysRevAccelBeams.25.040101
- [2] S. Lauber *et al.*, “Longitudinal phase space reconstruction for a heavy ion accelerator”, *Phys. Rev. Accel. Beams*, vol. 23, p. 114201. doi: 10.1103/PhysRevAccelBeams.23.114201
- [3] R. Singh *et al.*, “Comparison of Feschenko BSM and Fast Faraday Cup with Low Energy Ion Beams”, in *Proc. IBIC’21*, Pohang, Korea, Sep. 2021, pp. 407. doi: 10.18429/JACoW-IBIC2021-WEPP16
- [4] T. Milosic, “Feasibility Study on Longitudinal Phase-Space Measurements at GSI UNILAC using Charged-Particle Detectors”, PhD. thesis, Technical University of Darmstadt, Germany, 2014. https://tuprints.ulb.tu-darmstadt.de/4321/1/Milosic_PhD-Thesis_2013.pdf
- [5] P. Forck, “JUAS Lecture notes on beam instrumentation”, 2021
- [6] S. Ghosh *et al.*, “Method to reduce microphonics in superconducting resonators”, *Phys. Rev. ST Accel. Beams*, vol. 10, p. 042002, 2007. doi: 10.1103/PhysRevSTAB.10.042002
- [7] B. Zwicker, “Design of a Bunch Shape Monitor for High Current LINACs at GSI”, PhD thesis, University Frankfurt, 2016. https://www.gsi.de/fileadmin/SD/Theses/Thesis_DruckVersionDis_20160502.pdf
- [8] J. M. Bogaty *et al.*, “A Very Wide Bandwidth Faraday Cup Suitable for Measuring Gigahertz Structure on Ion Beams with Velocities Down to $\beta < 0.01$ ”, in *Proc. LINAC’90*, Albuquerque, NM, USA, Sep. 1990, pp. 465-467. <https://jacow.org/190/papers/tu457.pdf>
- [9] P. Strehl, “Beam instrumentation and diagnostics”, Springer Berlin, Heidelberg, 2006. doi: 10.1007/3-540-26404-3
- [10] W. R. Rawnsley *et al.*, “Bunch shape measurements using fast Faraday cups and an oscilloscope operated by LabVIEW over Ethernet”, *AIP Conference Proceedings*, vol. 546, p. 547, 2000. doi: 10.1063/1.1342629
- [11] M. Ferianis *et al.*, “Characterization of Fast Faraday cups at the ELETTRA LINAC”, in *Proc. DIPAC’03*, Mainz, Germany, May 2003, pp. 113-115. <https://jacow.org/d03/papers/PM10.pdf>
- [12] J. Matthew and A. Bajaj, “An improved strip-line fast Faraday cup for beam bunch measurements”, *Review of Scientific Instruments*, vol. 91, p. 113305, 2020. doi: 10.1063/5.0025457
- [13] J.-P. Carniero *et al.*, “Longitudinal beam dynamics studies at the PIP-II injector test facility”, *International Journal of Modern Physics A*, vol. 34, no. 36, 2019. doi: 10.1142/S0217751X19420132
- [14] A. Reiter *et al.*, “Investigation of Cross Talk in Secondary Electron Emission Grids”, Technical Note LOBI-TN-SEM-2012-001, GSI, Darmstadt, 2012.
- [15] R. Singh and T. Reichert, “Longitudinal charge distribution measurement of nonrelativistic ion beams using coherent transition radiation”, *Phys. Rev. Accel. Beams*, vol. 25, p. 032801, 2022. doi: 10.1103/PhysRevAccelBeams.25.032801

SIGNAL ESTIMATION AND ANALYSING OF COLD BUTTON BPMs FOR A LOW-BETA HELIUM / PROTON SUPERCONDUCTING LINAC*

Y. Zhang[†], X. J. Hu, Z. X. Li, H. Jia, S. H. Liu, H. M. Xie

Institute of Modern Physics, Chinese Academy of Sciences, Lanzhou, China

Abstract

We develop a formula including the low-beta effect and the influence of long cable issues for estimating the original signal of cold BPMs. A good agreement between the numerical and the measured signal with regard to two kinds of beam commissioning, helium and proton beams, in a low-beta helium and proton superconducting linac, proves that the developed numerical model could accurately estimate the output signal of cold button BPMs. Analysing the original signal between the first and the last cold BPM in the cryomodule, it is found that the signal voltage in the time domain is increased with the accelerated beam energy. However, the amplitude spectra in the frequency domain has more high frequency Fourier components and the amplitude at the first harmonic frequency reduces a lot. It results in a decline of the summed value from the BPM electronics. The decline is not proportional to a variety of the beam intensity. This is the reason why BPMs give only relative intensity and not absolute value for low-beta beams with a Gaussian distribution.

INTRODUCTION

Cold button BPM, as a normal diagnostic element in the Cryomodules (CMs), play an important function for monitoring the beam position, phase, and energy. Using the summed values from cold button BPMs to measure the beam intensity is our desirable thing. Thus, for a low-beta ion beam, estimating the original signal of cold button BPMs is important since the induced imaging bunch shape is expanded. Furthermore, the signal will be transmitted through a long cable to the electronics. An influence of cable's attenuation and dispersion on the transmission should be confirmed. If an accurate signal estimation in the time domain (TD) could be proven, we could perform the Fast Fourier Transform (FFT) to obtain the amplitude spectra in the frequency domain (FD) and analyse what signal is processed in the digital electronics. At last, we find the summed values of cold button BPMs processed by the digital electronics are decreasing along the superconducting (SC) linac. We will discuss these unexpected summed values and prove that they could not be used for monitoring the absolute beam intensity in a low-beta SC Linac

CAFe AND ITS COLD BUTTON BPMs

CAFe is a low-beta helium / proton superconducting LINAC. It is as a demo LINAC for China initiative

* Work was supported by National Natural Science Foundation of China (Grant No. 11675237) and the 2018 "Western Light" Talents Training Program of Chinese Academy of Sciences.

[†] zhangy@impcas.ac.cn

Accelerator-Driven System and constructed at the Institute of Modern Physics, Chinese Academy of Science, as shown in Fig. 1. This facility includes two ion sources with an output energy of 20 keV/u before a 4-vane type copper structure radio frequency quadrupole (RFQ) with an accelerated energy of 1.5 MeV/u. The first is an electron cyclotron resonance (ECR) proton source of 10 mA with an energy of 20 keV, and the second includes an ECR helium source of 2 mA. After the RFQ section, they have the same layout, including a medium energy beam transport (MEBT), four cryomodules (CMs) and a high energy beam transport (HEBT) line. In four CMs, there are 23 half-wave resonance (HWR) SC cavities, 23 SC solenoids, and 19 cold button BPMs [1-3].

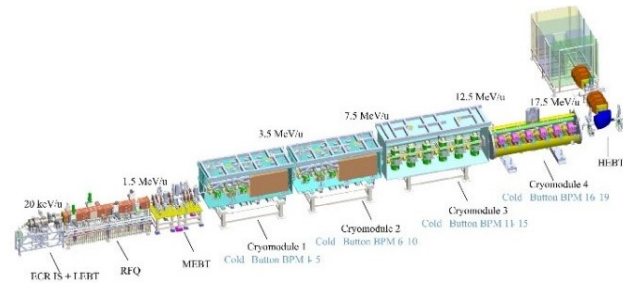


Figure 1: Schematic layout of Chinese ADS Front-end superconducting demo LINAC (CAFe).

Cold Button BPMs are both nonlinear and dependent on the position in the orthogonal plane. A general rule of thumb is that the button width should be approximately 60° wide, leaving a 30° gap between buttons. An initial design and test of the system was published in Ref. [4]. Our button parameter is optimized to an angular coverage ϕ of 62.2° to obtain high sensitivity. The surface is shaped as a section of a cylinder to be flush with the vacuum chamber surface, as shown in Fig. 2.

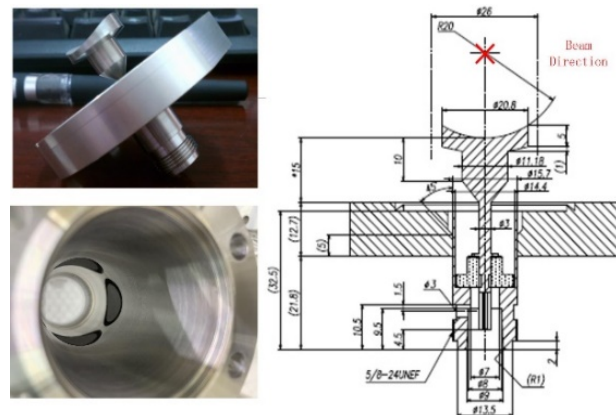


Figure 2: Button electrode, assembling picture and its drawing [4].

Content from this work may be used under the terms of the CC BY 4.0 licence (© 2022). Any distribution of this work must maintain attribution to the author(s), title of the work, publisher, and DOI

DESCRIPTION OF TWO KINDS OF BEAM COMMISSIONING

From the middle of 2020 to the beginning of 2021, there were two kinds of beam commissioning. One was Helium-4 ion beams with a peak current of 145 μA at an energy of 6–7 MeV/u, and the other was proton beams with a peak current of 4–10 mA at an energy of 16–20 MeV [3]. There are two ACCTs (AC current transformer from Bergoz Instruments, ACCT-CF6"-60.4-40 UHV) in the entrance of CM1 and the exit of CM4, respectively, to monitor the peak current [5]. Beam current is obtained by a data acquisition card with the sampling rate of 20 MHz/s (made in-house). It is recorded in a data base. The original data from cold button BPM 1 and 19 are obtained by an oscilloscope at the same time for the analysis. We choose the recorded current data during the obtaining time and show them in Fig. 3 and Fig. 4. The related beam size and energy at the location of cold button BPM1 and 19 are listed in Table 1. The beam orbit has been tuned to the center within less than 2 mm to prevent beam losses. In the next part, the signal estimation and the comparison of cold button BPMs are all based on the above-mentioned data.

Table 1: Parameters of Beam Size and Energy for Cold BPM1 and BPM19 During Two Kinds of Beam Commissioning

Beam parameters	$^4\text{He}^{2+}$		Proton	
	cold BPM1	cold BPM19	cold BPM1	cold BPM19
X_{rms} [mm]	1.66	1.93	1.51	1.31
Y_{rms} [mm]	1.66	2.84	1.42	1.31
Z_{rms} [°]	4.64	3.82	4.3	1.89
Energy [MeV/u]	1.59	6.89	1.78	16.93

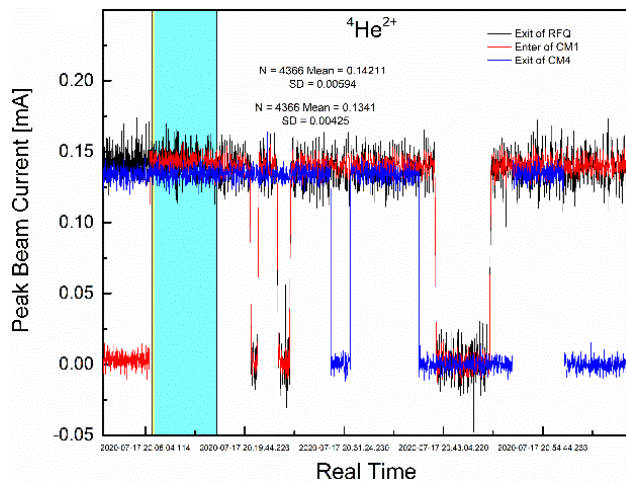


Figure 3: $^4\text{He}^{2+}$ beams' current in real time (from 20:08 to 20:54 on July 17, 2020).

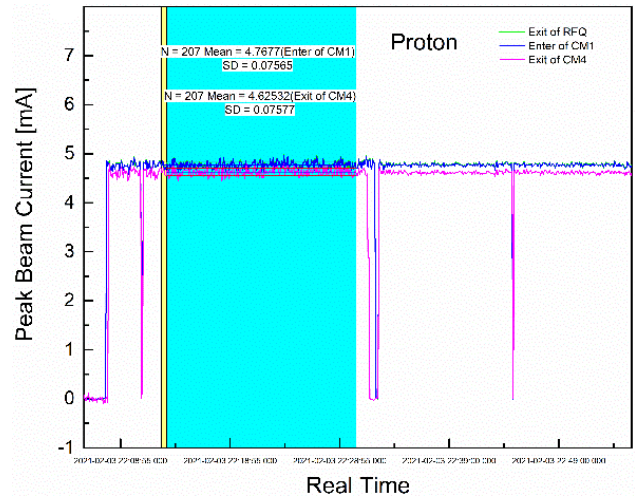


Figure 4: Proton beams' current in real time (from 22:08 to 22:49 on February 3, 2021).

SIGNAL ESTIMATION OF COLD BUTTON BPMs

3D Model and Simulated Results by CST PS

An accurate 3D model of cold button BPM is developed in SOLIDWORKS and then imported to CST PS for the simulation [6, 7]. The button electrode parameters are the same as the described in the last Section. Using an E-field monitor and voltage monitor, the output voltage of the electrode is simulated. A distribution of the bunched beam current and the related output voltage of cold BPM1 for $^4\text{He}^{2+}$ beams are simulated by CST PS with a PIC solver, as shown in Fig. 5. Furthermore, a numerical model is developed to check the simulated results.

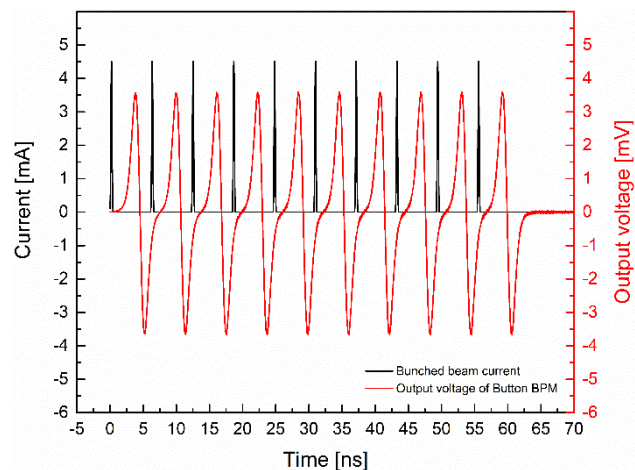


Figure 5: Simulated distribution of the bunched beam current and the output voltage of cold button BPM1 by CST PS with PIC solver.

Numerical Model and Comparisons of the Output Signal from Cold Button BPMs

Considering a Gaussian bunch shape, the beam current $I_b(t)$ of a single bunch is given by [8]:

$$I_b(t) = \frac{eN}{\sqrt{2\pi}\sigma} \cdot e^{\left(\frac{-t^2}{2\sigma^2}\right)}, \quad (1)$$

where N is the total particle number and σ is the rms bunch length. Assuming a symmetric bunch shape in time with a bunching period of T , the repetitive beam current could be represented by Fourier series expansion in TD as:

$$I_b(t) = \langle I_b \rangle + 2\langle I_b \rangle \cdot \sum_{m=1}^{\infty} A_m \cdot \cos(m\omega_0 t), \quad (2)$$

where $\langle I_b \rangle$ is the average dc current, ω_0 is the bunching angular frequency, m is the harmonic, and

$$A_m = e^{\left(\frac{-m^2\omega_0^2\sigma^2}{2}\right)}.$$

The length of the image charge distribution (opposite sign) is wider than the physical length of the bunch charge distribution for the low- β beam. The length of the image charge of the bunch is assumed,

$$\sigma_{im}^2 = \sqrt{\sigma^2 + \left(\frac{b}{\sqrt{2}\beta\gamma c}\right)^2},$$

where σ is the rms longitudinal bunch length, b is the radius of the beam pipe, βc is the beam velocity, and γ is the relativity factor.

Thus, the image current can be rewritten as:

$$I_{im}(t) = -\langle I_b \rangle - 2\langle I_b \rangle \cdot \sum_{m=1}^{\infty} B_m \cdot \cos(m\omega_0 t), \quad (3)$$

where

$$B_m = e^{\left(\frac{-m^2\omega_0^2\sigma_{im}^2}{2}\right)}. \quad (4)$$

The button electrode voltage on a termination of R is

$$V_{\text{button}}(t) = R \cdot i_s(t) = \frac{\Phi I R}{2\pi \beta c} \cdot \frac{dI_{im}(t)}{dt}. \quad (5)$$

Substituting Eqs. (3) and (4) into Eq. (5), the voltage of the button electrode for the low- β bunched ion beam is:

$$V_{\text{button}}(t) = -\langle I_b \rangle \cdot \frac{\Phi I R}{2\pi \beta c} \cdot \sum_{m=1}^{\infty} e^{\left(\frac{-m^2\omega_0^2\sigma_{im}^2}{2}\right)} \cdot (-m\omega_0) \cdot \sin(m\omega_0 t), \quad (6)$$

where the factor ϕI is equal to the button electrode surface area divided by b . Using Eqs. (2), (3) and (6), the bunched current distribution of low- β beams, its image current distribution and the related output signal of the button electrode are numerically calculated by a MATLAB code [9] and plotted in Fig. 6. There is a comparison between the CST simulated, the numerical calculated by Eq. (6) and the measured original signal from cold BPM1, shown in Fig. 7. It indicates that the assumed imaging bunch length for low- β

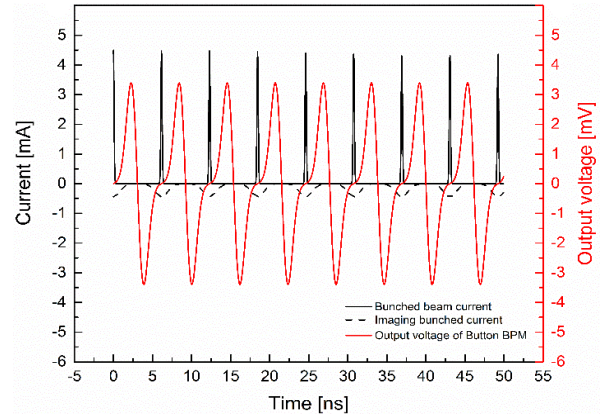


Figure 6: Numerical calculated distribution of the bunched beam current, image current and related output voltage of the button electrode by Eq. (2), Eq. (3) and Eq. (6).

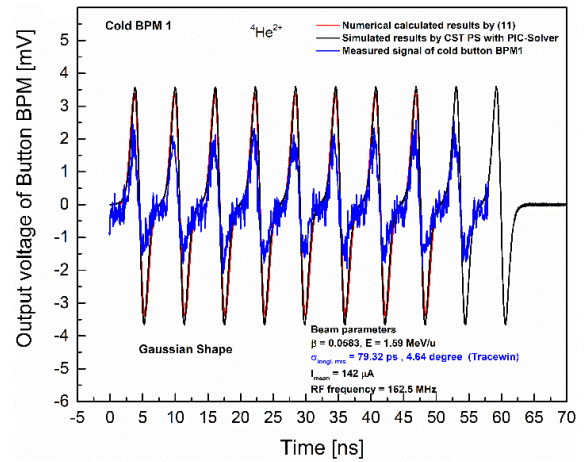


Figure 7: Comparisons between the simulation by CST PS with PIC solver, the numerical calculation by Eq. (6) and the measured output voltage of cold button BPM1.

beams is right. However, there is a large difference in the amplitude between the measured and the simulated values. This is due to the measured signal from the oscilloscope through a long cable transmission connected to the button electrode. The long cable transmission leads to an asymmetric measured signal. Thus, CST simulation and formula (6) only consider the output signal directly from the electrode. Furthermore, the signal estimation of cold button BPM including the influence of cable attenuation and dispersion is presented as the following.

If the bipolar output signal of the cold button pick-up can be written in the model (6), the signal with cable attenuation and dispersion could perform a convolution operation on Eq. (6). Then the complete expression for the attenuated button pick-up signal including cable attenuation and dispersion is Eq. (7), where α_m is the attenuation per unit length at frequency with the unit of nepers per meter. τ is the frequency-independent insertion delay for a lossless cable of length z . Other factors keep the same definition as listed in Eq. (6). The amplitudes of the individual frequency components are attenuated following the $f^{1/2}$ rule, and their relative phases are skewed because of the frequency-dependent dis-

person in the transmission line. In our case, the measured raw signal of cold button BPMs is obtained from an Agilent 90604A oscilloscope port, which is connected to a transmission line including a cold button feedthrough (port A), a 2.3 meter semirigid RF cable in CM, and a 30 m RF cable (TCOM240-PUR-FR from Times Microwave Systems) in the air.

$$V_{\text{button}}(t) = -\langle I_b \rangle \cdot \frac{\Phi I R}{2\pi\beta c} \cdot \sum_{m=1}^{\infty} \left\{ e^{-\alpha_m \sqrt{f} z} \cdot e^{\left(\frac{-m^2 \omega_0^2 \sigma_{im}^2}{2} \right)} \cdot (-m\omega_0) \cdot \sin \left(m\omega_0(t - \tau) - \alpha_m \sqrt{f} z \right) \right\} \quad (7)$$

Here, we only consider the influence of 30-meter cables since the specifications of semirigid RF cables are not very clear. We assume the semirigid cable with the same specification as TCOM240. Then, the total length z of cables is approximately 33 m, with respect to the time delay τ of 131 ns ($= 33/0.84/(3 \times 10^8)$).

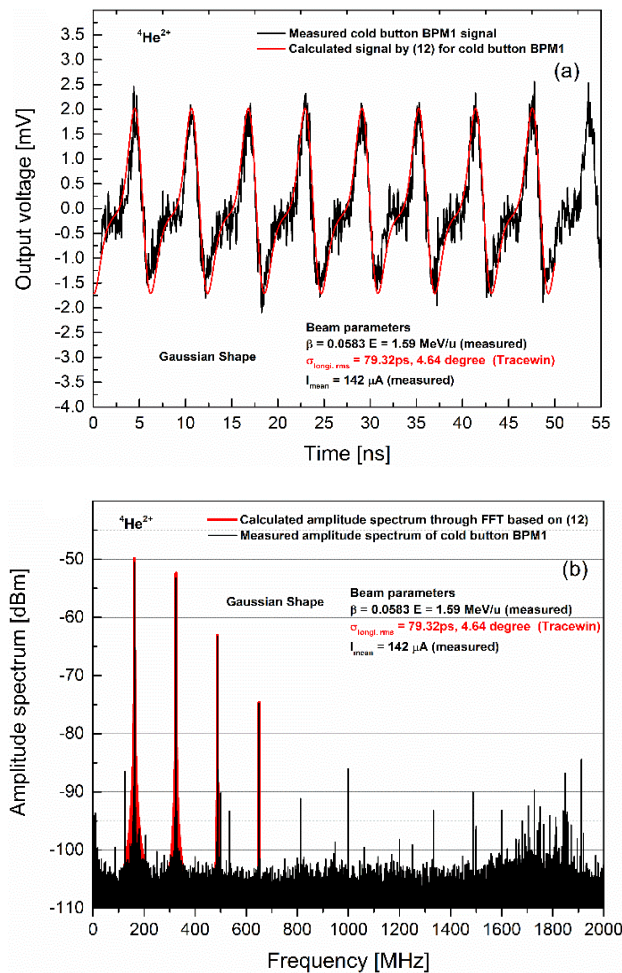


Figure 8: Comparisons between the calculated by Eq. (7) and the measured output voltage of cold button BPM1 in TD (a) and FD (b) during ${}^4\text{He}^{2+}$ beam commissioning.

The TCOM240 cable attenuation is calculated in nepers per meter by [10] $\alpha_m = (0.229148 \cdot \sqrt{f \text{ MHz}} + 0.000331 \cdot f \text{ MHz}) / 33 / 8.6$.

Substituting τ , z and α_m into Eq. (7), the numerical signal of the cold button BPM considering the low- β effect, cable attenuation and dispersion can be obtained. The measured and the calculated results for ${}^4\text{He}^{2+}$ beams and proton beams are compared and presented in Figs. 8 and 9. When a centred ${}^4\text{He}^{2+}$ beam with current of 142 μA enters the first SRF cavity, port A of cold button BPM1 shows an original signal with an asymmetric peak-to-peak voltage V_{pp} of 2 mV. The calculated result by Eq. (7) shows a good agreement with the measured in terms of the amplitude and shape, as shown in Fig. 8(a). The amplitude spectra in FD are transformed based on the estimated signal in TD. The spectra in FD also is coincided with the measured at the main harmonic frequencies (1st, 2nd, 3rd, 4th), as shown in Fig. 8(b). When proton beams with current of 4.76 mA enters the first SRF cavity and exits CM4 with current of 4.62 mA, port A of cold buttons BPM19 shows the original signals with asymmetric V_{pp} values of 135 mV, as shown in Fig. 9(a). Correspond-

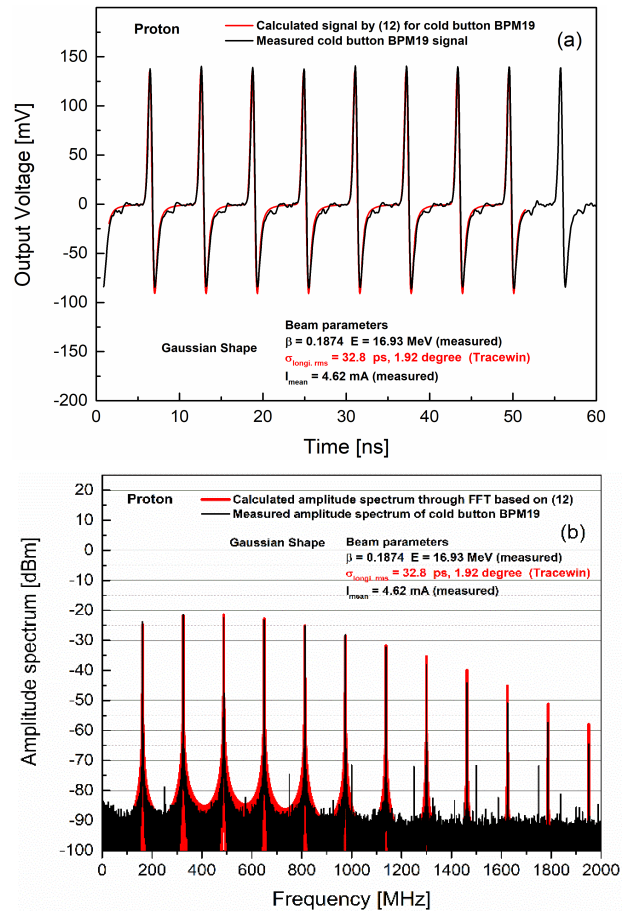


Figure 9: Comparisons between the calculated by Eq. (7) and the measured output voltage of cold button BPM19 in TD (a) and FD (b) during proton beam commissioning. ingly, the amplitude spectra in FD is coincided with together, as shown in Fig. 9(b). The induced imaging bunch shape and the amplitude of signal could have a good agreement with the measured results regardless of whether the signal is

Content from this work may be used under the terms of the CC BY 4.0 licence (© 2022). Any distribution of this work must maintain attribution to the author(s), title of the work, publisher, and DOI

from the helium beam or from the proton beam with different energies. At the same time, there is in agreement with the amplitude spectra in FD.

ANALYSIS OF SUMMED VALUES FOR COLD BUTTON BPMs

Based on the above results, we could use numerical model Eq. (7) to analyse the summed signal of cold button BPM1 and BPM19 with the centred beam. As shown in Figs. 3 and 4, the transmission efficiency from the entrance to the exit of CMs is approximately 95% ($= (142 - 134) / 142$) and 97.1% ($= (4.76 - 4.62) / 4.76$) during two kinds of beam commissioning, a low-power $^4\text{He}^{2+}$ beam and a high-power proton beam. As shown in Fig. 10, four color curves present Va, Vb, Vc, and Vd signals of cold button BPMs from the Libera Single Pass H (LSPH) [11]. For each BPM, four

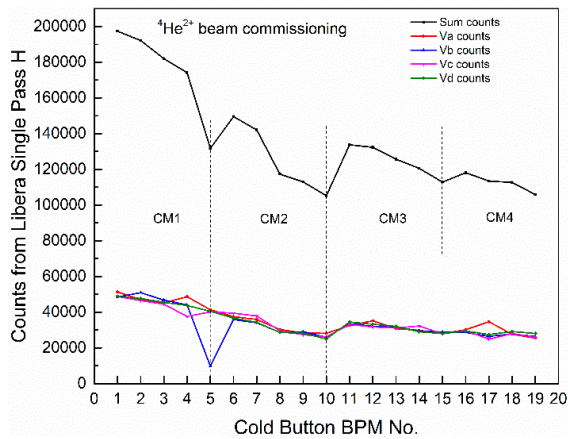


Figure 10: Trends of Sum, Va, Vb, Vc and Vd from cold button BPM1 to BPM19. These data are from the BPM electronics of Libera Single Pass H. The recording time is from 20:50 to 20:54 on July 17, 2020.

values remain similar except cold BPM5 since its Vb is very small. This means that $^4\text{He}^{2+}$ beam is around the center position. The summed values of four port signals ($= \text{Va} + \text{Vb} + \text{Vc} + \text{Vd}$) continue to decline in the counts, as shown in the black curve. The decrease ratio of summed values between BPM19 and BPM1 is up to 46% ($= (1.97 \times 10^5 - 1.06 \times 10^5) / 1.97 \times 10^5$). However, the beam current just has losses of 5%. Similarly, we perform the same comparison for proton beam. As shown in Fig. 11, the summed values between cold buttons BPM1 and BPM19 from LSPH has decreased by 44% ($= (8.9 \times 10^5 - 4.96 \times 10^5) / 8.9 \times 10^5$). However, the beam current difference is only 2.9%.

For our BPM electronics, LSPH uses narrowband processing to obtain a higher precision of the position reading. The summed counts of LSPH shown in Figs. 10 and 11 are all acquired at the first frequency. In fact, during a routine beam commissioning, it is not permitted to obtain the original signal of cold button BPMs through oscilloscopes because of the requirement from machine protect system (MPS). Thus, the numerical model Eq. (7) plays an important role to help us understand the raw signals of cold button

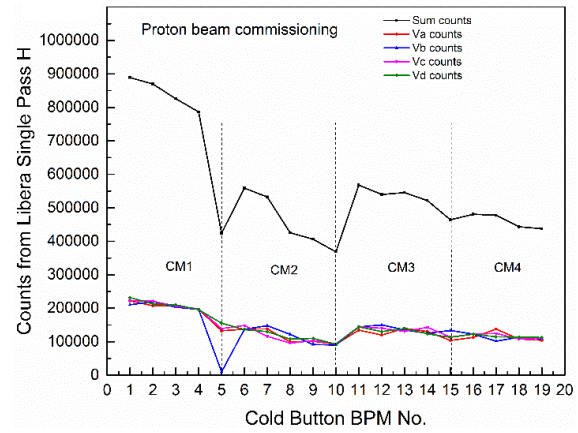


Figure 11: Trends of Sum, Va, Vb, Vc and Vd from cold button BPM1 to BPM19. These data are from the BPM electronics of Libera Single Pass H. The recording time is from 22:08 to 22:49 on Feb. 3, 2021.

BPMs, as shown in Figs. 12 and 13. Through FFT transforming from TD to FD on the calculated signal, it is found that the calculated differences between BPM1 and BPM19 are

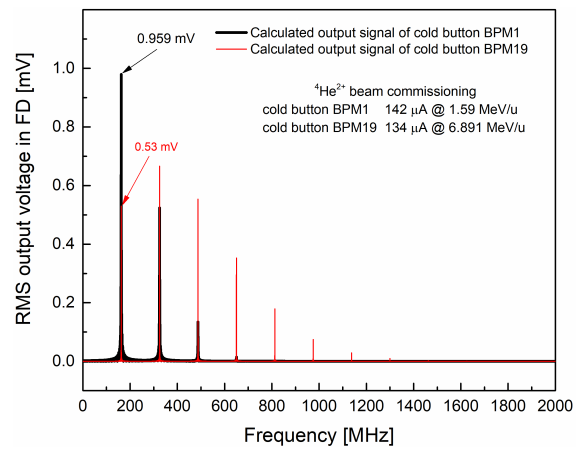


Figure 12: Comparison between the calculated signal in FD of cold button BPM1 and BPM19 during $^4\text{He}^{2+}$ beam commissioning.

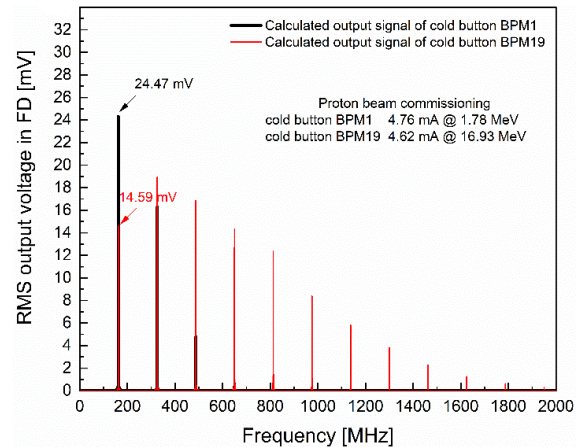


Figure 13: Comparison between the calculated output signal in FD of cold button BPM1 and BPM19 during proton beam commissioning.

44.7% ($= (0.959-0.53) / 0.959$), and 40% ($= (24.47-14.59) / 24.47$), which are similar to the measured differences at the first harmonic frequency.

For two kinds of beam commissioning, there are some similar conditions. Cold BPM5, the summed counts are particularly small because its V_b is small, as shown in Figs. 10 and 11, which indicates that port B of BPM5 has some problems. In CM2, cold BPM numbers is from 6 to 10. The measured data is smaller than the others. The only difference between CM2 and the others is that the semirigid RF cables are different. In CM2, we use semirigid cables with the dielectric material SiO_2 from MEGGITT. The others use semirigid RF cables with the dielectric material microporus PTFE from Times Microwave Systems. The different insert losses of semirigid cables might result in the summed value difference from cold button BPM6 to BPM10 in CM2. However, it could not change the decreasing trend of summed counts along CMs.

Figures 11 and 13 prove that the amplitude spectra of button BPMs in FD are widened with the beam energy increasing and the longitudinal length shortening, regardless of whether the signal from $^4\text{He}^{2+}$ beam or from proton beam. At the same time, the amplitude at the first harmonic frequency of 162.5 MHz is decreasing along the LINAC. Depending on the analysis of original signals in FD from the estimated signals by Eq. (7), we realize that the differential summed values of cold button BPMs could not monitor whether beam current has been lost or not in CMs. The summed values of BPM could only give us the relative current to prove there is a beam in CMs. This changes our interlock strategy for the low- β high-power proton SC LINAC.

CONCLUSION

In this paper, we use the simulated method and the numerical calculation to derive the output signal of button BPMs for a multi-bunched low- β beam. The simulated results from CST PS with the PIC solver and the numerical calculated results based on formula Eq. (6) confirm that the output signal shape width coincides with the measured value, which indicates that the assumed imaging bunch length for low- β beams is correct. Furthermore, we develop model Eq. (7) to estimate the output signal of cold button BPMs. A series of comparisons between the calculated and the measured signals from $^4\text{He}^{2+}$ and proton beam commissioning proves

model Eq. (7) to be accurate. It could help us understand what signal is processed by BPMs' electronics. Based on the FFT results, the amplitude spectra are expanded and have more high frequency components when the energy increasing and the longitudinal bunch length shortening. At the same time, the amplitude at the basic harmonic frequency of 162.5 MHz decreases, which leads to the summed values from LSPH showing a continuous decline in numbers. Because the BPM electronics LSPH processes the amplitude spectra of BPM signal in FD with a narrowband processing. We realize that the differential values between the different cold button BPMs could not monitor the beam current transmission efficiency. The summed values from cold button BPMs could only give the relative low- β beam intensity. Numerical model Eq. (7) is very useful for designing, estimating, and analysing the button BPM function when facing the centred low- β beam accelerated by an ion/proton low- β SC LINAC.

REFERENCES

- [1] Z. Wang, Y. He, H. Jia, *et al.*, "Beam commissioning for a superconducting proton LINAC," *Phys. Rev. Accel. Beams.*, vol. 19, no. 12, pp. 120101, Dec. 2016.
doi: 10.1103/PhysRevAccelBeams.19.120101
- [2] S. H. Liu, Z. J. Wang, H. Jia, Y. He, *et al.*, "Physics design of the CIADS 25 MeV demo facility," *Nucl. Instrum. Methods Phys. Res., Sect. A*, vol. 843, pp. 11-17, 2017.
doi: 10.1016/j.nima.2016.10.055
- [3] *High-power linac shows promise for accelerator-driven reactors*, <https://cerncourier.com/a/high-power-linac-shows-promise-for-accelerator-driven-reactors/>
- [4] Y. Zhang, J. X. Wu, G. Y. Zhu, H. Jia, *et al.*, "Capacitive beam position monitors for the low- β beam of the Chinese ADS proton LINAC," *Chinese Phys. C*, vol. 40, p. 027003, 2016. doi: 10.1088/1674-1137/40/2/027003
- [5] Bergoz instrumentation, www.bergoz.com
- [6] Dassault Systèmes, 3DS, www.3ds.com
- [7] Dassault Systèmes, SOLIDWORKS, www.solidworks.com
- [8] R. E. Shafer, "Beam position monitoring," *AIP Conf. Proc.*, vol. 212, p. 26, 1990. doi: 10.1063/1.39710
- [9] MathWorks, www.mathworks.com
- [10] Times Microwave Systems, www.timesmicrowave.com
- [11] I-Tech Instrumentation Technologies, www.i-tech.si

Table 1: Principal RFQ Parameters

Parameter (units)	Value
Operational mode	CW
Frequency	[MHz] 80
Injection Energy	[keV/u] 5.7 ($\beta=0.0035$)
Output Energy	[keV/u] 727 ($\beta=0.0395$)
Accelerated beam current	[μ A] 100
Charge states of accelerated ions [Q/A]	7-3

For the given input conditions, the main beam dynamics choices were aimed at minimizing the longitudinal and transverse emittance growths and to optimize the RF losses (<150 kW in order to take advantage of the available amplifier technologies) and transmission of the RFQ structure with the goal of a surface electric field below 1.8 Kilp. The RFQ cells were created using a home-made routine, based on the program used for the design of CERN linac3 RFQ, while the multiparticle transport was performed by PARMTEQM code package and TraceWin/Toutatis. With this design the RF power consumption is minimized, while a linear voltage profile allows accelerating the beam more effectively at higher velocities and achieving a shorter RFQ. A transition cell was used at both the entrance and exit of the RFQ. Table 2, Fig. 1 and Fig. 2 show the main parameters of the RFQ. The RFQ transmission is more than 95% of accelerated particles, the final longitudinal RMS emittance is 0.15 ns·keV/u (4.35 deg·keV/u). The 99% longitudinal emittance is 1.2 ns·keV/u. In Table 2 the main RFQ parameters as per Beam Dynamics Optimizations are shown, while in Figure 2 some of these parameters are shown as they evolve along the RFQ length.

Table 2: RFQ Design Parameters

Parameter (units)	Value
Inter-Vane Voltage [kV] ($A/q=7$)	63.81–85.84
Vane Length L [m]	6.95
Average Radius R_0 [mm]	5.33–6.79
Vane Radius ρ to average Radius ratio	0.76
Modulation Factor m	1.0/3.18
Minimum aperture a [mm]	2.45
Total number of Cells	321
Synchronous Phase [$^\circ$]	$-90^\circ / -20^\circ$
Focusing Strength B	4.7/4
Surface E field [kilp.]	1.74
Transmission [%]	95
Input Tr. RMS Emittance [mm·mrad]	0.1
Output Longitudinal RMS Emittance [keV·deg/u]/[ns·keV/u]	4.35/0.15

The RFQ performances were verified as well by performing a set of error studies, covering the input beam current variation (0 to 1 mA), input emittance (0.1 to 0.5π -mm·mrad), RFQ voltage ($\pm 6\%$ range), tuning errors

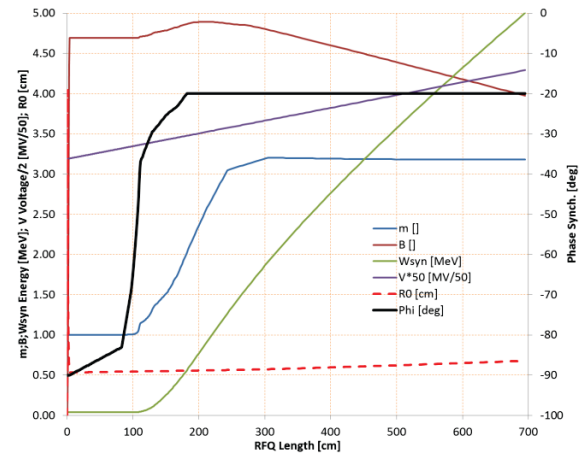


Figure 2: Main RFQ parameters vs length.

(i.e. voltage tilt and harmonic perturbations superimposed to the nominal law), and electrode displacement. As a conclusion, the RFQ keeps its transmission drop below 0.5% with respect to the nominal value and longitudinal emittance growth below 2,5% as far as the voltage variations and/or tilts are kept below $\pm 3\%$, which is, ultimately, the goal of the RFQ tuning.

Figure 3 shows the phase and the radial amplitude particle density along the RFQ, the plot is obtained from a Toutatis multiparticle simulation [2].

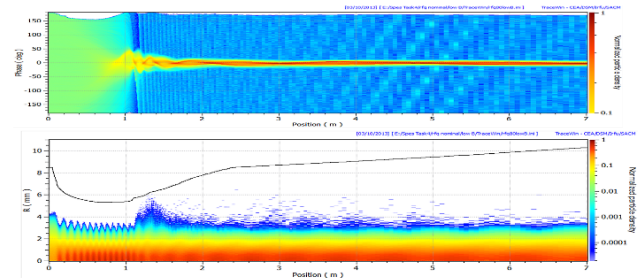


Figure 3: Phase and Radial density amplitude along the RFQ.

RFQ CAVITY DESIGN

The voltage law $V(z) = V(0) + b \cdot z$ with $b = 3.177$ kV/m and $V(0)$ depending on the A/q of the ion to be accelerated is obtained by proper shaping of the vane undercuts at both ends of the RFQ, by keeping the local TE_{21} cut-off frequency constant along z . Therefore, it was chosen to compensate the R_0 and ρ variations by capacitive tuning, by keeping the electrode thickness constant at 48 mm as well the angles $\alpha^1 = \alpha^2 = 30^\circ$, and the Tank radius $R = 377$ mm by varying the Y^4 parameter (Fig. 4).

The dimensioning of the vane undercut is made with a 45° angle and a tuning ring, machined on the end-plate (inner radius 150 mm, external radius 300 mm, thickness 0÷50 mm) is used for further tuning of the slope. The dimensions of the undercuts were optimized with HFSS simulations.

Content from this work may be used under the terms of the CC BY 4.0 licence (© 2022). Any distribution of this work must maintain attribution to the author(s), title of the work, publisher, and DOI

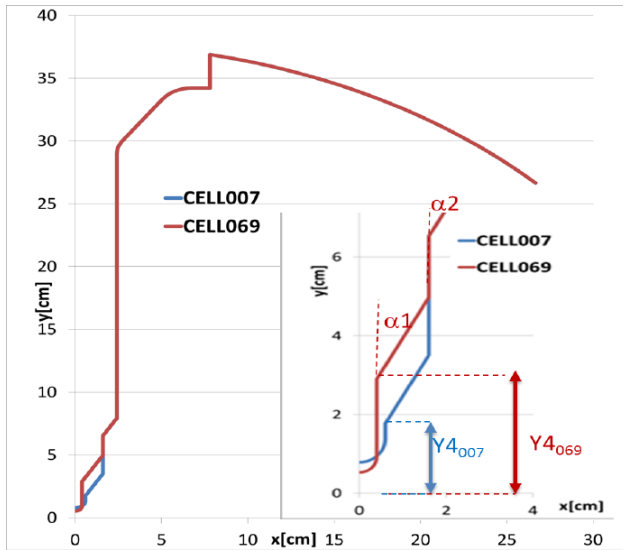


Figure 4: Capacitive tuning of the RFQ sections: maximum R_0 (blue curve) and minimum R_0 (red curve).

As it will explained in some detail later, in this RFQ the electrodes are assembled with the tank. Therefore, in order to allow proper operation of the RFQ, a RF joint must be placed longitudinally between the electrode and the tank. In addition, electrical properties of the joint have to comply with the possibility of ± 0.2 mm regulation of the electrode orthogonally with respect to beam axis. For this reason it was decided to use a multi-louver reed-shaped spring joint Contact louvers in copper, silver-plated and mounted on a stainless steel carrier, i.e. the LA-CUD/0,15 joint, by Multi-Contact® (400 louvers/m), which guarantees (in particular the LA-CUD joint) a current capability of tenth of Amperes per louver, the required regulation (± 0.6 mm, nominal), and a shrinkage force in the range of $(200\div 320)$ $\text{kg}\cdot\text{m}^{-1}$ of spring joint. The variation of this force, connected with the positioning of the electrode, causes the contact resistance to vary accordingly (Fig. 5).

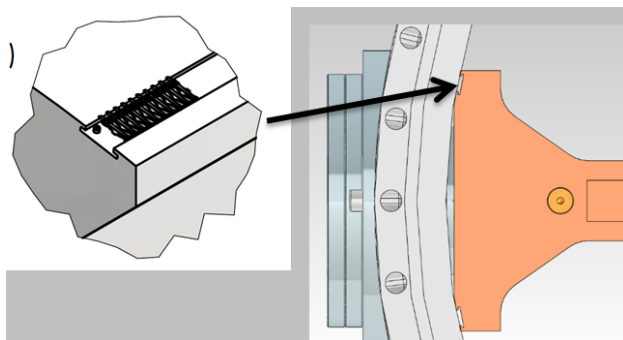


Figure 5: The RFQ electrode and the groove for the RF joint.

As for frequency sensitivities is concerned, it results that $\chi_{R_0} = \partial f / \partial R_0$ varies from 2.5 MHz/mm to 3.7 MHz/mm (average value 3.3 MHz/mm) and $\chi_R = \partial f / \partial R = -0.2$ MHz/mm. The frequency shift can be calculated as $\Delta f = \chi_{R_0} \Delta R_0 + \chi_R \Delta R \approx \chi_{R_0} \Delta R_0$ (in most cases the second term can be neglected). The number of tuners is $N_T = 68$ (17 per quadrant)

plus 3 extra tuners located at coupler position. The tuner radius is 59 mm the average tuner sensitivity is equal to about $\chi_{\text{tun}} = 13$ kHz/mm (all tuners). Therefore, the tuning range can be spanned with a range of tuner depths $h_t = [h_{\text{min}}, h_{\text{max}}] = [-10 \text{ mm}, 80 \text{ mm}]$, corresponding to a nominal tuner position of $h_0 = 35$ mm). In this case the tuning range of 1150 kHz, corresponds to frequency range of [79.39 MHz, 80.54 MHz] and a ΔR_0 range of ± 0.175 mm along all the RFQ, approximately equal to the electrode regulation range. The RF dissipated power value is equal to about 100 kW (with 30% margin for 3D details and RF joint), and, including a further 20% margin for LLRF regulation, the RF power is about 120 kW. In Table 3, the main RF parameters are shown.

Table 3: RFQ RF main Parameters (rated for $A/q=7$)

Parameter (units)	Value
Operational mode	CW
Frequency [MHz]	80
$TE_{21}[TE_{11}]$ cut-off frequency [MHz]	79.5 [77.3]
Q_0 value	14000
Shunt Impedance times length [k Ω ·m]	349–365
Dissipated Power in the cavity [kW]	100
RF power [kW]	120
Stored Energy [J]	2.87
Maximum Power density in the cavity sections [W/cm ²]	0.31
Maximum Power density in the cavity undercuts [W/cm ²]	11

Finally, the whole length RFQ (included modulation) underwent a combined ANSYS-HFSS RF and thermo-structural simulation. In Fig. 6 the vane voltage V calculated in some RFQ sections with the Faraday-Neumann law is shown in different cases, showing an agreement within $\pm 4\%$. This value (not yet tuned) can be considered as a validation of the RF design [3]. One interesting thing to be noticed is that the modulation made the Dipole-free region symmetric with respect to $f_{TE_{21}} = 79.5$ MHz. This symmetry is due to the fact that modulation has a little effect (less than 200 kHz) on Q modes and D modes with order >0 but shifts of 1 MHz lower in frequency the TE_{11} mode. Therefore, the RFQ is intrinsically «dipole free» and dipole rods are not needed [4].

RFQ ENGINEERING

Thermal Considerations

The RFQ Cooling System is designed to remove power and to finely tune the cavity resonant frequency during operation by temperature regulation. For such a purpose, it is necessary to have two independent water loops with two temperature set points: a “cold” circuit for the tank, end plates, the vacuum grids, the coupler and the tuners and a “warm” one for the vanes. By mixing with a 3-way valve the cold inlet water with part of the warm water coming from

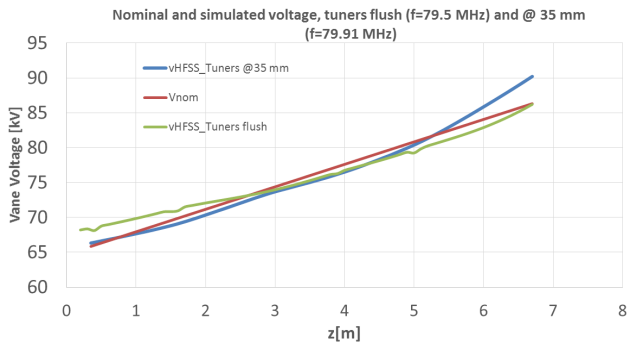


Figure 6: The RFQ voltage: nominal (red curve), tuner flush simulated (green curve), tuners at $h_{t0} = 35$ mm (blue curve). The simulation was performed on $\frac{1}{4}$ RFQ with 3 million mesh elements.

the cavity, it is possible to vary the resonant frequency of the RFQ and to tune the cavity accordingly. Let us observe that the vane and the tank are thermally insulated and that the RF power balance is approximately 60% on the vanes (Cu) and 40% on the tank (SS). The channel radii are $R_{c2} = 6$ mm on the vane and $R_{c1} = 4$ mm on the tank, the inlet water velocity is 2 m/s for the vane and 1.5 m/s for the tank. The reference inlet water temperatures are 15 °C for the tank and 20 °C for the vane. The cooling channel layout for the electrodes is shown in Fig. 7 [5].

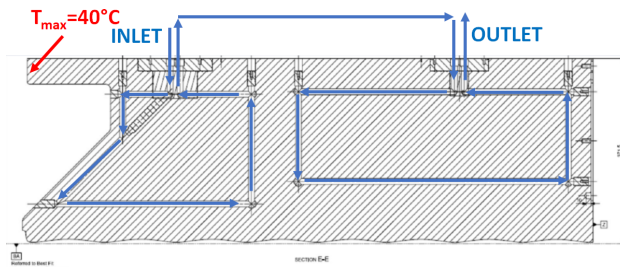


Figure 7: Cooling channel arrangement for the RFQ (case of high energy RFQ end).

In this case the water temperature increase is, in average, 2.6 °C, and the pressure drop is about 2 bars. The maximum temperature is about 40 °C and is reached in the upper part of the High Energy end undercut. As for the tank, there are 16 cooling channels, and the water temperature increase is 1.3 °C, while the maximum temperature of 47 °C occurs in the flange zone is higher, since the reduced thickness reduces heat conduction. In any case, the associated tip deformations are everywhere less than 20 μ m, with an overall effect on frequency less than 10 kHz. These results were obtained with a whole length RFQ (included modulation) combined ANSYS-HFSS RF and thermo-structural simulation. The vane temperature coefficient $\partial f/\partial T_2$ is equal to about -17 kHz/°C. Moreover, the frequency shift $\Delta f_{\text{on-off}}$ from maximum input power to zero input power is +85 kHz, and the vane + tank (isotropic) temperature coefficient $\partial f/\partial T_{1,2}$ (that is the frequency shift due to both T_1 and T_2 increase is -2 kHz/°C. Therefore, a temperature tuning range of about ± 85 kHz can be established for a T_2 variation in the range [15 °C, 25 °C]. Moreover, as power increases frequency in-

creases, as well as water temperature. Nevertheless, since $\partial f/\partial T_{1,2} < 0$, then a stabilizing mechanism is established, and a thermal runaway is avoided.

Mechanical Assembly Considerations

The RFQ is composed of 6 modules about 1.2 m long each. Each module is basically composed of an AISI 304 L SS Tank and four OFE Copper Electrodes (obtained by a single brazing cycle to avoid softening of the base material). A copper layer is plated on the tank inner surface and a spring joint between tank and electrode is used in order to seal the RF. Since the R_0 final values are determined by the electrode vs. tank positioning, the mechanical design and assembly procedure of the RFQ is aimed at obtaining both a precise and reliable assembly of the electrodes on the tank, as well as an accurate alignment of each RFQ module. For this reason, one can take advantage of the experience gained in IFMIF [6] project, by including some innovative elements in terms of the cavity assembly procedure.

The basic idea underlying the assembly procedure is to avoid on one hand large and/or not-round gasket mounting and on the other hand to decouple vacuum sealing and RF joints mounting, by avoiding simultaneous stresses on the components. For this reason, the interface joining the Electrode (EL) to the Tank (T) (Fig. 8) is made of two SS316LN Stainless Steel inserts, brazed on the electrode, on which cooling channel tube housings are placed, as well as an energized C-seal for vacuum sealing. The RF joints are to be contemporarily pushed against the inner tank surface with an overall max 8 kN force (8 N/louver) on the whole electrode length (2 RF joints/electrode). Indeed, each of the spring C-seal, needs 60 kN (167 N/mm on the circumference) for tightening, concentrated in the gasket diameter. Now, since the contemporarily tightening of the two C-seals would not be not feasible, the assembly interface was modelled in order to avoid dangerous stresses on the electrode, by making the assembly of one insert independent on the assembly of the other one. The Support Flange (SF) made of 316LN has the seats for two small gaskets and through holes (SF) for screws and cooling pipes. The external support flange hole pattern is in vacuum and will be enclosed in a donut-shaped Vacuum Cap (VC) via both an inner and an outer gasket. The stop surface in SF with the tank has to be machined according with mechanical/RF measurements to be performed in situ, in order both to avoid electrode deformations and proper electrode positioning with respect to tank axis. The Vacuum Cap (VC) has to guarantee vacuum tightness. Moreover, due to its relatively thin (1.5 mm) surface, it avoids stresses that could be induced by the non-parallelism of the two gasket stop surfaces. Finally, the Aluminium Extractor (EX) is such to house the SF, to tighten the RF joint, and to pull the electrode, as well as to allow the alignment pin insertion/extraction (Fig. 8). This setup was successfully prototyped before being employed as per brazing interface validation and the functionality of all the components, as well as determining possible issues in the electrode-vs-tank alignment assembly, via the usage of an

Content from this work may be used under the terms of the CC BY 4.0 licence (© 2022). Any distribution of this work must maintain attribution to the author(s), title of the work, publisher, and DOI

electrode simulacre with two inserts [3]. All the RFQ sealings are performed via spring energized gaskets.

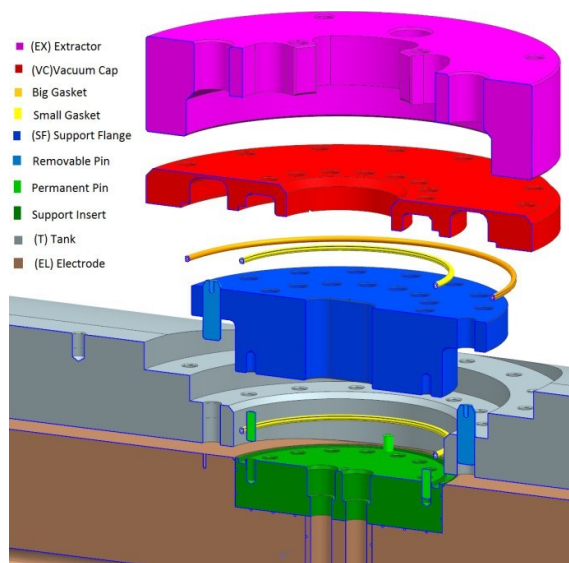


Figure 8: The assembly-alignment interface between electrodes and tank.

As for the inter-tank assembly, it has to be observed that slots for the bolt were added in order to increase the bending stiffness of the tank – tank interfaces and improve temperature uniformity. Moreover, calibrated shims will be bolted on a front face of a tank to obtain a correct relative positioning. Such shims could also be discontinuous to permit a He-leak test on the biggest seal of the cavity. As for tank positioning, no pins are used; relative positioning is made possible by the adjustable frame tools able to support any roll, pitch, and yaw effect of the inter tank planes (Fig. 9).

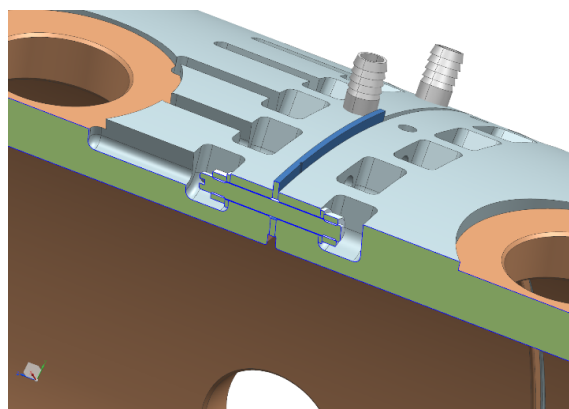


Figure 9: The inter-tank alignment detail: it is possible to recognise the slots for the bolts and the calibrated shims.

RFQ CONSTRUCTION AND TESTING

The construction of the electrodes (as well as tuners and vacuum grids) was done by CINEL Strumenti Scientifici s.r.l while the tanks were constructed by Fantini Sud Spa on the basis of design and drawings made at LNL; the Copperplating of the Tanks (copper thickness 70µm) was performed at CERN facilities. To date, all the electrodes and

tanks underwent complete construction and copper-plating. The first module to be assembled is module 5.

Despite to the electrodes with all the surfaces finished, the copper plated surfaces of the tank need to be re-finished with agate knife in order to avoid imperfections to obtain surfaces as smooth as possible, as experienced also in ESS [7]. Moreover, all the surfaces in contact with a vacuum gasket must be finished with a sandpaper with P320 grade to decrease the roughness and eliminate radial grooves due to the machining process. All tank surfaces were cleaned with isopropyl alcohol. After the re-finishing phase, metrological characterization of all the tank surfaces as well as the electrode surfaces was done in separate moments. A CMM arm 0.03 mm Maximum Permitted Error (MPE) with a ruby scanning probe was used. For all components a unique common coordinate system was defined. The superposition of the measured entities with the common reference system permits to obtain the ad-hoc geometry of Electrode/Tank interface components, i.e. the Support Flange (SF). The correct placement was determined by the CMM arm with respect to some common given reference surfaces. Module 5 has been assembled and passed all the tests (Fig. 10).

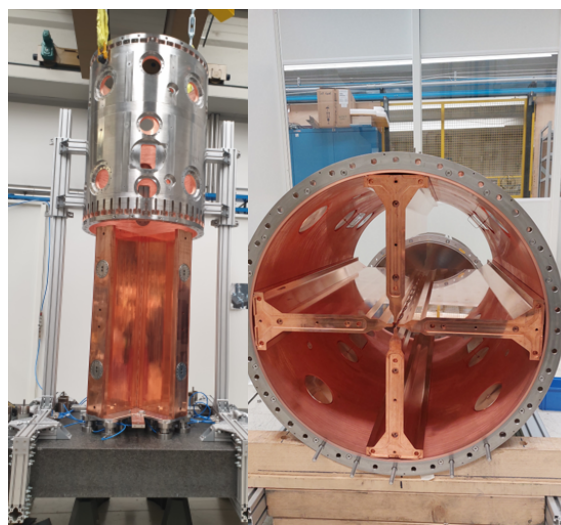


Figure 10: Initial positioning of Tank vs. electrodes (left), Final assembly of the RFQ module (right).

Tip positionings at the end faces of the module are within a range of ± 0.15 mm. Perpendicularity of the end faces of the module with respect to a representative beam axis, calculated using the tips deviations, are within 0.08 mm. Total tip deviations ΔR_0 at the middle plane of the module are about 0.02 mm. Vacuum test was carried out using the He spraying method. The pressure reached inside the chamber is about $1.2 \cdot 10^{-5}$ mbar and the maximum detected leak is about $3 \cdot 10^{-11}$ mbar-l/s].

A further validation step of the RFQ assembly procedure consists in RF measurements. In order to perform such characterization, the RFQ module is connected with a pair of hollow cylinders 0.5 m long each with the same diameter as the RFQ: the overall structure resonant frequencies are,

for electrode tips displacement in the order of ± 0.2 mm, in a linear relationship with the RFQ frequencies. Therefore it is possible to extrapolate the RFQ frequencies in these measurements for different electrode assemblies according to the relationship $f_{\text{QWG}} = c_1 * f_{\text{QRFO}} + c_0$, where f_{QWG} is the frequency of the Quadrupole mode of the RFQ connected with the cylinders, while f_{QRFO} is the frequency of the Quadrupole mode of the RFQ with perfect H boundary conditions at both ends. This setup is not optimized in terms of RF joints in cylinders, yet a Q_0 about 65% of the nominal value (for this particular configuration) was measured.

The measurements showed that, when assembled with nominal settings, the RFQ frequency only differs of 8 kHz from the simulated one and that, in three different alignment setups (#1: ruler checked alignment, no alignment pins, no machined flanges, no seals, #2: measuring arm checked alignment, alignment pins with 0.1 mm clearance, no seals, #3: measuring arm checked alignment, alignment pins with <0.05 mm clearance, seals installed), this difference decreases from +28 kHz (#1), to 18 kHz (#2), up to 8 kHz (#3). These measurements constitute a further validation of the RFQ alignment and assembly procedure.

As the testing and alignment procedure of the RFQ module is successfully established, it will be repeated for all the other RFQ modules. In particular, the next steps foresee the characterization of RFQ Module 4 and the intertank assembly and alignment.

RFQ ANCILLARIES

RFQ Support

The RFQ support and alignment frame was built by Fantini Sud srl upon LNL specifications and it is now installed in its final position. This support will also host the Solenoid immediately before the Low Energy End of the RFQ. After RFQ Module 5 was characterized, it was installed in its final position on the support (Fig. 11).



Figure 11: The Module 5 installed in its final position.

RF System

In an earlier phase of the project, it was thought to use a tetrode amplifier based on the 220 kW TH781 tube already

used for the IFMIF RFQ High Power Tests (175 MHz) nevertheless, due to some issues encountered in the availability of a commercial solution for a 200 kW 80 MHz cavity and the availability of MOSFETs with power capabilities in the order of 1.6–1.8 kW, it was decided to use a Solid State Amplifier with the same frequency and power, and the corresponding tendering is in phase of awarding. The SPES RFQ will make use of one coupler, based on the IFMIF RFQ design [8], and located approximately at halfway of the RFQ. In this case no circulator is foreseen, as the RF amplifier is rated to withstand up to 20% CW reflected power and full reflected power for 100 μ s. In order to compensate the dipole and quadrupole perturbations due to the presence of the loop, three tuners, located in the other RFQ quadrants at the same longitudinal position of the loop, are foreseen.

ACKNOWLEDGEMENTS

The authors wish to express their gratitude to the INFN Colleagues who took part to the achievements reached so far: Andrea Colombo (INFN-PD), Paolo Bottin and Riccardo Panizzolo (INFN-LNL) for their valuable contribution and help in all the RFQ assembly phase, and Enrico Fagotti (INFN-LNL) for fruitful discussion and encouragement.

REFERENCES

- [1] M. Comunian *et al.*, “Status of the SPES Exotic Beam Facility”, *J. Phys. Conf. Ser.*, vol. 1401, p. 012002, 2020.
doi:10.1088/1742-6596/1401/1/012002
- [2] M. Comunian, A. Palmieri, A. Pisent, and C. Roncolato, “The New RFQ as RIB Injector of the ALPI Linac”, in *Proc. IPAC’13*, Shanghai, China, May 2013, paper THPWO023, pp. 3812-3814.
- [3] L. Ferrari, A. Palmieri, and A. Pisent, “RF-Mechanical Design and Prototyping of the SPES RFQ”, in *Proc. IPAC’17*, Copenhagen, Denmark, May 2017, pp. 4166-4168.
doi:10.18429/JACoW-IPAC2017-THPIK033
- [4] A. Palmieri, INFN-LNL Annual Report 2015, https://www1.lnl.infn.it/~annrep/read_ar/2015/contributions/pdfs/207_G_105_G100.pdf
- [5] L. Ferrari, A. Palmieri, and A. Pisent, “Thermo-Mechanical Calculations for the SPES RFQ”, in *Proc. HIAT’15*, Yokohama, Japan, Sep. 2015, pp. 219-221.
doi:10.18429/JACoW-HIAT2015-WEPB13
- [6] E. Fagotti *et al.*, “Preparation and Installation of IFMIF-EVEDA RFQ at Rokkasho Site”, in *Proc. LINAC’16*, East Lansing, MI, USA, Sep. 2016, pp. 1005-1007.
doi:10.18429/JACoW-LINAC2016-THPLR066
- [7] P. Mereu *et al.*, “Details of the Manufacturing Processes of the ESS-DTL Components”, in *Proc. LINAC’18*, Beijing, China, Sep. 2018, pp. 260-263.
doi:10.18429/JACoW-LINAC2018-MOP0124
- [8] E. Fagotti *et al.*, “The Couplers for the IFMIF-EVEDA RFQ High Power Test Stand at LNL: Design, Construction and Operation”, in *Proc. LINAC’14*, Geneva, Switzerland, Aug.-Sep. 2014, paper TUPP093, pp. 643-645.

ALTERNATING PHASE FOCUSING BASED IH DTL FOR HEAVY ION APPLICATION

S. Lauber^{*, 1,2,3}, M. Basten^{1,2}, S. Yaramyshev^{1,2}, K. Aulenbacher^{1,2,3}, W. Barth^{1,2,3},
 C. Burandt^{1,2}, M. Droba⁴, F. Dziuba^{1,2,3}, P. Forck¹, V. Gettmann^{1,2}, T. Kürzeder^{1,2},
 J. List^{1,2,3}, M. Miski-Oglu^{1,2}, H. Podlech^{4,5}, A. Rubin¹, M. Schwarz⁴

¹GSI Helmholtzzentrum für Schwerionenforschung, Darmstadt, Germany

² Helmholtz Institute Mainz, Mainz, Germany

³Johannes Gutenberg-University, Mainz, Germany

⁴Institut für Angewandte Physik, Frankfurt, Germany

⁵Helmholtz Research Academy Hesse for FAIR, Frankfurt, Germany

Abstract

The continuous wave (CW) operated HELmholtz LInear ACcelerator (HELIAC) is going to reach the next milestone with the commissioning of the superconducting (SC) Advanced Demonstrator cryomodule, comprising four SC Crossbar H-mode (CH) cavities and SC steerer magnets. In parallel with the commissioning of the SC main accelerator, the normal conducting injector consisting of an ECR ion source, a RFQ and two Interdigital H-mode (IH) cavities will be built based on an Alternating Phase Focusing (APF) beam dynamics scheme. Both IH cavities will provide a beam energy gain from 300 keV/u to 1400 keV/u with a maximum mass to charge ratio of 6, requiring only one external quadrupole triplet and beam steerer elements between them. The APF concept allows stable and effective beam transport with transverse and longitudinal focusing, enabling an efficient and compact design. Due to the stringent requirements of the APF concept on the voltage distribution and the CW operation, optimization of each cavity in terms of RF, mechanical and thermal properties is crucial for successful operation of the HELIAC injector. The current layout of the APF based and CW operated injector will be presented.

INTRODUCTION

At GSI Helmholtzzentrum für Schwerionenforschung (GSI, Germany), the UNIVersal Linear ACcelerator (UNILAC) [1–3] is being upgraded to deliver high intensity, low repetition rate beam to the main synchrotron SIS100 [4] of the Facility for Antiproton and Ion Research (FAIR), which is currently under construction. The new scope of operation of UNILAC will have an impact on beam supply for the GSI material and superheavy element research program, which requires ideally a low peak current, continuous wave beam. To allow for further discoveries of new superheavy elements [5], a dedicated linear accelerator is under construction, namely the HELmholtz LInear ACcelerator (HELIAC, see Fig. 1). The operational parameters of the new machine are listed in Table 1; the machine has been specially designed to allow for a variable output beam energy [6, 7].

Whilst the variable output energy is attained by employing the EQUidistant mUltigap Structure (EQUUS [8]) beam

* s.lauber@gsi.de

Table 1: General Characteristics of the HELIAC Accelerator

Property	Value
Frequency	108.408 MHz (216.816 MHz ¹)
Mass-to-charge ratio	≤ 6
Repetition rate	Continuous wave
Beam current <i>I</i>	≤ 1 mA
Output energy	3.5 MeV/u to 7.3 MeV/u
Injector output energy	1.4 MeV/u
Normal conducting cavities	3
Superconducting cavities	12

¹ The SC CH cavities operate on the second harmonic.

dynamics concept in the superconducting accelerator [9, 10], the normal conducting injector has to deliver a fixed output energy and high beam quality. Thus, the normal conducting cavities in the warm injector are designed using a different beam dynamics approach, namely Alternating Phase Focusing (APF [11–15]).

This beam dynamics approach is very attractive, as it allows removing (costly) internal magnetic quadrupole multiplets from the cavities, and thus offers for a high beam quality, compact, and modular layout of the injector, supporting stable long-term operation of the machine. In order to omit internal magnetic lenses in the cavities, the beam is focused also transversally using the electric fields in between the drift tubes. Commonly, negative synchronous phases (i.e., the RF phase when the accelerated particle beam passes the RF gap) are employed to provide for longitudinal focusing (and transverse defocusing). Positive synchronous phases have the opposite effect on beam focusing, so that the beam is transversely focused and longitudinally defocused.

In order to alter the synchronous phases (and thus the focusing properties) in between individual gaps, the lengths of the neighboring tubes are adjusted

$$L_{\text{cell}} = \frac{\beta\lambda}{2} + \beta\lambda \frac{\Delta\phi}{360^\circ}, \quad (1)$$

with the relative velocity $\beta = v/c_0$, RF wavelength λ , and change of synchronous phase in between two neighboring gaps $\Delta\phi = \phi_{i+1} - \phi_i$.

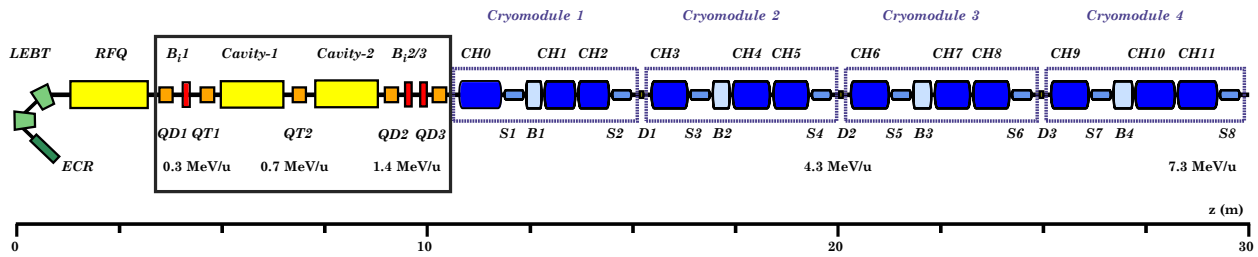


Figure 1: Layout of the HELIAC comprising four cryomodules and its dedicated injector; this publication focuses on the injector DTL with its relevant components: Quadrupole Doublets (QD), Bunchers (B), Quadrupole Triplets (QT), Interdigital H-Mode Cavities (IH), Crossbar H-Mode Cavities (CH), Solenoids (S)

The coupling of beam dynamics design on the cavity geometry imposes a circular dependency: The selection of synchronous phases impacts the geometry. The geometry alters the voltage in each gap. Ultimately, the altered gap voltage affects the beam dynamics, and a new optimum set of synchronous phases has to be found. The optimum solution is thus obtained iteratively.

METHODS

The APF cavities were designed in parallel from an RF and beam dynamics point of view. Two full length papers were submitted to peer-reviewed journals [14, 16] describing both views in detail. The RF design team had to take continuous wave operation into account, and design the cavities accordingly to reduce the thermal load in each cavity as much as possible. The tube and gap lengths are adjusted during the design of the beam dynamics with the aid of a Monte Carlo simulation, whereby the maximum temperature as well as the electrical peak fields at the drift tubes must be taken into account. Therefore, the tube-lengths in Cavity-1 were bound to range from 16 mm to 60 mm and in Cavity-2 from 20 mm to 80 mm. On one hand, this prevents too short tubes, which have a high power density and thus a high maximum surface temperature. On the other hand, the tip of too long tubes would be cooled ineffectively due to its distant position from the stem, which is mounted on the water-cooled girder.

The cavity is made from copper plated forged mild steel and the stems, tubes, and tuners are made from massive copper. The highest heat load (about 400 K) appears in the drift tubes for our design, as they are located relatively far from the embedded water cooling system in the Interdigital H-Mode (IH) cavity's girder.

Furthermore, the cavity is equipped with three capacitive frequency tuners to allow standard operation. The tuners were specially investigated to minimize their impact on the voltage in each individual gap (below 2% deviation from the design voltage distribution), allowing high beam quality even with mechanical expansion due to the temperature distribution.

As mentioned above, a Monte Carlo simulation (employing the beam dynamics solver DYNAMION [17]) has been developed to find the optimum set of synchronous phases $\vec{\phi}$ along a cavity. The optimum has been defined by means

of an objective function $f(\vec{\phi})$, targeting high beam quality (i.e., low emittance growth $\hat{\epsilon}$) and efficient energy gain ($E_{\text{target}} - E_{\text{out}}$) [14]:

$$f(\vec{\phi}) = \left(\frac{\hat{\epsilon}_{x,y} - 1}{t_{x,y}} \right)^2 + \left(\frac{\hat{\epsilon}_z - 1}{t_z} \right)^2 + \frac{E_{\text{target}} - E_{\text{out}}}{t_E} \quad (2)$$

A low longitudinal emittance growth is preferred. The longitudinal tolerance was set to $t_z = 0.5\%$ and the transverse tolerance to $t_{x,y} = 1\%$. A deviation from the design energy is tolerated with $t_E = 50$ keV.

RESULTS

The two cavities have been designed by means of Monte Carlo optimization using Eq. (2). An intermediate energy of 700 keV/u has been adopted to separate Cavity-1 and 2, allowing Cavity-1 to be designed for high beam quality transport and Cavity-2 to be stronger oriented towards acceleration of the ion bunches. The cavities are separated by an external quadrupole triplet, offering for additional transverse focusing, which improves the beam quality of our design and also offers the required adaptability of the machine for operation with very different ion species from Protons to Uranium ($A/Z \leq 6$).

The final layouts of the two cavities are depicted in Figs. 2 and 3. An average field gradient of 3 MV/m in Cavity-1 and 3.1 MV/m in Cavity-2 has been adopted, yielding a Kilpatrick value of 2.5 for both cavities (see Table 2).

The obtained set of synchronous phases of Cavity-1 (see Figure 2) is semi-sinusoidal, as present also for other APF linacs [18, 19]. The synchronous phase pattern in Cavity-2 is adapted to refocus the beam longitudinally, because it was defocused along the preceding intertank section. The effective refocusing to a 10° beam length allows embedded synchronous phases of about 0° for efficient acceleration with minor impact to the beam quality. The occurrence of negative phases below -90° is out of scope for this paper and discussed in [14].

The (average and maximum) envelopes within the cavity oscillate transversely and longitudinally in opposite direction of each other. In conventional (constant synchronous phase) linacs an oscillation of the beam length would indicate a mismatched beam. But for APF linacs this behavior is intended to allow for different focusing strength in longitudinal and transverse direction.

Content from this work may be used under the terms of the CC BY 4.0 licence (© 2022). Any distribution of this work must maintain attribution to the author(s), title of the work, publisher, and DOI

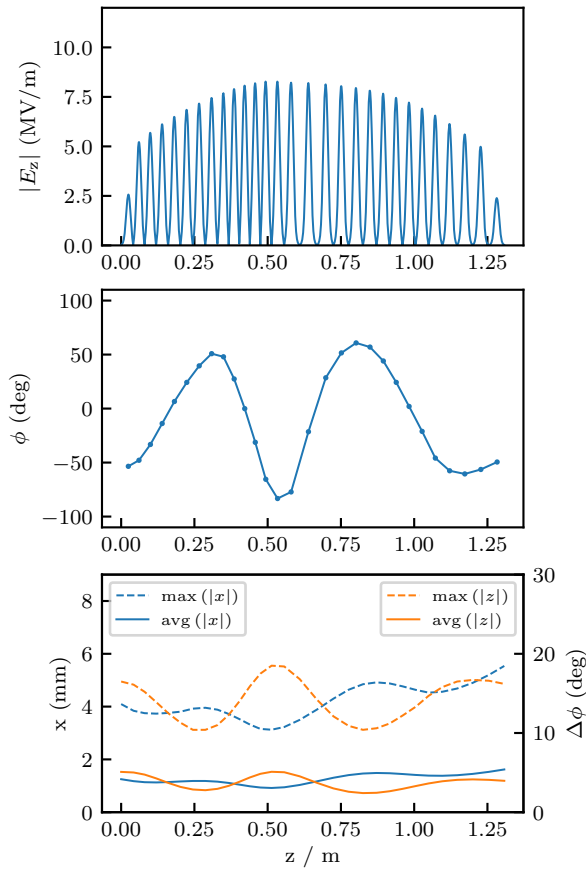


Figure 2: Gap voltages (*top*), synchronous phases (*center*) and resulting longitudinal and transverse beam envelopes (*bottom*) along Cavity-1.

Table 2: Final RF Parameters [16]

Property	Cavity-1	Cavity-2
Design frequency	108.408 MHz	108.408 MHz
Number of gaps	29	27
Effective length L_{eff}	1.31 m	1.75 m
Length (outer cavity)	1.5 m	2.0 m
Electric peak field	2.47 Kilpatrick	2.52 Kilpatrick
RF-Power (CW)	20 kW	48 kW
Quality factor Q_0	19000	22000
Shunt impedance Z_0	690 MΩ/m	425 MΩ/m
Max. temperature	≈ 413 K	≈ 441 K
Accelerating gradient	3.0 MV/m	3.1 MV/m
Effective accelerating gradient	2.61 MV/m	2.81 MV/m
Drift tube aperture radius	9 mm	9 mm
Drift tube outer radius	14 mm	17 mm

Finally, the beam is accelerated with full transmission from 300 keV/u to 1400 keV/u within 4.5 m (1.3 m Cavity-1 + 1.5 m intertank + 1.7 m Cavity-2) with low effective emittance growth of $\leq 5\%$ (accounting for 90 % of all particles, see Table 3).

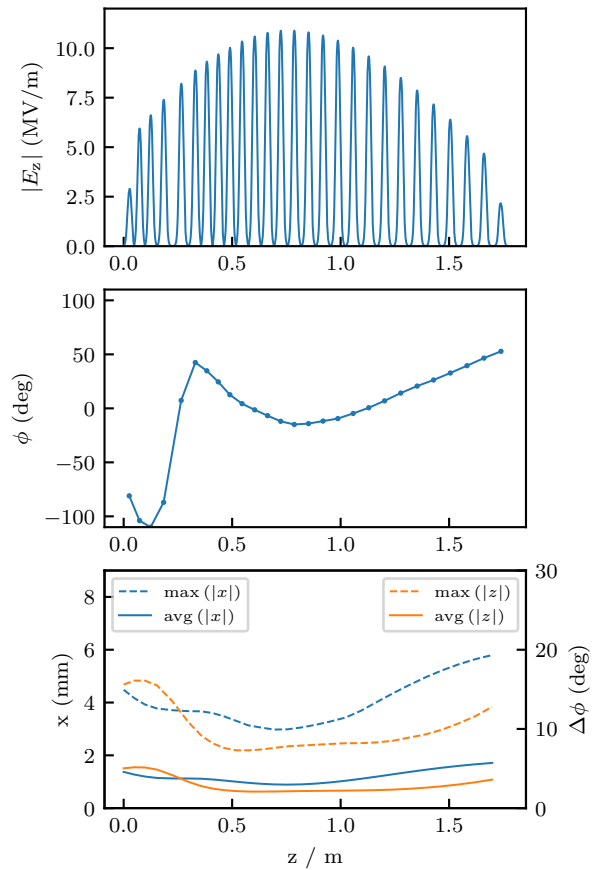


Figure 3: Gap voltages (*top*), synchronous phases (*center*) and resulting longitudinal and transverse beam envelopes (*bottom*) along Cavity-2.

Table 3: IH-DTL — Final Design Parameters and Beam Dynamics Results [14]

Property	Value
Beam transmission	100 %
Input beam energy	300.0 keV/u
Output beam energy	1400.0 keV/u
Mean beam spot radius	4 mm
Max beam spot radius	7 mm
Emittance Growth $\hat{\epsilon}_{90\%}$	
x	5.0 %
y	5.0 %
z	3.0 %
Emittance Growth $\hat{\epsilon}_{100\%}$	
x	23.0 %
y	23.0 %
z	17.0 %

CONCLUSION

A normal conduction continuous wave heavy ion Alternating Phase Focusing drift tube linac has been designed to serve as injector for the HELmholtz LInear ACcelerator. The designed DTL provides for full transmission and low

emittance growth below 5%. The associated RF layout of the cavity aims to limit heating of the cavities to 440 K and is designed so that the acceleration voltages are below a relative change of 2%.

REFERENCES

- [1] W. Barth, R. Hollinger, A. Adonin, M. Miski-Oglu, U. Scheeler, *et al.*, “LINAC developments for heavy ion operation at GSI and FAIR,” *Journal of Instrumentation*, vol. 15, no. 12, p. T12012, 2020, doi:10.1088/1748-0221/15/12/t12012
- [2] W. Barth, W. Bayer, L. Dahl, L. Groening, S. Richter, *et al.*, “Upgrade program of the high current heavy ion UNILAC as an injector for FAIR,” *Nucl. Instrum. Methods Phys. Res. A*, vol. 577, no. 1, pp. 211–214, 2007, doi:10.1016/j.nima.2007.02.054
- [3] W. Barth, G. C. L. Dahl, P. Gerhard, L. Groening, B. Lommel, *et al.*, “High current U⁴⁰⁺-operation in the GSI-UNILAC,” 2022.
- [4] P. Spiller, R. Balss, P. Bartolome, J. Blaurock, U. Blell, *et al.*, “The FAIR heavy ion synchrotron SIS100,” *Journal of Instrumentation*, vol. 15, no. 12, p. T12013, 2020, doi:10.1088/1748-0221/15/12/t12013
- [5] J. Khuyagbaatar, A. Yakushev, C. E. Düllmann, D. Ackermann, L. L. Andersson, *et al.*, “Search for elements 119 and 120,” *Phys. Rev. C*, vol. 102, no. 6, p. 064602, 2020, doi:10.1103/PhysRevC.102.064602
- [6] W. Barth, K. Aulenbacher, M. Basten, F. Dziuba, V. Gettmann, *et al.*, “A superconducting CW-linac for heavy ion acceleration at GSIX,” *EPJ Web Conf.*, vol. 138, p. 01026, 2017, doi:10.1051/epjconf/201713801026
- [7] M. Schwarz, S. Yaramyshev, K. Aulenbacher, W. Barth, M. Basten, *et al.*, “Reference beam dynamics layout for the SC CW heavy ion HELIAC at GSI,” *Nucl. Instrum. Methods Phys. Res. A*, p. 163044, 2019, doi:10.1016/j.nima.2019.163044
- [8] S. Minaev, U. Ratzinger, H. Podlech, M. Busch, and W. Barth, “Superconducting, energy variable heavy ion linac with constant β , multicell cavities of CH-type,” *Phys. Rev. ST Accel. Beams*, vol. 12, p. 120101, 2009, doi:10.1103/PhysRevSTAB.12.120101
- [9] W. Barth, K. Aulenbacher, M. Basten, M. Busch, F. Dziuba, *et al.*, “First heavy ion beam tests with a superconducting multi-gap CH cavity,” *Phys. Rev. Accel. Beams*, vol. 21, p. 020102, 2018, doi:10.1103/PhysRevAccelBeams.21.020102
- [10] W. Barth, K. Aulenbacher, M. Basten, M. Busch, F. Dziuba, *et al.*, “Superconducting CH-cavity heavy ion beam testing at GSI,” *J. Phys. Conf. Ser.*, vol. 1067, p. 052007, 2018, doi:10.1088/1742-6596/1067/5/052007
- [11] J. H. Adlam, “A method of simultaneously focusing and accelerating a beam of Protons,” *AERE GP/M*, no. 146, 1953.
- [12] M. L. Good, “Phase-reversal focusing in linear accelerators,” *Phys. Rev.*, vol. 92, p. 538, 1953, Berkeley Radiation Laboratory report.
- [13] I. B. Fainberg, “Alternating phase focusing,” in *Proc. Conf. on High Energy Accelerators*, 1956, doi:10.5170/CERN-1956-025.91
- [14] S. Lauber *et al.*, “An alternating phase focusing injector for heavy ion acceleration,” (submitted to NIMA).
- [15] S. Lauber, M. Basten, S. Yaramyshev, K. Aulenbacher, W. Barth, *et al.*, “Alternating phase focusing beam dynamics for drift tube linacs,” in *Proc. International Conference on Accelerators for Research and Sustainable Development: From Good Practices Towards Socioeconomic Impact*, 2022 (to be published).
- [16] M. Basten *et al.*, “Continuous wave interdigital H-mode cavities for alternating phase focusing heavy ion acceleration,” (submitted to RSI).
- [17] S. Yaramyshev, W. Barth, L. Groening, A. Kolomiets, and T. Tretyakova, “Development of the versatile multi-particle code DYNAMION,” *Nucl. Instrum. Methods Phys. Res. A*, vol. 558, no. 1, pp. 90–94, 2006, doi:10.1016/j.nima.2005.11.018
- [18] M. Otani, T. Mibe, M. Yoshida, K. Hasegawa, Y. Kondo, *et al.*, “Interdigital H-mode drift-tube linac design with alternative phase focusing for Muon linac,” *Phys. Rev. Accel. Beams*, vol. 19, no. 4, p. 040101, 2016, doi:10.1103/PhysRevAccelBeams.19.040101
- [19] Y. Iwata, S. Yamada, T. Murakami, T. Fujimoto, T. Fujisawa, *et al.*, “Alternating-phase-focused IH-DTL for an injector of heavy-ion medical accelerators,” *Nucl. Instrum. Methods Phys. Res. A*, vol. 569, no. 3, pp. 685–696, 2006, doi:10.1016/j.nima.2006.09.057

RECENT UNILAC UPGRADE ACTIVITIES

U. Scheeler¹, W. Barth^{1,2,3}, M. Miski-Oglu^{1,2}, H. Vormann¹, M. Vossberg¹, S. Yarymyshev^{1,2}

¹ GSI Helmholtzzentrum für Schwerionenforschung, Darmstadt, Germany

² Helmholtz Institute Mainz, Germany

³ Johannes Gutenberg-Universität Mainz, Mainz, Germany

Abstract

The GSI UNILAC is the section of the GSI accelerator facility that has been in operation the longest. UNILAC (Fig. 1) is able to accelerate ions from hydrogen to uranium up to 20 MeV (p+) and 13 MeV/u (uranium). The main focus of the recent upgrade measures is to meet the FAIR requirements and to provide reliable and long term beam operation conditions. Besides post stripper upgrade and upgrade of the UNILAC controls, a particular attention is paid to improve the performance of the High Current Injector (HSI) [1-7] and to intensify spare part management for the ageing accelerator. In order to ensure operational reliability, the main focus lies on extensive spare part management and replacement of outdated equipment. Modified beam dynamics design for the frontend system and the use of advanced technologies are needed to improve the UNILAC performance. Among other things, a modified Low and Medium Energy Beam Transport section design for the HSI and installation of reliable (non-destructive) high intensity beam diagnostics devices are in progress. This paper addresses the status of current development efforts and specific plans for the UNILAC upgrade.

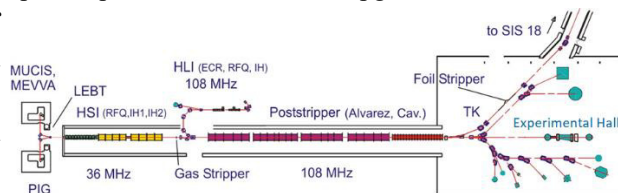


Figure 1: Overview of the UNILAC accelerator sections.

INTRODUCTION

In its more than 50 years of operation, the UNILAC (Fig. 1) has experienced extensions and optimizations in almost all sections. This has resulted in a diverse mix of components of different ages. The current strategy for maintaining and improving operational reliability can be classified into several categories. Complex components of the accelerator structures are being repaired or even replaced. Moreover, measures are being taken towards a complete system renewal. These include the installation of a new vacuum control system, the implementation of the current FAIR accelerator control system and the successive upgrade of the RF amplifier systems. Furthermore, two major linac projects have been started, which aim for the replacement or connection of a complete accelerator section such as the reconstruction of the Alvarez section (post-stripper upgrade) [8] and the link of the HELIAC (HELMholtz LInear ACcelerator) to supply the experimental hall

with cw-heavy ion beams. Finally, a comprehensive UNILAC upgrade program was defined that aims to achieve FAIR operating parameters, including the installation of the hydrogen gas stripper [9-12], increasing the intensity of the HSI and the development of non-destructive beam diagnostics to permanently monitor high current operation [13-17]. In particular, this proceeding reports on the individual measures of spare parts procurement and the upgrade activities to increase the beam intensity at the HSI.

SPARE PARTS MANAGEMENT

At the UNILAC Alvarez DTL accelerator section, about one drift tube per year has had to be replaced in the recent past due to water leakages. Operation is still possible, depending on which cooling circuit is affected. As a result, the focusing strength and/or the duty cycle is limited. In addition, two manufacturing types - solid copper body or stainless steel hollow body - are available for installation (Fig. 2). These are then brought to the specific length of each drift tube. In the last three years one type each has been newly manufactured. Especially for the copper version, drawings were required to be corrected and manufacturing processes had to be re-established, so that a relatively long manufacturing time of 12 months was required.



Figure 2: Drift tube of Alvarez section, as installed (left); opened drift tube with defective quadrupole lens (right).

In front of the three beam branches of the UNILAC experimental hall, a complex magnet septum has been in operation for decades, which deflects the beam into the three beam branches accordingly. So far, the water leaks that occurred at the coils of this septum magnet (see Fig. 3) could be repaired selectively, which is no longer successful due to the age-related poor condition of the coils. A complete rebuild of the beam section with the aim of separating the coils and the vacuum section is considered to be unaffordable at present. Thus, the 40-year-old manufacturing technology had to be reactivated. With regards to this it is crit-

Content from this work may be used under the terms of the CC BY 4.0 licence (© 2022). Any distribution of this work must maintain attribution to the author(s), title of the work, publisher, and DOI

ical to ensure dimensional accuracy of the individual conductive tracks and the vacuum suitability of the insulation. Here, the focus is once again on aluminum oxide. With the support of an external partner, manufacturing can now be implemented, the installation of the first coil is scheduled before start of the 2023 beam time period.

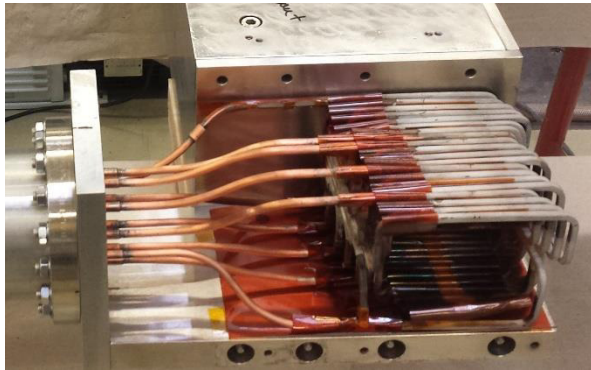


Figure 3: Septum coils with water supply (on the left) and the white insulation surface consisting of aluminum oxide.

The baffle plates in almost all dipoles of the previous generation are also affected by leakages. Besides preventing chamber destruction their ability to measure intensity has not been used for years. Re-manufacturing and replacement of the plates is very costly. In more recent chamber designs, a modified constructive solution is used, which ensures both the protective function and the separation of the vacuum area from the cooling channels. This option has to be manufactured and installed successively for the dipole chambers concerned over the next few years.

The failure rate of the dipole power supplies in the LEBT area of the HSI (the dipoles are needed for charge and mass separation) has increased in recent years. Due to the age of the power supplies, sustainable repair is becoming increasingly difficult. A failure would make beam operation in the affected source branch impossible. For this reason, a call for tender is currently being issued in order to replace these power supply units. The goal is to install them also before start of the 2023 beam time.

The lifetime of high duty/high current operable RFQ accelerators is typically 5-10 years depending on the damage due to the mode of operation. At the HSI RFQ, the 4th set of electrodes has been installed in 2018 (Fig. 4). Thanks to the proper preparation, the installation time requiring an interruption of operation could be reduced to 6-8 weeks. Before restarting the beam operation, an extensive RF conditioning program must be carried out.

Other critical components are the HSI-IH-DTL internal drift tubes housing quadrupole triplet lenses. Although spare parts have been manufactured in the course of previous failures, they are currently not sufficient to be installed. Therefore, a check of the magnetic properties is currently taking place and the copper surface is being refurbished. One drift tube still has an earth fault, here the possible repair approach still has to be coordinated and organized. The drift tube of the High Charge State Injector (HLI)-IH-DTL, which was recently destroyed due to overheating, must be

remanufactured. Fortunately, only one coil is affected, smoothly limited operation with only two quadrupoles is possible, as already practiced earlier at HSI-IH-DTL.

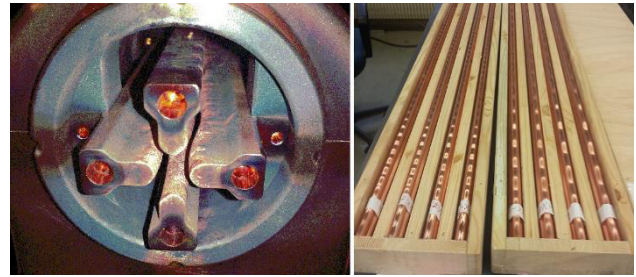


Figure 4: Installed HSI RFQ electrodes after 10 years' operation (left); newly fabricated electrodes just before assembly (right).

INTENSITY UPGRADE OF HSI

In order to provide for the requested Uranium beam intensity for FAIR, upgrade measures at HSI-frontend (Fig. 5) are initiated. The PRIDE project [24], consisting of an advanced Uranium terminal and a compact transport line to the existing LEBT has already been started. Increased ion source beam intensities are always associated with an increase of the beam emittance. However, even the recent high intensity Uranium beam emittance from the existing high current terminal cannot be fully matched to the HSI and must be collimated. In order to overcome this restriction, an increase in acceptance of the HSI RFQ and improved emittance is required. Technically, an increased aperture of the switching dipole and the exchange of the RFQ electrode design by trapezoidal shaped electrodes is foreseen. This measure also gains in the reduction of the tank voltage, while keeping the fields constant. Reversing the polarity of the quadrupole quartet used for beam matching to the RFQ significantly increased the overall high-current performance in heavy ion operation [2]. However, the Uranium record intensities achieved in 2016 cannot be obtained with the quadrupole quartet (with large aperture) installed in 2018.

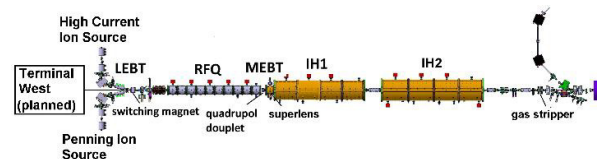


Figure 5: Sketch of the HSI, comprising existing LEBT with PIG and high current ion source terminal, as well as Terminal West and its compact transport line.

A further bottleneck is located at the MEBT comprising a quadrupole doublet and the superlens (SL). In addition to beam loading, operation of the SL is constrained by beam losses due to beam mismatch to the RFQ, resulting in additional transmitter power requirements of up to 20%. Beside improved RFQ-matching, the acceptance and quadrupole field strengths must be increased in order to ensure

matching conditions to the following two IH tank. A redesign of the quadrupoles is needed and a trapezoidal rod structure is also proposed for the SL, as well as for the RFQ.

Converting the gas stripper to hydrogen operation provides the key contribution to intensity increase and reduces the strong heavy ion HSI intensity requirement ($> 30\text{emA}$, $^{238}\text{U}^{4+}$) to a feasible level. Applying a pulsed hydrogen stripper gas target with high target density, the yield of $^{238}\text{U}^{28+}$ ions is increased from 12.5% to 21.0% [12]. The principle function has recently been verified in several beam times with different accelerated ion beams.

HIGH CURRENT BEAM DIAGNOSTICS

Currently, the UNILAC delivers up to 20% of the FAIR heavy ion beam brilliance [2]. The achieved intensities already place immense demands on beam diagnostics, requiring for the development of non-beam destroying diagnostics. Thus three systems move into the center of attention. First of all, the transmission measurement based on existing beam transformers is to be revised in order to provide for a pulse-exact beam current measurement. Due to the low repetition rate and intensity fluctuation of the beam pulses, only in this way a well-founded evaluation of the accelerator setting and its monitoring and optimization is possible.

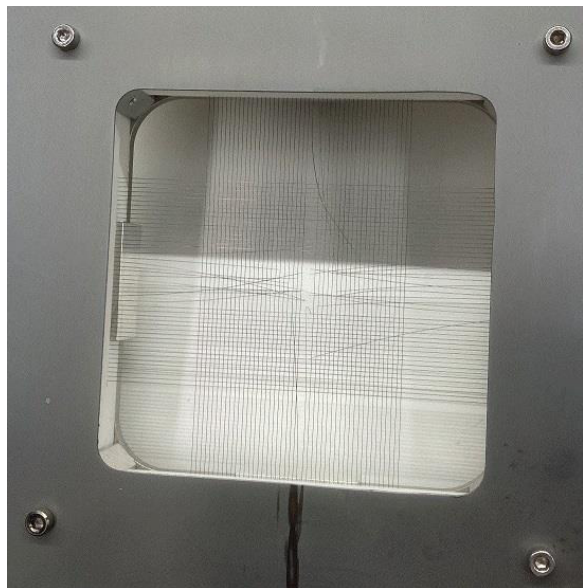


Figure 6: Damaged SEM profile grid.

Wire profile grids currently used for beam position and width measurements can only be operated to a limited extent. This is also reflected by an increased number of repairs due to defective wires. After the 2021 beam time 12 SEM-grids (Fig. 6) had to be dismantled, repaired and reinstalled. During recent beam time period, again five profile grids have already been destroyed.

For enabling high current operation, six BIF (Beam Induced Fluorescence monitor) stations are already installed, although the handling and optimization of the operating pa-

rameters is currently ongoing and extensive efforts are required for an adequate integration into the operating environment. The existing four split phase probe system used for beam energy measurement by ToF (Time of Flight) is also capable for beam position measurements along entire UNILAC. A corresponding display software is currently being developed. To improve the operability, the limitations in the measurement accuracy due to the fluctuation in the bunch intensity have to be addressed.

CONCLUSION

The presented upgrade measures refer to many different single tasks. As not all of this subprojects can be performed in parallel, the preparation, prioritization, coordination and realization is in an ongoing process to be managed in parallel to the strong efforts taken to realize the FAIR project. UNILAC upgrade for FAIR is the most important in the line of several GSI linac projects [18-23].

ACKNOWLEDGEMENTS

Success of UNILAC operation and of all described upgrade measures is the result of tremendous effort provided by the untiring commitment of experts from the different departments of GSI accelerator division.

REFERENCES

- [1] W. Barth *et al.*, “Upgrade program of the high current heavy ion unilac as an injector for FAIR”, *Nucl. Instrum. Methods Phys. Res., Sect. A*, vol. 577, pp. 211-214, July 2007.
- [2] W. Barth *et al.*, “High Brilliance Beam Investigations at UNILAC”, *Phys. Rev. Acc. Beams*, vol. 25, p. 040101, 2022. DOI: <https://doi.org/10.1103/PhysRevAccelBeams.25.040101>.
- [3] W. Barth *et al.*, “LINAC developments for heavy ion operation at GSI and FAIR”, *Journal of Instrumentation*, vol. 15, number 12, p. T12012, 2020. doi:10.1088/1748-0221/15/12/t12012
- [4] A. Adonin *et al.*, “Production of high current proton beams using complex H-rich molecules at GSI”, *Rev. Sci. Instrum.*, vol. 87, no. 2, 2016. doi:10.1063/1.4934620.
- [5] W. Barth *et al.*, “Heavy ion linac as a high current proton beam injector”, *Phys. Rev. Accel. Beams*, vol. 18, p. 050102, 2015. doi:10.1103/PhysRevSTAB.18.050102
- [6] S. Yaramyshev *et al.*, “Development of the versatile multi-particle code DYNAMION”, *Nucl. Instrum. Methods Phys. Res., Sect. A*, vol. 558, pp. 90-94, March 2006. doi:10.1016/j.nima.2005.11.018
- [7] W. Barth *et al.*, “High brilliance uranium beams for the GSI FAIR”, *Phys. Rev. Accel. Beams*, vol. 20, p. 050101, May 2017. doi: 10.1103/PhysRevAccelBeams.20.050101
- [8] L. Groening *et al.*, “Technical Design Report of the Alvarez 2.0 post-Stripper DTL (V13b) for the UNILAC, ALV2_note_20210915, GSI Darmstadt (2021).
- [9] W. Barth *et al.*, “U28+-intensity record applying a H2-gas-stripper cell”, *Phys. Rev. Accel. Beams*, vol. 18, p. 040101, 2015.
- [10] P. Gerhard *et al.*, “Development of Pulsed Gas Strippers for Intense Beams of Heavy and Intermediate Mass Ions”, in

- Proc. LINAC'18*, Beijing, China, Sep. 2018, pp. 982-987.
doi:10.18429/JACoW-LINAC2018-FR1A05
- [11] P. Scharrer *et al.*, “Electron stripping of Bi ions using a modified 1.4 MeV/u gas stripper with pulsed gas injection”, *J. Radioanal. Nucl. Chem.*, vol. 305, pp. 837-842, Mar. 2015. doi:10.1007/s10967-015-4036-2
- [12] P. Scharrer *et al.*, “Applications of the pulsed gas stripper technique at the GSI UNILAC”, *Nucl. Instrum. Methods Phys. Res., Sect. A*, vol. 863, pp. 20-25, 2017.
doi:10.1016/j.nima.2017.05.015
- [13] S. Lauber *et al.*, “Longitudinal phase space reconstruction for a heavy ion accelerator”, *Phys. Rev. Accel. Beams*, vol. 23, p. 114201, 2020.
doi:10.1103/PhysRevAccelBeams.23.114201
- [14] S. Yaramyshev *et al.*, “Virtual charge state separator as an advanced tool coupling measurements and simulations”, *Phys. Rev. ST Accel. Beams*, vol. 18, p. 050103, May 2015.
doi:10.1103/PhysRevSTAB.18.050103
- [15] S. Lauber *et al.*, “A dynamic collimation and alignment system for the Helmholtz linear accelerator”, *Review of Scientific Instruments*, vol. 92, no. 11, p. 113306, 2021.
doi.org/10.1063/5.0069824
- [16] A. Adonin and R. Hollinger, “Beam brilliance investigation of high current ion beams at GSI heavy ion accelerator facility”, *Rev. Sci. Instrum.* vol. 85, p. 02A727, 2014.
doi:10.1063/1.4833931
- [17] R. Singh *et al.*, “Longitudinal Beam Diagnostics R&D at GSI-UNILAC”, presented at 15th Int. Conf. On Heavy Ion Technology (HIAT'22), Darmstadt, Germany, June 2022, paper TH2C2, this conference
- [18] W. Barth *et al.*, “A superconducting CW-linac for heavy ion acceleration at GSIX”, *EPJ Web Conf.* 138, p. 01026, 2017.
doi:10.1051/epjconf/201713801026
- [19] W. Barth *et al.*, “First heavy ion beam tests with a superconducting multigap CH cavity”, *Phys. Rev. Accel. Beams*, vol. 21, p. 020102, Feb. 2018.
- [20] M. Schwarz, S. Yaramyshev, K. Aulenbacher, W. Barth, M. Basten, *et al.*, “Reference beam dynamics layout for the SC CW heavy ion HELIAC at GSI”, *Nucl. Instrum. Meth. Phys. Res. Sect. A*, p. 163044, 2019.
doi:10.1016/j.nima.2019.163044
- [21] F. Herfurth *et al.*, “The HITRAP facility for slow highly charged ions”, *Physica Scripta*, vol. 2015, no. T166, p. 014065, Nov. 2015.
doi:10.1088/0031-8949/2015/T166/014065
- [22] S. Busold *et al.*, “Shaping laser accelerated ions for future applications – the LIGHT collaboration”, *Nucl. Instrum. Meth. Phys. Res. Sect. A*, vol. 740, pp. 94–98, 2014.
doi:10.1016/j.nima.2013.10.025
- [23] U. Ratzinger *et al.*, “The 70 MeV p-injector design for FAIR”, in: *AIP Conf. Proc.*, vol. 773, pp. 249–253, 2005.
doi:10.1063/1.1949539
- [24] A. Adonin *et al.*, “The PRIDE project”, poster at ICIS 2019, Lanzhou, China, 2019, not published.

HIGH INTENSITY PROTON BEAMS AT GSI (HEAVY ION) UNILAC

W. Barth^{1,2,3,†}, M. Miski-Oglu^{1,2}, U. Scheeler¹, H. Vormann¹, M. Vossberg¹, S. Yaramyshev^{1,2}
¹ GSI Helmholtzzentrum für Schwerionenforschung, Darmstadt, Germany
² Helmholtz Institute Mainz, Germany
³ Johannes Gutenberg-Universität Mainz, Mainz, Germany

Abstract

A significant part of the experimental program at FAIR is dedicated to pbar physics requiring a high number of cooled pbars per hour. The primary proton beam has to be provided by a 70 MeV proton linac followed by two synchrotrons. The new FAIR proton linac will deliver a pulsed high intensity proton beam of up to 35 mA of 36 μ s duration at a repetition rate of 4 Hz. The GSI heavy ion linac (UNILAC) is able to deliver intense heavy ion beams for injection into SIS18, but it is not suitable for FAIR relevant proton beam operation. In an advanced machine investigation program it has been shown, that the UNILAC provides for sufficient high intensities of CH₃-beam, cracked (and stripped) in a supersonic nitrogen gas jet into protons and carbon ions. This new operational approach results in up to 3 mA of proton intensity at a maximum beam energy of 20 MeV, 100 μ s pulse duration and a rep. rate of 4 Hz. For some time now, UNILAC proton beam operation with higher intensities has been offered as standard for users. Recent linac beam measurements will be presented, showing that the UNILAC is able to bridge the time until the FAIR-proton linac delivers high-intensity proton beams.

INTRODUCTION

Besides two ion source terminals and a low energy beam transport system (LEBT) the High Current Injector (HSI) [1] of the UNILAC (Fig. 1) comprises a 36 MHz IH-RFQ (2.2 keV/u up to 120 keV/u) and an IH-DTL with two separate tanks, accelerating the beam up to the final HSI-energy of 1.4 MeV/u. After stripping and charge state separation the Alvarez DTL provides for beam acceleration up to $\beta = 0.155$. In the transfer line (TK) to the synchrotron SIS18 a foil stripper and another charge state separator system can be used. In order to provide the highest heavy ion beam currents (15 e mA, U²⁸⁺), as required for FAIR, the HSI must deliver up to $2.8 \cdot 10^{12}$ U⁴⁺ ions per pulse [2].

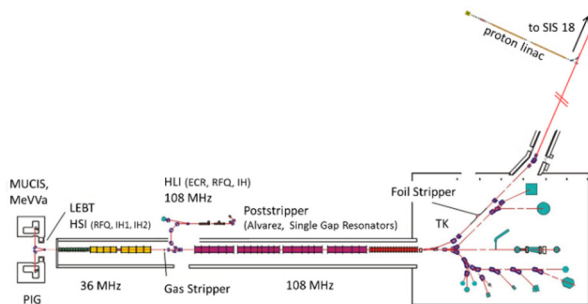


Figure 1: Schematic overview of the GSI UNILAC, experimental area and new FAIR proton linac.

† email address: w.barth@gsi.de

Highly charged heavy ion beams as well as protons, both with high average intensities (but low pulse intensities), from an ECR ion source of CAPRICE-type are accelerated in the High Charge State Injector (HLI) to 1.4 MeV/u. The HLI as well as the HSI serve in a time sharing mode for the Alvarez DTL. The FAIR proton linac [3] has to provide the high intensity primary proton beam for the production of antiprotons. It will deliver a 70 MeV beam to the SIS18 with a repetition rate of 4 Hz. The proton linac will be located north of the existing UNILAC complex. The main beam parameters are listed in Table 1.

Table 1: Main Parameters of the FAIR Proton Linac

Final energy	70 MeV
Pulse current	up to 70 mA
Protons per pulse	$7 \cdot 10^{12}$
Repetition rate	4 Hz
Transversal beam emittance	4.2 μ m (tot. norm.)
rf-frequency	325.224 MHz

PROTON BEAMS AT HEAVY ION LINACS

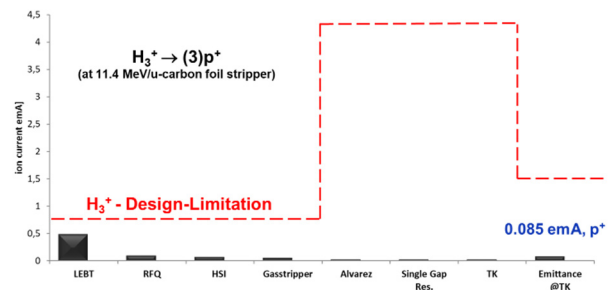


Figure 2: Standard proton beam operation at GSI-UNILAC.

The GSI heavy ion linac (UNILAC) is able to deliver intense heavy ion beam for injection into SIS18, but it is not suitable for FAIR relevant proton beam operation. A strong limitation for light ion beam operation is the low extraction voltage, applied at the ion source due to the fixed specific ion energy of 2.2 keV/u at the RFQ entrance. This limits strongly the extracted beam current from the ion source. Due to the huge emittance in the LEBT only $\leq 20\%$ of the H₃⁺-beam could be accepted by the HSI-RFQ, minor additional particle losses in the matching section to the HSI-IH-DTL limits the overall HSI-transmission to 17%.

Anyway, the significantly higher design limit at Alvarez DTL for H₃⁺-beam and for high energy proton beam behind carbon foil stripping can by far not be utilized in standard operation (see Fig. 2).

Content from this work may be used under the terms of the CC BY 4.0 licence (© 2022). Any distribution of this work must maintain attribution to the author(s), title of the work, publisher, and DOI

UNILAC MACHINE INVESTIGATIONS

Recently an advanced investigation program at the existing UNILAC was successfully pushed to deliver high intensity proton beams up to the UNILAC (Alvarez DTL) design limit for a dedicated experimental program at SIS18. In this frame CH_3^+ -beam operation with a MULTI Cusp Ion Source (MUCIS) [4] was established (see Fig. 3). The maximum achieved beam current (for methane operation) was 11 mA for the not analyzed beam and 4 mA for the CH_3^+ ion beam. The ion source operation has been performed with a repetition frequency of 2 Hz and a pulse length of 1 ms. The ethane gas tests have been carried out with the same ion source and under the same conditions, but the mass spectrum is more complex than for methane operation (see Fig. 3). The production maximum was obtained for C_2H_4^+ , while a maximum beam current of 2.0 emA in front of the RFQ was achieved. However, assuming the same transmission through the HSI, CH_3^+ beam operation results in a higher proton yield. Due to the higher applied extraction voltage and the enhanced HSI design limit for CH_3^+ -beam operation, the improved beam transmission compared to a pure proton beam is evident. Furthermore a triple particle output (for protons) from each CH_3^+ molecule behind the stripping section [5] can be anticipated.

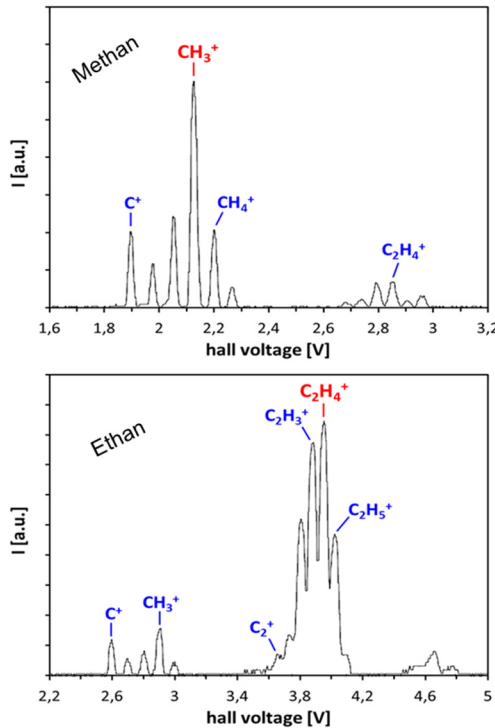


Figure 3: Ion source development in order to provide for high intensity hydro carbon compound beams. [6]

Acceleration of protons at UNILAC implicates special challenges for the settings of the high power rf sections. Designed and normally operated at rf levels between some 100 kW up to 2 MW, in particular the low level part (amplitude and phase control) has to be adjusted to handle very

low signal levels. The cavity voltage for the Alvarez tank 3, shown in Fig. 4 corresponds to an output power of approximately 21 kW. The adjustment of the rise time setting has to ensure a constant gap voltage (flat top) at the time when the beam pulse is passing the cavity. The overall loop gain had to be increased up to a non-risky level. The reaction on the proton beam is shown in Fig. 4 as well. Due to the lowered cavity impedance while the beam is present the control loop increases rf power in the range of 4 kW in addition to the 21 kW for the cavity losses.

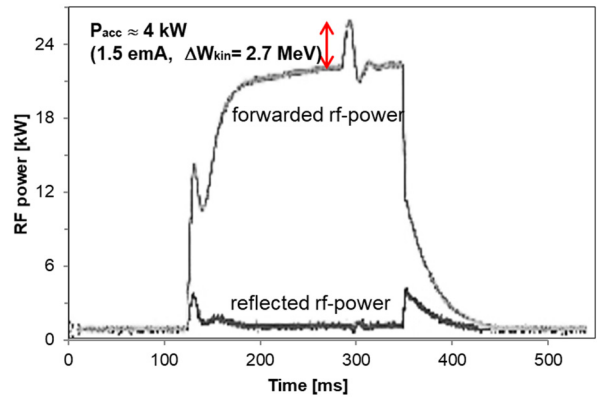


Figure 4: RF-amplifier optimizations. [6]

HIGH INTENSITY MEASUREMENTS

A dedicated machine investigation program was carried out to push the proton beam intensity at GSI-UNILAC. The highest proton intensity of 4 mA (at 1.4 MeV) was achieved in a test experiment with C_2H_4^+ -beam from the HSI. Finally in 2016, a thirty times higher proton current was available at standard beam energy of 11.4 MeV/u. Strong efforts were launched to push the high current proton beam transmission through the entire poststripper and transfer line to a value of up to 80% (for 2.0 mA).

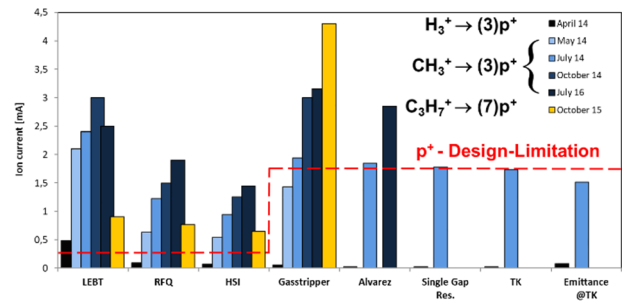


Figure 5: Proton beam intensity at UNILAC. [6]

The high current transverse beam emittance was measured with high resolution in all sections of the UNILAC and the transfer line (Fig. 6). The transverse emittance growth inside the entire Alvarez section could be minimized to 17% only. Even though a transmission loss was observed in the transfer line to the SIS18, the beam brilliance was kept constant during beam transport. The bottleneck of the beam transport line is a 22.5 degree bending

Content from this work may be used under the terms of the CC BY 4.0 licence (© 2022). Any distribution of this work must maintain attribution to the author(s), title of the work, publisher, and DOI

magnet with a limited aperture implicating transmission loss of approx. 10% for high current proton beam operation.

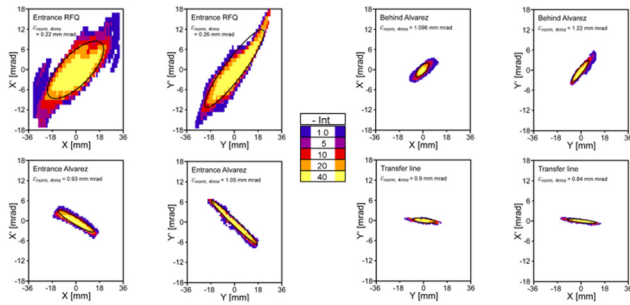


Figure 6: Proton beam emittance measurements corresponding to Fig. 5 (May 2014). [6]

HIGH PERFORMANCE PROTON BEAM OPERATION

For the applied (pulsed) H₂-gas target at 1.4 MeV/u strip-per section the CH₃⁺-molecules are stripped and cracked in one carbon ion and three protons. In the charge separating system comprising three dipole magnets the high intensity proton beam is separated from the carbon beam. The measured charge spectrum (Fig. 7) shows a proton fraction, which is (above a certain threshold) independent on the density of the supersonic nitrogen gas jet target. The average charge of the carbon spectrum depends on the target density. A maximum at Z = 4 for lower gas pressure and at Z = 6 for highest gas pressure was observed. For advanced proton beam operation the lowest target density, providing for high beam intensities as well as for minimum beam straggling (minimum emittance growth), has been adjusted. The entire spectrum is influenced by the different secondary electron multiplying factors of proton and carbon beams; especially the relatively low measured proton beam current signal (compared to the carbon beam current signal) was not investigated in detail.

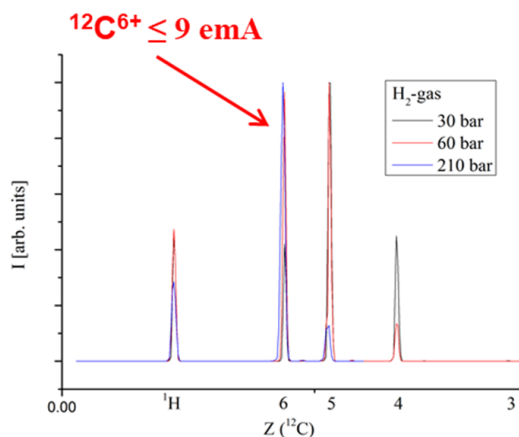


Figure 7: Stripper spectrum optimized for C⁶⁺. [6]

Proton acceleration in the Alvarez post stripper requires very low rf voltages, as long as the regular synchronous phase of -30° (resp. -25° for Alvarez tank 3 and 4) is ap-

plied. In order to operate at these low voltages, the rf transmitters have to be tuned carefully providing for stable and reliable proton beam operation. This strong effort and long lasting tuning procedure can be avoided, when larger negative phases for the reference particle are chosen: For the same peak voltage the instantaneous voltage for the reference particle is then lower ($U(\varphi) = U_{\text{peak}} \cdot \cos(\varphi)$). Accordingly, for the same reference particle voltage higher rf peak voltages can be applied. During 2020 machine experiment campaign with high current (2 emA) proton beams it turned out that a phase value of -57° is the best compromise for sufficient beam properties at manageable rf control-voltages for all Alvarez-tanks. As shown in Fig. 8 the beam emittance is increased by almost a factor of, 2 while beam transmission is not significantly changed.

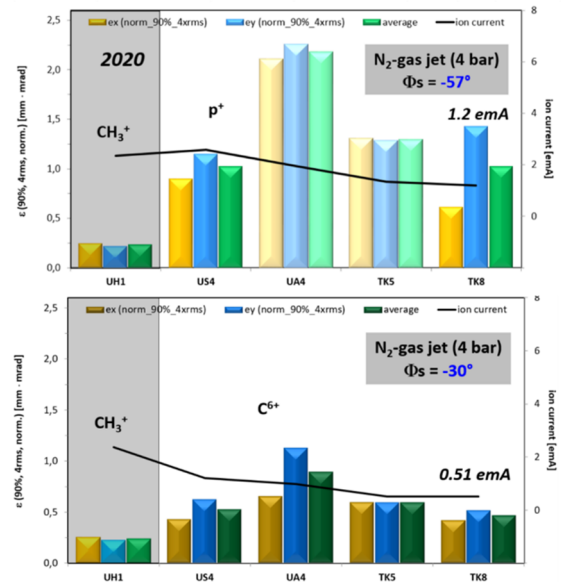


Figure 8: Simultaneous poststripper operation with high intensity carbon and proton beam.

After cracking of CH₃⁺-molecules and stripping into protons and carbon ions simultaneous proton and carbon beam operation (C⁶⁺) in the post stripper has been enabled. For further poststripper acceleration the Alvarez dc quadrupole gradients were adjusted to an average A/Z-value of 1.35, sufficient for proton- (A/Z = 1) and C⁶⁺ (A/Z = 2) operation. Avoiding strong scattering effects for the proton beam a relatively low stripper target density is required. In contradiction fully stripped carbon ions can only be achieved by high target densities. For 2021 and 2022 user runs simultaneous high intensity proton and carbon operation at UNILAC based on a sufficiently balanced target thickness could be first time carried out successfully.

SUMMARY AND OUTLOOK

The UNILAC serves as heavy ion accelerator since 1975. An R&D-program started seven years ago with the goal to operate UNILAC with high intensity proton beams until the dedicated FAIR proton linac is available. Since 2016 UNILAC can provide for up to 3 emA high brilliance proton beam) at a maximum beam energy of 20 MeV.

2×10^{11} protons per second could be achieved at SIS18 extraction. Taking the achieved beam current, emittance and energy into account the UNILAC can provide for up to 1.5×10^{12} protons per second [6-9]. An advanced and simplified UNILAC-proton operation at a synchronous phase $\Phi_s \approx -57^\circ$ high intensity proton beam operation has been established. Simultaneous high intensity proton/carbon (6+) operation from a single ion source has been made available for user operation since 2021 [10, 11]. Simultaneous operation at maximum proton and C^{6+} -intensity is facilitated when the pulsed hydrogen gas stripper is put into operation.

ACKNOWLEDGEMENTS

Successful beam testing could not be accomplished without strong support of highly committed people from different GSI-departments.

REFERENCES

- [1] O. Kester, W. Barth, O. Dolinsky, F. Hagenbuck, K. Knie, H. Reich-Sprenger, H. Simon, P.J. Spiller, U. Weinrich, M. Winkler, R. Maier and D. Prasuhn, "Status of the FAIR Accelerator Facility", in *Proc. IPAC'14*, Dresden, Germany, Jun. 2014, pp. 2084-2087
doi:10.18429/JACoW-IPAC2014-WEPRO060
- [2] H. Vormann, W. Barth, L. Dahl, W. Vinzenz, S. Yaramyshev, U. Ratzinger, R. Tiede, A. Kolomiets, S. Minaev, "Advanced UNILAC Upgrade for FAIR", in *Proc. LINAC'10*, Tsukuba, Japan, Sep. 2010, paper MOP040, pp. 142-144.
- [3] R. M. Brodhage, G. Clemente, W. Vinzenz, and U. Ratzinger, "First Coupled CH Power Cavity for the FAIR Proton Injector", in *Proc. IPAC'14*, Dresden, Germany, Jun. 2014, pp. 3232-3234. doi:10.18429/JACoW-IPAC2014-THPME011
- [4] R. Keller, Multi charged Ion Production with MUCIS, GSI Scientific. Rep. 1987, p. 385. (1987)
- [5] W. Barth and P. Forck, "The New Gas Stripper and Charge State Separator of the GSI High Current Injector", in *Proc. LINAC'00*, Monterey, CA, USA, Aug. 2000, paper MOD13, p. 235.
- [6] W. Barth *et al.*, "Heavy ion linac as a high current proton beam injector", *Phys. Rev. ST Accel. & Beams*, vol. 18, p. 050102, 2015. doi:10.1103/PhysRevSTAB.18.050102
- [7] S. Appel and O. Boine-Frankenheim, "Multi-turn injection into a heavy ion synchrotron in the presence of space charge". doi:10.48550/arXiv.1403.5972
- [8] U. Ratzinger, G. Clemente, C. Commenda, H. Liebermann, H. Podlech, R. Tiede, W. Barth and L. Groening, "A 70-MeV Proton Linac for the FAIR Facility Based on CH - Cavities", in *Proc. LINAC'06*, Knoxville, TN, USA, Aug. 2006, paper TH1004, p. 186
- [9] W. Vinzenz, "p-linac status and plans", 12th FAIR Machine Advisory Committee, 2014.
- [10] H. Vormann *et al.*, "Machine investigations with 209Bi- and proton-beam at the GSI-UNILAC", https://www.gsi.de/fileadmin/Beschleunigerbetrieb/Dokumente/UNILAC_Report_ACC_Exp_05_06_2020.pdf
- [11] H. Vormann, U. Scheeler, W. Barth, and S. Yaramyshev, "Investigation of advanced UNILAC Operation Modes", GSI Ann. Rep. 2020, Darmstadt, Germany, 2021.

MODE ANALYSIS OF SINGLE SPOKE RESONATOR TYPE-2 (SSR2) FOR RISP *

Myung Ook Hyun[†], Rare Isotope Science Project (RISP), Institute of Basic Science (IBS),
 Daejeon, South Korea

ABSTRACT

Rare Isotope Science Project (RISP) in the Institute of Basic Science (IBS), Daejeon, South Korea, is developing the high-energy superconducting (SC) linac composed of two types of superconducting cavities, single spoke resonator type-1 (SSR1) and type-2 (SSR2) [1]. Both cavities have same RF frequency of 325MHz, but different beta, 0.3 for SSR1 and 0.51 for SSR2. For operating SC cavity within the target frequency, all external disturbances must be removed or avoided. From a view of mechanical vibration, comparably low frequency up to 20kHz always happens as a consequence of combination between outer disturbance and resonant frequency of SC cavity. In this paper, we will show the design layout and the specifications. Also, the mechanical resonance analysis for both bare and dressed cavity will be conducted with a numerical analysis program.

SSR2 SC CAVITY

SSR2 SC cavity prototyping was started from 2018, and its design concept was balloon-variant which came from the research collaboration with TRIUMF, the national laboratory of Canada [2]. For suppressing multipacting, the balloon-variant design is applied to both SSR1 and SSR2 of RISP. Table 1. shows the comparison result of SSR1 and SSR2 specifications [3].

Table 1: Specifications of SSR1 and SSR2

Spec.	SSR1	SSR2
Operating Frequency	325MHz	
Beta	0.3	0.51
Epeak	35MV/m	
Vacc	> 2.4MV	> 4.1MV
Q0	>3.2E9	>5E9
df/dP	<10Hz/mbar	
Aperture	50mm	
Pressure Envelope @ 300K	2 bars	
Pressure Envelope @ 2K	5 bars	

* This work was supported by the Rare Isotope Science Project (RISP) in the Institute of Basic Science (IBS) funded by the Ministry of Science and ICT (MSIT) and National Research Foundation (NRF) of South Korea.

[†] atikus43@ibs.re.kr

Figure 1 shows the layout of SSR2 SC cavity. RISP is now making six SSR2 SC cavities for prototyping [4]. Until now, 4 cavities are fabricated as a bare cavity and ready for cryogenic test, and 2 cavities are now on the electron beam welding (EBW) stage. Figure 2 shows the EBW finished SSR2 bare cavity.

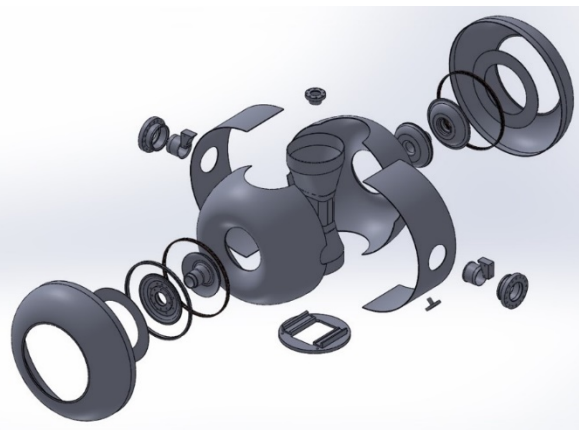


Figure 1: Layout of SSR2 Dressed Cavity.



Figure 2: Fabricated SSR2 Bare Cavity.

SSR2 MODE ANALYSIS

Same as SSR1 [5], the finite element method (FEM) simulation was proceeded for evaluating the mechanical characteristics of SSR2 SC cavity such as Von Mises stress and deformation/strain. Also, mode analysis and harmonic response were calculated for defining its structural characteristics. However, unlikely to SSR1, SSR2 SC cavity fabrication process is not finished yet, thus the vibration test of SSR2 SC cavity is not proceeded.

Nonetheless of the absence of vibration test for SSR2 SC cavity, mode analysis of this paper make it possible to estimate the mechanical resonance of SSR2 SC cavity. Because during the previous studies and experiments [5,6], current numerical analysis method and code is verified for predicting mechanical resonance of other systems such as quarter wave resonator (QWR) or single spoke resonator type-1 (SSR1) precisely. Therefore, in this paper we will discuss only with numerical analysis with commercial code, ANSYS ver.18 [7].

MODEL SETUP AND ANALYSIS

Figure 3 shows the meshed shape of dressed SSR2 SC cavity. SSR2 SC cavity is mainly composed with two materials, pure niobium for bare cavity and 316L stainless steel for liquid helium jacket. Table 2 shows the material properties of pure niobium and 316L stainless steel [8].

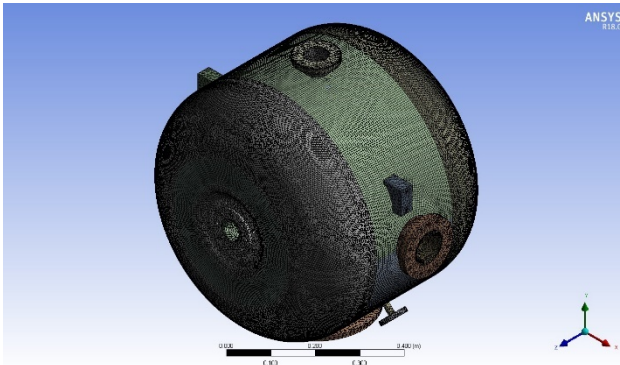


Figure 3: Mesh Shape of SSR2 SC cavity.

Table 2: Material Properties

Spec.	RRR300 Niobium	Stainless Steel 316L
Young's Modulus	107 GPa	193GPa
Poisson's Ratio	0.36	0.25
Yield Strength	51MPa	170MPa
Maximum Tensile Strength	134MPa	483MPa

Figure 4 shows the boundary conditions for numerical analysis. We applied fixed support condition to jacket support block – bottom side, gravitational force condition for its own weight, and 0.2 MPa pressure condition at the outer surface of bare cavity and inner surface of liquid helium jacket.

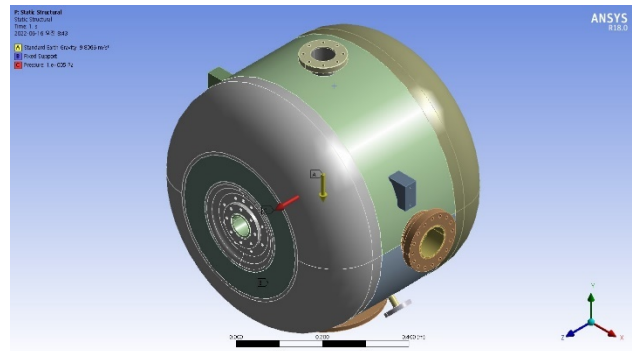


Figure 4 : Boundary conditions.

After finishing structural analysis, we proceeded modal and harmonic response analysis. Same as SSR1 simulation, harmonic response was calculated at three points, spoke centre, free cover and fixed cover. Free cover means no connection between cavity stiffener ring and jacket, and fixed cover means TIG weldment between cavity stiffener ring and jacket. Figure 5 to 8 show the four harmonic response analysis results, spoke centre, free cover, fixed cover and three-points combined. At figure 5, the four highest and dominant peaks are shown around 585, 420, 220, 40 Hz. We can define other peaks at different points from figure 6 to 8 as same as figure 5.

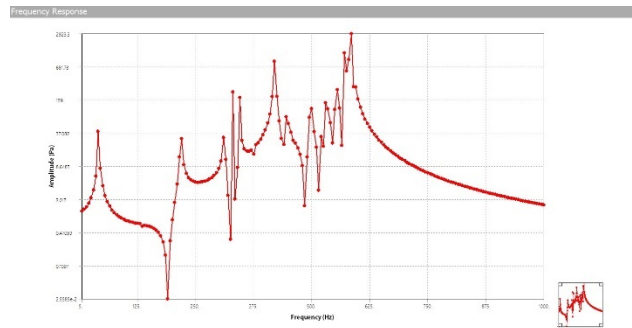


Figure 5 : Harmonic Response – Spoke Centre.

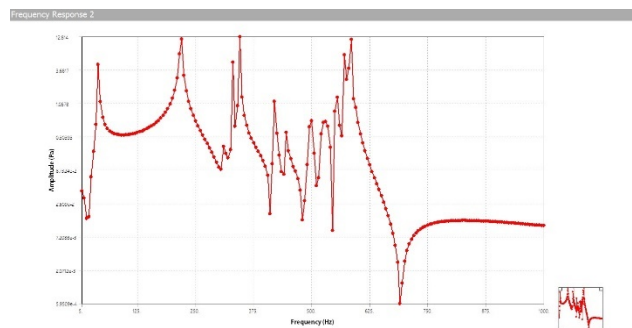


Figure 6 : Harmonic Response – Free Cover.

Content from this work may be used under the terms of the CC BY 4.0 licence (© 2022). Any distribution of this work must maintain attribution to the author(s), title of the work, publisher, and DOI

Content from this work may be used under the terms of the CC BY 4.0 licence (© 2022). Any distribution of this work must maintain attribution to the author(s), title of the work, publisher, and DOI

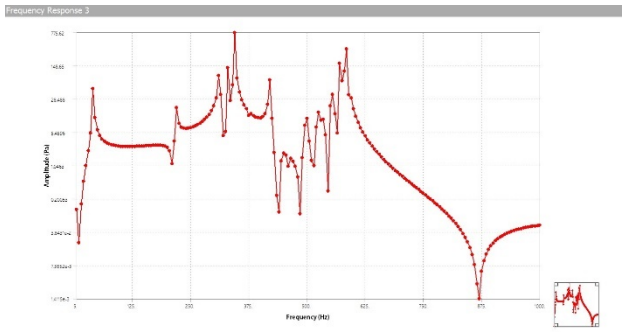


Figure 7 : Harmonic Response – Fixed Cover.

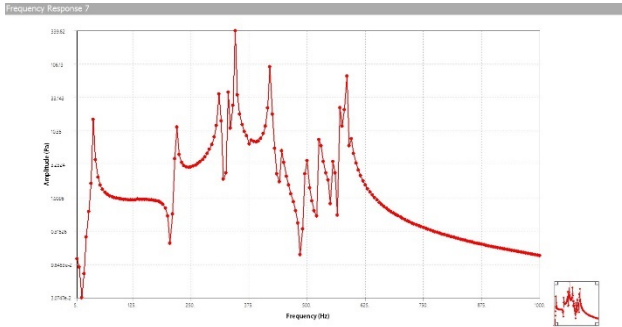


Figure 8 : Harmonic Response – Combined.

Table 3 shows the summary of highest and dominant peaks of three points each and combined. With this summary, we can observe five main dominant peaks. Figure 9 to 13 show the mode summary of each peak.

Table 3: Mode Summary

Points	First (Hz)	Second (Hz)	Third (Hz)	Fourth (Hz)	Fifth (Hz)
Spoke	40	220		420	585
Centre					
Free Cover	40	220	345		585
Fixed Cover	40		345	420	585
Com-bined	40	220	345	420	585

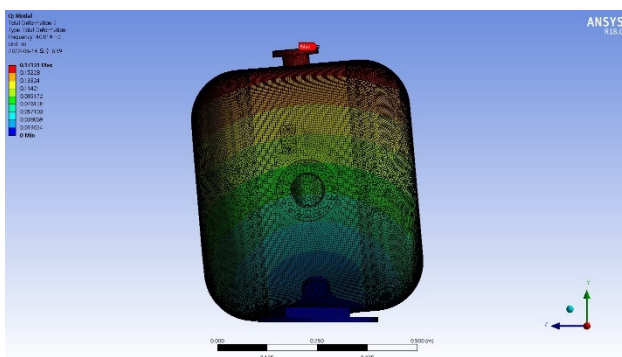


Figure 9 : 1st Mode – Simply Bending (pitching).

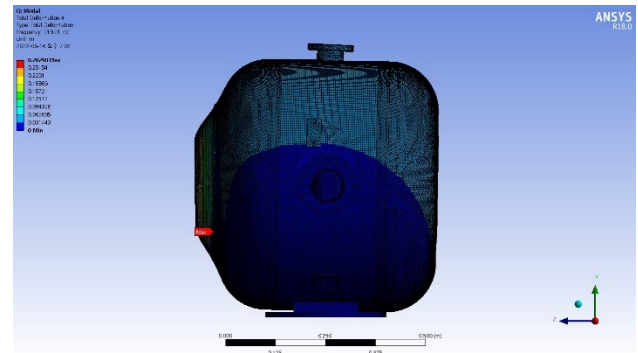


Figure 10 : 2nd Mode – Free Cover Fluctuation.

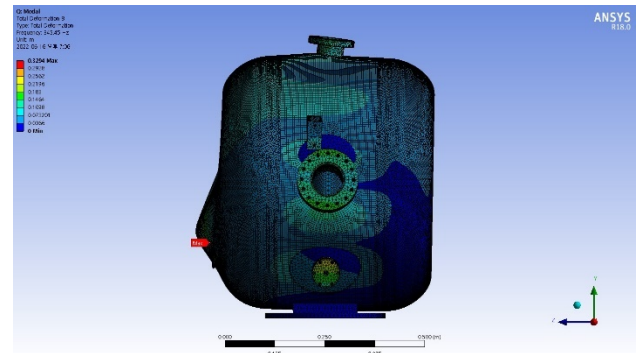


Figure 11 : 3rd Mode – Complex Mode.

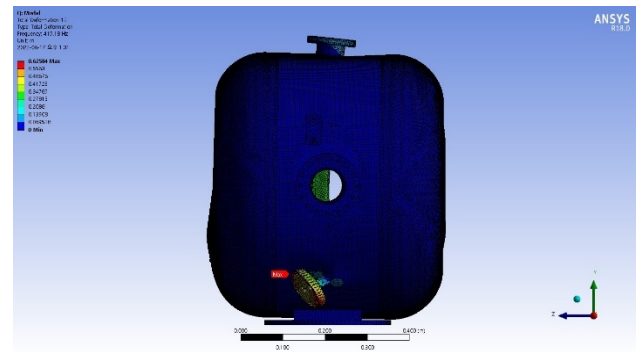


Figure 12 : 4th Mode – Helium Inlet Bending.

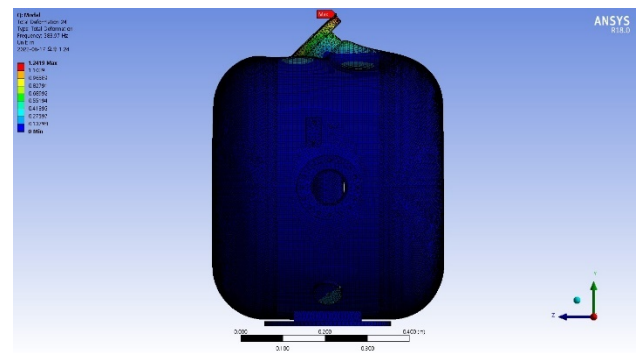


Figure 13 : 5th Mode – Helium Outlet Bending.

ANALYSIS COMPARISON

Comparing with SSR1 mode analysis results, we found that there was a similarity between SSR1 and SSR2 mode shape. Table 4 shows the comparison of SSR1 and SSR2 mode analysis results.

Table 4: Comparison of SSR1 and SSR2 Modes

Num.	SSR2 Mode (Hz)	Mode Def.	SSR1 Mode (Hz)	Mode Def.
1st	40.82	Bending	46.73	Bending
2nd	218.2	Fluctuate	240.8	Fluctuate
3rd	-	-	265.5	He Inlet
4th	345.5	Torsion	349.4	Torsion
5th	419.2	He Inlet	-	-
6th	584.0	He Outlet	579.6	He Outlet
7th	-	-	710.1	Complex

From the table 4, SSR1 and SSR2 mode analysis results are very similar. The first mode of both cavities exists near 40Hz, 46.73Hz for SSR1 and 40.82Hz for SSR2. The second and the fourth modes of both cavities are also so close each other, 240.8Hz for SSR1 and 218.2Hz for SSR2 in the free cover fluctuation mode, 349.4Hz for SSR1 and 345.5Hz for SSR2 in the free cover torsional mode. Through this comparison, it can be assumed that shape similarity between two cavities makes structural similarity and mechanical resonances appear very similar to the outer disturbance. Nonetheless, there is a slight difference between the mode analysis of two cavities. It might come from the weight(mass) difference. SSR2 is heavier than SSR1, so the resonant frequency of SSR1 can be smaller than that of SSR2, because the frequency of system is directly proportional to the stiffness and is inversely proportional to the mass.

We will proceed the vibration test of dressed SSR2 SC cavity after finishing our cryogenic test.

CONCLUSION

Through analysis, we can find that SSR2 mode is very similar to SSR1. RISP are now preparing for the next stage, pre-production of SCL2 which has a plan for fabrication of modified SSR1 and SSR2 model. For activating next stage, RISP will finish the current SSR1 and SSR2 prototyping stage within this year.

ACKNOWLEDGEMENTS

This paper was supported by the Rare Isotope Science Project (RISP), which had been funded by the Ministry of Science and ICT (MSIT) and National Research Foundation (NRF) of the Republic of Korea.

REFERENCES

- [1] D. Jeon *et al*, “Design of the RAON accelerator systems”, *Journal of Korean Physical Society*, vol. 65, no. 7, pp. 1010-1019, Oct. 2014. doi:10.3938/jkps.65.1010
- [2] Z. Y. Yao, R. E. Laxdal, and V. Zvyagintsev, “Balloon Variant of Single Spoke Resonator”, in *Proc. 17th Int. Conf. RF Superconductivity (SRF'15)*, Whistler, Canada, Sep. 2015, paper THPB021, pp. 1110-1114.
- [3] M. O. Hyun, Y. W. Jo, H. C. Jung, and Y. Kim, “Mechanical Design of Single Spoke Resonator Type-2 (SSR2) Superconducting Cavity for RISP”, in *Proc. 14th Int. Conf. on Heavy Ion Accelerator Technology (HIAT'18)*, Lanzhou, China, Oct. 2018, pp. 125-128. doi:10.18429/JACoW-HIAT2018-WE0YA01
- [4] M. O. Hyun, J. Joo, H. C. Jung, and Y. Kim, “Fabrication Process of Single Spoke Resonator Type-2 (SSR2) for RISP”, presented at the 20th International Conference on RF Superconductivity (SRF'21), East Lansing, MI, USA, Jun.-Jul. 2021, paper MOPCAV011, to be published. doi:10.18429/JACoW-SRF2021-MOPCAV011
- [5] M. O. Hyun, Y. W. Jo, H. C. Jung, Y. Kim, and M. Lee, “Modal Analysis and Vibration Test of Single Spoke Resonator Type-1 (SSR1) for RISP”, presented at the 20th International Conference on RF Superconductivity (SRF'21), East Lansing, MI, USA, Jun.-Jul. 2021, paper THPCAV001, to be published. doi:10.18429/JACoW-SRF2021-THPCAV001
- [6] M. O. Hyun, H. C. Jung, Y. Kim, and M. Lee, “Modal Analysis and Vibration Test for Quarter Wave Resonator for RAON”, in *Proc. 19th Int. Conf. RF Superconductivity (SRF'19)*, Dresden, Germany, Jun.-Jul. 2019, pp. 485-487. doi:10.18429/JACoW-SRF2019-TUP032
- [7] Ansys | Engineering Simulation Software, <https://www.ansys.com>
- [8] Online Materials Information Resource – MatWeb, <https://www.matweb.com>

List of Authors

Bold papercodes indicate primary authors; ~~crossed-out~~ papercodes indicate 'no submission'

— A —

Adachi, T. ~~M04I1~~
 Adam, T. ~~TU3I2~~, ~~TUP14~~
 Adegun, J.A. ~~TU2C4~~
 Agustsson, R.B. ~~M03I1~~
 Ames, F. ~~M02I2~~, ~~TU2C4~~
 Andelkovic, Z. ~~TU3C3~~
 Andres, A. ~~TU2C4~~
 Anger, P. ~~TUP02~~
 Angot, J. ~~M02C3~~
 Araujo, A. ~~M03I1~~
 Ates, A. ~~TU1C4~~
 Aulenbacher, K. ~~TH3C2~~, ~~TH1C4~~
 Aumüller, S. ~~TUP05~~, ~~TUP06~~
 Aurnia, S. ~~TUP15~~

— B —

Baartman, R.A. ~~TU2C4~~, ~~TUP19~~
 Back, B. ~~TUP11~~, ~~TUP12~~
 Bagri, H. ~~TU2C4~~
 BalSS, R. ~~TUP03~~
 Bambade, P. ~~TU3I2~~
 Bandyopadhyay, A. ~~TU2I2~~
 Bandyopadhyay, S. ~~TU2I2~~
 Barazzuol, L. ~~M03C2~~
 Barth, W.A. ~~TH1C4~~, ~~TH3C2~~, ~~TH3C3~~,
~~TH4C3~~
 Basten, M. ~~TUP10~~, ~~TH1C4~~, ~~TH3C2~~
 Battison, S.T. ~~M01C3~~
 Baylac, M.A. ~~M02C3~~
 Bechtold, A. ~~M04C3~~
 Beeckman, W. ~~M04C3~~
 Bellamy, R. ~~TUP14~~
 Bellan, L. ~~TH3I1~~
 Ben Abdillah, S.M. ~~TU3I2~~
 Bender, M. ~~TU1C2~~
 Benedetto, E. ~~WE1I4~~
 Bernal, E. ~~TH1C3~~
 Beyer, M. ~~FR1C2~~
 Bhattacharya, S. ~~TU2I2~~
 Bhattacharyya, P. ~~TU2I2~~
 Bhattacharyya, T. ~~TU2I2~~
 Bhunia, U. ~~TU2I2~~
 Blaum, K. ~~TUP05~~
 Blomberg, B.R. ~~TUP11~~, ~~TUP12~~, ~~TH1I2~~
 Bosch, R.A. ~~M01C3~~
 Both, S. ~~M03C2~~
 Bouquerel, E. ~~TU3I2~~
 Bozyk, L.H.J. ~~TUP05~~, ~~TUP06~~
 Brandenburg, S. ~~M03C2~~
 Bultman, N.K. ~~M04I2~~
 Bunnell, K.J. ~~TUP11~~, ~~TH1I2~~
 Burandt, C. ~~TH3C2~~

— C —

Caruso, A.C. ~~TUP15~~
 Casagrande, F. ~~WE1I3~~
 Castel, C. ~~TUP14~~
 Castro, G. ~~TH4C1~~
 Celona, L. ~~TH4C1~~
 Chaddha, N. ~~TU2I2~~
 Chang, W. ~~TH1C3~~
 Chen, L.H. ~~FR2I1~~
 Cheymol, B. ~~TU3I2~~
 Chines, F. ~~TH4C1~~
 Clark, J.A. ~~TUP11~~, ~~TUP12~~
 Comunian, M. ~~TH3I1~~
 Conrad, T. ~~TH1C4~~
 Cooper, A. ~~M01C3~~
 Coppes, R.P. ~~M03C2~~
 Costanzo, G. ~~TH4C1~~
 Cui, B.Q. ~~FR2I1~~

— D —

D'Agostino, G. ~~TUP17~~
 Dantsuka, T. ~~M04I1~~
 Daudin, L. ~~TU3I2~~
 Dauvergne, D. ~~TU3I2~~
 Daykin, E. ~~TH1C3~~
 De Luca, G. ~~TUP15~~
 Debnath, J. ~~TU2I2~~
 Delerue, N. ~~TU3I2~~
 Dendooven, P.G. ~~M03C2~~
 Dey, M.K. ~~TU2I2~~
 Dickerson, C. ~~TUP12~~, ~~TUP13~~, ~~TH1I1~~
 Droba, M. ~~TH3C2~~
 Dunn, G.M. ~~TH1I2~~
 Durand, T. ~~TU3I2~~, ~~TUP14~~
 Dutta Gupta, A. ~~TU2I2~~
 Dziuba, F.D. ~~TH1C4~~, ~~TH3C2~~

— E —

Ezawa, K. ~~TU2C4~~

— F —

Fedoroko, W. ~~TU2C4~~
 Fedotova, S. ~~TU3C3~~
 Ferrari, L. ~~TH3I1~~
 Fomichev, A.S. ~~M04C3~~
 Forck, P. ~~TH3C2~~
 Forest, F. ~~M04C3~~
 Franberg Delahaye, H. ~~WE2I1~~
 Fujii, H. ~~M04I1~~
 Fujimaki, M. ~~M04I1~~
 Fukunishi, N. ~~M04I1~~
 Fukushima, K. ~~WE1I3~~

— G —

Gallin-Martel, M.-L. ~~TU3I2~~

Content from this work may be used under the terms of the CC BY 4.0 licence (© 2022). Any distribution of this work must maintain attribution to the author(s), title of the work, publisher, and DOI

Gammino, S. ~~TH4C1~~
 Geithner, W. **TU3C3**
 Gerbershagen, A. **M03C2**
 Gerhard, P. **M03I3, TU3C3**
 Gettmann, V. **TH1C4, TH3C2**
 Ghosh, S. **TU2I2**
 Gonzalez, A.J. **TUP08**
 Gorshkov, A.V. **M04C3**
 Grabenhofer, A.F. ~~TUP13~~
 Graehling, P.G. **TUP14**
 Guler, H. **TU3I2**
 Guo, B. ~~FR2I1~~
 Gutierrez, E. **TH1C3**

— H —

Haddad, F. **TUP14**
 Hähnel, H. **TUP09, TU1C4**
 Hannweg, A. ~~TU1C3~~
 Hartung, W. **TH1C3**
 Hasebe, H. ~~M04I1~~
 He, J.J. ~~FR2I1~~
 Heighway, J.K. **M01C3**
 Heilig, R. ~~FR1C2~~
 Heilmann, M. **TH1C4**
 Heine, M. **TUP14**
 Hendricks, M.R. **TUP11, TUP12**
 Herfurth, F. **TU3C3**
 Hess, R. ~~TU3I1~~
 Higurashi, Y. ~~M04I1~~
 Hinde, D.J. **M01C3**
 Höltermann, H. **TUP09**
 Hollmann, D. ~~FR1C2~~
 Hu, X.J. **TH2C4**
 Husson, A.A. **TU3I2**
 Hwang, K. **WE1I3**
 Hyun, M.O. **FR1C3**

— I —

Ikegami, M. **WE1I3**
 Imao, H. ~~M04I1~~

— J —

Jamet, C. **TU3I2**
 Jia, H. **TH2C4**
 Jones, B.N. **M03C2**
 Joseph, R. ~~TU3I1~~
 Jung, P.M. **TU2C4**

— K —

Kafer, C. **M01C3**
 Kamigaito, O. ~~M04I1~~
 Kanemura, T. **M04I2, WE1I3**
 Kedzie, M. ~~TUP13~~
 Kelly, M.P. ~~TUP13~~
 Kester, O.K. **TU2C4, TUP19**
 Kidera, M. ~~M04I1~~
 Kim, S.H. **WE1I3, TH1C3**
 Kitchen, T. **M01C3**
 Kiy, S. **TU2C4, TUP19**

Kleeven, W.J.G.M. **TUP17**
 Klingbeil, H. **TUP03**
 Komiyama, M. ~~M04I1~~
 Koser, D. **TUP10**
 Koubek, B. **TUP09**
 Koumeir, C. **TU3I2, TUP14**
 Kowalska, M. ~~M02I1~~
 Kraus, I. **TU3C3**
 Krupko, S.A. **M04C3**
 Kürzeder, T. **TH1C4, TH3C2**
 Kumagai, K. ~~M04I1~~
 Kunjir, S.R. **TH1C3**
 Kutsaev, S.V. **M03I1**

— L —

Lachacinski, B. **TU3I2**
 Laier, U. **TUP03**
 Larter, T.L. **TH1C3**
 Lau, M. ~~FR1C2~~
 Lauber, S. **TH1C4, TH3C2**
 LaVere, M.J. **M04I2**
 Lens, D.E.M. **TUP03**
 Leonard, O. ~~TH4C1~~
 Letcher, E. **TH1I2**
 Li, J.H. ~~FR2I1~~
 Li, J.Q. ~~FR2I1~~
 Li, Z.X. **TH2C4**
 Lian, G. ~~FR2I1~~
 Lidia, S.M. **WE1I3**
 Linardakis, P. **M01C3**
 List, J. **TH1C4, TH3C2**
 Litvinov, S.A. ~~TU3I1~~
 Liu, J.L. ~~FR2I1~~
 Liu, S.H. **TH2C4**
 Liu, W.P. ~~FR2I1~~
 Liu, Y.G. ~~FR2I1~~
 Lobanov, N.R. **M01C3**
 Longhitano, A. **TUP15**
 Lorentz, B. ~~TU3I1~~
 Lucow, K.E. **TU2C4**

— M —

Maazouzi, C. **TU3I2, TUP14**
 Machicoane, G. **WE1I3**
 Madendorp, R. **M04I2**
 Maie, T. ~~M04I1~~
 Maier, M.T. **M03I3, TU3C3**
 Malferrari, L. ~~TH4C1~~
 Mandal, A. **TU2I2**
 Marti, F. **M04I2**
 Martinez Marin, J.L. **TH1I2**
 Maruta, T. **M04I2, WE1I3**
 Massara, A. ~~TH4C1~~
 Maugeri, C. ~~TH4C1~~
 Meyer, D.A. **M03I1**
 Michaud, J. **TU3I2**
 Migliore, M. **M02C3**
 Miski-Oglu, M. **TH1C4, TH3C2, TH3C3,**

	TH4C3
Miyake, Y.M.	M04I1
Molle, R.	TU3I2
Momozaki, Y.	M04I2
Morris, D.G.	WE1I3, TH1C3
Moscatello, M.H.	TUP02
Mustapha, B.	M03I1, TUP12, TH1I2
— N —	
Nabhiraj, P.Y.	TU2I2
Nagatomo, T.	M04I1
Nakagawa, T.	M04I1
Nakamura, M.	M04I1
Nandi, C.	TU2I2
Naser, Z.A.	TU2I2
Nasser, J.	TU2C4
Nassiri, A.	M03I1
Neri, L.	TH4C1
Nishi, T.	M04I1
Nolen, J.A.	M04I2, TH1I1
Notthoff, C.	M01C3
— O —	
Odorici, F.	TH4C1
Ohnishi, J.	M04I1
Okuno, H.	M04I1
Osswald, F.R.	TU3I2, TUP14, TUP16
Ostroumov, P.N.	M04I2, WE1I3
Ozeki, K.	M04I1
— P —	
Pal, S.	TU2I2
Pal, S.	TU2I2
Palmieri, A.	TH3I1
Panda, U.	TU2I2
Passarello, S.	TH4C1
Peaucelle, C.	TU3I2
Peters, C.E.	TUP11
Petersen, T.B.	TUP13
Pisent, A.	TH3I1
Planche, T.	TU2C4
Plastun, A.S.	M04I2, TUP08, WE1I3
Platania, L.	TUP15
Podlech, H.	TUP10, TH3C2, TUP07, TUP09, TH1C4
Poirier, F.	TU3I2, TUP14
Popielarski, J.T.	TH1C3
Popp, U.	TU3I1
Pradhan, J.	TU2I2
— R —	
Raatz, J.E.	M01C3
Ratzinger, U.	TUP09, TU1C4
Rädel, S.D.	TU2C4
Reid, T.	TUP13
Reitano, R.	TH4C1
Reiter, A.	TU3C3
Ren, H.T.	M04I2, WE1I3, TH1C3
Reyna, J.	TUP11

Roncolato, C.R.	TH3I1
Rossi, L.	M01I2
Roy, A.	TU2I2
Rubin, A.	TH1C4, TH3C2
Russo, F.	TH4C1
— S —	
Saha, S.	TU2I2
Sakamoto, N.	M04I1
Savajols, H.	TUP02
Savard, G.	TUP11, TUP12, TH1I1
Scheeler, U.	TH3C3, TH4C3
Schippers, J.M.	M03C2
Schmidt, J.S.	TUP03
Schnase, A.	TH1C4
Schreiber, J.	M01I1
Schultz, B.E.	TU2C4
Schwarz, M.	TH1C4, TH3C2
Schweizer, M.	FR1C2
Scott, R.H.	TUP12
Seth, S.	TU2I2
Shelbaya, O.	TU2C4, TUP19
Siliato, D.	TH4C1
Singh, R.	TH2I2
Smirnov, A.Yu.	M03I1
Som, S.	TU2I2
Song, J.	TH1I1
Spartà, A.	TUP15
Spiller, P.J.	TUP05, TUP06, WE1I2
Stallkamp, N.S.	TU3C3
Stanton, D.	TUP11, TH1I2
Steck, M.	TU3I1
Stringer, B.	TU2C4
Suda, K.	M04I1
Sun, L.T.	WE2I2, FR2I1
— T —	
Tang, X.D.	FR2I1
Tarvainen, O.A.	M02C3
Tasset-Maye, O.	M04C3
Taylor, A.	M04I2
Tempra, T.	M01C3
Ter-Akopian, G.M.	M04C3
Thakur, S.K.	TU2I2
Thiebaut, C.	TU3I2
Thomin, K.G.	TUP03
Thomson, D.C.	TU2C4
Thuillier, T.	M02C3
Torims, T.	TU1I1
Tranter, B.	M01C3
Tranter, R.	M01C3
Trautmann, C.	TU1C2
Trichet, H.	TUP14
Tunningley, T.B.	M01C3
— U —	
Uchiyama, A.	M04I1

Content from this work may be used under the terms of the CC BY 4.0 licence (© 2022). Any distribution of this work must maintain attribution to the author(s), title of the work, publisher, and DOI

— V —

Van Der Graaf, E.R.	M03C2
van Goethem, M.-J.	M03C2
Van Luijk, P.	M03C2
Varenne, F.	TUP02
Velthaus, V.	TU1C2
Verderi, M.	TU3I2
Voisin, E.J.	M04C3
Vondrasek, R.C.	TUP12
Vormann, H.	TH3C3, TH4C3
Vorobyev, G.	TU3C3
Vossberg, M.	TH3C3, TH4C3
Vretenar, M.	WE1I4

— W —

Wagner, S.R.	TUP10
Wang, C.	TH2I1
Wang, D.Y.	TU2C4
Wang, P.P.	FR2I1
Watanabe, T.	M04I1
Watanabe, Y.	M04I1
Weber, J.	FR1C2
Weber, L.	TUP11
Wei, J.	M04I2, WE1I3
Willeke, F.J.	FR1I1
Winnefeld, T.	TUP03
Wu, K.C.	TU2C4
Wu, Q.	FR2I1

Wunderlich, S. TUP04

— X —

Xia, J.W.	WE2I2
Xiao, G.Q.	WE2I2
Xie, H.M.	TH2C4
Xu, H.S.	WE2I2
Xu, T.	WE1I3
Xu, T.	TH1C3

— Y —

Yamada, K.	M04I1
Yang, J.C.	WE2I2
Yang, Y.	M03I1
Yaramyshev, S.	TH1C4, TH3C2, TH3C3, TH4C3

Yuan, Y.J. WE2I2

— Z —

Zhan, W.-L.	WE2I2
Zhang, C.	TUP04, TUP07
Zhang, T.	WE1I3
Zhang, T.J.	TH2I1
Zhang, Y.	TH2C4
Zhao, H.W.	WE2I2, FR2I1
Zhao, Q.	M04I2, WE1I3
Zhao, S.	WE1I3, TH1C3
Zhou, X.H.	WE2I2
Zipfel, B.	TUP03

Institutes List

ANL

Lemont, Illinois, USA

- Back, B.
- Blomberg, B.R.
- Bunnell, K.J.
- Clark, J.A.
- Dickerson, C.
- Dunn, G.M.
- Hendricks, M.R.
- Kedzie, M.
- Kelly, M.P.
- Letcher, E.
- Martinez Marin, J.L.
- Meyer, D.A.
- Momozaki, Y.
- Mustapha, B.
- Nassiri, A.
- Nolen, J.A.
- Peters, C.E.
- Petersen, T.B.
- Reid, T.
- Reyna, J.
- Savard, G.
- Scott, R.H.
- Song, J.
- Stanton, D.
- Vondrasek, R.C.
- Weber, L.
- Yang, Y.

BEVATECH

Frankfurt, Germany

- Hähnel, H.
- Höltermann, H.
- Koubek, B.
- Ratzinger, U.

BNL

Upton, New York, USA

- Willeke, F.J.

BNU

Haidian District Beijing, People's Republic of China

- He, J.J.

CAS

Beijing, People's Republic of China

- Zhan, W.-L.

CERN

Meyrin, Switzerland

- Kowalska, M.
- Vretenar, M.

CIAE

Beijing, People's Republic of China

- Chen, L.H.
- Cui, B.Q.
- Guo, B.
- Li, J.H.

- Lian, G.
- Liu, W.P.
- Wang, C.
- Zhang, T.J.

CNAO Foundation

Pavia, Italy

- Maugeri, C.
- Russo, F.

Cyclotron ARRONAX

Saint-Herblain, France

- Bellamy, R.
- Castel, C.
- Durand, T.
- Haddad, F.
- Koumeir, C.
- Poirier, F.
- Trichet, H.

FRIB

East Lansing, Michigan, USA

- Bernal, E.
- Bultman, N.K.
- Casagrande, F.
- Chang, W.
- Daykin, E.
- Fukushima, K.
- Gonzalez, A.J.
- Gutierrez, E.
- Hartung, W.
- Hwang, K.
- Ikegami, M.
- Kanemura, T.
- Kim, S.H.
- Kunjir, S.R.
- Larter, T.L.
- Lidia, S.M.
- Machicoane, G.
- Madendorp, R.
- Marti, F.
- Maruta, T.
- Momozaki, Y.
- Morris, D.G.
- Nolen, J.A.
- Ostroumov, P.N.
- Plastun, A.S.
- Popielarski, J.T.
- Ren, H.T.
- Taylor, A.
- Wei, J.
- Xu, T.
- Zhang, T.
- Zhao, Q.
- Zhao, S.

GANIL

Caen, France

- Anger, P.
- Franberg Delahaye, H.

- Jamet, C.
- Moscatello, M.H.
- Savajols, H.
- Varenne, F.

GSI

Darmstadt, Germany

- Andelkovic, Z.
- Aulenbacher, K.
- Aumüller, S.
- BalSS, R.
- Barth, W.A.
- Basten, M.
- Bender, M.
- Bozyk, L.H.J.
- Burandt, C.
- Dziuba, F.D.
- Fedotova, S.
- Forck, P.
- Geithner, W.
- Gerhard, P.
- Gettmann, V.
- Heilmann, M.
- Herfurth, F.
- Hess, R.
- Joseph, R.
- Klingbeil, H.
- Kraus, I.
- Kürzeder, T.
- Laier, U.
- Lauber, S.
- Lens, D.E.M.
- List, J.
- Litvinov, S.A.
- Lorentz, B.
- Maier, M.T.
- Miski-Oglu, M.
- Popp, U.
- Reiter, A.
- Rubin, A.
- Scheeler, U.
- Schmidt, J.S.
- Schnase, A.
- Singh, R.
- Spiller, P.J.
- Steck, M.
- Thomin, K.G.
- Trautmann, C.
- Velthaus, V.
- Vormann, H.
- Vorobyev, G.
- Vossberg, M.
- Winnefeld, T.
- Wunderlich, S.
- Yaramyshev, S.
- Zhang, C.
- Zipfel, B.

HBH Microwave GmbH

Stutensee, Germany

- Beyer, M.

HFHF

Frankfurt am Main, Germany

- Podlech, H.

HIM

Mainz, Germany

- Aulenbacher, K.
- Barth, W.A.
- Basten, M.
- Burandt, C.
- Dziuba, F.D.
- Gettmann, V.
- Kürzeder, T.
- Lauber, S.
- List, J.
- Miski-Oglu, M.
- Yaramyshev, S.

IAP

Frankfurt am Main, Germany

- Ateş, A.
- Conrad, T.
- Droba, M.
- Hähnel, H.
- Koser, D.
- Podlech, H.
- Ratzinger, U.
- Schwarz, M.
- Wagner, S.R.

IBA

Louvain-la-Neuve, Belgium

- D'Agostino, G.
- Kleeven, W.J.G.M.

IBS

Daejeon, Republic of Korea

- Hyun, M.O.

IKF

Frankfurt am Main, Germany

- Stallkamp, N.S.

IKP

Mainz, Germany

- Aulenbacher, K.

IMP/CAS

Lanzhou, People's Republic of China

- Hu, X.J.
- Jia, H.
- Li, J.Q.
- Li, Z.X.
- Liu, J.L.
- Liu, S.H.
- Liu, Y.G.
- Sun, L.T.
- Tang, X.D.
- Wang, P.P.
- Wu, Q.
- Xia, J.W.
- Xiao, G.Q.
- Xie, H.M.
- Xu, H.S.
- Yang, J.C.

- Yuan, Y.J.
- Zhang, Y.
- Zhao, H.W.
- Zhou, X.H.

INFN-Bologna

Bologna, Italy

- Malferrari, L.
- Odorici, F.

INFN-Pavia

Pavia, Italy

- Costanzo, G.

INFN/LASA

Segrate (MI), Italy

- Rossi, L.

INFN/LNL

Legnaro (PD), Italy

- Bellan, L.
- Comunian, M.
- Ferrari, L.
- Palmieri, A.
- Pisent, A.
- Roncolato, C.R.

INFN/LNS

Catania, Italy

- Aurnia, S.
- Caruso, A.C.
- Castro, G.
- Celona, L.
- Chines, F.
- De Luca, G.
- Gammino, S.
- Leonardi, O.
- Longhitano, A.
- Massara, A.
- Neri, L.
- Passarello, S.
- Reitano, R.
- Siliato, D.
- Spartà, A.

IPHC

Strasbourg Cedex 2, France

- Adam, T.
- Bouquerel, E.
- Graehling, P.G.
- Heine, M.
- Maazouzi, C.
- Osswald, F.R.

JINR/FLNR

Moscow region, Russia

- Fomichev, A.S.
- Gorshkov, A.V.
- Krupko, S.A.
- Ter-Akopian, G.M.

KPH

Mainz, Germany

- Aulenbacher, K.
- Barth, W.A.
- Dziuba, F.D.
- Lauber, S.
- List, J.

LLR

Palaiseau, France

- Thiebaut, C.
- Verderi, M.

LMU

Garching, Germany

- Schreiber, J.

LP Electronics di Platania Luca

Pedara, CT, Italy

- Platania, L.

LP2I

Gradignan, France

- Daudin, L.
- Husson, A.A.
- Lachacinski, B.
- Michaud, J.

LPSC

Grenoble Cedex, France

- Angot, J.
- Baylac, M.A.
- Cheymol, B.
- Dauvergne, D.
- Gallin-Martel, M.-L.
- Migliore, M.
- Molle, R.
- Peaucelle, C.
- Thuillier, T.

MPI-K

Heidelberg, Germany

- Blaum, K.

MSU

East Lansing, Michigan, USA

- LaVere, M.J.

NEC

Middleton, Wisconsin, USA

- Ratz, J.E.

Northern Illinois University

DeKalb, Illinois, USA

- Grabenhofer, A.F.

NTG Neue Technologien GmbH & Co KG

Gelnhausen, Germany

- Bechtold, A.

PARTREC

Groningen, The Netherlands

- Barazzuol, L.
- Both, S.
- Brandenburg, S.

- Coppes, R.P.
- Dendooven, P.G.
- Gerbershagen, A.
- Jones, B.N.
- Schippers, J.M.
- Van Der Graaf, E.R.
- van Goethem, M.-J.
- Van Lwijk, P.

Pfeiffer Vacuum GmbH

Aslar, Germany
 ▪ Hannweg, A.

RadiaBeam

Los Angeles, California, USA
 ▪ Agustsson, R.B.
 ▪ Araujo, A.
 ▪ Kutsaev, S.V.
 ▪ Smirnov, A.Yu.

Research School of Physics and Engineering, Australian National University

Canberra, Australian Capitol Territory, Australia
 ▪ Battisson, S.T.
 ▪ Cooper, A.
 ▪ Heighway, J.K.
 ▪ Hinde, D.J.
 ▪ Kafer, C.
 ▪ Kitchen, T.
 ▪ Linardakis, P.
 ▪ Lobanov, N.R.
 ▪ Notthoff, C.
 ▪ Tempra, T.
 ▪ Tranter, B.
 ▪ Tranter, R.
 ▪ Tunngley, T.B.

Riga Technical University

Riga, Latvia
 ▪ Torims, T.

RIKEN

Saitama, Japan
 ▪ Adachi, T.
 ▪ Miyake, Y.M.

RIKEN Nishina Center

Wako, Japan
 ▪ Dantsuka, T.
 ▪ Fujii, H.
 ▪ Fujimaki, M.
 ▪ Fukunishi, N.
 ▪ Hasebe, H.
 ▪ Higurashi, Y.
 ▪ Imao, H.
 ▪ Kamigaito, O.
 ▪ Kidera, M.
 ▪ Komiyama, M.
 ▪ Kumagai, K.
 ▪ Maie, T.
 ▪ Nagatomo, T.
 ▪ Nakagawa, T.
 ▪ Nakamura, M.

- Nishi, T.
- Ohnishi, J.
- Okuno, H.
- Ozeki, K.
- Sakamoto, N.
- Suda, K.
- Uchiyama, A.
- Watanabe, T.
- Watanabe, Y.
- Yamada, K.

SEEIIST

Geneva, Switzerland
 ▪ Benedetto, E.

SIGMAPHI S.A.

Vannes, France
 ▪ Beeckman, W.
 ▪ Forest, F.
 ▪ Tasset-Maye, O.
 ▪ Voisin, E.J.

STFC/RAL/ISIS

Chilton, Didcot, Oxon, United Kingdom
 ▪ Tarvainen, O.A.

SUBATECH

Nantes, France
 ▪ Haddad, F.

TEMF, TU Darmstadt

Darmstadt, Germany
 ▪ Klingbeil, H.

TRIUMF

Vancouver, Canada
 ▪ Ames, F.
 ▪ Andres, A.
 ▪ Baartman, R.A.
 ▪ Bagri, H.
 ▪ Ezawa, K.
 ▪ Fedorko, W.
 ▪ Jung, P.M.
 ▪ Kester, O.K.
 ▪ Kiy, S.
 ▪ Lucow, K.E.
 ▪ Nasser, J.
 ▪ Planche, T.
 ▪ Radel, S.D.
 ▪ Schultz, B.E.
 ▪ Shelbaya, O.
 ▪ Stringer, B.
 ▪ Thomson, D.C.
 ▪ Wang, D.Y.
 ▪ Wu, K.C.

TRUMPF Huettinger GmbH

Freiburg, Germany
 ▪ Heilig, R.
 ▪ Hollmann, D.
 ▪ Lau, M.
 ▪ Schweizer, M.
 ▪ Weber, J.

UCAS

Beijing, People's Republic of China

- Sun, L.T.

Università degli Studi di Catania

Catania, Italy

- Reitano, R.

Université Paris-Saclay, CNRS/IN2P3, IJCLab

Orsay, France

- Bambade, P.
- Ben Abdillah, S.M.
- Delerue, N.
- Guler, H.

UVIC

Victoria, Canada

- Adegun, J.A.

UW-Madison/SRC

Madison, Wisconsin, USA

- Bosch, R.A.

VECC

Kolkata, India

- Bandyopadhyay, A.
- Bandyopadhyay, S.
- Bhattacharya, S.
- Bhattacharyya, P.
- Bhattacharyya, T.
- Bhunia, U.
- Chaddha, N.
- Debnath, J.
- Dey, M.K.
- Dutta Gupta, A.
- Ghosh, S.
- Mandal, A.
- Nabhiraj, P.Y.
- Nandi, C.
- Naser, Z.A.
- Pal, S.
- Panda, U.
- Pradhan, J.
- Roy, A.
- Saha, S.
- Seth, S.
- Som, S.
- Thakur, S.K.

Participants List

— A —

Açksöz, Sevim

Adonin, Aleksey
GSI, Germany

Ali, Rahbar
Gandhi Faiz-e-Aam College,
Shahjahanpur, India

Ames, Friedhelm
TRIUMF, Canada

Andelkovic, Zoran
GSI, Germany

Andreev, Aleksandr
GSI, Germany

Anger, Pascal
CEA/GANIL, France

Angot, Julien
CNRS/LPSC-IN2P3, France

Aumüller, Simone
GSI, Germany

— B —

Bahng, Jungbae
Korea Univesity, South Korea

Barth, Winfried
GSI/HIM/JGU, Germany

Beeckman, William
Sigmaphi, France

Beike, Pascal
Aurion Anlagentechnik
Germany

Benedetto, Elena
SEEHST Association
Switzerland

Berezov, Rustam
GSI, Germany

Birli, Larissa
GSI, Germany

Blaurock, Jörg
GSI, Germany

Block, Michael
GSI, Germany

Blomberg, Ben
ANL, USA

Bozyk, Lars
GSI, Germany

Budelmann, Dirk
Pfeiffer Vacuum, Germany

— C —

Caruso, Antonino
INFN-LNS, Italy

Castro, Giuseppe
INFN-LNS, Italy

Cee, Rainer
HIT, Germany

Celona, Luigi
INFN-LNS, Italy

Conrad, Thorsten
IAP, Germany

— D —

D'Agostino, Grazia
Ion Beam Applications
Belgium

Durand, Teddy
GIP ARRONAX/Subatech
France

— F —

Fork, Peter
GSI, Germany

Franberg Delahaye, Hanna
CEA/GANIL, France

— G —

Geitner, Wolfgang
GSI, Germany

Gerhard, Peter
GSI, Germany

Gonzalez, Alec
FRIB, MSU, USA

Groening, Lars
GSI, Germany

Groß, Kerstin
GSI, Germany

— H —

Hähnel, Hendrik
IAP, Germany

Hannweg, Andre
Pfeiffer Vacuum, Germany

He, Yuan
IMP, China

Herfurth, Frank
GSI, Germany

Hollinger, Ralph
GSI, Germany

Hyun, Myung Ook
RISP/IBS, South Kora

— J —

Jones, Brian
UMCG-PARTREC
The Netherlands

— K —

Kamigaito, Osamu
RIKEN, Japan

Kanemura, Takuji
MSU, USA

Kester, Oliver
TRIUMF,

Kiba Bassandi, Romain
A A S E, Congo

Kikuati Ntotila, Claude
I.S.I.P.A., Congo

Kıçgedik, Atacan
Marmara University, Türkiye

Kiy, Spencer
TRIUMF, Canada

Klingbeil, Harald
TU Darmstadt/GSI, Germany

Kowalska, Magdalena
CERN, Switzerland

Kumar Prajapat, Rinku
IIT Roorkee, India

— **L** —

Laier, Ulrich
GSI, Germany

Lau, Marcus
TRUMPF Hüttinger, Germany

Lauber, Simon
GSI/HIM, Germany

Leitner, Daniela
LBNL, USA

Lens, Dieter
GSI, Germany

Lindenberg, Paola
GSI, Germany

Longhitano, Alberto
INFN LNS, Italy

— **M** —

Maimone, Fabio
GSI, Germany

Martinez-Marin, Jose L
ANL, USA

Müller, Raphael
GSI, Germany

Mustapha, Brahim
ANL, USA

— **N** —

Navitski, Alexander
Research Instruments, Germany

Nikitovic, Lazar

Notthoff, Christian
The Australian National
University, Australia

— **O** —

Oswald, Francis
CNRS/IN2P3/IPHC, France

Ostroumov, Peter
MSU, USA

— **P** —

Palmieri, Antonio
INFN-LNL, Italy

Peters, Andreas
HIT, Germany

Petit-Jean-Genaz, Christine
CERN, Switzerland

Platow, Wilhelm
Axcelis Technologies, USA

Podlech, Holger
IAP, Germany

Poirier, Freddy
Arronax/CNRS, France

— **Q** —

Qian, Cheng
Jindai Physics Institute, China

— **R** —

Rossi, Lucio
Università degli Studi di Milano,
INFN-Milano, LASA Llab, Italy

Reimann, Stephan
GSI, Germany

— **S** —

Savard, Guy
ANL, USA

Schaa, Volker RW
GSI, Germany

Scheeler, Uwe
GSI, Germany

Schmidt, Janet
GSI, Germany

Schreiber, Jörg
LMU Munich, Germany

Schwemmer, Harald
AXON Kabel, Germany

Schreiber, Jörg
LMU Munich, Germany

Schütt, Petra
GSI, Germany

Schwickert, Marcus
GSI, Germany

Singh, Rahul
GSI, Germany

Siwach, Surender
Banaras Hindu University, India

Som, Sumit
VECC, India

Spiller, Peter
GSI, Germany

Steck, Markus
GSI, Germany

Sun, Liangting
IMP, CAS, China

— **T** —

Teja, Cadez Sirca
Instrumentation Technologies
Slovenia

Tinta, Dejan
Instrumentation Technologies
Slovenia

Torims, Toms
Riga Technical University
Latvia

Tschunke, Wolfgang
CPI, Germany

— **V** —

Velthaus, Verena
GSI, Germany

Vormann, Hartmut
GSI, Germany

Content from this work may be used under the terms of the CC BY 4.0 licence (© 2022). Any distribution of this work must maintain attribution to the author(s), title of the work, publisher, and DOI

— W —

Wagner, Stephan
IAP, Germany

Weinrich, Udo
GSI, Germany

Willeke, Ferdinand
BNL, USA

Wunderlich, Stefan
GSI, Germany

— Y —

Yang, Jiancheng
IMP, China

— Z —

Zhai, Yuhan
IMP, China

Zhang, Chuan
GSI, Germany

Zhang, Yong
IMP, China

Zhao, Shen
FRIB/MSU, USA

Zhou, Bowen
GSI, Germany

Zweibäumer, Lucas
Research Instruments
Germany